Title
Development of a Chilean Ground Motion Database for the NGA-Subduction Project

Author
Contreras, Victor

Publication Date
2017

Peer reviewed|Thesis/dissertation

UNIVERSITY OF CALIFORNIA

Los Angeles

Development of a Chilean Ground Motion Database for the NGA-Subduction Project

A thesis submitted in partial satisfaction

of the requirements for the degree of Master of Science

in Civil Engineering

by

Víctor Contreras

2017

ABSTRACT OF THE THESIS

Development of a Chilean Ground Motion Database

for the NGA-Subduction Project

by

Víctor Contreras

Master of Science in Civil Engineering

University of California, Los Angeles, 2017

Professor Jonathan Paul Stewart, Chair

The Next-Generation Attenuation (NGA) projects provide uniformly-processed ground motion data from earthquakes recorded in different tectonic settings and regions around the world. Since 2008, three separate NGA projects have been developed: NGA-West and NGA-West2 for shallow crustal earthquakes in active tectonic regions like California; and NGA-East for stable continental regions like central and eastern North America. Currently, the NGA-Subduction project is under development, focusing on gathering data for regions affected by subduction-zone earthquakes like the Pacific Northwest (PNW) and Alaska regions of North America, Japan, Taiwan, Mexico, and South America, among other areas.

As part of the effort of assembling and characterizing the ground motion dataset for South America, this thesis describes the development of a Chilean ground motion database for the NGA-Subduction project. First, the tectonics and seismicity of South America are discussed to highlight the importance of these subduction-zone earthquakes, with a particular emphasis on Chilean events. Subsequently, an overview of the seismic data providers in Chile is presented, describing the evolution of the different institutions and seismic networks that have recorded ground motions in the country. In addition, prior works on ground motion datasets and ground motion modeling for South America and Chile are introduced and briefly described. The importance of regional considerations in the development of global models, particularly with respect to path terms, is emphasized by comparing attenuation features observed in past work on the 2010 **M** 8.8 Maule Chile and **M** 9.0 Tohoku Japan events.

A significant effort was made to collect and characterize required metadata to accompany the ground motion database, including source, path, and site information. This thesis is primarily focused on presenting the development of parameters describing seismic sources. To date, the NGA-Subduction event catalog for the South American region consists of 826 earthquakes that extend from 1985 to 2016, 689 of which have been recorded in Chilean territory. The moment magnitude ranges from **M** 2.5 to **M** 8.8. In terms of number of recordings, the data obtained in Chile (4,213 time histories) represents approximately 68% of the total dataset in South America. The event database is controlled by interface and instraslab earthquakes, having 404 and 223 events respectively, with considerably fewer shallow crustal and outer-rise events. When possible, seismic sources are defined using suitable finite fault models (FFM) from the literature. Processes are introduced here to interpret published FFMs in a way that the most salient portion of the fault plane is used for site-to-source distance calculations. These processes improve upon those that had

been used previously and have been adopted elsewhere in the NGA-Subduction project (e.g., Japan). In the case of the events without available FFMs, source characterization is similar to that used previously in NGA-projects.

Path and site parameters are currently being characterized and preliminary results are briefly explained in the final chapter. The results presented in this thesis regarding source information, along with the results from path and site characterization, will be part of a data PEER report describing the Chilean dataset.

The thesis of Víctor Contreras is approved.

Scott J. Brandenberg

Robert E. Kayen

Yousef Bozorgnia

Jonathan P. Stewart, Committee Chair

University of California, Los Angeles

2017

TABLE OF CONTENTS

LIST OF FIGURES

LIST OF TABLES

LIST OF EQUATIONS

ACKNOWLEDGMENTS

First, I would like to acknowledge the Chilean National Commission for Scientific and Technological Research (CONICYT) for the financial support through the CONICYT-Becas Chile program and for giving me the opportunity to pursue graduate level education at UCLA.

I would also like to thank CSN and RENADIC, both at the University of Chile, for providing the strong motion data and the information regarding the strong motion stations, especially to Professors Fabián Rojas and Rubén Boroschek for transferring the raw data from RENADIC to UCLA. I am also grateful to FUCHIGE (*Fundación Chilena de Geotecnia*) for providing various geotechnical data and reports for several stations, and to Francisco Ruz for providing numerous unpublished V_S profiles.

I am grateful to Tadahiro Kishida at UC Berkeley for overseeing the signal processing of the Chilean ground motion recordings according to PEER's standard processing methods. I would also like to thank the earthquake source working group including Bob Darragh, Tadahiro Kishida, Bob Youngs, and Jonathan Stewart for numerous meetings and for their help with the review of the seismic sources in Chile, and especially thanks to Bob Darragh (Pacific Engineering and Analysis) for reviewing the seismic source characteristics in Latin America.

A special thank you to my advisor, Jonathan P. Stewart, who has provided much time and guidance throughout my M.S. work, offering suggestions on coursework and research, and advice during the preparation of this thesis. I would also like to express my gratitude to the other members serving on my committee: Scott Brandenberg, for his helpful comments and advice; Robert Kayen, for his advice and providing geophysical fieldwork data for Chilean stations; and Yousef Bozorgnia, for

his advice and suggestions during the development of the NGA-Subduction project. I would also like to thank all of them for sharing their knowledge and expertise while I was learning from them during their lectures.

I would like to thank my classmates for their friendship and their help during the course work, especially Bolun, Claudia, Guangze, Omar, Pengfei, and Xiangdong. My gratitude also goes to my officemates for all their technical help and friendship, especially to Sean Ahdi who helped me assemble the V_S profile database for Chile.

I would also like to thank my family for their support, especially to my parents, without whom none of this would have been possible. Finally, I would like to thank Carla, for all she has done to help me reach my goals. This would not have been possible without her support, love, sacrifices, and help.

1 INTRODUCTION

1.1 Tectonics and seismicity in South America and Chile

Chile is located in one of the most seismically active zones on Earth known as the Circum-Pacific region. This region is defined by subduction zone plate boundaries that are responsible for approximately 80% of earthquakes worldwide and have over 400 active volcanoes, as shown in Figure 1.1. Within this framework, the occurrence of earthquakes in western South America, including Chilean territory, is dominated by the subduction of the oceanic Nazca plate beneath the continental South American plate at rates of convergence ranging from 5.6 cm per year in Ecuador to 6.3 cm per year in northern Chile, according to GPS observations. This process generates more than 800 measured earthquakes every year in South America and has shaped the 5,900 km long Peru-Chile trench (IRIS, 2007). A schematic cross section in central Chile along parallel 33.7°S is shown in Figure 1.2 to illustrate the geometry and the main features of this subduction zone.

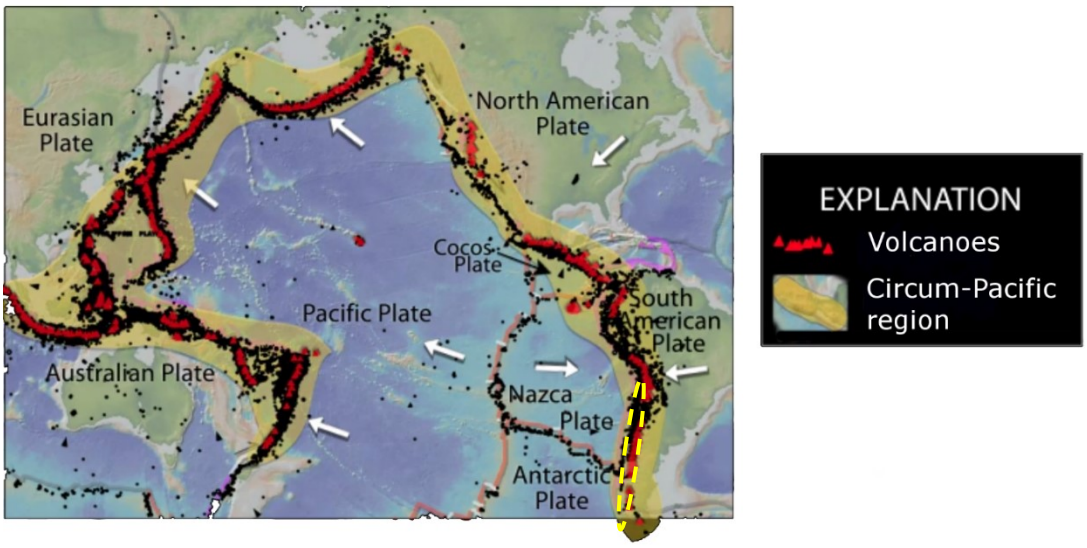

Figure 1.1 Map of the Circum-Pacific region showing the main tectonic plates and their relative movements (white arrows), distribution of the seismicity (black circles), and the position of volcanoes (red triangles). The yellow ellipse represents the approximate location of Chilean territory (modified from IRIS, 2017).

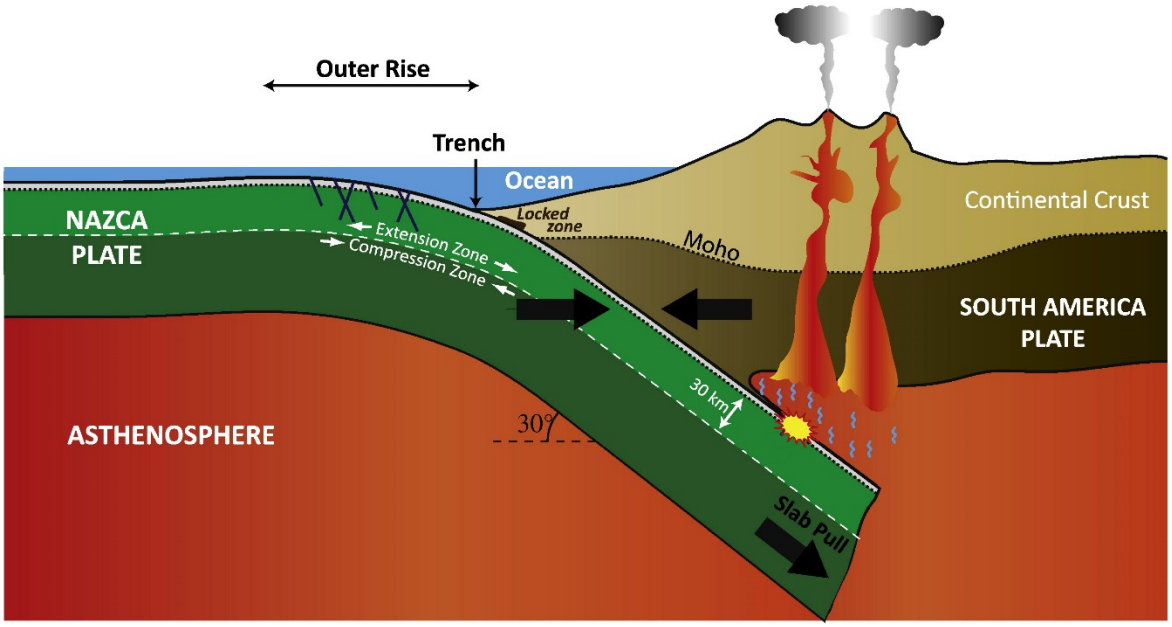

Figure 1.2 Schematic profile of the subduction zone along 33.7°S (modified from Marot et al. 2012).

To more closely examine the South American subduction zone, Figure 1.3(a) presents a map depicting the seismicity associated with earthquakes that occurred between 1900 and 2014 with magnitude 6.5 or larger, slab contours representing the depth of the Nazca plate, and the Peru-Chile trench along with the convergence rates at some specific areas. According to this information, the relative movement of the Nazca plate with respect to the continental plate reaches a rate of convergence of 7.4 cm per year in southern Chile (Wald, 2016). Figure 1.3(b) shows an overview map of the South American subduction zone with the location of significant earthquakes (**M** $\geq$ 7.5 only) from the 20th and 21st centuries. Bathymetry and convergence rate are also included, as well as the focal mechanisms for other moderate magnitude earthquakes.

A substantial number of the great magnitude 8.0 or larger earthquakes world-wide have occurred in western South America. Particularly, the Chilean subduction zone was the source of the largest earthquake ever recorded, the 1960 **M** 9.5 Valdivia megathrust earthquake, and has been very

active recently due to the occurrence of three large events: the 2010 **M** 8.8 Maule earthquake in central Chile, and the 2014 **M** 8.15 Iquique and 2015 **M** 8.31 Illapel earthquakes in northern Chile.

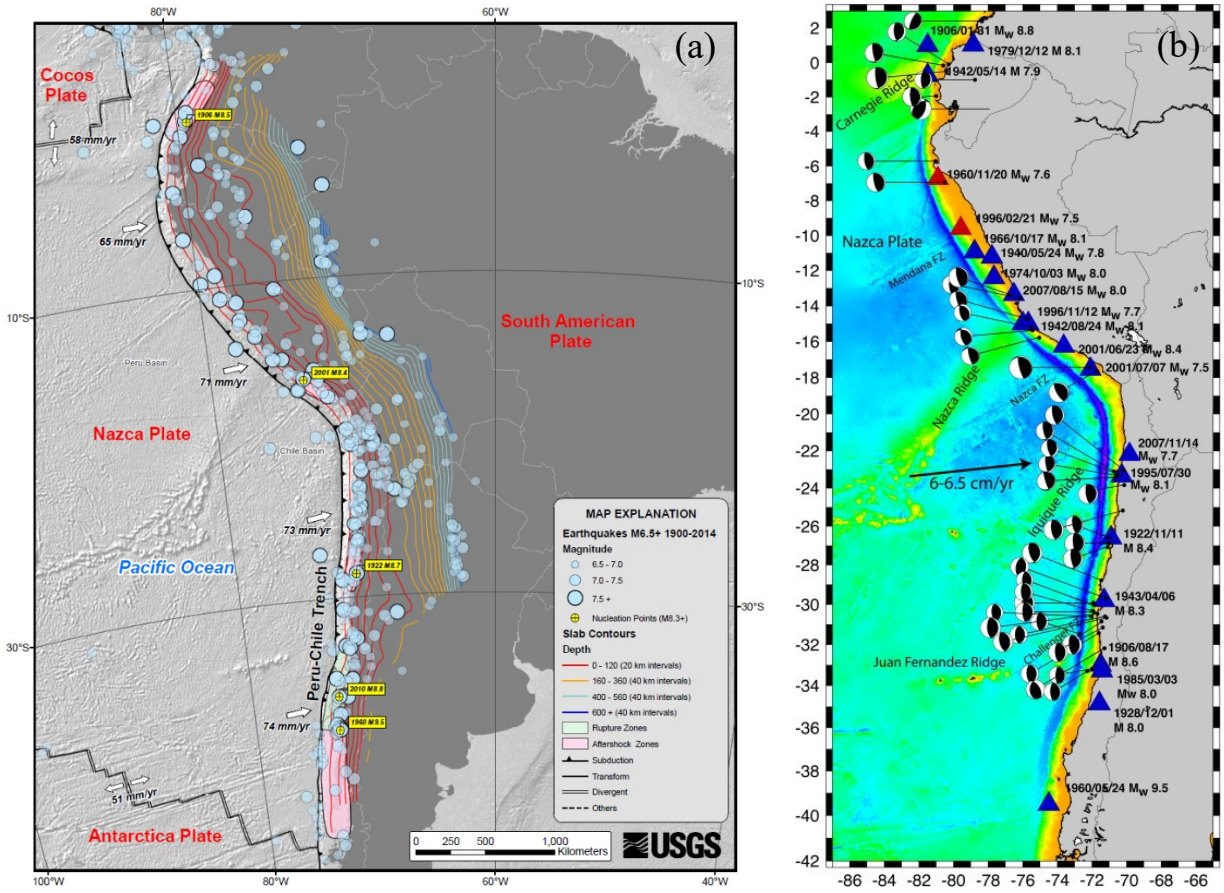

Figure 1.3 Map of the South America subduction zone: (a) Seismicity of **M**6.5+ earthquakes between 1900-2014 (circles), slab contours (color lines) and plate boundaries (Wald, 2016); (b) Significant earthquakes with magnitudes **M**7.5+ (triangles), bathymetry, and focal mechanisms of other moderate events (Bilek, 2010).

1.2 Overview of the NGA-Subduction project

The Next-Generation Attenuation (NGA) projects provide uniformly-processed ground motion data from earthquakes recorded in different tectonic settings and regions, including time series and intensity measure values, such as peak ground acceleration (*PGA*), peak ground velocity (*PGV*), pseudo spectral acceleration (*PSa*), Arias Intensity (I_A) and significant duration. The databases and

the corresponding documentation that result from these efforts are public and available on the Internet, freely allowing researchers and practitioners to access and use these resources continuously. Three separate NGA projects have been coordinated by the Pacific Earthquake Engineering Research Center (PEER):

a) NGA-West (Power et al., 2008) and NGA-West2 (Bozorgnia et al., 2014), for shallow crustal earthquakes in active tectonic regimes such as California, Japan, Turkey, Taiwan, and Italy, among other regions (information available at http://peer.berkeley.edu/ngawest and http://ngawest2.berkeley.edu).

b) NGA-East (Goulet et al., 2014), for stable continental regions like central and eastern North America, an important portion of Europe, South Africa, and others (information available at http://peer.berkeley.edu/ngaeast).

c) NGA-Subduction, for subduction-zone earthquakes in active tectonic regimes like the Pacific Northwest (PNW) region of North America, northern California and Alaska in the United States, Japan, Taiwan, Mexico, and South America, among other areas. This project is currently under development (Kishida et al., 2017; Ahdi et al., 2017).

More specifically, NGA-Subduction is a major multi-year international project in engineering seismology utilizing a multidisciplinary approach to develop database resources and ground motion models (GMMs) for subduction-zone earthquakes. As already mentioned, the project is coordinated by the PEER center and numerous partnering institutions, and is funded by the Factory Mutual Insurance Company (FM Global), the United States Geological Survey (USGS), and the California Department of Transportation (Caltrans). NGA-Subduction involves highly

collaborative research with extensive technical interaction and cooperation among many organizations and participants from different countries around the world.

The NGA-Subduction project database is currently under development. Figure 1.4(a) shows the hypocenters of earthquakes included in the database as of January 2017 along with the locations of the strong motion recording stations (additional events and stations have been added since that time). The magnitude-distance distribution of the recordings associated with these earthquakes is presented in Figure 1.4(b), with differentiation by region. The ground motion database includes the processed recordings and supporting source, path, and site metadata from Japan, Taiwan, the PNW and Alaska in the United States and Canada, and Central and South America (Kishida et al., 2017). Recently acquired data from New Zealand, Mexico, and Central America, that are not shown in the map, are currently being incorporated into the database in ongoing work.

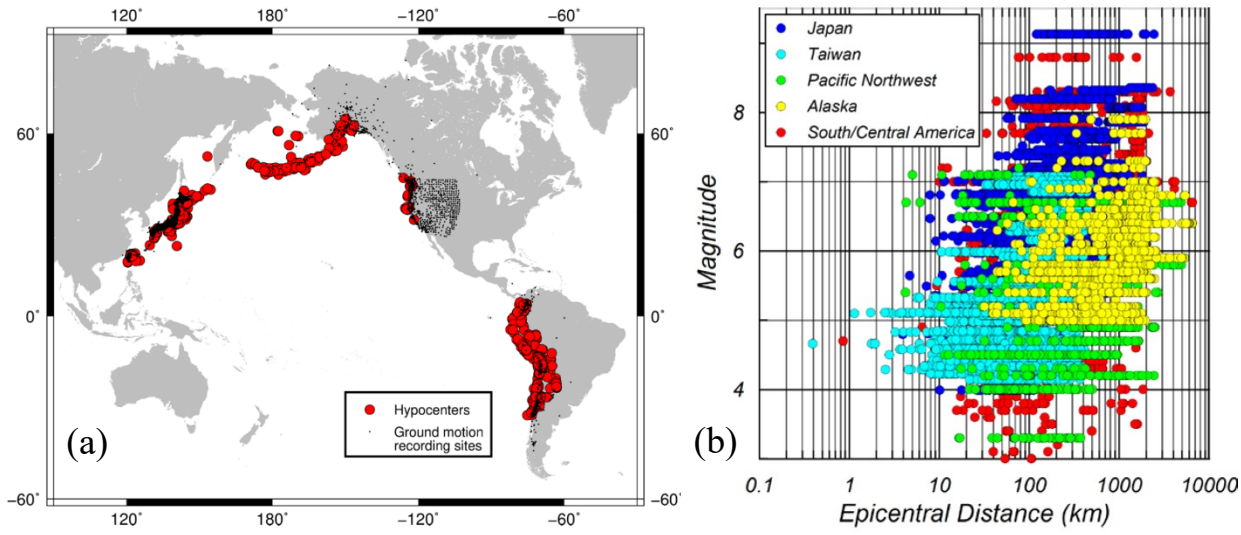

Figure 1.4 NGA-Subduction database: (a) Map showing the hypocenters of the earthquakes (red circles) and the locations of the strong motion recording stations (black dots); (b) Magnitude versus epicentral distance distribution with distinction by region (Kishida et al., 2017).

The main objective of this project is to define a new set of state-of-the-art global GMMs for subduction-zone earthquakes, with regional adjustments as appropriate for path and site terms. These GMMs will significantly improve upon current models which rely on much more limited data sets, mainly from moderate magnitude events. The NGA-Subduction approach aims to largely increase the considered recordings and therefore reduce the lack of information within certain magnitude-distance ranges and site conditions.

This project seeks to make the data catalogue as complete as possible, and as such the inclusion of seismic data from Chile is of utmost importance. In fact, given the high rate of seismicity and the major subduction earthquakes that have occurred in Chilean territory, including the 2010 **M** 8.8 Maule earthquake and other large-magnitude interface earthquakes that struck Chile in recent years (2014 **M** 8.15 Iquique and 2015 **M** 8.31 Illapel), the NGA-Subduction research program considers that Chilean participation is relevant for the success of the project.

2 REVIEW OF CHILEAN GROUND MOTION ARRAYS AND PREDICTION MODELS

2.1 Overview of Chilean seismic data providers

The University of Chile has operated and maintained strong motion arrays since 1968, when the Department of Geophysics, Seismology, and Geodesy began the installation of a network of instruments that could register future earthquakes in Chile (Husid, 1973). This first effort initiated the Central Chile Accelerograph Network that was operated later by the Department of Geophysics and Geodesy (DGG) and the Department of Civil Engineering (DIC) at the University of Chile. The locations of the strong motion recording (SMR) stations in this network, hereafter referred to as the DGG network, are shown in Figure 2.1. Despite the relatively limited number of recordings from this network (1% of the total of recordings collected in Chile), these data are relevant mainly because of the accelerograms recorded at 26 sites during the interface **M** 7.98 Valparaiso earthquake that occurred March 3, 1985. This earthquake is one of the first major subduction-zone events that was well recorded and studied, thanks to data acquired in locations with various geological conditions and at relatively close distances to the fault rupture plane, ranging from approximately 25 to 220 km. In addition, three important aftershocks to this event were also recorded by this network. The instruments are analog accelerographs (Kinemetrics model SMA-1 or similar) and the strong motion recordings are available at the Virtual Data Center of the Consortium of Organizations for Strong-Motion Observation Systems (COSMOS) at http://www.strongmotioncenter.org/vdc. Most of the DGG stations are no longer in operation.

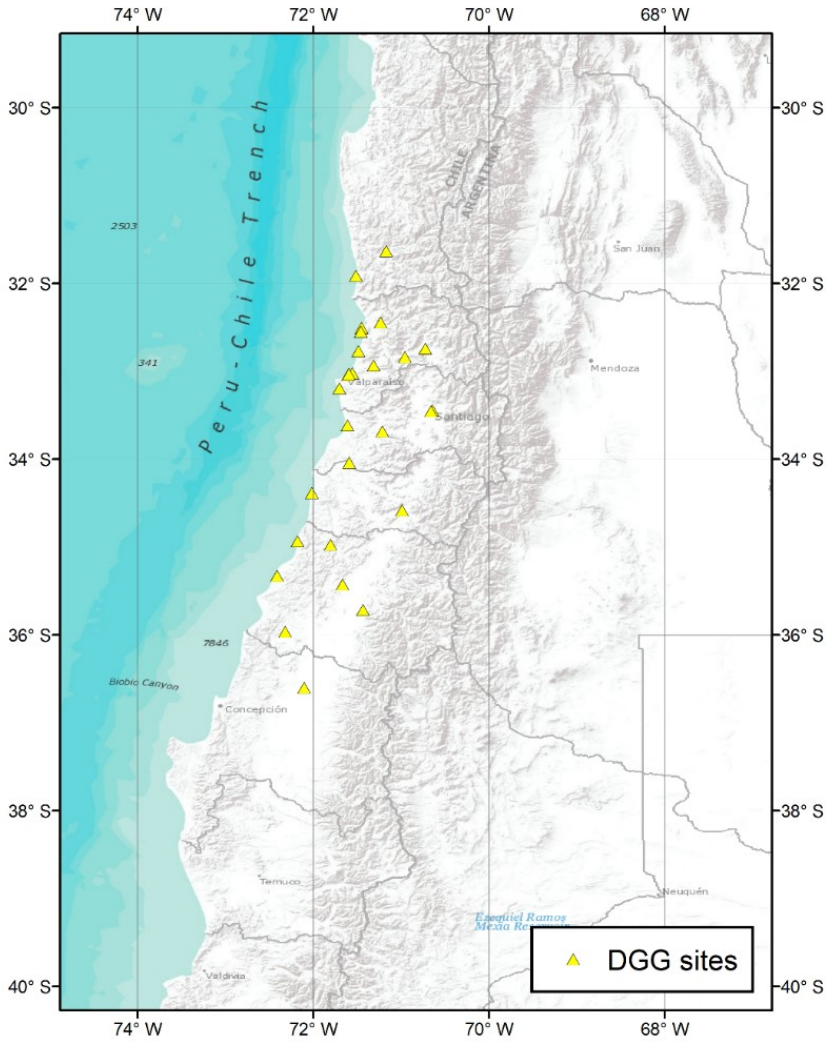

Figure 2.1 DGG network: 27 SMR stations.

After the 1985 Valparaiso earthquake, the DIC has continued operating and maintaining an accelerographic network called RENADIC (from its Spanish name *Red de cobertura Nacional de Acelerógrafos del DIC*), which includes 7 DGG stations that remain in operation and 55 new stations in northern and central Chile. The locations of the 62 SMR stations that are part of this network are shown in Figure 2.2. The instruments are both analog and digital accelerometers, and their recorded strong motion data are partially available from 1995 to 2010 at the RENADIC website http://www.renadic.cl, including the recordings of the 2010 **M** 8.8 Maule earthquake.

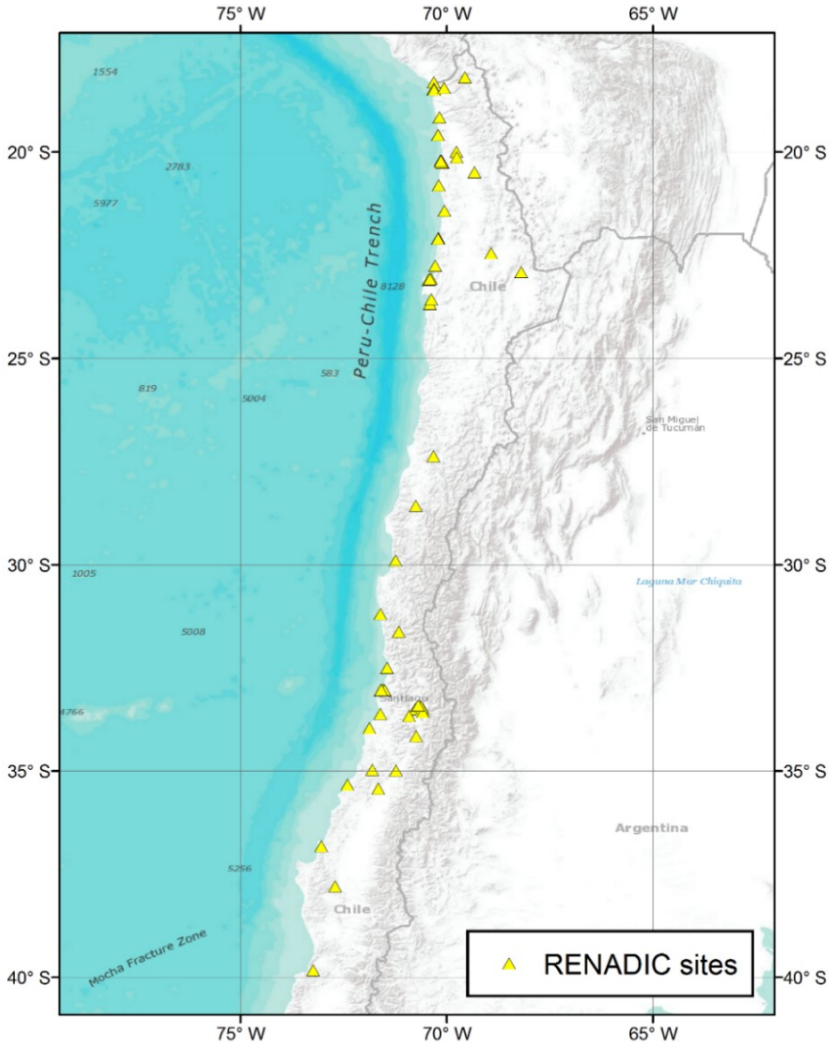

Figure 2.2 RENADIC network: 62 SMR stations.

As part of this research project, an agreement was reached between the DIC and NGA-Subduction to include additional recordings from the RENADIC network into the NGA-Subduction database, specifically the data recorded after 2010. The RENADIC network is presently operative and contributes almost 30% of the recordings in the Chilean database for the NGA-Subduction project.

Since 1991 the Department of Geophysics at the University of Chile (DGF) has operated the Chilean National Seismic Network, known as the C network, which consists of 55 stations located along the country, as shown in Figure 2.3.

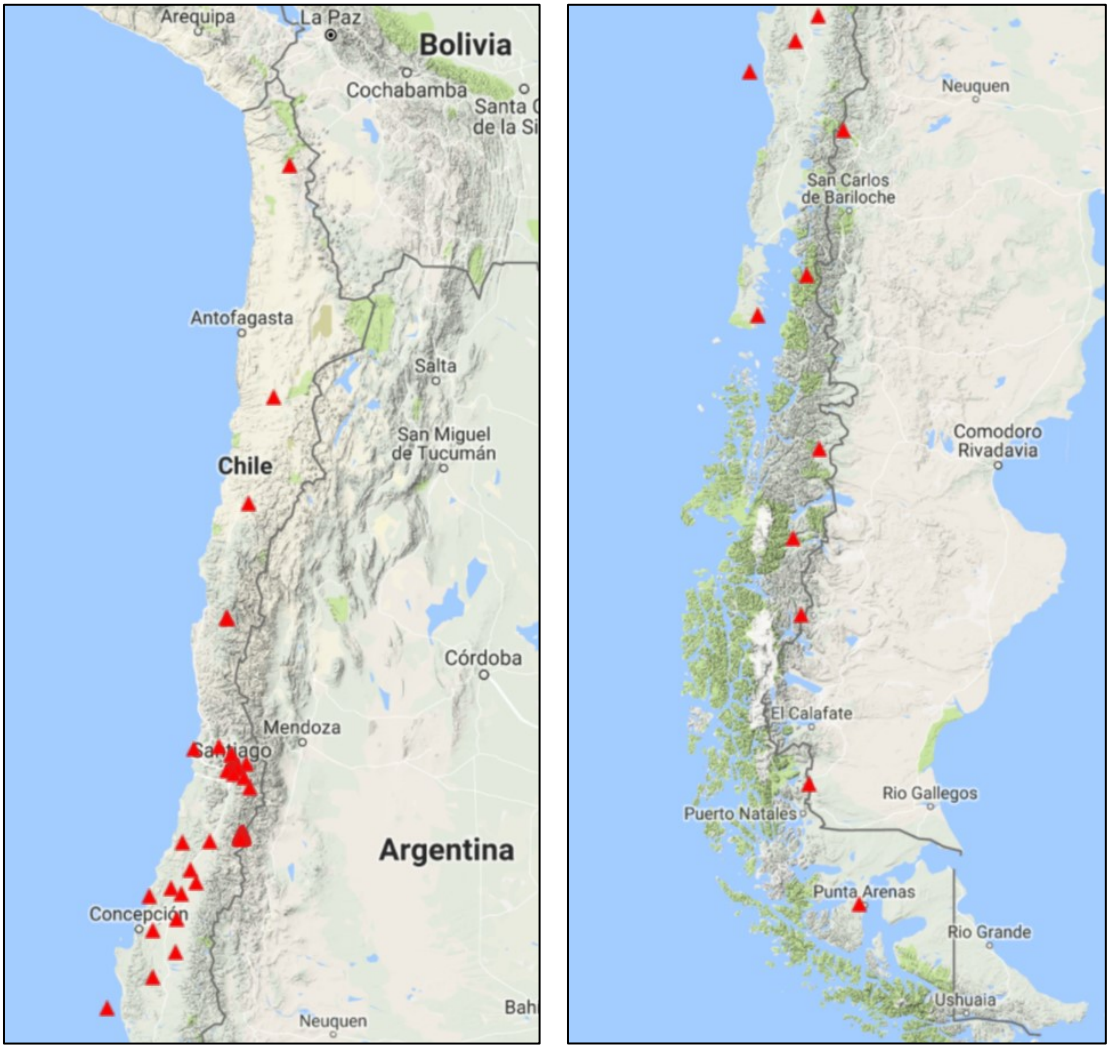

Figure 2.3 C network: 55 stations in total; 34 SMR stations with usable recordings (FDSN, 2017).

The instruments are digital accelerometers and broadband sensors, and the strong motion data are available from the IRIS Data Management Center (IRISDMC, 2017). Usable ground motion recordings were obtained only from 34 SMR stations due to the frequency range characteristics of

the instruments. The C network also recorded the 2010 **M** 8.8 Maule earthquake and is presently operative, contributing approximately 6% of the recordings in the Chilean database for the NGA-Subduction project.

Another important data provider is the IPOC seismic network, also known as the CX network, which is located in northern Chile from the Peru-Chile border south to the city of Antofagasta. This network is part of the Integrated Plate boundary Observatory Chile (IPOC), a European-Chilean collaboration effort that connects institutions and researchers studying earthquakes and crustal deformations in this zone. The CX network was created in 2006 by the German Research Centre for Geosciences, Potsdam, Germany (GFZ) and the *Institut des Sciences de l'Univers-Centre National de la Recherche* (CNRS-INSU), being jointly operated by the GFZ, the *Institut de Physique du Globe Paris* (IPGP), the Chilean National Seismological Center (CSN), the University of Chile (UdC) and the *Universidad Católica del Norte, Antofagasta, Chile* (UCNA).

The locations of the 25 stations in the CX network are shown in Figure 2.4. The instruments are digital accelerometers and broadband sensors, and the strong motion recordings are available from the IRIS Data Management Center (IRISDMC, 2017) and at the IPOC website http://www.ipoc-network.org. Usable ground motion data were obtained only from 20 SMR stations due to the frequency range characteristics of the instruments. The CX network is presently operative and contributes more than 28% of the recordings that are included in the Chilean database for the NGA-Subduction project.

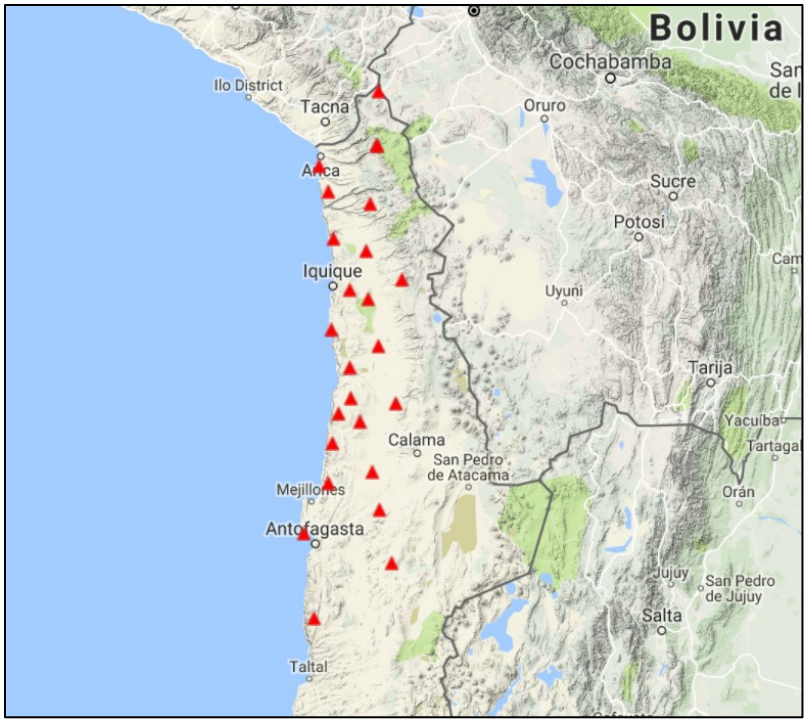

Figure 2.4 CX network: 25 stations in total; 20 SMR stations with usable recordings (FDSN, 2017).

After the 2010 Maule earthquake, due to the relatively limited number of broadband and strong motion recordings that were obtained during this event, and because of the clear importance of such data, the need of improving the quality and size of the Chilean seismic networks became evident. In December 2012, the National Emergency Office (ONEMI) signed an agreement with the University of Chile to form the National Seismological Center (CSN). The CSN replaces the previous agency, National Seismologic Service (SSN), and has the mission of monitoring seismic activity in the country and to rapidly characterize and disseminate seismic information (De la Llera et al., 2016). This agreement has incorporated new stations that constitute the C1 network.

The locations of the C1 network stations are shown in Figure 2.5. The instruments are digital accelerometers and broadband sensors, and the strong motion data are available at the CSN strong motion database site at http://evtdb.csn.uchile.cl. Usable ground motion recordings were obtained

only from 47 out of 71 stations due to the frequency range characteristics of the instruments. The C1 network has been operative since 2013 and contributes approximately 3% of the recordings in the Chilean database for the NGA-Subduction project.

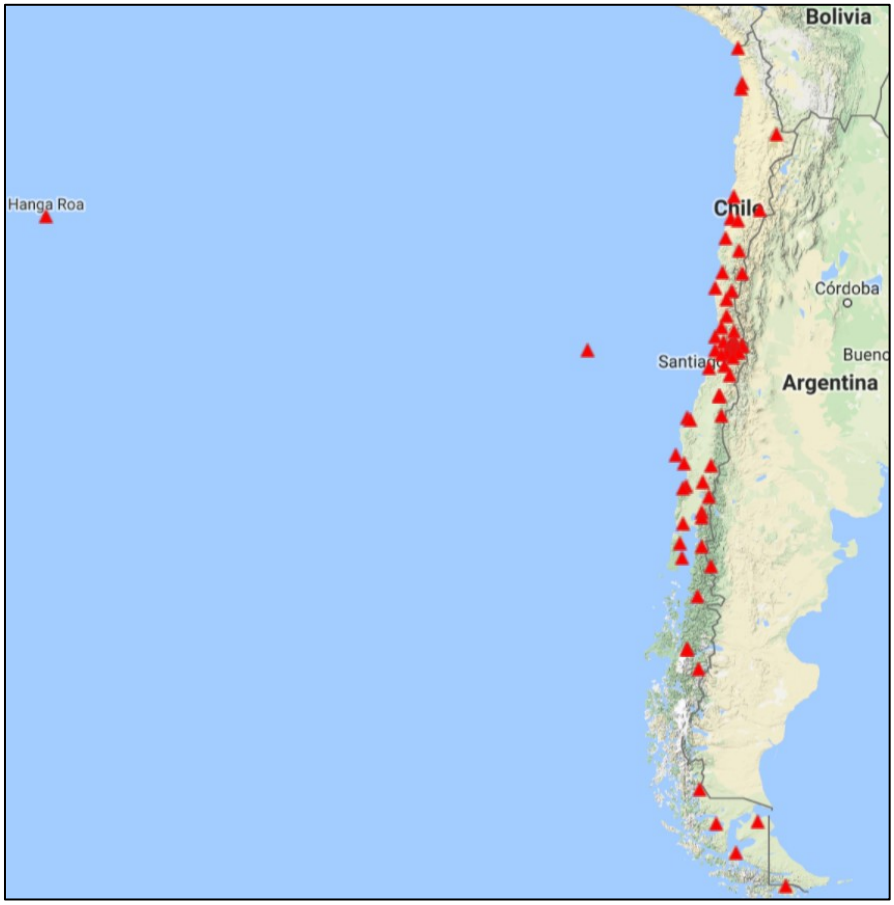

Figure 2.5 C1 network: 71 stations in total; 47 SMR stations with usable recordings (FDSN, 2017).

Additionally, the CSN-ONEMI agreement also considers the incorporation of the Accelerographic National Network with nearly 300 SMR stations, named RNA from its Spanish name *Red Nacional de Acelerógrafos*. These stations are being deployed as part of a large effort by the ONEMI and the Ministry of Housing and Urbanism (MINVU) in a variety of cities and site conditions across the country (Leyton et al., 2017). Figure 2.6 shows the locations of the 75 SMR stations that are currently part of the RNA network and contribute with recordings to the NGA-Subduction

database. The instruments are digital accelerometers and the strong motion data are also available at the CSN strong motion database site at http://evtdb.csn.uchile.cl. The RNA network has been operative since 2013 contributing approximately 23% of the recordings in the Chilean database for the NGA-Subduction project.

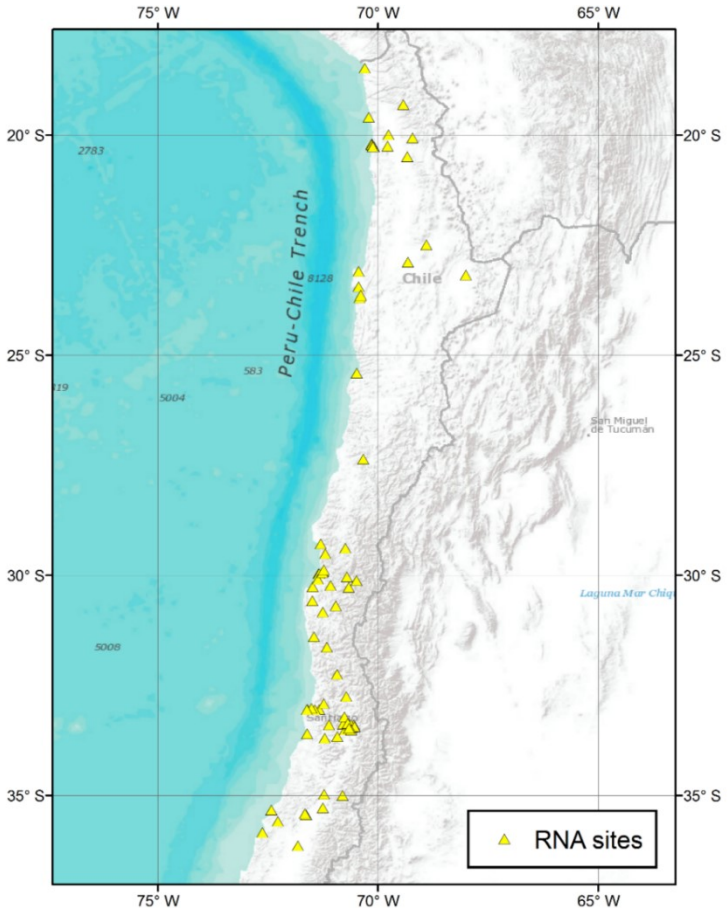

Figure 2.6 RNA network: 75 SMR stations.

As a result of the recent rapid growth of the Chilean seismic networks, currently the CSN assembles and distributes online the uncorrected strong motion recordings from the C, CX, C1 and RNA networks for earthquakes with magnitudes equal or greater than 4.0. The recordings obtained from all these networks provide useful information from moderate to large earthquakes that have

occurred recently in Chile (e.g., the 2014 **M** 8.15 Iquique and 2015 **M** 8.31 Illapel earthquakes, along with their aftershocks).

The networks that have been described in this section (DGG, RENADIC, C, CX, C1 and RNA) contribute approximately 90% of the recordings obtained in Chilean territory that are part of the NGA-Subduction database. Additionally, the following networks (most of them temporary) provide the remaining 10% of the data:

1. IU: Global Seismograph Network (GSN). Permanent network contributing approximately 3% of the recordings. Operated by the Albuquerque Seismological Laboratory since 1988.
2. XS: Maule Earthquake (Chile) Aftershock Experiment. Temporary network that contributes approximately 2% of the recordings. Operated by the *Reseau Sismologique et Géodésique Français* (RESIF) from 2010 to 2011.
3. XY: RAMP response for 2010 earthquake, Chile RAMP. Temporary network contributing approximately 2% of the recordings. Operated by the University of Florida in 2010.
4. Y9: Tocopilla. Temporary network that contributes approximately 1% of the recordings. Operated by the GEOFON Program (GFZ-Postdam, Germany) from 2007 to 2008.
5. YC: Slab Geometry in the Southern Andes. Temporary network that contributes approximately 1% of the recordings. Operated by IRIS/PASSCAL from 2000 to 2002.
6. ZA: PISCO94 PS. Temporary network contributing approximately 0.7% of the recordings. Operated by the GEOFON Program (GFZ-Postdam, Germany) in 1994.
7. XJ, YJ, ZW, G. Other networks contributing in total less than 1% of the data.

Figure 2.7 and Figure 2.8 show the locations of the stations for the listed networks IU, XS, XY, Y9, YC and ZA (FDSN, 2017). It is important to notice that not all the stations shown in these Figures provide strong motion recordings to the NGA-Subduction database.

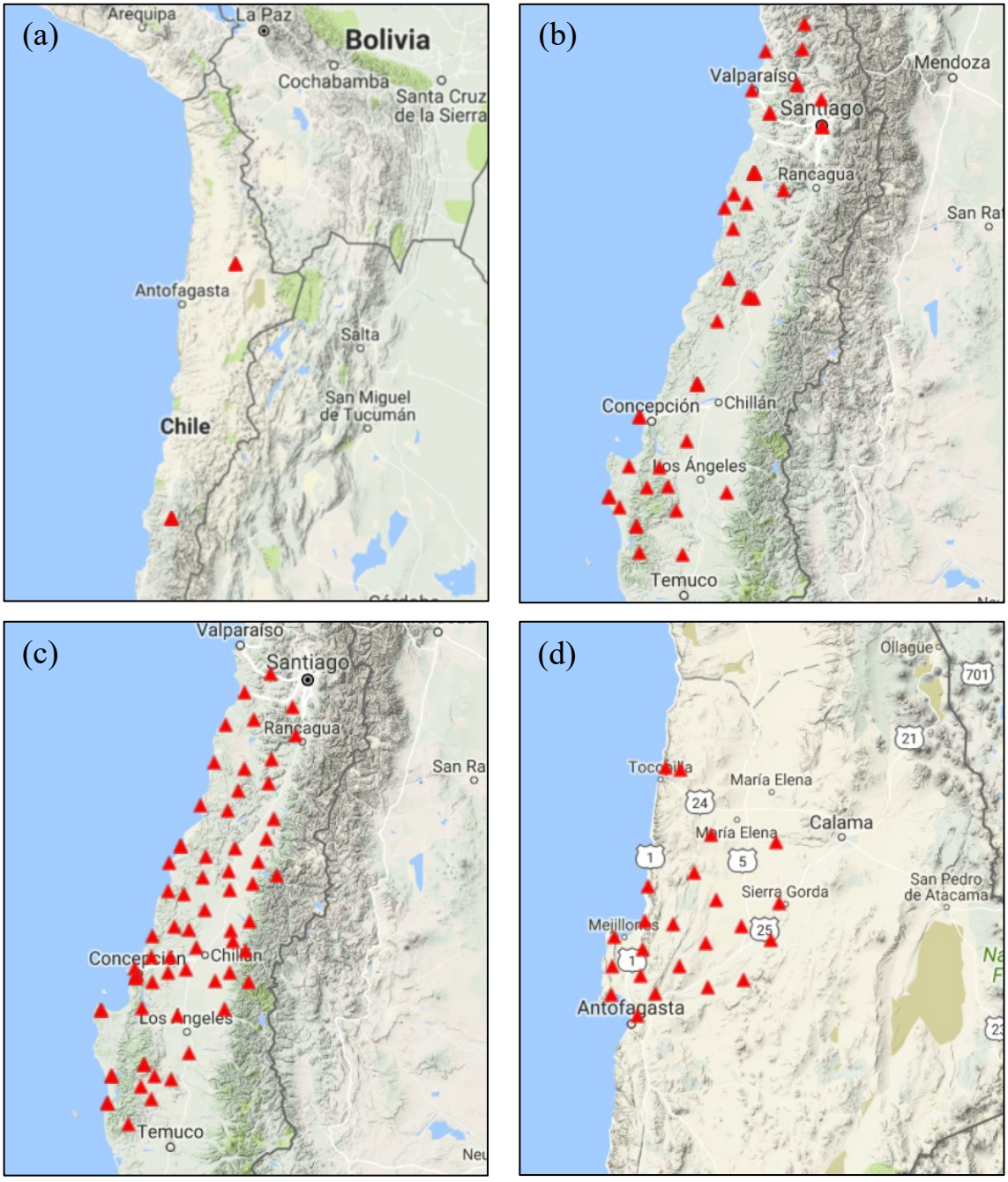

Figure 2.7 Other data providers: (a) IU network. (b) XS network. (c) XY network. (d) Y9 network.

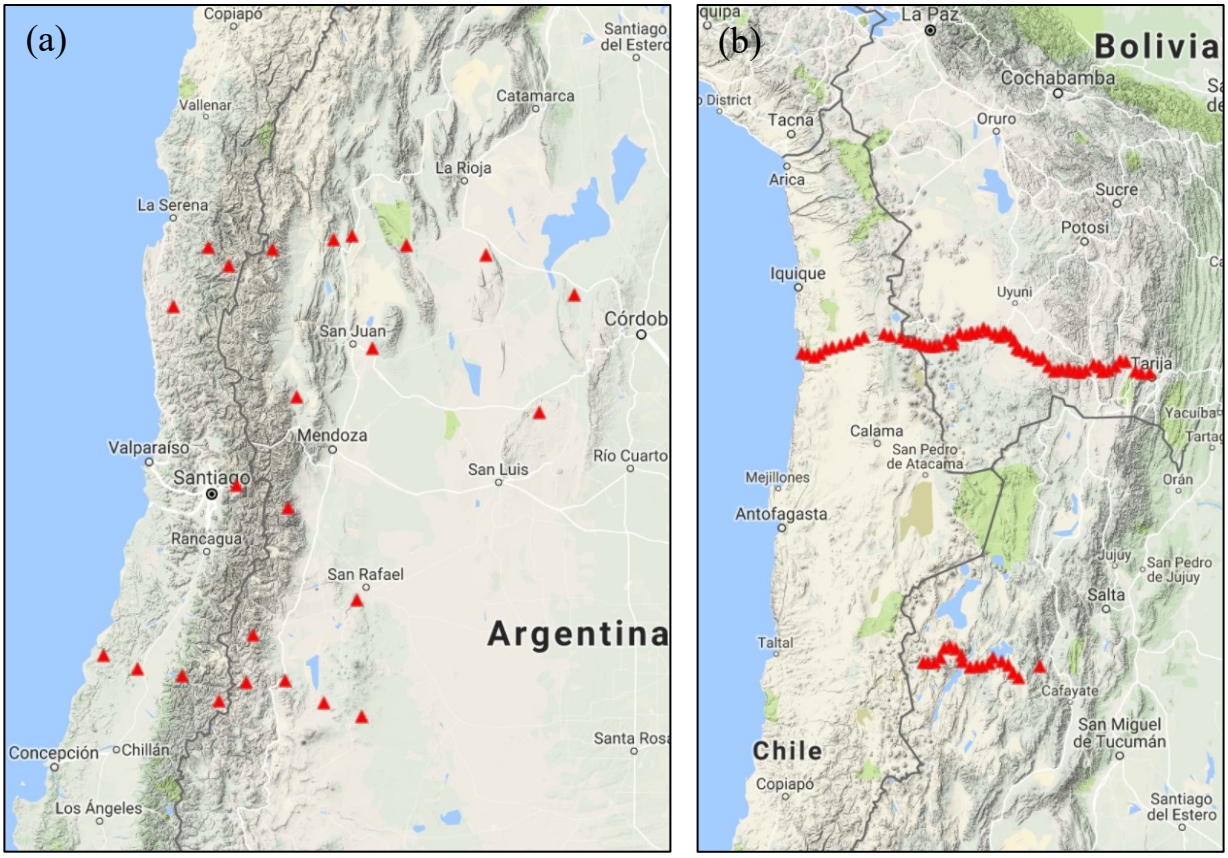

Figure 2.8 Other data providers: (a) YC network. (b) ZA network.

Table 2.1 summarizes the institutions that currently provide or have provided ground motion recordings in Chile, presenting the ID codes and the names of the different networks, the periods of operation, the operator institutions, the number of stations (total and stations with usable recordings), and the approximate percentage of stations and recordings contributed by each network relative to the total Chilean dataset that is presently part of the NGA-Subduction database.

Table 2.1 Summary of seismic data providers in Chile.

Network Code	Network Name	Operation Period	Network Operator	Number of Stations		Percent. of Stations	Percent. of Recordings
				Total	Usable		
DGG	Department of Geophysics and Geodesy Network	1968-1985	DGG, DIC	27	27	6%	1%
RENADIC	DCI National Accelerographic Network	1985 to present	DIC	62	62	15%	29%
C	Chilean National Seismic Network	1991 to present	DGF, CSN	55	34	8%	6%
CX	IPOC Seismic Network	2006 to present	GFZ, IPGP, CSN, UdC, UCNA	25	20	5%	28%
C1	*Red Sismológica Nacional*	2013 to present	DGF, CSN	71	47	11%	3%
RNA	Accelerographic National Network	2013 to present	CSN	75	75	18%	23%
Others: IU, XS, XY, Y9, YC, ZA, XJ, YJ, ZW	Several	Varies	Varies	-	153	37%	10%

2.2 Prior work on ground motion datasets and ground motion modeling in Chile

In this section, I describe previous efforts to compile strong motion datasets for Chile and prior ground motion modeling efforts for the country. Differences between the data set compilation efforts in prior work and in the NGA-Subduction effort for Chile are discussed in Section 5.1.

Ruiz and Saragoni (2005) assembled the first ground motion dataset of recordings obtained in Chilean territory, which clearly differentiates interface and intraslab events and characterizes the SMR stations based on shear wave velocity (V_S) values. This dataset consists of approximately 90 recordings from 8 interface earthquakes and 9 intraslab events that occurred between 1945 and

2005, with surface-wave magnitudes (M_S) ranging from 5.6 to 7.9. The distance range of the recordings is approximately 35-350 km according to the measure used by the authors (hypocentral distance, R_{hyp}). Afterward, Contreras and Boroschek (2012, 2015) developed a Chilean strong motion dataset including 285 recordings from interface earthquakes and 246 recordings from intraslab events (more than 530 recordings in total) obtained between 1985 and 2010, including the ground motion recordings of the **M** 8.8 Maule event. The distances range from 25 to 700 km utilizing the closest distance to the fault rupture plane (R_{rup}), whereas the magnitude range is M_W 5.0-8.8 for interface earthquakes and M_W 5.0-7.8 for intraslab earthquakes.

Arango et al. (2011) compiled the first strong motion dataset for the South and Central American subduction-zone, which contains 98 recordings from sites in Chile and Peru. This dataset consists of 15 earthquakes between 1966 and 2007, with moment magnitudes ranging from 6.3 to 8.4, recorded at 55 different SMR stations at distances of about R_{rup} 25-420 km. A later regional initiative is the South America Risk Assessment (SARA) project, which lasted between 2013 and 2016 and was promoted by the Global Earthquake Model (GEM) foundation. This project was developed within a community-based effort by the GEM team in collaboration with a group of scientists from South America. As part of the hazard component of the program, the SARA project also developed a South American ground motion database (Castillo et al., 2016) consisting of 4110 recordings from Brazil (566), Chile (2197), Colombia (695), Ecuador (586), and Peru (66). The distance range is R_{rup} 20-1200 km approximately and the magnitude range is M_W 2.0-8.8. The SARA project flat file is available at https://sara.openquake.org/hazard_rt6.

The most complete ground motion dataset for Chile is the work developed by Bastías and Montalva (2016), which presents a public database containing 3572 recordings from 477 earthquakes

recorded between 1985 and 2015, including the mega-thrust 2010 Maule (**M** 8.8), 2014 Iquique (**M** 8.15) and 2015 Illapel (**M** 8.31) events. Figure 2.9 shows the magnitude versus distance distribution of this dataset, along with magnitude versus focal depth. The magnitude range is M_W 4.6-8.8, whereas the distance range is R_{rup} 20-650 km. The recordings were obtained at 181 SMR stations characterized with V_{S30} values ranging from 110 to 1,951 m/s. The reported intensity measures are *PGA, PGV*, I_A, and *PSa* values for periods from 0.01 to 10 s. On the other hand, Idini et al. (2017) compiled a dataset of 1207 ground motion recordings obtained at 154 different SMR stations from 184 earthquakes recorded between 1985 and 2015. These authors only consider events with moment magnitudes (M_W) ranging from 5.5 to 8.8 for interface earthquakes and from 5.0 to 7.8 for intraslab earthquakes, including the large events previously mentioned (2010, 2014 and 2015 interface earthquakes). The reported intensity measures are *PGA* and *PSa* values for periods from 0.01 to 10 s.

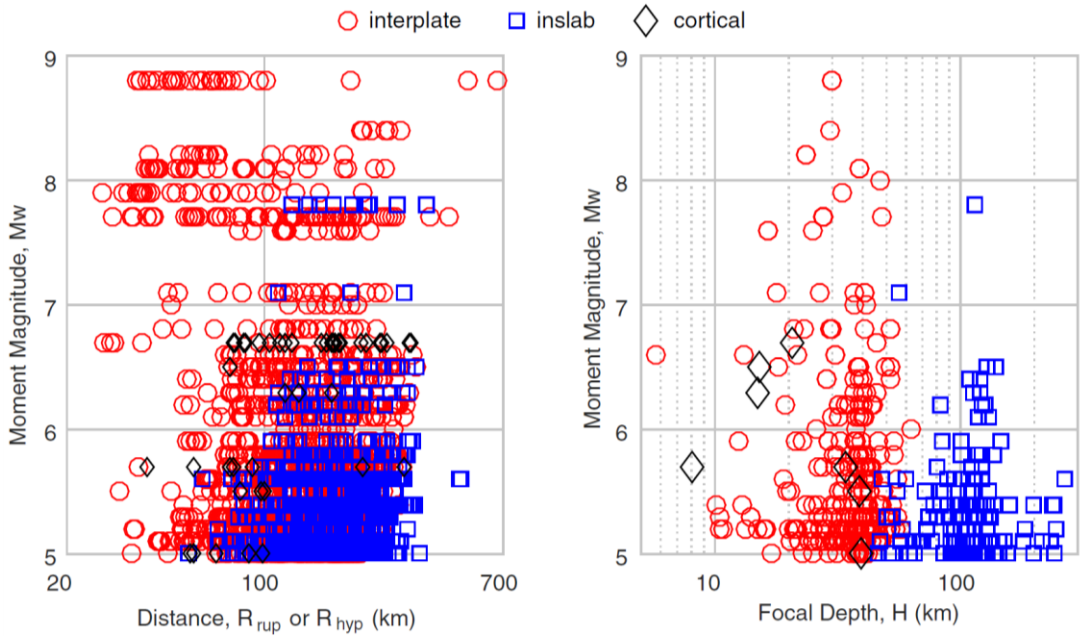

Figure 2.9 Bastías and Montalva (2016) database: magnitude versus distance and magnitude versus focal depth distribution.

With regard to local GMMs, several studies to estimate *PGA* values were developed in Chile between 1976 and 1998 utilizing the limited data available at the time (Ruiz and Saragoni, 2005). Those GMMs typically do not distinguish earthquake mechanism, treat site response effects as linear, and have relatively rudimentary path models (lack of anelastic attenuation, lack of M-dependent geometric spreading, etc.).

The first GMM for the Chilean subduction zone that separates the effects of interface and intraslab seismic sources was proposed by Ruiz and Saragoni (2005, RS2005) based on the dataset described previously in this section, which contains approximately 90 recordings. This GMM only estimates *PGA* values and uses M_S as the magnitude measure and R_{hyp} as the distance measure. Additionally, the model utilizes two broad site categories named "hard rock" and "rock and stiff soil", defined by means of a broad shear wave velocity range used as representative of each site class ($V_S > 1500$ m/s for hard rock; 1500 m/s > V_S > 360 m/s for rock and stiff soil). Subsequently, Contreras and Boroscheck (2012, 2015; CB2015) produced the first GMM that estimates both *PGA* and *PSa* values up to periods of 3 seconds for Chile, based on the dataset compiled by these authors which consists of 531 recordings, including the ground motion recordings of the **M** 8.8 Maule event. The GMM evaluates both interface and intraslab earthquakes and considers two site categories: generic rock, which is taken as $V_{S30} \geq 900$m/s (where V_{S30} is defined as the time-averaged shear wave velocity in the upper 30 m of a site) and generic soil, which is taken as $V_{S30} < 900$m/s. In this case, the local GMM does not include data from the numerous Maule earthquake aftershocks or the recent large events in 2014 (**M** 8.15) and 2015 (**M** 8.31). In the case of the SARA project, Montalva et al. (2016, MEA2016) produced an adaptation of the Abrahamson et al. (2016) GMM calibrated to Chilean strong motion data included in the SARA project dataset.

Two recent local GMMs were published by Montalva et al. (2017, MEA2017) and Idini et al. (2017, IEA2017) for the Chilean subduction zone. The magnitude versus distance distribution of the recordings utilized in the development of these GMMs is shown in Figure 2.10 for each case. The data used by MEA2017 is an updated version of the Bastías and Montalva (2016) dataset and include 3774 recordings from 473 earthquakes, divided into 2461 recordings from 281 interface events and 1313 recordings from 192 intraslab events. These ground motion recordings were obtained at 235 SMR stations characterized with V_{S30} values ranging from 108 to 1951 m/s. On the other hand, IEA2017 utilizes a new subset of 483 recordings (out of the initial 1207 recordings) for the GMM derivation, consisting of 114 strong motion recordings from 38 intraslab earthquakes and 369 strong motion recordings from 65 interface events. The subset is defined after applying two specific selection criteria to remove bias caused by the trigger threshold of accelerometers and to avoid using recordings that had lost high frequency content after the processing methodology,

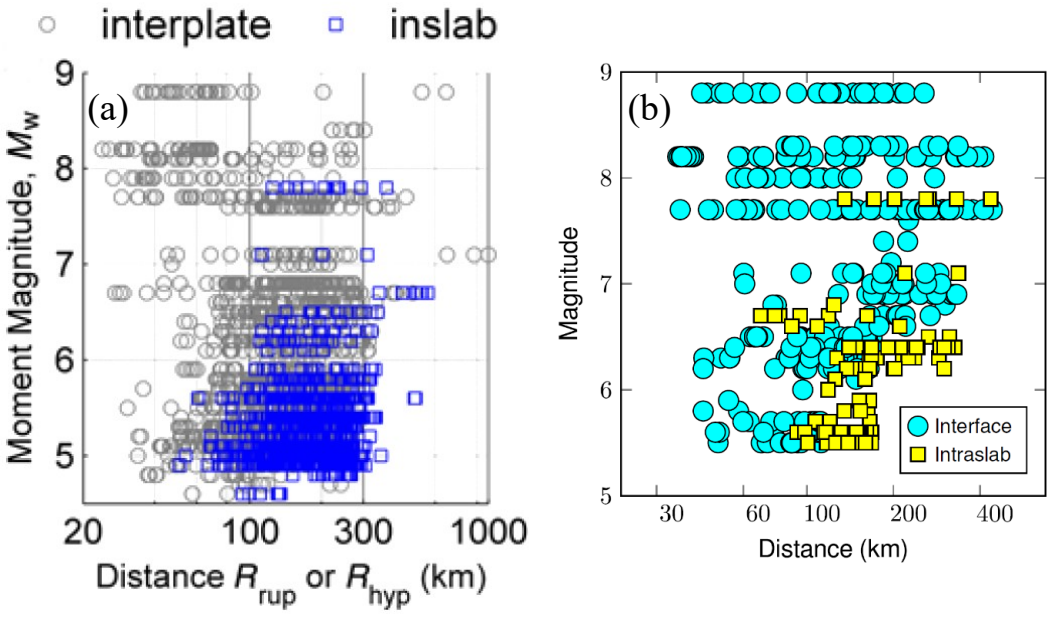

Figure 2.10 Magnitude versus distance distribution of the datasets used in the development of recent local GMMs: (a) Montalva et al. (2017); (b) Idini et al. (2017).

Table 2.2 presents a summary of the different ground motion datasets that include recordings obtained in Chile, along with the GMMs that have been produced using these databases.

Table 2.2 Ground motion datasets and GMMs for the Chilean subduction zone.

Author	Region	Time Frame	# Events	# Recordings	Magnitude range, M_W	Distance Range, R_{rup}	GMM
Ruiz and Saragoni [(*)] (2005)	Chile	1945-2005	8 interface 9 intraslab	49 41	6.4 - 7.8 5.6 - 7.9	35 - 315 km 62 - 350 km	RS2005
Arango et al. (2011)	Chile, Perú	1966-2007	10 interface 5 intraslab	66 32	6.3 - 8.4 6.6 - 7.8	26 - 231 km 54 - 420 km	-
Contreras and Boroschek (2015)	Chile	1985-2010	200 interface & intraslab	285 246	5.0 - 8.8 5.0 - 7.8	25 – 700 km	CB2015
SARA project, Castillo et al. (2016)	South America	1985-2015	286 interface 161 intraslab 126 other	2,176 986 948	4.1 - 8.8 4.1 - 7.8 2.0 - 6.8	20 - 1200 km	MEA2016
Bastías and Montalva (2016)	Chile	1985-2015	279 interface 191 intraslab 7 crustal	2,229 1,300 43	4.6 - 8.8 4.6 - 7.8 4.9 - 6.7	20 - 650 km	MEA2017
Idini et al. (2017)	Chile	1985-2015	184 interface & intraslab	1207	5.5 - 8.8 5.0 - 7.8	N.S.	IEA2017

[(*)] Ruiz and Saragoni (2005) utilizes M_S and R_{hyp} (instead of M_W and R_{rup}).

N.S. = Not Specified

Several probabilistic seismic hazard analysis (PSHA) models have been developed in Chile since the mid-1980s at the national level, such as the studies by Villablanca and Riddell (1985), Martin (1990), Algermissen et al. (1992), and Fischer et al. (2002). Interface (thrust) and intraslab earthquakes were evaluated in these models; however, shallow crustal sources were not considered due to the lack of information relative to the location, seismic activity, seismic recurrence, size, and other features regarding geological faults and shallow seismicity in general. Most of these models only consider *PGA* as the intensity measure and use old-fashioned local GMMs, whose limitations were already mentioned. The most recent PSHA models at the national level were

presented by Leyton et al. (2009), Núñez et al. (2015), and Garcia et al. (2016). Figure 2.11 presents some results from these models showing intensity measure values (*PGA*, and in some cases, *PSa*) with a 10% probability of exceedance in 50 years (475-year return period hazard level). The main characteristics of these models are briefly summarized as follows:

a) Leyton et al. (2009) provide only *PGA* values. The authors utilize a local GMM (RS2005) that separates the effects of interface and intraslab seismic sources. The intensity measure values are estimated for rock and stiff soil, both included in the same broad site class.

b) Núñez et al. (2015) have developed a model that estimates both *PGA* and *PSa* values up to periods of 3 seconds, based on the use of logic trees that combine the global subduction-zone GMMs by Youngs et al. (1997), Atkinson and Boore (2003, 2008), Zhao et al. (2006), and Abrahamson et al. (2016) with a local GMM, CB2015, which includes the ground motion recordings of the **M** 8.8 Maule event. Both interface and intraslab earthquakes are evaluated and the intensity measures are estimated for generic rock, which is taken as V_{S30} > 900m/s.

c) Garcia et al. (2016) have generated a model for South America as part of the hazard component of the SARA project. Both interface and intraslab earthquakes are modeled with a 3D geometry, whereas shallow seismicity is modeled using a combination of distributed seismicity and crustal fault sources. Three GMMs are considered to estimate the intensity measures (*PGA* and *PSa*) for interface and intraslab events: Zhao et al. (2006), Abrahamson et al. (2016) and MEA2016. A logic tree scheme is used to account for the alternative GMMs that are utilized in the SARA project.

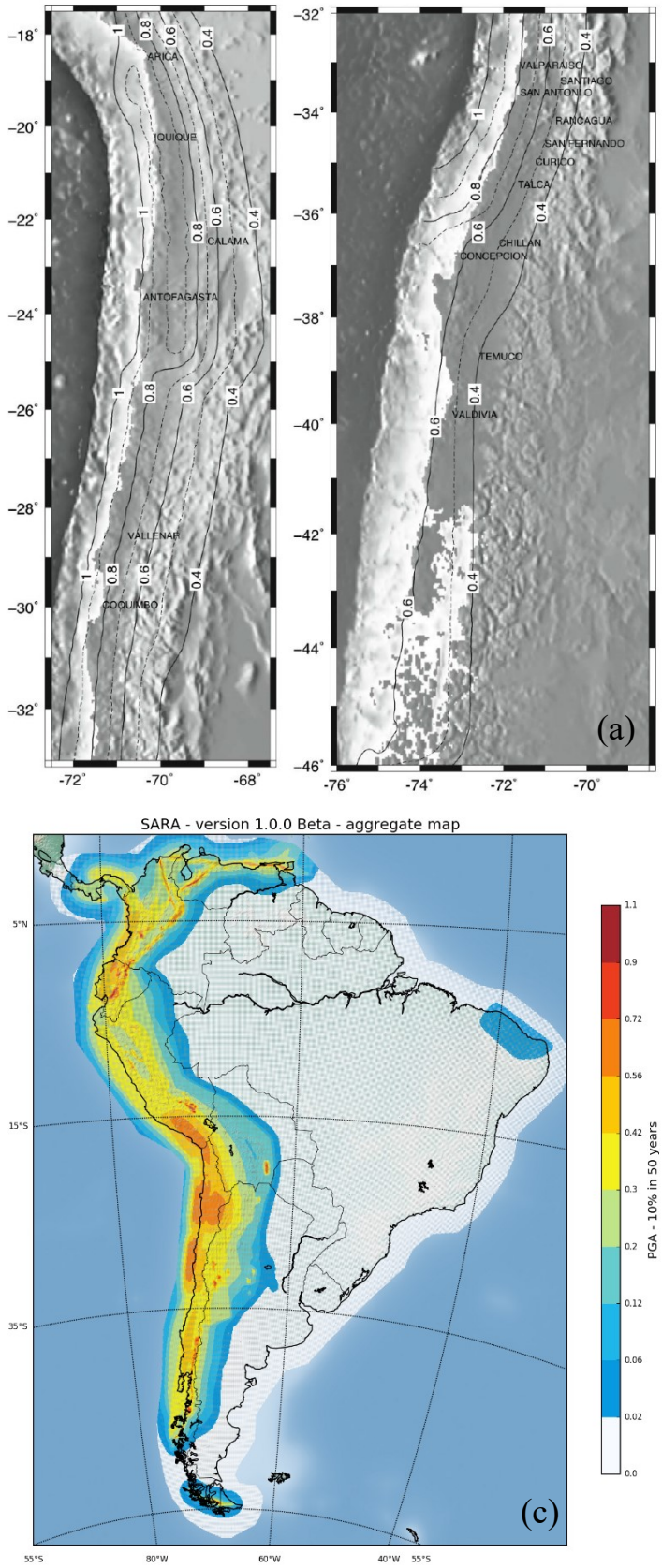

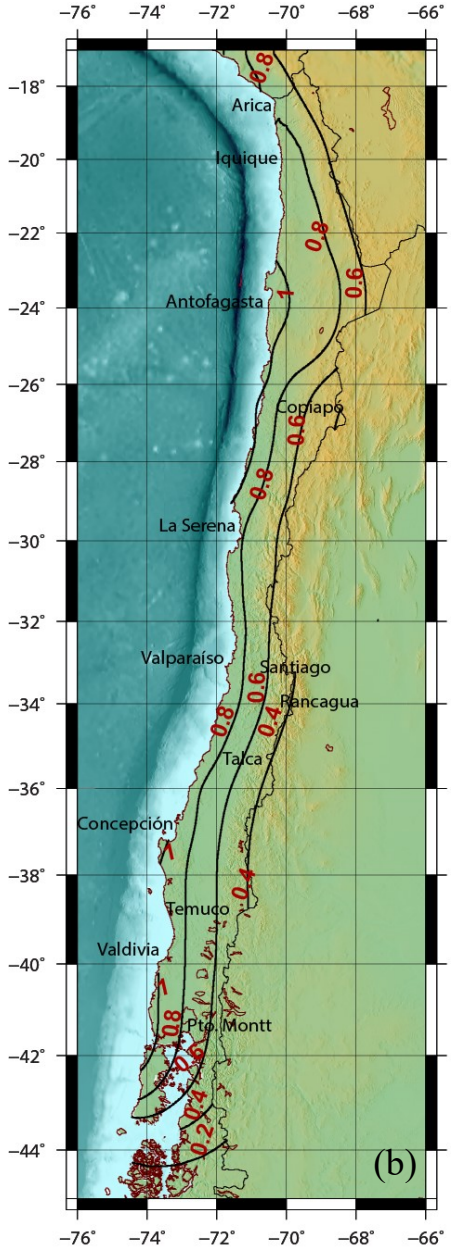

Figure 2.11 Results from recent PSHA models in Chile at the national level, considering 475 years of return period:

(a) Leyton et al. (2009), *PGA* on rock or stiff soil;

(b) Núñez et al. (2015), *PSa* at 0.2s on rock;

(c) Garcia et al. (2016), *PGA*.

An important aspect regarding the development of GMMs is the need to consider regional variability of path effects, as the attenuation of ground motions with distance is faster in some regions than in others. For instance, Figure 2.12 shows a comparison between the attenuation of the 2010 **M** 8.8 Maule strong motion recordings and the trend predicted using the global GMMs by Atkinson and Boore (2003, AB2003) and Zhao et al. (2006, ZEA2006). Both models underpredict the intensities in the distance range of 70 km to 150 km. At closer distance, however, the AB2003 model underpredicts whereas the ZEA2006 model overpredicts. This is a product of the significantly different distance attenuation rates in the two models. AB2003 captures better the attenuation rate for this event, while the ZEA2006 presents a too-fast attenuation rate. This helps to highlight the importance of considering the Chilean data as part of NGA-Subduction. As many distinct regions as possible are needed to understand these differences and obviously, the differences are critical for seismic hazard applications within Chile and elsewhere.

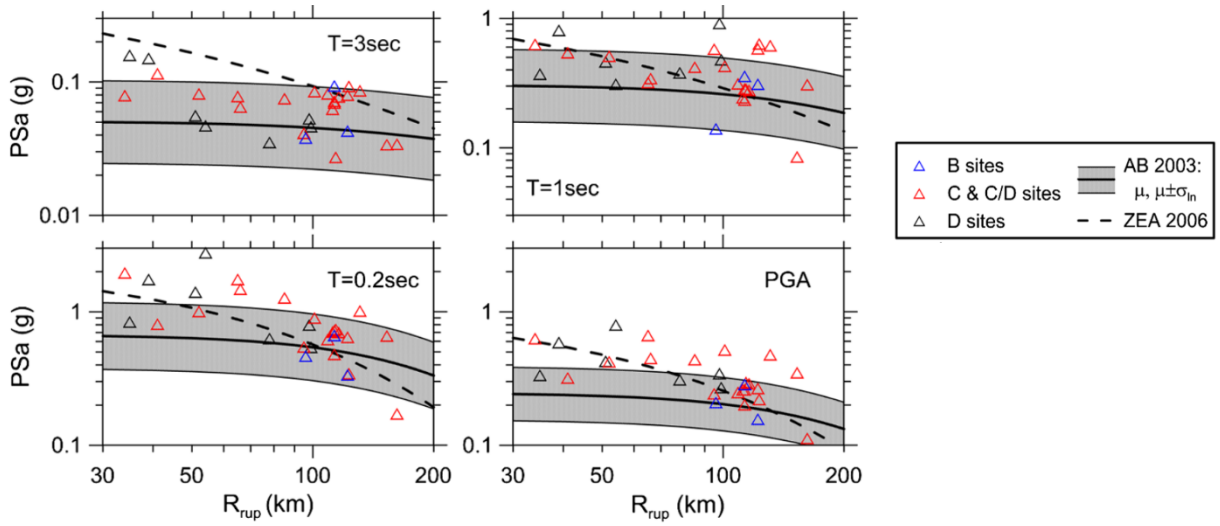

Figure 2.12 Attenuation of PGA and spectral accelerations with distance and comparison to GMMs for C/D site condition. For AB2003, both the median (μ) and median one standard deviation ($\mu \pm \sigma_{ln}$) are shown; for ZEA2006, the median is shown. The data are plotted as geometric means. ZEA2006 applies to the geometric mean, whereas AB2003 to random component. No correction to the AB2003 median has been applied (modified from Boroschek et al., 2012).

Another remarkable example that illustrates the regional variability of path effects is the case of the 2011 **M** 9.0 Tohoku-Oki Japan earthquake, which produced approximately 2,000 ground motion recordings. Stewart et al. (2013) utilized 1,238 accelerograms to evaluate the performance of global GMMs for subduction zones (AB2003, ZEA2006 and the GMM by Abrahamson et al. 2016, AEA2016). The authors calculate total residuals for these models, using the appropriate source distance and site condition for each data point, as follows:

$$R_i = \ln(IM_i)_{rec} - (\mu_i)_{GMM} \qquad \text{Equation 2-1}$$

where $(IM_i)_{rec}$ = value of ground motion intensity measure from recording i and $(\mu_i)_{GMM}$ = mean value of the same IM (in natural log units) from the GMMs. Positive values represent underestimation whereas negative values represent overestimation by the models.

Figure 2.13 shows the residuals versus distance (R_{rup}) for the AB2003, ZEA2006 and AEA2016 GMMs, considering *PGA* and *PSa* values at T=0.1, 1.0 and 3.0 seconds as the IMs, in both forearc and backarc regions. For high-frequency IMs, the AEA2016 model best captures the distance attenuation trends, and particularly for rupture distances under about 200 km to 300 km, all of the models underpredict the attenuation rate in backarc regions. On the other hand, at long periods the distance attenuation rate is too-slow for AB2003, about right for ZEA2006, and too-fast for AEA2016. Additionally, the distance attenuation trends are different from those from the Maule earthquake for high-frequency IMs (Boroschek et al., 2012), where distance attenuation rates were slower than for the Tohoku-Oki event, being overpredicted by the ZEA 2006 model, but well captured by the AB2003 model.

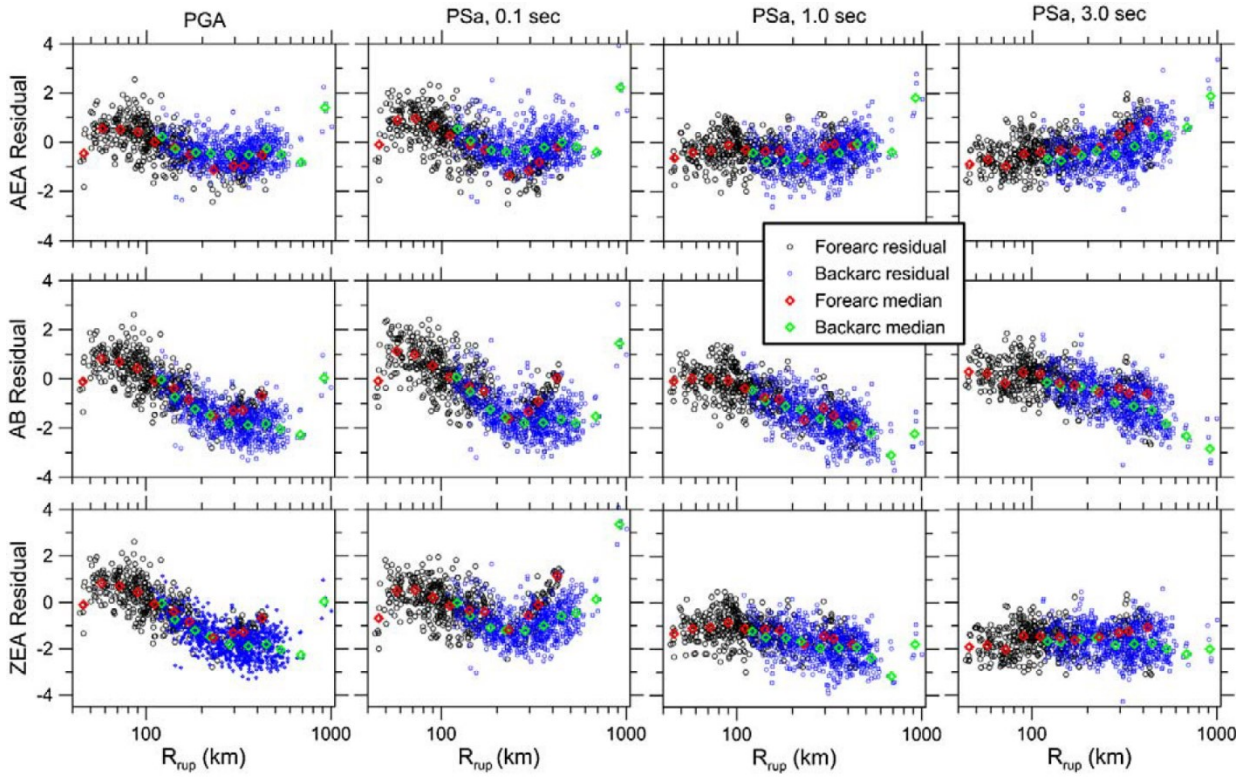

Figure 2.13 Total residuals of Tohoku-Oki recordings within forearc and backarc regions relative to AB2003, AEA2016, and ZEA2006 GMMs along with mean residuals within distance bins (Stewart et al., 2013).

3 EARTHQUAKE CATALOG AND GENERAL SOURCE PARAMETERS

The earthquake catalogue for the NGA-Subduction project has been generated by reviewing past studies for subduction zones, such as those developed by Crouse (1991), Youngs et al. (1997), Atkinson and Boore (2003), and Abrahamson et al. (2016), and including recent earthquakes with available ground motion recordings. Regional reports and studies on subduction events have also been reviewed along with interaction between numerous international experts to identify the earthquakes included in the database (Kishida et al., 2017).

3.1 Earthquakes recorded in Chile with available ground motions

The NGA-Subduction event catalog for the South American region consists of 826 earthquakes that extend from 1985 to 2016. Figure 3.1 shows the geographical distribution of the epicenters of these earthquakes with distinction by hypocentral depth and magnitude. As expected, most of the seismic activity is concentrated close to the Peru-Chile trench and hypocenter depths increase eastward. The largest earthquakes included in the dataset (red circles in Figure 3.1(b)) are located in Chile and Peru.

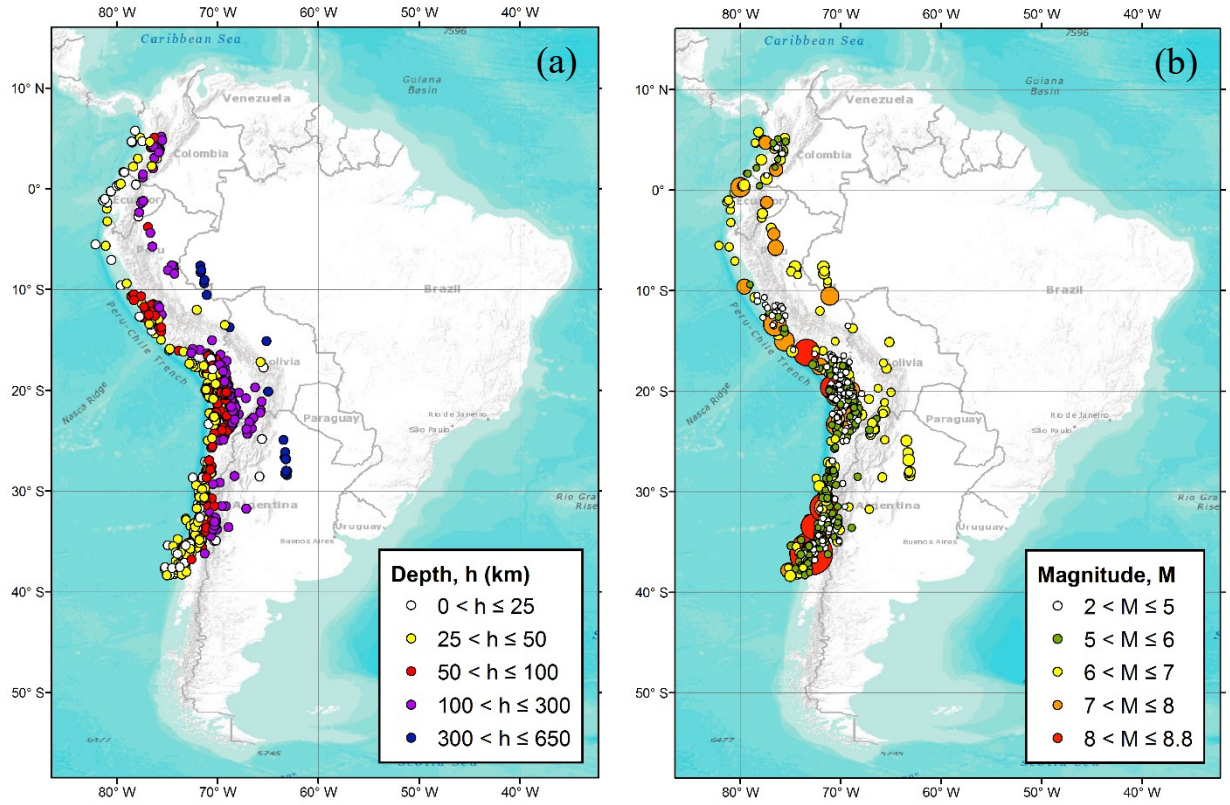

Figure 3.1 Map of South America showing the distribution of the epicenters of the 826 earthquakes included in the NGA-Subduction project: (a) by hypocentral depth; (b) by magnitude; size of the circles is proportional to the seismic moment, M_0.

At the time of writing this document, the total number of ground motion recordings in the NGA-Subduction database for the South American region reaches 6,168 entries. Considering only the recordings obtained in Chilean territory at the SMR stations presented in Chapter 1, the number of recordings decreases to 4,213, which represents approximately 68% of the NGA-Subduction database for South America. These 4,213 recordings are from 689 earthquakes (out of 826) whose epicenters are shown in Figure 3.2, with distinction by hypocentral depth and magnitude. Most of the events are located in Chile, however, some earthquakes located in Argentina, Bolivia, Peru, and even in Brazil, were recorded at Chilean SMR stations as well. The source characterization described in the next sections of this document has been focused on this subset of 689 earthquakes.

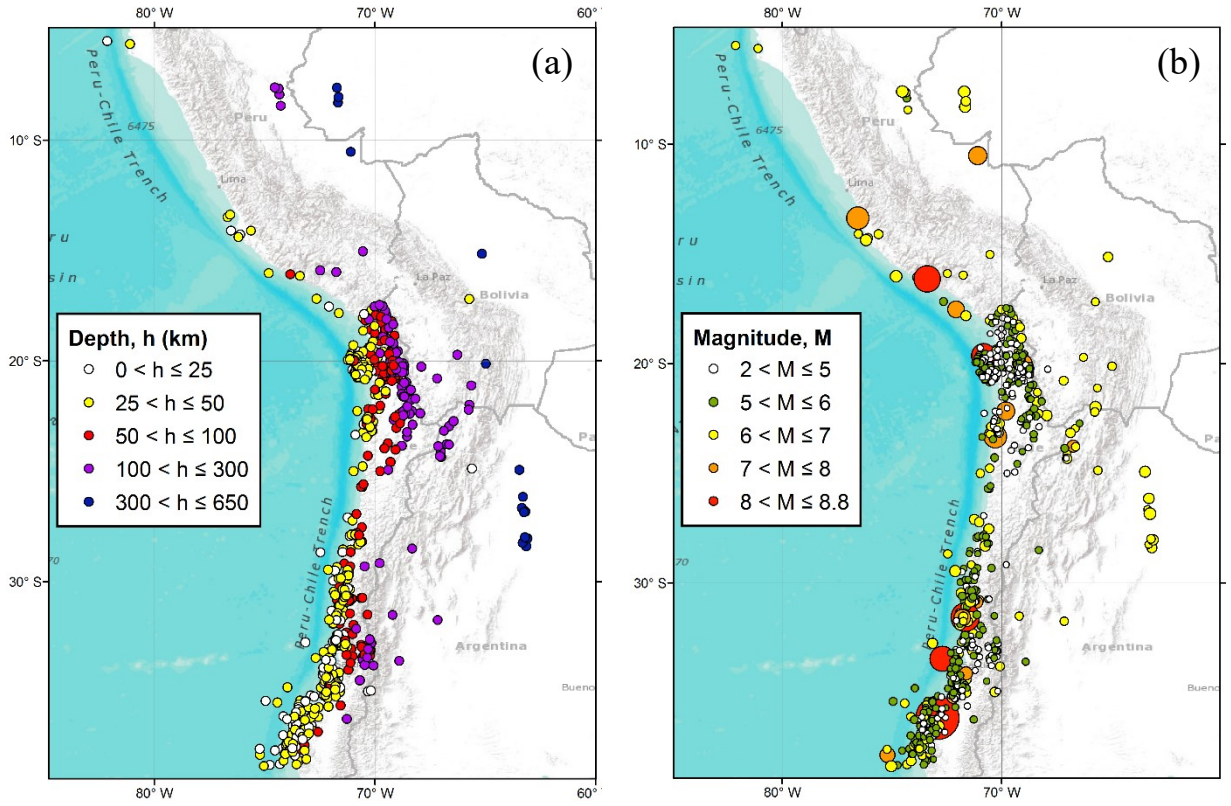

Figure 3.2 Map showing the distribution of the epicenters of the 689 earthquakes with ground motion recordings obtained in Chilean territory: (a) by hypocentral depth; (b) by magnitude; size of the circles is proportional to the seismic moment, M_0.

3.2 Distribution of the earthquake database

A brief analysis of the distribution of the Chilean event dataset is presented in the following Figures, showing event occurrence over time, magnitude distribution, and the classification of the events according to the type of earthquake, as either interface, intraslab, outer-rise, or shallow crustal earthquakes. The methodology to obtain these general source parameters (moment magnitude and earthquake classification) is explained in detail in the next chapter. Some of the presented parameters, like earthquake classification, are preliminary and need further review.

Figure 3.3 shows the number of earthquakes per year which extend from 1985 to 2015. Most of the events are concentrated in 2010, 2014, and 2015, associated with the occurrence of the 2010

Maule **M** 8.8, 2014 Iquique **M** 8.15, and 2015 **M** 8.31 Illapel earthquakes and their aftershocks. In addition, this is probably also related to the installation of new SMR stations after the 2010 Maule earthquake, which increased the number of events being recorded.

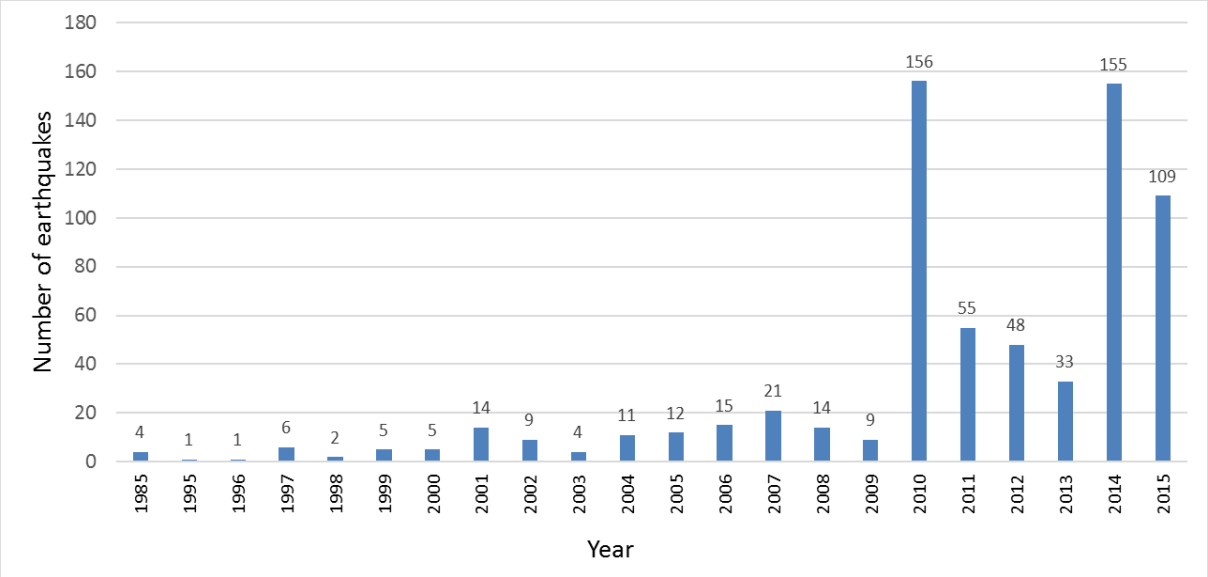

Figure 3.3 Number of earthquakes per year.

Figure 3.4 shows the magnitude distribution of the events. There are six earthquakes with magnitude equal or greater than **M** 8.0, all of them mega-thrust events. As expected, most of the earthquakes are moderate events (**M** 5.0 – 6.0), whereas minor events (**M** < 5.0) are significantly fewer, probably due to the limited capability of the seismic networks to record low-amplitude ground motions. The event database is controlled by interface and intraslab earthquakes as shown in Figure 3.5, representing approximately 59% and 32% of the total number of events, respectively. On the other hand, shallow crustal and outer-rise earthquakes are approximately 6% and 2% of the dataset, respectively. The geographical distribution of these earthquakes is shown in Figure 3.6, with distinction by earthquake type. Due to the geometry of the Chilean subduction zone, interface events (red triangles) are generally located to the west of intraslab events (blue squares).

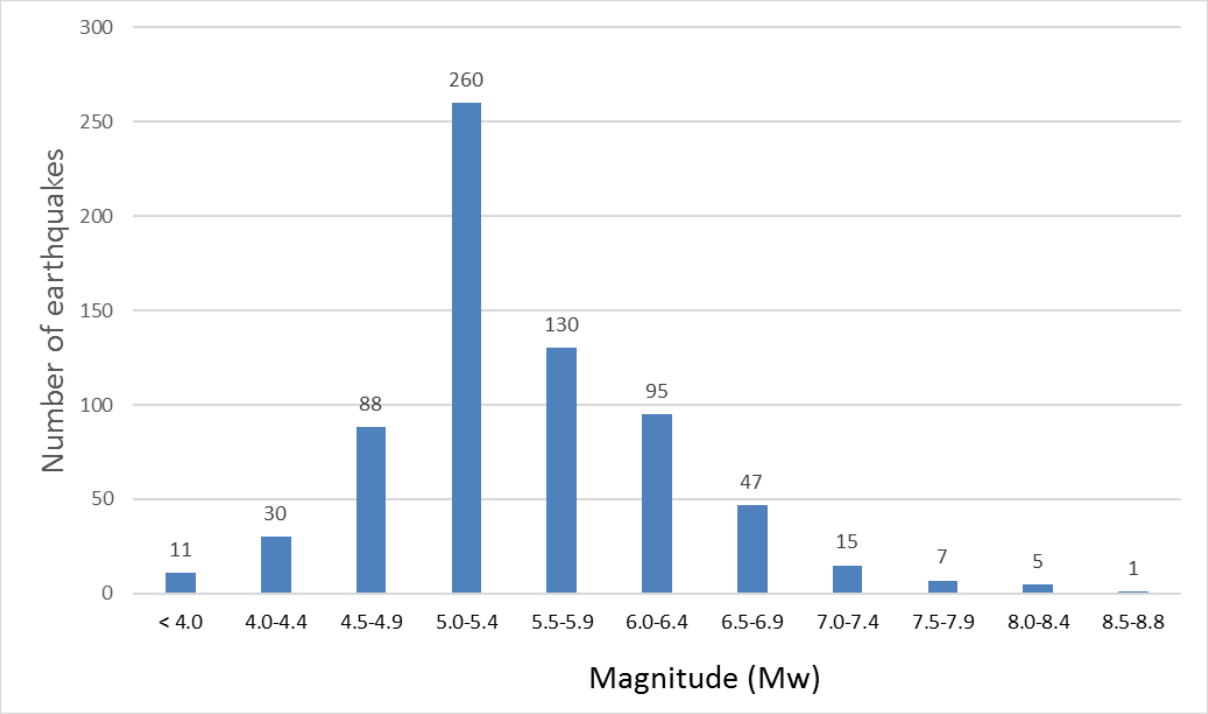

Figure 3.4 Number of earthquakes per magnitude.

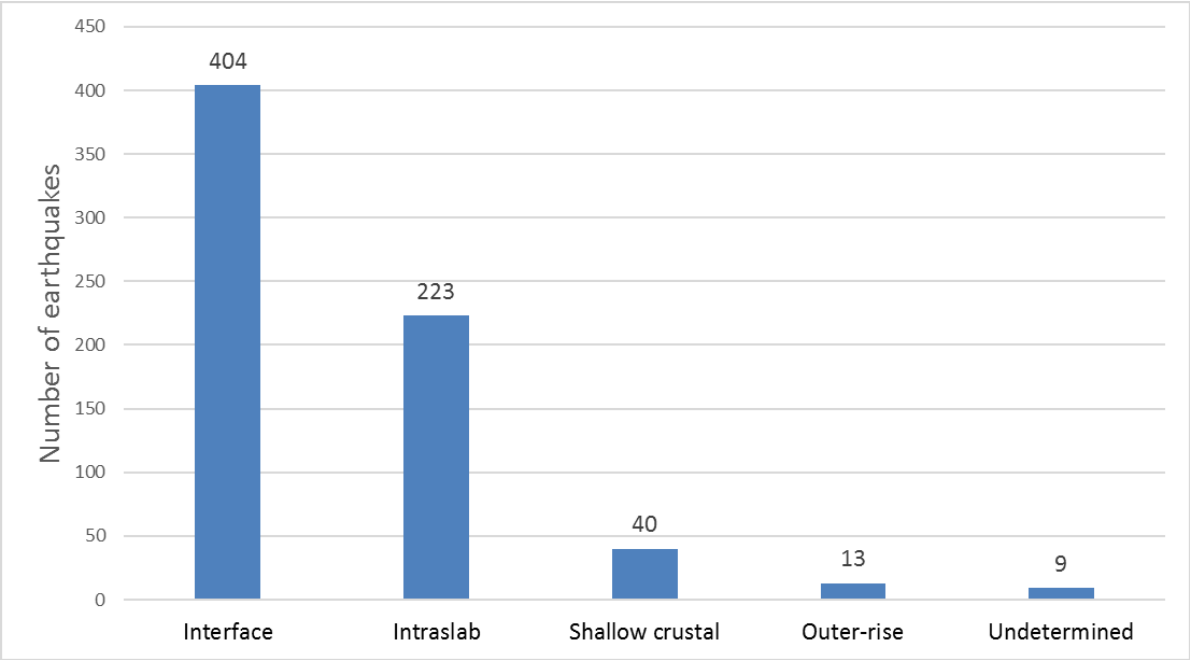

Figure 3.5 Distribution of the events according to earthquake type.

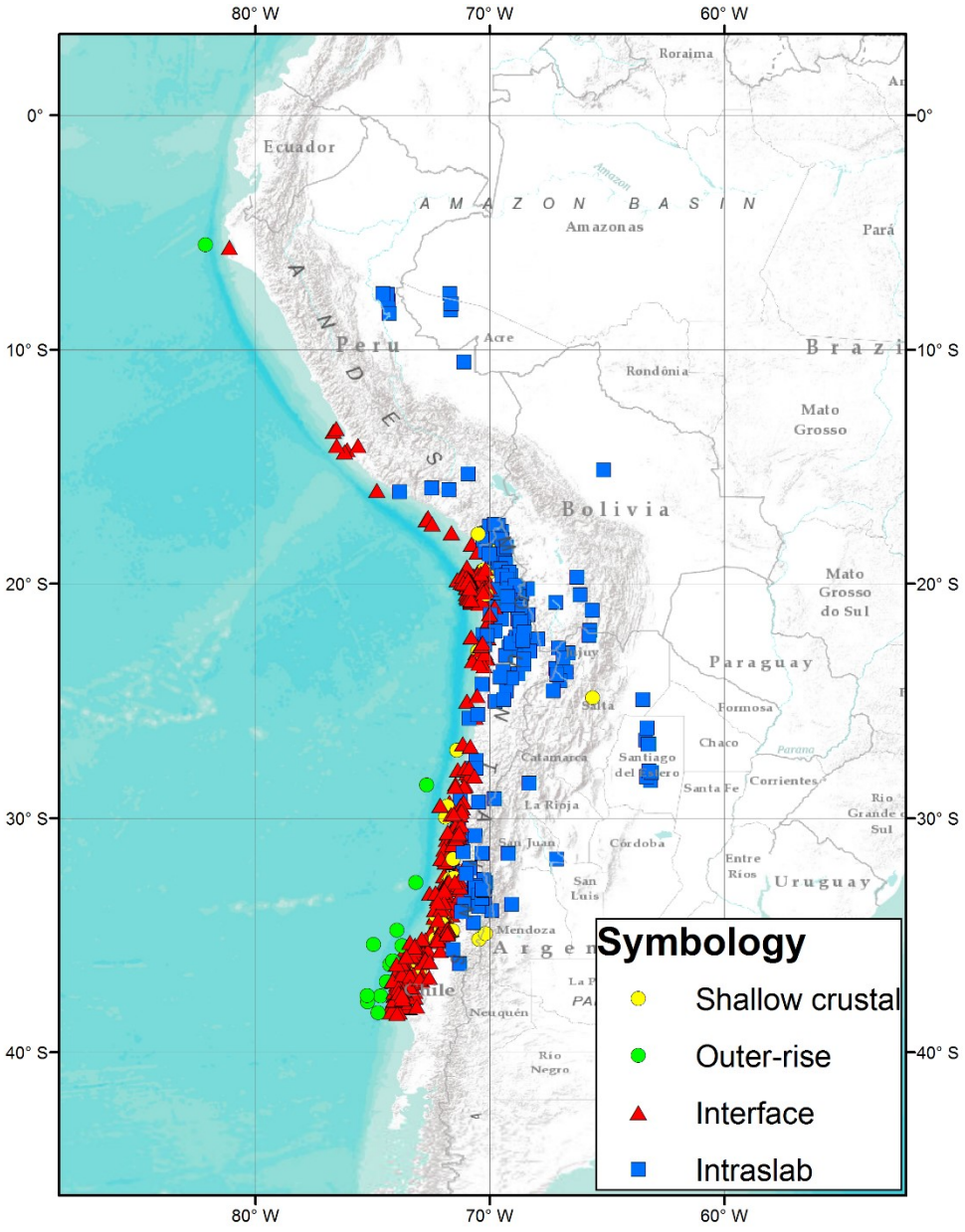

Figure 3.6 Map showing the spatial distribution of the epicenters of the 689 earthquakes included in the database. Epicenters are plotted using a different symbol for each type of earthquake.

4 SOURCE CHARACTERIZATION

For the events considered in the NGA-Subduction project, a series of descriptive source parameters is needed to support GMM development. Those parameters are compiled in a source database file, and here I describe the manner by which that file was assembled for Chilean earthquakes. The processes developed here improve somewhat on those that have been used previously in NGA-Subduction and other NGA projects, and hence are having impact for events elsewhere as well (e.g., Japan). The methodology for this task was developed collaboratively with other member of an NGA-Subduction source database working group having the following participants:

a) Contreras, Víctor. Graduate student, Civil and Environmental Engineering Department, University of California, Los Angeles, CA.
b) Darragh, Robert B. Senior Seismologist, Pacific Engineering and Analysis, El Cerrito, CA.
c) Kishida, Tadahiro. Assistant Project Scientist, University of California, Berkeley, CA.
d) Stewart, Jonathan P. Professor and Chair of the Civil and Environmental Engineering Department, University of California, Los Angeles, CA.
e) Youngs, Robert R. Senior Seismologist, AMEC Foster Wheeler, Oakland, CA.

The events considered for the development of the Chilean source database are those that were recorded at SMR stations located in Chilean territory, which includes some events whose epicenters have been located in other regions of South America. The main parameters that are considered to characterize these events are date, origin time, moment magnitude (**M**), hypocenter location (latitude, longitude, and focal depth), and the following features regarding earthquake mechanism and source geometry:

a) Classification of events as either interface, intraslab, outer-rise, or shallow crustal earthquakes.

b) Fault rupture plane dimensions: length (L), width (W), and area (A).

c) Strike (ϕ), dip (δ), and rake (λ) angles.

d) Location of the fault rupture plane.

e) Depth to top of the fault rupture plane (Z_{TOR}).

Whenever possible, the finite fault parameters listed above are taken from published models, as described in Section 4.1. When such models are not available, which is the case for most events, simulation procedures described in Section 4.2 are used to approximate finite fault effects for the purpose of closest distance calculation for ground motion stations.

4.1 Source parameters for earthquakes with finite fault models

As a part of earthquake source database, finite fault models (FFM) have been collected by reviewing past studies published in the literature. Several websites, including those given below, have been utilized to help locate suitable FFMs for Chilean events:

a) SRCMOD website (Mai and Thingbaijam, 2014), available at http://equake-rc.info/SRCMOD/ (last accessed May 2017).

b) Source Models of Large Earthquakes, Caltech Tectonic Observatory, available at http://www.tectonics.caltech.edu/slip_history/index.html (last accessed 2017).

c) Rupture processes of global large earthquakes ($M_W > 7$), Chen Ji, UC Santa Barbara, available at http://www.geol.ucsb.edu/faculty/ji/big_earthquakes/home.html (last accessed May 2017).

Table 4.1 summarizes the earthquakes with available FFMs or published information regarding source parameters. The seismic moment (M_0) was collected from different agencies, namely the Global Centroid Moment Tensor (CMT, Ekström et al. 2012), the National Earthquake Information Center (NEIC) at the United States Geological Survey, the International Seismological Centre (ISC, 2014), and the Chilean National Seismological Center (CSN). We prefer magnitudes from the CMT catalog when available. We then compute moment magnitude **M** using the following equation from Hanks and Kanamori (1977):

$$\mathbf{M} = \frac{2}{3}\log M_0 - 10.7 \qquad \text{Equation 4-1}$$

Hypocenter locations from the CSN, NEIC, and ISC catalogs are also presented in this table, along with the type of earthquake (interface or intraslab), the number of recordings included in the NGA-Subduction database (235 in total for these earthquakes), and the number of recordings identified from other datasets but currently not included in the project (17 in total; efforts are being done to incorporate these ground motions and improve the database).

The compilation in Table 4.1 is for nine events for which more than 40 FFMs are available. Three studies related to the fault rupture plane of the 1997 **M** 7.1 Punitaqui event are listed as well. Figure 4.1 shows the epicenters of the earthquakes with available FFMs summarized in Table 4.1. There are seven interface earthquakes with **M** ranging from 7.7 to 8.8 and two intraslab earthquakes with **M** = 7.1 and 7.8.

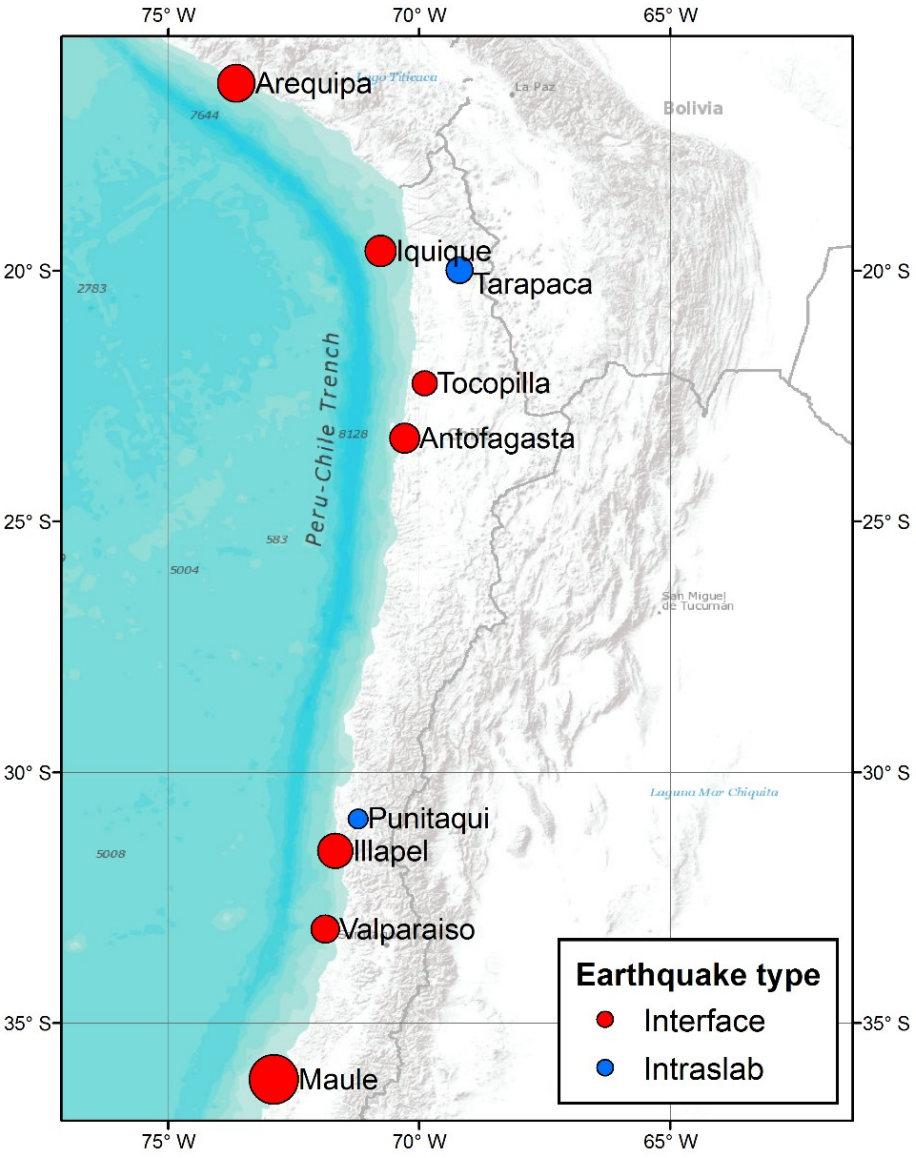

Figure 4.1 Map showing the epicenters of the nine earthquakes with available FFMs or published information regarding fault rupture plane. The size of the circles is proportional to the seismic moment, M_0.

Table 4.1 Earthquakes with available FFMs and/or related publications.

#	Earthquake	Date (UTC)	Time (UTC)	Moment Magnitude M	Hypocenter Location				Mechanism/ Tectonic Environment	# Recordings		FFM References
					Agency	Lat (°)	Lon (°)	Depth (km)		Included	Not included	
1	Maule	2010/02/27	6:34:08	8.8	CSN NEIC ISC	-36.29 -36.122 -36.1485	-73.239 -72.898 -72.9327	30 22.9 28.1	Interface	45	5	1. Sladen (2010) 2. Hayes (2010, 2017a) 3. Luttrell et al. (2011) 4. Shao et al. (2010) 5. Delouis et al. (2010) 6. Lorito et al. (2011) 7. Pollitz et al. (2011)
2	Arequipa (Southern Perú)	2001/06/23	20:34:23	8.4	CSN NEIC ISC	N.A. -16.265 -16.303	N.A. -73.641 -73.561	N.A. 33 2.2	Interface	19	0	1. Skarlatoudis et al. (2015) 2. Shao and Ji (2001) 3. Lay et al. (2010)
3	Illapel	2015/09/16	22:54:28	8.3	CSN NEIC ISC	-31.553 -31.573 -31.557	-71.864 -71.674 -71.585	11.1 22.4 26	Interface	48	6	1. Hayes (2017b) 2. Heidarzadeh et al. (2016) 3. Li et al. (2016) 4. Ruiz et al. (2016) 5. Zhang et al. (2016) 6. Tilmann et al. (2016)

Table 4.1 Earthquakes with available FFMs and/or related publications.

#	Earthquake	Date (UTC)	Time (UTC)	Moment Magnitude M	Hypocenter Location				Mechanism/ Tectonic Environment	# Recordings		FFM References
					Agency	Lat (°)	Lon (°)	Depth (km)		Included	Not included	
3	Illapel (cont.)	2015/09/16	22:54:28	8.3	CSN NEIC ISC	-31.553 -31.573 -31.557	-71.864 -71.674 -71.585	11.1 22.4 26	Interface	48	6	7. Melgar et al. (2016) 8. Li and Ghosh (2016) 9. Okuwaki et al. (2016) 10. Lee et al. (2016) 11. Ye et al. (2016) 12. Fuentes et al. (2016)
4	Iquique	2014/04/01	23:46:45	8.1	CSN NEIC ISC	-19.572 -19.61 -19.453	-70.908 -70.769 -70.747	38.9 25 10	Interface	37	0	1. Wei (2014) 2. Lay et al. (2014) 3. Barrientos (2014) 4. Ruiz et al. (2016) 5. Duputel et al. (2015)
5	Antofagasta	1995/07/30	5:11:57	8.0	CSN NEIC ISC	N.A. -23.34 -23.3033	N.A. -70.294 -70.2052	N.A. 45.6 42.6	Interface	2	1	1. Shao and Ji (n.d.) 2. Delouis et al. (1997)
6	Valparaíso	1985/03/03	22:47:39	7.9	CSN NEIC ISC	N.A. -33.135 -33.0777	N.A. -71.871 -71.7222	N.A. 33 36.2	Interface	26	0	1. Mendoza et al. (1994)

Table 4.1 Earthquakes with available FFMs and/or related publications.

#	Earthquake	Date (UTC)	Time (UTC)	Moment Magnitude M	Hypocenter Location				Mechanism/ Tectonic Environment	# Recordings		FFM References
					Agency	Lat (°)	Lon (°)	Depth (km)		Included	Not included	
7	Tarapacá	2005/06/13	22:44:30	7.8	CSN NEIC ISC	-20.054 -19.987 -19.9172	-69.328 -69.197 -69.2156	114.9 115.6 111.9	Intraslab	30	3	1. Delouis and Legrand (2007) 2. Kuge et al. (2010) 3. Peyrat and Favreau (2010) 4. Hayes (2017c)
8	Tocopilla	2007/11/14	15:40:49	7.7	CSN NEIC ISC	-22.314 -22.247 -22.3208	-70.078 -69.89 -69.7803	47.7 40 33.6	Interface	25	1	1. Sladen (2007) 2. Béjar-Pizarro et al. (2010) 3. Motagh et al. (2010) 4. Ji (2007) 5. Zeng et al. (2007) 6. Hayes (2017d) 7. Delouis et al. (2009) 8. Schurr et al. (2012)
9	Punitaqui (*)	1997/10/15	1:03:43	7.1	CSN NEIC ISC	N.A. -30.933 -30.8907	N.A. -71.22 -71.139	N.A. 58 54.1	Intraslab	3	1	1. Lemoine et al. (2001) 2. Pardo et al. (2002) 3. Gardi et al. (2006)

(*) FFMs are not available for the 1997 Punitaqui earthquake, but the listed references discuss source parameters and fault plane location. / N.A. = Not Available.

A detailed review of the collected FFMs has been carried out to select the most appropriate model for each earthquake. To illustrate the methodology and the specific criteria behind this process, the 2010 **M** 8.8 Maule earthquake is utilized as an example. For this specific event, seven different FFMs have been analyzed and the model by Delouis et al. (2010) was finally preferred. The epicenter of the Maule earthquake (from the preferred FFM) along with the SMR stations that recorded this event are shown in Figure 4.2.

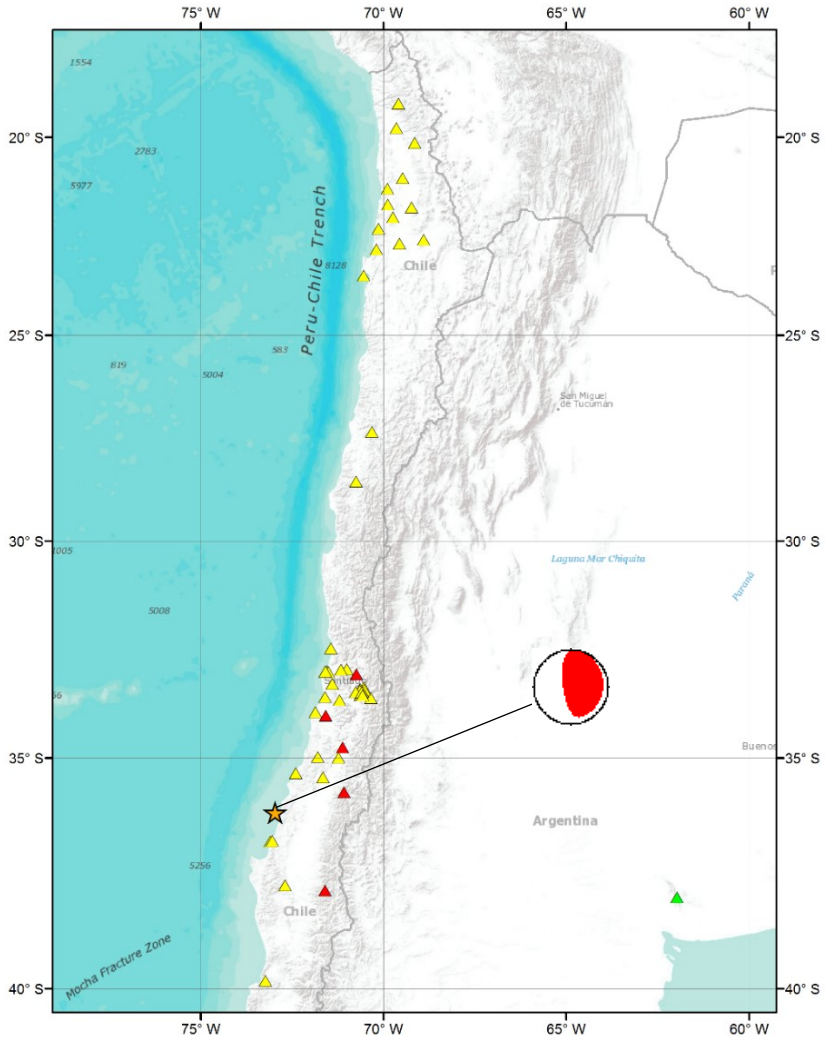

Figure 4.2 Map of the 2010 **M** 8.8 Maule earthquake showing the hypocenter (star), the mechanism from the CMT, and the SMR stations located in Chile with recordings included (yellow triangles) and not included (red triangles) in the NGA-Subduction database. A SMR station in Argentina (green triangle) is also shown.

Once a published FFM model is selected, it is typically necessary to apply some trimming of the rupture dimensions. This is important because faults are often set as large geometric objects at the outset of the inversion so as to avoid "missing" areas of potential rupture. As a result, the inverted fault may contain broad regions with relatively little slip, in addition to concentrated areas of high slip. This need for trimming is not unique to NGA-Subduction, and was addressed earlier in the NGA-West1 project (Power et al., 2008). At that time, on average, a threshold of 50 cm of slip was generally applied, meaning that portions of the fault having slip below this value were trimmed (excluded) in the development of representative fault geometries used for distance calculations. Similar procedures were subsequently used in NGA-West2.

Initially, all seven FFMs were trimmed removing the zones with slip values lower than 50 cm, in accordance with the aforementioned procedures. Figure 4.3 shows the trimmed models that resulted from utilizing this approach for the Maule earthquake. Important differences are observed in the location of the fault rupture planes, which produces a significant variability in terms of source-to-site distances among the FFMs. Table 4.2 presents the distances (R_{rup}) for the 35 stations that recorded this event computed using all the FFMs, and confirms that in several cases the differences are considerable, especially for sites located close to the rupture (see highlighted values in Table 4.2).

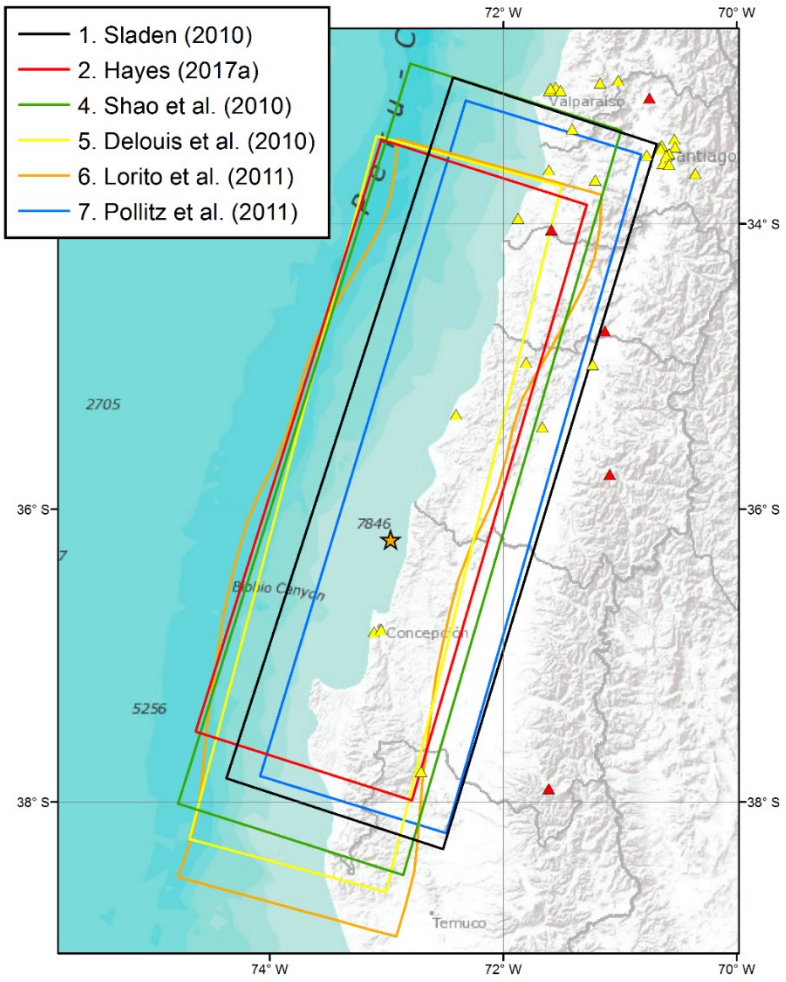

Figure 4.3 FFMs for the 2010 **M** 8.8 Maule earthquake using a trimming threshold of 50 cm of slip.

Table 4.2 Computed distances (R_{rup}) using the seven FMMs for the Maule earthquake.

Recorded Strong Motion				**Closest distance to the fault rupture plane, R_{rup} (km)**								
No	**RSN**	**Station**	**Network**	**FFM 1**	**FFM 2**	**FFM 3**	**FFM 4**	**FFM 5**	**FFM 6**	**FFM 7**	**Range (min - max)**	
1	1814	REN31	RENADIC	652	716	726	652	711	710	661	652	726
2	1820	REN32	RENADIC	512	576	586	511	572	570	520	511	586
3	1819	REN36	RENADIC	82	142	150	82	137	135	86	**82**	**150**
4	1829	REN37	RENADIC	39	88	94	41	83	80	36	**36**	**94**
5	1810	REN38	RENADIC	39	88	93	42	83	80	36	**36**	**93**
6	1827	REN41	RENADIC	36	84	90	38	80	76	32	**32**	**90**
7	1828	REN42	RENADIC	37	86	92	39	81	78	33	**33**	**92**
8	1817	REN43	RENADIC	39	43	40	42	43	41	30	30	43

Table 4.2 Computed distances (R_{rup}) using the seven FMMs for the Maule earthquake.

Recorded Strong Motion				Closest distance to the fault rupture plane, R_{rup} (km)								
No	RSN	Station	Network	FFM 1	FFM 2	FFM 3	FFM 4	FFM 5	FFM 6	FFM 7	Range (min - max)	
9	1824	REN44	RENADIC	63	88	91	66	93	83	54	54	93
10	1821	REN45	RENADIC	60	80	81	63	83	75	51	51	83
11	1822	REN46	RENADIC	65	91	94	70	97	86	56	56	97
12	1811	REN47	RENADIC	65	89	91	69	95	84	56	56	95
13	1823	REN48	RENADIC	66	87	90	71	95	83	57	57	95
14	1818	REN50	RENADIC	36	36	28	38	38	34	26	26	38
15	1815	REN51	RENADIC	64	66	60	66	74	68	54	54	74
16	1816	REN52	RENADIC	48	49	38	51	49	51	38	38	51
17	1825	REN53	RENADIC	57	57	46	59	58	63	47	46	63
18	1813	REN54	RENADIC	36	36	27	38	36	40	26	26	40
19	1809	REN55	RENADIC	35	35	25	37	32	38	24	24	38
20	1812	REN56	RENADIC	54	54	41	56	50	53	43	41	56
21	1826	REN57	RENADIC	189	215	146	163	146	120	197	**120**	**215**
22	1799	CCSP	C	34	33	24	35	30	36	22	22	36
23	1807	MELP	C	50	55	50	53	54	52	41	41	55
24	1805	CLCH	C	66	99	103	70	104	93	58	**58**	**104**
25	1802	SJCH	C	73	101	105	84	113	96	66	66	113
26	1803	STL	C	63	90	93	66	95	85	54	**54**	**95**
27	1804	ANTU	C	65	84	86	68	92	80	55	55	92
28	1800	LACH	C	66	96	100	71	103	91	57	**57**	**103**
29	1801	ROC1	C	61	112	116	63	106	104	59	**59**	**116**
30	1806	CSCH	C	41	68	71	44	64	61	32	**32**	**71**
31	1808	OLMU	C	54	105	109	56	99	97	52	**52**	**109**
32	3551	PB02	CX	1316	1376	1388	1312	1374	1372	1326	1312	1388
33	3560	PB11	CX	1491	1551	1562	1487	1549	1547	1501	1487	1562
34	3549	MNMCX	CX	1561	1620	1632	1557	1619	1617	1571	1557	1632
35	3550	PB01	CX	1354	1416	1427	1352	1414	1412	1364	1352	1427
36	3552	PB03	CX	1240	1301	1312	1237	1299	1297	1249	1237	1312
37	3553	PB04	CX	1200	1261	1272	1197	1259	1257	1210	1197	1272
38	3554	PB05	CX	1143	1203	1215	1139	1201	1199	1153	1139	1215
39	3555	PB06	CX	1172	1235	1246	1171	1233	1231	1182	1171	1246
40	3556	PB07	CX	1272	1332	1344	1268	1331	1328	1282	1268	1344
41	3557	PB08	CX	1460	1522	1533	1457	1520	1517	1469	1457	1533
42	3558	PB09	CX	1279	1342	1353	1277	1339	1337	1288	1277	1353
43	3559	PB10	CX	1064	1124	1135	1060	1122	1120	1074	1060	1135

Table 4.2 Computed distances (R_{rup}) using the seven FMMs for the Maule earthquake.

Recorded Strong Motion				Closest distance to the fault rupture plane, R_{rup} (km)								
No	**RSN**	**Station**	**Network**	**FFM 1**	**FFM 2**	**FFM 3**	**FFM 4**	**FFM 5**	**FFM 6**	**FFM 7**	**Range (min - max)**	
44	785	LVC	IU	1200	1264	1274	1199	1259	1258	1209	1199	1274
45	786	TRQA	IU	897	932	937	922	943	937	897	897	943

As a result of the large differences in rupture distance shown in Table 4.2, the selection of the most appropriate model for each earthquake is of some practical significance and was given serious consideration by the source database working group. This section process focused on the quality of the models, including the type of study (preliminary or published article) and the type and amount of data used in the source inversions. This information along with some comments have been summarized for each FFM in Table 4.3. We indicate in that table the preferred model, or the FFM candidates in case there are two or more options. Ideally, the preferred FFM should have appeared in a peer-reviewed document (not preliminary or automatic solution) produced utilizing as much data as possible, including data from strong motion or broadband recordings. In the case of the Maule earthquake, the FFM by Delouis et al. (2010) and both the average and the best FFMs developed by Lorito et al. (2011) were selected as candidates. Figure 4.4 presents a comparison between the computed source-to-site distances using these models. For large distances ($R_{rup} > 500$ km) the selection of the model is not a critical issue, whereas for closer distances to the fault rupture plane ($R_{rup} < 200$ km) important differences are observed.

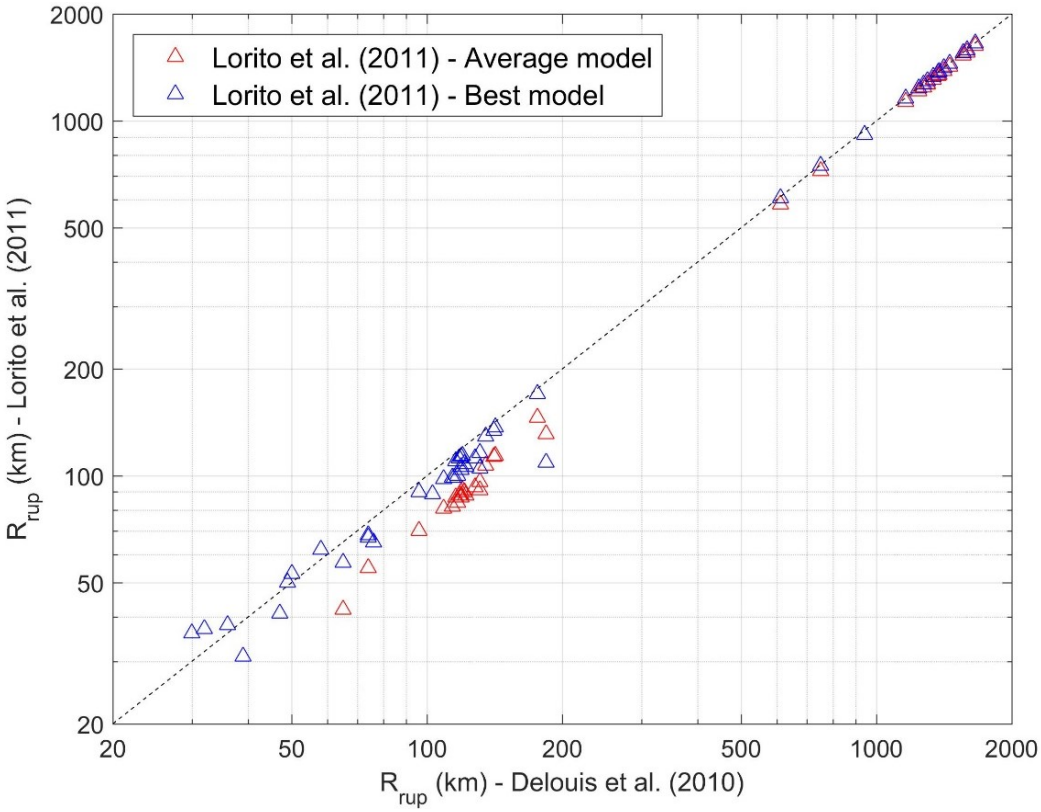

Figure 4.4 Comparison between the distances (R_{rup}) obtained using the different FFM candidates for the Maule earthquake (trimming threshold of 50 cm of slip). The dashed line is the 1:1 relationship.

Table 4.3 Summary of the available FFMs and model selection.

EQ	#	Finite Fault Model	Type of Publication	Data / Number of Stations	M_0 (Nm)	M	Comments and Preferred FFMs
Maule 2010	1	Sladen (2010)	Preliminary result Caltech, Maule 2010	24 teleseismic waveforms (GSN broadband): 24 P waves.	1.74E+22	8.76	Model has not been updated.
	2	Hayes (2010, 2017a)	Preliminary result NEIC, Maule 2010	77 teleseismic waveforms.	1.60E+22	8.77	
			Updated model NEIC, Maule 2010	43 teleseismic waveforms (GSN broadband): 29 P and 14 SH + 48 long period surface waves.	2.50E+22	8.9	Updated model has 5 plane segments.
	3	Luttrell et al. (2011)	Journal paper J. Geophys. Res., 2011	InSAR + 24 GPS stations.	1.78E+22	8.8	
	4	Shao et al. (2010)	Preliminary result UCSB, Maule 2010	35 teleseismic waveforms (GSN broadband): body waves + 35 long period surface waves.	2.51E+22	8.9	Model has not been updated.
	5	Delouis et al. (2010)	Journal paper Geophys. Res. L., 2010	24 teleseismic waveforms (GSN broadband) + InSAR (1172 points) + 40 GPS stations.	1.78E+22	8.8	**FFM candidate.**
	6	Lorito et al. (2011) - Average	Journal paper Nature Geoscience, 2011	InSAR + 25 GPS stations + 19 sea-level recordings (tsunami data) + 34 land level-change measurements. Model has 200 plane segments with different strike and dip angles.	1.55E+22	8.8	**FFM candidate.** Average model is representative of almost equally acceptable solutions.
		Lorito et al. (2011) - Best					**FFM candidate.** Best model might be an extreme solution.
	7	Pollitz et al. (2011)	Journal paper Geophys. Res. L., 2011	InSAR + GPS.	1.97E+22	8.8	

Table 4.3 Summary of the available FFMs and model selection.

EQ	#	Finite Fault Model	Type of Publication	Data / Number of Stations	M_0 (Nm)	M	Comments and Preferred FFMs
Arequipa 2001	1	Skarlatoudis et al. (2015)	Journal paper Seismol. Res. Lett., 2003 BSSA, 2015	Not specified.	Not reported	8.3	This model is a forward simulation.
	2	Shao and Ji (2001)	Preliminary result UCSB, Arequipa 2001	41 teleseismic waveforms (GSN broadband): 26 P and 15 SH + 40 long period surface waves.	5.22E+21	8.4	Model has not been updated.
	3	Lay et al. (2010)	Journal paper BSSA, 2010	46 teleseismic waveforms (GSN broadband): 26 P and 20 SH + shortarc (R1) Rayleigh waves (GSN).	5.50E+21	8.4	**Preferred FFM.**
Illapel 2015	1	Hayes (2017b)	Preliminary result NEIC, Illapel 2015	88 teleseismic waveforms (GSN broadband): 62 P and 26 SH + 49 long period surface waves.	2.9E+21	8.2	
	2	Heidarzadeh et al. (2016)	Journal paper Geophys. Res. L., 2016	62 teleseismic waveforms (0.003-1.0Hz) + 33 tsunami records (3 stations + 30 coastal tide gauges).	4.42E+21	8.4	
	3	Li et al. (2016)	Journal paper Geophys. Res. L., 2016	102 teleseismic waveforms: 60 P and 42 SH (0.005–0.9 Hz) + tsunami signals (recorded at 3 stations and tide gauges).	2.6E+21	8.21	
	4	Ruiz et al. (2016)	Journal paper Seismol. Res. Lett., 2016	High-rate GPS data at 15 stations (0.2 and 1 Hz).	3.94E+21	8.3	
	5	Zhang et al. (2016)	Journal paper Pure&App. Geoph., 2016	InSAR data.	3.28E+21	8.3	
	6	Tilmann et al. (2016)	Journal paper Geophys. Res. L., 2016	Joint inversion of teleseismic (23 stations), strong motion (9 stations) and high-rate GPS (8 stations) waveforms, static displacements from GNSS (17 stations) and InSAR.	Not reported	8.28	

Table 4.3 Summary of the available FFMs and model selection.

EQ	#	Finite Fault Model	Type of Publication	Data / Number of Stations	M_0 (Nm)	M	Comments and Preferred FFMs
Illapel 2015	7	Melgar et al. (2016)	Journal paper Geophys. Res. L., 2016	Joint inversion of InSar, high-rate GPS, strong motion, tsunami, and teleseismic backprojection data.	Not reported	8.3	**Preferred FFM.**
	8	Li and Ghosh (2016)	Journal paper Pure&App. Geoph., 2016	Teleseismic backprojection (187 stations) using two frequency bands (0.1–0.5 and 0.25–1 Hz).	Not reported	8.3	
	9	Okuwaki et al. (2016)	Journal paper Pure&App. Geoph., 2016	Hybrid inversion of 42 teleseismic waveform (0.3–2.0 Hz and 0.001–0.36 Hz analyses) and backprojection data.	3.30E+21	8.3	
	10	Lee et al. (2016)	Journal paper Geophys. Res. L., 2016	Teleseismic data (57 records filtered using two passbands 0.003–0.04 Hz and 0.003–0.02 Hz): P waves, S waves, reflections, and surface waves. Green's functions computed with a 3D spectral-element method.	5.48E+21	8.43	
	11	Ye et al. (2016)	Journal paper Pure&App. Geoph., 2016	Teleseismic P (60 recordings) and SH (42 recordings) waves in the passband 0.005–0.9 Hz. Various models: dip ranges from 16° to 22°.	3.7E+21 2.7E+21	8.35 8.25	Highest moment magnitude (**M**8.35) associated with dip=16° and lowest (**M**8.25) associated with dip=22°.
	12	Fuentes et al. (2016)	Journal paper Pure&App. Geoph., 2016	Comparison of USGS and Melgar et al. (2016) models.	-	-	Not focused on producing a new FFM.
Iquique 2014	1	Wei (2014)	Preliminary result Caltech, Iquique 2014	91 teleseismic waveforms (GSN broadband): P and SH.	1.58E+21	8.1	Model has not been updated.
	2	Lay et al. (2014)	Journal paper Geophys. Res. L., 2014	101 teleseismic waveforms (broadband): P and SH (Period band: 1.1-200 s) + short-period teleseismic wave backprojections and inversion of deepwater tsunami wave recordings.	1.70E+21	8.1	**FFM candidate.**
	3	Barrientos (2014)	Report (prel. solution) CSN, 2014	16 GPS + gCMT solution.	1.69E+21	8.1	

Table 4.3 Summary of the available FFMs and model selection.

EQ	#	Finite Fault Model	Type of Publication	Data / Number of Stations	M_0 (Nm)	M	Comments and Preferred FFMs
Iquique 2014	4	Ruiz et al. (2014)	Journal paper Science, 2014	22 far-field broad-band recordings (FDSN network).	Not reported	8.1	
	5	Duputel et al. (2015)	Journal paper Geophys. Res. L., 2014	InSAR + 16 static GPS + 5 tsunami tide gauges + 5 high-rate GPS + 14 strong motion recordings.	1.60E+21	8.1	**FFM candidate.**
Antofagasta 1995	1	Shao and Ji (n.d.)	Preliminary result UCSB, Antofagasta 1995	33 teleseismic waveforms (GSN broadband): 21 P and 12 SH + 31 long period surface waves.	2.11E+21	8.14	**Preferred FFM.** Model has not been updated.
	2	Delouis et al. (1997)	Journal paper BSSA, 1997	Teleseismic waveforms (broadband) from 26 stations + aftershocks distribution analysis + 1 strong motion accelerogram.	1.2E+21	8.0	FFM is not an inversion (dislocation model).
Valparaíso 1985	1	Mendoza et al. (1994)	Journal paper BSSA, 1994	16 teleseismic body wave + 10 long-period surface waves + 12 local strong motions. Model has 2 plane segments with different dip angles.	1.96E+21	8.16	**Preferred FFM.**
Tarapacá 2005	1	Delouis and Legrand (2007)	Journal paper Geophys. Res. L., 2007	20 teleseismic waveforms (broadband): P and SH, only 10 used in the inversion, all 20 for fault plane + 6 strong motion accelerograms. Model has 2 plane segments with different dip angles.	5.47E+20	7.8	**FFM candidate.**
	2	Kuge et al. (2010)	Journal paper J. Geophys. Res., 2010	Teleseismic waveforms: 33 P and 11 pP waves + 5 strong motion accelerograms.	5.4E+20	7.8	**FFM candidate.** Results are similar to Delouis and Legrand (2007) FFM.

Table 4.3 Summary of the available FFMs and model selection.

EQ	#	Finite Fault Model	Type of Publication	Data / Number of Stations	M_0 (Nm)	M	Comments and Preferred FFMs
Tarapacá 2005	3	Peyrat and Favreau (2010)	Journal paper Geophys, J. Int., 2010	Only strong motion data (5 recordings) + simplified slip patch kinematic parametization. Assumes two ellipsse shaped asperities.	5.6E+20	7.8	Method only produces ellipsoidal ruptures (assumed geometry).
	4	Hayes (2017c)	Preliminary result NEIC, Tarapaca 2005	35 teleseismic waveforms (GSN broadband): 27 P and 8 SH.	Not reported	7.7	Model has not been updated.
Tocopilla 2007	1	Sladen (2007)	Preliminary result Caltech, Tocopilla 2007	38 teleseismic waveforms (GSN broadband): 33 P and 5 SH.	3.98E+20	7.7	Model has not been updated.
	2	Béjar-Pizarro et al. (2010) - 1	Journal paper Geophys, J. Int., 2010	11 GPS	3.98E+20	7.7	
		Béjar-Pizarro et al. (2010) - 2		InSAR			
		Béjar-Pizarro et al. (2010) - 3		Joint inversion (11 GPS + InSAR)			
	3	Motagh et al. (2010)	Journal paper Tectonophysics, 2010	InSAR + Aftershocks distribution analysis	5.62E+20	7.8	
	4	Ji (2007)	Preliminary result UCSB, Tocopilla 2007	20 teleseismic waveforms (GSN broadband): 13 P and 7 SH + 25 long period surface waves	5.82E+20	7.81	Model has not been updated.
	5	Zeng et al. (2007)	Preliminary result USGS, 2007	42 teleseismic waveforms	3.98E+20	7.7	Model has not been updated.

Table 4.3 Summary of the available FFMs and model selection.

EQ	#	Finite Fault Model	Type of Publication	Data / Number of Stations	M_0 (Nm)	M	Comments and Preferred FFMs
Tocopilla 2007	6	Hayes (2017d)	Preliminary result NEIC, Tocopilla 2007	51 teleseismic waveforms (GSN broadband): 32 P and 19 SH + 56 long period surface waves	4.3E+20	7.7	Model has not been updated.
	7	Delouis et al. (2009)	Journal paper BSSA, 2009	37 teleseismic waveforms: 21 P and 16 SH + 6 strong motion accelerograms	4.5E+20	7.7	**FFM candidate.**
	8	Schurr et al. (2012)	Journal paper J. Geophys. Res., 2012	InSAR + 11 GPS + 7 strong motion accelerograms + 7 broadband sensors	6.24E+20	7.83	**FFM candidate.**
Punitaqui 1997 (*)	1	Lemoine et al. (2001)	Journal paper Geophys. Res. Lett., 2001	*"From the directivity, we found that its rupture plane was almost vertical with a downward rupture. It was a down-dip compressional mechanism which is rare in Chile"*	-	-	
	2	Pardo et al. (2002)	Journal paper Tectonophysics, 2002	*"The main event focal mechanism indicates normal faulting with the more vertical plane considered as the active fault"*	4.92E+19	7.1	
	3	Gardi et al. (2006)	Journal paper J. Geophys. Res., 2006	Figure 7 in Gardi et al. (2006) schematically shows the position of the fault plane.	-	-	

(*) FFMs are not available for the 1997 Punitaqui earthquake, but the listed references discuss source parameters and fault plane location.

As part of this project, we re-examined the source models that were used to develop the 50 cm threshold in previous NGA projects. The models were of the 7 shallow crustal events in California summarized in Table 4.4, which shows the calculation of the average threshold that was utilized in the trimming of the source models. These events had maximum slips in the approximate range of 45 to 790 cm, so that on average the 50 cm threshold corresponded to approximately 15% of the maximum. For NGA-Subduction, we elected to consider this percentage of the maximum slip, in lieu of the 50 cm threshold directly. This was considered to be appropriate given the large rupture dimensions and slip values involved in subduction-zone earthquakes when compared to the **M**6-7 shallow crustal events upon which the original criteria had been based. When the 15% criteria was applied to Chilean events with FFMs, the results were judged to be reasonable by the source working group. Accordingly, we trim the FFMs by applying a threshold of 15% of the maximum slip and then drawing one or more rectangles around the high slip areas.

Table 4.4 Summary of trimming applied for NGA-West and NGA-West 2 projects.

EQ ID	Earthquake name	Magnitude M	Maximum slip in the FFM (cm)	Maximum slip in the trimmed row or column of the FFM (cm)	Percentage of the maximum trimmed value relative to the maximum slip
48	Coyote Lake	5.9	120	0	0%
87	Borah Peak	6.8	128	9	7%
101	North Palm Springs	6.2	45	9-11	22%
113*	Whittier Narrows	5.9	90	No trim (< 58 cm)	No trim (<64)
125	Landers	7.3	790	60	8%
127*	Northridge	6.7	319	No trim (< 140 cm)	No trim (<46)
118*	Loma Prieta	6.9	513	0 (< 105 cm)	0 (< 20 cm)
280	El Mayor-Cucupah	7.2	700	180	26%
177	San Simeon	6.5	300	70	23%
179	2004 Parkfield	6.0	52	18	35%
		Average**	**305 cm**	**50 cm**	**~15%**

* Events 113 (Whittier Narrows), 127 (Northridge), and 118 (Loma Prieta) applied models as published, because trimming appears to have been done by the FFM authors.

**Average is computed without the pre-trimmed events.

Table 4.5 presents a summary of the preferred models, including hypocenter location, seismic moment, moment magnitude, and notes on trimming. Also provided in Table 4.5 is justification for the selected model from among alternatives, as applicable. In addition, Table 4.6 lists parameters describing the rectangles that define the fault plane for each event. Geometric parameters considered in the rectangle definitions are explained in Figure 4.5.

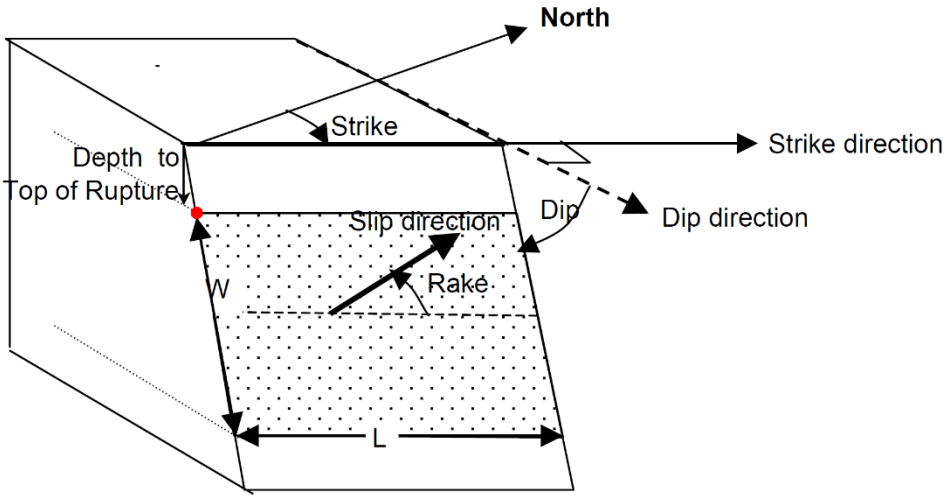

Figure 4.5 Schematic representation of the fault rupture plane. The red point represents the bottom-left corner listed in Table 4.6 (Modified from Chiou et al., 2005).

Figures 4.6 to 4.13 show for each event studied in this section a map displaying hypocenter, stations locations, and the mechanism from the CMT catalog. (For the 2010 **M** 8.8 Maule earthquake see Figure 4.2). Subsequently, Figures 4.14 to 4.21 show for each event with a finite fault model the following figures: (a) map view of fault model, (b) view of slip distribution and applied trimming.

Table 4.5 Summary of the preferred FFMs.

#	Earthquake	Mechanism/ Environment	M*	Finite Fault Model	M_0 (Nm)	Hypocenter location			Comments
						lat (°)	lon (°)	depth (km)	
1	Maule 2010	Interface	8.81	Delouis et al. (2010)	1.78E+22	-36.208	-72.963	31.64	This model is preferred because is a published paper which uses most of the waveforms data. Additionally, its geometry is simpler than other candidates (Lorito et al., 2011), which facilitates trimming and distance calculation.
2	Arequipa 2001	Interface	8.41	Lay et al. (2010)	4.2E+21	-16.2099	-73.6233	29.6	This model is preferred over other preliminary solutions, because is a published paper with most of the data used in the inversion. Slip values are not reported (only relative distribution). The model is already trimmed using approx. 15-20% of maximum slip as limit.
3	Illapel 2015	Interface	8.31	Melgar et al. (2016)	3.7023E+21	-31.5571	-71.6617	29.81	This model is preferred because of the data used in the inversion, that is a joint inversion of various data, including strong motions records. The model was trimmed using 3 rectangles (with the same strike angle). Model assumes irregular fault surface using Hayes et al. (2012) geometry of the slab.
4	Iquique 2014	Interface	8.15	Lay et al. (2014)	1.70E+21	-19.642	-70.817	20.0	This model is preferred over the other candidate (Duputel et al., 2015), because the dimensions of the trimmed area are more consistent with M-RA relations for subduction zones. The model is already trimmed using approx. 15-20% of maximum slip as limit.
5	Antofagasta 1995	Interface	8.02	Shao and Ji (n.d.)	2.11E+21	-23.4317	-70.4542	36.86	Even though this model is a preliminary result, it is preferred over the other candidate (Delouis et al., 1997) because the latter is not an inversion. The model was trimmed using two rectangles (with the same dip and strike angles). Hypocenter was relocated to be consistent with the FFM.

#	Earthquake	Mechanism/ Environment	M*	Finite Fault Model	M_0 (Nm)	Hypocenter location			Comments
						lat (°)	lon (°)	depth (km)	
6	Valparaiso 1985	Interface	7.98	Mendoza et al. (1994)	1.96E+21	-33.125	-71.610	40.0	This model is the only candidate for this event. It was judged to be a good quality model, based on the use of strong motion recordings and the geometry of the model. The model was trimmed using two rectangles (with the same strike angle but different dip angles).
7	Tarapaca 2005	Intraslab	7.78	Kuge et al. (2010)	5.4E+20	-20.03	-69.28	110.0	This model is preferred because it builds on the other candidate model (Delouis and Legrand, 2007). The results are nearly identical with two asperities over a 45 by 40 km fault plane at about 110 km depth. The model is already trimmed using approx. 15-20% of maximum slip as limit.
8	Tocopilla 2007	Interface	7.75	Schurr et al. (2012)	6.24E+20	-22.3421	-70.0235	49.844	This model is preferred because uses the most complete dataset. Hypocenter was relocated to be consistent with the FFM.
9	Punitaqui 1997	Intraslab	7.09	**FFM not available**	4.92E+19	-31.02	-71.23	68.0	Seismic moment and hypocenter location from Pardo et al. (2002). Strike, dip and rake from CMT catalog (consistent with Gardi et al. 2006).

*** M** based on seismic moment from the CMT catalog,

Table 4.6 Summary of fault rupture plane parameters for the preferred FFMs.

#	Earthquake	M	Finite Fault Model	strike (°)	dip (°)	rake (°)	Slip (cm)		Rupture dimensions				Bottom-left corner *		
							Max	Trimmed	L (km)	W (km)	A (km²)	L/W	lat (°)	lon (°)	Z_{TOR} (km)
1	Maule 2010	8.81	Delouis et al. (2010)	15.0	18.0	109.33	2129	319	480	160	76800	3.0	-37.9013	-74.5714	0.74
2	Arequipa 2001	8.41	Lay et al. (2010)	310.0	18.0	62.0	N/A	N/A	264	145	38280	1.8	-18.1438	-72.4969	0.24
3	Illapel 2015	8.31	Melgar et al. (2016)	3.7	N/A	N/A	1070	161	240	50	24470	N/A	-32.1323	-72.6559	~7.40
									140	38			-31.6209	-72.098	~16.51
									130	55			-31.9660	-71.7437	~27.62
4	Iquique 2014	8.15	Lay et al. (2014)	357.0	18.0	N/A	670	101	157.5	105	16538	1.5	-20.3422	-71.0114	12.20
5	Antofagasta 1995	8.02	Shao and Ji (1995)	4.0	18.0	N/A	387	58	180	91	24180	N/A	-24.9535	-71.4106	9.10
									150	52			-24.3346	-70.5125	37.21
6	Valparaiso 1985	7.98	Mendoza et al. (1994)	5.0	15.0	90.0	329	49	255	75	29925	N/A	-34.6053	-72.809	6.4
					30.0	110.0			180	60			-34.1241	-71.9772	25.81
7	Tarapaca 2005	7.78	Kuge et al. (2010)	187.0	23.0	-73.0	>1000	200	47.5	45	2138	1.1	-19.8061	-69.0518	101.21
8	Tocopilla 2007	7.75	Schurr et al. (2012)	3.0	20.0	98.0	258	39	180	60	10800	3.0	-23.2347	-70.5316	32.78
9	Punitaqui 1997	7.09	**FFM not available**	173.0	80.0	-83.0	N/A	N/A	N/A	N/A	N/A	N/A	N/A	N/A	N/A

* Bottom-left corner of the rectangle looking in the direction of the strike (see Figure 4.5). N/A = not available / not applicable.

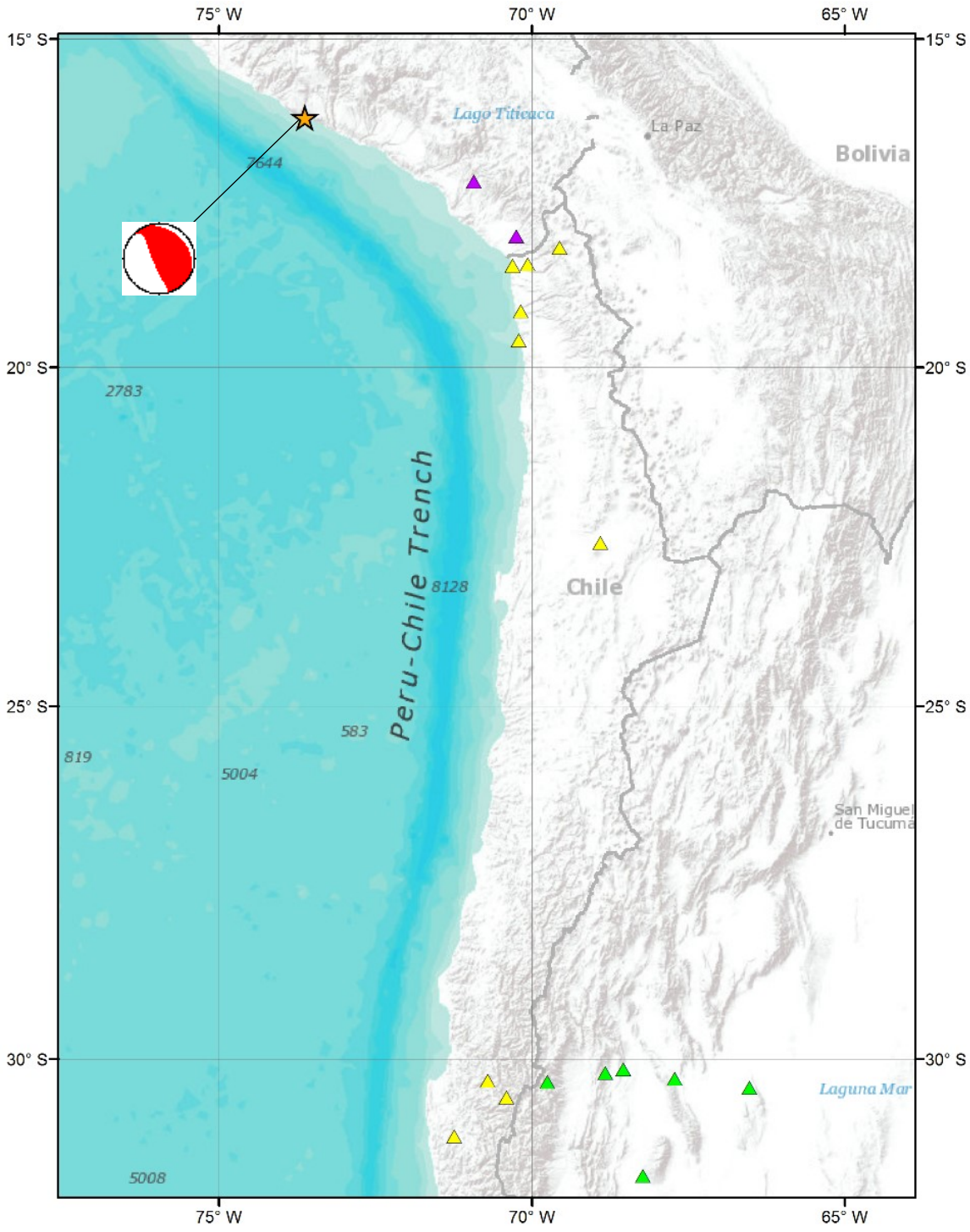

Figure 4.6 Map of the 2001 **M** 8.4 Arequipa earthquake showing the hypocenter (star), the mechanism from the CMT, and the SMR stations located in Chile (yellow triangles) with recordings included in the NGA-Subduction database. SMR stations in Argentina (green triangles) and in Peru (purple triangles) are also shown.

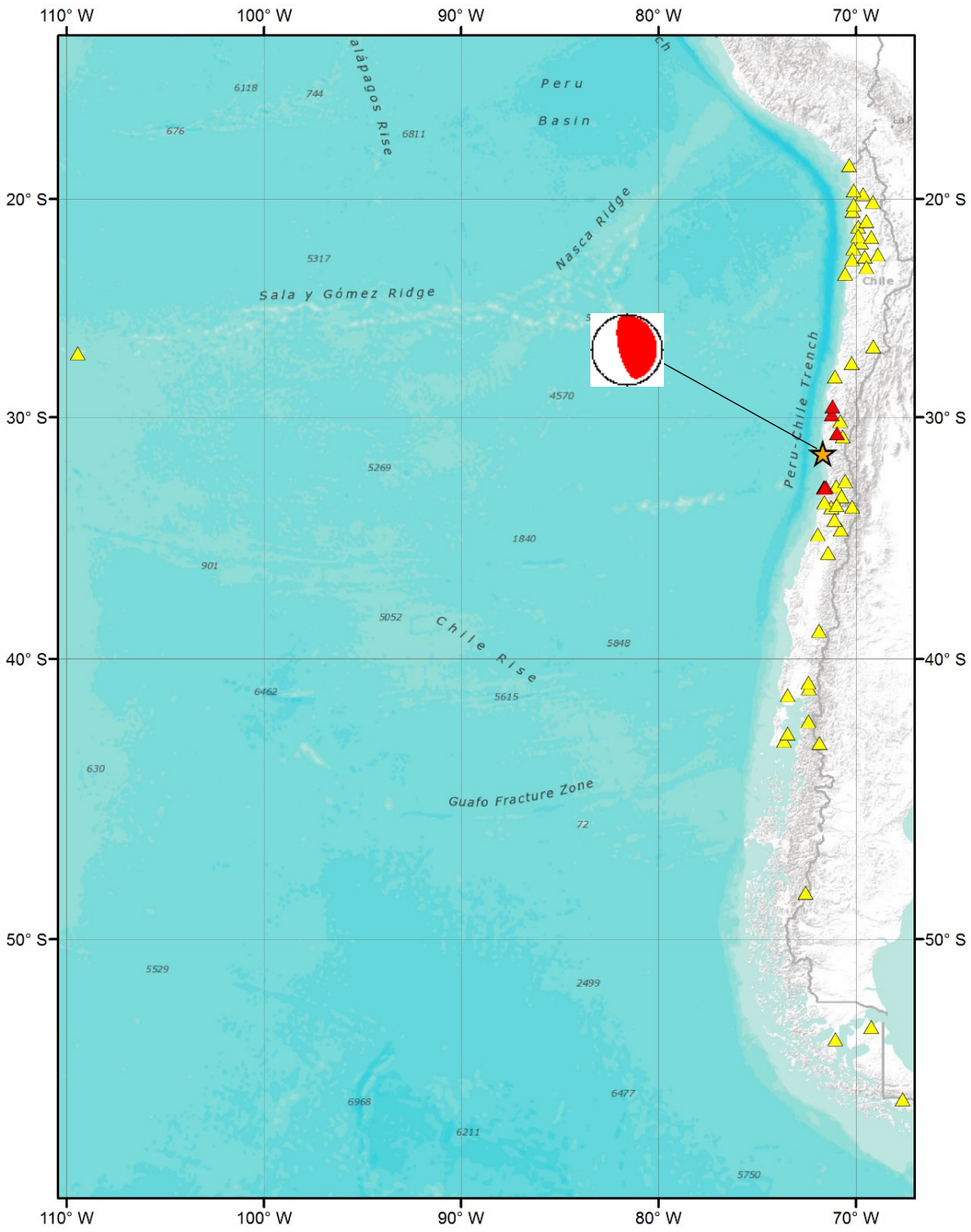

Figure 4.7 Map of the 2015 **M** 8.3 Illapel earthquake showing the hypocenter (star), the mechanism from the CMT, and the SMR stations located in Chile with recordings included (yellow triangles) and not included (red triangles) in the NGA-Subduction database.

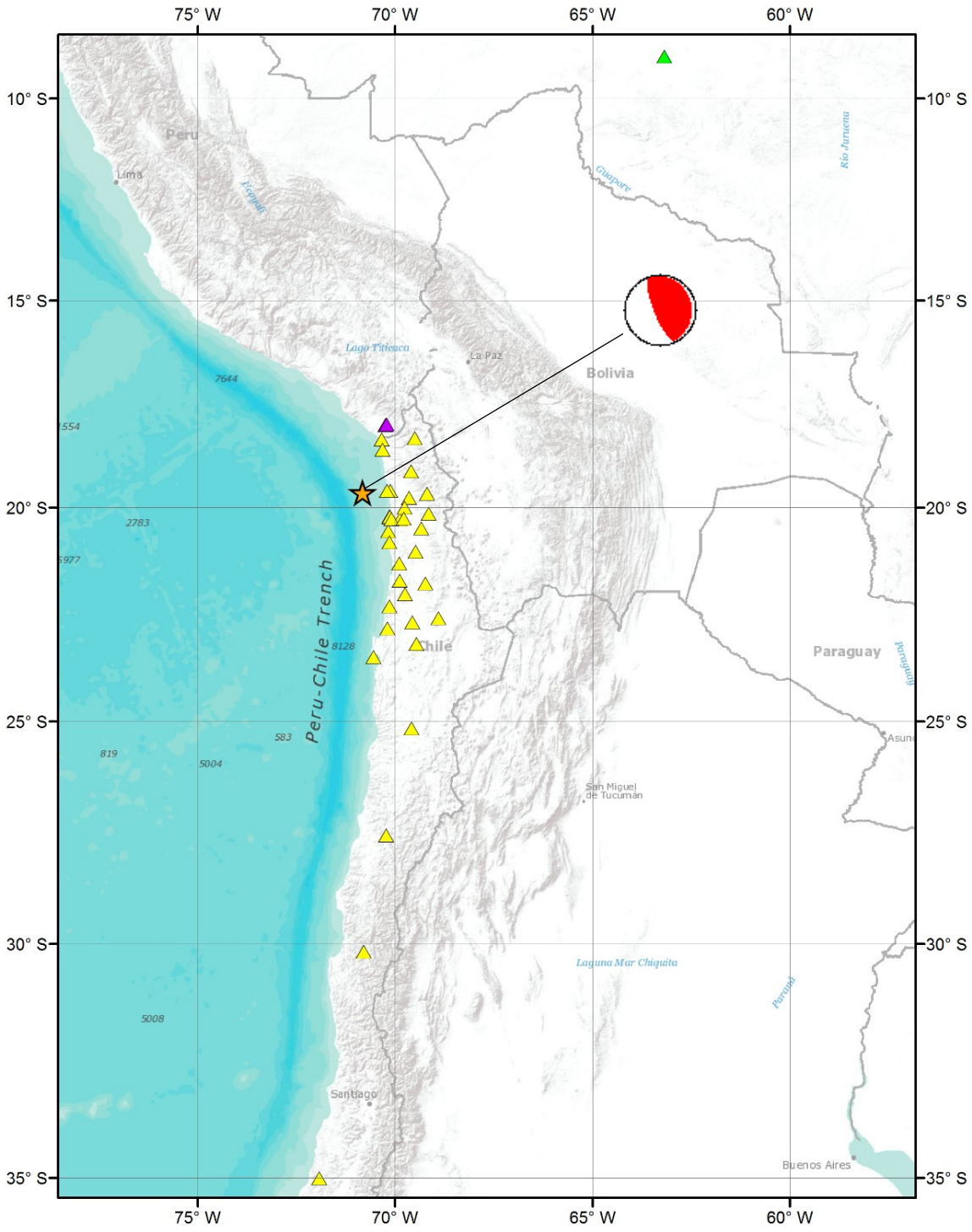

Figure 4.8 Map of the 2014 **M** 8.1 Iquique earthquake showing the hypocenter (star), the mechanism from the CMT, and the SMR stations located in Chile (yellow triangles) with recordings included in the NGA-Subduction database. SMR stations in Peru (purple triangles) and Brazil (green triangle) are also shown.

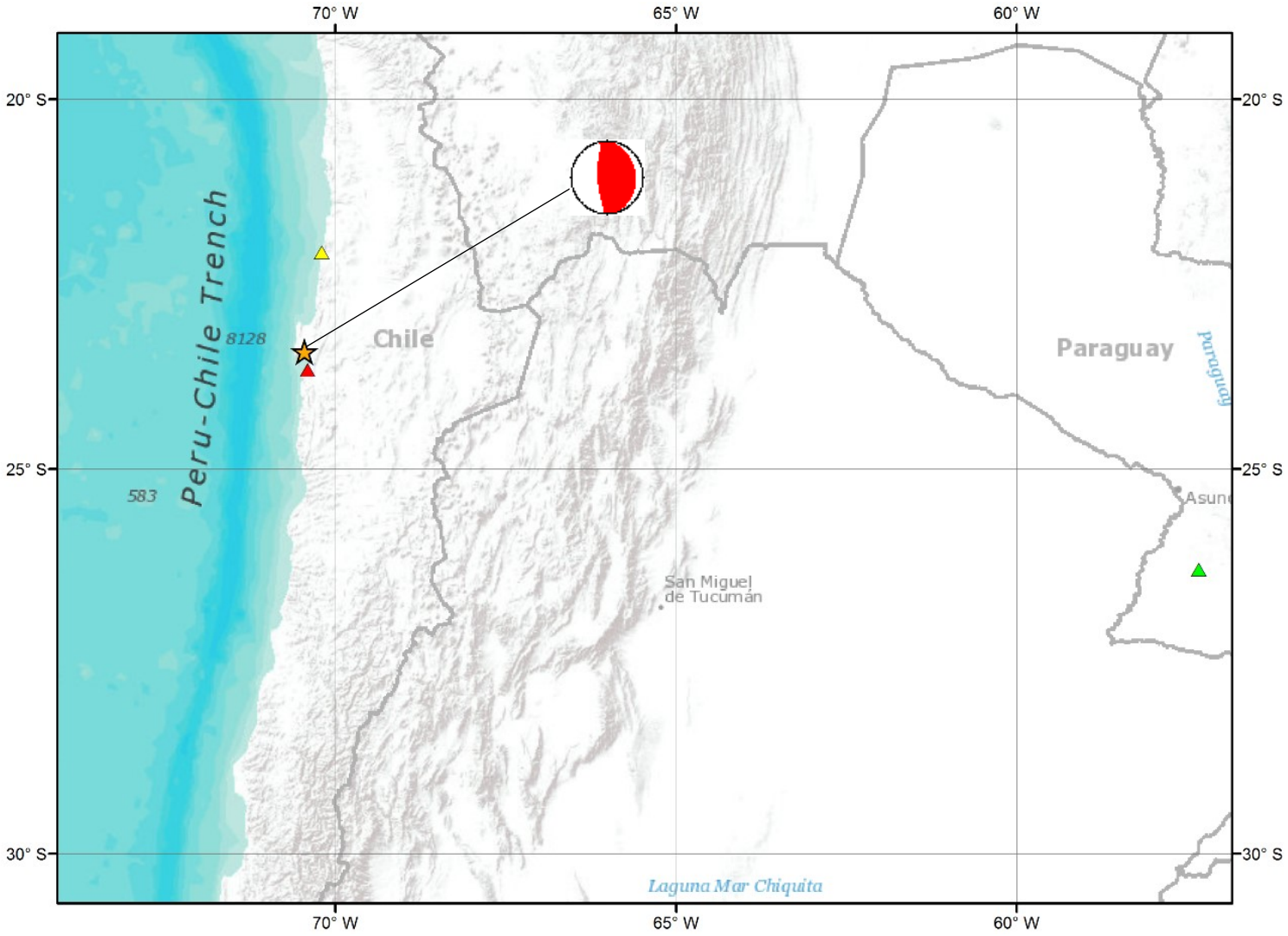

Figure 4.9 Map of the 1995 **M** 8.0 Antofagasta earthquake showing the hypocenter (star), the mechanism from the CMT, and the SMR stations located in Chile with recordings included (yellow triangles) and not included (red triangles) in the NGA-Subduction database. A SMR station in Paraguay (green triangle) is also shown.

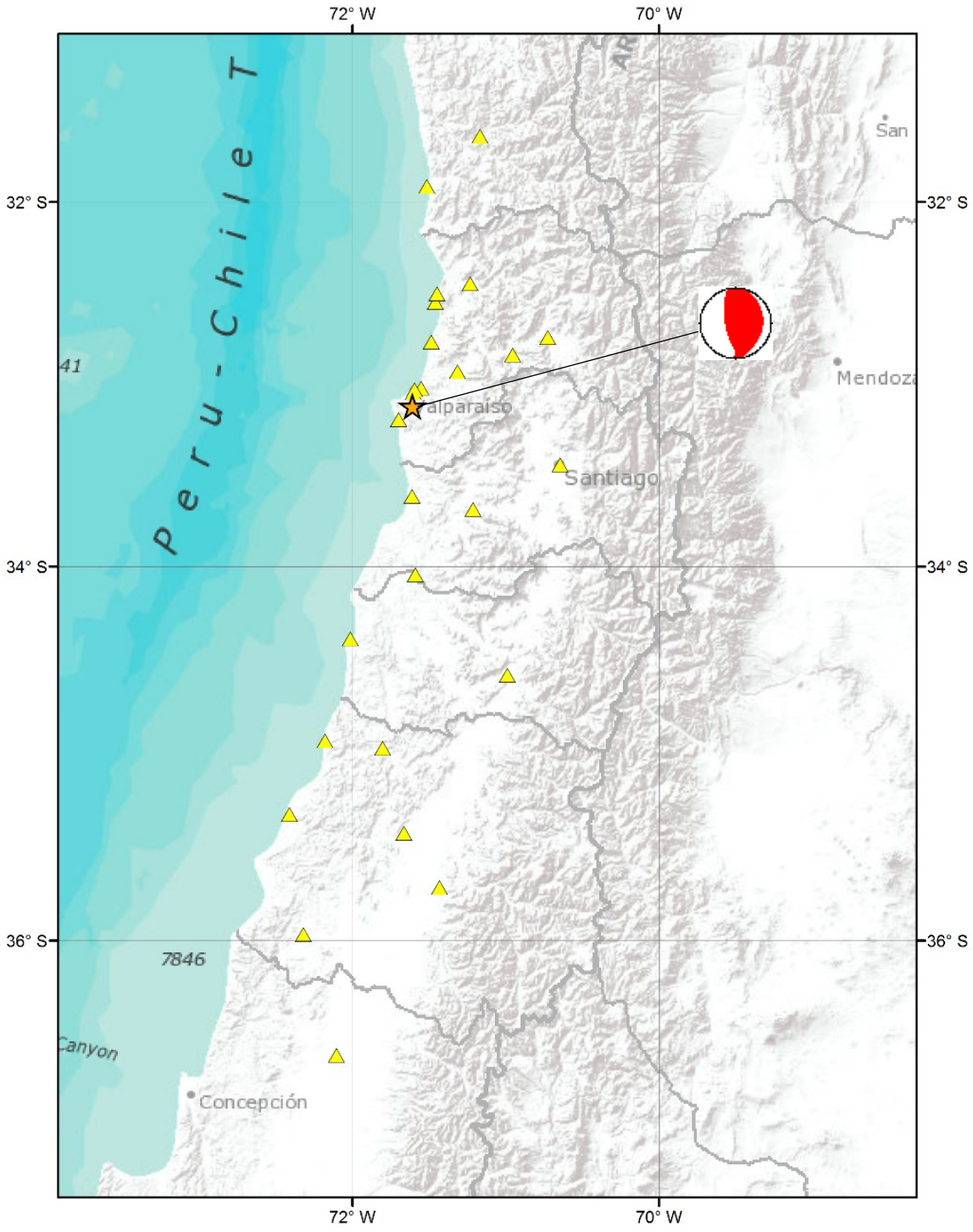

Figure 4.10 Map of the 1985 **M** 7.9 Valparaiso earthquake showing the hypocenter (star), the mechanism from the CMT, and the SMR stations located in Chile (yellow triangles) with recordings included in the NGA-Subduction database.

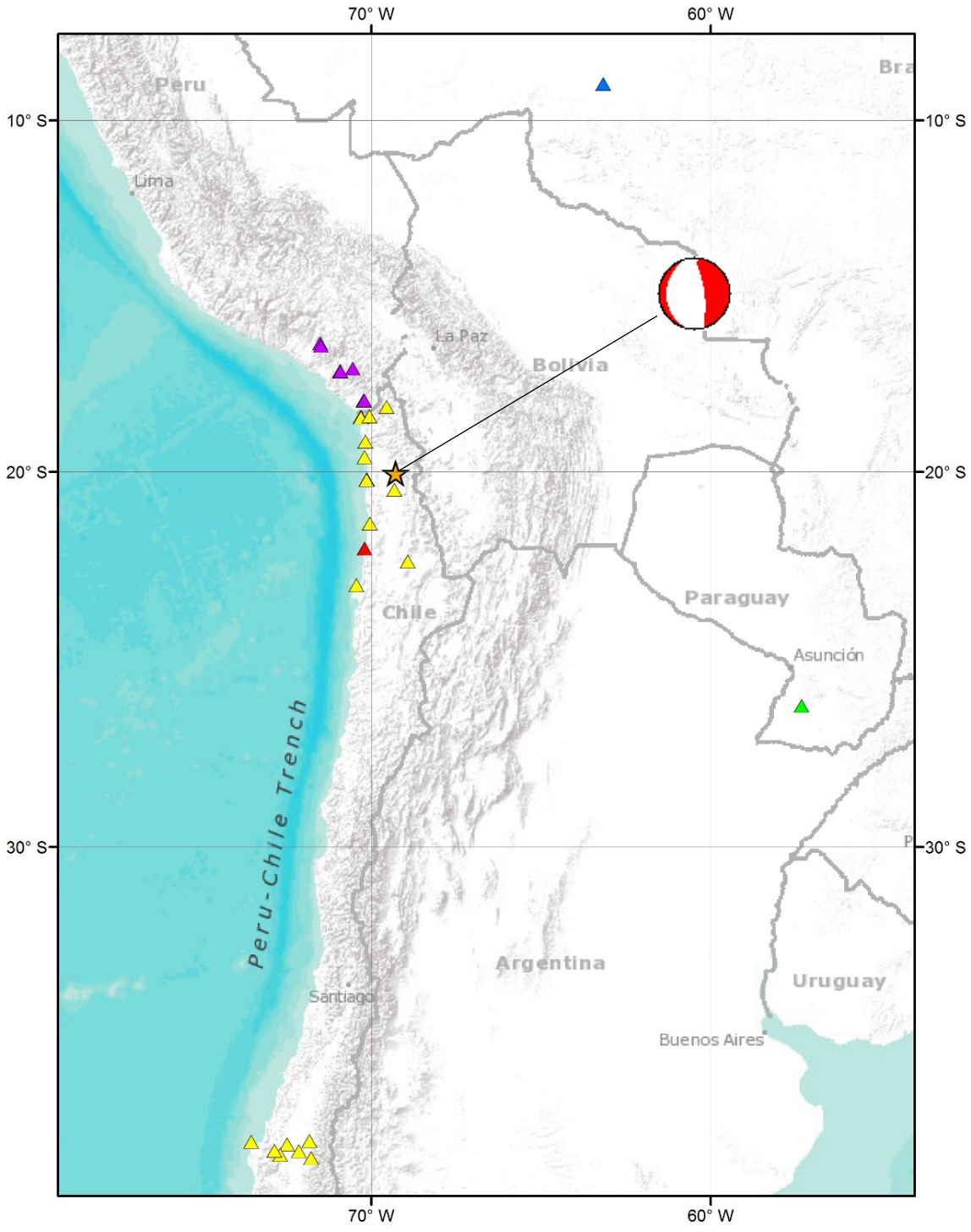

Figure 4.11 Map of the 2005 **M** 7.8 Tarapacá earthquake showing the hypocenter (star), the mechanism from the CMT, and the SMR stations located in Chile with recordings included (yellow triangles) and not included (red triangles) in the NGA-Subduction database. SMR stations in Paraguay (green triangle) and in Brazil (blue triangle) are also shown.

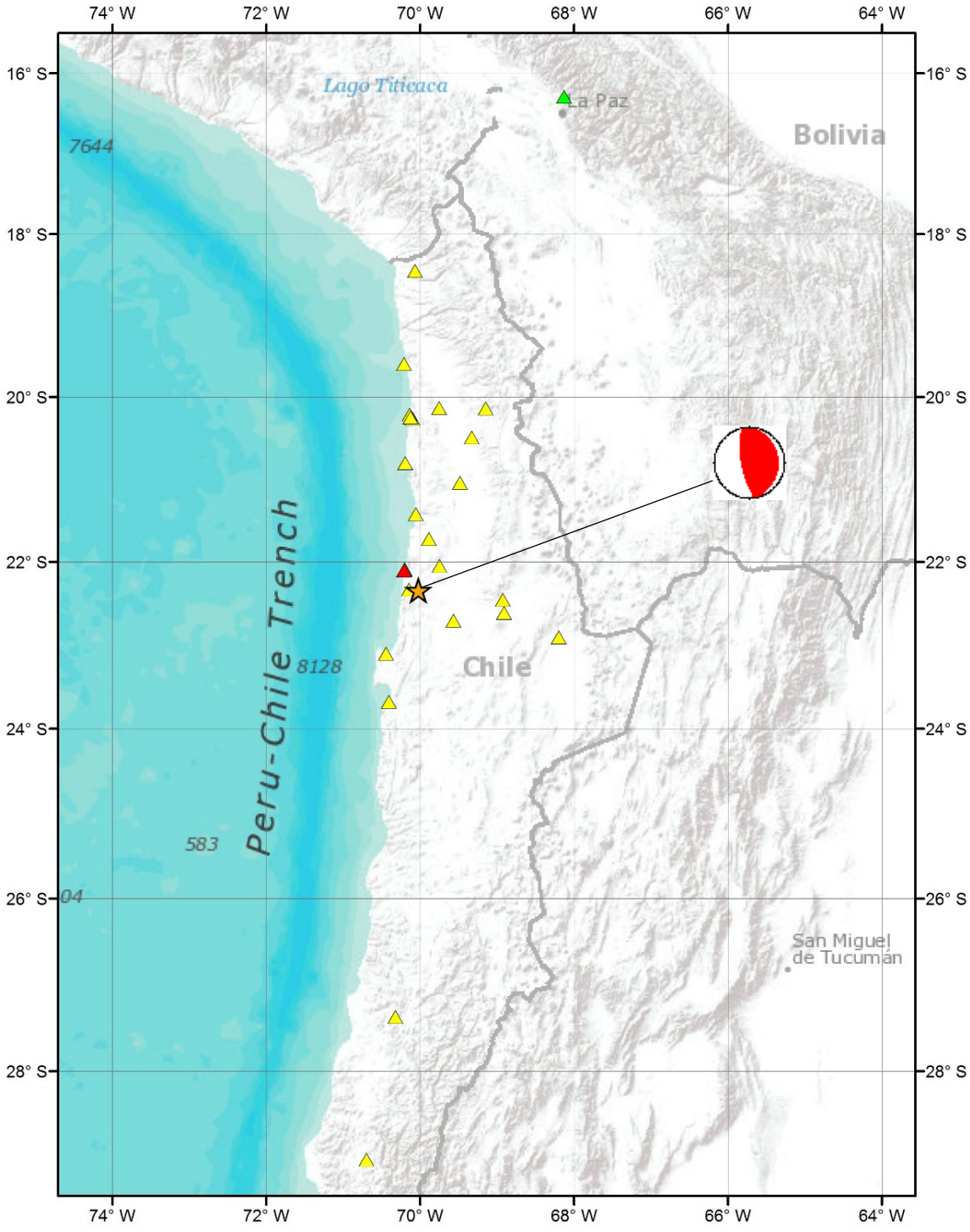

Figure 4.12 Map of the 2007 **M** 7.7 Tocopilla earthquake showing the hypocenter (star), the mechanism from the CMT, and the SMR stations located in Chile with recordings included (yellow triangles) and not included (red triangles) in the NGA-Subduction database. A SMR station in Bolivia (green triangle) is also shown.

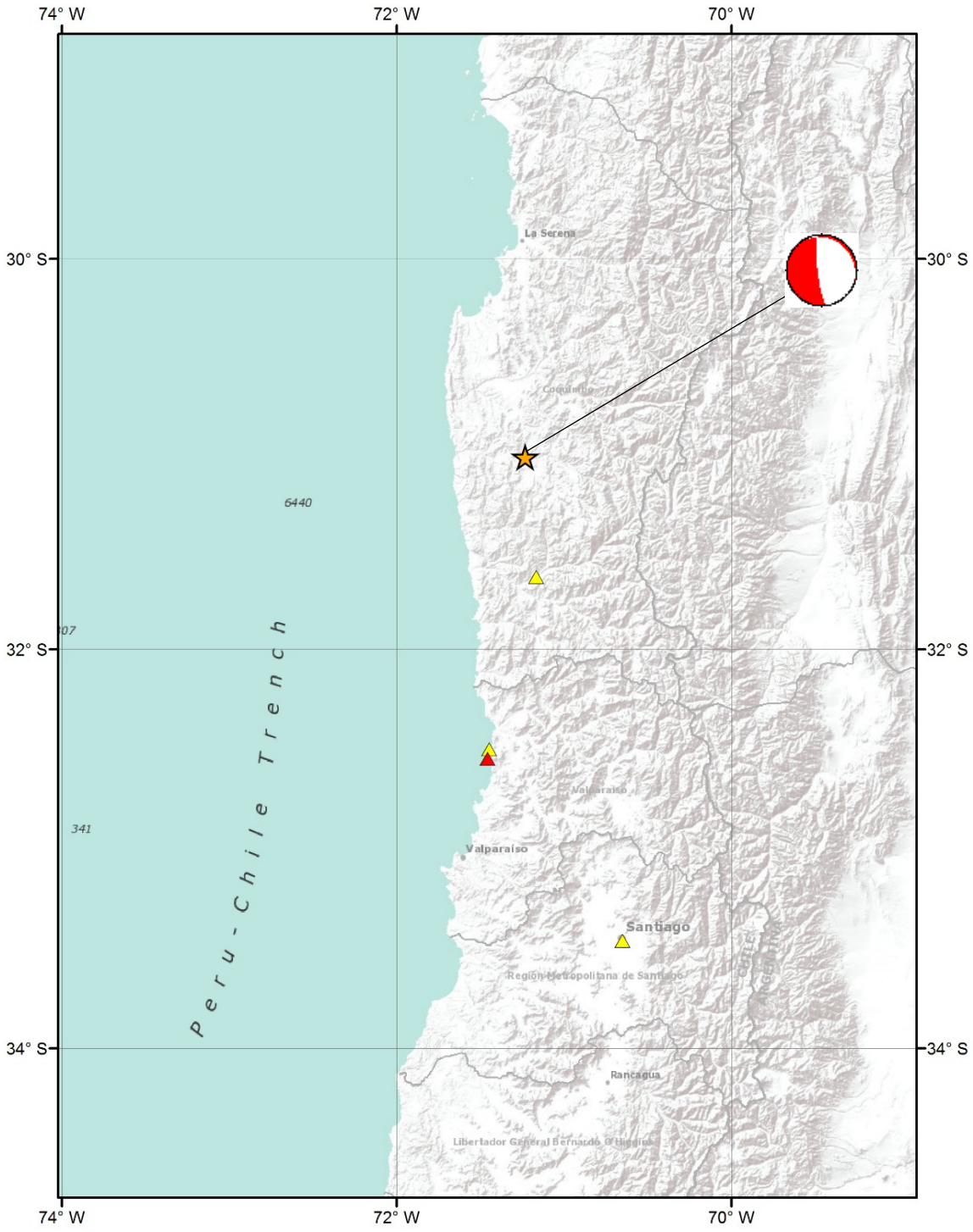

Figure 4.13 Map of the 1997 **M** 7.1 Punitaqui earthquake showing the hypocenter (star), the mechanism from the CMT, and the SMR stations located in Chile with recordings included (yellow triangles) and not included (red triangles) in the NGA-Subduction database.

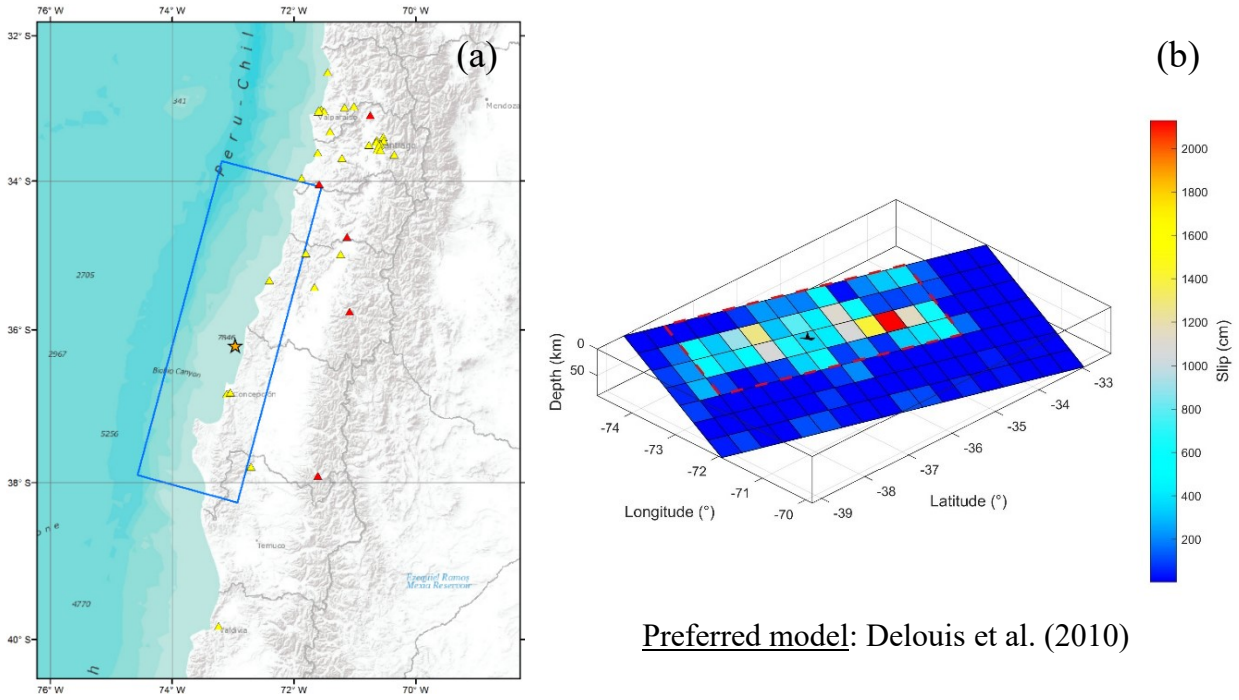

Figure 4.14 Preferred FFM for the 2010 **M** 8.8 Maule earthquake: (a) Map showing the epicenter, the fault rupture plane, and the SMR stations closest to the fault; (b) Finite fault slip distribution and applied trimming (red dashed line).

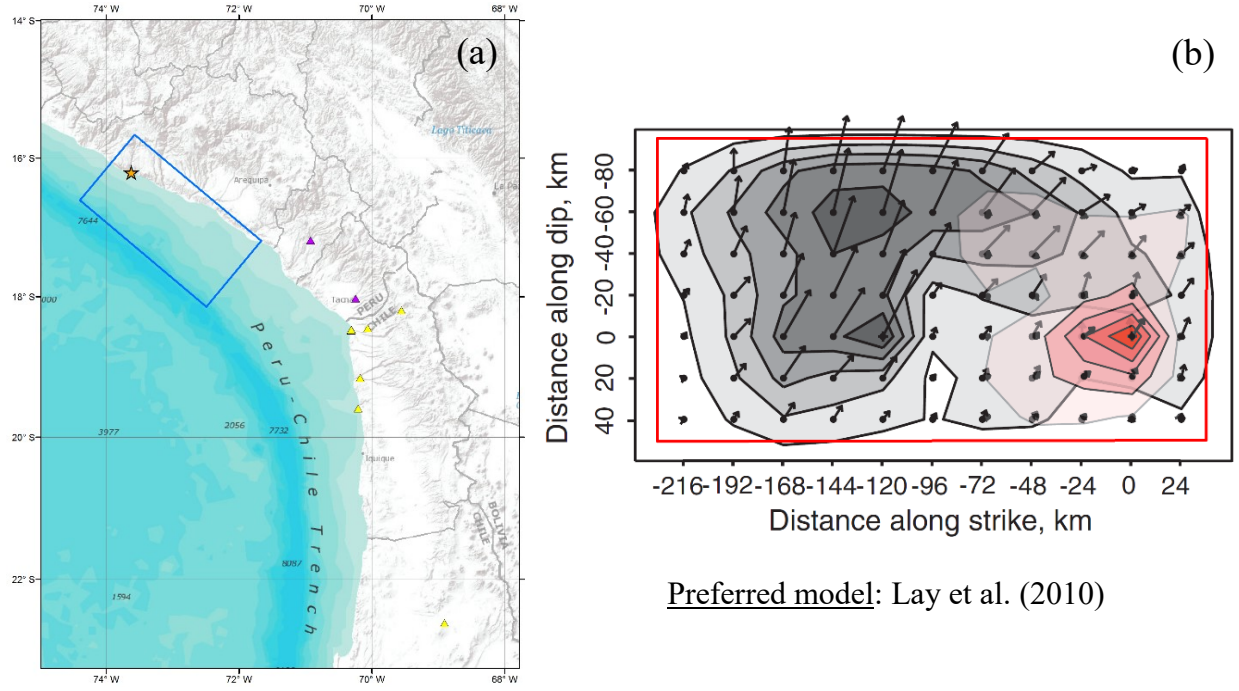

Figure 4.15 Preferred FFM for the 2001 **M** 8.4 Arequipa earthquake: (a) Map showing the epicenter, the fault rupture plane, and the SMR stations closest to the fault; (b) Finite fault slip distribution and applied trimming (red line).

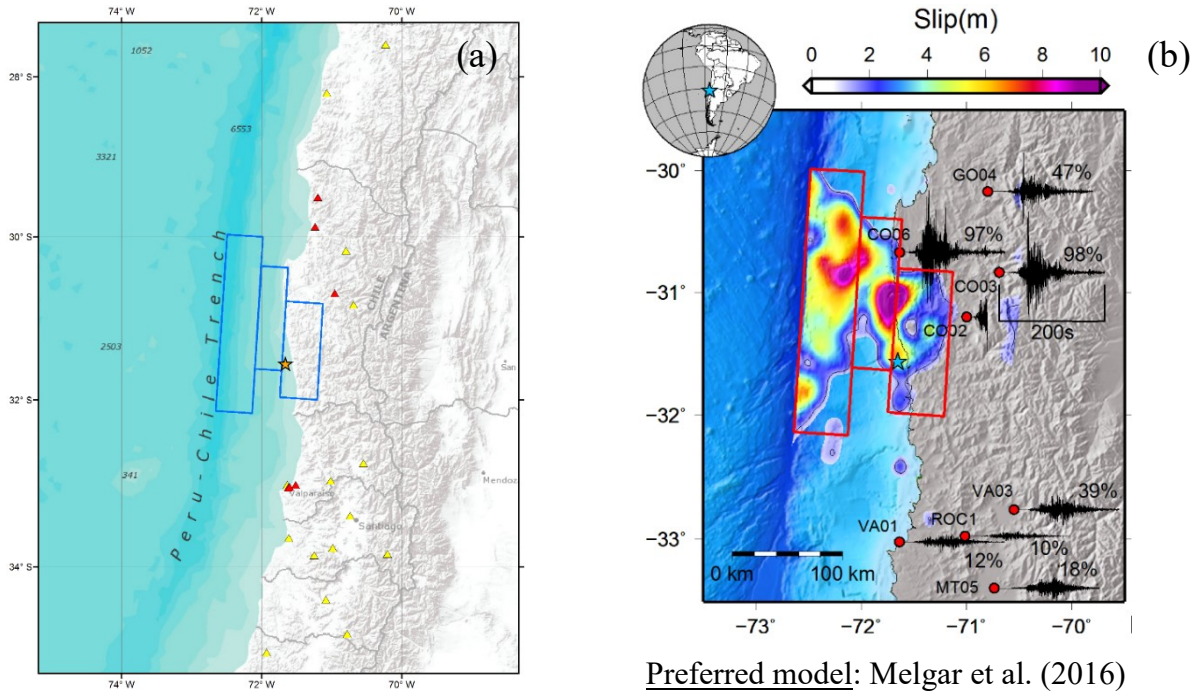

Preferred model: Melgar et al. (2016)

Figure 4.16 Preferred FFM for the 2015 **M** 8.3 Illapel earthquake: (a) Map showing the epicenter, the fault rupture plane, and the SMR stations closest to the fault; (b) Finite fault slip distribution and applied trimming (red line).

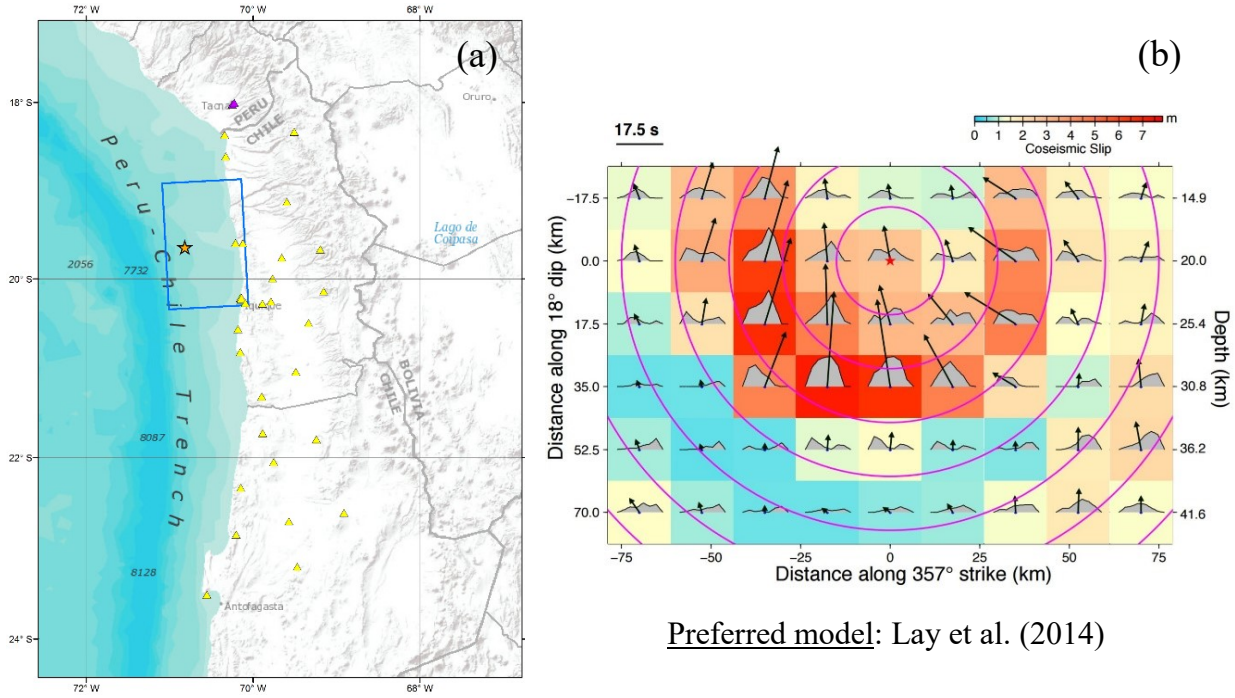

Preferred model: Lay et al. (2014)

Figure 4.17 Preferred FFM for the 2014 **M** 8.1 Iquique earthquake: (a) Map showing the epicenter, the fault rupture plane, and the SMR stations closest to the fault; (b) Finite fault slip distribution. (FFM is already trimmed by the authors).

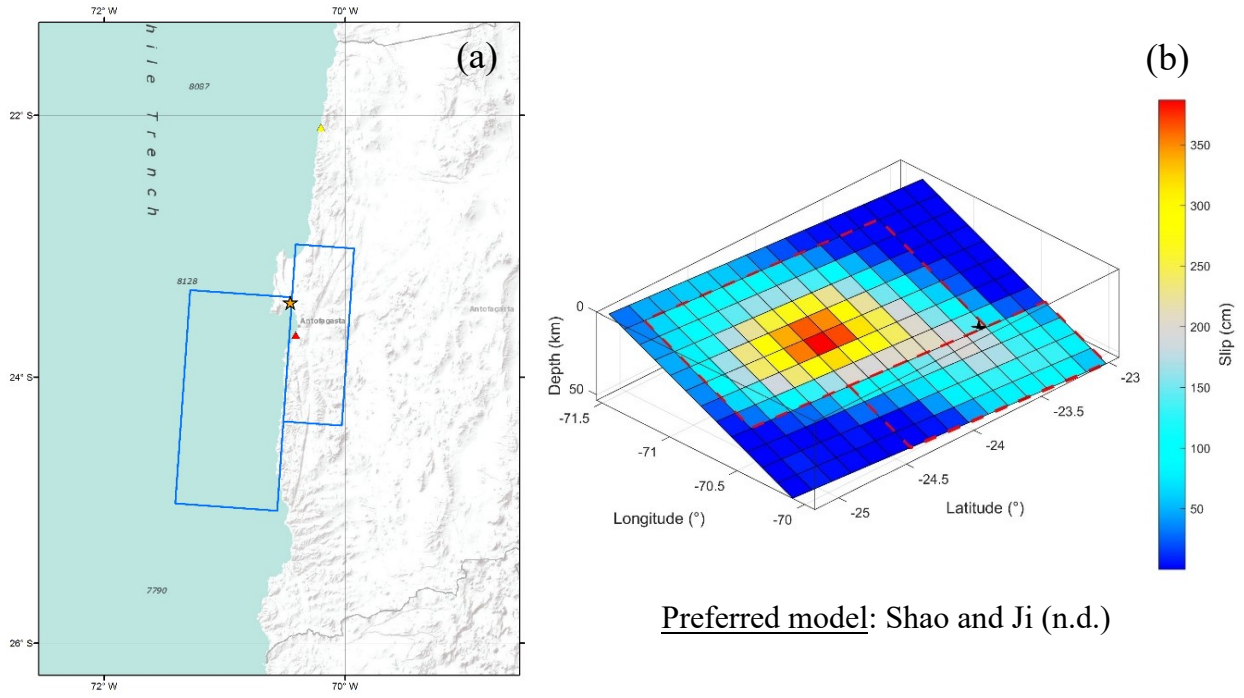

Figure 4.18 Preferred FFM for the 1995 **M** 8.0 Antofagasta earthquake: (a) Map showing the epicenter, the fault rupture plane, and the SMR stations closest to the fault; (b) Finite fault slip distribution and applied trimming (red dashed line).

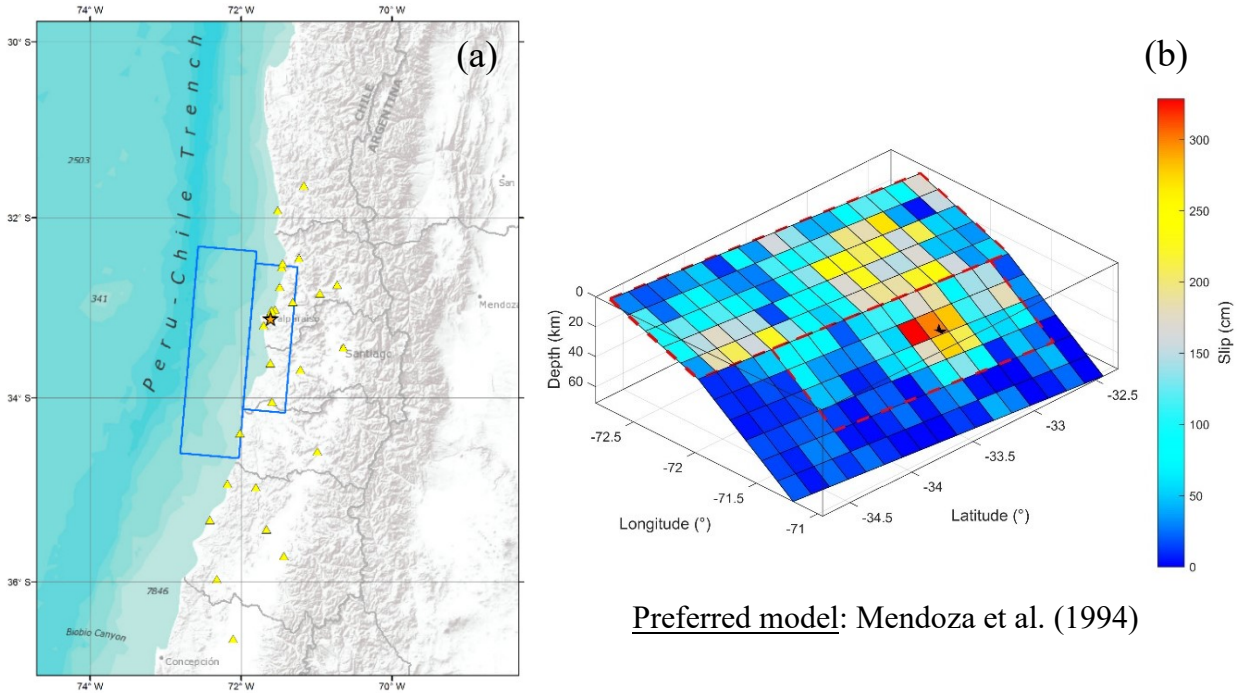

Figure 4.19 Preferred FFM for the 1985 **M** 7.9 Valparaíso earthquake: (a) Map showing the epicenter, the fault rupture plane, and the SMR stations closest to the fault; (b) Finite fault slip distribution and applied trimming (red dashed line).

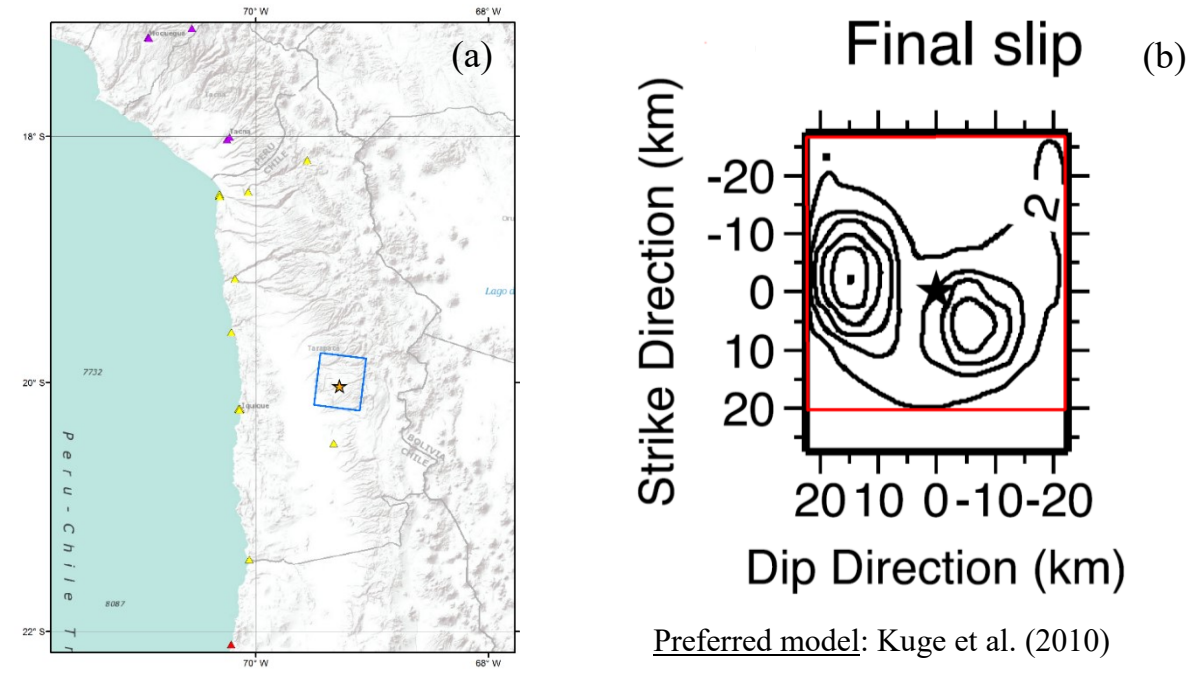

Figure 4.20 Preferred FFM for the 2005 **M** 7.8 Tarapacá earthquake: (a) Map showing the epicenter, the fault rupture plane, and the SMR stations closest to the fault; (b) Finite fault slip distribution and applied trimming (red line).

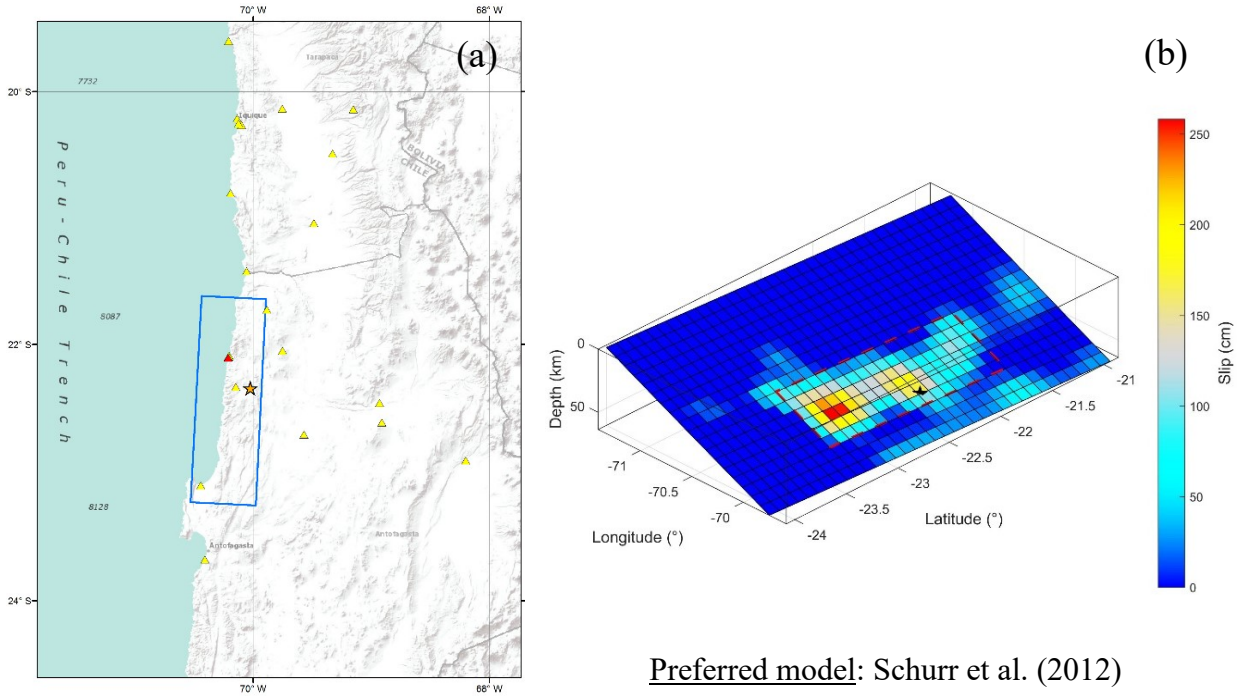

Figure 4.21 Preferred FFM for the 2007 **M** 7.7 Tocopilla earthquake: (a) Map showing the epicenter, the fault rupture plane, and the SMR stations closest to the fault; (b) Finite fault slip distribution and applied trimming (red dashed line).

FFMs are not available from the literature for the 1997 **M** 7.1 Punitaqui earthquake (intraslab event). However, some features regarding the fault rupture plane are inferred from the compiled references. Figure 4.22 (Gardi et al., 2016) shows the approximate location of the rupture for this earthquake, which is close to a vertical plane (dip angle is 80°, approximately). This is consistent with the solution from the CMT catalog.

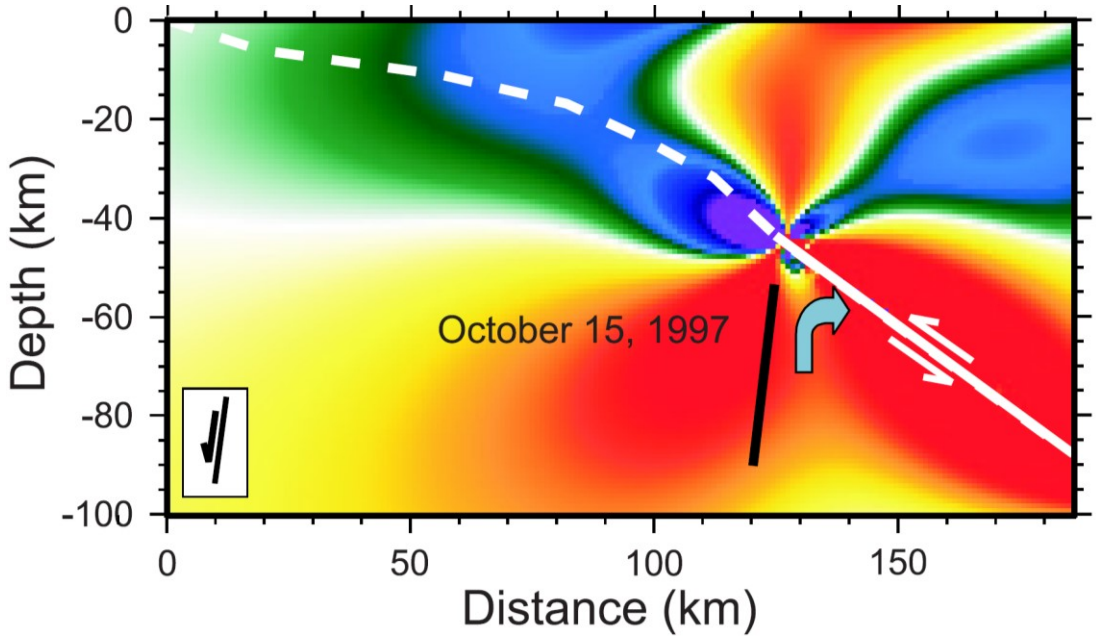

Figure 4.22 Coulomb stress changes on the 1997 Punitaqui fault. The black line represents the rupture of the Punitaqui event (from Gardi et al., 2006).

Figure 4.23 shows the magnitude-distance distributions for the nine events studied in this section and listed in Table 4.1. Results are shown for the full distance range and for rupture distances up to 500 km. These data occupy a very important portion of the parameter space for model development, filling in gaps present between **M** 8 and 8.8 that would otherwise be present.

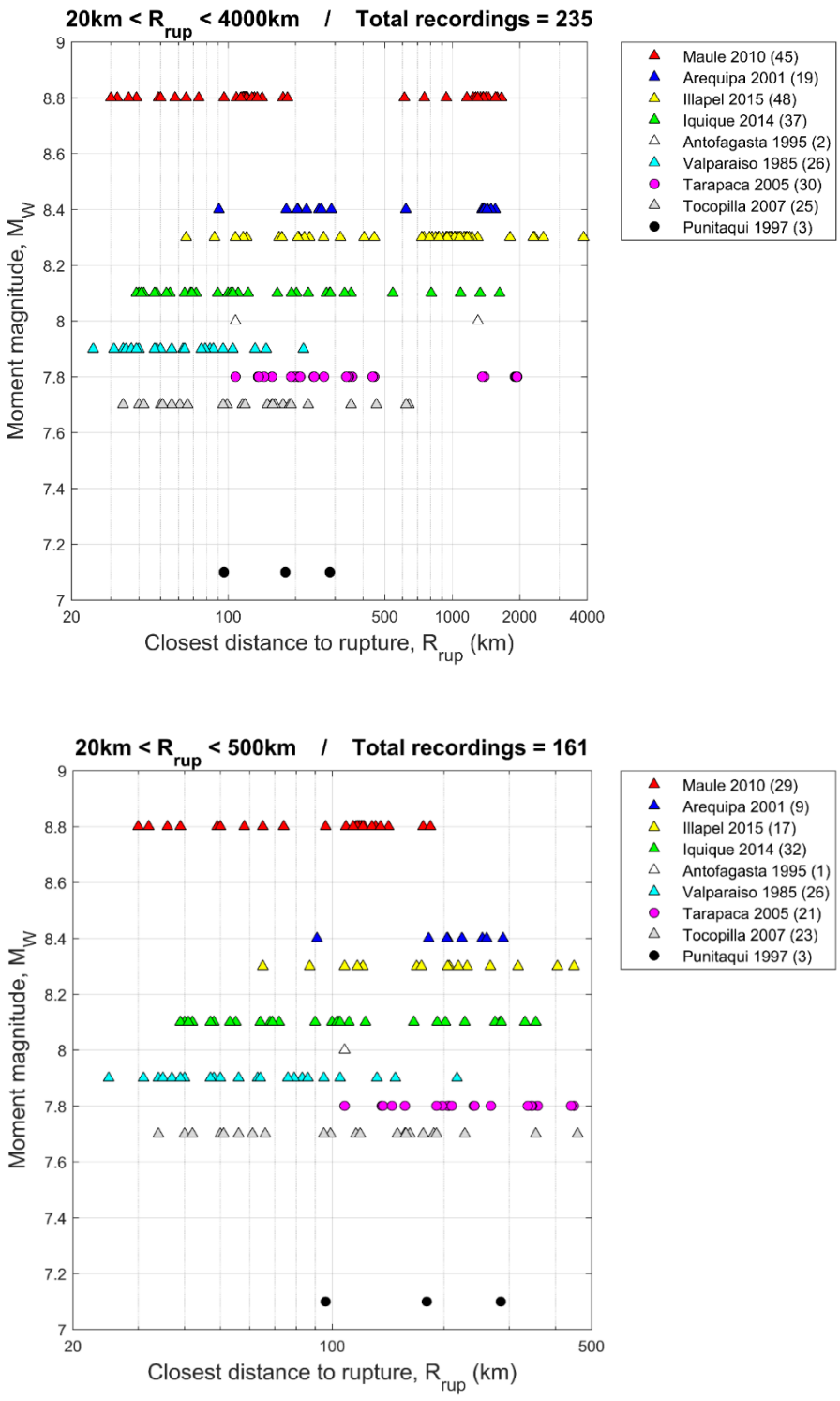

Figure 4.23 Data distribution in magnitude-closest distance space using full data range (top) and limiting distance of 500 km (bottom). Triangles are data from interface events, whereas circles are data from intraslab earthquakes.

Having developed preferred FFMs for the eight events in Table 4.5, we sought to test the degree to which the resulting rupture surface areas are consistent with those found in other global subduction zones. This test is most readily performed for interface events, for which we have seven models. We considered two data sources for non-Chilean events:

1. Finite fault models presented by Skarlatoudis et al. (2016) for interface subduction zone earthquakes, who also present magnitude-area scaling relations derived from the data.
2. Finite fault models developed within the NGA-Subduction project for Japanese events by Tadahiro Kishida (*personal communication*, June 2017). The protocols used in this work match those described here for the Chilean events.

In some cases, events considered by Skarlatoudis et al. (2016) match those considered in this work (Chile) and by Kishida (Japan), in which case the values developed in NGA-Subduction are used. Figure 4.24 shows the resulting data points and the results of a regression fit performed using the following equation:

$$\log_{10} RA = a_0 + \mathbf{M} \qquad (\sigma_{\ln} = 0.62) \qquad \text{Equation 4-2}$$

where RA is rupture area in km^2 and a_0 = -3.829 is the regression parameter. Note that self-similarity is assumed, which is typical in models of this sort, meaning that the coefficient in front of **M** is unity.

The fit provided by Skarlatoudis et al. (2016) was on RA directly, not its logarithm. Accordingly, Eq. 4-2 fits the mean of the log of the data, which is lower for a log-normally distributed quantity. This explains why the fit using Eq. 4-2 falls below that of Skarlatoudis et al. (2016). Our fit essentially matches that of Murotani et al. (2013).

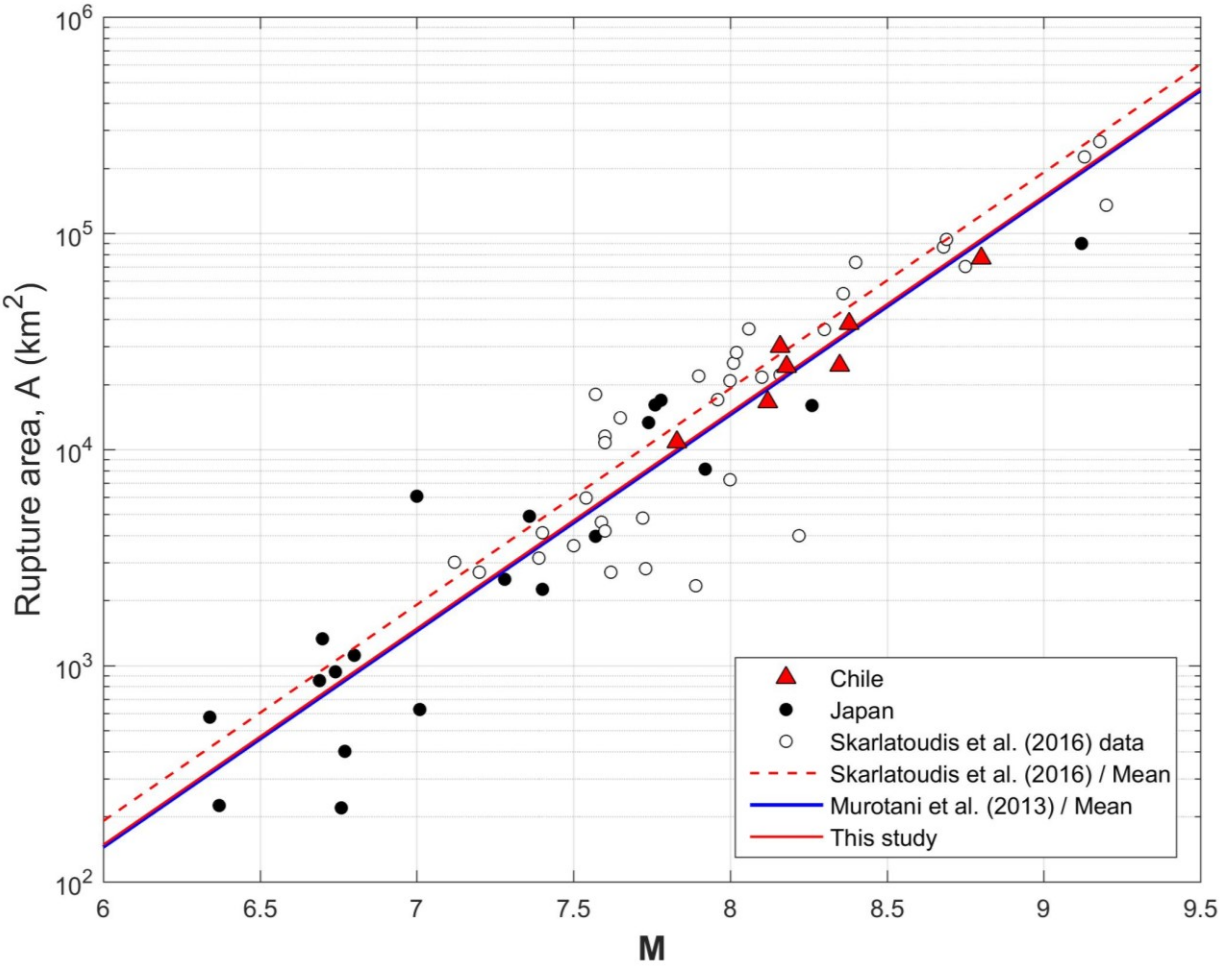

Figure 4.24 Data and model fits for rupture area vs **M** from Skarlatoudis et al. (2016) and NGA-Subduction studies for Japan and Chile events. Fit per Eq. 4-2 is shown along with prior models by Skarlatoudis et al. (2016) (fit is on *RA*, not log *RA*) and Murotani et al. (2013).

4.2 Source parameters for earthquakes without finite fault models

In this section, we describe the methodology used to characterize source characteristics for events without an available FFM in the literature. There are three objectives:

1. Identify seismic moment, moment magnitude, focal mechanism, and hypocenter location.
2. Identify sources as interface, intraslab, outer-rise, or shallow crustal.
3. Estimate fault dimensions and approximate position of rupture to facilitate calculation of source-to-site distances.

The seismic moment (M_0) was collected from the agencies mentioned in the preceding section (CMT, NEIC, ISC and CSN) and the information from the CMT catalog was preferred, when available. The moment magnitude **M** is computed using the equation from Hanks and Kanamori (1977, Equation 4-1). For those events without a reported M_0 value, linear relationships between different magnitude scales are utilized to estimate **M**. These relations, shown in the following equations and in Figure 4.25 and Figure 4.26, have been developed by Bastías and Montalva (2016) and Leyton et al. (2009) using only information from Chilean earthquakes. These correlations were developed for M_W whereas we use **M**. Accordingly, we increase intercept terms by 0.033 in the relations that follow:

Modified from Bastías and Montalva (2016)	$\mathbf{M} = 0.915M_L + 0.524 \quad (\sigma = 0.26)$	Equation 4-3
	$\mathbf{M} = 0.847M_L + 0.727 \quad (\sigma = 0.25)$	Equation 4-4
Modified from Leyton et al. (2009)	$\mathbf{M} = 0.887M_S + 1.095$	Equation 4-5
	$\mathbf{M} = 1.173m_b - 0.634$	Equation 4-6

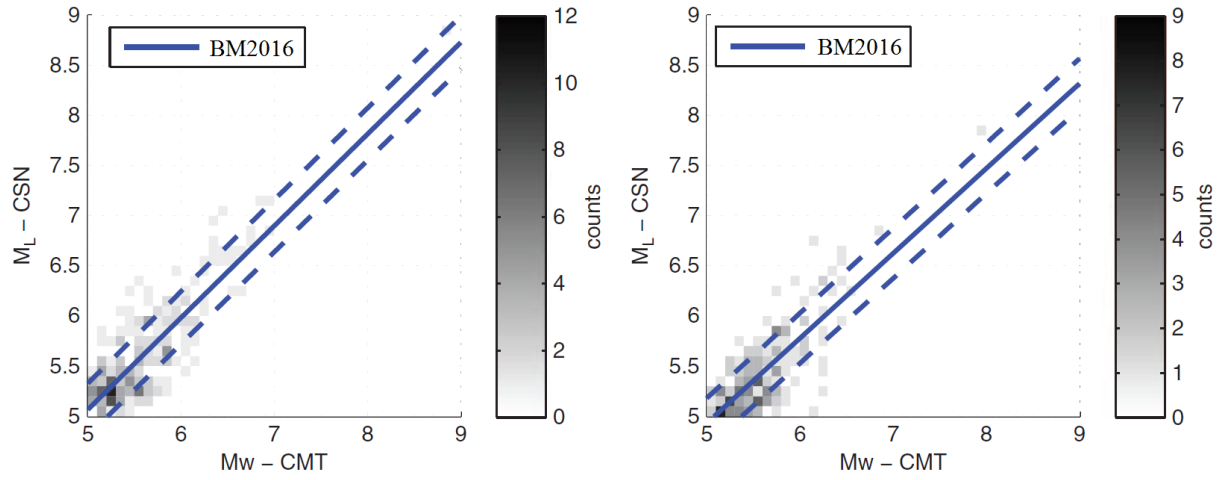

Figure 4.25 M_W-M_L relationships from Bastías and Montalva (2016). Left: Eq. 4-3 for shallow-focus earthquakes ($H \leq 50$ km); Right: Eq. 4-4 for deep-focus earthquakes ($H > 50$ km). We use a slightly modified form of the relation (shifted up 0.033 to reflect **M**).

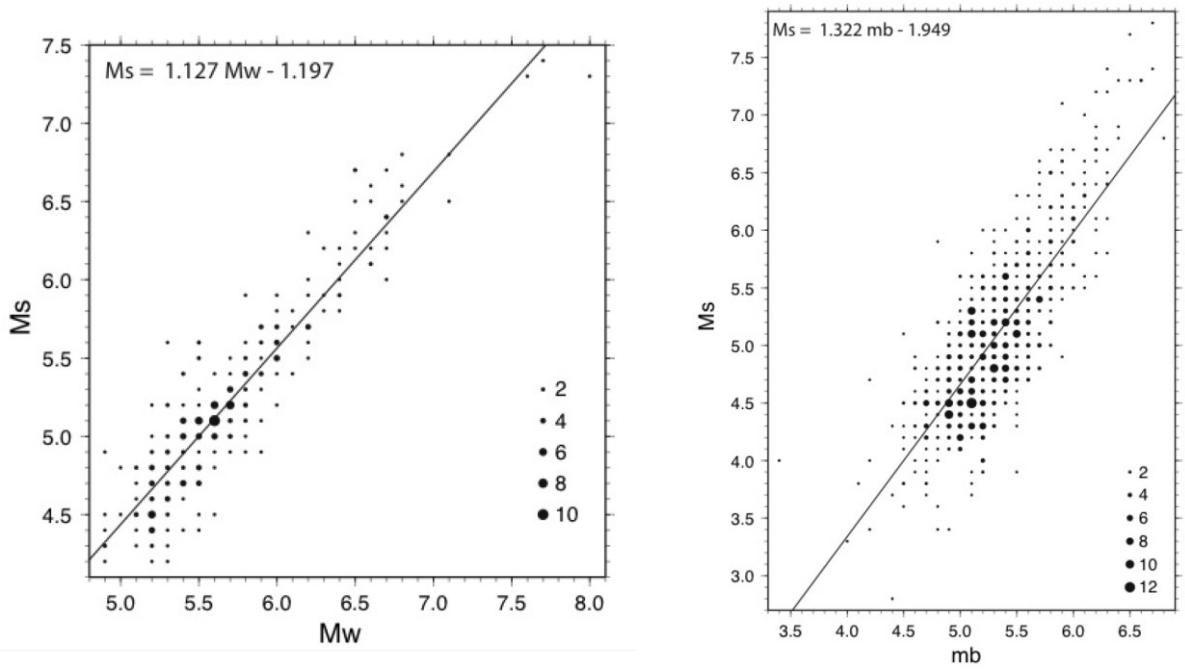

Figure 4.26 M_S-M_W and M_S-m_b relations from Leyton et al. (2009) Left: Eq. 4-5; Right: Original M_S-m_b relation reported by the authors. We use a slightly modified form of the M_S-M_W relation (shifted up 0.033 to reflect **M**).

Hypocenter locations from the CSN, NEIC, and ISC catalogs were collected. We use local agency results (CSN) and where that is unavailable, we take hypocenter locations from ISC or NEIC, in this order. In addition, moment tensor solutions are compiled when available from the CMT and NEIC catalogs, identifying strike, dip and rake angles. In the future, we plan to augment this information with results from inversion studies, hypocenter relocation studies, or from the EBH catalog.

We employed an automated process to identify earthquake type (interface, intraslab, shallow crustal and outer-rise). This process considers the location of the hypocenter relative to the geometry of the Nazca plate defined by Hayes et al. (2012, Figure 4.27). Also considered is the event focal mechanism. Event classification are based on event location relative to the interface, as shown for Event 455 in Figure 4.28. The blue solid line is the geometry of the interface of the Nazca plate and the dashed lines represent the estimated error of the Hayes et al. (2012) model (±10 km). Three zones are defined:

i. Zone A: depth of the Nazca plate < 10 km

ii. Zone B: 10 km ≤ depth of the Nazca plate ≤ 55 km

iii. Zone C: depth of the Nazca plate > 55 km

Based on the event location, the classifications are as follows:

1. Outer rise: yellow area

2. Interface: cyan area

3. Intraslab: gray area (and probably all the earthquakes with H > 60 km)

4. Shallow crustal: green area

Following these assignments, results are checked using moment tensor solution. Interface earthquakes should have reverse mechanism. If an event near the interface is not reverse, we assign a shallow crustal designation. Procedures similar to these have been used previously by Poblete (2008) and Contreras (2009).

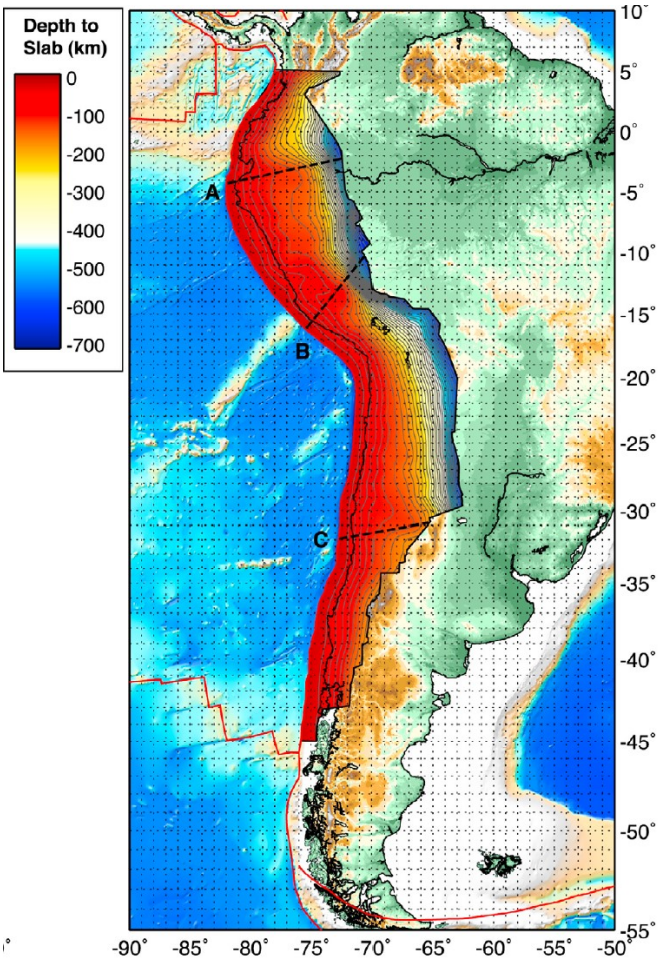

Figure 4.27 Subduction interface geometry of the Nazca plate from Hayes et al. (2012).

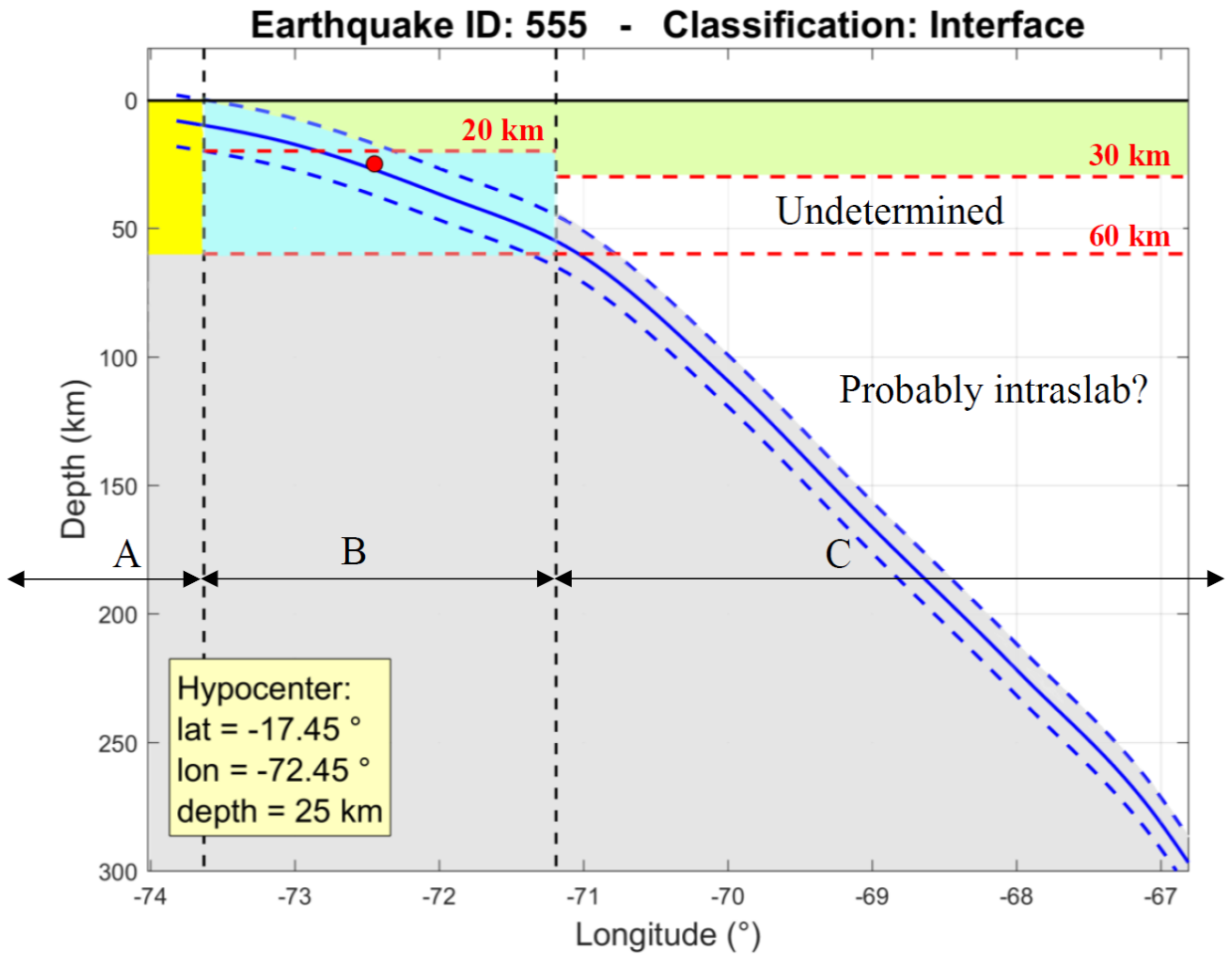

Figure 4.28 Event classification scheme based on hypocenter location relative to the interface of the of Nazca plate. Example event is Earthquake ID 555 – interface.

Figures 4.29 to 4.33 show examples of events classified as interface, intraslab, outer-rise, and shallow crustal. An event for which the classification is undetermined is also shown. We find 59% of events to be interface and 32% intra-slab. Figure 3.6 shows a map of Chile with events of different classification.

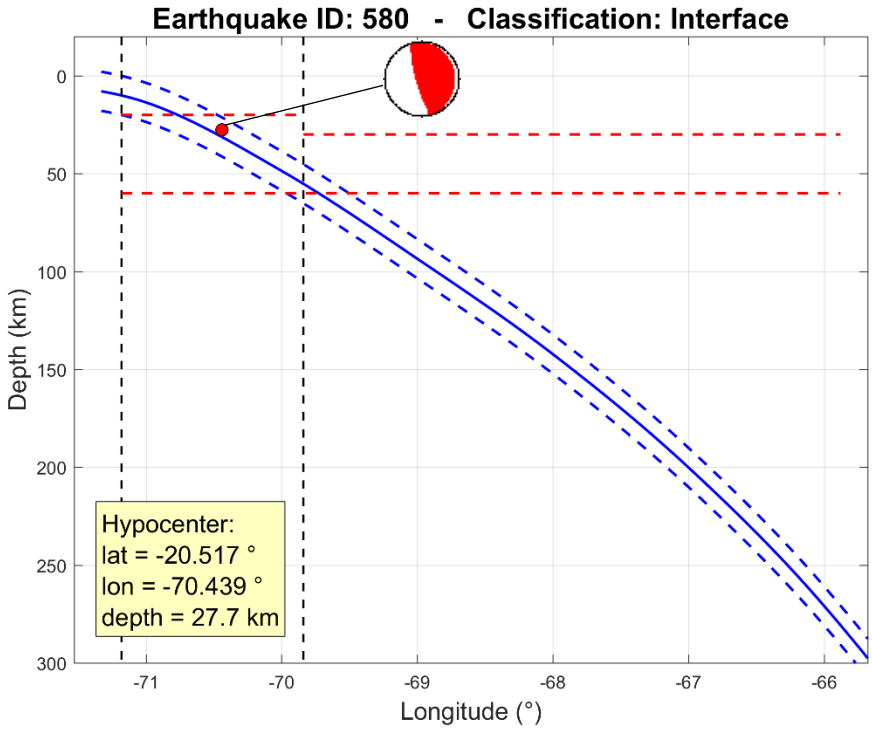

Figure 4.29 Example of event classified as interface.

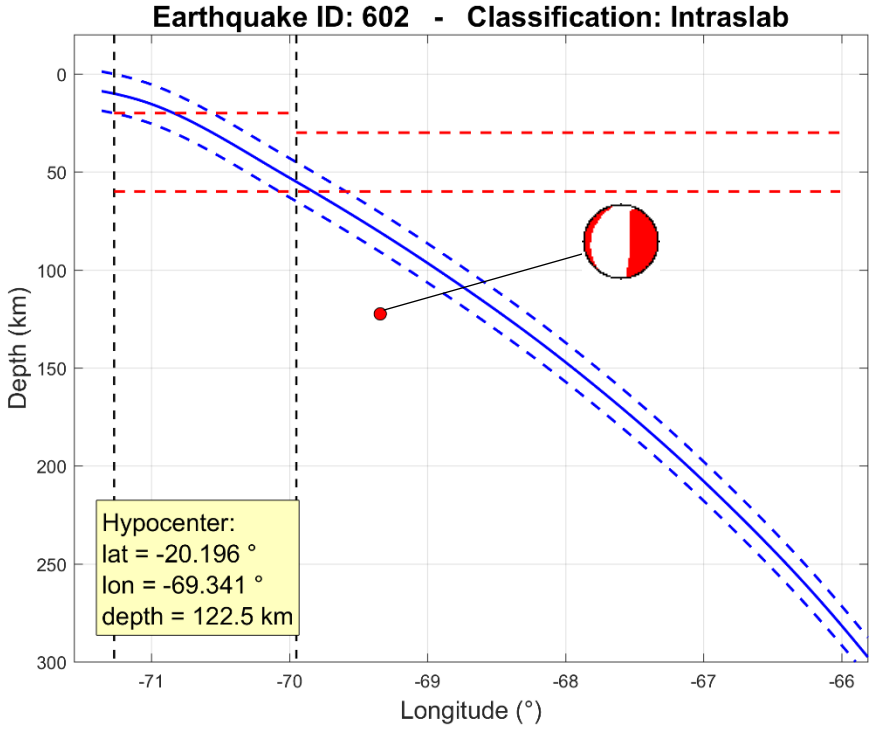

Figure 4.30 Example of event classified as intraslab.

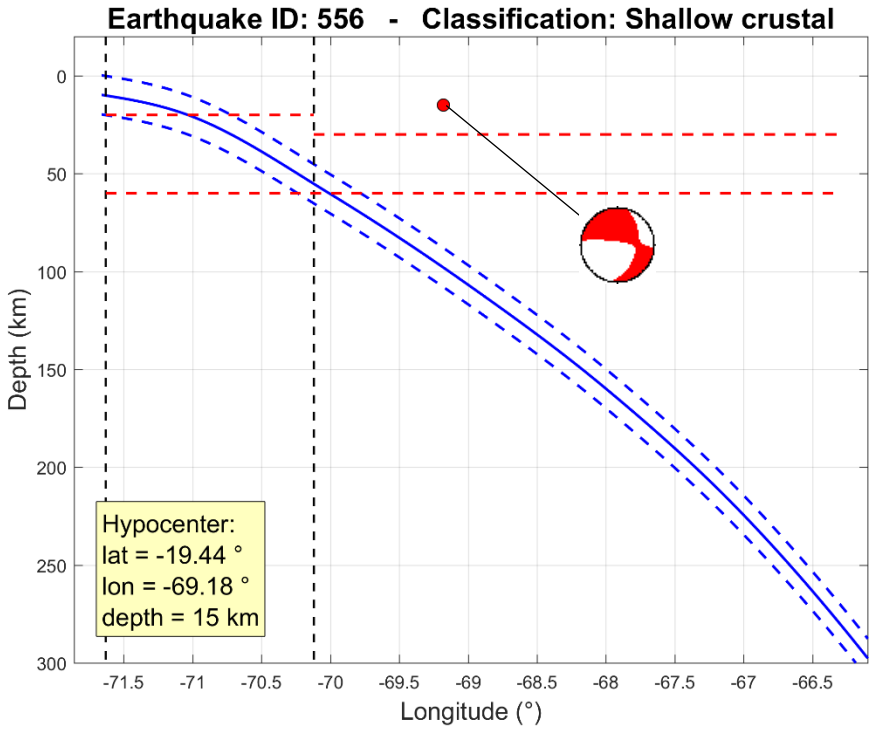

Figure 4.31 Example of event classified as shallow crustal.

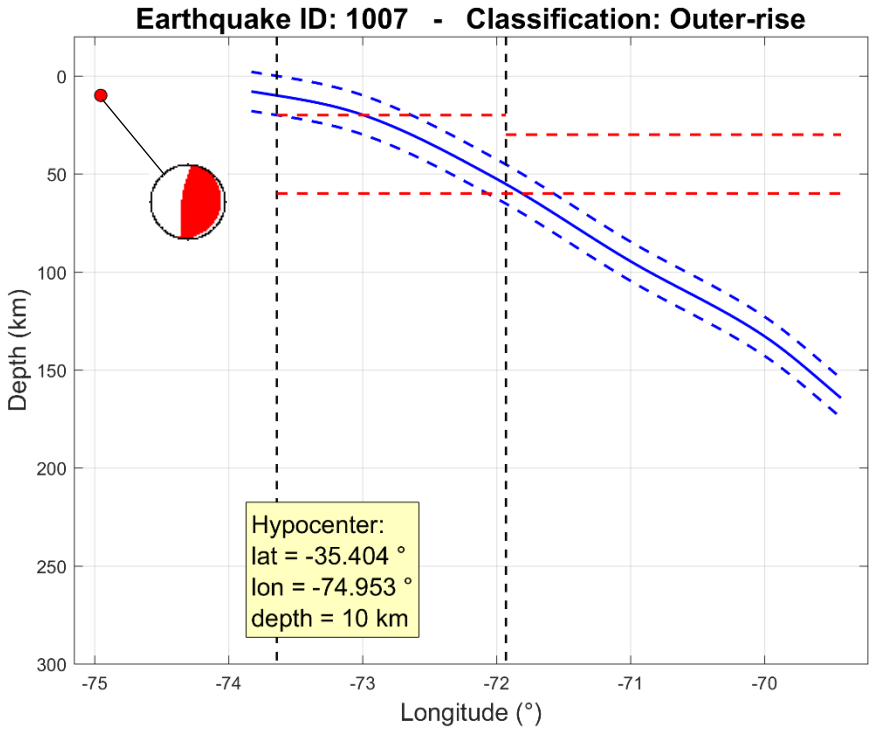

Figure 4.32 Example of event classified as outer-rise.

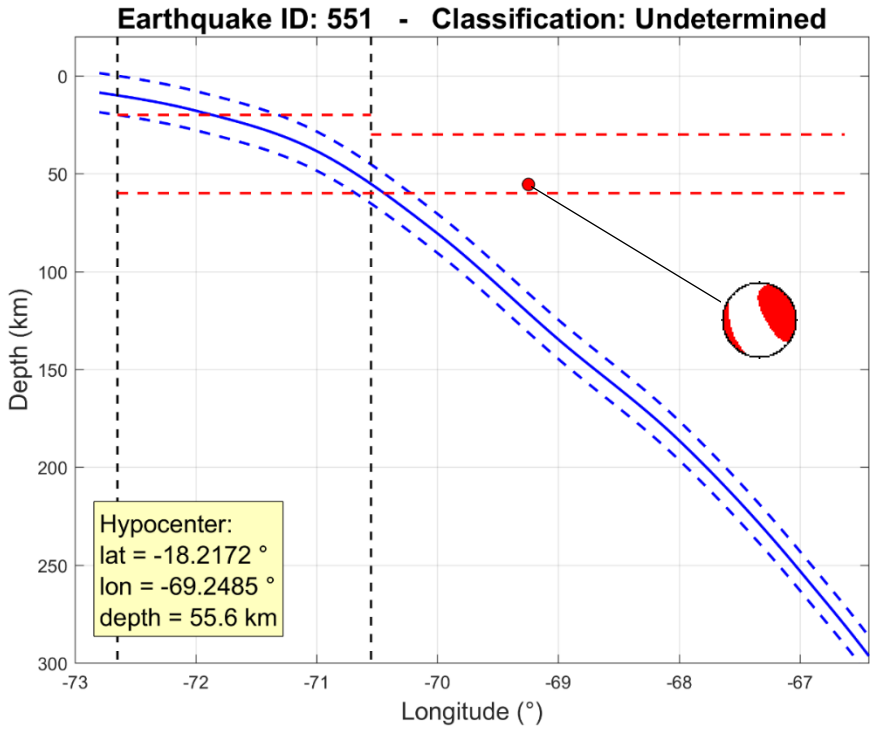

Figure 4.33 Example of event for which the classification is undetermined.

Because the events considered in this section lack a finite fault model, simulations procedures are used to generate approximate fault dimensions conditional on the magnitude of the earthquake (**M**), the hypocenter location (latitude, longitude and focal depth), and focal mechanism. The procedure operates as follows (adapted from Chiou and Youngs, 2008):

1. Locate hypocenter, which is assumed to have a mean location at the midpoint of the fault (along strike) and about 60% down-dip from the top of the fault. The down-dip locations are being checked in ongoing work.
2. Compute *RA* and its standard deviation using the model in Figure 4.24 and a similar relation by Strasser et al. (2010) for intraslab events.
3. Compute fault aspect ratio L/W (along-strike length / down-dip width) using the relations in Figure 4.34.

4. For interface events, use the dip from the CMT catalogue (using nodal plane that aligns with Nazca plate). For other event types, consider both nodal planes.
5. Compute many possible fault planes given the distribution of location (Step 1), RA (Step 2), and aspect ratio (Step 3) for one or two dip angles, as required by Step 4. Compute rupture distances for all realizations with their respective weights (derived from the probability densities of the underlying distributions). We take the median rupture distance among these results.

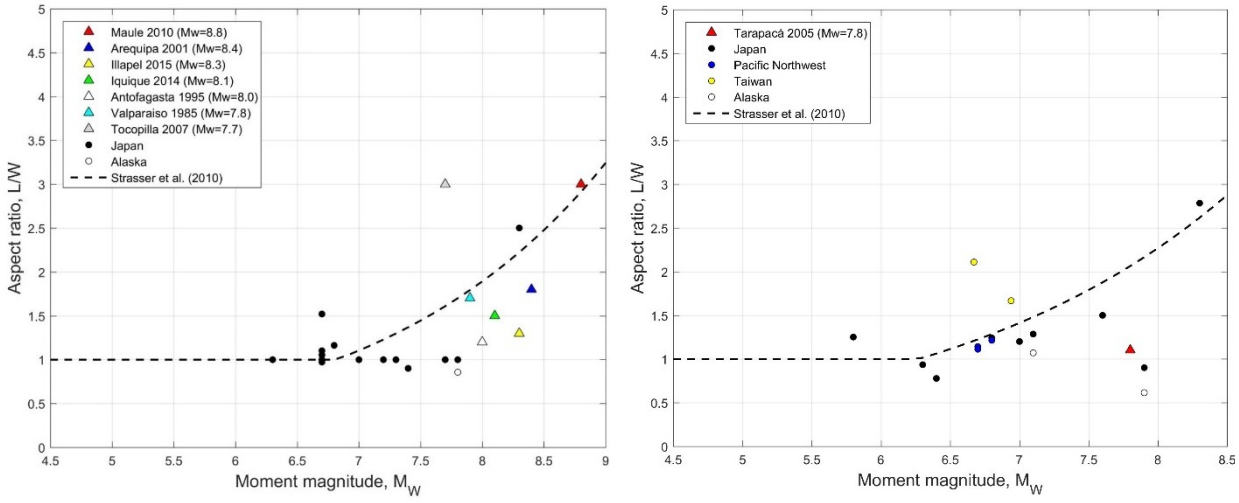

Figure 4.34 Relations for fault aspect ratio L/W versus data.

Results are summarized in Appendix A and Appendix B.

5 SUMMARY AND CONCLUSIONS

5.1 Summary

The following is a summary of the work completed for this thesis and the principle findings to date:

1. The NGA-Subduction project is currently under development, focusing on gathering data for regions affected by subduction-zone earthquakes like the Pacific Northwest (PNW) and Alaska regions of North America, Japan, Taiwan, Mexico, and South America, among other areas. The work undertaken for this thesis has focused on the creation of a Chilean ground motion database for the NGA-Subduction project.

2. Data from the South American subduction zone, and particularly from Chilean earthquakes, are relevant for the success of NGA-Subduction due to the availability of data from many large (**M** > 7.5) events and the importance of significant regional path effects previously observed in Chile (Boroschek et al. 2012) but not evident elsewhere. The subduction of the Nazca plate beneath the South American plate generates more than 800 measured earthquakes every year and has been responsible for the occurrence of extreme events like the 2010 **M** 8.8 Maule earthquake, among many others.

3. Strong motion arrays have been maintained in Chile since 1968. However, recordings are available from 1985, when the **M** 7.9 Valparaiso earthquake became the first major event that was well-recorded in the country. Approximately 90% of the recordings were obtained by permanent networks consisting of more than 250 strong motion recording (SMR) stations in total, whereas the remaining 10% were recorded by temporary networks having

approximately 150 SMR stations in total. The most important arrays are the RENADIC network, the CX (IPOC) network in northern Chile, and the RNA network, which contribute 29%, 28% and 23% of the recordings of the Chilean dataset for NGA-Subduction, respectively. The number of SMR stations in Chile has increased significantly since the 2010 Maule earthquake, thanks to the installation of nearly 300 new instruments that started in 2012 and that remains under implementation by the CSN.

4. Different authors have compiled ground motion datasets for Chile and South America, including Ruiz and Saragoni (2005), Arango et al. (2011), Contreras and Boroschek (2012, 2015), the SARA/GEM project in 2016, Bastías and Montalva (2016), and Idini et al. (2017). Prior to the present work, the most complete ground motion dataset for Chile is the work developed by Bastías and Montalva (2016), consisting of 3572 recordings from 477 earthquakes. These datasets have been used to generate local GMMs for Chilean earthquakes and PSHA studies. The most recent GMMs are those developed by Montalva et al. (2017) and Idini et al. (2017).

5. To date the event database for South America consists of 826 earthquakes that extend from 1985 to 2016, of which 689 have been recorded in Chilean SMR stations. Most of the events with recorded ground motions in Chile, are concentrated in 2010, 2014, and 2015, associated with the occurrence of the 2010 Maule **M** 8.8, 2014 Iquique **M** 8.1, and 2015 **M** 8.3 Illapel earthquakes and their aftershocks. The moment magnitude ranges from **M** 2.5 to **M** 8.8. There are six earthquakes with $\mathbf{M} \geq 8.0$, all of them mega-thrust interface events. As expected, most of the earthquakes are moderate events (**M** 5.0–6.0), whereas minor events ($\mathbf{M} < 5.0$) are significantly fewer, probably due to the limited capability of

the seismic networks to record low-amplitude ground motions. The event database contains interface, intraslab, shallow crustal and outer-rise earthquakes; however, is dominated by interface (59%) and intraslab (32%) events. In terms of number of recordings, the data obtained in Chile (4,213 three-component records) represents approximately 68% of the total dataset in South America (6,168 three-component records).

6. As a part of earthquake source database, finite fault models (FFM) have been collected by reviewing past studies published in the literature. Processes are introduced here to interpret published FFMs in a way that the most salient portion of the fault plane is used for site-to-source distance calculations. These processes improve upon those that had been used previously and have been adopted elsewhere in the NGA-Subduction project (e.g., Japan).

7. For the large number of events that lack published FFMs, we present uniform protocols for assigning seismic moment, **M**, hypocenter location, moment tensor from results in the literature. We assign each event according to one of four types (interface, intraslab, outer-rise, shallow crustal) following uniform procedures. Site-source distances are computed using a simulation-based representation of finite fault parameters that is similar to that used previously in NGA-projects. We develop an M-rupture area scaling relationship that is used in the simulation routine.

8. The resulting data set improves upon those already in the literature, as summarized in Section 2.2.

5.2 Ongoing work and future research

The work presented in this thesis is primarily related to source characterization. Additional, ongoing work pertains to the development of path and site parameters for the Chilean data set. Essential path parameters include mainly source-to-site distance calculation and definition of forearc and backarc regions. The distance calculation is a straightforward application of the finite fault models presented here.

In terms of site characterization, geotechnical information regarding shear-wave velocity profiles and V_{S30} values have been collected from different sources. There are approximately 80 SMR stations with measured profiles, most of them derived using surface waves methods. For the sites without in situ V_{S30} measurements, a proxy-based model is currently being developed based on terrain classes defined using a procedure similar applied previously in California and Japan.

Once the dataset is complete, as part of Ph.D. work, I will investigate the scaling of ground motions in Chile with respect to source, path, and site parameters. These studies could be focused on adapting global ground motion models to the Chilean case, analysis of source, path and site effects, single-station sigma values, and estimation of duration parameters s for subduction earthquakes in Chile.

APPENDIX A

EARTHQUAKE DATABASE

Table A.1 Earthquake catalog.

ID	Date and Time			M_W	Hypocenter		
	YEAR	MODY	HRMN		Lat (°)	Lon (°)	Depth (km)
808	1985	0303	2247	7.9	-33.125	-71.61	40
809	1985	0303	2338	7.3	-33.0616	-71.3012	36.7
810	1985	0408	2327	5.2	-33.0483	-72.0938	14.8
811	1985	0409	0157	7.1	-34.131	-71.618	37
581	1995	0730	0511	8	-23.4317	-70.4542	36.86
664	1996	0222	1340	5.9	-33.63	-71.63	46
583	1997	0123	0215	7.1	-21.999	-65.719	276.2
665	1997	0325	0014	5.5	-33.46	-70.78	83
551	1997	0401	1842	6.1	-18.2172	-69.2485	55.6
667	1997	1015	0103	7.1	-31.02	-71.23	68
668	1997	1022	0626	4.7	-31.9114	-71.5999	81.2
666	1997	1103	1917	6.2	-30.66	-71.79	44
669	1998	0417	1948	5.3	-32.7616	-71.4181	55.9
636	1998	0729	0714	6.4	-32.38	-71.46	39
670	1999	0206	0636	3.8	-34.605	-72.299	13.3
671	1999	0802	0106	5.5	-33.104	-70.197	105.3
585	1999	0915	0301	6.4	-20.799	-67.176	184.8
672	1999	1104	0538	4.7	-32.746	-71.667	52.4
673	1999	1130	0401	6.6	-19.01	-69.37	138.2
586	2000	0108	1159	6.3	-23.169	-70.122	36
587	2000	0512	1843	7.1	-23.779	-66.74	193.5
637	2000	0616	0755	6.4	-33.95	-69.92	109.1
674	2000	0811	1731	5.1	-17.9	-69.95	90.8
588	2000	1129	1025	6.3	-25.005	-70.965	34.5
638	2001	0409	0900	6.6	-32.754	-73.15	10
557	2001	0623	2033	8.4	-16.2099	-73.6233	29.6
558	2001	0623	2127	6.4	-17.181	-72.642	33
559	2001	0626	0418	6.7	-17.831	-71.63	33
560	2001	0629	1835	6	-19.725	-66.272	271.9
553	2001	0704	1209	6.1	-17.191	-65.727	33
554	2001	0705	1353	6.5	-16.083	-73.839	71.3
555	2001	0707	0938	7.6	-17.45	-72.45	25
556	2001	0724	0500	6.4	-19.44	-69.18	15
681	2001	0724	1742	5.2	-32.878	-71.785	54.8
677	2001	0809	0333	5.5	-18.35	-69.42	129.9

Table A.1 Earthquake catalog.

ID	Date and Time			M_W	Hypocenter		
	YEAR	MODY	HRMN		Lat (°)	Lon (°)	Depth (km)
639	2001	1128	1054	4.5	-32.718	-71.806	33
680	2001	1202	2144	3.8	-20.733	-69.046	124.6
640	2001	1228	2130	4.4	-32.879	-71.742	38.4
684	2002	0226	0832	5.4	-17.97	-69.83	100.4
614	2002	0401	1959	6.3	-29.634	-71.27	72.7
616	2002	0418	1608	6.6	-27.535	-70.586	62
685	2002	0523	1552	5.9	-30.718	-71.41	53.7
686	2002	0524	0023	5.5	-32.185	-71.132	39.7
615	2002	0618	1356	6.6	-30.826	-71.341	52.2
617	2002	0924	0357	6.2	-31.519	-69.2	119.6
545	2002	1012	2009	6.9	-8.3159	-71.6696	516.4
687	2002	1112	1306	5.2	-20.31	-68.77	91.3
529	2003	0620	0619	7	-7.6253	-71.7128	572
618	2003	0620	1330	6.7	-30.659	-71.788	23.1
641	2003	0709	1923	5.1	-32.6926	-71.5822	38.8
711	2003	1020	1913	3.9	-18.5931	-69.9256	10
717	2004	0105	2119	4.5	-20.8161	-68.9423	97.2
718	2004	0110	0725	5.6	-30.925	-71.84	47.8
720	2004	0223	2040	3.8	-20.3773	-68.8112	105
589	2004	0317	0321	6.1	-21.1257	-65.6315	290.9
735	2004	0430	1003	5	-33.516	-70.566	95.8
642	2004	0503	0436	6.6	-37.8063	-73.4165	17
723	2004	0805	1323	4.4	-18.8452	-69.9769	10
729	2004	0825	0512	5.1	-20.643	-69.612	112.4
643	2004	0828	1341	6.5	-35.187	-70.459	15.1
732	2004	0927	2258	5.5	-32.688	-71.743	32.9
620	2004	1112	0636	6.1	-26.6664	-63.3346	561.1
644	2005	0313	2038	5.2	-32.731	-71.718	10.8
741	2005	0319	0135	5.3	-20.424	-68.622	109
591	2005	0321	1223	6.8	-24.9411	-63.4567	576.6
746	2005	0325	0354	5.1	-20.436	-69.212	95
590	2005	0602	1056	6	-24.1334	-67.0103	194.9
561	2005	0613	2244	7.8	-20.03	-69.28	110
747	2005	0627	0053	4.9	-19.5797	-69.6422	39.2
745	2005	0705	1706	4.4	-32.8423	-71.4272	55.7

Table A.1 Earthquake catalog.

ID	Date and Time			M_W	Hypocenter		
	YEAR	MODY	HRMN		Lat (°)	Lon (°)	Depth (km)
749	2005	0713	1206	5.7	-17.847	-70.109	79.9
751	2005	0814	0239	5.8	-19.839	-69.271	117.1
753	2005	1017	1923	5.7	-17.775	-69.486	123
592	2005	1117	1926	6.8	-22.3676	-67.9421	161.7
645	2006	0210	1751	5.2	-32.599	-71.561	33.8
760	2006	0327	0523	5.2	-20.799	-69.469	58
757	2006	0407	0453	2.5	-34.934	-70.177	17.8
759	2006	0409	2050	5.7	-20.792	-70.772	35
622	2006	0430	1917	6.6	-27.097	-71.399	5.7
762	2006	0430	2141	6.5	-26.839	-71.149	18
756	2006	0606	1357	5	-20.8043	-69.0881	90.8
646	2006	0620	0214	5	-32.919	-71.638	42
623	2006	0716	1142	6.2	-28.579	-72.688	30
593	2006	0825	0044	6.6	-24.561	-67.282	175
624	2006	0917	0934	6.2	-31.7531	-67.1463	142
761	2006	1012	1805	6.3	-31.34	-71.702	36.9
546	2006	1020	1048	6.7	-13.4967	-76.6679	34.3
621	2006	1113	0126	6.8	-26.1608	-63.2916	581.9
763	2006	1120	1438	5.5	-17.664	-70.228	39
765	2007	0214	1421	5.3	-19.588	-69.823	53
764	2007	0302	1307	5.4	-30.88	-71.682	33.1
648	2007	0422	1022	5.5	-32.408	-71.432	20.2
769	2007	0426	1213	5.2	-28.157	-70.78	45.4
647	2007	0510	0531	4.3	-32.5738	-71.3803	67.4
533	2007	0712	0523	6.1	-7.9279	-74.3249	152.4
599	2007	0721	1534	6.4	-22.2136	-65.7495	290.6
771	2007	0815	1200	4.5	-20.675	-69.0654	82.5
772	2007	0815	2340	8	-13.3836	-76.5555	41.2
562	2007	0816	0516	6.4	-14.2784	-76.0919	24.7
774	2007	1025	0835	5.6	-21.314	-69.849	100
595	2007	1114	1540	7.7	-22.3421	-70.0235	49.844
766	2007	1114	1613	4.3	-23.1849	-70.1419	47.2
596	2007	1115	1503	6.3	-22.94	-70.575	37
768	2007	1115	1506	6.8	-23.002	-70.489	29.7
770	2007	1117	0307	5.5	-22.989	-70.326	40.2

Table A.1 Earthquake catalog.

ID	Date and Time			M_W	Hypocenter		
	YEAR	MODY	HRMN		Lat (°)	Lon (°)	Depth (km)
773	2007	1118	0702	5.3	-19.12	-69.9	98.4
598	2007	1120	1755	6.1	-22.8806	-70.5143	13.7
594	2007	1213	0723	6.2	-23.29	-70.742	43.1
767	2007	1215	1822	5.9	-32.706	-71.754	37.4
597	2007	1216	0809	6.7	-22.96	-70.202	45.2
779	2008	0122	0909	5.2	-19.955	-70.101	49.4
600	2008	0204	1701	6.3	-20.271	-70.274	45.9
601	2008	0216	1445	6.1	-21.3193	-68.3628	131.8
776	2008	0301	1951	5.6	-20.413	-70.186	43.8
602	2008	0324	2039	6.2	-20.196	-69.341	122.5
563	2008	0708	0913	6.2	-15.9861	-71.7482	122.6
781	2008	0731	0003	4.1	-19.541	-70.057	26.7
535	2008	0826	2100	6.4	-7.6632	-74.3692	153.9
626	2008	0903	1125	6.3	-26.83	-63.1933	570.6
786	2008	0910	1611	5.7	-20.45	-69.491	34.2
787	2008	0910	1628	4	-20.5641	-69.5188	31.1
606	2008	1012	2055	6.2	-20.471	-66.144	393.7
1274	2008	1218	2118	6.1	-32.476	-71.9	24.8
662	2008	1219	0936	5.7	-32.458	-71.949	32.2
788	2009	0211	2045	5.4	-20.335	-69.217	116.8
566	2009	0417	0208	6.1	-19.666	-70.68	37.2
789	2009	0525	0510	5.3	-28.55	-71.461	50.1
567	2009	0712	0612	6.1	-15.3	-70.912	190
790	2009	0715	1521	5.4	-20.444	-69.34	119.9
782	2009	1029	0125	4.9	-20.764	-69.62	66.5
564	2009	1113	0305	6.5	-19.508	-70.505	39
603	2009	1114	1944	6.2	-22.965	-66.641	220.4
783	2009	1222	2301	5.2	-28.607	-71.035	45
784	2010	0113	0352	5.2	-20.383	-69.237	94.8
1275	2010	0212	1202	5.8	-33.686	-69.06	192.4
604	2010	0227	1545	6.2	-24.872	-65.602	10
649	2010	0227	0634	8.8	-36.208	-72.963	31.64
650	2010	0227	0801	7.4	-37.84	-75.2105	35
651	2010	0227	0825	6.8	-34.8047	-72.4495	34.2
652	2010	0227	1030	6.1	-33.281	-71.955	35

Table A.1 Earthquake catalog.

ID	Date and Time			M_W	Hypocenter		
	YEAR	MODY	HRMN		Lat (°)	Lon (°)	Depth (km)
653	2010	0227	1724	6.1	-36.3859	-73.1192	25
654	2010	0227	1900	6.2	-33.4675	-72.028	19
785	2010	0227	0659	5.4	-33.9492	-71.9279	19
655	2010	0228	1125	6.2	-35.01	-71.924	19.4
656	2010	0303	1744	6.1	-36.5647	-73.2926	27
990	2010	0303	1956	5.8	-33.429	-72.223	38.9
605	2010	0304	2239	6.3	-22.613	-68.798	126.3
991	2010	0304	0158	6	-33.219	-72.554	34.5
657	2010	0305	0919	6.1	-36.6319	-73.239	34.3
658	2010	0305	1147	6.6	-36.575	-73.923	17.5
992	2010	0305	0334	5.3	-34.546	-71.85	8.5
993	2010	0305	0355	5.2	-34.659	-71.755	34.1
994	2010	0306	0123	5.5	-37.057	-73.521	10
995	2010	0307	0446	5.3	-33.166	-72.064	18.8
1017	2010	0307	1559	5.9	-38.105	-73.436	41.8
996	2010	0308	1649	4.8	-32.693	-71.771	6.9
997	2010	0309	0553	5.2	-37.103	-73.321	10.8
1089	2010	0310	0904	5.4	-36.699	-73.189	27.3
1276	2010	0310	0937	5.4	-37.15	-73.276	4
659	2010	0311	1439	6.9	-34.301	-72.13	33.1
660	2010	0311	1455	7	-34.451	-72.206	31
998	2010	0311	1505	5.9	-34.444	-72.096	28.6
999	2010	0311	1554	5.1	-34.507	-72.124	12.7
1000	2010	0311	2011	5.8	-34.381	-71.979	8
1123	2010	0311	1656	5.4	-34.463	-72.052	30.4
1001	2010	0312	0610	5	-34.488	-71.823	22.9
1002	2010	0312	0644	4.9	-34.346	-71.978	33.8
1003	2010	0313	1034	5.8	-37.603	-74.081	13.5
1004	2010	0313	1522	5.2	-34.56	-71.747	36.4
1005	2010	0314	0731	5.5	-34.27	-71.985	30.1
1139	2010	0314	1459	5.3	-36.604	-72.985	10.1
1007	2010	0315	1108	6.2	-35.404	-74.953	10
661	2010	0316	0221	6.6	-36.471	-73.9	25
1006	2010	0316	0304	5.9	-36.491	-73.689	21.2
1008	2010	0317	1900	5.2	-36.754	-73.324	44.2

Table A.1 Earthquake catalog.

ID	Date and Time			M_W	Hypocenter		
	YEAR	MODY	HRMN		Lat (°)	Lon (°)	Depth (km)
1009	2010	0318	0157	5.5	-36.511	-73.183	28.1
1010	2010	0318	0318	5.3	-34.361	-72.008	35
1019	2010	0319	1710	5.1	-34.445	-72.044	16.3
1011	2010	0325	0258	5	-35.106	-71.954	37.8
1020	2010	0325	1357	5.1	-35.992	-72.731	33.8
1124	2010	0325	1839	5.3	-20.345	-69.486	122.9
625	2010	0326	1452	6.1	-28.089	-70.964	51.2
1012	2010	0326	1030	4.9	-35.27	-72.152	39.8
1013	2010	0327	0954	5.4	-37.547	-73.991	14.8
1028	2010	0328	2138	6	-35.364	-73.423	27.8
1014	2010	0329	0735	5.8	-34.881	-71.935	34.1
1140	2010	0330	0812	4.1	-36.976	-73.067	16.8
1015	2010	0401	1541	5.1	-34.891	-71.918	38.3
1021	2010	0402	1934	5.5	-36.118	-72.898	29
1022	2010	0402	1958	5.9	-36.216	-73.162	28.2
1125	2010	0402	1038	4.9	-36.698	-73.617	26.5
1277	2010	0402	2312	5.1	-36.28	-73.178	25.7
1016	2010	0405	0332	4.8	-33.385	-71.014	68.6
1027	2010	0405	2236	5.8	-20.022	-69.246	106.6
1278	2010	0406	0904	5	-35.209	-72.74	17.9
1023	2010	0407	0918	5.4	-20.014	-69.306	110.9
1126	2010	0407	1750	4.9	-37.127	-73.254	18.7
1018	2010	0408	0803	5	-35.161	-72.317	14.3
1127	2010	0408	2115	4.6	-34.375	-72.091	15
1038	2010	0409	2223	5.8	-28.512	-68.303	113.4
1024	2010	0410	1506	5.5	-25.707	-70.618	55
1025	2010	0411	1028	5.3	-34.76	-71.889	32.1
1128	2010	0411	0234	4.5	-35.946	-72.763	33.7
1029	2010	0412	2059	4.9	-36.543	-73.277	15.1
1129	2010	0413	1507	4.7	-36.869	-73.381	24.7
1141	2010	0416	2315	5.7	-37.604	-74.658	20
1026	2010	0418	0149	5.6	-37.377	-74.018	9.1
1030	2010	0423	1003	6	-37.486	-73.315	54.4
1031	2010	0425	1542	4.9	-37.612	-73.346	50.7
1032	2010	0426	0844	4.8	-37.413	-73.186	56.2

Table A.1 Earthquake catalog.

ID	Date and Time			M_W	Hypocenter		
	YEAR	MODY	HRMN		Lat (°)	Lon (°)	Depth (km)
1130	2010	0426	2233	5	-36.183	-72.923	39.5
1033	2010	0428	1233	5.2	-34.654	-71.673	42.6
1279	2010	0428	0026	4.8	-35.753	-72.72	30
1034	2010	0429	1340	5.2	-36.854	-73.183	33.9
1035	2010	0501	1441	5.3	-33.194	-72.312	35.3
1036	2010	0502	1451	5.9	-34.29	-72.088	32.1
1037	2010	0503	0649	5	-34.278	-72.126	9.2
1054	2010	0503	2309	6.2	-38.268	-74.345	22.9
1039	2010	0504	1355	5	-34.141	-72.336	22.5
1040	2010	0505	1524	5.4	-35.565	-73.441	28.3
565	2010	0506	0242	6.2	-18.316	-70.766	38.9
1280	2010	0508	1752	5	-36.113	-73.637	31.6
1041	2010	0509	0329	5.1	-33.991	-72.138	36.5
1131	2010	0511	1304	5.2	-35.705	-73.006	28.6
1043	2010	0513	2039	5	-34.237	-72.362	23.4
1132	2010	0513	2256	5.2	-37.02	-73.288	28.6
1042	2010	0517	2116	5.1	-36.686	-73.267	34.7
1044	2010	0519	0304	5	-22.626	-68.833	114.1
1050	2010	0521	1852	5.6	-34.645	-71.97	7.3
548	2010	0524	1618	6.4	-8.0537	-71.6386	575.8
1045	2010	0524	2357	5.4	-36.342	-73.601	26.9
1049	2010	0524	1912	5.4	-35.769	-72.856	31.4
1046	2010	0525	1309	5.8	-37.645	-73.183	47.9
1047	2010	0530	0227	5.2	-34.796	-71.722	46.9
1048	2010	0601	1605	5.7	-36.886	-73.543	25.3
830	2010	0605	1518	5.2	-21.545	-70.02	26.8
1051	2010	0609	1358	5.2	-20.475	-69.006	116
1052	2010	0610	0610	4.9	-22.671	-69.113	120
1053	2010	0611	0854	5.1	-34.728	-72.081	17.9
1055	2010	0616	0919	5.7	-36.227	-71.277	137.1
1056	2010	0619	2130	5.2	-38.066	-73.501	41.8
1072	2010	0624	1324	5.2	-37.115	-73.975	22.8
1057	2010	0625	1433	5.2	-32.641	-71.793	35.7
831	2010	0626	1901	5.4	-19.109	-69.626	105.9
1059	2010	0629	0140	5.5	-37.883	-73.622	25.4

Table A.1 Earthquake catalog.

ID	Date and Time			M_W	Hypocenter		
	YEAR	MODY	HRMN		Lat (°)	Lon (°)	Depth (km)
1058	2010	0701	2056	5.6	-35.655	-72.63	39.9
1060	2010	0703	0005	5.2	-34.78	-71.642	54.8
1070	2010	0706	1354	5.4	-35.664	-72.111	46.3
1061	2010	0708	0549	5	-34.496	-72.049	7.8
607	2010	0712	0011	6.3	-22.354	-68.633	125.3
1062	2010	0713	2112	5.2	-27.896	-70.724	66.7
1067	2010	0714	0832	6.6	-38.113	-74.131	26.9
1133	2010	0714	1505	5.8	-38.291	-73.868	20.9
1063	2010	0715	0036	5.5	-34.153	-72.303	8.8
1064	2010	0715	2257	5.2	-35.16	-72.905	25.3
1065	2010	0717	0607	6	-24.299	-70.322	86.1
1066	2010	0719	0100	5.1	-20.551	-70.466	40.3
1071	2010	0720	2249	5.4	-37.341	-73.972	42.9
1090	2010	0723	1350	5.1	-37.02	-73.546	9.3
1068	2010	0805	0601	5.9	-37.42	-74.073	33.5
1069	2010	0805	1749	5.7	-37.562	-73.772	29.3
1075	2010	0805	0627	5.4	-37.531	-73.821	36.3
1073	2010	0822	0349	5.4	-36.533	-73.72	19.1
832	2010	0825	1202	5.1	-22.704	-69.184	76.9
1091	2010	0901	1724	5.1	-22.832	-68.853	90.9
1074	2010	0906	0320	5.4	-37.486	-73.575	17
1142	2010	0907	2333	4.1	-36.005	-72.763	28.8
663	2010	0909	0728	6.2	-36.986	-74.397	28.8
1076	2010	0923	1636	5.4	-34.972	-71.887	47.7
1092	2010	0923	0720	4.4	-36.719	-72.882	33.2
1077	2010	0929	1629	5.6	-34.804	-71.795	51
1078	2010	0930	0026	5.6	-36.249	-74.256	20.2
1079	2010	1004	1643	4.8	-36.504	-73.564	32.6
1081	2010	1012	0921	4.8	-36.802	-73.716	25.6
1086	2010	1013	2238	4.4	-36.044	-72.754	36
1080	2010	1016	1203	5.1	-35.144	-72.246	28.2
1082	2010	1021	0249	5.9	-34.792	-73.957	32.6
833	2010	1022	1931	5.8	-21.01	-68.806	136.3
834	2010	1023	0138	5.6	-29.5649	-71.1702	54.9
1083	2010	1023	1056	5.4	-36.955	-73.771	36.9

Table A.1 Earthquake catalog.

ID	Date and Time			M_W	Hypocenter		
	YEAR	MODY	HRMN		Lat (°)	Lon (°)	Depth (km)
1084	2010	1023	1546	5.5	-36.608	-73.505	20.7
1095	2010	1023	0558	5.5	-37.791	-74.088	45.5
1085	2010	1027	2009	5.6	-19.121	-69.76	88.3
1087	2010	1105	0453	4.9	-36.136	-72.559	28.8
1134	2010	1106	1215	5	-18.965	-69.49	105.3
1088	2010	1110	0123	4.9	-36.431	-73.56	21.9
1094	2010	1125	0327	5.2	-32.139	-70.841	105
1093	2010	1128	0819	5.6	-34.672	-72.043	41.9
1098	2010	1204	0315	4.2	-19.89	-70.188	47
627	2011	0101	0956	7	-26.8513	-63.2373	584.3
1165	2011	0102	2020	7.1	-38.343	-73.961	17.8
1096	2011	0104	2259	5	-29.175	-69.788	128
835	2011	0110	0602	5.9	-35.604	-73.604	22.8
1097	2011	0111	0533	5.1	-35.687	-73.462	25.1
836	2011	0118	2130	5.6	-19.201	-69.397	102.7
1099	2011	0205	1611	5.7	-37.761	-74.088	27.4
1101	2011	0210	1558	5.1	-32.714	-71.893	21
837	2011	0211	2005	6.8	-36.679	-73.593	20.9
1100	2011	0212	0117	6	-36.958	-74.155	25.4
838	2011	0213	0851	5.9	-36.673	-73.742	21.4
839	2011	0213	1035	5.9	-36.73	-73.397	32.3
840	2011	0213	1344	5.6	-36.94	-72.904	55
1102	2011	0214	2156	5.6	-20.038	-69.302	105
1166	2011	0214	0340	6.6	-35.46	-73.735	21.5
841	2011	0228	0129	5.8	-37.36	-73.695	31.5
842	2011	0228	2045	5.3	-20.457	-69.271	101.4
1103	2011	0303	0758	5.5	-37.34	-73.859	18
568	2011	0306	1231	6.3	-18.309	-69.44	112.4
1108	2011	0313	1751	4.9	-34.658	-72.022	51.2
1104	2011	0316	2236	5.6	-32.564	-71.726	32.7
1281	2011	0317	1114	5.2	-32.59	-71.692	13.3
843	2011	0319	0912	4.9	-20.322	-69.538	109.3
1105	2011	0328	0610	5.2	-34.889	-71.837	45
1106	2011	0329	0508	5.2	-34.775	-71.718	48.1
1170	2011	0402	1059	5.9	-19.684	-69.355	100.5

Table A.1 Earthquake catalog.

ID	Date and Time			M_W	Hypocenter		
	YEAR	MODY	HRMN		Lat (°)	Lon (°)	Depth (km)
1107	2011	0410	2024	5	-36.196	-73.768	23.8
1109	2011	0413	1514	5.4	-33.771	-72.209	31.1
1110	2011	0519	1705	5.2	-34.754	-71.668	36.5
1114	2011	0601	1255	6.3	-37.58	-75.224	9.6
1111	2011	0605	1025	5.3	-35	-72.19	32.4
1112	2011	0608	0306	6.2	-17.534	-70.004	146.5
608	2011	0620	1636	6.5	-21.874	-68.668	128.7
1113	2011	0629	0536	5.1	-33.906	-72.341	19.7
1115	2011	0715	1455	5.4	-21.177	-68.781	125.1
1116	2011	0716	0026	5.7	-33.901	-72.099	26
1117	2011	0723	0256	5.9	-29.318	-70.465	135.7
1118	2011	0723	2245	5	-20.208	-70.683	17
1119	2011	0725	1115	5.4	-37.714	-73.728	32.8
1120	2011	0728	1605	5.2	-35.829	-73.488	20.1
1121	2011	0728	1950	5.6	-35.786	-73.464	19
1122	2011	0806	1322	5.5	-35.884	-73.334	31.9
536	2011	0824	1746	7	-7.6203	-74.538	149.3
628	2011	0902	1347	6.7	-28.4135	-63.136	592.7
1135	2011	0903	1620	5.8	-38.312	-74.753	17.2
1136	2011	0909	0233	5.4	-22.416	-68.9	98.7
1138	2011	0913	2118	5.2	-37.258	-73.906	31.8
1137	2011	0914	0702	5.9	-32.696	-71.797	37
844	2011	1003	1735	5	-20.199	-69.249	102.1
1159	2011	1025	1627	3.9	-34.346	-72.201	28.4
569	2011	1028	1854	6.9	-14.3822	-76.1843	29
845	2011	1105	0713	5.7	-23.506	-70.236	43.2
1143	2011	1111	0808	5.2	-38.048	-73.118	36.8
570	2011	1122	1848	6.6	-15.1438	-65.1489	552.4
629	2011	1207	2223	6.1	-27.949	-71.359	31.9
1144	2012	0109	2130	5.2	-32.55	-71.53	16.2
1182	2012	0117	2320	5.7	-31.765	-71.906	37.5
571	2012	0130	0510	6.4	-14.1089	-75.6184	41
1145	2012	0201	0243	4.3	-32.678	-71.336	52.1
1148	2012	0221	1546	4.6	-19.982	-70.222	47.1
1146	2012	0226	0808	5.4	-18.912	-69.642	106.7

Table A.1 Earthquake catalog.

ID	Date and Time			M_W	Hypocenter		
	YEAR	MODY	HRMN		Lat (°)	Lon (°)	Depth (km)
846	2012	0303	1101	5.2	-30.189	-71.448	34.6
847	2012	0304	1627	5.1	-21.602	-70.061	47.1
630	2012	0305	0746	6.1	-28.246	-63.294	553.9
1150	2012	0307	2013	4.7	-19.993	-70.228	47.8
1147	2012	0309	1612	4.9	-19.113	-69.603	98
848	2012	0310	0226	5.2	-19.738	-69.25	101
851	2012	0319	2152	4.9	-25.005	-69.752	100.5
849	2012	0324	0728	5.1	-33.052	-71.063	68.8
850	2012	0325	2237	7.1	-35.2	-72.217	40.7
852	2012	0401	0731	5	-23.056	-69.316	93.8
1149	2012	0403	0725	5	-19.647	-69.092	114.1
1152	2012	0417	0350	6.7	-32.787	-71.812	35
1151	2012	0419	0114	4.9	-30.868	-71.188	65.1
853	2012	0430	0739	5.6	-29.8	-71.641	43.1
1157	2012	0505	1318	4.4	-19.692	-70.211	51.3
572	2012	0514	1000	6.2	-18.115	-70.237	119.6
1153	2012	0514	1620	3.9	-20.578	-70.599	38.6
854	2012	0519	0835	5.9	-25.741	-70.858	83.6
1154	2012	0520	0644	4.7	-20.197	-69.159	96.3
631	2012	0528	0507	6.7	-28.043	-63.094	586.9
573	2012	0607	1603	6.2	-15.9117	-72.4723	106.7
1155	2012	0611	2337	4.8	-17.929	-69.964	96.6
1156	2012	0621	1622	4.6	-20.471	-69.288	95.1
1158	2012	0718	1824	5.2	-20.796	-70.556	28.1
549	2012	0802	0938	6	-8.454	-74.2726	148.8
855	2012	0807	0039	5.3	-27.878	-70.579	73.5
856	2012	0827	0039	5.2	-23.739	-69.414	99.9
857	2012	0830	0804	5.2	-37.199	-73.397	23
1160	2012	0907	0237	5	-22.391	-68.625	125.2
1282	2012	0915	1039	3.8	-18.647	-70.524	39.9
858	2012	0921	1217	5.4	-19.719	-69.335	100.8
1161	2012	0926	1744	5.2	-22.295	-68.658	115.1
1162	2012	0929	1748	5.3	-17.503	-69.633	125.3
859	2012	1008	0150	5.8	-21.828	-68.537	121.3
860	2012	1011	1722	5.5	-32.879	-70.651	95

Table A.1 Earthquake catalog.

ID	Date and Time			M_W	Hypocenter		
	YEAR	MODY	HRMN		Lat (°)	Lon (°)	Depth (km)
1163	2012	1025	0537	4.9	-32.773	-70.165	104.7
1164	2012	1108	0824	4.2	-20.462	-69.933	72.6
861	2012	1113	0311	5	-20.54	-69.03	93
632	2012	1114	1902	6.2	-29.237	-71.235	82.3
862	2012	1116	0038	5	-21.506	-69.488	61.7
1167	2012	1224	0531	4.9	-18.123	-70.269	104
1168	2012	1226	1317	5.4	-37.348	-73.7	33.1
864	2013	0101	0351	4.9	-20.81	-69.67	58.6
1169	2013	0109	1838	4.7	-18.002	-69.726	95.3
863	2013	0113	2123	5.3	-20.116	-69.315	89.9
633	2013	0130	2015	6.8	-28.178	-70.882	52.2
1172	2013	0210	1954	5.4	-33.458	-72.1	46.5
634	2013	0222	1201	6.1	-27.993	-63.195	585.8
1171	2013	0223	2200	4.5	-19.949	-70.02	52.7
865	2013	0302	1142	5	-22.851	-70.375	50.7
1173	2013	0512	1251	5.3	-20.996	-68.673	132.6
1174	2013	0521	2310	4.8	-20.572	-69.576	85.6
1207	2013	0609	0122	4	-19.123	-70.079	41.7
1175	2013	0619	2129	5.2	-32.621	-70.236	107.1
1257	2013	0709	2051	5.1	-19.145	-69.304	115.9
866	2013	0710	1432	5.6	-19.367	-69.522	112.9
1176	2013	0805	0540	5.3	-20.189	-70.705	29.8
537	2013	0812	0949	6.2	-5.52	-82.13	12
1177	2013	0816	2217	5.2	-28.665	-71.098	54.3
1178	2013	0819	1939	5.4	-21.503	-68.784	129.3
867	2013	0823	0834	5.8	-22.278	-68.855	117.5
1179	2013	0830	1048	5	-34.475	-70.684	111.7
868	2013	0907	1913	5.2	-19.617	-69.299	100.1
574	2013	0925	1642	7	-16.03	-74.81	46.1
869	2013	0929	2306	5.3	-37.469	-73.753	49.3
870	2013	0929	2323	5.5	-37.472	-73.883	42.5
1180	2013	1011	0332	5	-19.988	-69.196	91.6
1181	2013	1020	2151	3.9	-18.59	-70.183	58.2
871	2013	1029	0340	5.1	-30.705	-71.279	46.9
1283	2013	1030	0251	6.3	-35.314	-73.395	41.5

Table A.1 Earthquake catalog.

ID	Date and Time			M_W	Hypocenter		
	YEAR	MODY	HRMN		Lat (°)	Lon (°)	Depth (km)
1284	2013	1030	0228	5.9	-35.439	-73.193	39.2
635	2013	1031	2303	6.5	-30.372	-71.501	52
872	2013	1204	0539	5.2	-24.578	-69.295	72.4
1183	2013	1217	1229	5.5	-25.5886	-70.5093	65
873	2013	1222	0153	4.9	-32.872	-70.621	95.3
1184	2014	0102	2239	4.9	-32.948	-71.383	44.5
1185	2014	0104	0011	5.3	-20.687	-70.795	26.1
1194	2014	0105	1509	4.3	-32.828	-71.329	45.1
1186	2014	0106	0359	4.9	-20.774	-70.652	26.6
1187	2014	0106	1623	4.2	-20.518	-68.982	103.6
874	2014	0107	0343	5.3	-20.989	-69.729	97.3
1188	2014	0108	0420	5.7	-20.774	-70.678	30.2
1285	2014	0110	1645	4	-20.236	-69.655	66.9
1189	2014	0119	0526	4.5	-20.996	-69.789	40.3
875	2014	0129	1001	5.6	-18.5087	-69.3735	120
876	2014	0205	1151	5.2	-21.377	-69.517	39.6
1190	2014	0209	0407	4.3	-22.036	-69.748	71.5
877	2014	0212	1143	5.8	-22.348	-68.724	98.7
1191	2014	0212	1335	5.1	-34.801	-71.584	21.1
1192	2014	0215	1252	5	-22.472	-68.72	101.8
878	2014	0223	2340	4.9	-23.847	-68.785	105.8
1193	2014	0304	1051	5.7	-33.6046	-71.957	20
1197	2014	0306	0437	5.3	-33.333	-71.28	59.7
538	2014	0315	2351	6.3	-5.65	-81.1	32.5
575	2014	0315	0859	6.1	-14.1	-76.53	21.9
1195	2014	0315	1446	5.2	-34.742	-71.784	44.6
576	2014	0316	2116	6.7	-19.965	-70.814	20.6
609	2014	0317	0511	6.4	-19.928	-70.944	28.3
879	2014	0317	0519	5.2	-19.994	-70.885	36.2
880	2014	0317	1112	5	-19.899	-70.892	35.5
881	2014	0318	2126	5.8	-19.958	-70.944	38.1
882	2014	0318	2133	5.1	-20.023	-70.835	22.1
883	2014	0320	1841	5.1	-24.0271	-69.0615	93.2
577	2014	0322	1259	6.2	-19.836	-71.384	31.8
884	2014	0322	1314	5.3	-19.767	-70.849	13.9

Table A.1 Earthquake catalog.

ID	Date and Time			M_W	Hypocenter		
	YEAR	MODY	HRMN		Lat (°)	Lon (°)	Depth (km)
578	2014	0323	1820	6.3	-19.794	-70.943	33.8
1258	2014	0323	2204	4.8	-19.761	-70.747	42.3
799	2014	0324	1545	5.7	-19.594	-70.791	43
885	2014	0324	1126	5.7	-19.846	-70.828	40.6
886	2014	0324	1132	5.4	-19.796	-70.808	42.1
887	2014	0324	1140	5.7	-19.822	-70.868	41.1
1196	2014	0325	0015	5.2	-19.784	-70.821	40.9
801	2014	0331	1253	5.6	-19.511	-69.174	114.5
579	2014	0401	2346	8.1	-19.642	-70.817	20
888	2014	0401	2358	7	-19.4255	-70.2639	18
901	2014	0401	2357	6.9	-19.8927	-70.9455	28.4
889	2014	0402	0003	5.9	-19.84	-70.917	29
890	2014	0402	0129	5.2	-20.076	-70.961	25.2
891	2014	0402	0037	5.2	-20.031	-70.494	42.8
892	2014	0402	0340	5.1	-19.966	-71.116	33.3
893	2014	0402	0446	5.7	-20.134	-70.792	38.6
1199	2014	0402	0412	4.9	-19.573	-70.53	33.7
1243	2014	0402	0020	5.2	-19.788	-71.113	45.1
1259	2014	0402	0419	5.2	-19.89	-71.112	39
1260	2014	0402	1107	5.3	-19.993	-71.024	39.4
1286	2014	0402	0033	5.4	-20.196	-70.767	33.2
1287	2014	0402	0508	4.8	-20.382	-70.585	26.3
580	2014	0403	0243	7.7	-20.517	-70.439	27.7
610	2014	0403	0158	6.6	-20.314	-70.583	30.7
611	2014	0403	0526	6.5	-20.798	-70.651	38
894	2014	0403	0311	5.2	-20.601	-70.511	40.6
895	2014	0403	0345	5.1	-19.976	-70.887	30.6
896	2014	0403	0417	5.1	-20.584	-70.669	26.8
897	2014	0403	0551	5.5	-20.756	-70.425	36.1
898	2014	0403	0923	5.2	-20.595	-70.708	28.5
899	2014	0403	2337	5.2	-20.178	-70.627	41.1
1198	2014	0403	1433	4.9	-20.583	-70.899	35.6
1218	2014	0403	0255	5.3	-20.733	-70.559	27.7
1219	2014	0403	0654	4.8	-20.625	-70.635	30.1
1220	2014	0403	0908	4.9	-20.284	-70.468	37.1

Table A.1 Earthquake catalog.

ID	Date and Time			M_W	Hypocenter		
	YEAR	MODY	HRMN		Lat (°)	Lon (°)	Depth (km)
1261	2014	0403	1150	4.8	-20.64	-70.31	37.1
612	2014	0404	0137	6.2	-20.616	-70.566	40.2
900	2014	0404	0434	4.8	-22.1907	-70.2949	61.5
902	2014	0404	0952	5.4	-31.5039	-70.3232	96.2
903	2014	0405	0222	5.6	-32.669	-71.295	42.3
904	2014	0405	0544	5.3	-20.161	-70.538	43.2
1200	2014	0405	0033	5.1	-20.173	-70.505	43.4
1262	2014	0405	0404	5.1	-20.707	-70.688	30.1
1288	2014	0405	0528	4.7	-20.604	-70.67	18.5
905	2014	0406	1406	5.3	-20.414	-70.983	45.1
906	2014	0407	1343	5.8	-20.131	-70.905	35.6
907	2014	0407	1347	5.1	-20.135	-70.921	20.3
908	2014	0407	1403	5.1	-20.136	-70.9	38.7
909	2014	0408	0103	5.1	-19.768	-70.481	39.1
910	2014	0408	0520	5	-19.875	-70.865	39.8
911	2014	0408	1014	5.6	-20.558	-70.978	38.2
912	2014	0409	1114	5.2	-20.631	-70.935	31.8
1263	2014	0409	1105	5	-20.772	-70.79	31.6
1201	2014	0410	1748	5.1	-19.987	-71.03	38.4
613	2014	0411	0001	6.1	-20.717	-70.649	38.9
913	2014	0411	0855	5.1	-19.941	-70.927	39.4
914	2014	0411	1200	5.3	-20.077	-70.5	35.5
1223	2014	0411	0001	6.1	-20.71	-70.653	37.4
915	2014	0413	1211	5.4	-20.585	-70.713	23.6
1264	2014	0414	0555	5.3	-20.726	-70.774	34.3
916	2014	0415	1609	5.3	-20.204	-70.858	39.9
917	2014	0415	1621	5.1	-20.183	-70.844	27.9
918	2014	0415	1859	5.1	-20.16	-70.991	38.7
919	2014	0416	0314	5	-20.172	-70.858	37.8
1202	2014	0417	1319	5.1	-22.534	-69.091	98.7
920	2014	0419	2054	5.8	-19.965	-71.112	40
921	2014	0421	1339	5.3	-19.683	-70.938	39.3
1265	2014	0424	1026	5.1	-19.903	-71.132	41.5
922	2014	0428	0459	5.1	-19.563	-70.377	43.6
923	2014	0430	1800	5.3	-32.723	-71.746	21.3

Table A.1 Earthquake catalog.

ID	Date and Time			M_W	Hypocenter		
	YEAR	MODY	HRMN		Lat (°)	Lon (°)	Depth (km)
1289	2014	0501	1645	5.1	-19.959	-71.222	31.7
1266	2014	0504	0446	5.1	-20.004	-71.028	38.1
924	2014	0505	1121	5.4	-20.196	-70.742	41.1
925	2014	0505	1338	4.8	-20.213	-68.384	176.2
1203	2014	0505	0902	4.9	-19.299	-70.98	41.6
1290	2014	0505	0251	4.7	-19.906	-70.815	40.7
1291	2014	0505	2252	4.9	-19.856	-70.872	42.2
1292	2014	0507	1326	4.9	-19.961	-70.941	39.8
1293	2014	0510	0311	4.6	-20.175	-69.219	92.4
1294	2014	0512	1153	4.7	-20.637	-70.865	43.2
926	2014	0514	0338	5.6	-22.739	-67.063	265.3
927	2014	0514	0551	5.3	-19.682	-71.143	42.3
928	2014	0516	1708	5.5	-23.4456	-68.5388	105
929	2014	0517	0911	5.6	-19.989	-70.896	42.6
930	2014	0521	0900	5.1	-30.452	-71.311	36.2
1295	2014	0527	0334	4.8	-20.856	-70.447	40.6
931	2014	0530	1141	5.1	-21.309	-69.974	67.8
932	2014	0530	1532	5.6	-21.302	-69.999	59.6
1204	2014	0530	2205	5.1	-33.552	-72.223	25.1
1224	2014	0530	1532	5.6	-21.302	-69.999	59.6
1205	2014	0604	1703	5.1	-20.652	-70.761	38.8
933	2014	0605	2019	5.1	-20.343	-70.224	40.5
1206	2014	0607	1355	4.5	-35.19	-71.782	41.1
946	2014	0612	1228	5	-30.745	-70.564	52.6
941	2014	0614	2213	4.8	-24.943	-69.401	108
934	2014	0616	0917	5	-23.97	-69.564	90.7
935	2014	0619	0938	5.8	-19.931	-70.906	38.8
936	2014	0619	1954	5.8	-19.815	-70.941	40.1
937	2014	0619	1959	5.3	-19.84	-70.889	39.3
938	2014	0620	1953	5.5	-19.772	-70.942	39.7
939	2014	0620	2022	5.8	-19.744	-71.002	38.2
940	2014	0703	0250	5	-34.758	-71.835	41.3
942	2014	0713	0316	4.8	-32.949	-71.255	44.1
943	2014	0713	0718	5.3	-30.748	-70.62	83.4
944	2014	0713	2054	5.5	-20.238	-70.309	40.7

Table A.1 Earthquake catalog.

ID	Date and Time			M_W	Hypocenter		
	YEAR	MODY	HRMN		Lat (°)	Lon (°)	Depth (km)
945	2014	0723	2139	5.6	-20.238	-68.74	122
1270	2014	0723	2139	5.6	-20.238	-68.74	122
947	2014	0814	0002	5.3	-20.158	-70.023	50.9
948	2014	0823	0445	5.6	-20.187	-69.081	100.2
949	2014	0823	2232	6.4	-32.737	-71.498	40.1
1208	2014	0904	0926	5	-20.702	-70.343	38
1256	2014	0924	1114	6.2	-23.622	-67.163	257.6
950	2014	0928	0846	5.3	-35.623	-73.209	10.4
951	2014	1007	0509	5.4	-19.653	-69.469	109.2
1296	2014	1007	1232	5.2	-19.993	-70.952	52.1
1297	2014	1012	1043	5	-22.894	-68.296	144.3
952	2014	1020	1018	5.1	-35.609	-71.555	91.4
1209	2014	1023	2131	4.9	-20.255	-69.199	101.6
1271	2014	1110	1138	5.6	-21.631	-68.725	111.3
1210	2014	1117	0033	5	-32.959	-70.6	86.2
1298	2014	1125	0854	5	-20.536	-68.761	111.1
1299	2014	1129	1417	5.4	-19.948	-71.129	30.1
1211	2014	1203	0937	5.1	-22.607	-70.201	70
1212	2014	1212	1234	5.2	-19.847	-70.917	33.7
1213	2014	1218	0624	5.2	-20.381	-68.867	103.3
1272	2015	0109	1148	5.1	-20.401	-69.025	110.4
1300	2015	0110	1754	5.4	-21.63	-68.658	109.8
1301	2015	0112	0336	3.6	-20.434	-69.246	85.1
1302	2015	0115	0520	4.8	-33.683	-71.097	68.2
953	2015	0120	1734	5.1	-23.409	-70.457	47.4
1214	2015	0122	1615	4.5	-22.99	-70.222	48.2
1303	2015	0123	1412	5	-18.121	-69.469	119.6
954	2015	0125	0847	5.2	-34.756	-71.813	43.4
1215	2015	0202	1521	5.3	-22.272	-70.8	40.1
1221	2015	0208	0603	4.1	-22.652	-70.396	41.8
955	2015	0211	1707	4.9	-30.214	-71.32	67.7
1273	2015	0211	1857	6.7	-23.167	-66.863	238.9
1222	2015	0212	1209	4.2	-22.205	-70.103	67.1
956	2015	0217	1435	5.4	-32.383	-70.988	77.5
1216	2015	0228	0345	5.2	-36.884	-72.991	35.4

Table A.1 Earthquake catalog.

ID	Date and Time			M_W	Hypocenter		
	YEAR	MODY	HRMN		Lat (°)	Lon (°)	Depth (km)
957	2015	0302	1653	5.2	-27.8657	-71.065	33.7
958	2015	0303	1245	5.2	-20.358	-69.145	106.2
959	2015	0305	2130	5.3	-29.319	-71.111	60
960	2015	0314	1603	5.3	-27.865	-70.889	47
1225	2015	0314	0123	4.1	-20.455	-70.148	18.2
961	2015	0318	1827	6.1	-36.101	-74.138	23
1226	2015	0318	1827	6.1	-36.101	-74.138	23
962	2015	0323	0451	6.4	-18.416	-69.269	121
1217	2015	0324	2246	4.8	-20.68	-70.785	15.5
963	2015	0328	1636	5.6	-22.191	-68.7	111.7
964	2015	0401	0817	5.4	-29.3442	-71.718	31.6
1304	2015	0419	0233	4	-19.37	-70.181	39
1227	2015	0512	0036	4	-33.307	-70.47	93.3
965	2015	0514	1508	5.1	-28.6662	-71.4742	18.4
1228	2015	0516	0851	4.6	-33.08	-71.933	33.3
1229	2015	0521	2034	4.8	-34.891	-71.795	40.4
966	2015	0522	1939	5.3	-20.1892	-70.8373	17.2
1230	2015	0526	1032	5.6	-22.061	-68.522	133.6
967	2015	0529	0428	5.2	-28.216	-70.649	43.8
968	2015	0610	1352	6	-22.425	-68.581	130.5
1305	2015	0614	1721	3.5	-22.638	-70.356	41.3
1306	2015	0620	0224	6	-36.239	-73.972	23.3
1307	2015	0622	0612	4.9	-33.779	-70.467	105.1
969	2015	0707	1335	4.7	-33.3711	-70.22	94.8
1308	2015	0707	1343	5.2	-33.435	-70.336	117.3
970	2015	0713	2116	5	-33.0941	-70.232	98.5
1309	2015	0713	1815	5.1	-33.054	-70.305	111.9
971	2015	0716	1048	5	-29.5	-71.8098	7.7
972	2015	0717	1111	5.2	-35.5031	-73.2219	10
973	2015	0724	2314	5.3	-20.29	-70.174	38.2
1310	2015	0725	0106	4.6	-26.942	-70.826	55.1
974	2015	0728	1805	4.8	-34.9564	-71.8116	44.7
1231	2015	0804	1111	4.7	-20.591	-69.263	108.1
975	2015	0810	0940	5.4	-29.4727	-71.2415	38.9
1311	2015	0811	2023	4.1	-17.889	-70.493	22.5

Table A.1 Earthquake catalog.

ID	Date and Time			M_W	Hypocenter		
	YEAR	MODY	HRMN		Lat (°)	Lon (°)	Depth (km)
976	2015	0812	0014	5.5	-31.6968	-71.6227	30
977	2015	0823	2310	5.7	-29.723	-71.25	50.1
1247	2015	0823	2020	4.2	-20.357	-70.277	46.1
1232	2015	0824	0125	4.9	-20.415	-69.141	111.5
1312	2015	0824	0516	5.2	-29.882	-71.252	44.7
1313	2015	0825	0456	4.3	-20.371	-69.046	100.8
978	2015	0901	1528	5.4	-19.785	-69.245	97.2
1314	2015	0903	1355	4.9	-36.81	-72.579	60
826	2015	0916	2254	8.3	-31.5571	-71.6617	29.81
979	2015	0916	2318	7.1	-31.589	-71.791	16.5
980	2015	0916	2259	6.3	-31.618	-71.745	26.7
1248	2015	0916	2315	6.2	-31.901	-71.899	29.2
1249	2015	0916	2321	7.6	-31.589	-71.791	16.5
1250	2015	0916	2338	6	-31.882	-71.888	35.1
1315	2015	0916	2303	6.1	-31.733	-71.677	30
981	2015	0917	0141	6.5	-31.113	-71.651	49.5
982	2015	0917	0410	6.7	-31.542	-71.748	40.7
983	2015	0917	2040	5.7	-29.9614	-71.8851	5.7
987	2015	0917	1604	5	-31.3359	-71.9539	14.6
988	2015	0917	0312	5.1	-30.922	-71.264	47.1
989	2015	0917	0355	6.3	-31.461	-71.704	53.3
1251	2015	0917	0111	6.6	-31.542	-71.748	40.7
1316	2015	0918	1955	4.8	-31.734	-72.071	26.4
984	2015	0919	0907	5.8	-31.128	-71.578	34.2
1233	2015	0919	1045	4.5	-34.001	-71.199	70.6
985	2015	0920	0302	5.5	-30.79	-71.319	48.3
986	2015	0921	0539	6.1	-31.759	-71.737	40.7
1238	2015	0921	1739	6.7	-31.759	-71.553	13
1267	2015	0922	0712	6.1	-31.451	-71.13	63.3
1234	2015	0924	1612	5.3	-30.705	-71.398	50
1317	2015	0924	0723	4.8	-20.214	-69.15	99.8
1235	2015	0925	0330	5.3	-20.91	-69.221	90.7
1236	2015	0926	0252	6.3	-30.794	-71.418	40.3
1318	2015	0928	1529	6	-23.875	-67.121	249.9
1268	2015	1003	1122	5.3	-29.858	-71.644	38.8

Table A.1 Earthquake catalog.

ID	Date and Time			M_W	Hypocenter		
	YEAR	MODY	HRMN		Lat (°)	Lon (°)	Depth (km)
1319	2015	1003	0622	6.1	-37.556	-73.743	20
1320	2015	1003	0628	5.9	-30.368	-71.371	33.9
1269	2015	1005	1635	5.9	-30.35	-71.466	29
1237	2015	1007	0800	5.2	-30.298	-71.228	24.5
1239	2015	1016	0453	4.8	-20.07	-68.894	115.2
1252	2015	1020	1007	5.2	-30.736	-71.443	50.2
1240	2015	1021	1448	4.8	-20.374	-69.298	100.5
1321	2015	1025	1314	4.7	-29.721	-71.201	44.5
1241	2015	1101	1516	5.9	-23.232	-68.535	114.6
1322	2015	1107	0731	6.7	-30.87	-71.431	47.8
1323	2015	1107	1055	5.8	-30.719	-71.367	48
1242	2015	1108	0819	5.5	-17.472	-69.791	194.4
1324	2015	1111	0155	6.8	-29.46	-72.12	32.9
1325	2015	1111	0247	6.8	-29.46	-72.12	32.9
1326	2015	1121	2305	5.8	-30.607	-71.797	34.9
1327	2015	1124	2250	7.6	-10.53	-71.09	604
1244	2015	1127	2100	6.2	-24.779	-70.546	37.2
1328	2015	1203	0834	5.1	-29.84	-71.54	48.1
1245	2015	1205	1028	4.7	-22.536	-70.316	38.7
1246	2015	1207	1802	4.5	-18.738	-70.002	99.6
1253	2015	1210	0031	5.4	-35.914	-73.562	14.4
1329	2015	1219	1927	5.8	-30.637	-71.308	49.5
1254	2015	1223	2353	4.4	-20.539	-69.215	112.1
1255	2015	1226	1141	4.1	-18.424	-70.012	39.9

Table A.2 Earthquake source parameters.

ID	EQ Classification		Fault Plane 1			Fault Plane 2		
	Automatic	Preferred	Strike (°)	Dip (°)	Rake (°)	Strike (°)	Dip (°)	Rake (°)
808	Interface	Interface	5	15/30	90/110			
809	Interface	Pending						
810	Interface	Pending						
811	Interface	Interface	0	21	99	170	69	86
581	Interface	Interface	4	18	N/A			
664	Interface	Interface	93	40	49	321	61	119
583	Intraslab	Pending	85	4	-175	351	90	-86
665	Intraslab	Intraslab	158	59	-161	58	74	-33
551	Undetermined	Pending	188	21	-51	327	74	-104
667	Intraslab	Intraslab	173	80	-83			
668	Intraslab	Pending						
666	Interface	Interface	352	31	88	175	59	91
669	Interface	Pending						
636	Interface	Interface	181	40	116	329	55	70
670	Shallow crustal	Pending						
671	Intraslab	Pending	141	19	-151	23	81	-73
585	Intraslab	Pending	102	21	-159	351	82	-70
672	Interface	Pending						
673	Intraslab	Intraslab	236	19	-29	354	81	-107
586	Interface	Pending	356	18	98	167	72	87
587	Intraslab	Pending	214	12	-62	5	80	-96
637	Intraslab	Intraslab	219	33	-67	11	60	-105
674	Intraslab	Intraslab	128	19	-128	347	75	-78
588	Interface	Pending	207	12	-56	352	80	-97
638	Outer-rise	Outer-rise	219	44	-86	33	46	-94
557	Interface	Interface	310	18	62			
558	Interface	Pending						
559	Interface	Pending	314	19	75	150	71	95
560	Intraslab	Pending	199	22	-52	339	73	-104
553	Undetermined	Pending	88	23	44	316	74	107
554	Intraslab	Pending	118	22	-89	297	68	-91
555	Interface	Interface	306	14	52	165	79	99
556	Shallow crustal	Shallow crustal	14	46	-169	276	82	-44
681	Interface	Interface	334	40	87	158	50	93

Table A.2 Earthquake source parameters.

ID	EQ Classification		Fault Plane 1			Fault Plane 2		
	Automatic	Preferred	Strike (°)	Dip (°)	Rake (°)	Strike (°)	Dip (°)	Rake (°)
677	Intraslab	Intraslab	122	21	-120	335	72	-79
639	Interface	Pending						
680	Intraslab	Pending						
640	Interface	Pending						
684	Intraslab	Intraslab	215	22	-21	324	83	-110
614	Intraslab	Pending	274	30	-22	23	79	-118
616	Intraslab	Pending	253	56	168	350	80	35
685	Interface	Interface	358	35	89	179	55	91
686	Interface	Interface	9	40	107	167	52	76
615	Interface	Interface	353	29	96	166	61	87
617	Intraslab	Pending	27	39	-94	212	51	-87
545	Intraslab	Pending	353	40	-75	153	51	-103
687	Intraslab	Intraslab	122	57	-165	24	78	-34
529	Intraslab	Pending	353	47	-65	139	49	-114
618	Interface	Interface	1	27	93	177	63	88
641	Interface	Pending						
711	Shallow crustal	Pending						
717	Intraslab	Pending						
718	Interface	Intraslab	70	48	-144	314	64	-48
720	Intraslab	Pending						
589	Intraslab	Pending	286	28	-18	32	82	-117
735	Intraslab	Intraslab	157	35	-133	26	65	-64
642	Shallow crustal	Pending	0	116	118	151	76	82
723	Shallow crustal	Pending						
729	Intraslab	Intraslab	213	42	-30	326	70	-128
643	Shallow crustal	Shallow crustal	21	61	-178	290	88	-29
732	Interface	Interface	17	21	109	177	70	83
620	Intraslab	Pending	31	36	-61	176	59	-109
644	Shallow crustal	Shallow crustal	9	24	103	175	66	84
741	Intraslab	Intraslab	252	54	4	160	86	144
591	Intraslab	Pending	64	18	-8	161	88	-107
746	Intraslab	Intraslab	244	12	-37	11	82	-100
590	Intraslab	Pending	183	29	-95	9	61	-87
561	Intraslab	Intraslab	187	23	-73			

Table A.2 Earthquake source parameters.

ID	EQ Classification		Fault Plane 1			Fault Plane 2		
	Automatic	Preferred	Strike (°)	Dip (°)	Rake (°)	Strike (°)	Dip (°)	Rake (°)
747	Undetermined	Pending						
745	Interface	Pending						
749	Intraslab	Intraslab	118	33	-113	325	60	-75
751	Intraslab	Intraslab	165	17	-93	348	73	-89
753	Intraslab	Intraslab	238	22	-27	353	80	-110
592	Intraslab	Pending	126	26	-149	7	77	-68
645	Interface	Interface	11	32	97	183	59	86
760	Undetermined	Intraslab	321	66	178	52	88	24
757	Shallow crustal	Pending						
759	Interface	Interface	49	30	106	211	61	81
622	Shallow crustal	Interface	11	14	106	175	76	86
762	Interface	Interface	14	18	112	171	73	83
756	Intraslab	Pending						
646	Interface	Interface						
623	Outer-rise	Outer-rise	357	46	-111	205	48	-70
593	Intraslab	Intraslab	194	36	-48	326	64	-115
624	Intraslab	Pending	147	17	-147	25	81	-76
761	Interface	Interface	3	26	96	176	65	87
546	Interface	Pending	327	16	73	165	74	95
621	Intraslab	Pending	344	7	-87	160	83	-90
763	Undetermined	Shallow crustal	220	41	28	108	72	127
765	Undetermined	Intraslab	150	29	-133	17	70	-70
764	Interface	Interface	7	35	100	176	55	83
648	Interface	Interface						
769	Interface	Interface	33	43	128	166	58	60
647	Intraslab	Pending						
533	Intraslab	Pending	215	37	-29	329	73	-124
599	Intraslab	Pending	240	3	-24	353	89	-93
771	Intraslab	Pending						
772	Interface	Pending	321	28	63	171	65	104
562	Interface	Pending	327	18	63	176	74	98
774	Intraslab	Intraslab	194	32	-32	312	73	-118
595	Interface	Interface	3	20	98	170	71	87
766	Interface	Pending						

Table A.2 Earthquake source parameters.

ID	EQ Classification		Fault Plane 1			Fault Plane 2		
	Automatic	Preferred	Strike (°)	Dip (°)	Rake (°)	Strike (°)	Dip (°)	Rake (°)
596	Interface	Interface	5	21	106	168	70	84
768	Interface	Interface	360	16	98	172	74	88
770	Interface	Interface	14	13	119	164	79	84
773	Intraslab	Intraslab	246	44	-17	349	78	-133
598	Shallow crustal	Pending	1	13	99	172	78	88
594	Interface	Interface	9	15	106	173	75	86
767	Interface	Interface	359	21	89	179	69	90
597	Interface	Interface	246	6	159	357	88	84
779	Interface	Interface						
600	Interface	Interface	1	27	107	162	64	81
601	Intraslab	Pending	223	18	-54	6	76	-100
776	Interface	Interface	357	29	102	163	62	83
602	Intraslab	Intraslab	198	22	-73	1	69	-97
563	Intraslab	Pending	177	44	-23	284	74	-132
781	Shallow crustal	Pending						
535	Intraslab	Pending	198	39	-60	341	57	-112
626	Intraslab	Pending	26	21	-36	150	78	-108
786	Undetermined	Shallow crustal	289	44	138	52	62	54
787	Undetermined	Pending						
606	Intraslab	Intraslab	257	18	-2	349	89	-108
1274	Interface	Interface	360	19	94	175	71	89
662	Interface	Interface	2	19	100	172	72	87
788	Intraslab	Intraslab						
566	Interface	Interface	355	24	102	161	67	85
789	Interface	Intraslab	192	20	-84	5	70	-92
567	Intraslab	Intraslab	101	26	-112	306	66	-80
790	Intraslab	Intraslab						
782	Intraslab	Intraslab						
564	Interface	Interface	342	24	92	160	66	89
603	Intraslab	Pending	180	11	-79	350	79	-92
783	Interface	Interface						
784	Intraslab	Intraslab						
1275	Intraslab	Intraslab	69	57	-156	325	70	-35
604	Shallow crustal	Pending	169	25	97	342	66	87

Table A.2 Earthquake source parameters.

ID	EQ Classification		Fault Plane 1			Fault Plane 2		
	Automatic	Preferred	Strike (°)	Dip (°)	Rake (°)	Strike (°)	Dip (°)	Rake (°)
649	Interface	Interface	15	18	109.33			
650	Outer-rise	Pending	3	46	-102	200	46	-78
651	Interface	Pending						
652	Interface	Interface	3	27	97	175	64	86
653	Interface	Pending						
654	Interface	Pending	3	27	97	175	64	86
785	Interface	Pending						
655	Shallow crustal	Interface	17	25	113	171	67	80
656	Interface	Pending	15	12	103	182	78	87
990	Interface	Interface	2	17	94	178	73	89
605	Intraslab	Intraslab	155	26	-115	2	67	-78
991	Interface	Interface	10	19	97	183	71	88
657	Interface	Pending	11	8	116	164	83	87
658	Interface	Interface	9	16	98	180	74	88
992	Shallow crustal	Pending						
993	Interface	Pending						
994	Shallow crustal	Pending						
995	Interface	Pending						
1017	Interface	Pending	348	12	84	174	78	91
996	Shallow crustal	Pending						
997	Shallow crustal	Pending						
1089	Interface	Pending						
1276	Shallow crustal	Pending						
659	Interface	Pending	324	35	-90	145	55	-90
660	Interface	Pending	16	6	-53	155	78	-90
998	Interface	Interface						
999	Shallow crustal	Pending						
1000	Shallow crustal	Pending						
1123	Interface	Pending						
1001	Interface	Pending						
1002	Interface	Pending						
1003	Interface	Interface	7	19	102	175	71	86
1004	Interface	Pending						
1005	Interface	Pending						

Table A.2 Earthquake source parameters.

ID	EQ Classification		Fault Plane 1			Fault Plane 2		
	Automatic	Preferred	Strike (°)	Dip (°)	Rake (°)	Strike (°)	Dip (°)	Rake (°)
1139	Shallow crustal	Pending						
1007	Outer-rise	Pending	21	15	103	187	76	87
661	Interface	Interface	12	14	107	175	77	86
1006	Interface	Interface	19	14	112	177	77	85
1008	Interface	Pending						
1009	Interface	Pending						
1010	Interface	Pending						
1019	Shallow crustal	Pending						
1011	Interface	Pending						
1020	Interface	Pending						
1124	Intraslab	Pending						
625	Interface	Interface	176	38	70	21	54	105
1012	Interface	Pending						
1013	Interface	Pending						
1028	Interface	Interface	28	16	112	185	75	84
1014	Interface	Pending						
1140	Shallow crustal	Pending						
1015	Interface	Pending						
1021	Interface	Interface						
1022	Interface	Pending						
1125	Interface	Pending						
1277	Interface	Pending						
1016	Intraslab	Pending						
1027	Intraslab	Intraslab	183	15	-58	330	77	-98
1278	Interface	Pending						
1023	Intraslab	Pending						
1126	Shallow crustal	Pending						
1018	Shallow crustal	Pending						
1127	Shallow crustal	Pending						
1038	Intraslab	Pending						
1024	Interface	Intraslab	237	25	-15	341	84	-114
1025	Interface	Pending						
1128	Interface	Pending						
1029	Shallow crustal	Pending						

Table A.2 Earthquake source parameters.

ID	EQ Classification		Fault Plane 1			Fault Plane 2		
	Automatic	Preferred	Strike (°)	Dip (°)	Rake (°)	Strike (°)	Dip (°)	Rake (°)
1129	Interface	Pending						
1141	Outer-rise	Pending	31	15	115	185	77	84
1026	Interface	Pending						
1030	Interface	Pending	7	14	141	135	81	79
1031	Interface	Pending						
1032	Interface	Pending						
1130	Interface	Pending						
1033	Interface	Pending						
1279	Interface	Pending						
1034	Interface	Pending						
1035	Interface	Pending						
1036	Interface	Pending	26	25	-36	149	76	-110
1037	Shallow crustal	Pending						
1054	Interface	Interface	357	14	89	178	76	90
1039	Interface	Pending						
1040	Interface	Pending	19	14	106	182	76	86
565	Interface	Interface	357	37	104	160	54	80
1280	Interface	Pending						
1041	Interface	Pending						
1131	Interface	Pending						
1043	Interface	Pending						
1132	Interface	Pending						
1042	Interface	Pending						
1044	Intraslab	Intraslab						
1050	Shallow crustal	Pending						
548	Intraslab	Pending	349	37	-82	159	54	-96
1045	Interface	Pending						
1049	Interface	Pending						
1046	Interface	Pending						
1047	Interface	Pending						
1048	Interface	Pending						
830	Interface	Interface						
1051	Intraslab	Pending						
1052	Intraslab	Intraslab						

Table A.2 Earthquake source parameters.

ID	EQ Classification		Fault Plane 1			Fault Plane 2		
	Automatic	Preferred	Strike (°)	Dip (°)	Rake (°)	Strike (°)	Dip (°)	Rake (°)
1053	Shallow crustal	Pending						
1055	Intraslab	Pending						
1056	Interface	Pending						
1072	Interface	Pending						
1057	Interface	Pending						
831	Intraslab	Intraslab	154	27	-101	347	64	-84
1059	Interface	Interface	330	27	126	110	69	73
1058	Interface	Interface						
1060	Interface	Pending						
1070	Interface	Pending						
1061	Shallow crustal	Pending						
607	Intraslab	Intraslab	167	40	-73	325	52	-104
1062	Intraslab	Pending						
1067	Interface	Pending	7	9	97	180	81	89
1133	Interface	Interface	353	14	88	175	76	91
1063	Shallow crustal	Pending						
1064	Interface	Pending						
1065	Intraslab	Intraslab	29	24	130	165	72	74
1066	Interface	Interface						
1071	Interface	Pending						
1090	Shallow crustal	Pending						
1068	Interface	Interface	6	13	97	179	78	88
1069	Interface	Interface						
1075	Interface	Pending	355	30	86	180	60	92
1073	Interface	Pending						
832	Intraslab	Intraslab						
1091	Intraslab	Intraslab						
1074	Interface	Pending						
1142	Interface	Pending						
663	Outer-rise	Pending	11	14	99	182	76	88
1076	Interface	Pending						
1092	Interface	Pending						
1077	Interface	Pending						
1078	Outer-rise	Outer-rise	9	17	98	180	73	87

Table A.2 Earthquake source parameters.

ID	EQ Classification		Fault Plane 1			Fault Plane 2		
	Automatic	Preferred	Strike (°)	Dip (°)	Rake (°)	Strike (°)	Dip (°)	Rake (°)
1079	Interface	Pending						
1081	Interface	Pending						
1086	Interface	Pending						
1080	Interface	Pending						
1082	Outer-rise	Outer-rise	2	45	-136	237	60	-54
833	Intraslab	Intraslab	89	20	-141	322	78	-74
834	Interface	Pending						
1083	Interface	Pending						
1084	Interface	Interface						
1095	Interface	Interface	31	16	123	177	76	81
1085	Intraslab	Intraslab						
1087	Interface	Pending						
1134	Intraslab	Intraslab	263	32	-6	358	87	-122
1088	Interface	Pending						
1094	Intraslab	Pending						
1093	Interface	Pending						
1098	Interface	Pending						
627	Intraslab	Pending	360	20	-64	152	72	-99
1165	Interface	Interface	5	13	97	178	77	88
1096	Intraslab	Pending						
835	Interface	Interface	22	14	105	187	76	86
1097	Interface	Interface	138	15	60	349	77	98
836	Intraslab	Intraslab						
1099	Interface	Interface	9	17	98	180	73	88
1101	Interface	Pending						
837	Interface	Interface	15	13	104	180	77	87
1100	Interface	Interface	12	15	98	183	75	88
838	Interface	Interface	13	11	101	182	79	88
839	Interface	Interface	12	18	97	184	72	88
840	Interface	Interface	9	15	95	184	75	89
1102	Intraslab	Pending						
1166	Outer-rise	Interface	25	17	105	189	74	86
841	Interface	Interface	6	16	97	179	74	88
842	Intraslab	Intraslab	201	15	-61	351	77	-97

Table A.2 Earthquake source parameters.

ID	EQ Classification		Fault Plane 1			Fault Plane 2		
	Automatic	Preferred	Strike (°)	Dip (°)	Rake (°)	Strike (°)	Dip (°)	Rake (°)
1103	Interface	Pending						
568	Intraslab	Intraslab	210	26	-37	335	75	-111
1108	Interface	Pending						
1104	Interface	Interface	15	28	105	179	63	83
1281	Shallow crustal	Interface	6	28	101	174	62	84
843	Intraslab	Intraslab						
1105	Interface	Interface	29	32	119	176	62	73
1106	Interface	Pending						
1170	Intraslab	Intraslab	230	24	-35	352	76	-110
1107	Interface	Pending						
1109	Interface	Interface	9	23	100	178	67	86
1110	Interface	Interface	19	32	118	167	62	74
1114	Outer-rise	Pending	1	17	88	183	73	91
1111	Interface	Interface	24	31	118	172	63	74
1112	Intraslab	Intraslab	208	32	-27	321	76	-119
608	Intraslab	Intraslab	261	11	-9	360	88	-101
1113	Interface	Pending						
1115	Intraslab	Pending						
1116	Interface	Interface	14	21	108	174	70	83
1117	Intraslab	Pending						
1118	Interface	Interface	351	27	90	171	63	90
1119	Interface	Interface	3	15	95	178	75	89
1120	Interface	Interface	24	19	103	191	71	86
1121	Interface	Interface	344	17	61	194	75	98
1122	Interface	Interface	49	9	131	188	83	84
536	Intraslab	Pending	197	40	-57	336	58	-114
628	Intraslab	Pending	70	34	-45	199	67	-115
1135	Outer-rise	Pending						
1136	Intraslab	Intraslab	209	50	-40	328	60	-132
1138	Interface	Interface						
1137	Interface	Interface	359	16	84	185	74	92
844	Intraslab	Intraslab	155	19	-95	341	71	-88
1159	Interface	Pending						
569	Interface	Pending	326	15	68	168	76	96

Table A.2 Earthquake source parameters.

ID	EQ Classification		Fault Plane 1			Fault Plane 2		
	Automatic	Preferred	Strike (°)	Dip (°)	Rake (°)	Strike (°)	Dip (°)	Rake (°)
845	Interface	Interface	237	26	140	4	74	70
1143	Interface	Interface	346	20	76	181	71	95
570	Intraslab	Pending	163	11	102	331	79	88
629	Interface	Interface	17	25	109	176	67	81
1144	Shallow crustal	Interface	11	23	100	180	68	86
1182	Interface	Interface	355	29	87	178	61	91
571	Interface	Pending	323	31	64	174	63	105
1145	Interface	Pending						
1148	Interface	Pending						
1146	Intraslab	Intraslab						
846	Interface	Interface	179	23	88	1	67	91
847	Interface	Interface	17	36	119	163	59	71
630	Intraslab	Pending	302	24	-86	118	66	-92
1150	Interface	Pending						
1147	Intraslab	Intraslab						
848	Intraslab	Intraslab	179	19	-91	1	71	-89
851	Intraslab	Intraslab						
849	Intraslab	Intraslab	68	64	2	337	88	154
850	Interface	Interface	20	16	112	177	76	84
852	Intraslab	Intraslab	260	48	-18	2	77	-137
1149	Intraslab	Intraslab	110	12	-130	331	81	-82
1152	Interface	Interface	2	24	95	176	66	88
1151	Intraslab	Intraslab						
853	Interface	Interface	330	47	35	214	65	131
1157	Interface	Pending						
572	Intraslab	Intraslab	203	25	-25	315	80	-113
1153	Interface	Pending						
854	Intraslab	Intraslab	23	44	125	160	55	62
1154	Intraslab	Pending						
631	Intraslab	Pending	28	23	-44	160	74	-107
573	Intraslab	Pending	110	56	173	204	84	34
1155	Intraslab	Pending						
1156	Intraslab	Pending						
1158	Interface	Interface	358	22	96	171	68	88

Table A.2 Earthquake source parameters.

ID	EQ Classification		Fault Plane 1			Fault Plane 2		
	Automatic	Preferred	Strike (°)	Dip (°)	Rake (°)	Strike (°)	Dip (°)	Rake (°)
549	Intraslab	Pending	222	26	-66	16	67	-101
855	Intraslab	Intraslab	276	38	180	6	90	52
856	Intraslab	Pending						
857	Interface	Pending						
1160	Intraslab	Intraslab	121	24	-123	336	70	-77
1282	Interface	Pending						
858	Intraslab	Intraslab	184	5	-66	339	85	-92
1161	Intraslab	Intraslab	151	35	-107	351	57	-78
1162	Intraslab	Intraslab	252	40	-3	344	88	-130
859	Intraslab	Intraslab	158	35	-114	7	59	-74
860	Intraslab	Intraslab	170	84	-174	80	84	-6
1163	Intraslab	Pending						
1164	Intraslab	Pending						
861	Intraslab	Intraslab	83	29	-150	326	76	-64
632	Intraslab	Intraslab	248	23	-28	4	79	-111
862	Intraslab	Intraslab	285	39	137	51	65	59
1167	Intraslab	Pending						
1168	Interface	Interface	4	17	92	182	73	89
864	Intraslab	Intraslab						
1169	Intraslab	Pending						
863	Intraslab	Intraslab	217	19	-39	345	78	-105
633	Interface	Interface	31	30	119	178	64	75
1172	Interface	Interface	6	24	100	176	66	86
634	Intraslab	Pending	17	25	-37	142	75	-110
1171	Interface	Pending						
865	Interface	Intraslab	199	34	-40	323	69	-118
1173	Intraslab	Intraslab	164	6	-95	349	84	-89
1174	Intraslab	Pending						
1207	Undetermined	Pending						
1175	Intraslab	Intraslab	190	45	-111	39	48	-70
1257	Intraslab	Intraslab	221	33	-44	350	68	-115
866	Intraslab	Intraslab	194	11	-66	350	80	-94
1176	Interface	Interface	356	27	97	168	63	86
537	Outer-rise	Pending	179	40	-82	349	50	-97

Table A.2 Earthquake source parameters.

ID	EQ Classification		Fault Plane 1			Fault Plane 2		
	Automatic	Preferred	Strike (°)	Dip (°)	Rake (°)	Strike (°)	Dip (°)	Rake (°)
1177	Interface	Interface	148	34	47	16	66	115
1178	Intraslab	Intraslab	238	25	-33	358	77	-111
867	Intraslab	Intraslab	224	28	-44	355	71	-110
1179	Intraslab	Intraslab	338	45	-18	81	77	-133
868	Intraslab	Pending						
574	Interface	Pending	307	31	84	133	59	93
869	Interface	Interface	4	20	92	182	70	89
870	Interface	Interface	358	20	86	182	70	91
1180	Intraslab	Intraslab						
1181	Intraslab	Pending						
871	Interface	Interface						
1283	Interface	Interface	19	17	92	196	73	89
1284	Interface	Interface	15	18	91	194	72	90
635	Interface	Interface	5	28	98	175	62	85
872	Intraslab	Pending						
1183	Intraslab	Pending						
873	Intraslab	Intraslab						
1184	Interface	Pending						
1185	Interface	Pending						
1194	Interface	Pending						
1186	Interface	Pending						
1187	Intraslab	Pending						
874	Intraslab	Pending						
1188	Interface	Interface	355	22	92	173	68	89
1285	Intraslab	Pending						
1189	Interface	Pending						
875	Intraslab	Pending						
876	Undetermined	Pending						
1190	Intraslab	Pending						
877	Intraslab	Intraslab	190	41	-57	329	57	-115
1191	Shallow crustal	Pending						
1192	Intraslab	Pending						
878	Intraslab	Pending						
1193	Interface	Pending						

Table A.2 Earthquake source parameters.

ID	EQ Classification		Fault Plane 1			Fault Plane 2		
	Automatic	Preferred	Strike (°)	Dip (°)	Rake (°)	Strike (°)	Dip (°)	Rake (°)
1197	Interface	Pending						
538	Interface	Pending	205	38	112	358	56	74
575	Interface	Pending	333	19	76	168	71	95
1195	Interface	Pending						
576	Interface	Interface	284	26	54	144	69	106
609	Interface	Interface	352	17	94	168	73	89
879	Interface	Interface						
880	Interface	Interface	348	25	89	169	65	90
881	Interface	Interface	13	17	101	182	73	87
882	Interface	Interface						
883	Intraslab	Pending						
577	Interface	Interface	346	20	90	167	70	90
884	Interface	Interface						
578	Interface	Interface	350	21	100	160	69	86
1258	Interface	Pending						
799	Interface	Interface	347	21	90	166	69	90
885	Interface	Interface	352	22	94	168	68	89
886	Interface	Interface	351	26	92	169	64	89
887	Interface	Interface	353	20	91	171	70	90
1196	Interface	Pending						
801	Intraslab	Intraslab	275	48	-36	31	64	-132
579	Interface	Interface	357	18	N/A			
888	Shallow crustal	Pending	347	26	81	177	65	94
901	Interface	Pending						
889	Interface	Interface						
890	Interface	Interface						
891	Interface	Interface						
892	Interface	Interface						
893	Interface	Interface						
1199	Interface	Interface						
1243	Interface	Interface						
1259	Interface	Interface						
1260	Interface	Interface						
1286	Interface	Interface						

Table A.2 Earthquake source parameters.

ID	EQ Classification		Fault Plane 1			Fault Plane 2		
	Automatic	Preferred	Strike (°)	Dip (°)	Rake (°)	Strike (°)	Dip (°)	Rake (°)
1287	Interface	Interface						
580	Interface	Interface	358	14	103	165	76	87
610	Interface	Interface	354	23	96	167	67	87
611	Interface	Interface	4	27	104	168	63	83
894	Interface	Interface						
895	Interface	Interface						
896	Interface	Interface						
897	Interface	Interface						
898	Interface	Interface						
899	Interface	Interface						
1198	Interface	Interface						
1218	Interface	Pending						
1219	Interface	Interface						
1220	Interface	Interface						
1261	Interface	Interface						
612	Interface	Interface	1	25	109	160	67	81
900	Intraslab	Pending						
902	Intraslab	Pending						
903	Interface	Interface	359	28	78	193	63	96
904	Interface	Interface	358	28	104	162	63	83
1200	Interface	Interface	355	27	95	169	63	88
1262	Interface	Interface	355	27	95	169	63	88
1288	Interface	Interface						
905	Interface	Interface	81	6	-167	338	89	-84
906	Interface	Interface	46	26	35	284	76	112
907	Interface	Interface						
908	Interface	Interface						
909	Interface	Interface						
910	Interface	Interface	344	28	90	164	62	90
911	Interface	Interface	1	18	70	202	73	97
912	Interface	Interface	350	22	91	169	68	90
1263	Interface	Interface						
1201	Interface	Interface	327	25	65	175	67	101
613	Interface	Interface	328	28	43	198	72	111

Table A.2 Earthquake source parameters.

ID	EQ Classification		Fault Plane 1			Fault Plane 2		
	Automatic	Preferred	Strike (°)	Dip (°)	Rake (°)	Strike (°)	Dip (°)	Rake (°)
913	Interface	Interface						
914	Interface	Interface						
1223	Interface	Interface	328	28	43	198	72	111
915	Interface	Interface	350	21	97	162	69	87
1264	Interface	Interface	356	21	95	170	69	88
916	Interface	Interface	343	26	81	173	64	95
917	Interface	Interface	76	36	73	276	55	102
918	Interface	Interface	343	30	81	174	60	95
919	Interface	Interface	300	45	121	79	52	62
1202	Intraslab	Pending						
920	Interface	Interface	339	26	79	171	64	96
921	Interface	Interface	349	24	93	166	66	89
1265	Interface	Interface	347	28	88	170	62	91
922	Interface	Interface						
923	Interface	Pending						
1289	Interface	Interface	318	34	70	162	58	103
1266	Interface	Interface	166	66	91	344	24	88
924	Interface	Interface	354	30	91	173	60	89
925	Intraslab	Intraslab						
1203	Interface	Shallow crustal	39	48	-141	281	62	-49
1290	Interface	Interface						
1291	Interface	Interface						
1292	Interface	Interface						
1293	Intraslab	Intraslab						
1294	Interface	Interface						
926	Intraslab	Intraslab						
927	Interface	Interface	332	23	78	164	67	95
928	Intraslab	Pending						
929	Interface	Interface	344	25	86	169	65	92
930	Interface	Pending						
1295	Interface	Interface						
931	Intraslab	Intraslab	353	56	23	250	71	143
932	Interface	Intraslab	2	85	4	272	86	175
1204	Interface	Pending						

Table A.2 Earthquake source parameters.

ID	EQ Classification		Fault Plane 1			Fault Plane 2		
	Automatic	Preferred	Strike (°)	Dip (°)	Rake (°)	Strike (°)	Dip (°)	Rake (°)
1224	Interface	Pending						
1205	Interface	Interface	347	26	89	168	64	90
933	Interface	Interface						
1206	Undetermined	Pending						
946	Undetermined	Pending						
941	Intraslab	Pending						
934	Intraslab	Pending						
935	Interface	Interface	349	21	92	167	69	89
936	Interface	Interface	351	22	91	169	68	90
937	Interface	Interface	161	63	83	355	28	103
938	Interface	Interface	349	24	94	164	66	88
939	Interface	Interface	344	21	84	171	70	92
940	Interface	Pending						
942	Interface	Pending						
943	Intraslab	Pending						
944	Interface	Interface	341	29	108	140	63	80
945	Intraslab	Intraslab	212	36	-30	327	73	-122
1270	Intraslab	Intraslab	212	36	-30	327	73	-122
947	Interface	Pending						
948	Intraslab	Intraslab	304	6	45	168	86	94
949	Interface	Interface	5	26	92	183	64	89
1208	Interface	Interface	357	31	104	161	60	82
1256	Intraslab	Intraslab	177	31	-97	5	59	-86
950	Interface	Interface	21	19	106	185	72	85
951	Intraslab	Intraslab	137	23	-126	355	71	-76
1296	Interface	Interface	342	27	84	168	64	93
1297	Intraslab	Intraslab	135	25	-99	324	66	-86
952	Intraslab	Intraslab						
1209	Intraslab	Intraslab						
1271	Intraslab	Intraslab	259	43	-26	8	73	-130
1210	Intraslab	Intraslab						
1298	Intraslab	Intraslab	189	28	-77	354	63	-97
1299	Interface	Interface	339	22	78	172	69	95
1211	Intraslab	Intraslab	240	31	-68	35	61	-103

Table A.2 Earthquake source parameters.

ID	EQ Classification		Fault Plane 1			Fault Plane 2		
	Automatic	Preferred	Strike (°)	Dip (°)	Rake (°)	Strike (°)	Dip (°)	Rake (°)
1212	Interface	Interface	340	24	83	168	66	93
1213	Intraslab	Pending						
1272	Intraslab	Intraslab						
1300	Intraslab	Intraslab	117	35	-122	334	61	-70
1301	Intraslab	Pending						
1302	Intraslab	Pending						
953	Interface	Interface	22	36	103	187	55	81
1214	Interface	Pending						
1303	Intraslab	Intraslab	184	5	-57	330	86	-93
954	Interface	Interface						
1215	Interface	Interface	60	61	165	158	76	29
1221	Interface	Pending						
955	Intraslab	Intraslab						
1273	Intraslab	Intraslab	168	19	-104	3	72	-85
1222	Intraslab	Pending						
956	Intraslab	Intraslab	339	80	170	70	80	10
1216	Interface	Interface						
957	Interface	Pending						
958	Intraslab	Pending						
959	Interface	Pending						
960	Interface	Pending						
1225	Shallow crustal	Pending						
961	Outer-rise	Pending	9	17	87	192	73	91
1226	Outer-rise	Pending	9	17	87	192	73	91
962	Intraslab	Intraslab	228	17	-32	349	81	-105
1217	Interface	Pending						
963	Intraslab	Intraslab	153	32	-113	359	61	-77
964	Interface	Pending						
1304	Interface	Pending						
1227	Intraslab	Pending						
965	Interface	Pending						
1228	Interface	Pending						
1229	Interface	Pending						
966	Interface	Pending						

Table A.2 Earthquake source parameters.

ID	EQ Classification		Fault Plane 1			Fault Plane 2		
	Automatic	Preferred	Strike (°)	Dip (°)	Rake (°)	Strike (°)	Dip (°)	Rake (°)
1230	Intraslab	Intraslab	113	32	-171	16	85	-58
967	Interface	Pending						
968	Intraslab	Intraslab	139	38	-80	306	52	-98
1305	Interface	Pending						
1306	Interface	Pending						
1307	Intraslab	Pending						
969	Intraslab	Pending						
1308	Intraslab	Pending						
970	Intraslab	Pending						
1309	Intraslab	Pending						
971	Shallow crustal	Pending						
972	Interface	Pending						
973	Interface	Interface	327	29	72	167	63	100
1310	Interface	Pending						
974	Interface	Pending						
1231	Intraslab	Pending						
975	Interface	Pending						
1311	Shallow crustal	Pending						
976	Interface	Pending						
977	Interface	Interface	17	38	81	208	52	97
1247	Interface	Pending						
1232	Intraslab	Pending						
1312	Interface	Pending						
1313	Intraslab	Pending						
978	Intraslab	Intraslab						
1314	Interface	Pending						
826	Interface	Interface	3.7	Varies	Varies			
979	Interface	Interface						
980	Interface	Interface						
1248	Interface	Interface						
1249	Interface	Pending						
1250	Interface	Interface						
1315	Interface	Interface						
981	Interface	Interface						

Table A.2 Earthquake source parameters.

ID	EQ Classification		Fault Plane 1			Fault Plane 2		
	Automatic	Preferred	Strike (°)	Dip (°)	Rake (°)	Strike (°)	Dip (°)	Rake (°)
982	Interface	Interface	1	29	96	174	61	87
983	Shallow crustal	Pending						
987	Interface	Pending						
988	Interface	Interface						
989	Interface	Interface						
1251	Interface	Pending						
1316	Interface	Pending						
984	Interface	Interface	353	29	92	171	61	89
1233	Intraslab	Pending						
985	Interface	Interface						
986	Interface	Interface	5	27	103	171	64	84
1238	Shallow crustal	Interface	2	27	92	180	63	89
1267	Intraslab	Intraslab	3	28	104	167	63	83
1234	Interface	Interface						
1317	Intraslab	Pending						
1235	Intraslab	Pending						
1236	Interface	Interface	357	32	93	174	58	88
1318	Intraslab	Intraslab	143	3	-122	355	87	-88
1268	Interface	Pending						
1319	Interface	Pending						
1320	Interface	Pending	13	35	108	171	57	77
1269	Interface	Pending	8	34	101	175	57	83
1237	Interface	Pending						
1239	Intraslab	Pending						
1252	Interface	Pending						
1240	Intraslab	Pending						
1321	Interface	Pending						
1241	Intraslab	Pending						
1322	Interface	Pending	359	33	97	171	58	86
1323	Interface	Pending	349	31	86	174	59	92
1242	Intraslab	Pending						
1324	Interface	Pending	2	22	93	179	68	89
1325	Interface	Pending	358	21	90	178	69	90
1326	Interface	Pending	5	28	102	171	63	84

Table A.2 Earthquake source parameters.

ID	EQ Classification		Fault Plane 1			Fault Plane 2		
	Automatic	Preferred	Strike (°)	Dip (°)	Rake (°)	Strike (°)	Dip (°)	Rake (°)
1327	Intraslab	Pending	350	30	-81	160	61	-95
1244	Interface	Pending	13	26	113	167	66	79
1328	Interface	Pending						
1245	Interface	Pending						
1246	Intraslab	Pending						
1253	Interface	Pending						
1329	Interface	Pending						
1254	Intraslab	Pending						
1255	Undetermined	Pending						

APPENDIX B

AUTOMATED EARTHQUAKE CLASSIFICATION

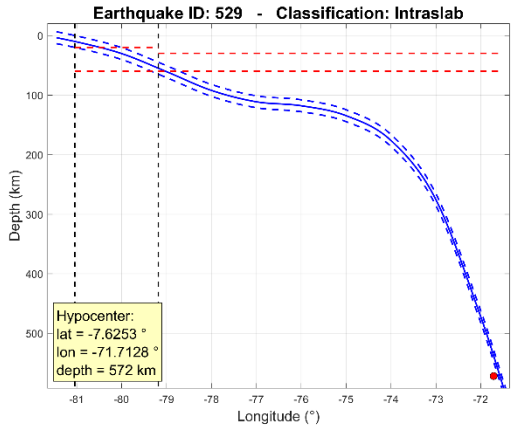

Figure B. 1: Event 529

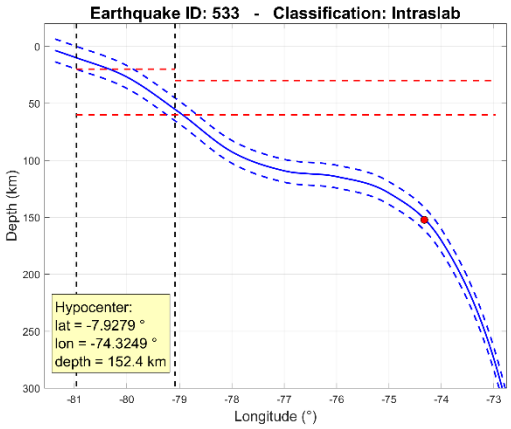

Figure B. 2: Event 533

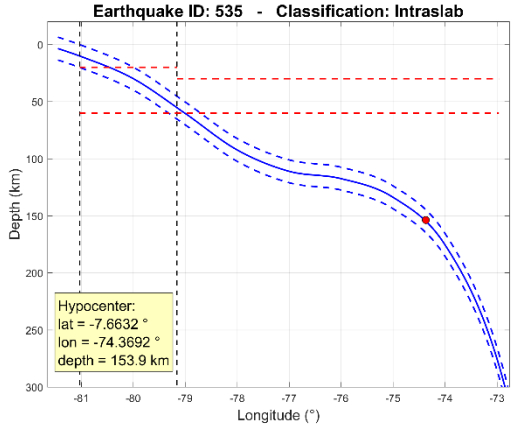

Figure B. 3: Event 535

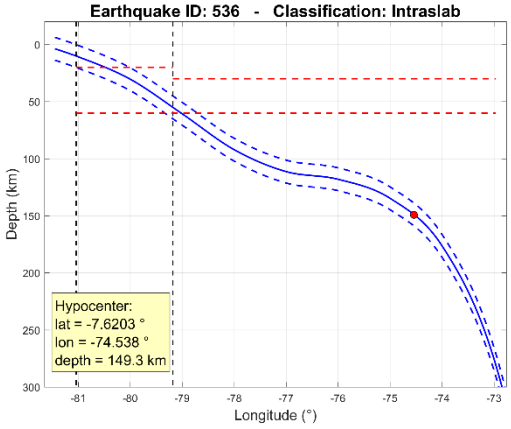

Figure B. 4: Event 536

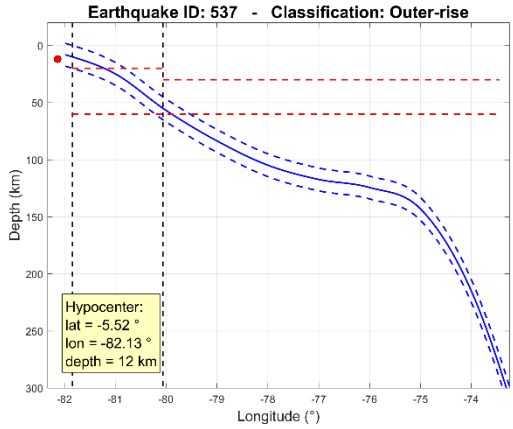

Figure B. 5: Event 537

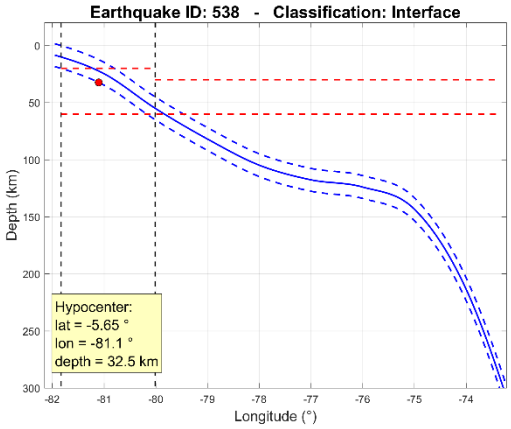

Figure B. 6: Event 538

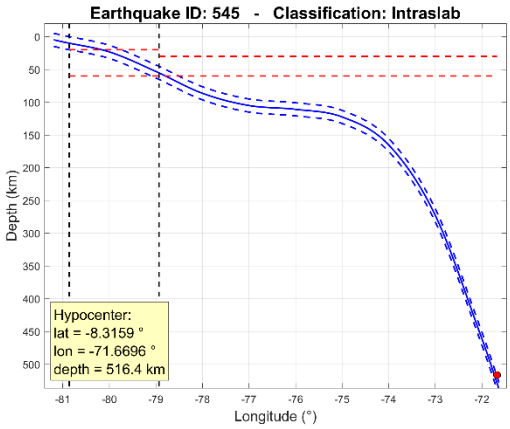

Figure B. 7: Event 545

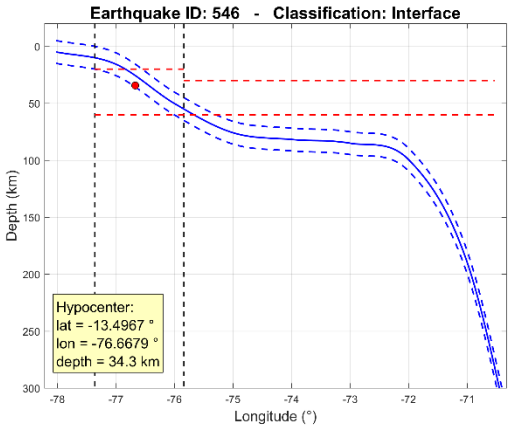

Figure B. 8: Event 546

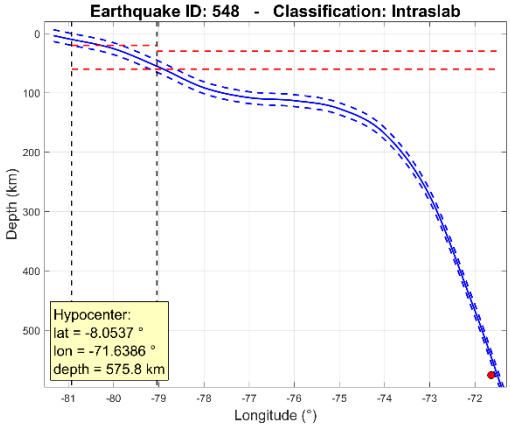

Figure B. 9: Event 548

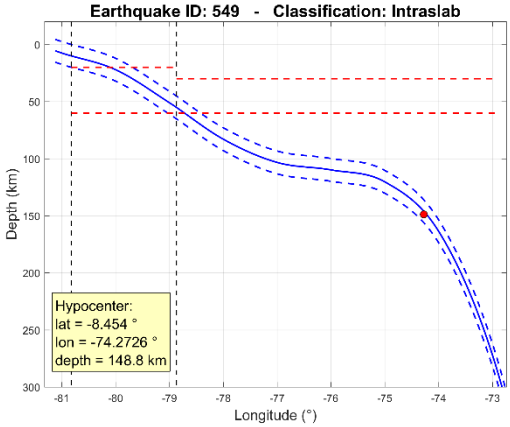

Figure B. 10: Event 549

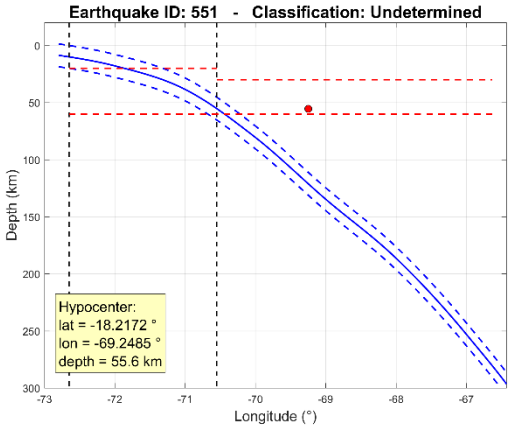

Figure B. 11: Event 551

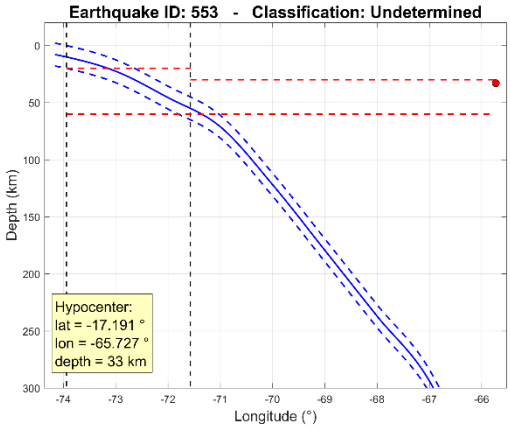

Figure B. 12: Event 553

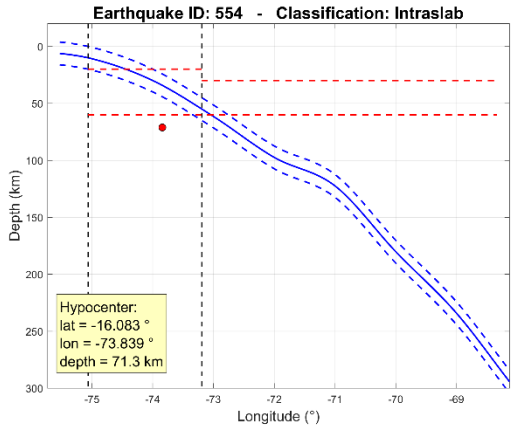

Figure B. 13: Event 554

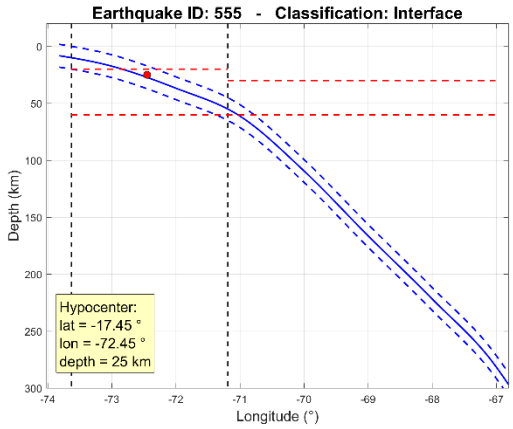

Figure B. 14: Event 555

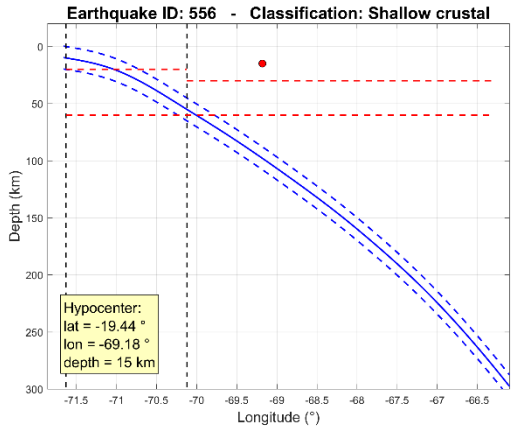

Figure B. 15: Event 556

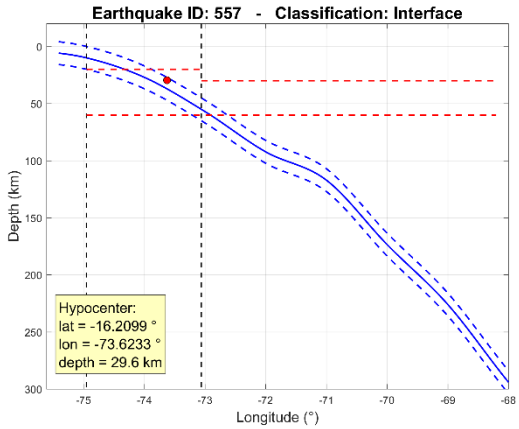

Figure B. 16: Event 557

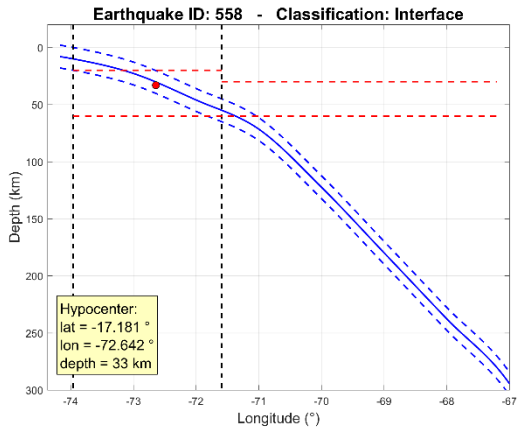

Figure B. 17: Event 558

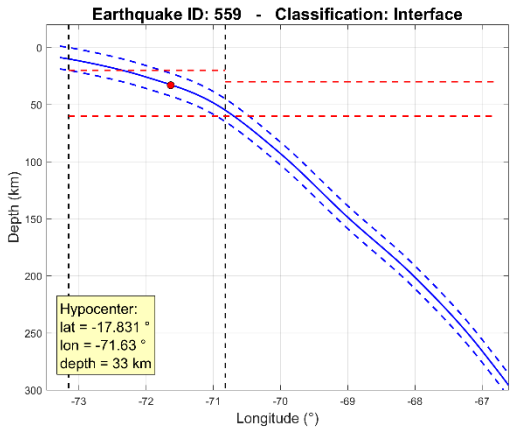

Figure B. 18: Event 559

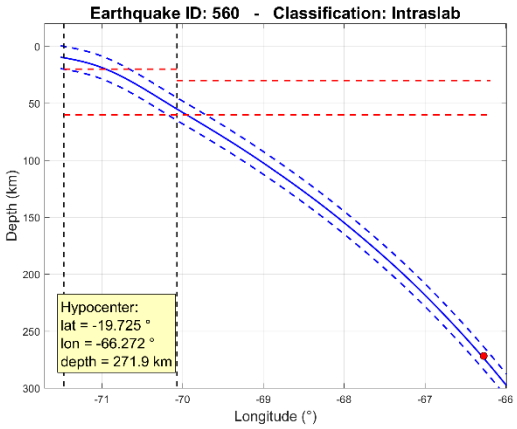

Figure B. 19: Event 560

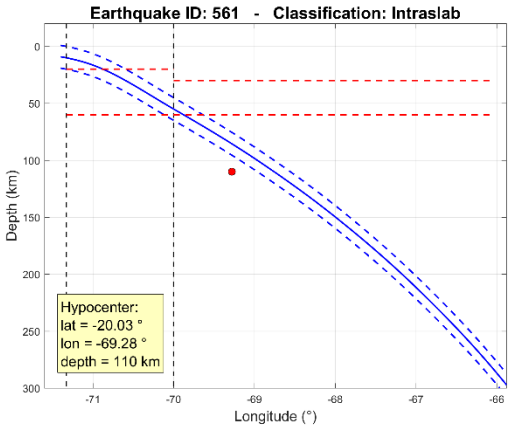

Figure B. 20: Event 561

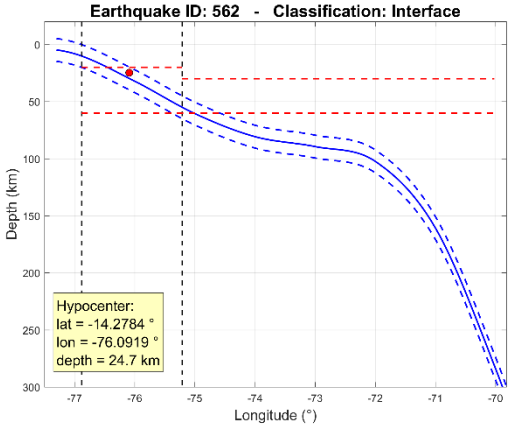

Figure B. 21: Event 562

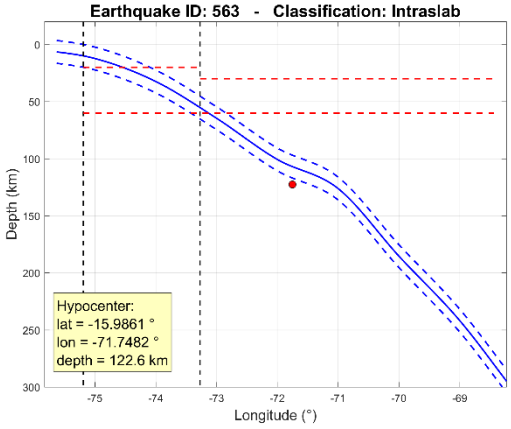

Figure B. 22: Event 563

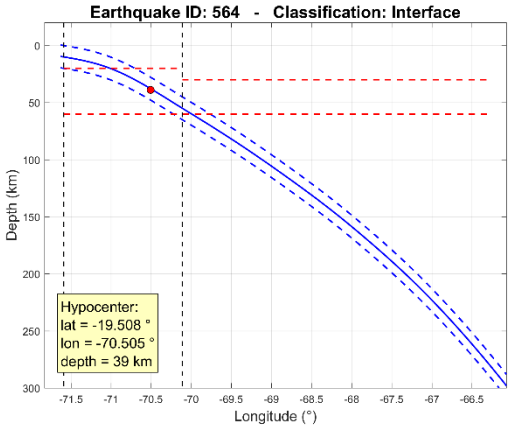

Figure B. 23: Event 564

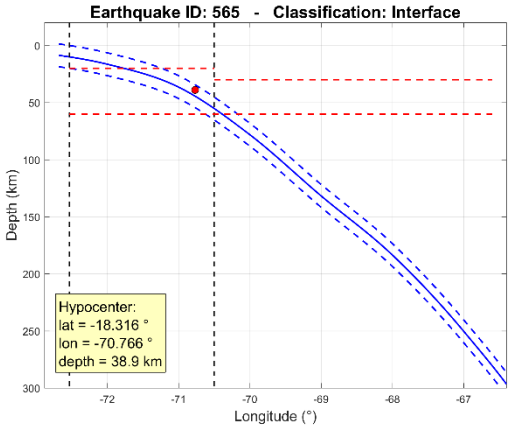

Figure B. 24: Event 565

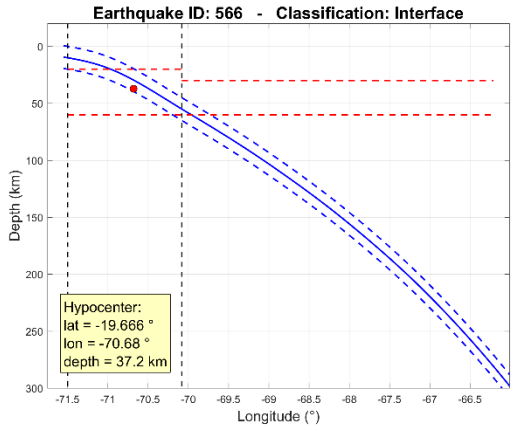

Figure B. 25: Event 566

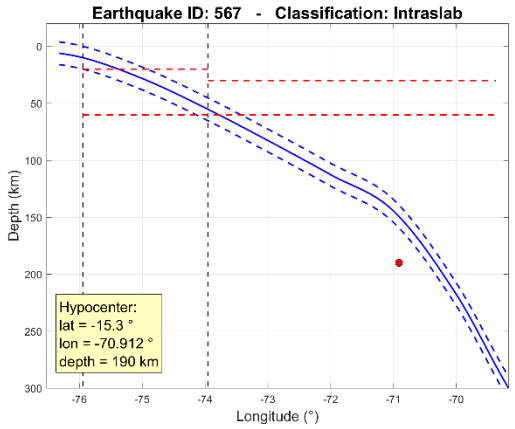

Figure B. 26: Event 567

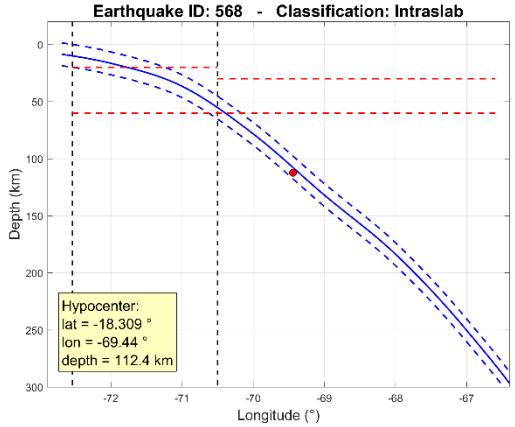

Figure B. 27: Event 568

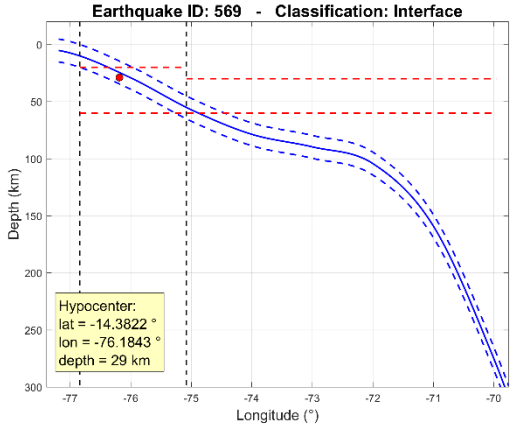

Figure B. 28: Event 569

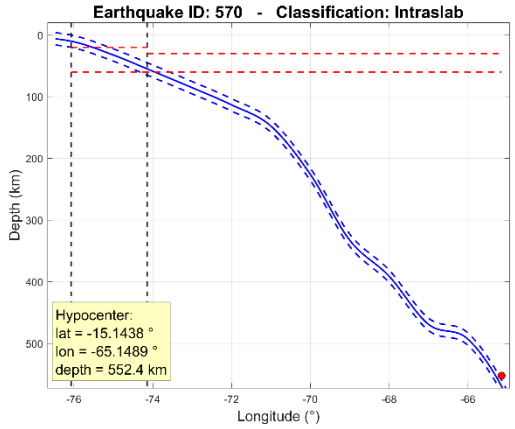

Figure B. 29: Event 570

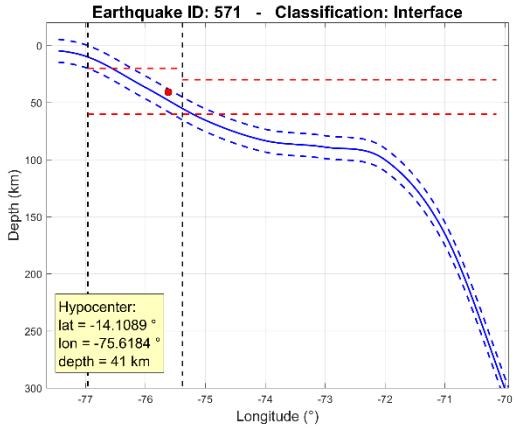

Figure B. 30: Event 571

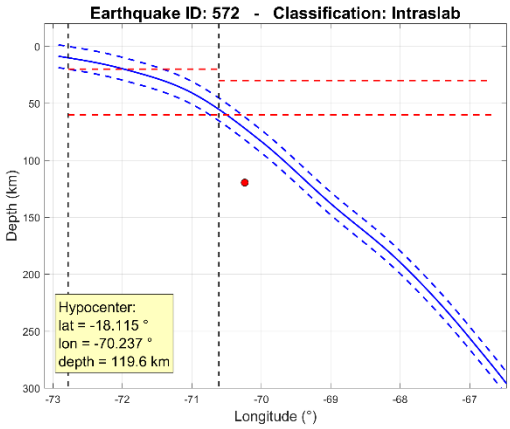

Figure B. 31: Event 572

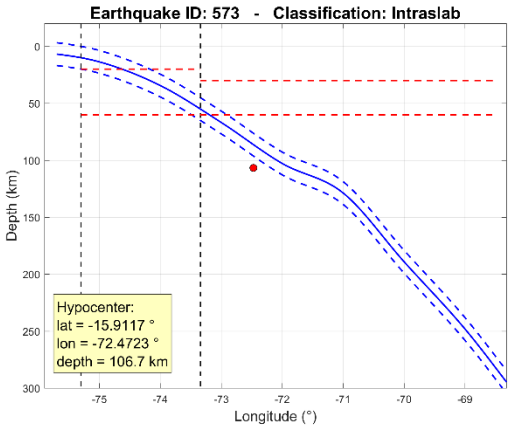

Figure B. 32: Event 573

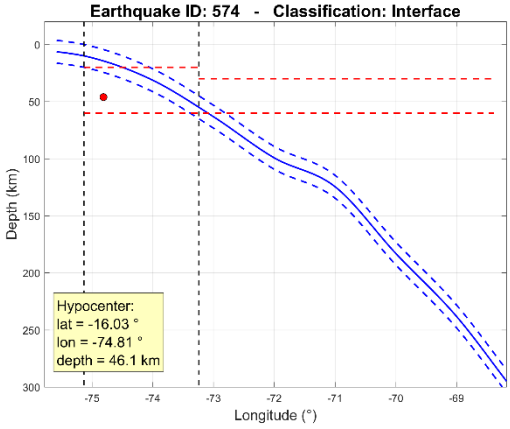

Figure B. 33: Event 574

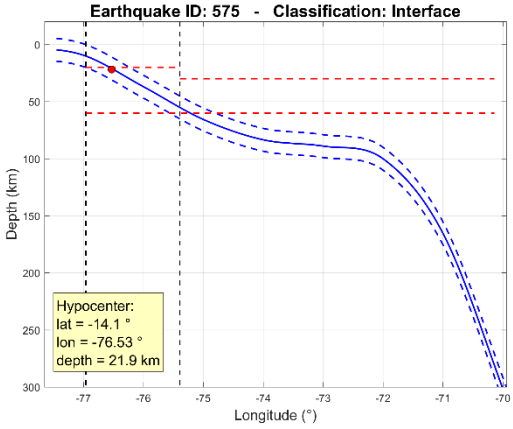

Figure B. 34: Event 575

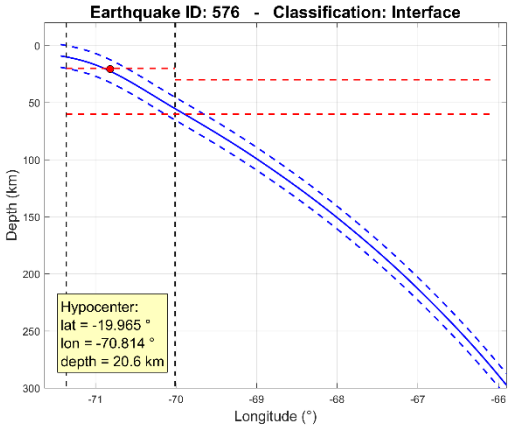

Figure B. 35: Event 576

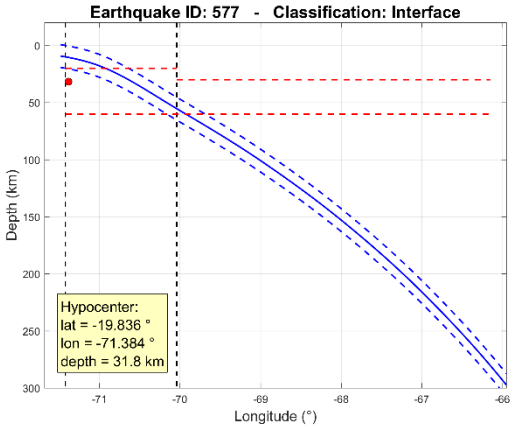

Figure B. 36: Event 577

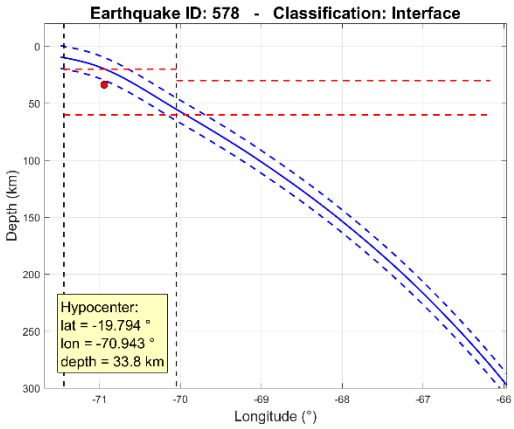

Figure B. 37: Event 578

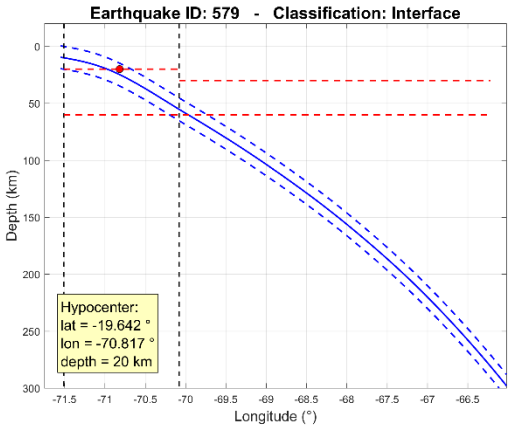

Figure B. 38: Event 579

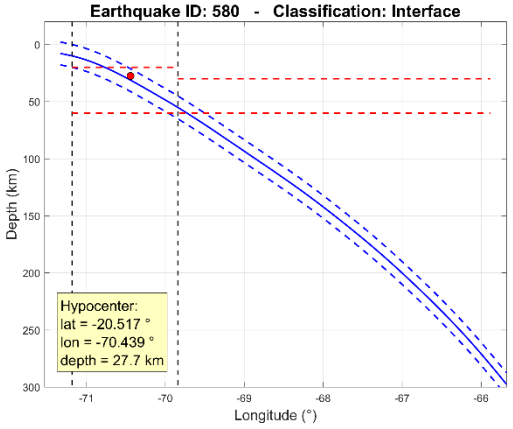

Figure B. 39: Event 580

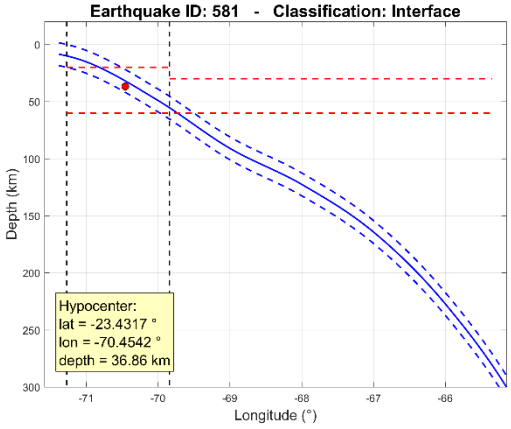

Figure B. 40: Event 581

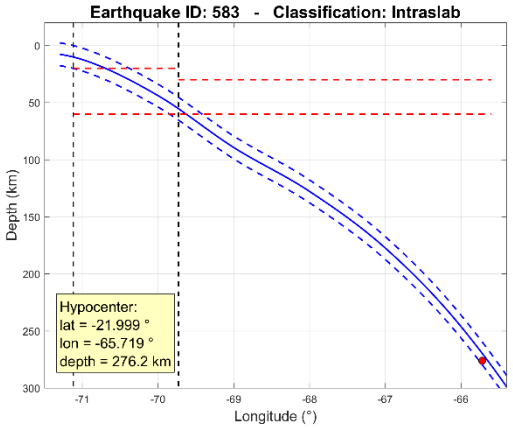

Figure B. 41: Event 583

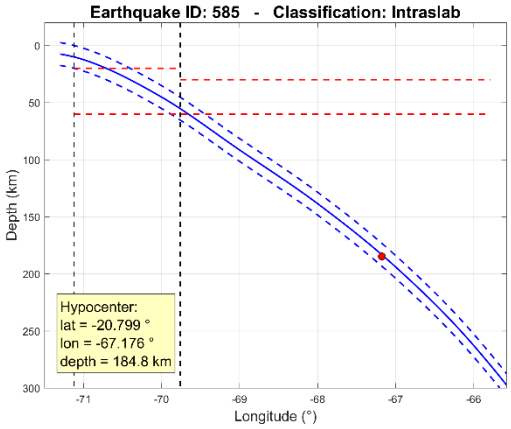

Figure B. 42: Event 585

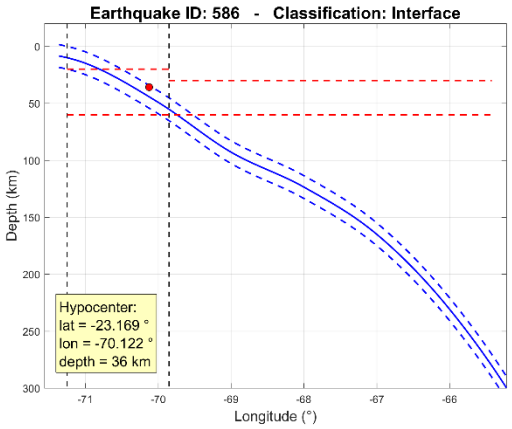

Figure B. 43: Event 586

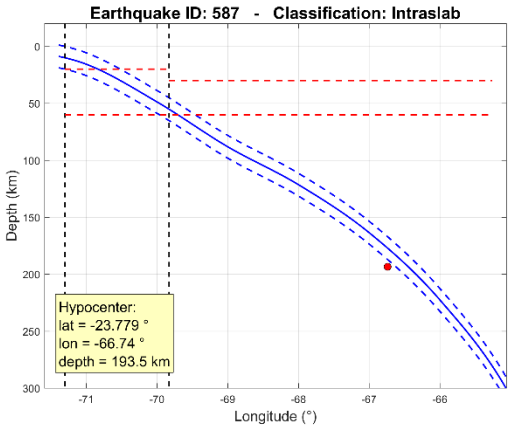

Figure B. 44: Event 587

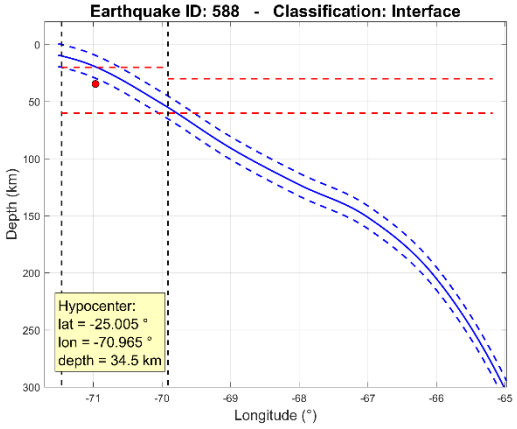

Figure B. 45: Event 588

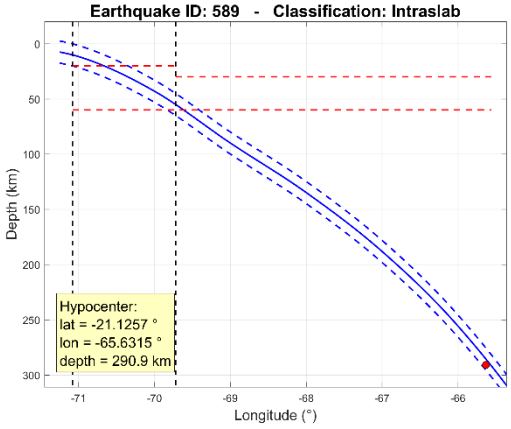

Figure B. 46: Event 589

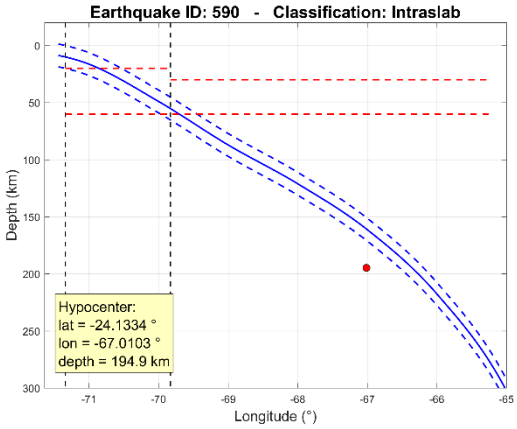

Figure B. 47: Event 590

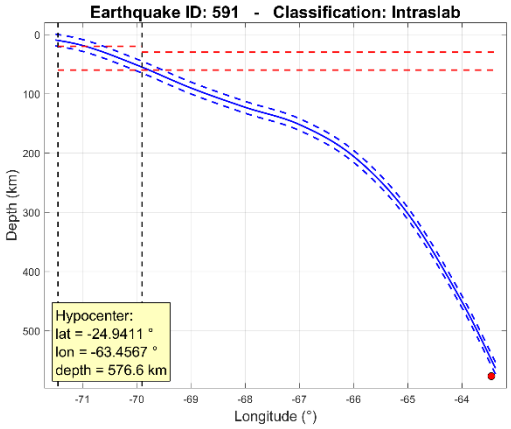

Figure B. 48: Event 591

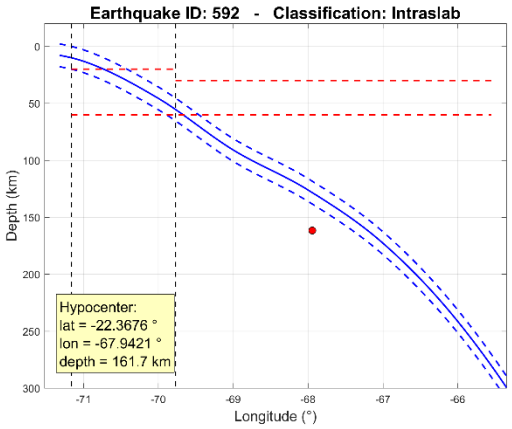

Figure B. 49: Event 592

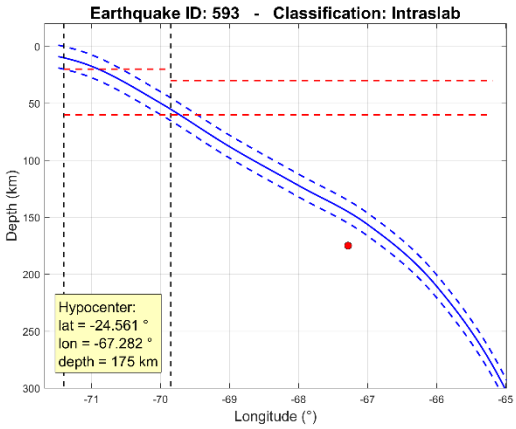

Figure B. 50: Event 593

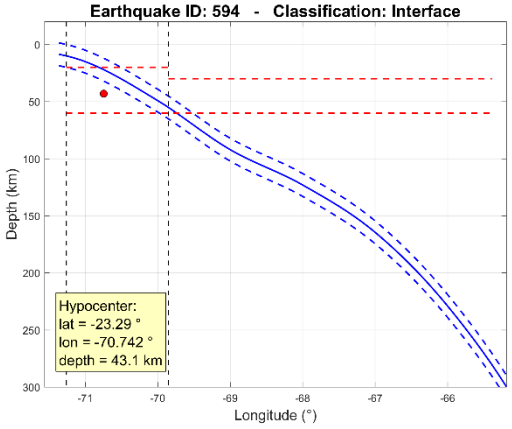

Figure B. 51: Event 594

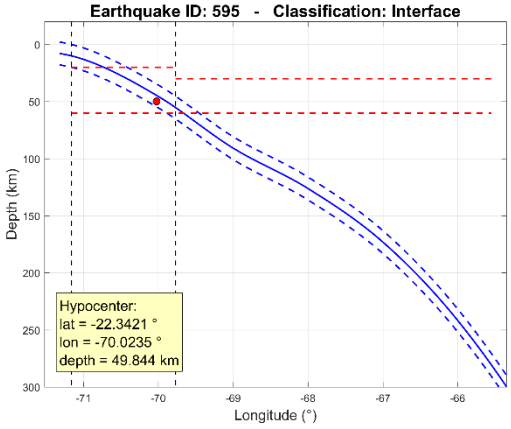

Figure B. 52: Event 595

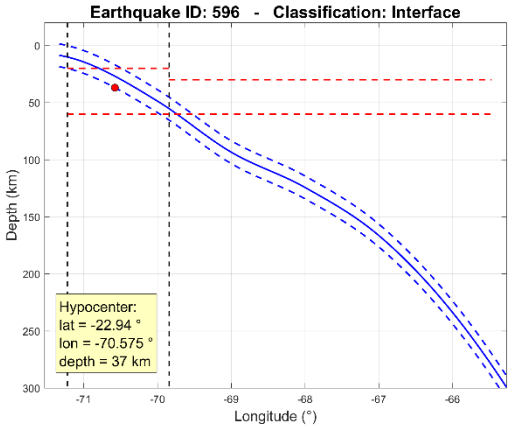

Figure B. 53: Event 596

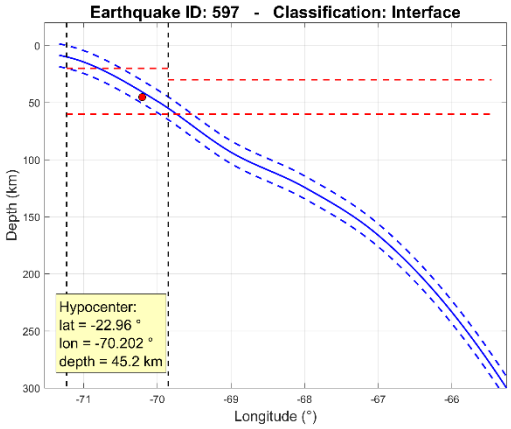

Figure B. 54: Event 597

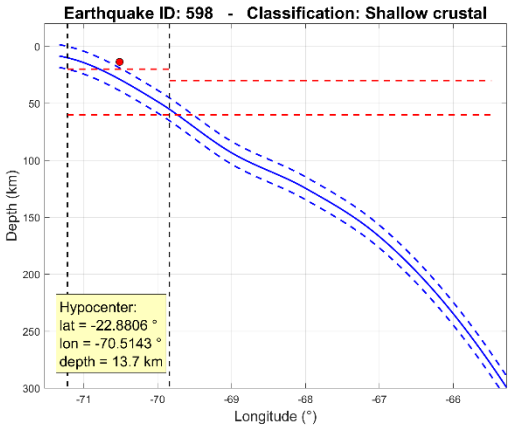

Figure B. 55: Event 598

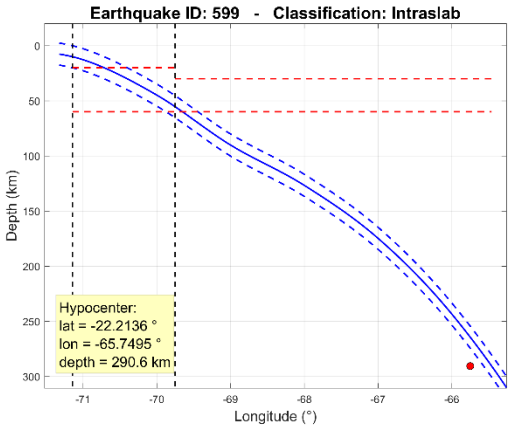

Figure B. 56: Event 599

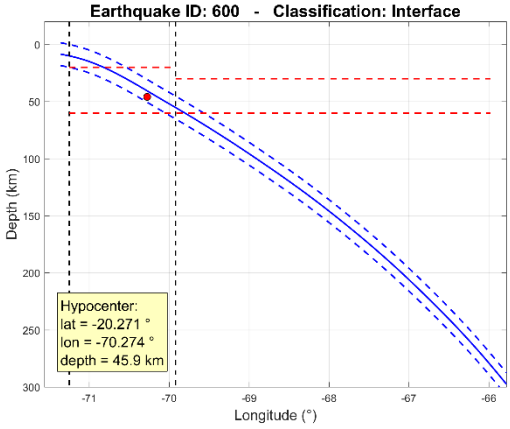

Figure B. 57: Event 600

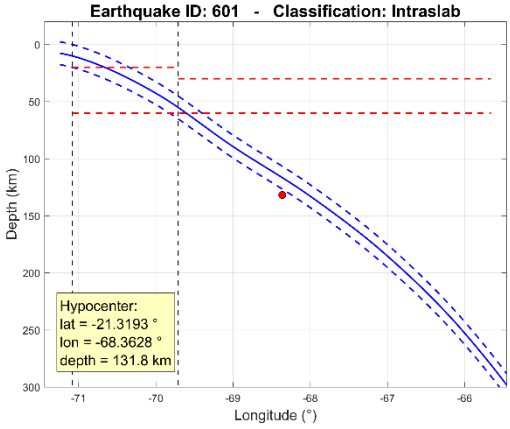

Figure B. 58: Event 601

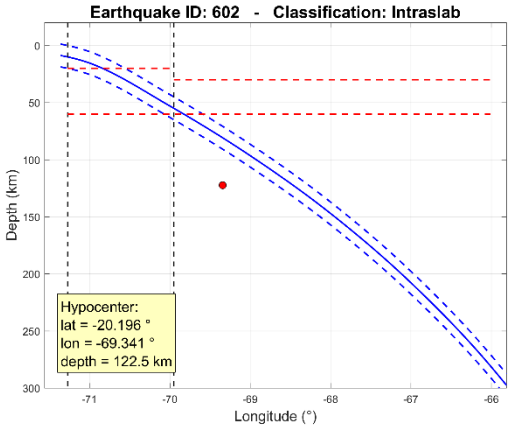

Figure B. 59: Event 602

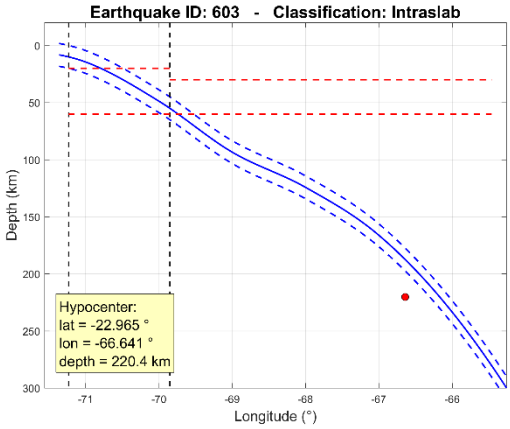

Figure B. 60: Event 603

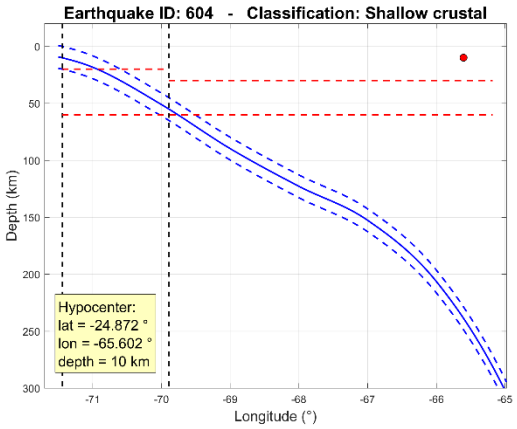

Figure B. 61: Event 604

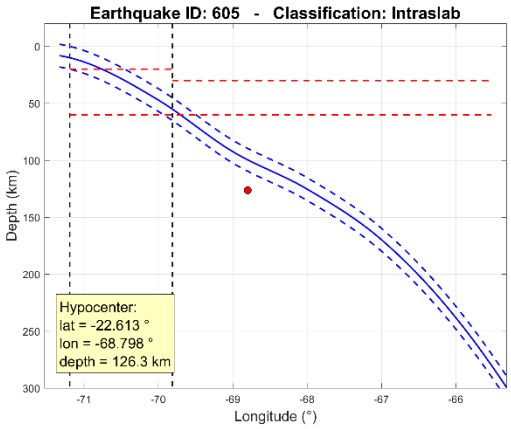

Figure B. 62: Event 605

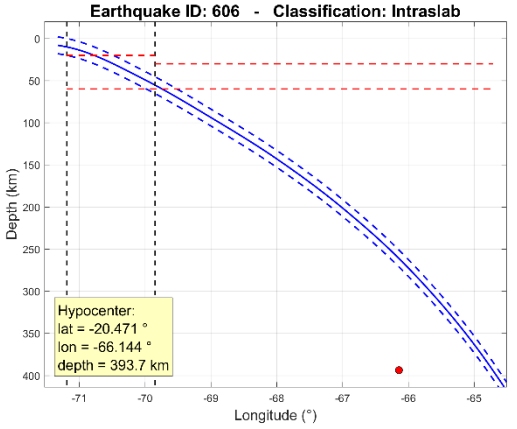

Figure B. 63: Event 606

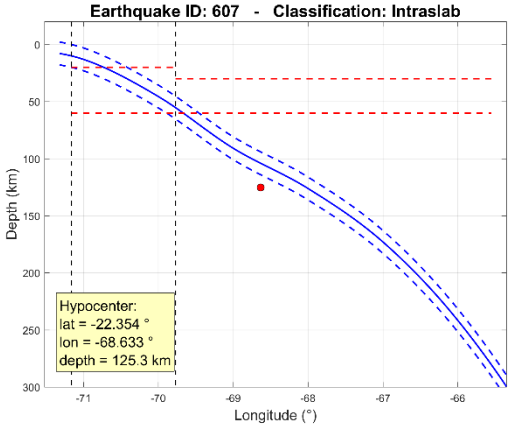

Figure B. 64: Event 607

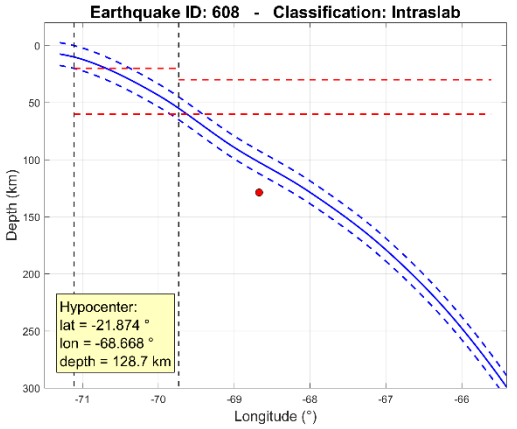

Figure B. 65: Event 608

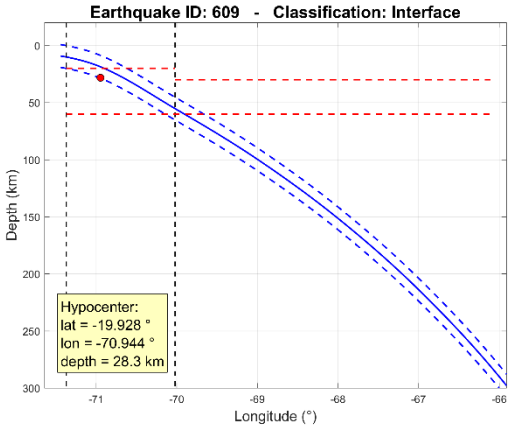

Figure B. 66: Event 609

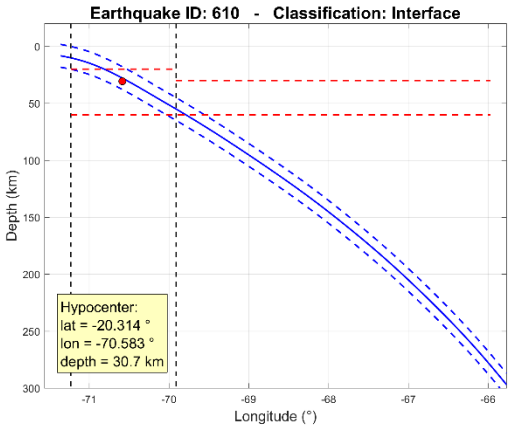

Figure B. 67: Event 610

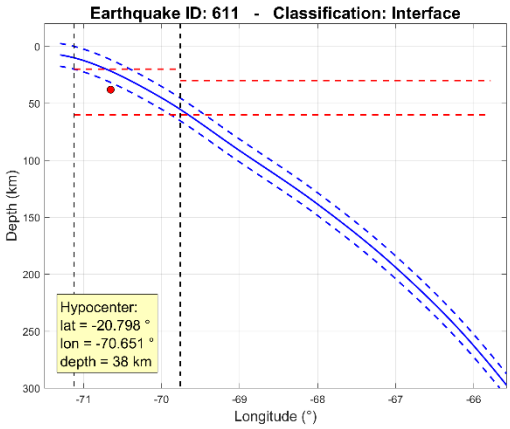

Figure B. 68: Event 611

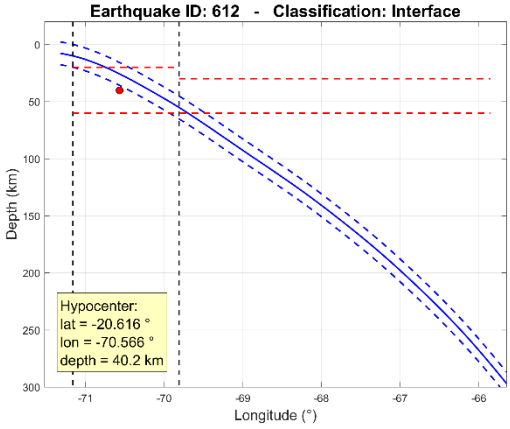

Figure B. 69: Event 612

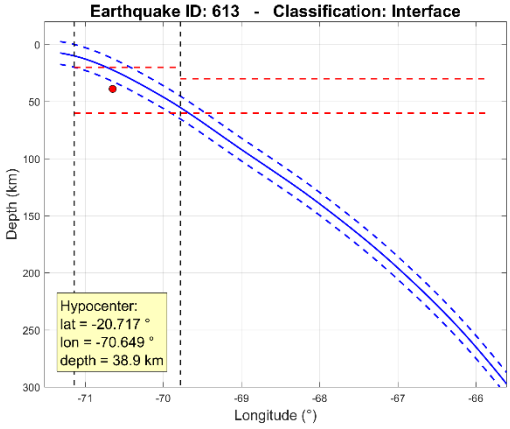

Figure B. 70: Event 613

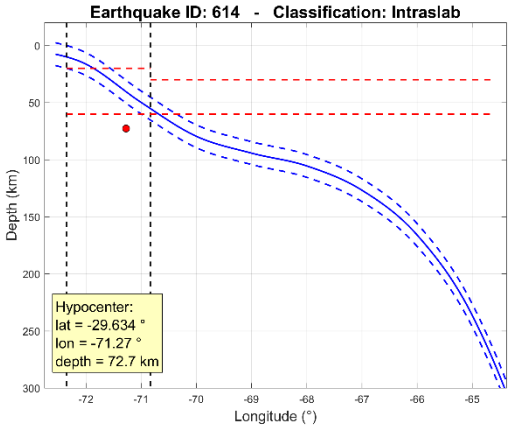

Figure B. 71: Event 614

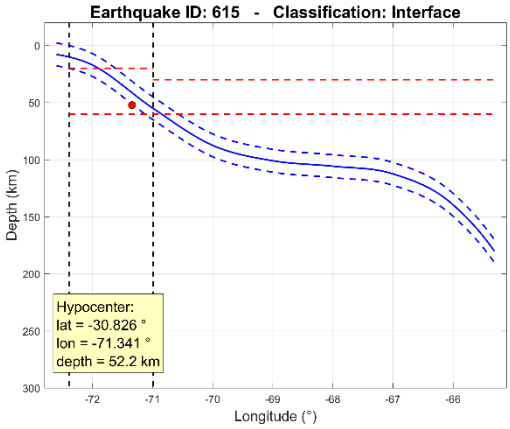

Figure B. 72: Event 615

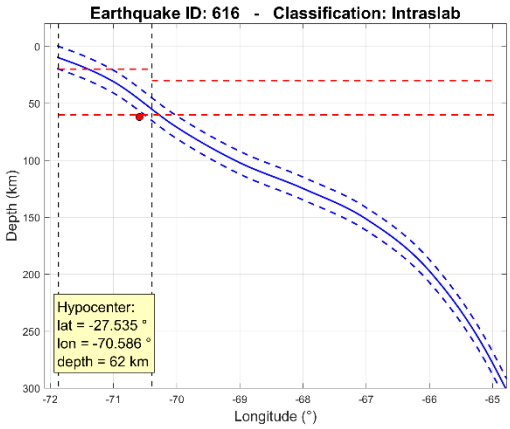

Figure B. 73: Event 616

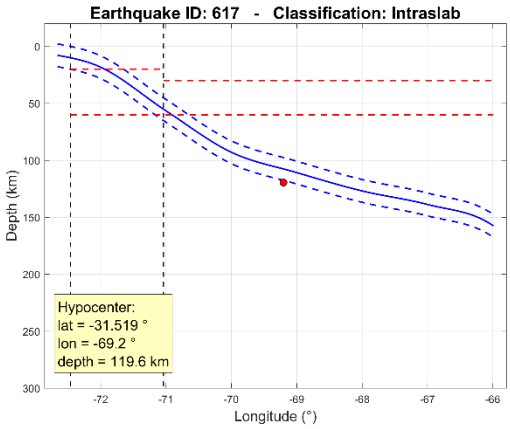

Figure B. 74: Event 617

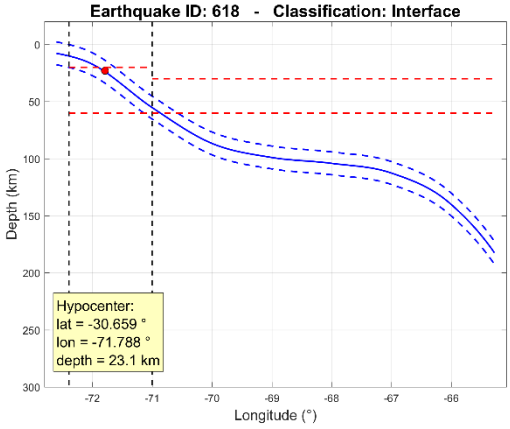

Figure B. 75: Event 618

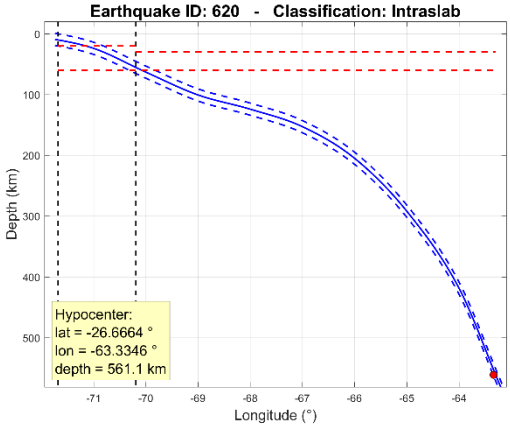

Figure B. 76: Event 620

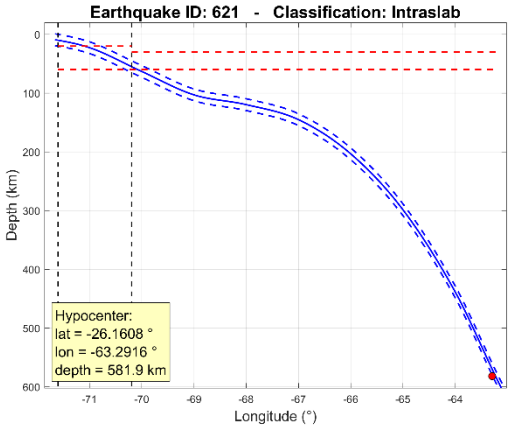

Figure B. 77: Event 621

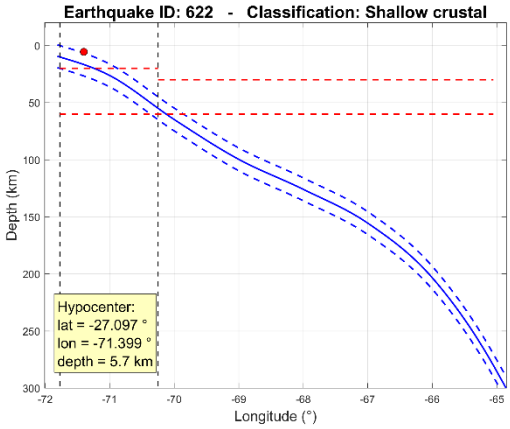

Figure B. 78: Event 622

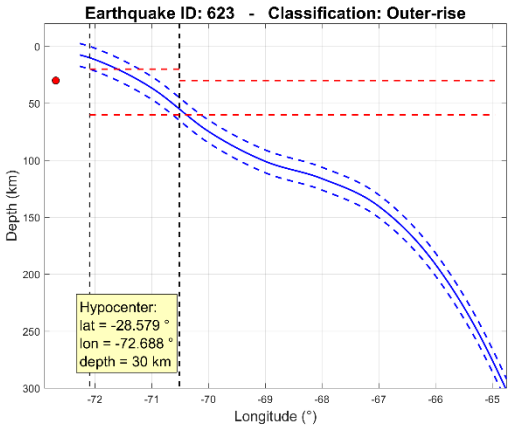

Figure B. 79: Event 623

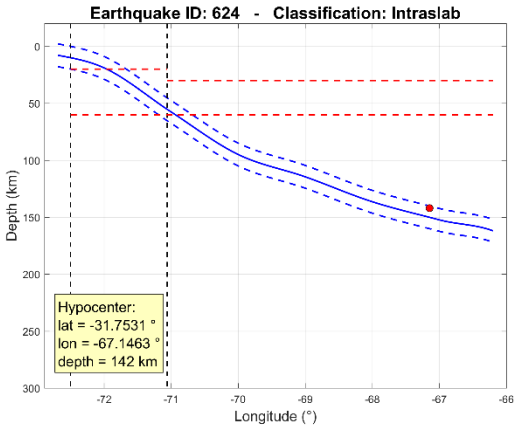

Figure B. 80: Event 624

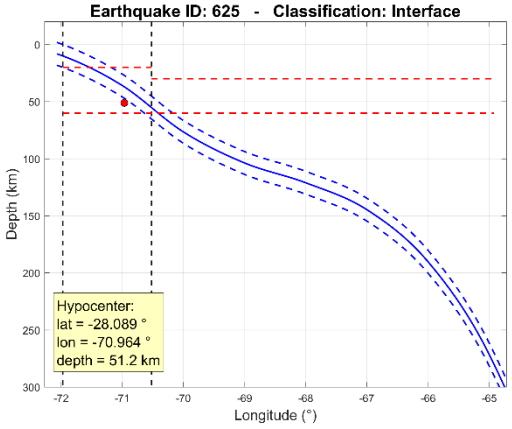

Figure B. 81: Event 625

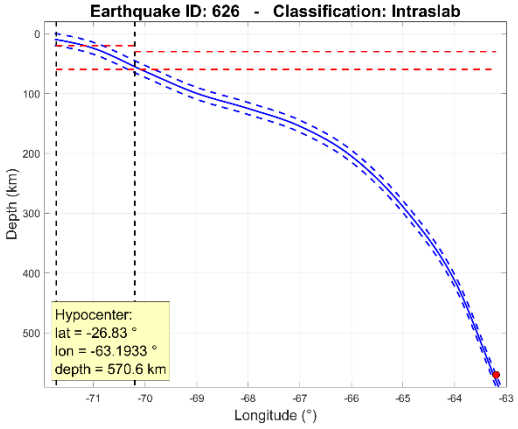

Figure B. 82: Event 626

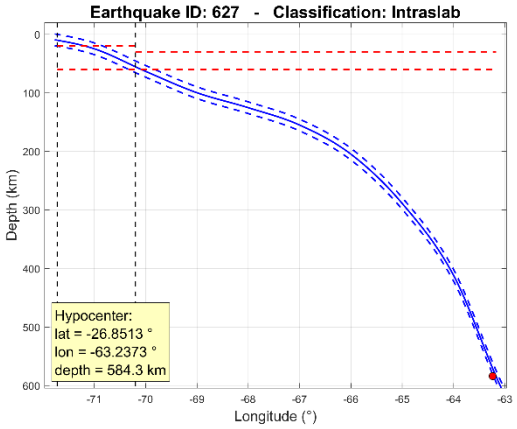

Figure B. 83: Event 627

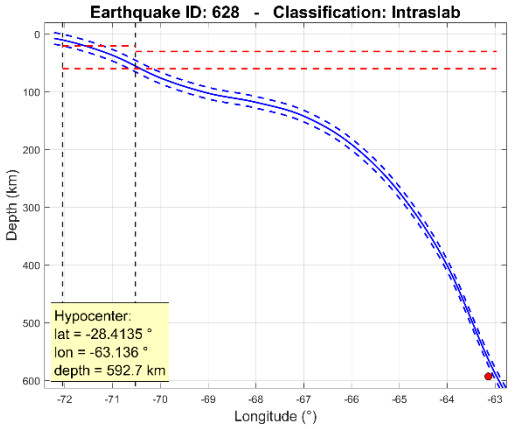

Figure B. 84: Event 628

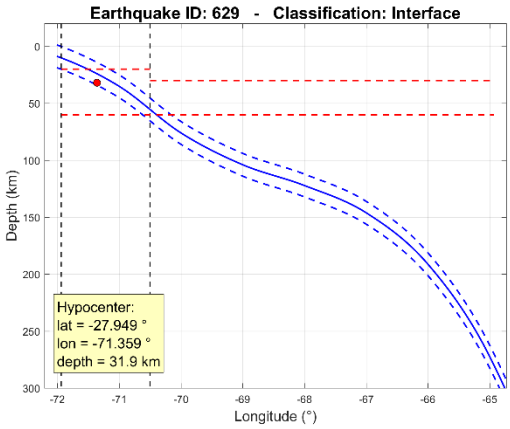

Figure B. 85: Event 629

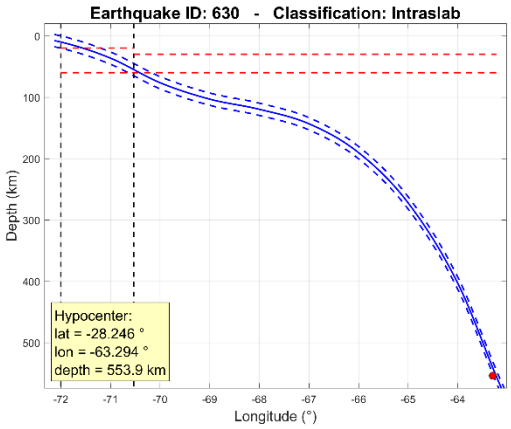

Figure B. 86: Event 630

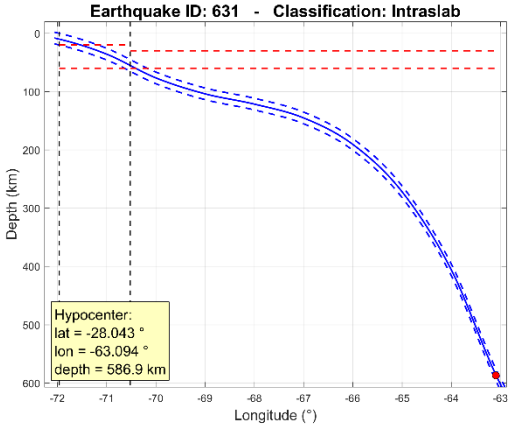

Figure B. 87: Event 631

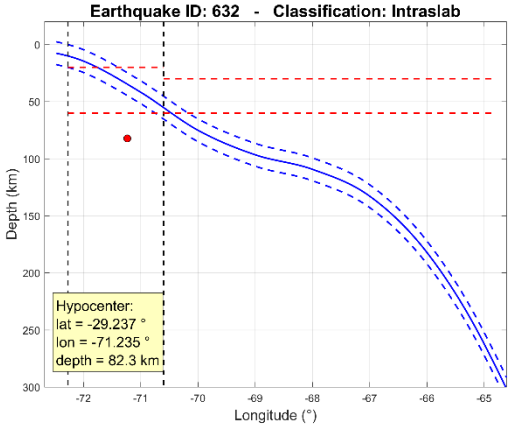

Figure B. 88: Event 632

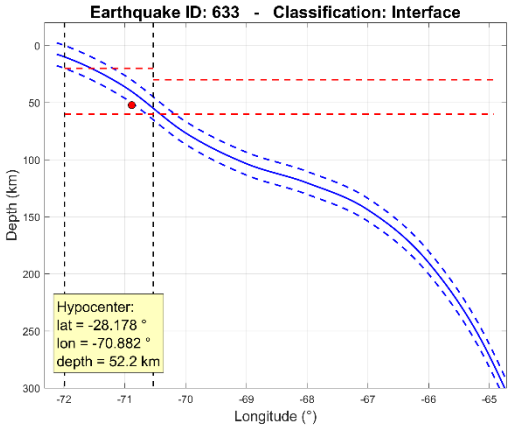

Figure B. 89: Event 633

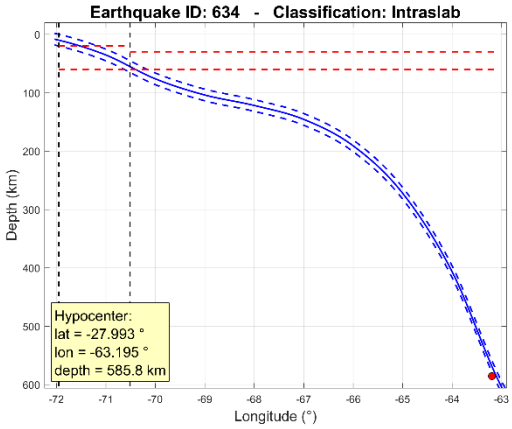

Figure B. 90: Event 634

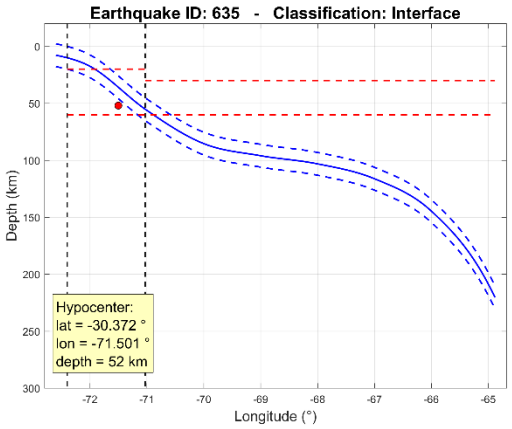

Figure B. 91: Event 635

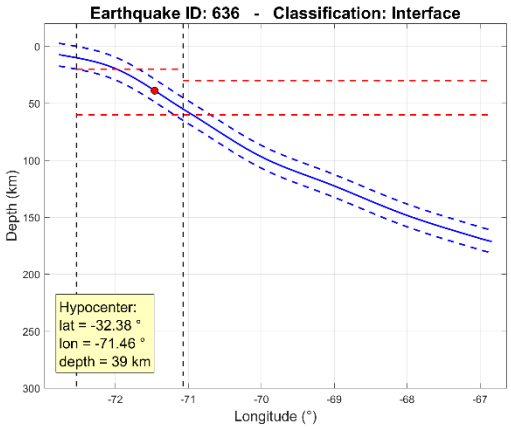

Figure B. 92: Event 636

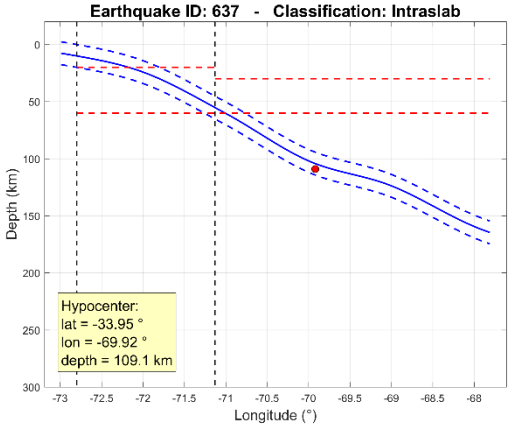

Figure B. 93: Event 637

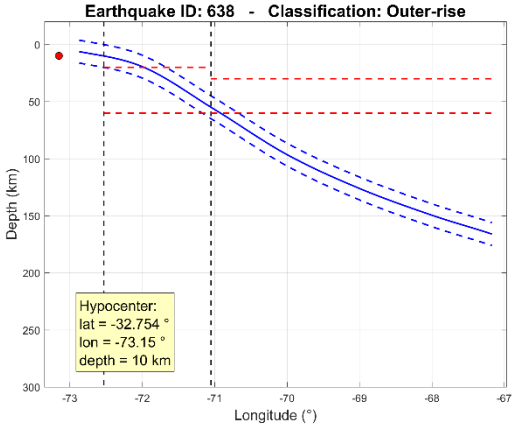

Figure B. 94: Event 638

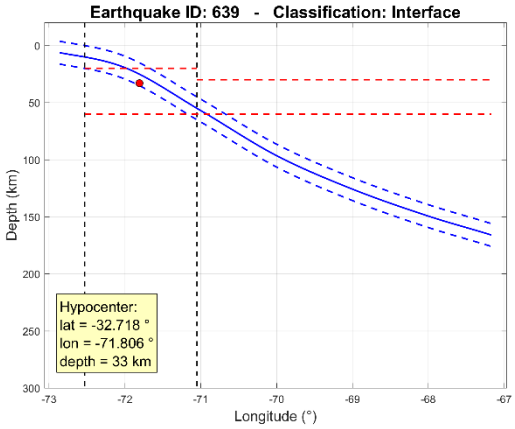

Figure B. 95: Event 639

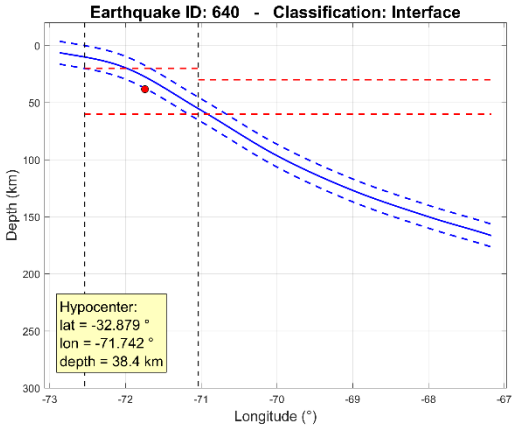

Figure B. 96: Event 640

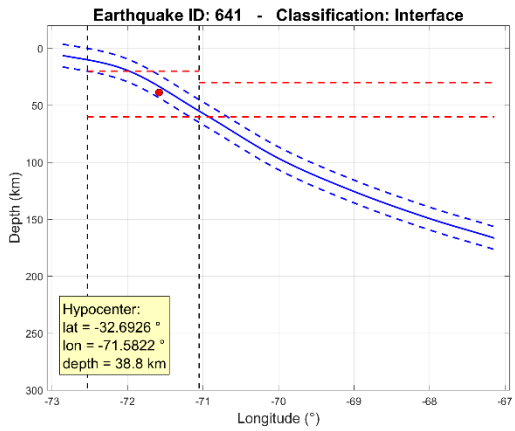

Figure B. 97: Event 641

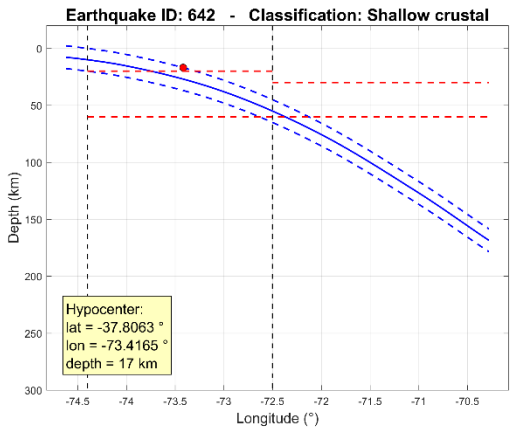

Figure B. 98: Event 642

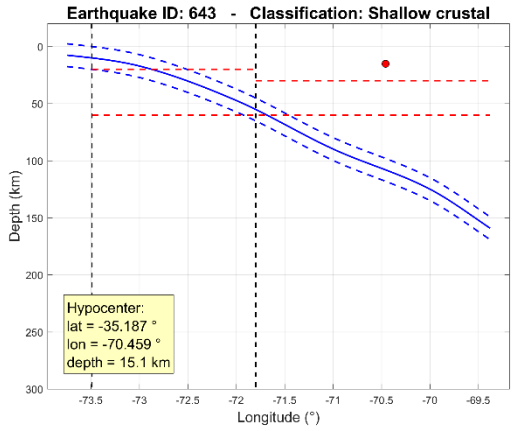

Figure B. 99: Event 643

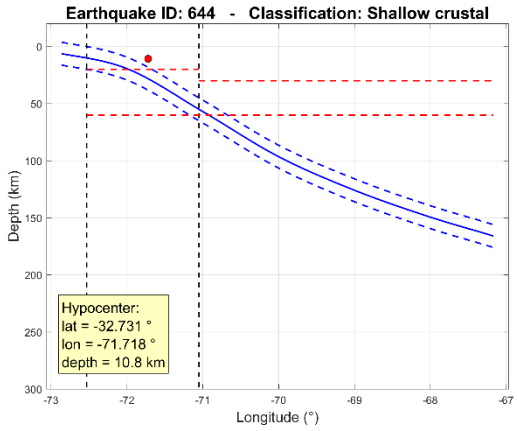

Figure B. 100: Event 644

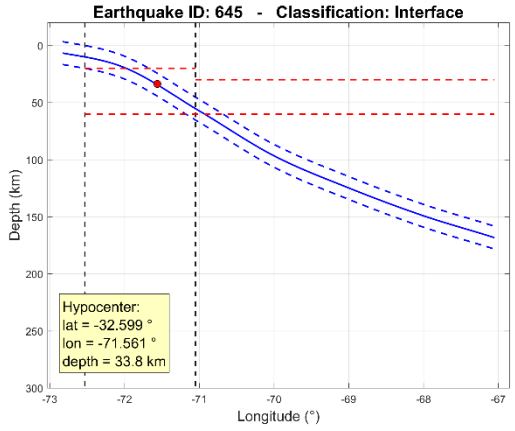

Figure B. 101: Event 645

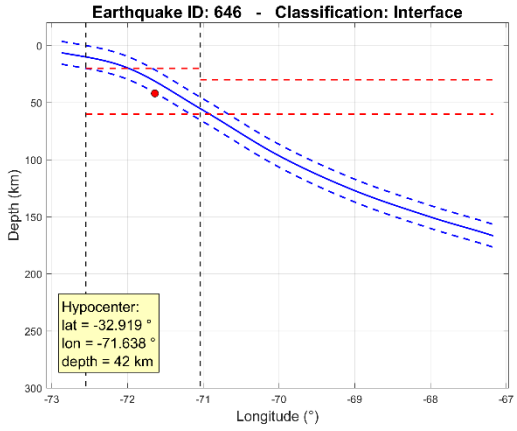

Figure B. 102: Event 646

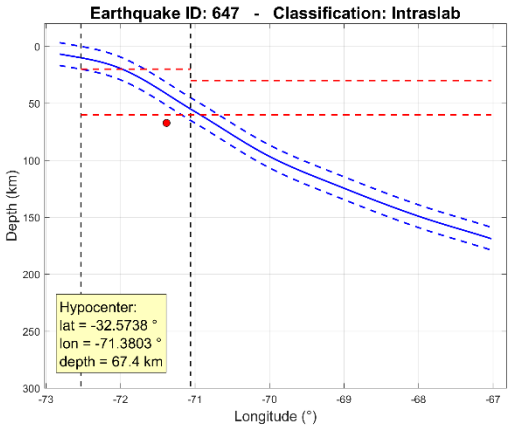

Figure B. 103: Event 647

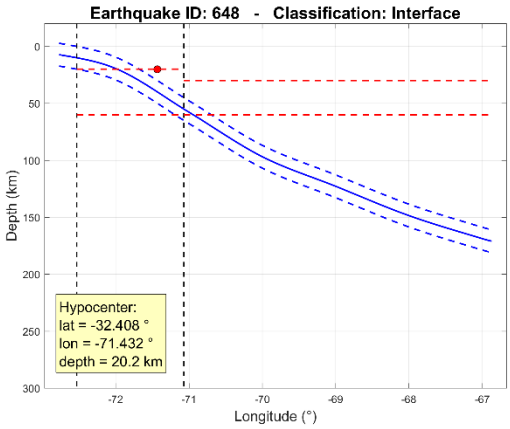

Figure B. 104: Event 648

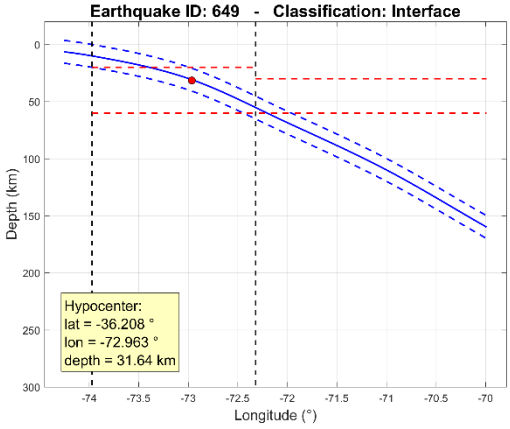

Figure B. 105: Event 649

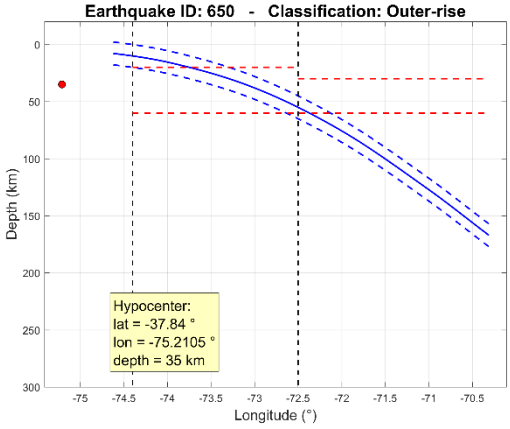

Figure B. 106: Event 650

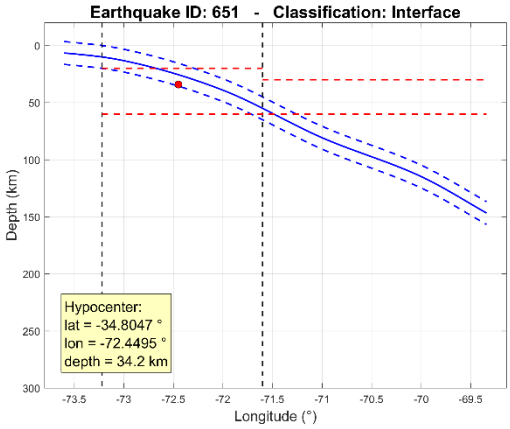

Figure B. 107: Event 651

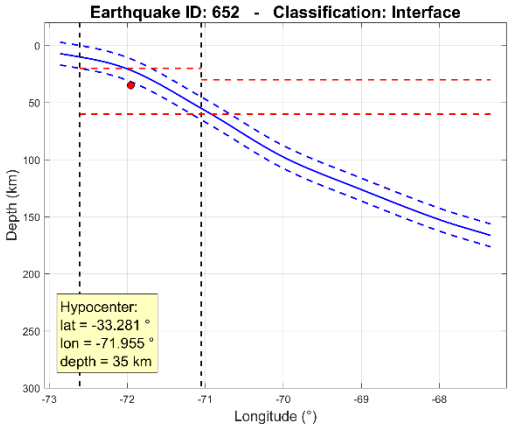

Figure B. 108: Event 652

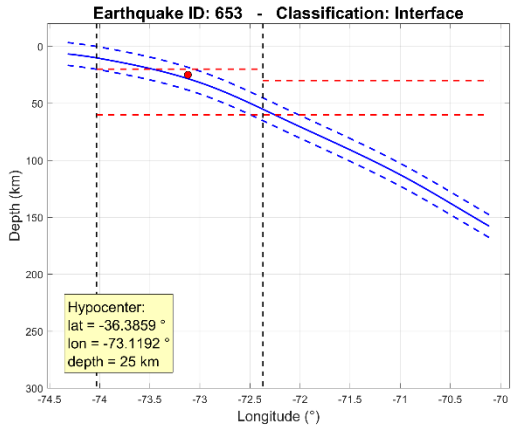

Figure B. 109: Event 653

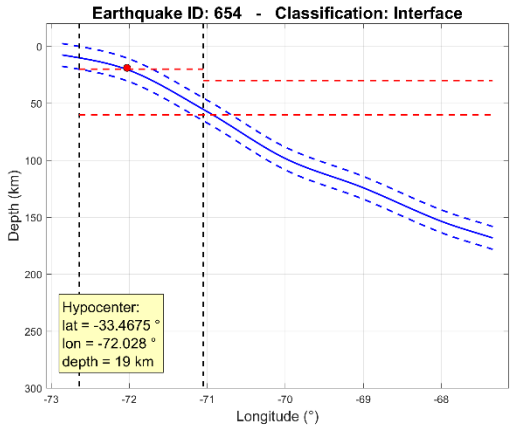

Figure B. 110: Event 654

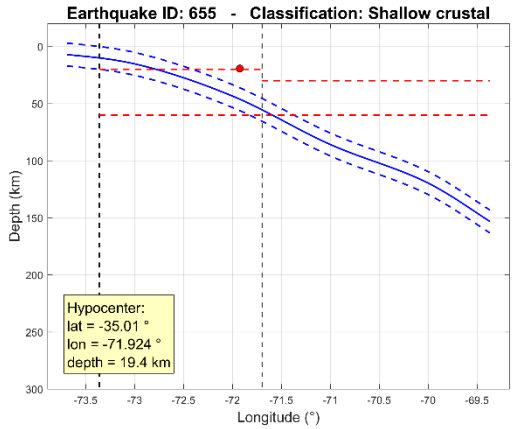

Figure B. 111: Event 655

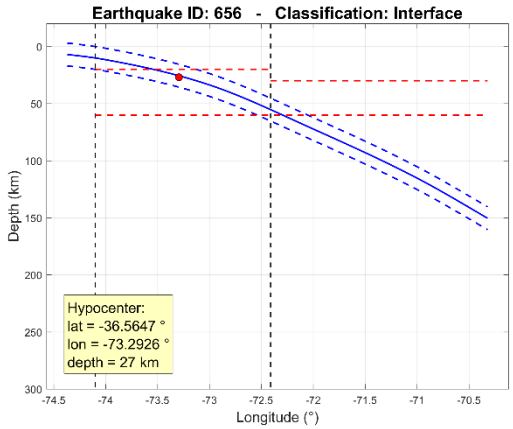

Figure B. 112: Event 656

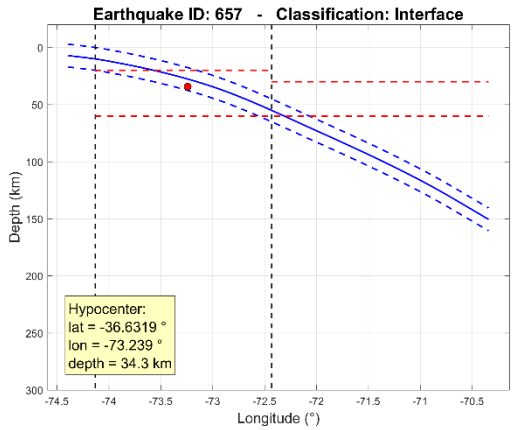

Figure B. 113: Event 657

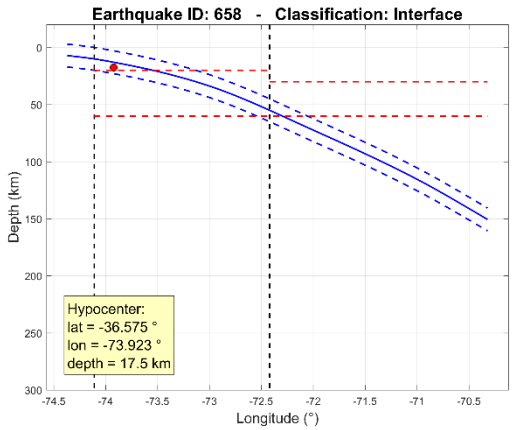

Figure B. 114: Event 658

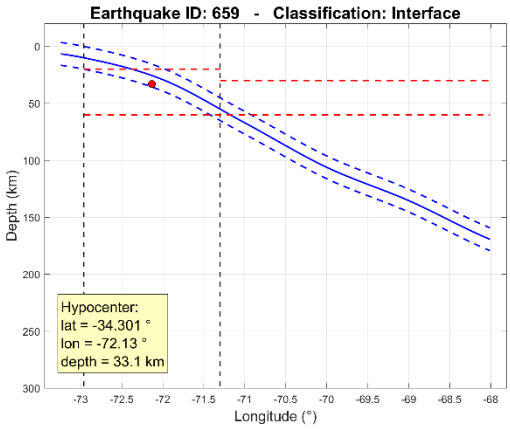

Figure B. 115: Event 659

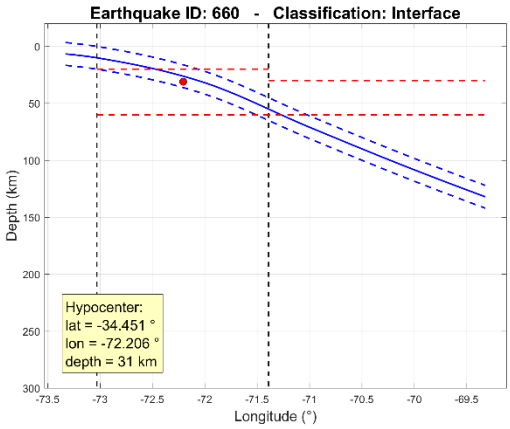

Figure B. 116: Event 660

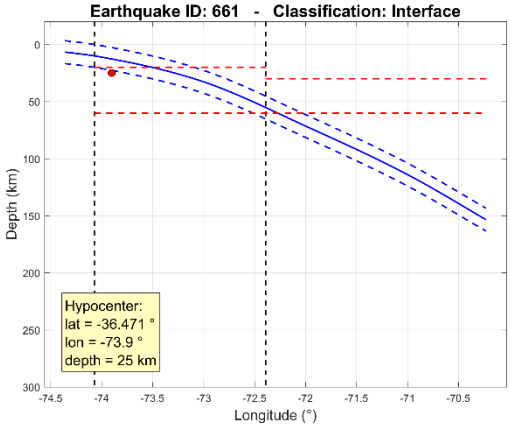

Figure B. 117: Event 661

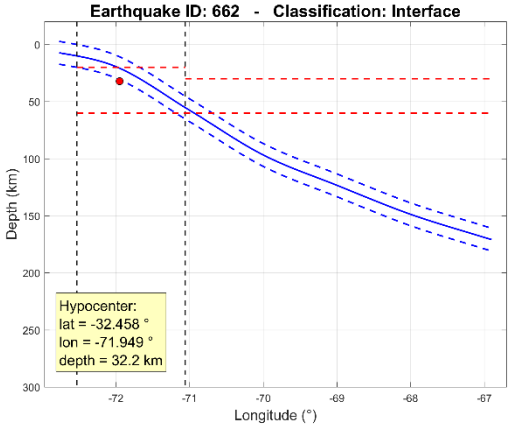

Figure B. 118: Event 662

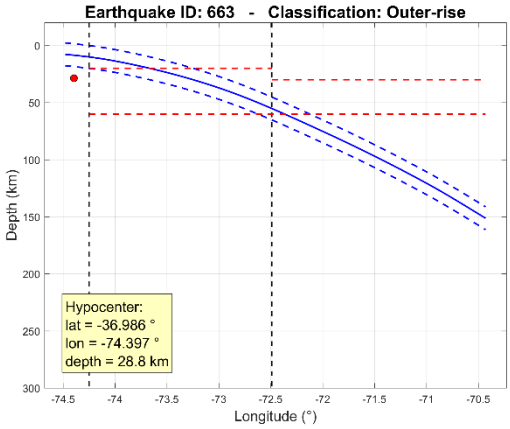

Figure B. 119: Event 663

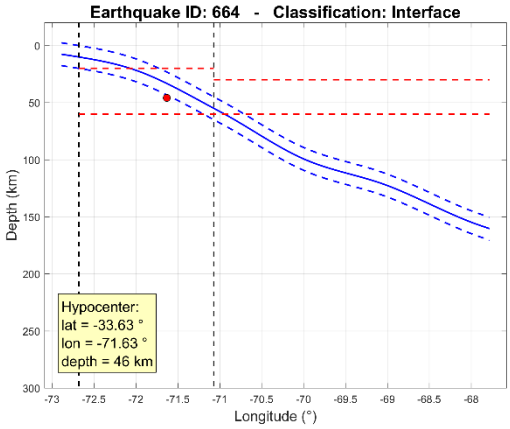

Figure B. 120: Event 664

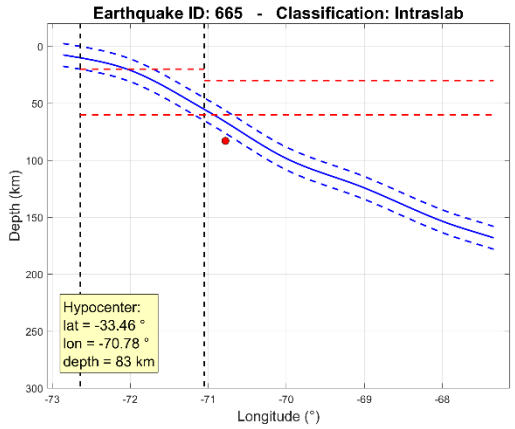

Figure B. 121: Event 665

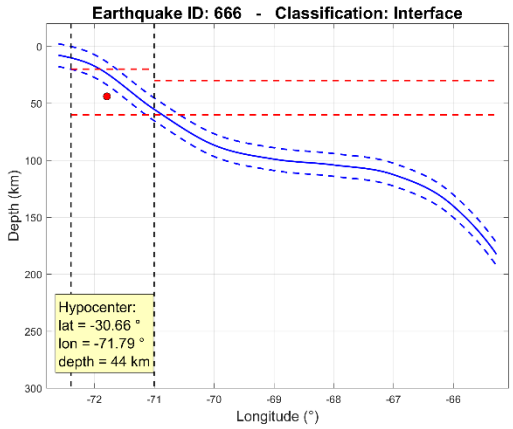

Figure B. 122: Event 666

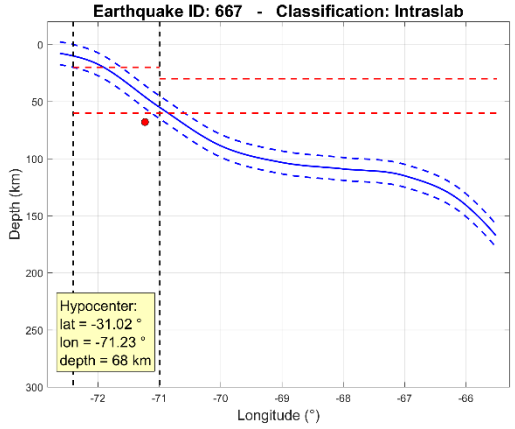

Figure B. 123: Event 667

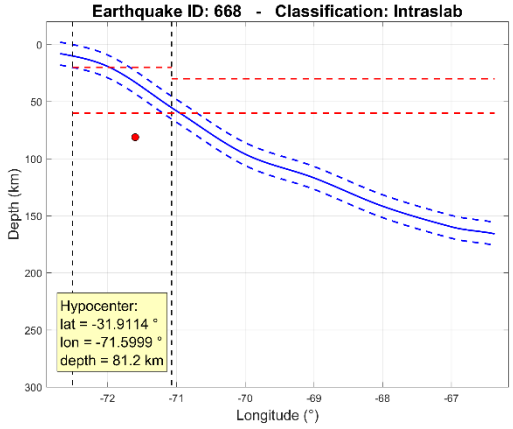

Figure B. 124: Event 668

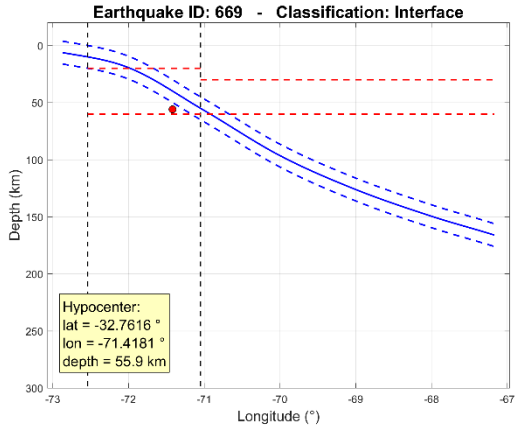

Figure B. 125: Event 669

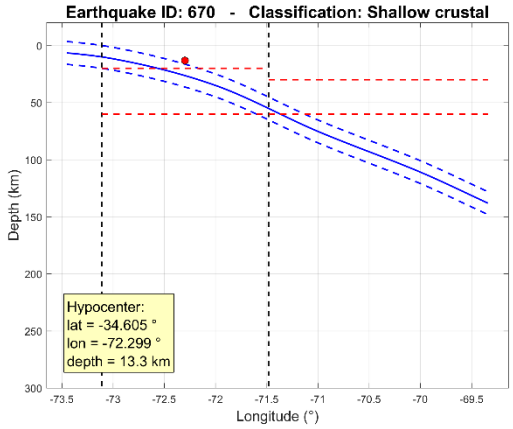

Figure B. 126: Event 670

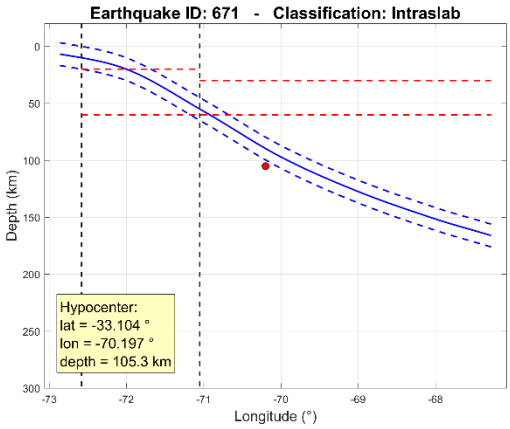

Figure B. 127: Event 671

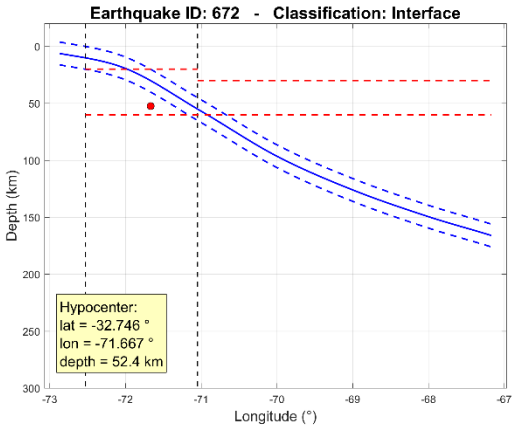

Figure B. 128: Event 672

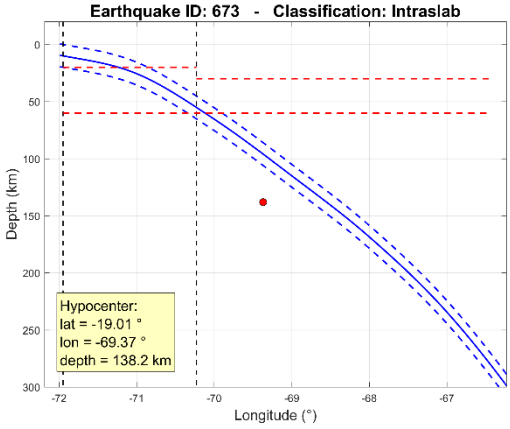

Figure B. 129: Event 673

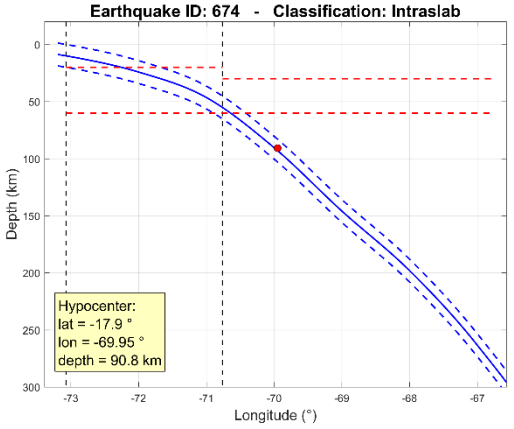

Figure B. 130: Event 674

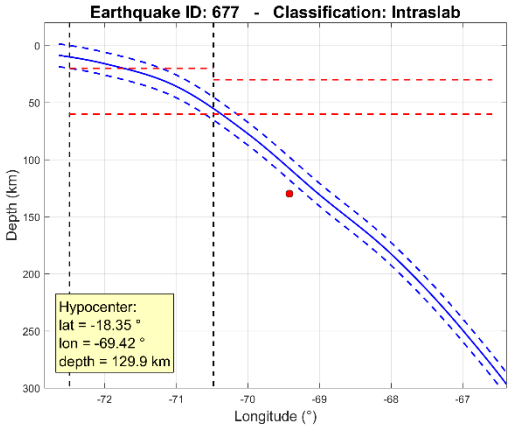

Figure B. 131: Event 677

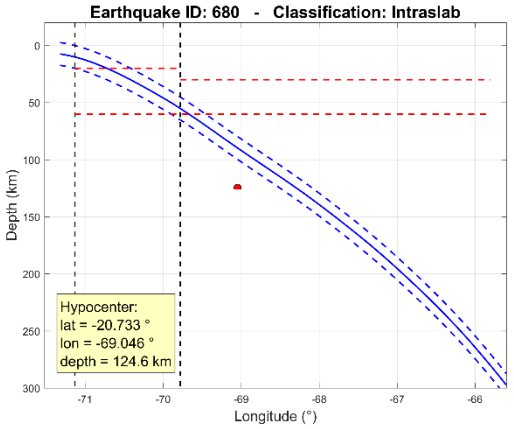

Figure B. 132: Event 680

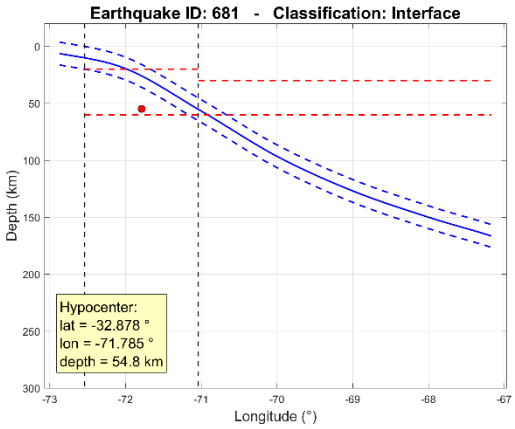

Figure B. 133: Event 681

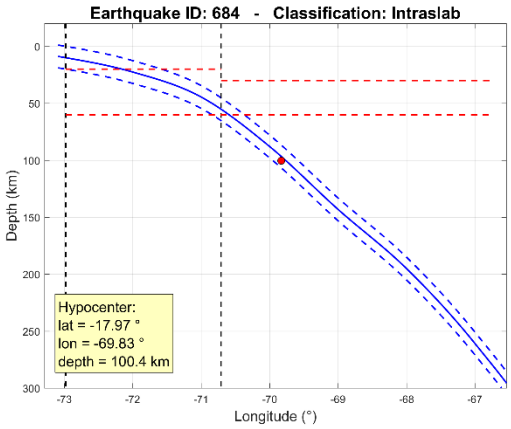

Figure B. 134: Event 684

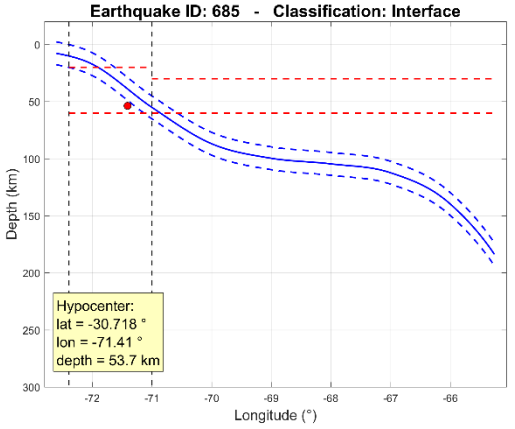

Figure B. 135: Event 685

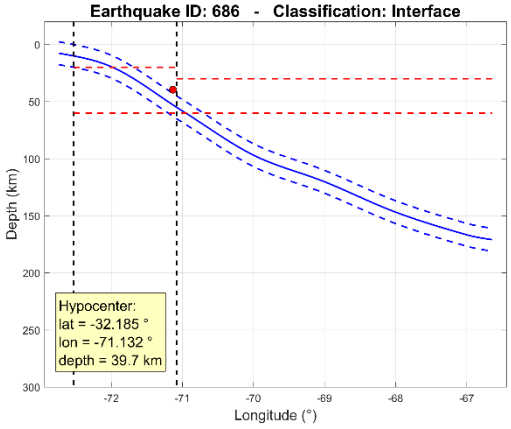

Figure B. 136: Event 686

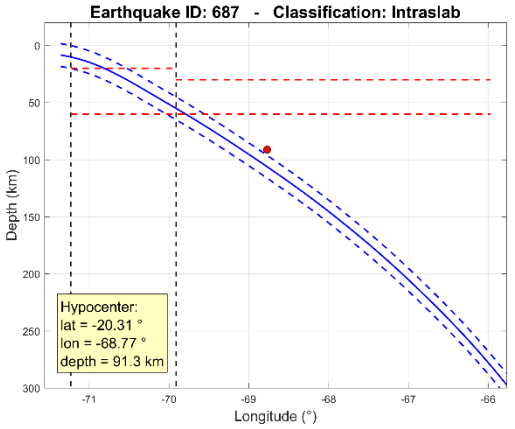

Figure B. 137: Event 687

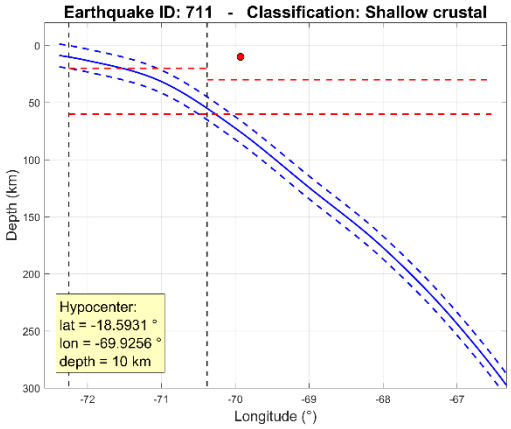

Figure B. 138: Event 711

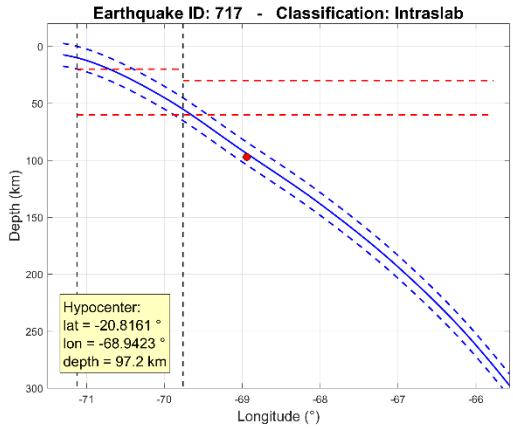

Figure B. 139: Event 717

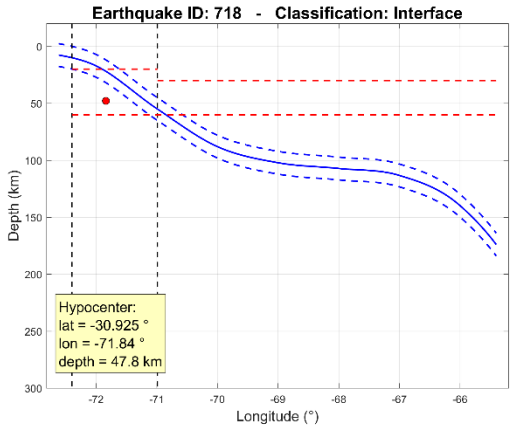

Figure B. 140: Event 718

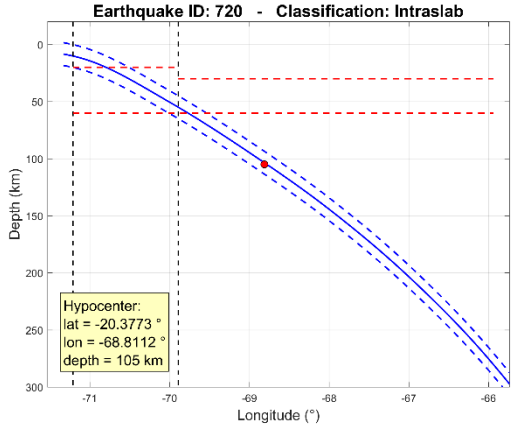

Figure B. 141: Event 720

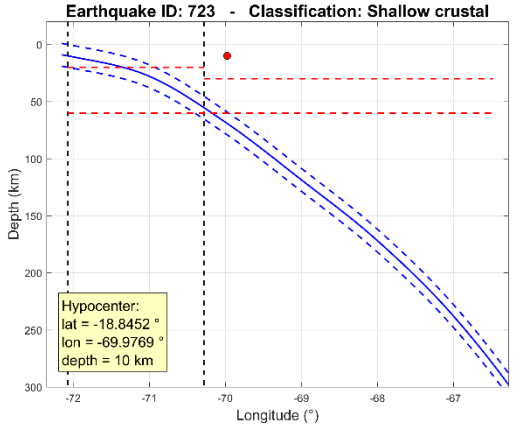

Figure B. 142: Event 723

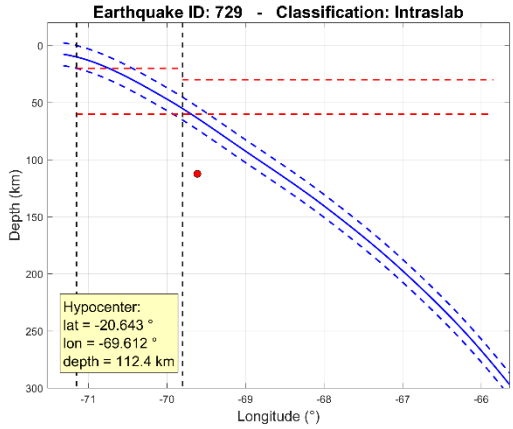

Figure B. 143: Event 729

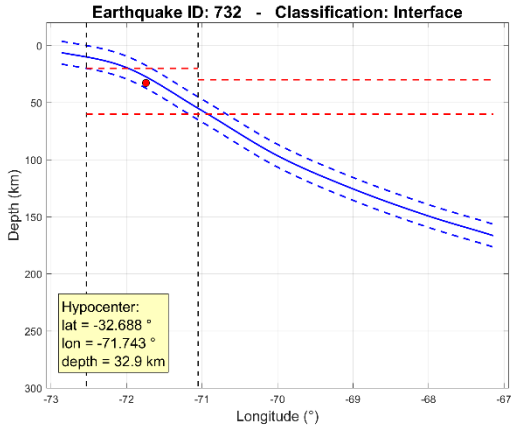

Figure B. 144: Event 732

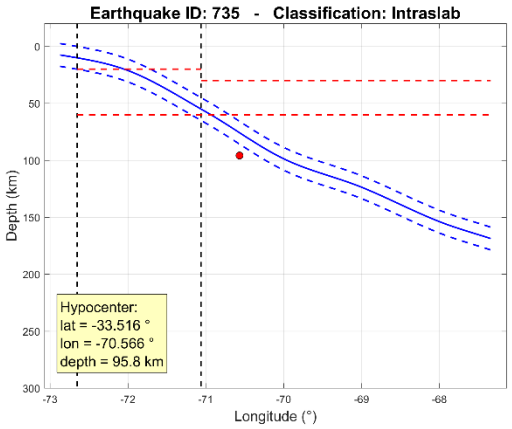

Figure B. 145: Event 735

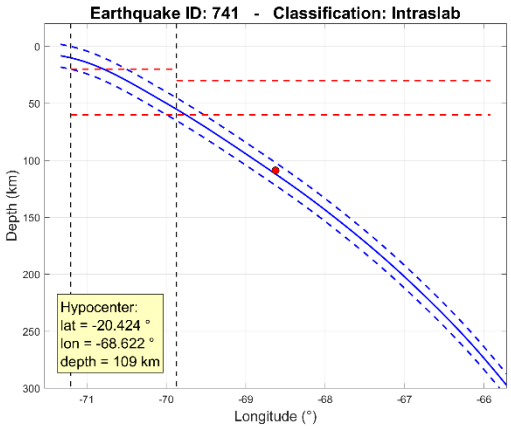

Figure B. 146: Event 741

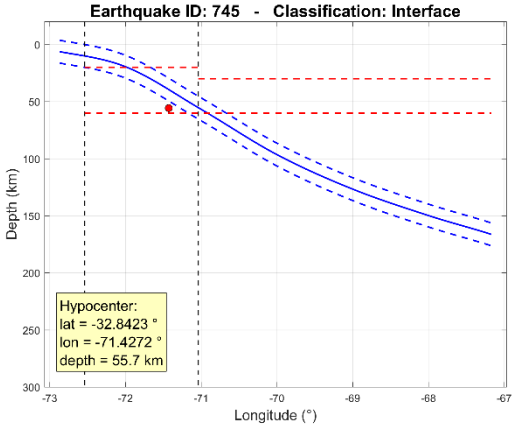

Figure B. 147: Event 745

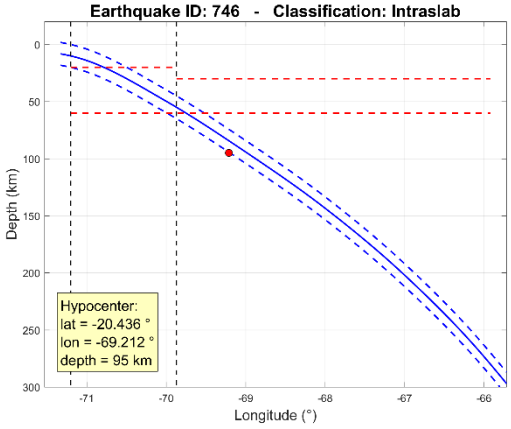

Figure B. 148: Event 746

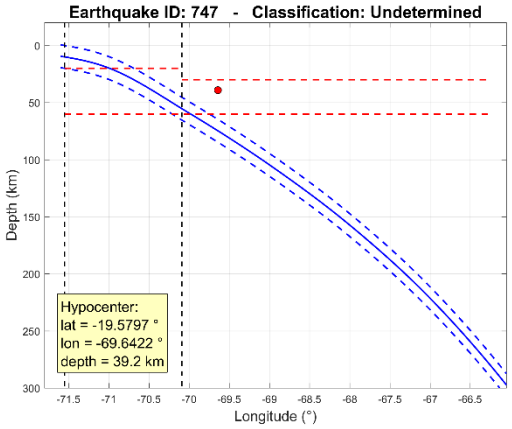

Figure B. 149: Event 747

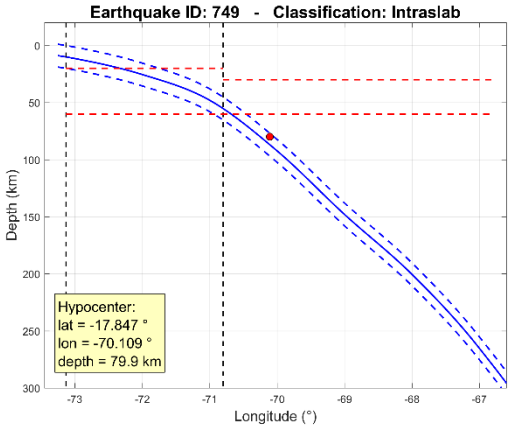

Figure B. 150: Event 749

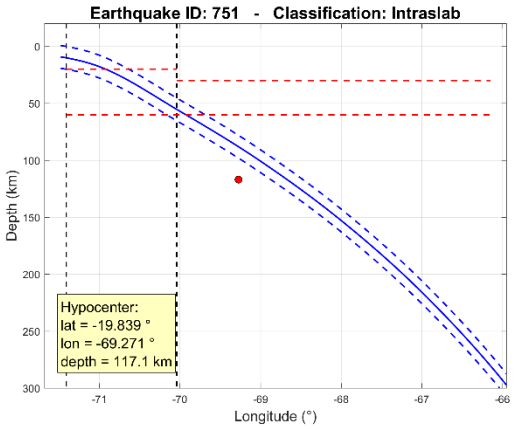

Figure B. 151: Event 751

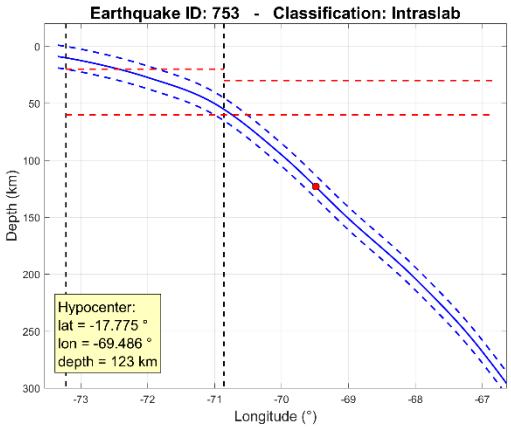

Figure B. 152: Event 753

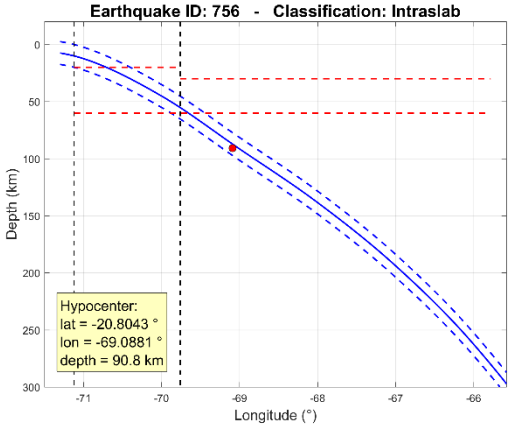

Figure B. 153: Event 756

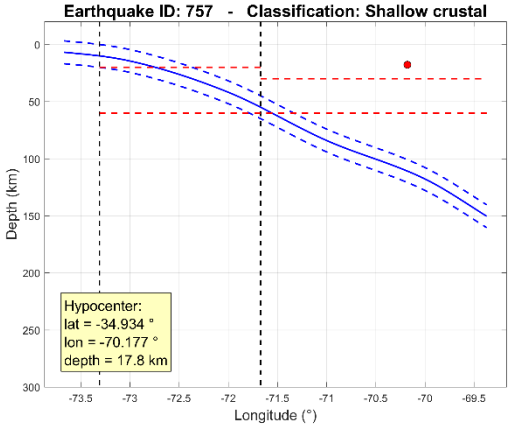

Figure B. 154: Event 757

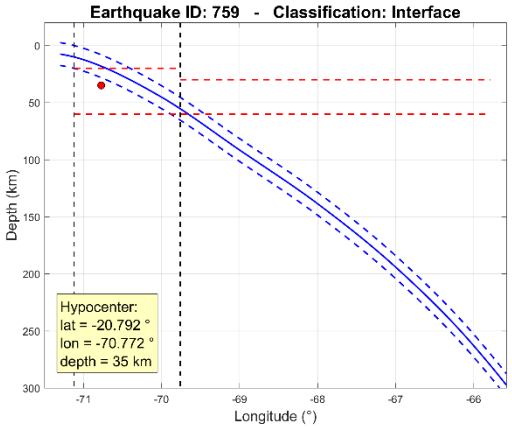

Figure B. 155: Event 759

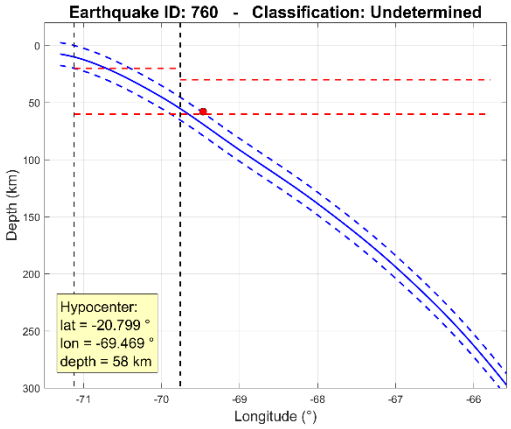

Figure B. 156: Event 760

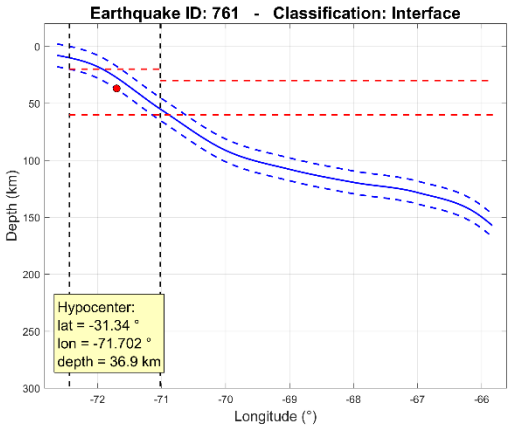

Figure B. 157: Event 761

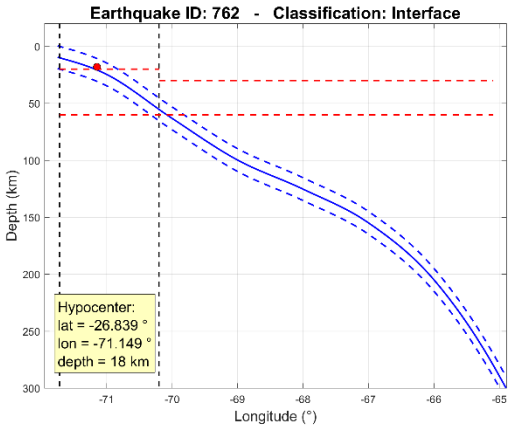

Figure B. 158: Event 762

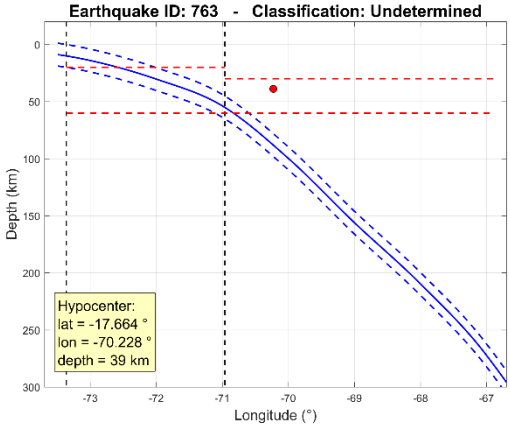

Figure B. 159: Event 763

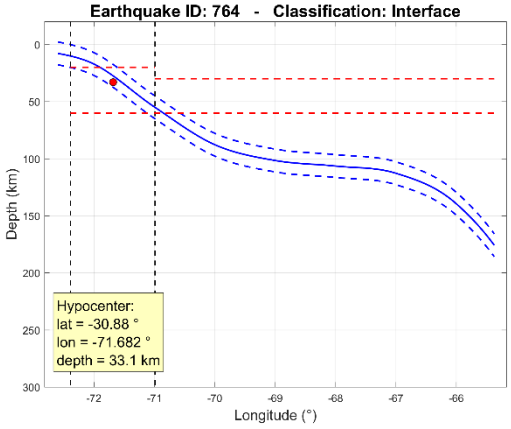

Figure B. 160: Event 764

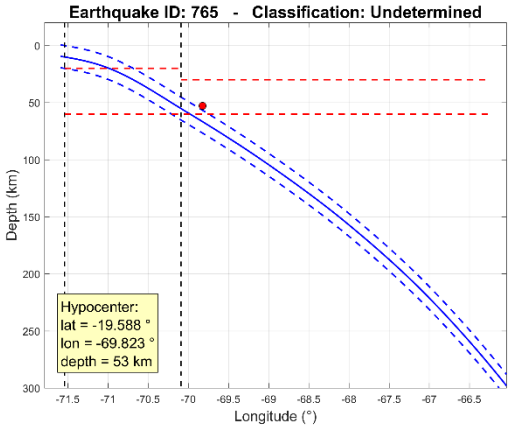

Figure B. 161: Event 765

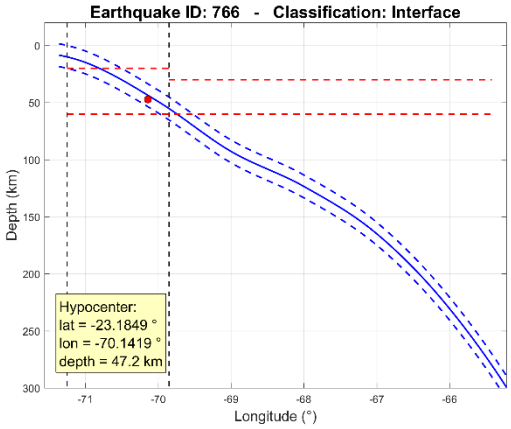

Figure B. 162: Event 766

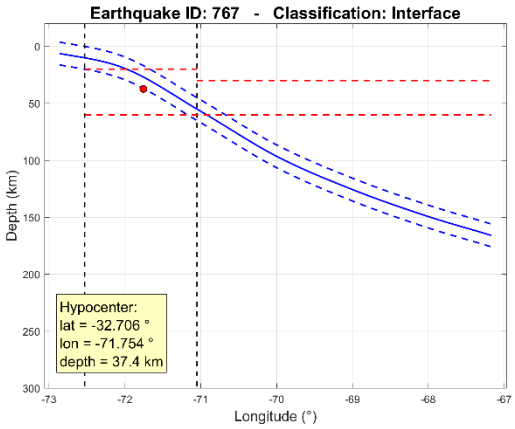

Figure B. 163: Event 767

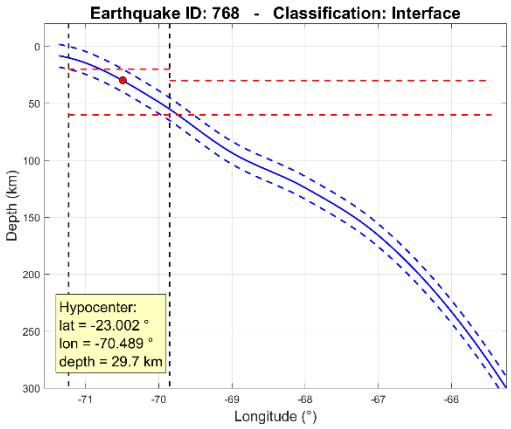

Figure B. 164: Event 768

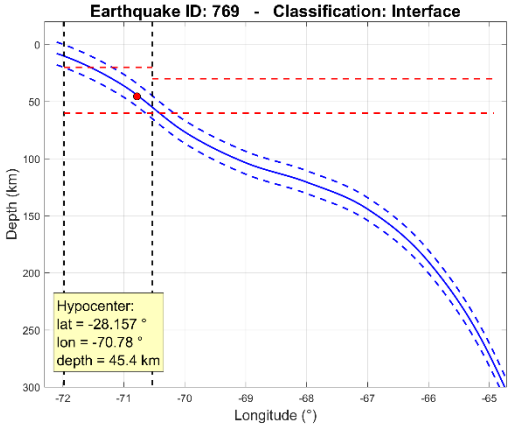

Figure B. 165: Event 769

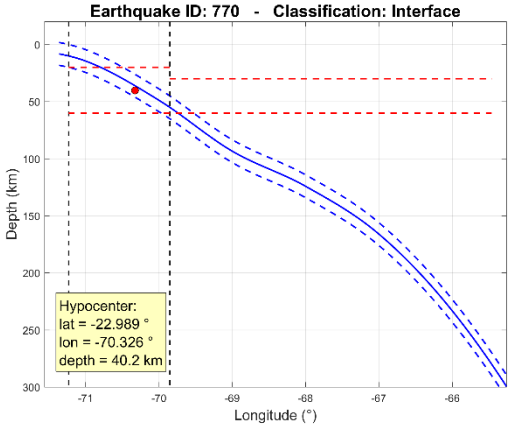

Figure B. 166: Event 770

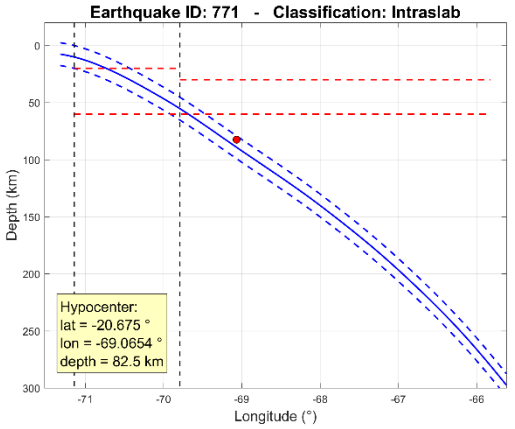

Figure B. 167: Event 771

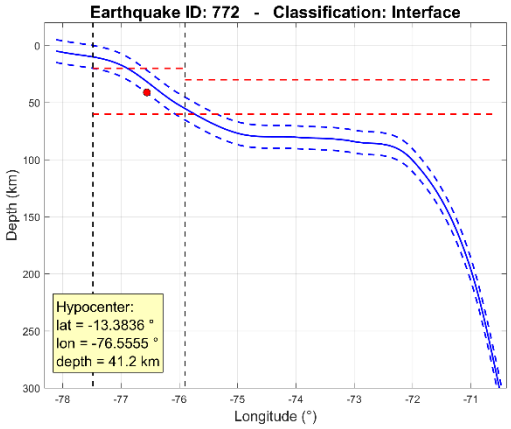

Figure B. 168: Event 772

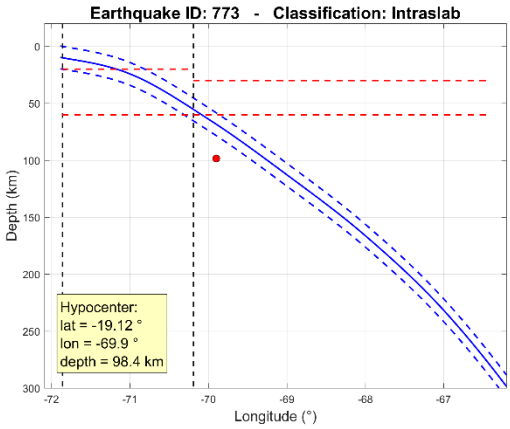

Figure B. 169: Event 773

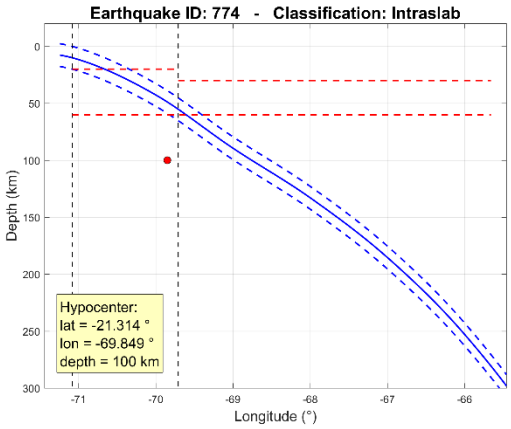

Figure B. 170: Event 774

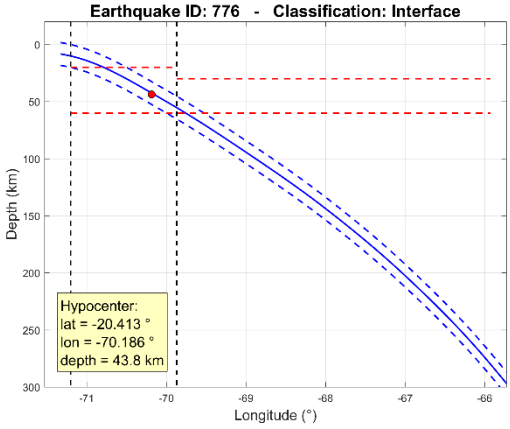

Figure B. 171: Event 776

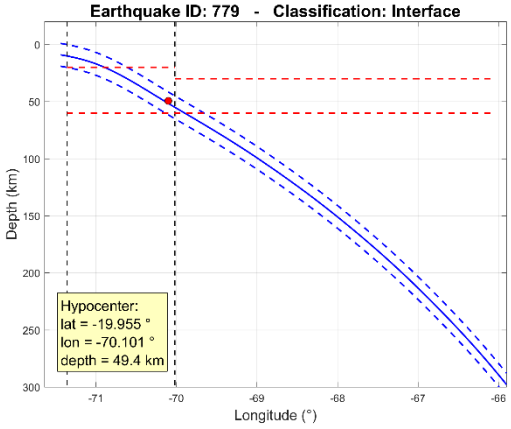

Figure B. 172: Event 779

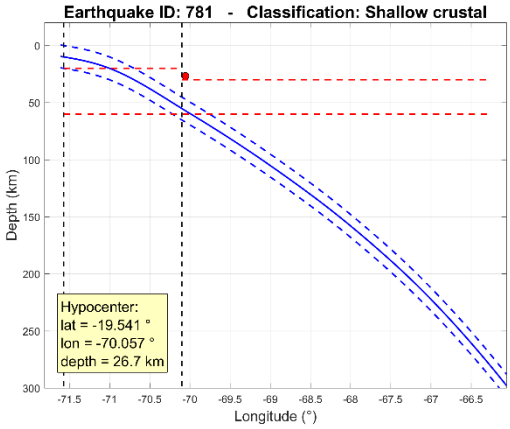

Figure B. 173: Event 781

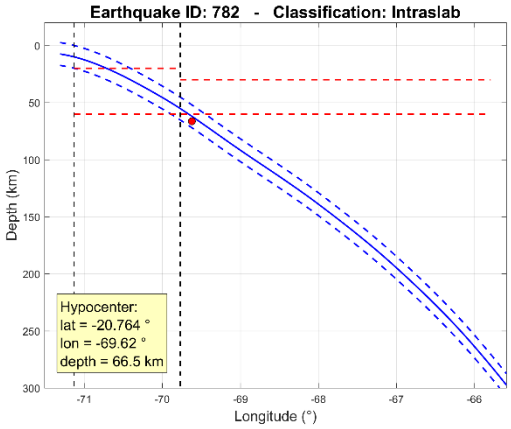

Figure B. 174: Event 782

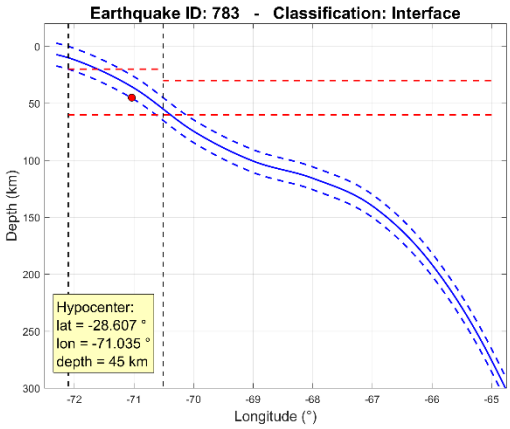

Figure B. 175: Event 783

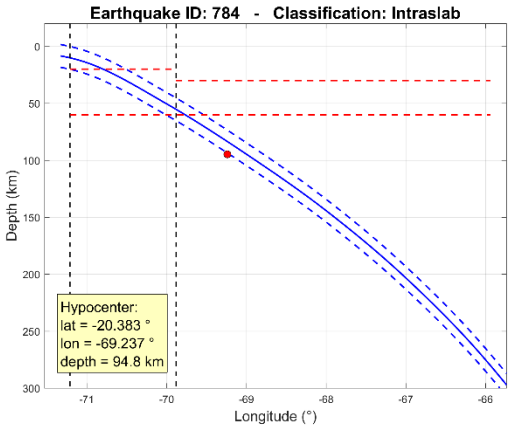

Figure B. 176: Event 784

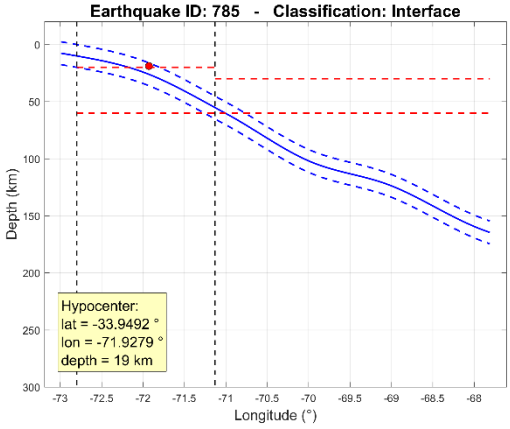

Figure B. 177: Event 785

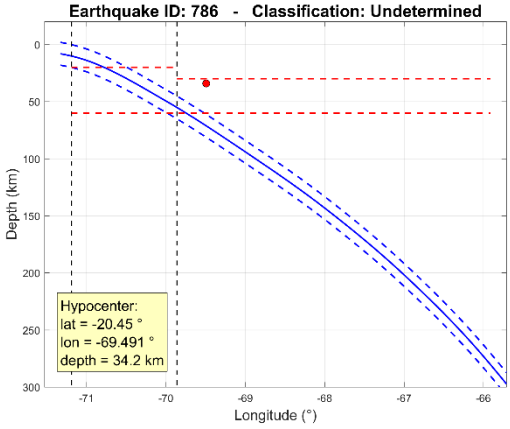

Figure B. 178: Event 786

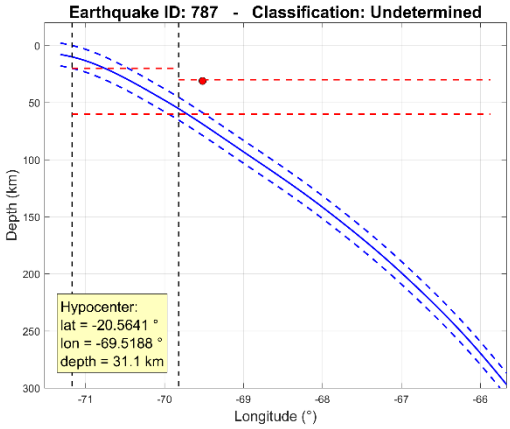

Figure B. 179: Event 787

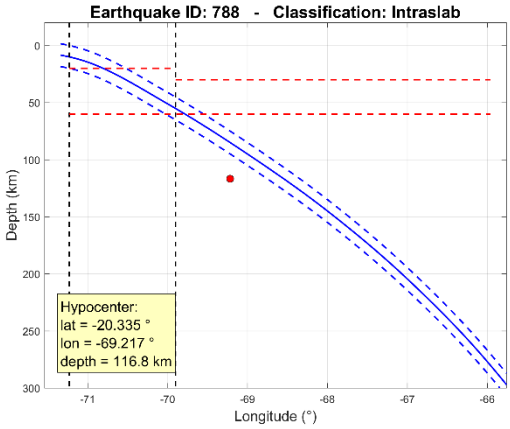

Figure B. 180: Event 788

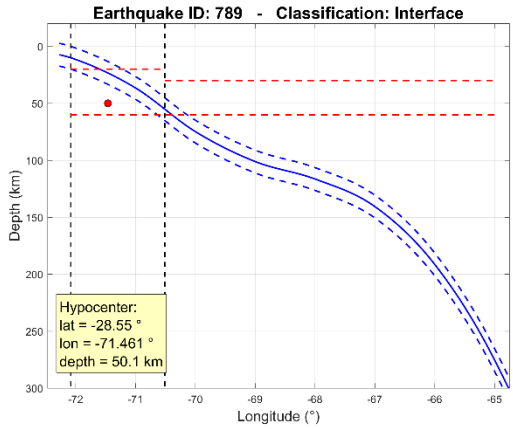

Figure B. 181: Event 789

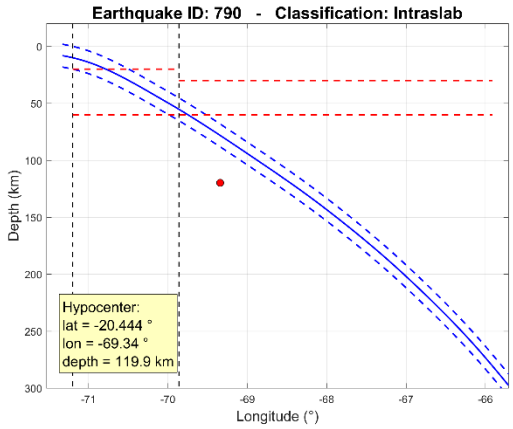

Figure B. 182: Event 790

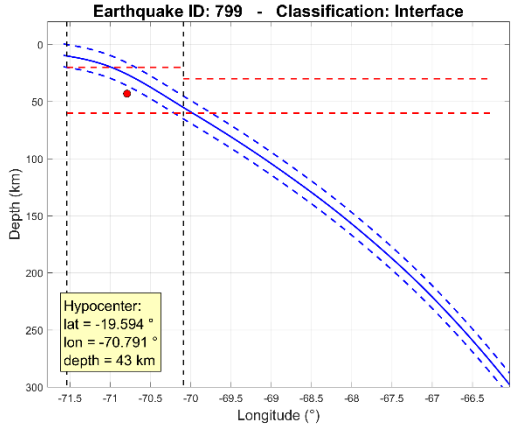

Figure B. 183: Event 799

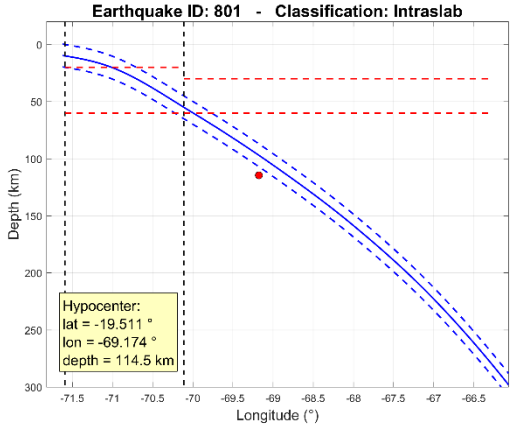

Figure B. 184: Event 801

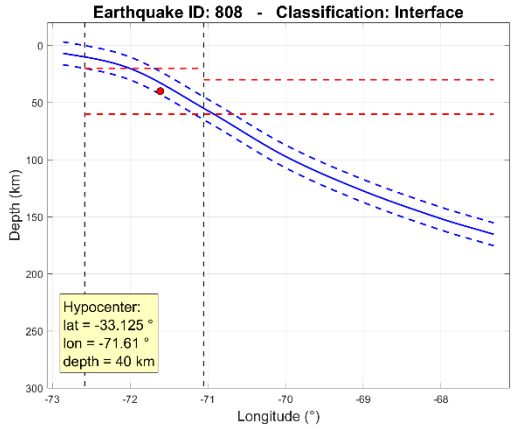

Figure B. 185: Event 808

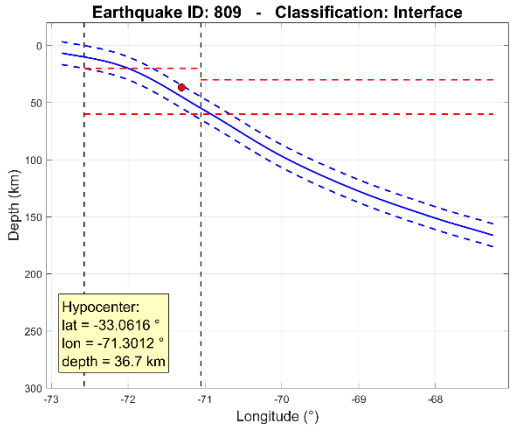

Figure B. 186: Event 809

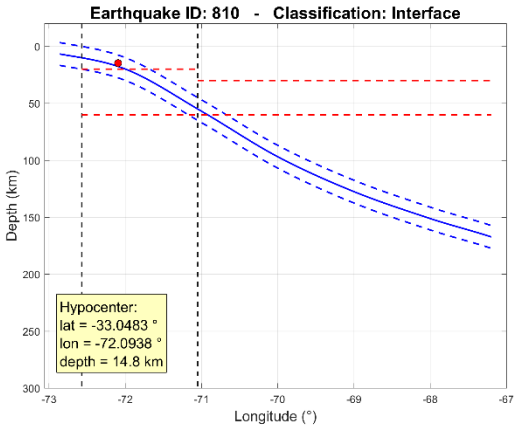

Figure B. 187: Event 810

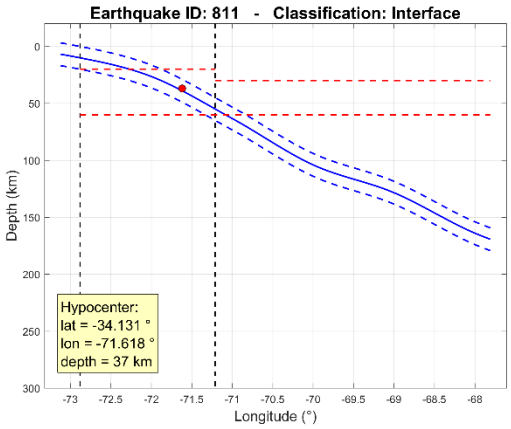

Figure B. 188: Event 811

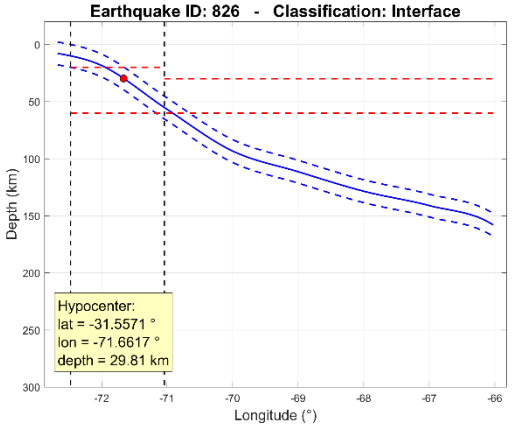

Figure B. 189: Event 826

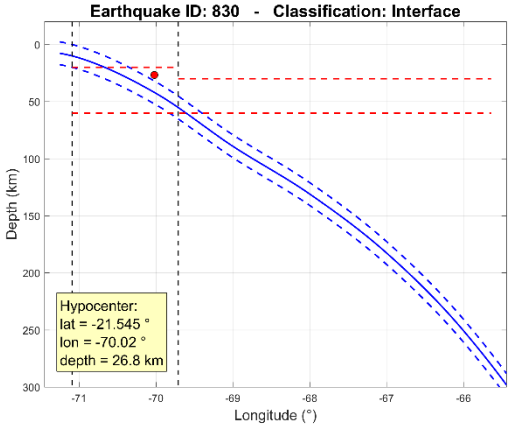

Figure B. 190: Event 830

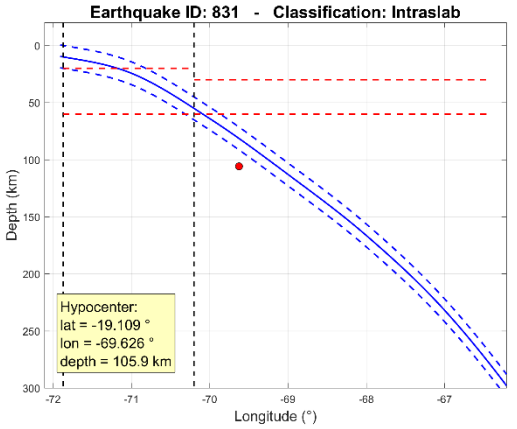

Figure B. 191: Event 831

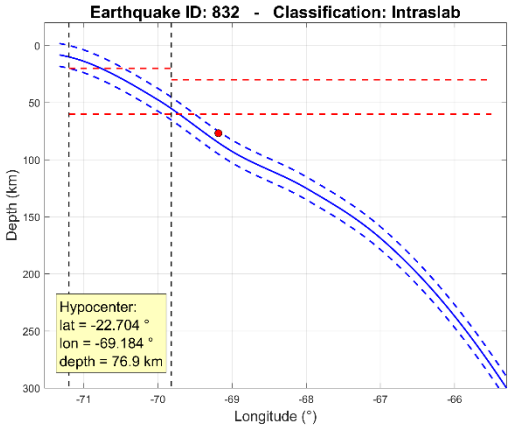

Figure B. 192: Event 832

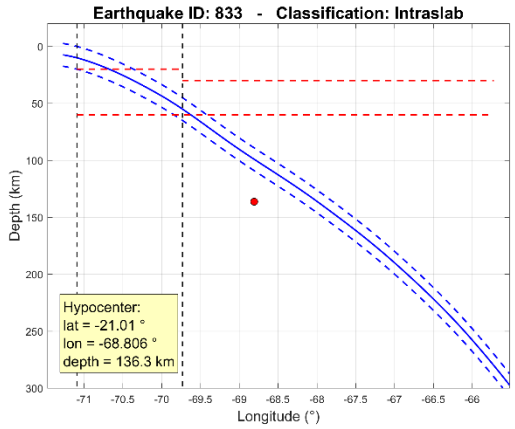

Figure B. 193: Event 833

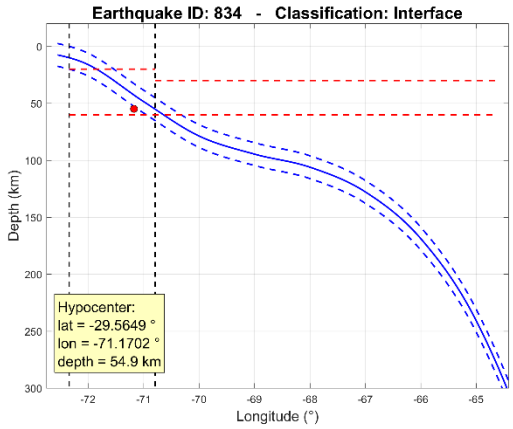

Figure B. 194: Event 834

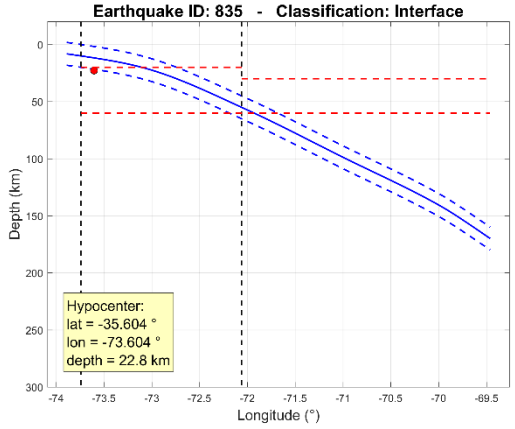

Figure B. 195: Event 835

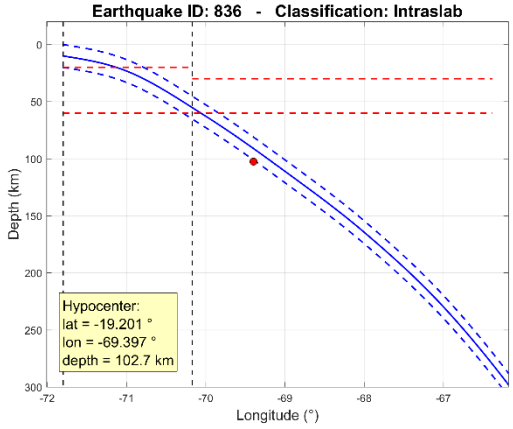

Figure B. 196: Event 836

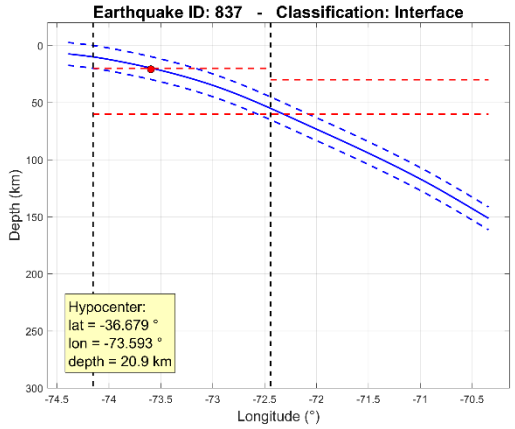

Figure B. 197: Event 837

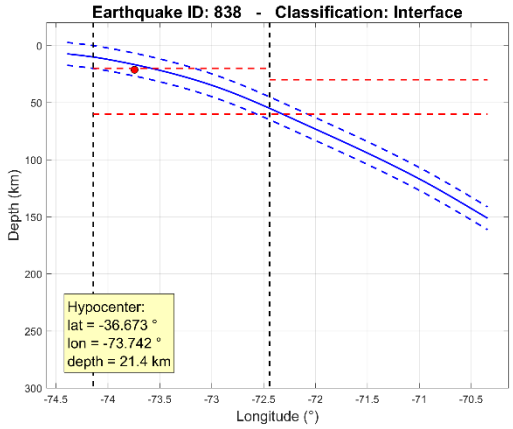

Figure B. 198: Event 838

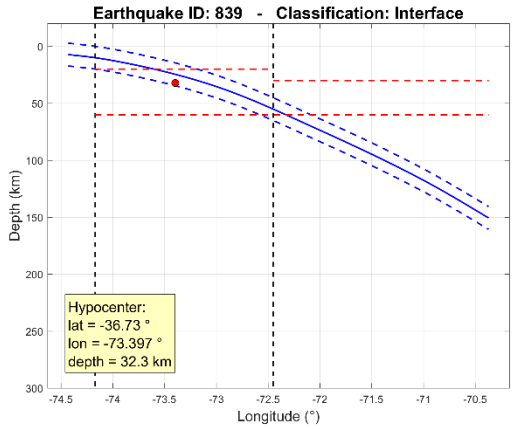

Figure B. 199: Event 839

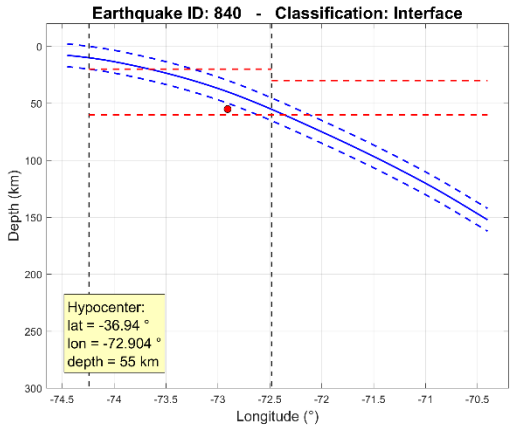

Figure B. 200: Event 840

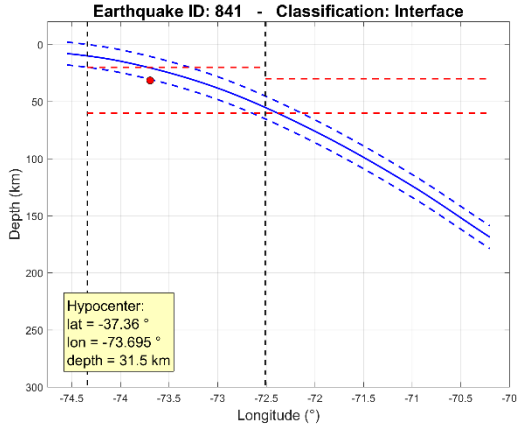

Figure B. 201: Event 841

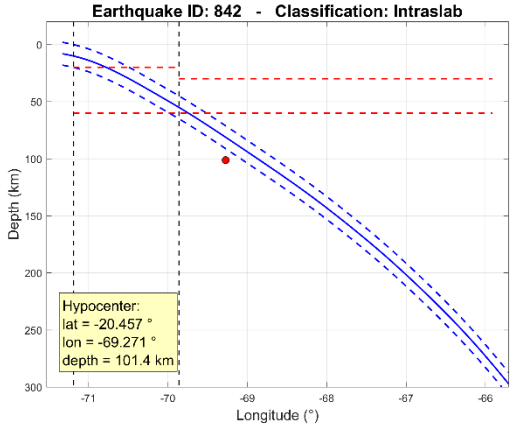

Figure B. 202: Event 842

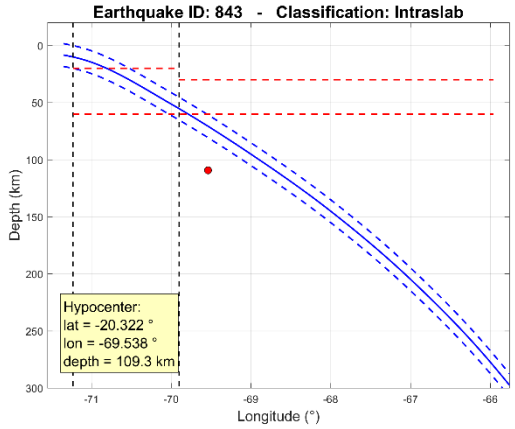

Figure B. 203: Event 843

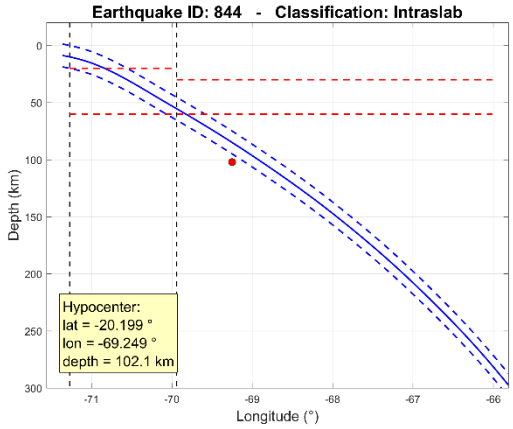

Figure B. 204: Event 844

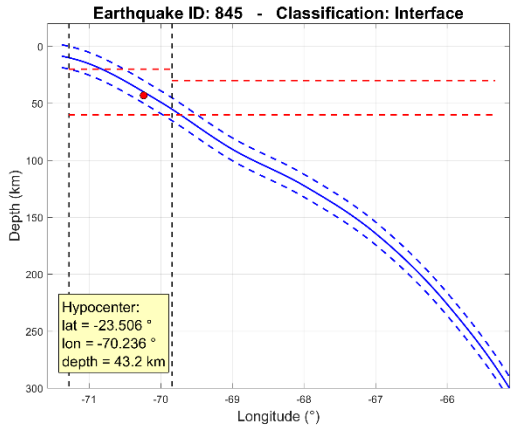

Figure B. 205: Event 845

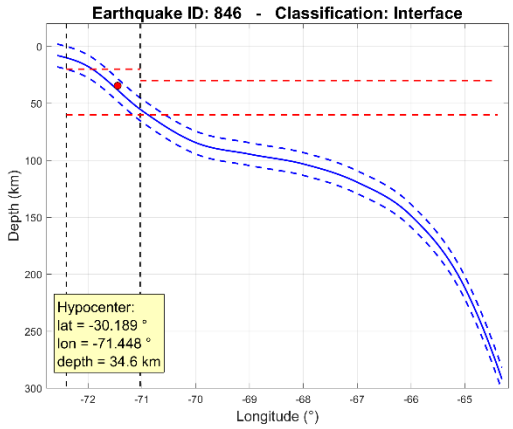

Figure B. 206: Event 846

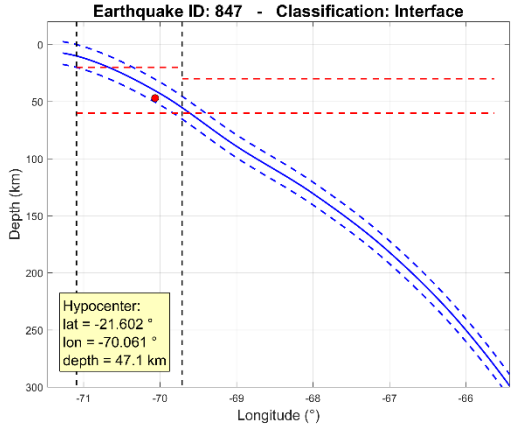

Figure B. 207: Event 847

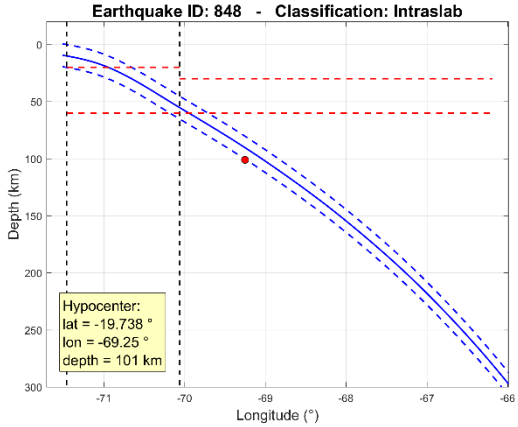

Figure B. 208: Event 848

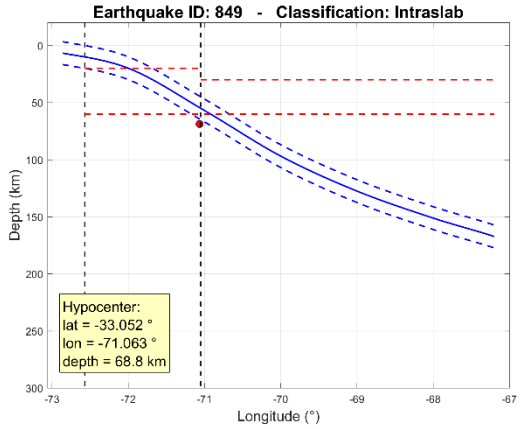

Figure B. 209: Event 849

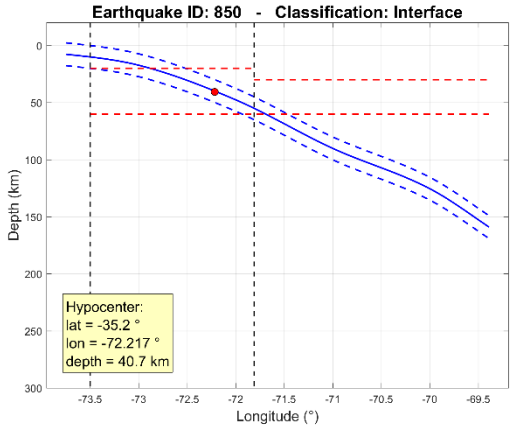

Figure B. 210: Event 850

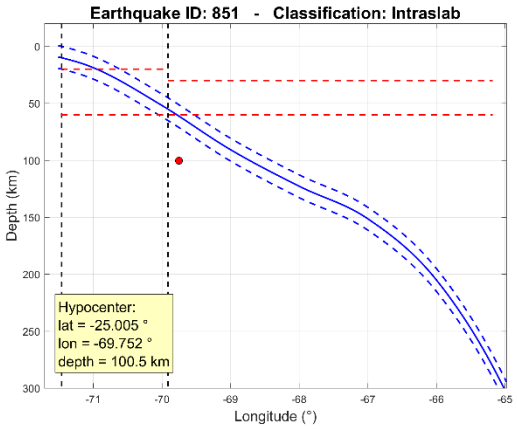

Figure B. 211: Event 851

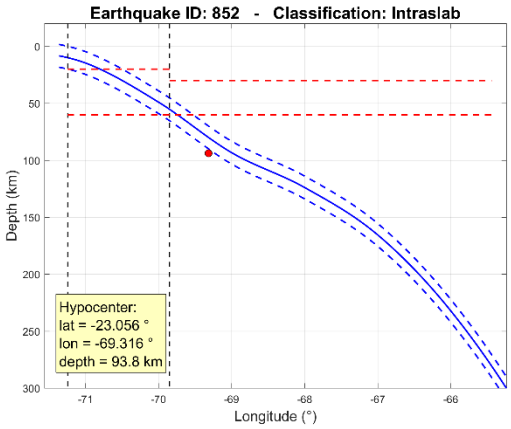

Figure B. 212: Event 852

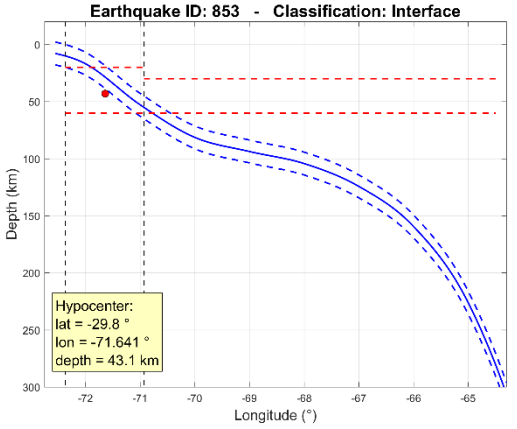

Figure B. 213: Event 853

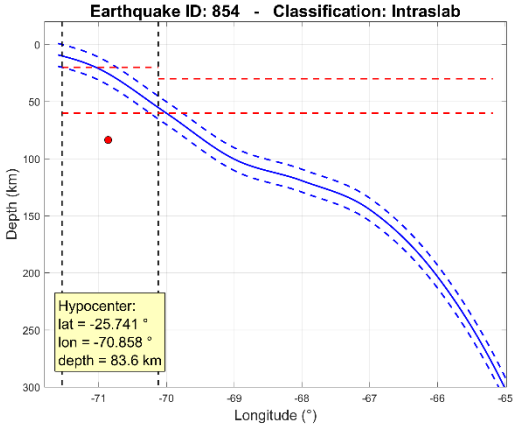

Figure B. 214: Event 854

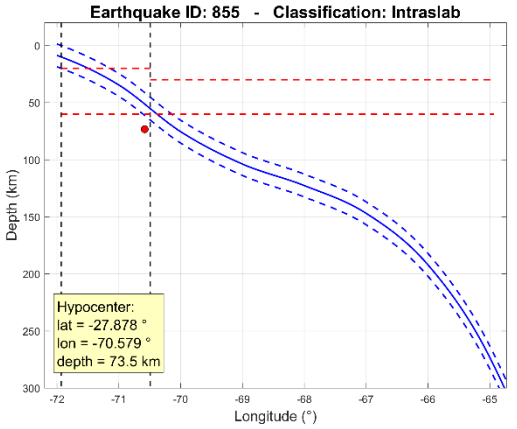

Figure B. 215: Event 855

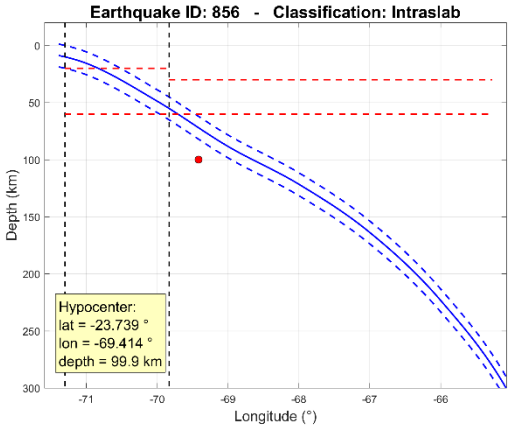

Figure B. 216: Event 856

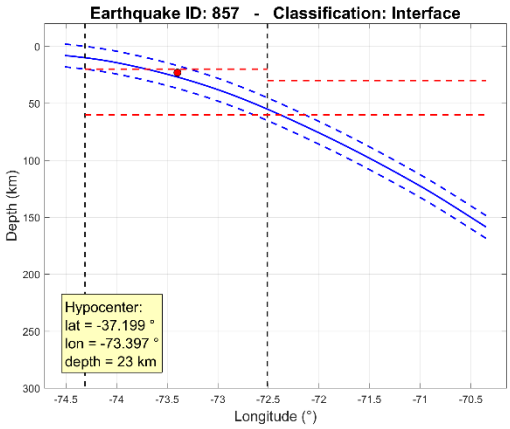

Figure B. 217: Event 857

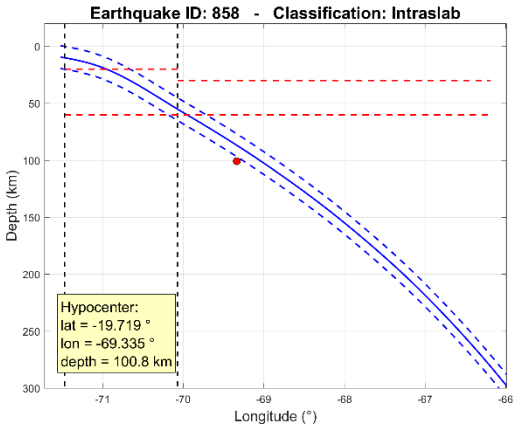

Figure B. 218: Event 858

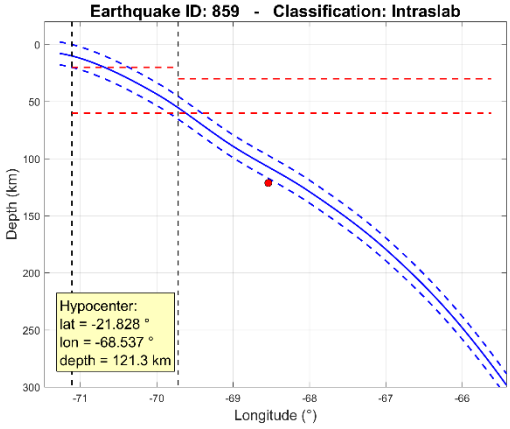

Figure B. 219: Event 859

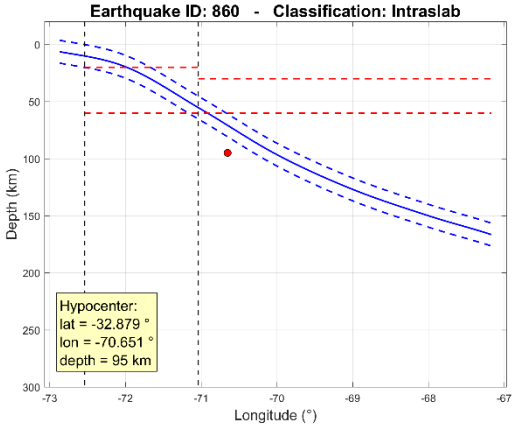

Figure B. 220: Event 860

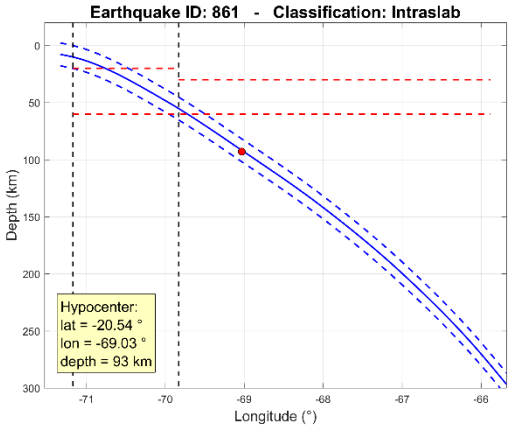

Figure B. 221: Event 861

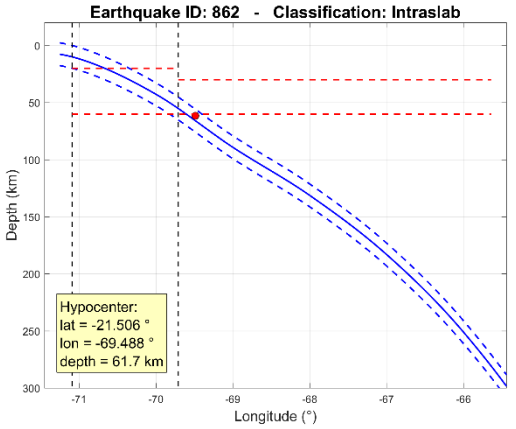

Figure B. 222: Event 862

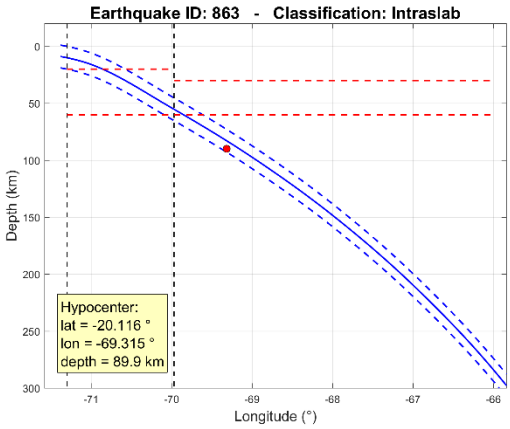

Figure B. 223: Event 863

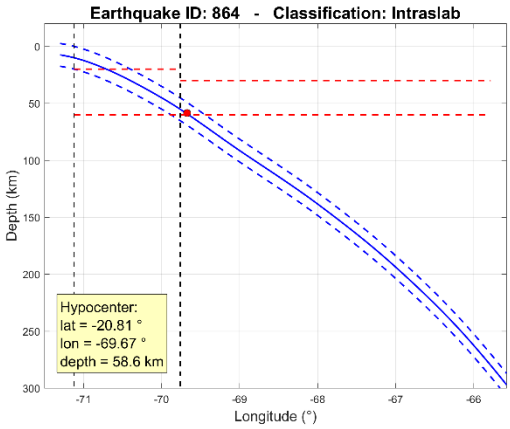

Figure B. 224: Event 864

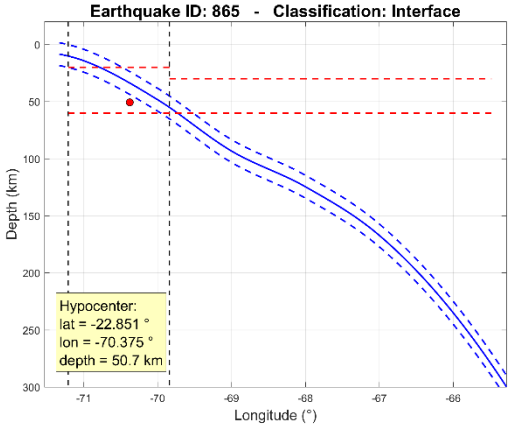

Figure B. 225: Event 865

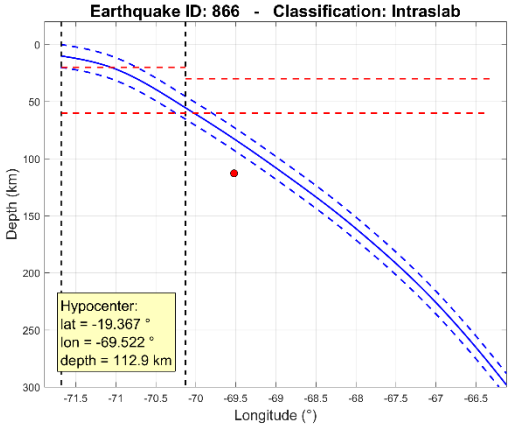

Figure B. 226: Event 866

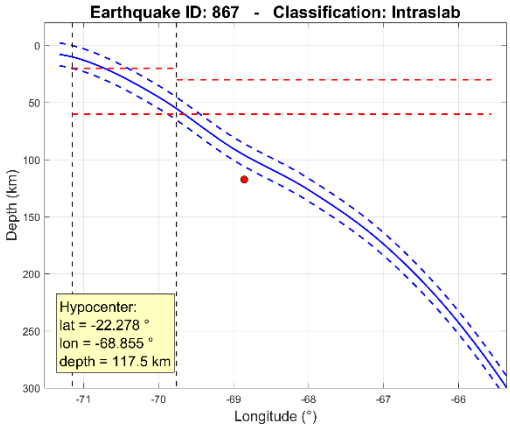

Figure B. 227: Event 867

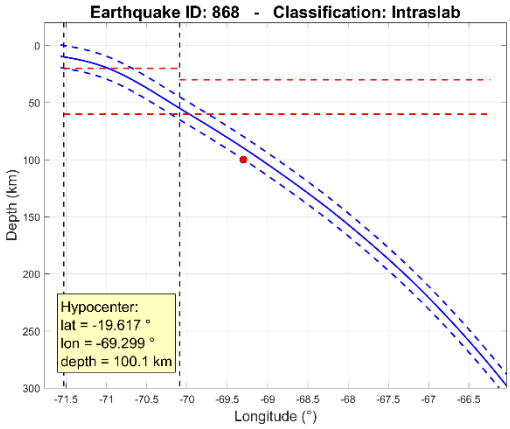

Figure B. 228: Event 868

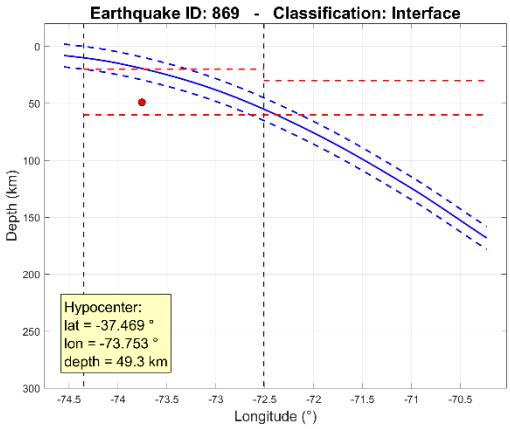

Figure B. 229: Event 869

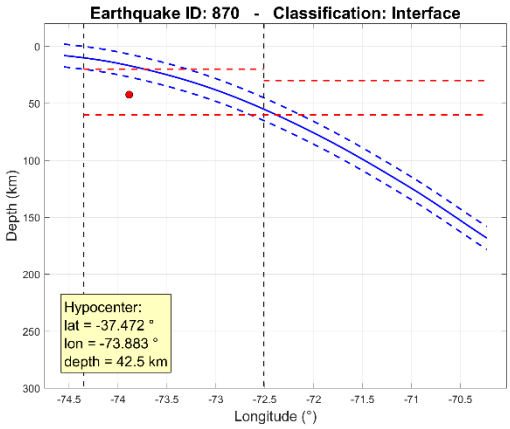

Figure B. 230: Event 870

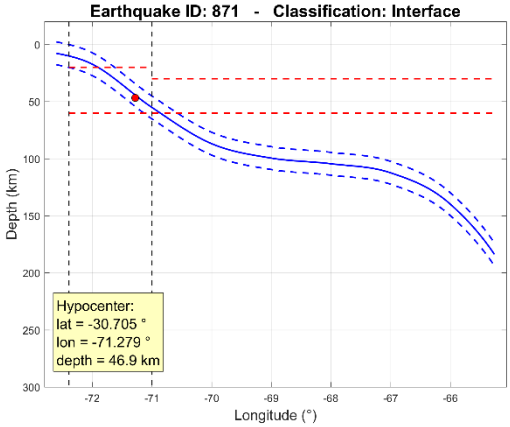

Figure B. 231: Event 871

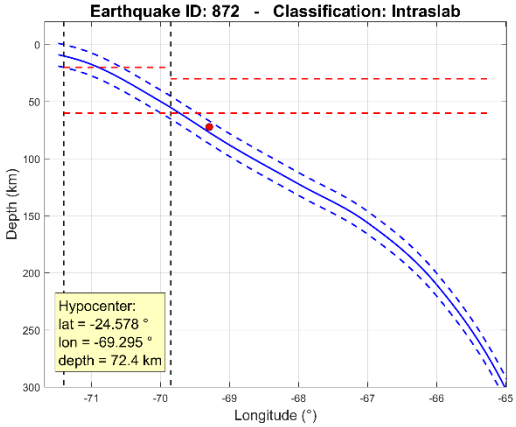

Figure B. 232: Event 872

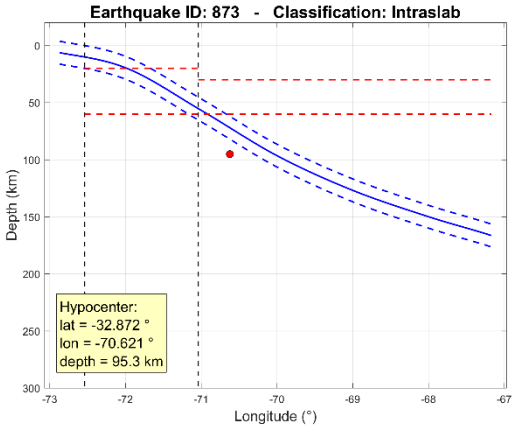

Figure B. 233: Event 873

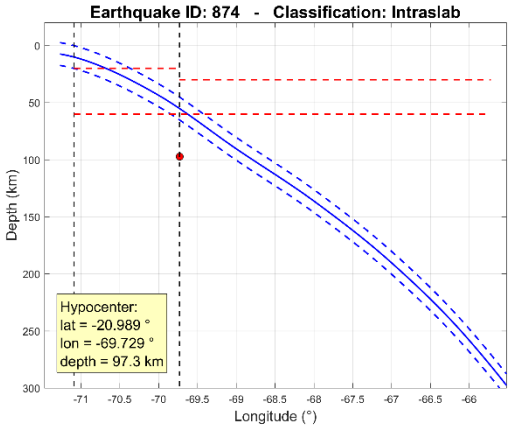

Figure B. 234: Event 874

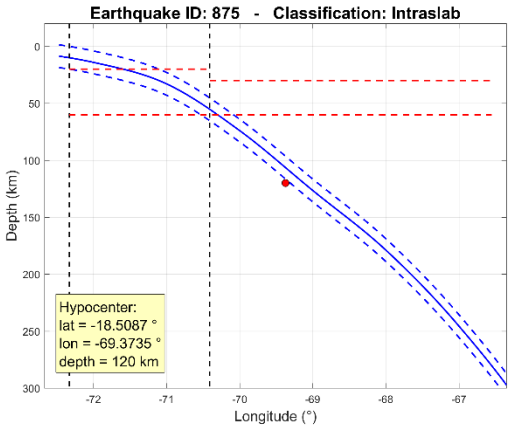

Figure B. 235: Event 875

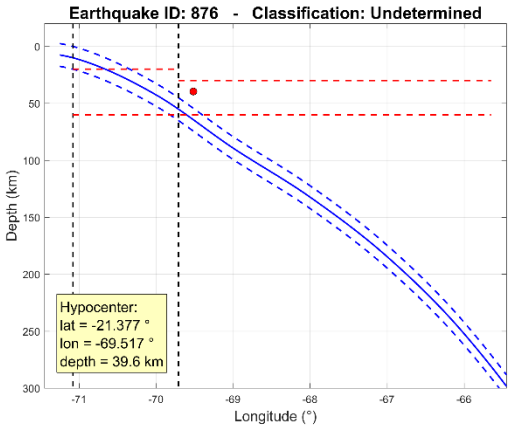

Figure B. 236: Event 876

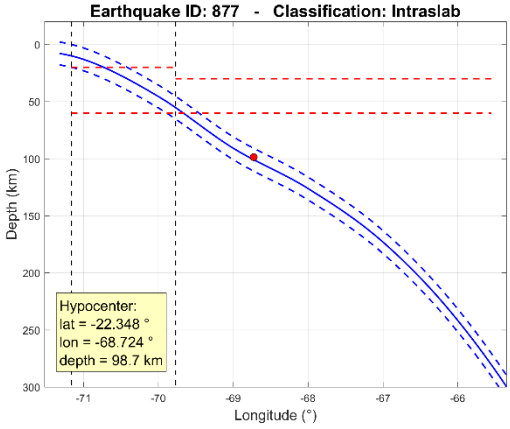

Figure B. 237: Event 877

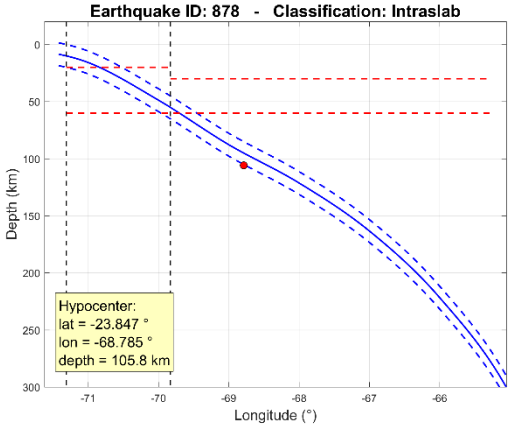

Figure B. 238: Event 878

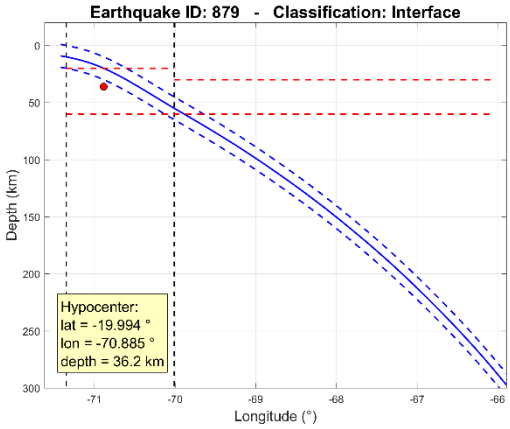

Figure B. 239: Event 879

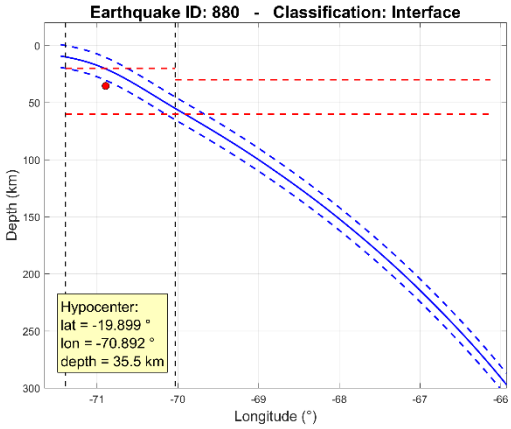

Figure B. 240: Event 880

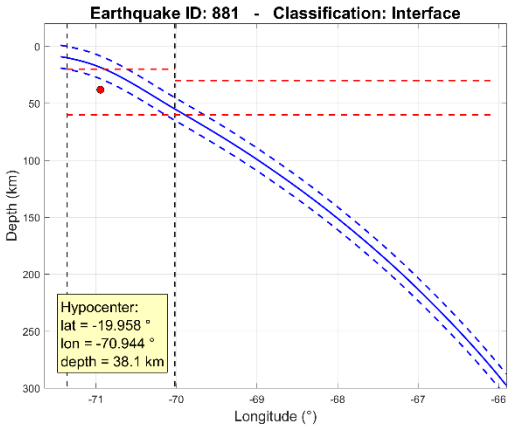

Figure B. 241: Event 881

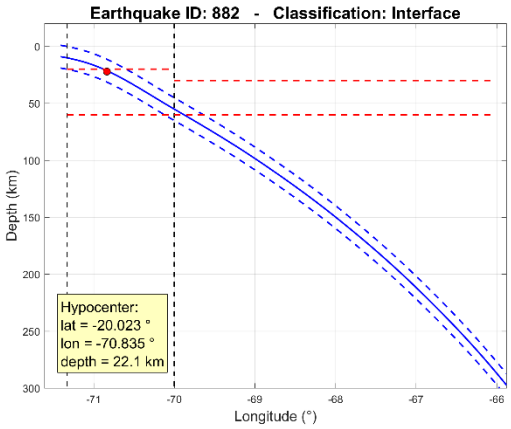

Figure B. 242: Event 882

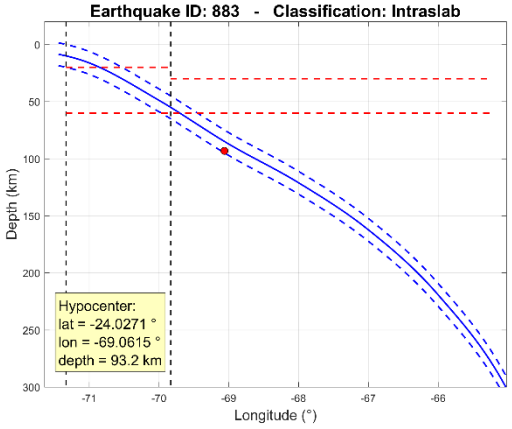

Figure B. 243: Event 883

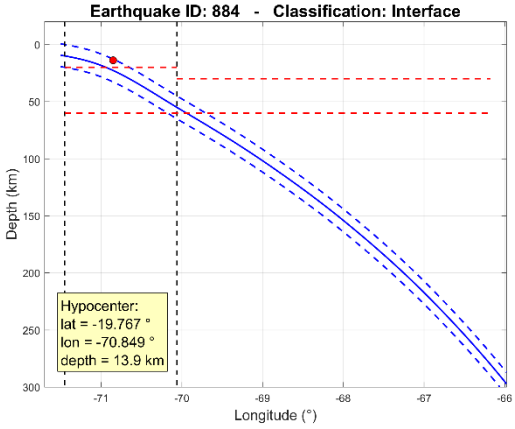

Figure B. 244: Event 884

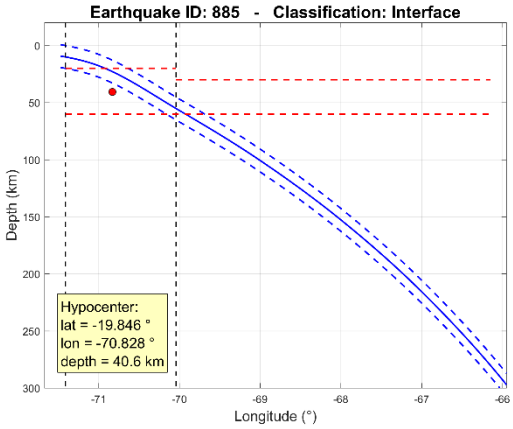

Figure B. 245: Event 885

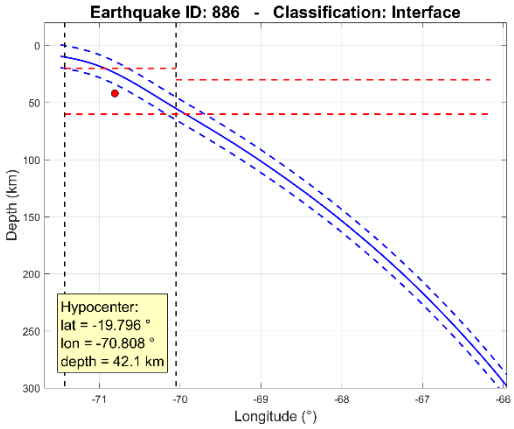

Figure B. 246: Event 886

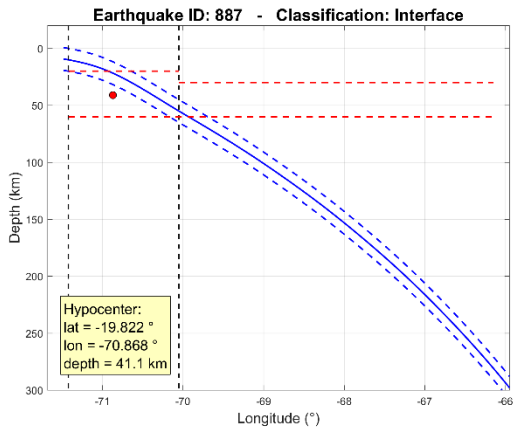

Figure B. 247: Event 887

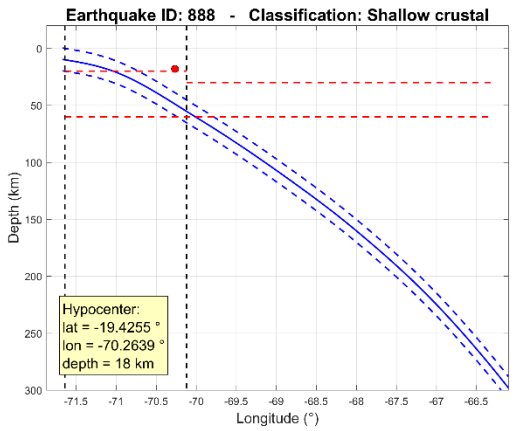

Figure B. 248: Event 888

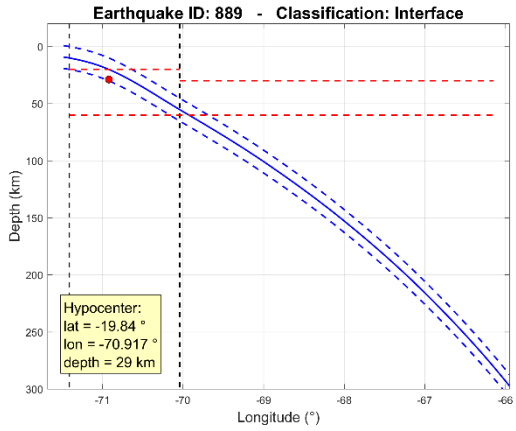

Figure B. 249: Event 889

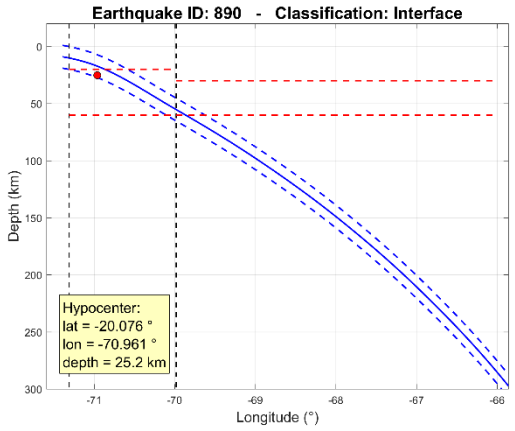

Figure B. 250: Event 890

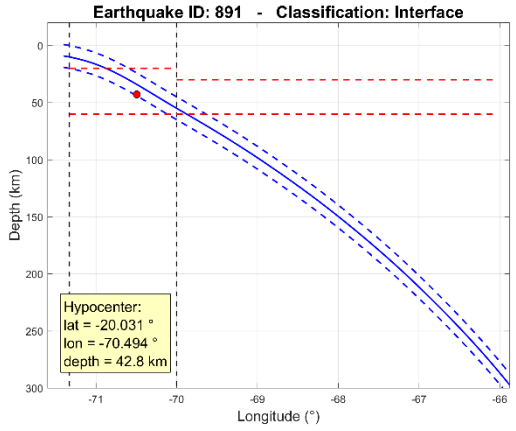

Figure B. 251: Event 891

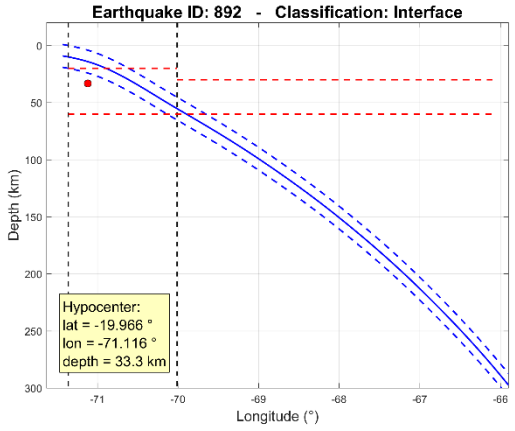

Figure B. 252: Event 892

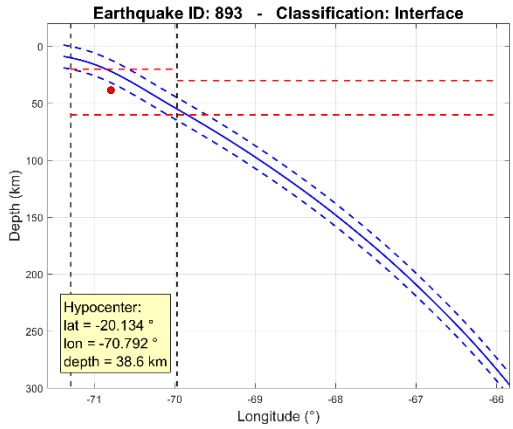

Figure B. 253: Event 893

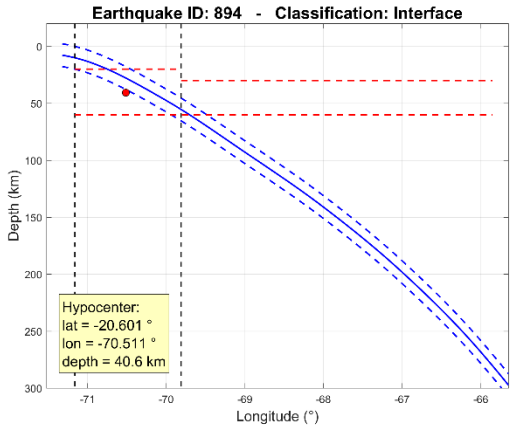

Figure B. 254: Event 894

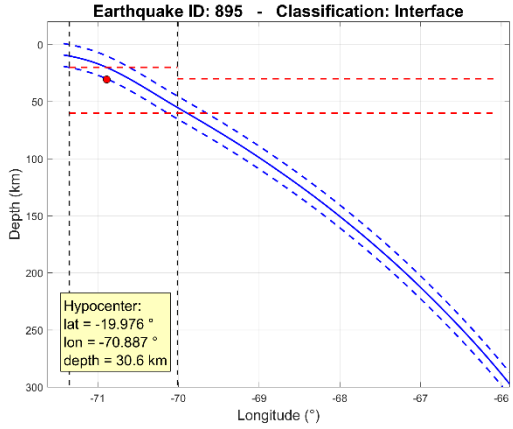

Figure B. 255: Event 895

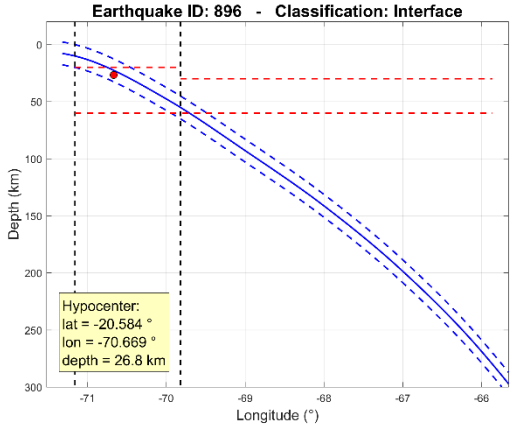

Figure B. 256: Event 896

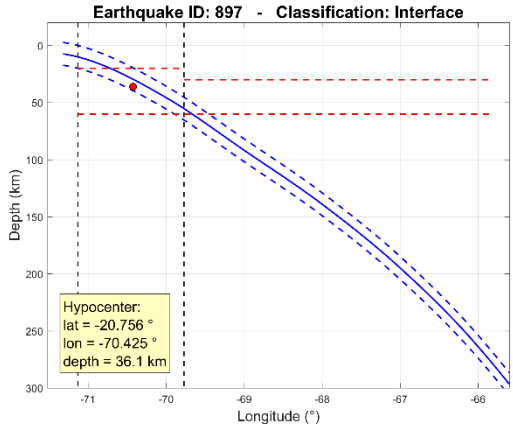

Figure B. 257: Event 897

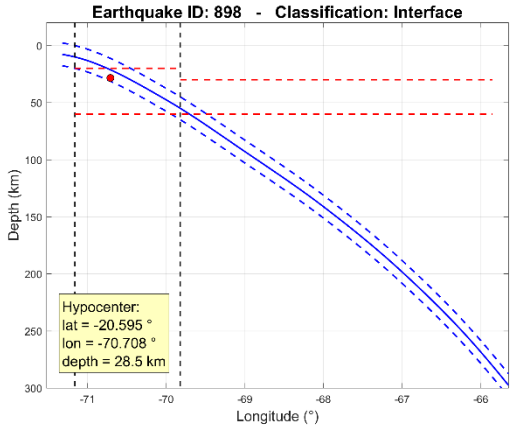

Figure B. 258: Event 898

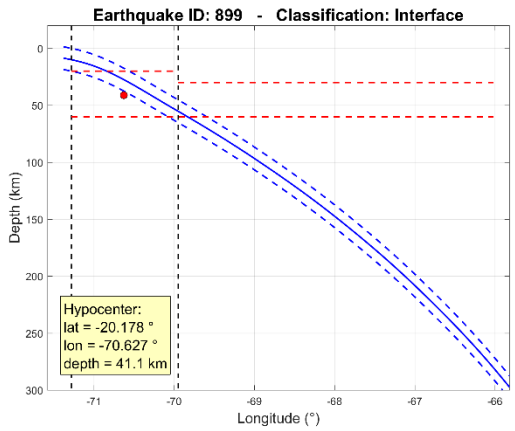

Figure B. 259: Event 899

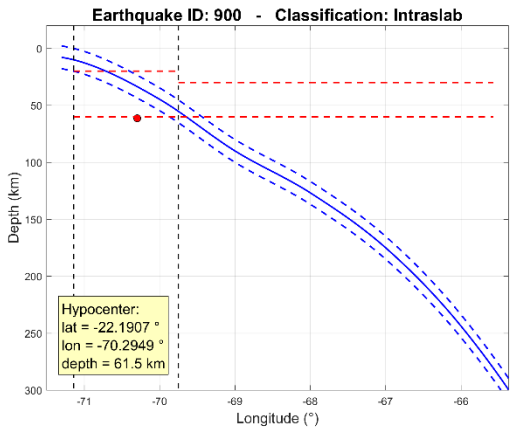

Figure B. 260: Event 900

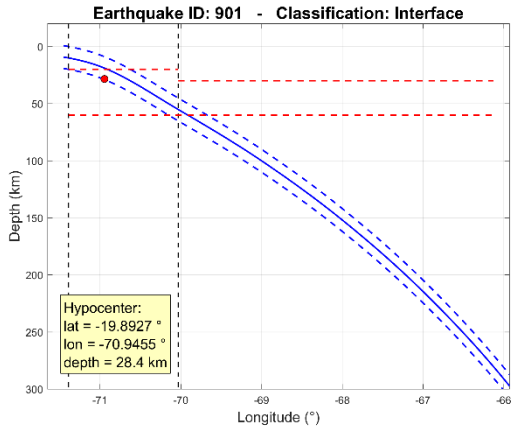

Figure B. 261: Event 901

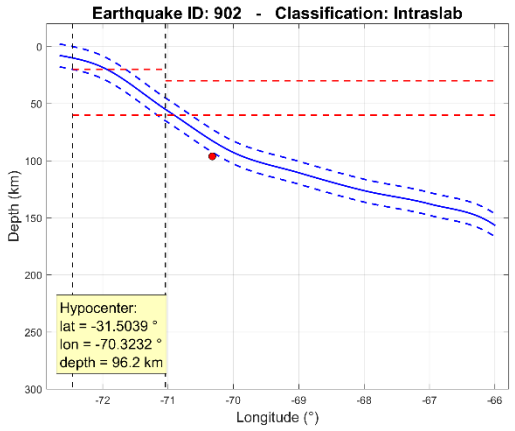

Figure B. 262: Event 902

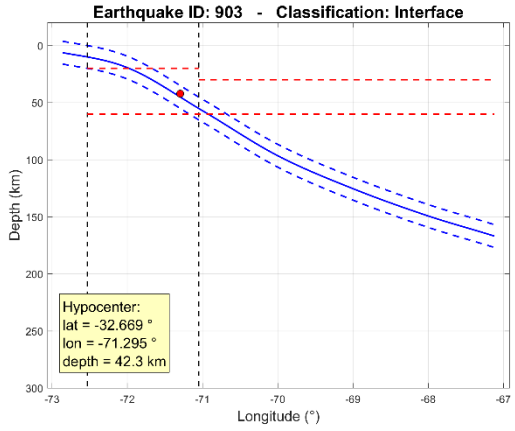

Figure B. 263: Event 903

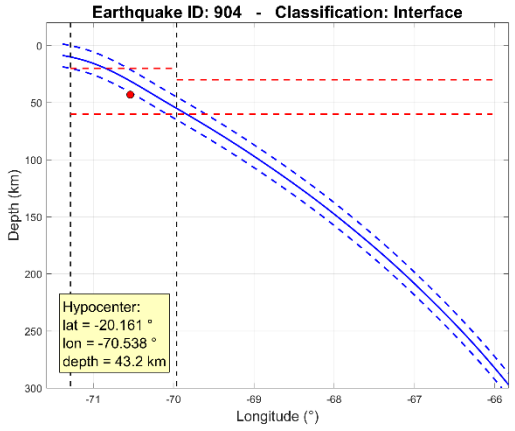

Figure B. 264: Event 904

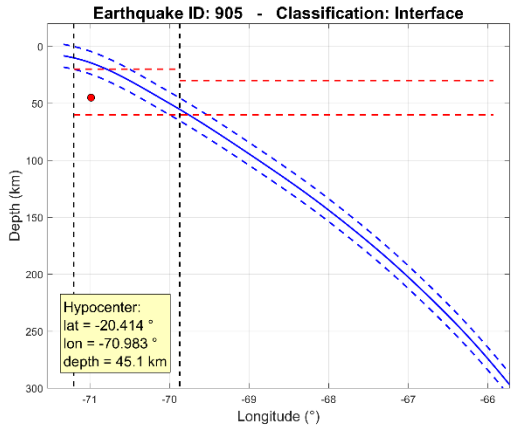

Figure B. 265: Event 905

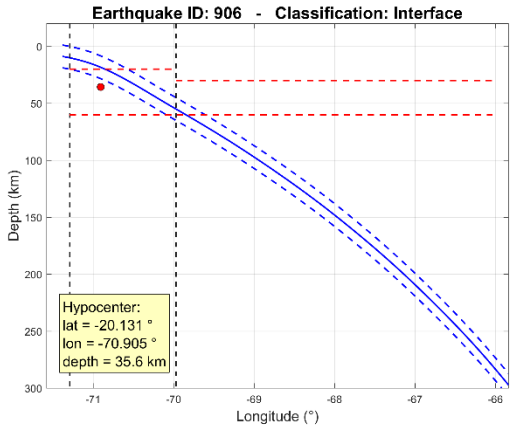

Figure B. 266: Event 906

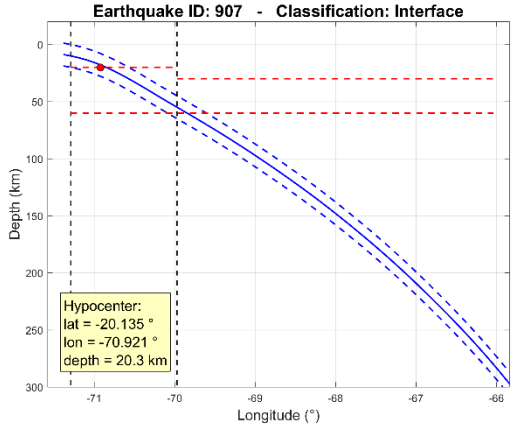

Figure B. 267: Event 907

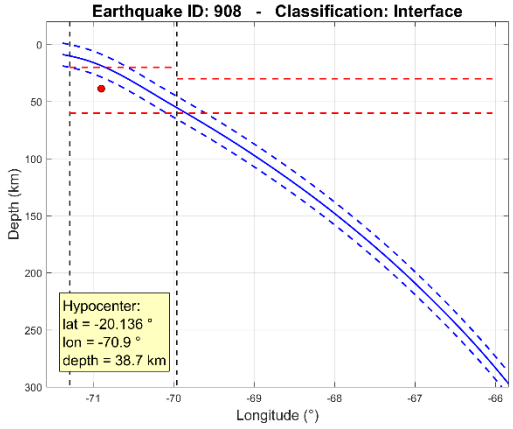

Figure B. 268: Event 908

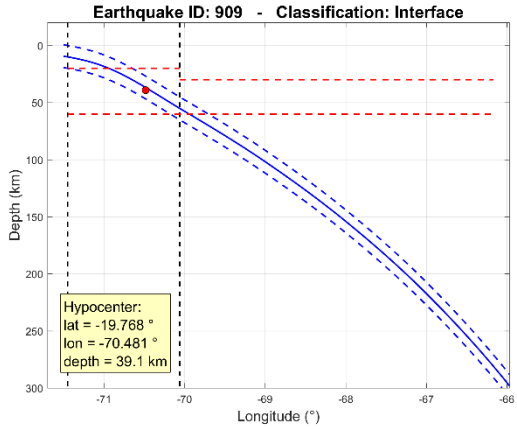

Figure B. 269: Event 909

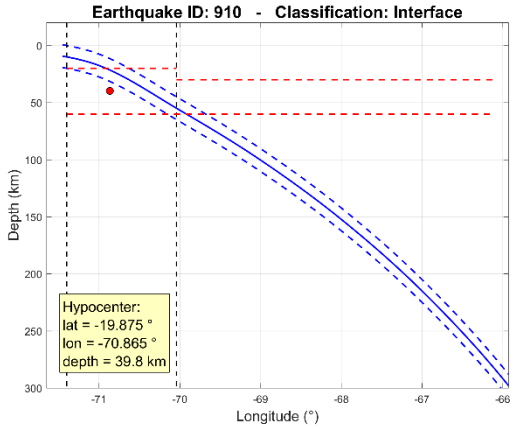

Figure B. 270: Event 910

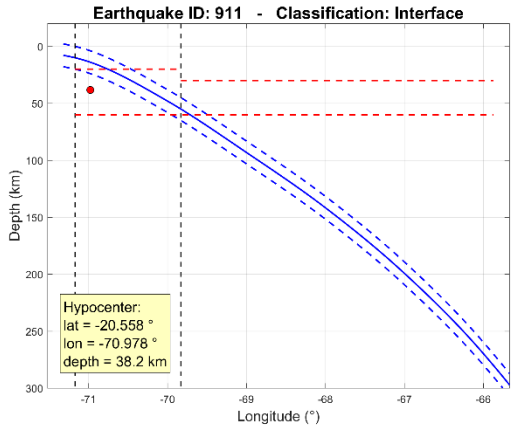

Figure B. 271: Event 911

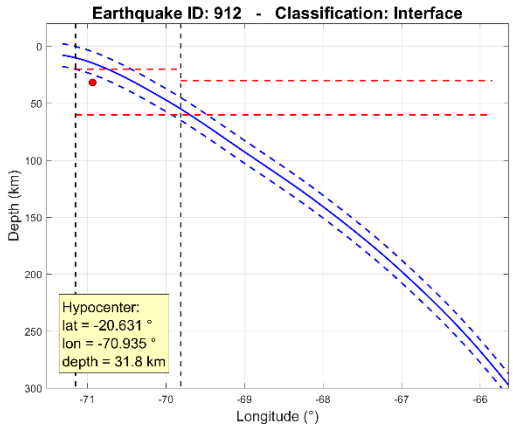

Figure B. 272: Event 912

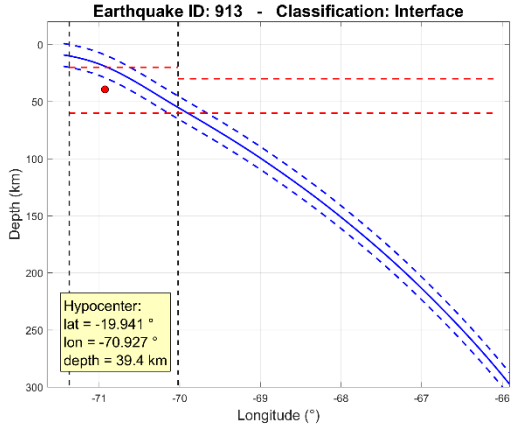

Figure B. 273: Event 913

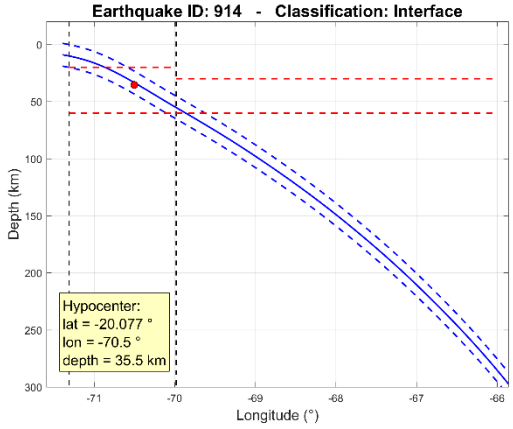

Figure B. 274: Event 914

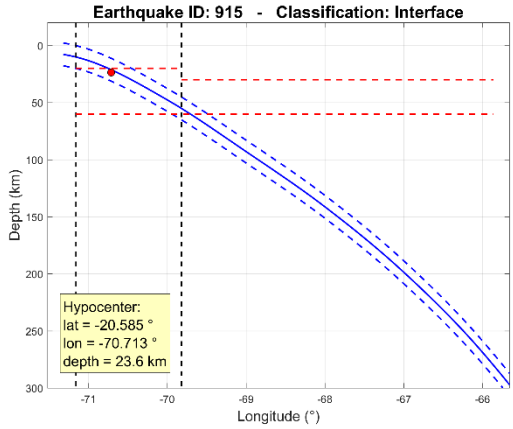

Figure B. 275: Event 915

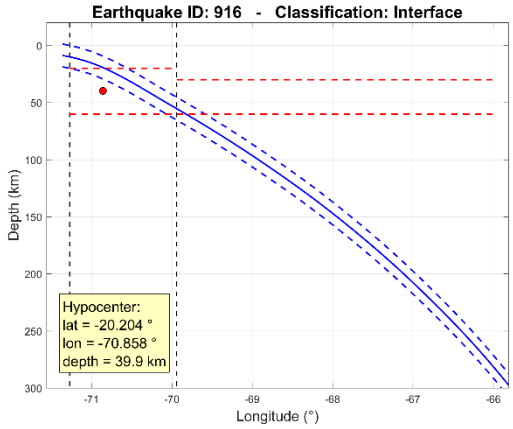

Figure B. 276: Event 916

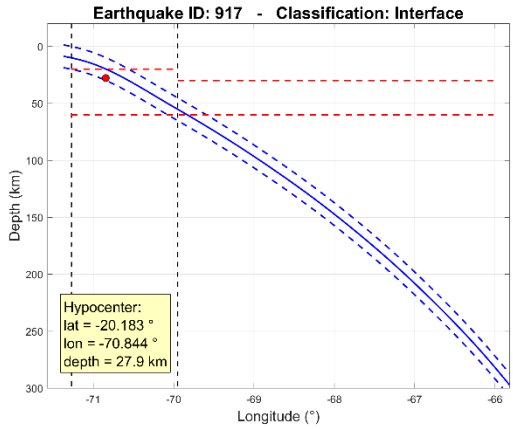

Figure B. 277: Event 917

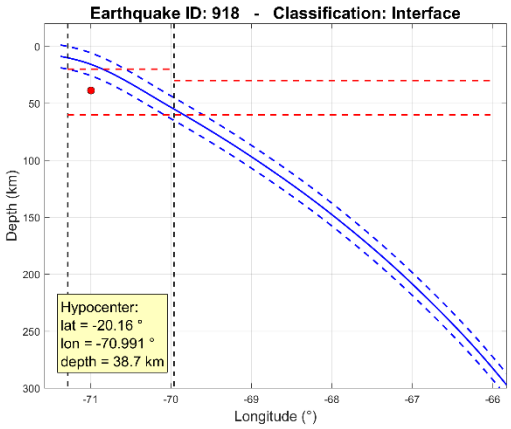

Figure B. 278: Event 918

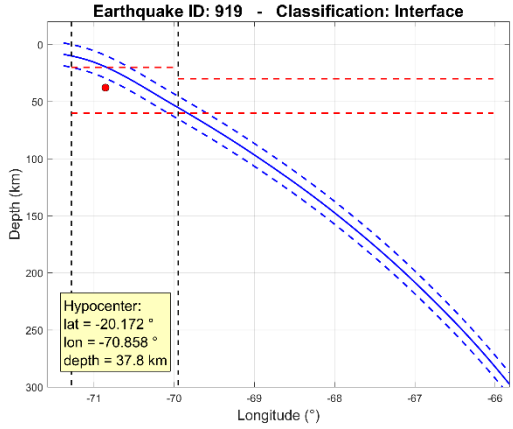

Figure B. 279: Event 919

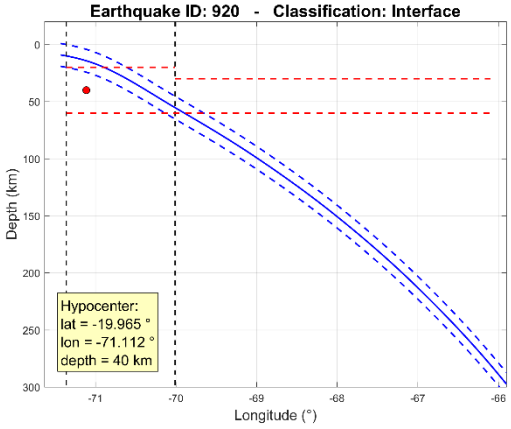

Figure B. 280: Event 920

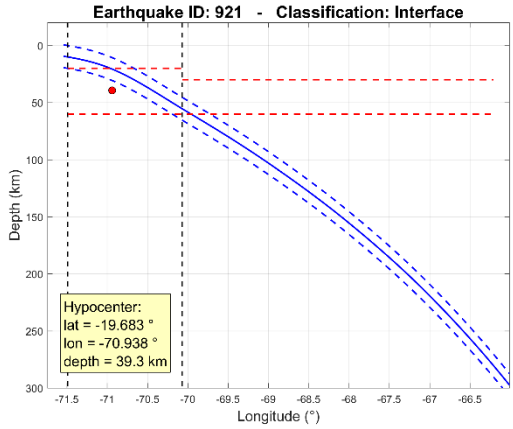

Figure B. 281: Event 921

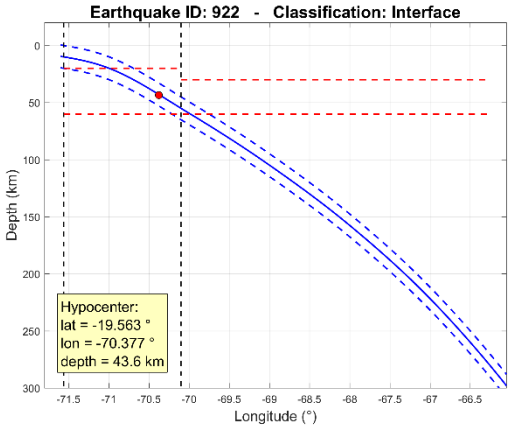

Figure B. 282: Event 922

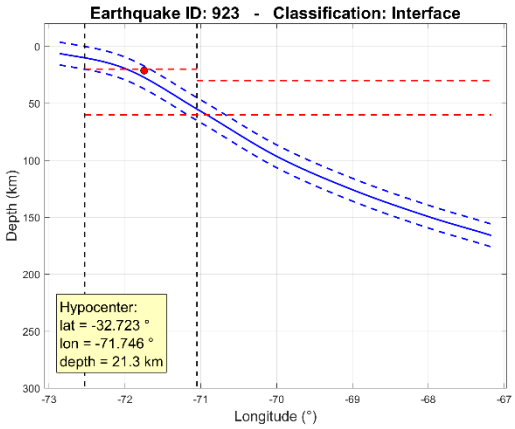

Figure B. 283: Event 923

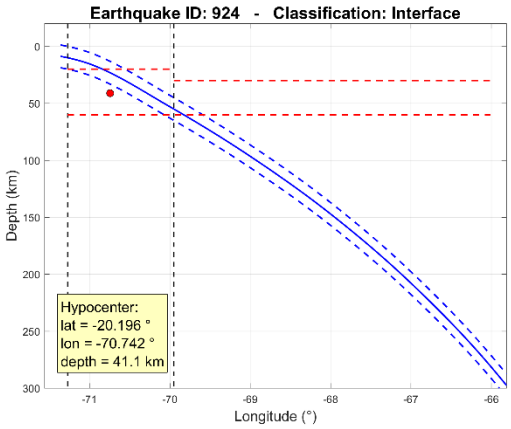

Figure B. 284: Event 924

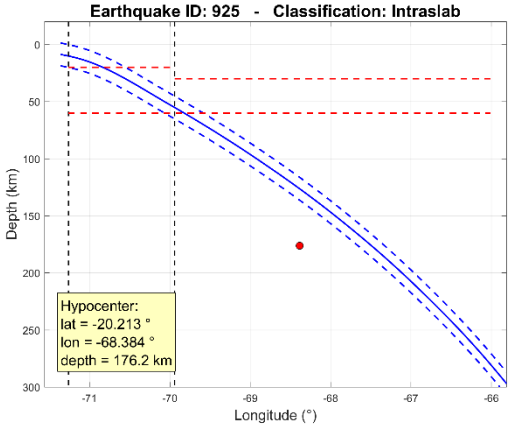

Figure B. 285: Event 925

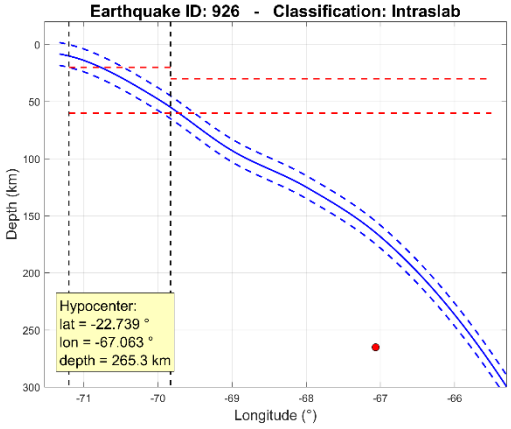

Figure B. 286: Event 926

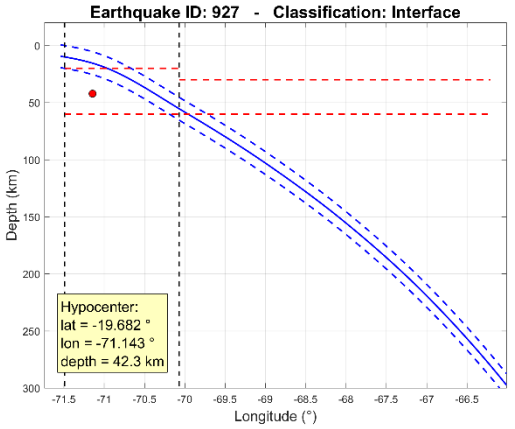

Figure B. 287: Event 927

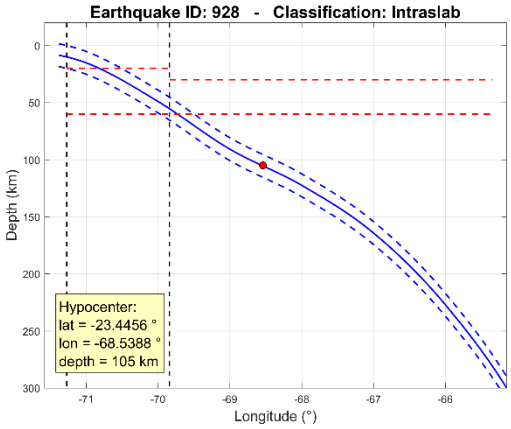

Figure B. 288: Event 928

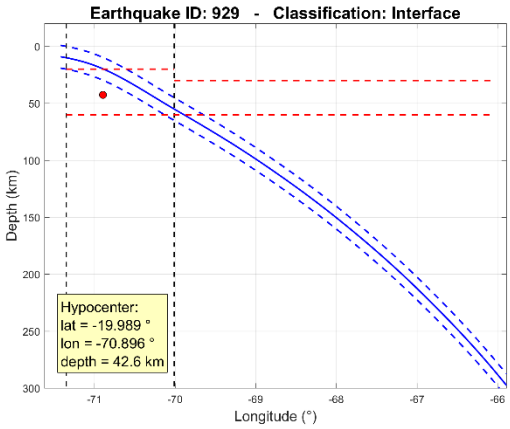

Figure B. 289: Event 929

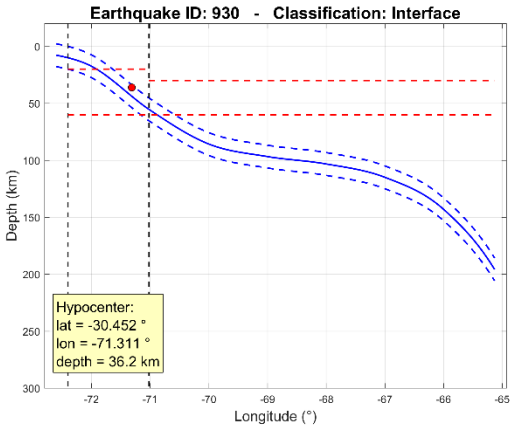

Figure B. 290: Event 930

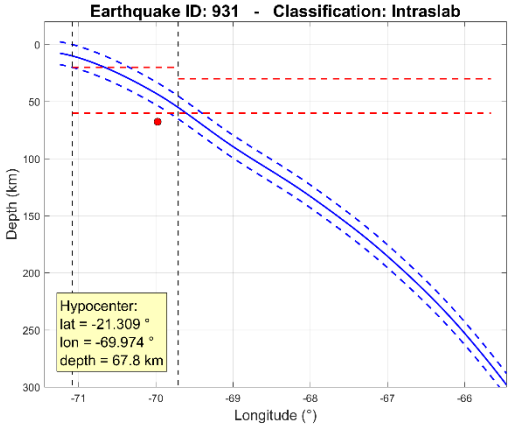

Figure B. 291: Event 931

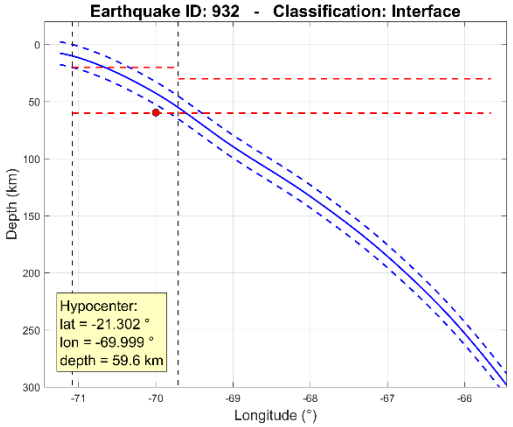

Figure B. 292: Event 932

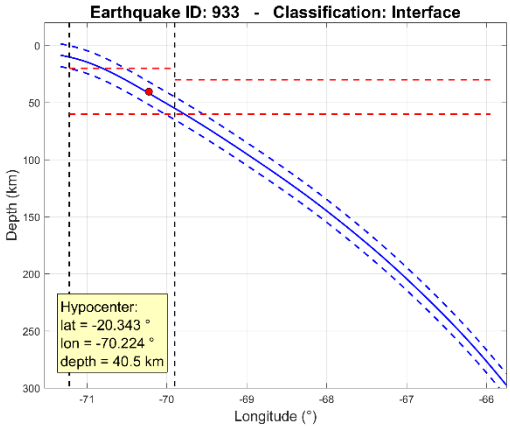

Figure B. 293: Event 933

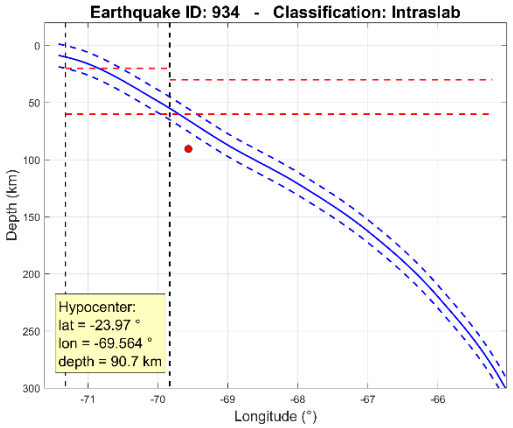

Figure B. 294: Event 934

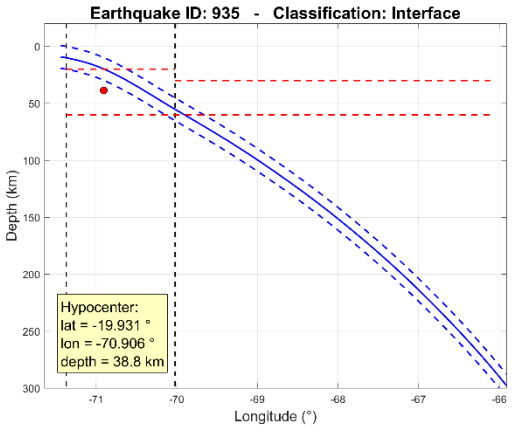

Figure B. 295: Event 935

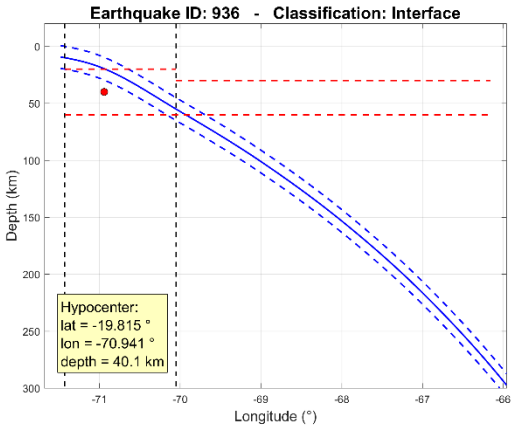

Figure B. 296: Event 936

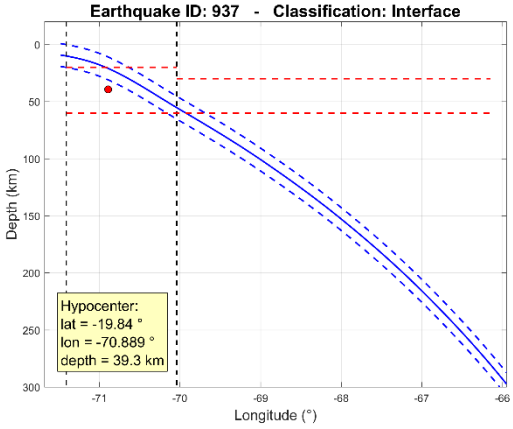

Figure B. 297: Event 937

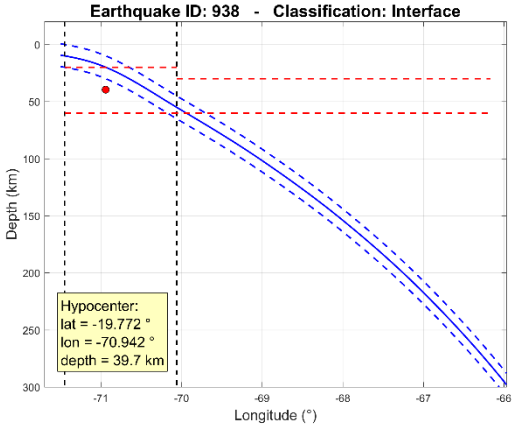

Figure B. 298: Event 938

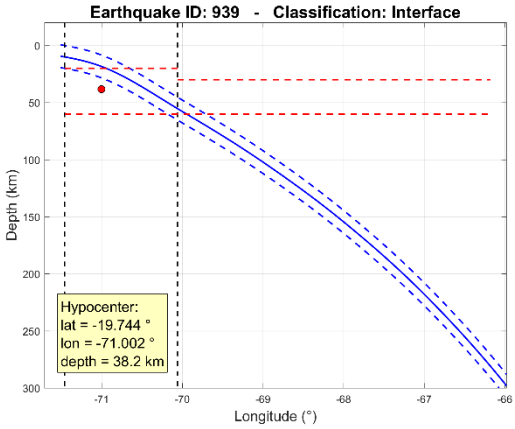

Figure B. 299: Event 939

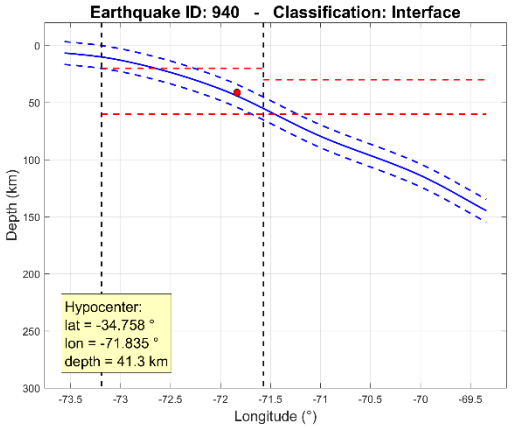

Figure B. 300: Event 940

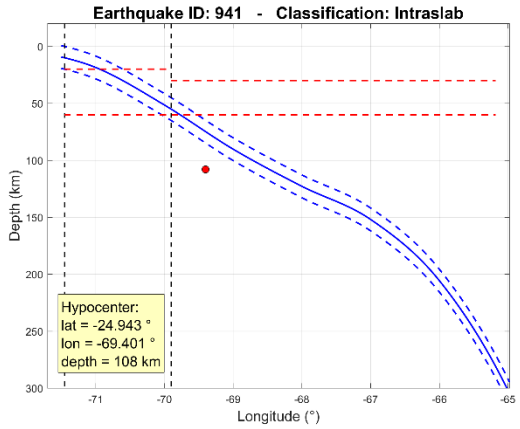

Figure B. 301: Event 941

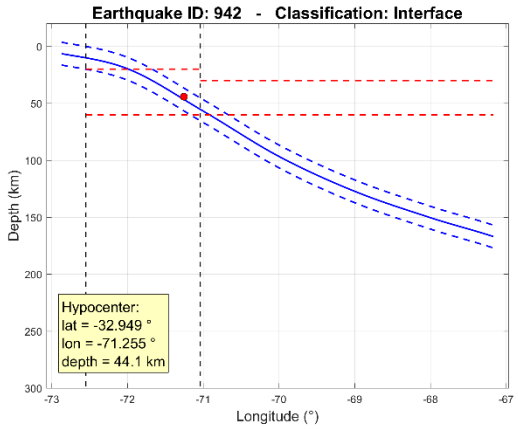

Figure B. 302: Event 942

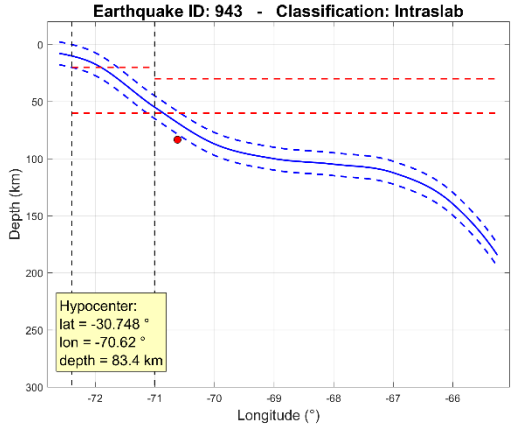

Figure B. 303: Event 943

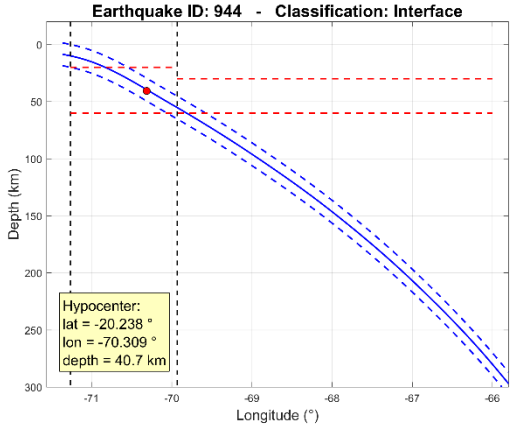

Figure B. 304: Event 944

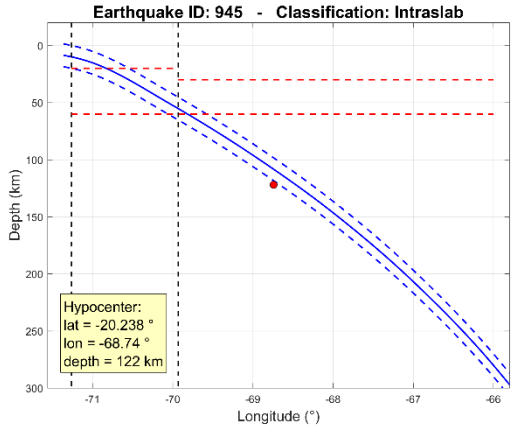

Figure B. 305: Event 945

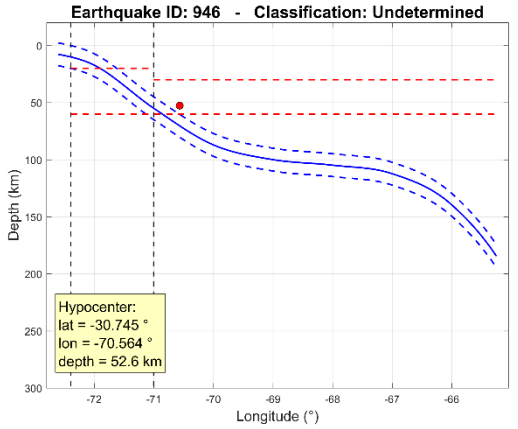

Figure B. 306: Event 946

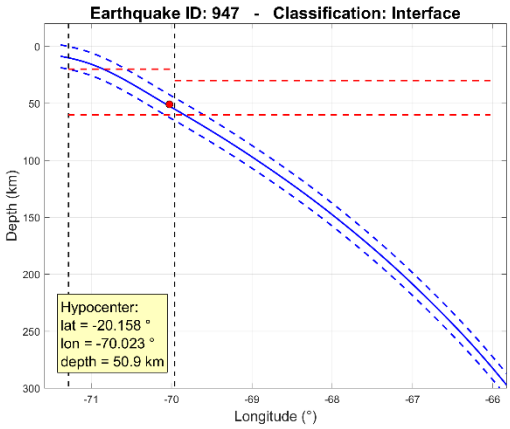

Figure B. 307: Event 947

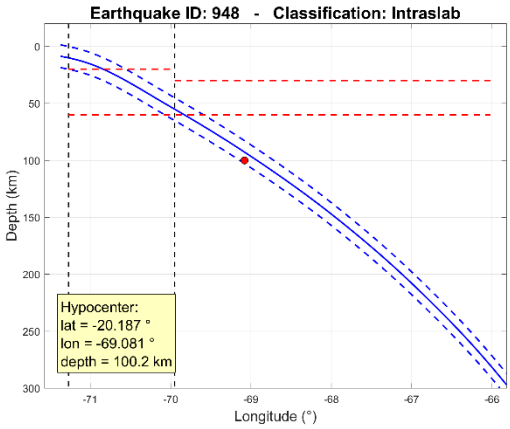

Figure B. 308: Event 948

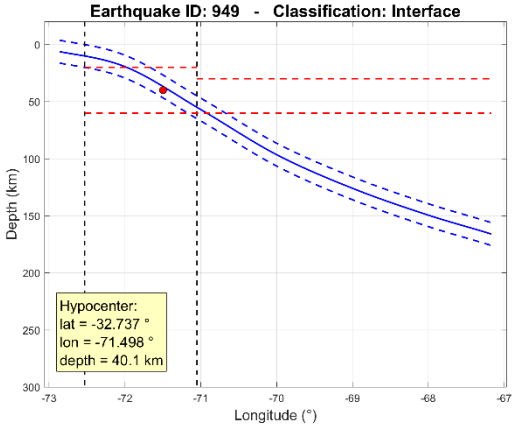

Figure B. 309: Event 949

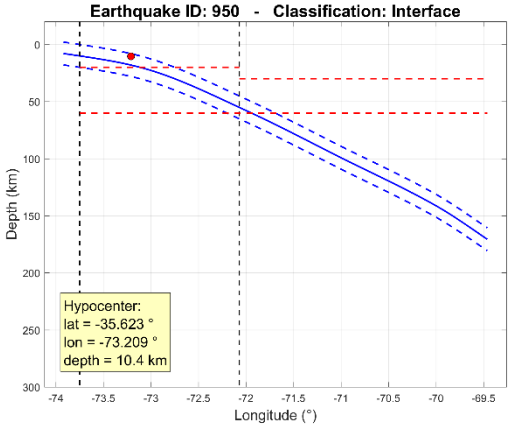

Figure B. 310: Event 950

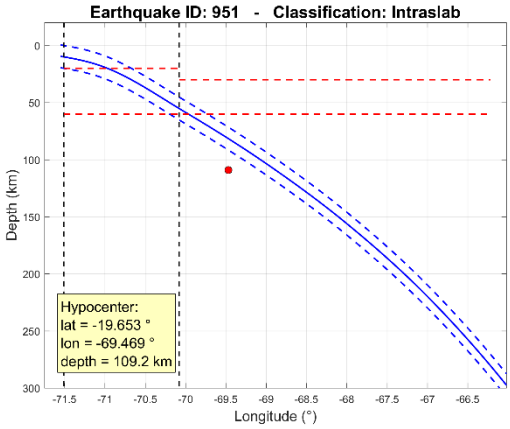

Figure B. 311: Event 951

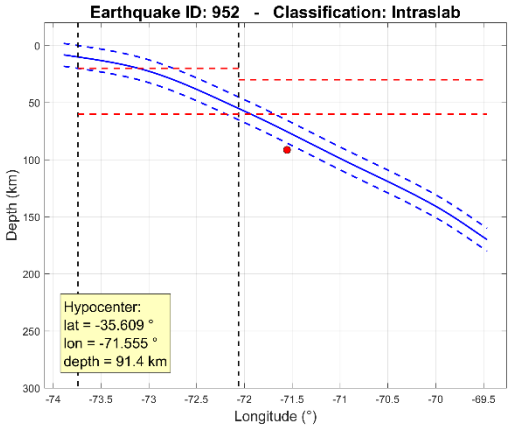

Figure B. 312: Event 952

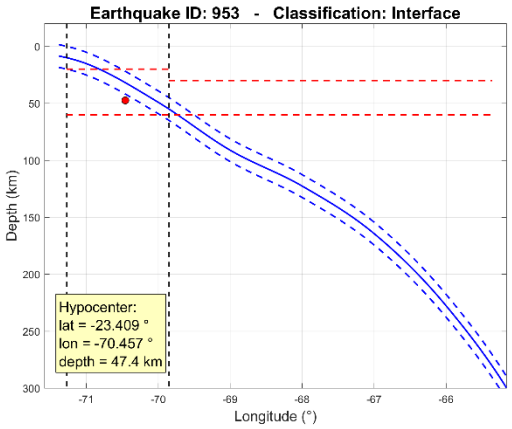

Figure B. 313: Event 953

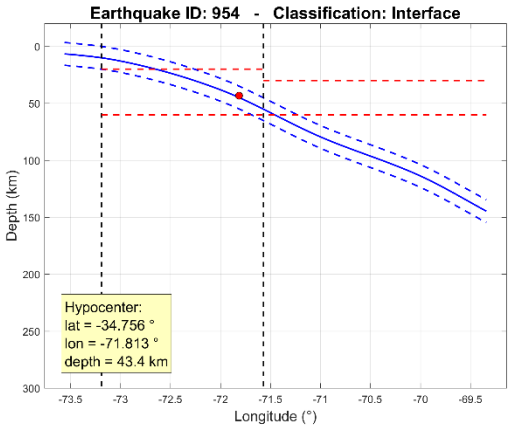

Figure B. 314: Event 954

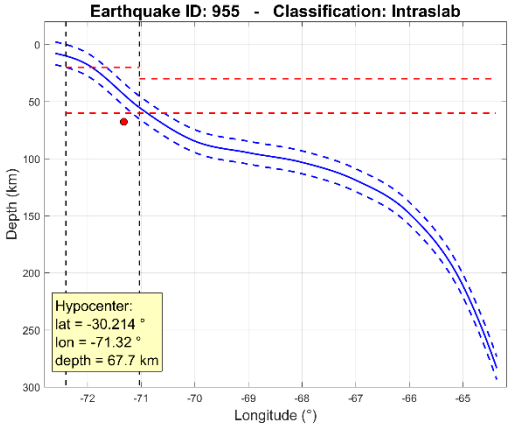

Figure B. 315: Event 955

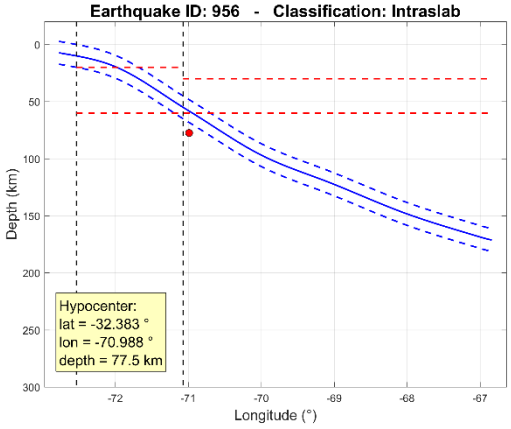

Figure B. 316: Event 956

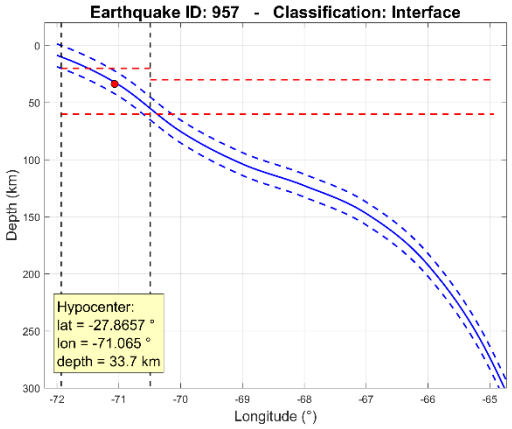

Figure B. 317: Event 957

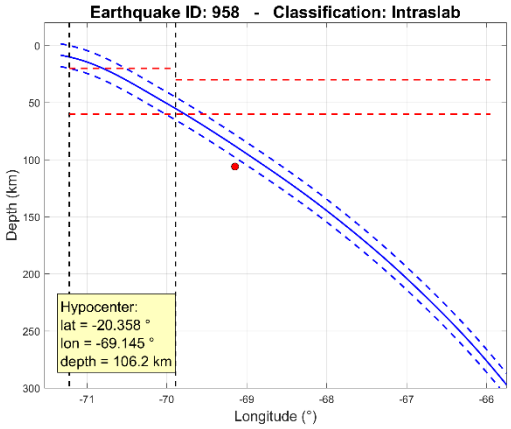

Figure B. 318: Event 958

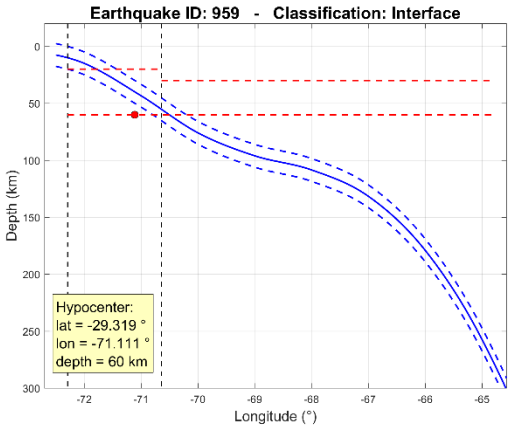

Figure B. 319: Event 959

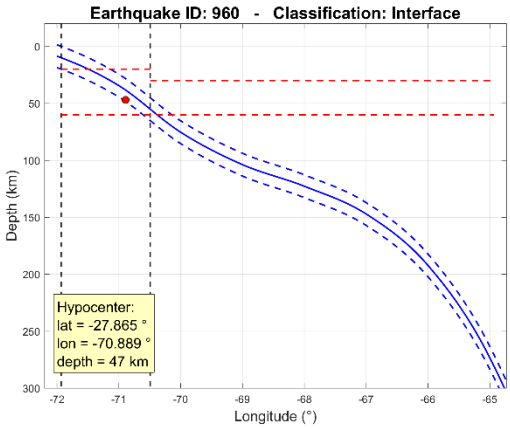

Figure B. 320: Event 960

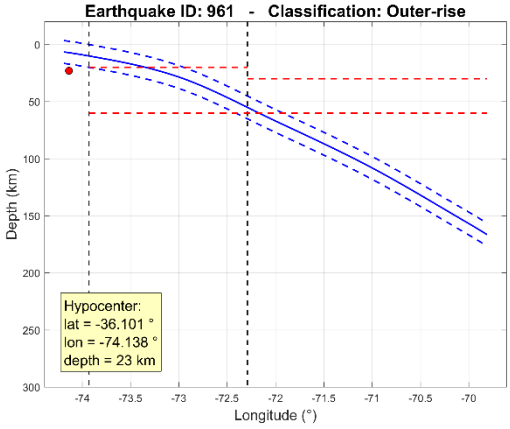

Figure B. 321: Event 961

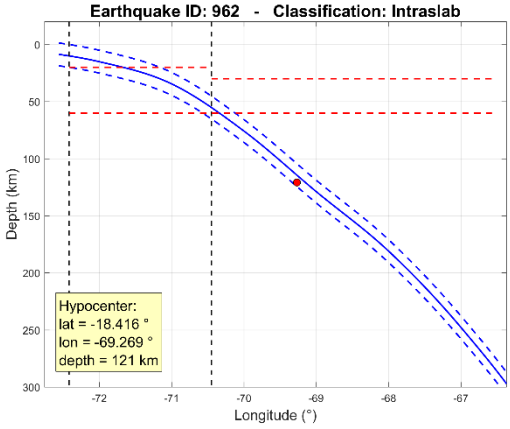

Figure B. 322: Event 962

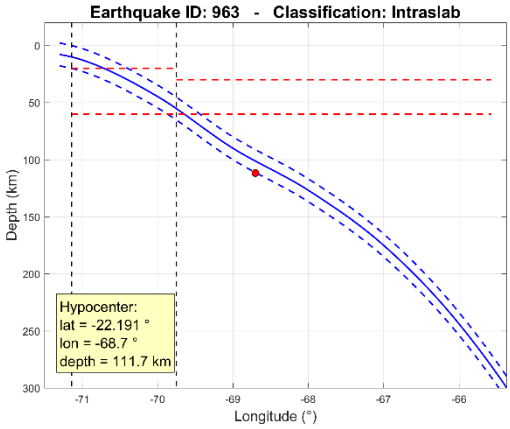

Figure B. 323: Event 963

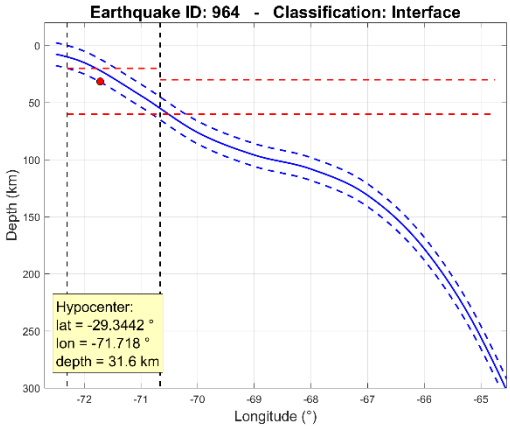

Figure B. 324: Event 964

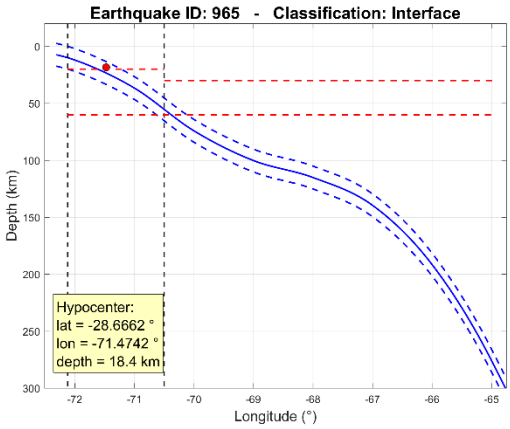

Figure B. 325: Event 965

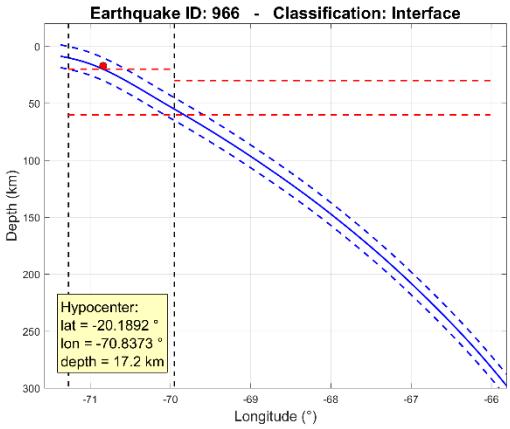

Figure B. 326: Event 966

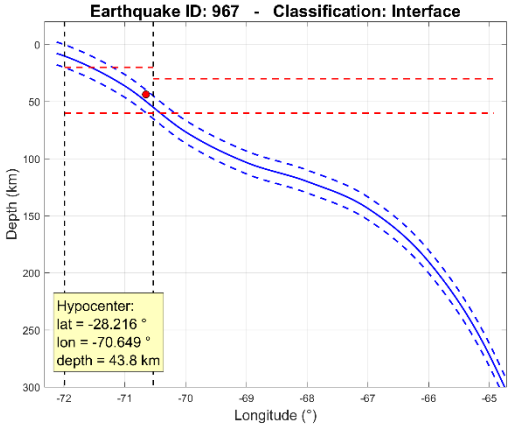

Figure B. 327: Event 967

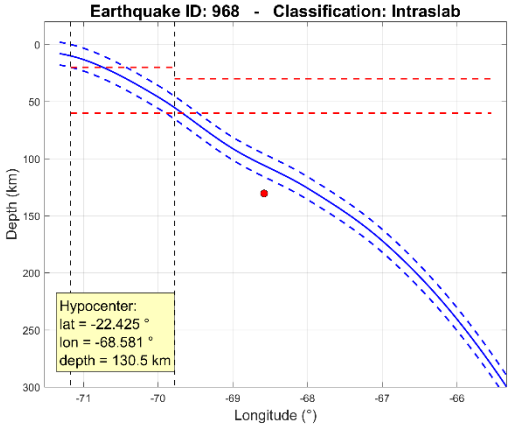

Figure B. 328: Event 968

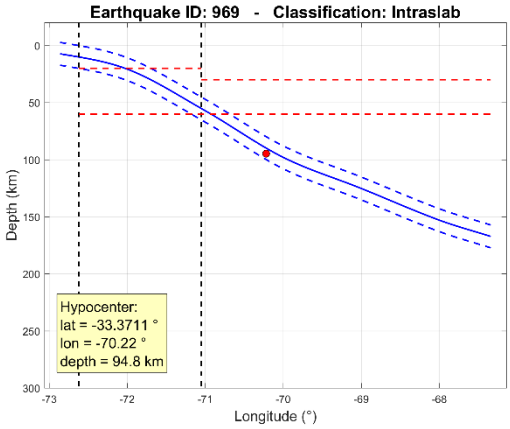

Figure B. 329: Event 969

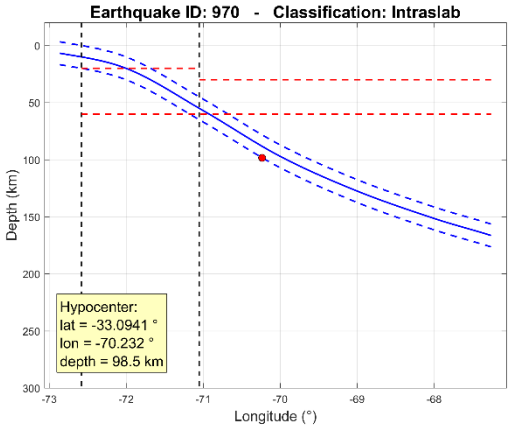

Figure B. 330: Event 970

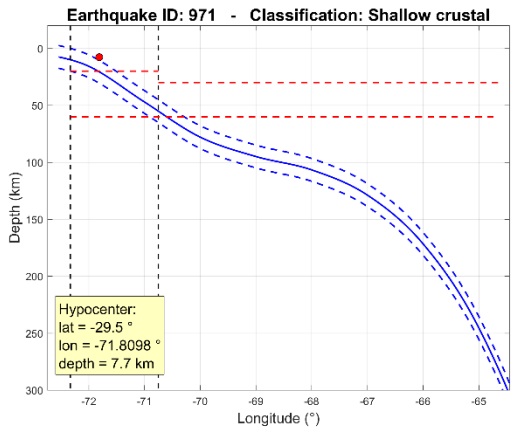

Figure B. 331: Event 971

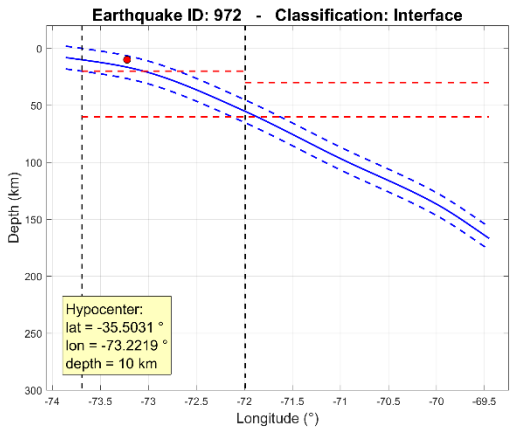

Figure B. 332: Event 972

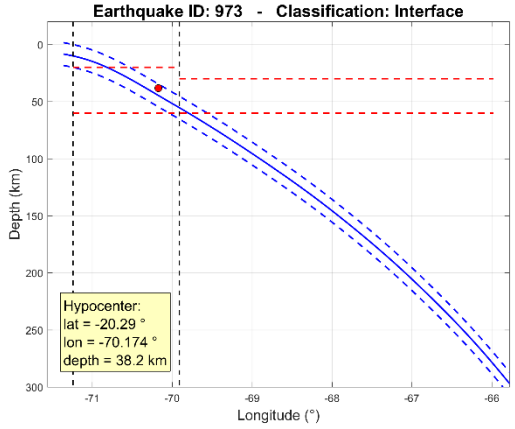

Figure B. 333: Event 973

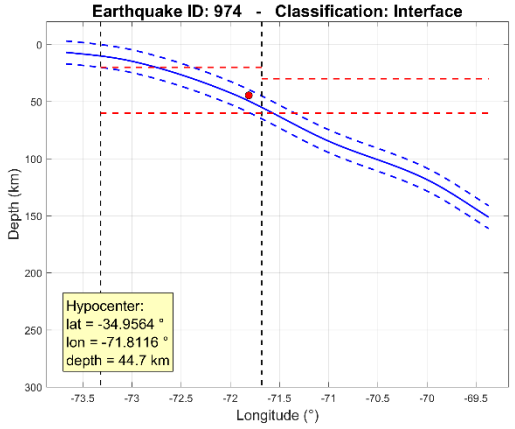

Figure B. 334: Event 974

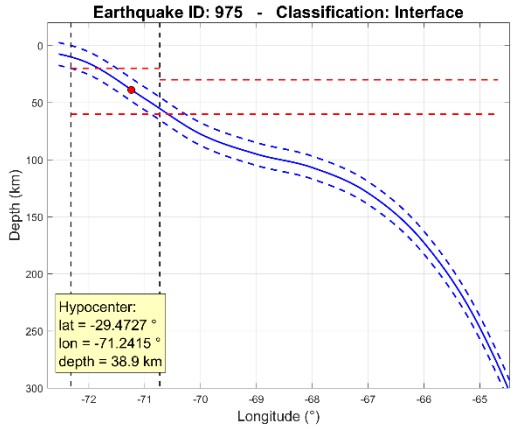

Figure B. 335: Event 975

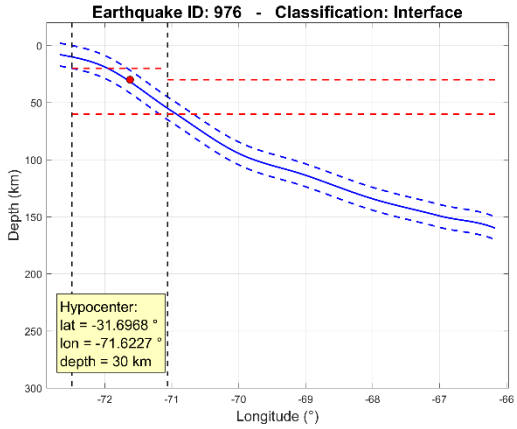

Figure B. 336: Event 976

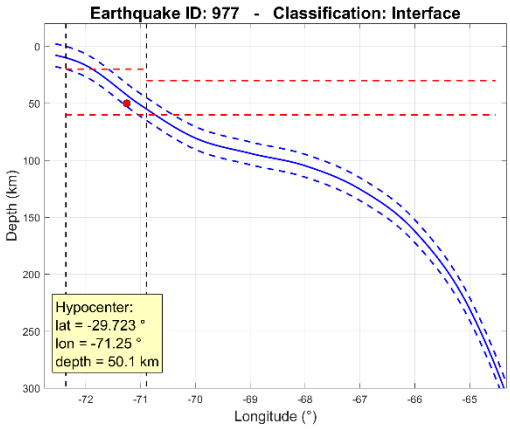

Figure B. 337: Event 977

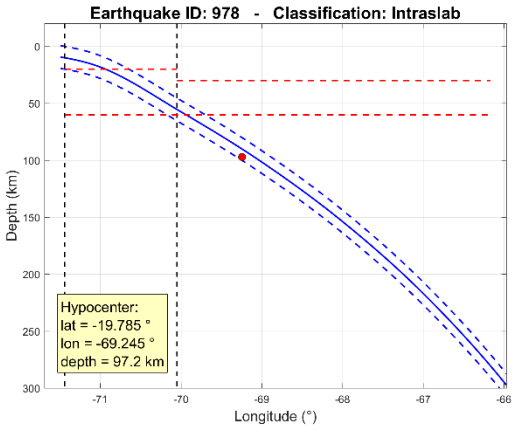

Figure B. 338: Event 978

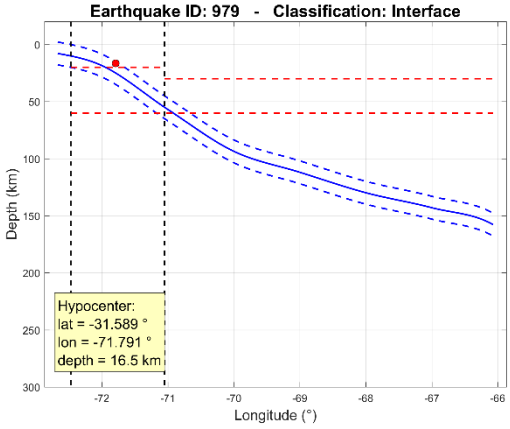

Figure B. 339: Event 979

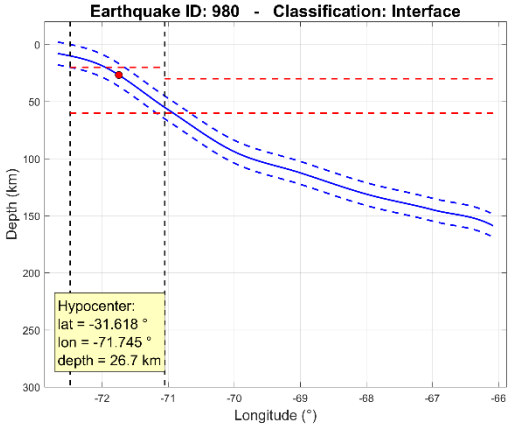

Figure B. 340: Event 980

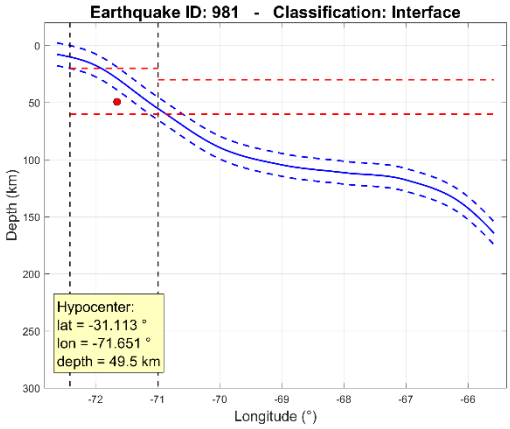

Figure B. 341: Event 981

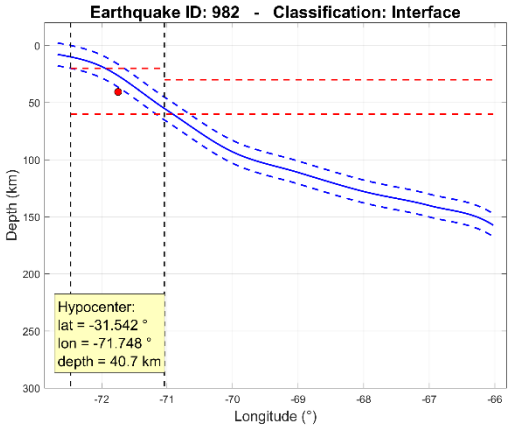

Figure B. 342: Event 982

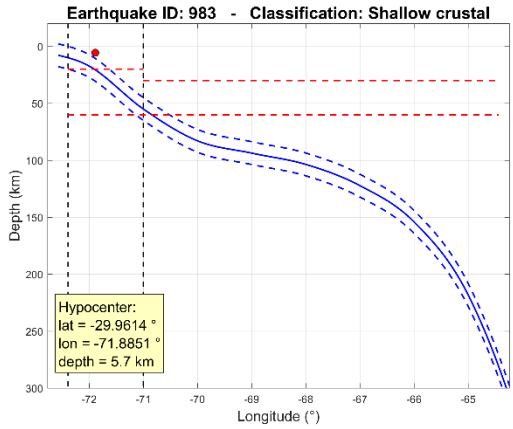

Figure B. 343: Event 983

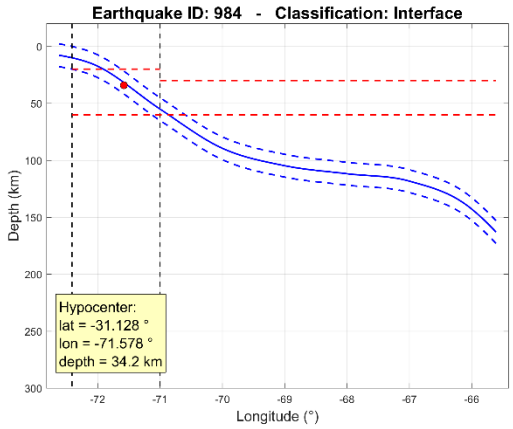

Figure B. 344: Event 984

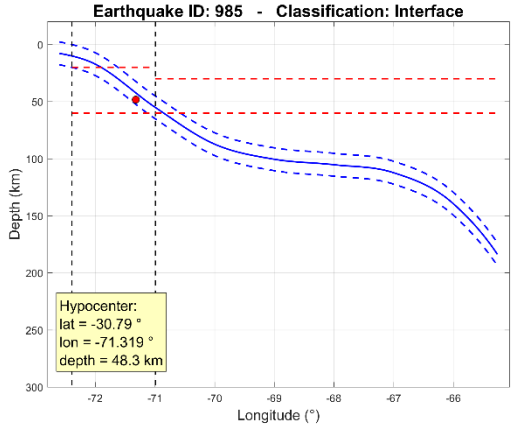

Figure B. 345: Event 985

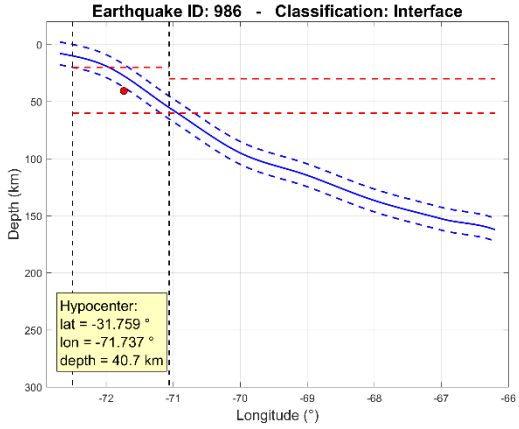

Figure B. 346: Event 986

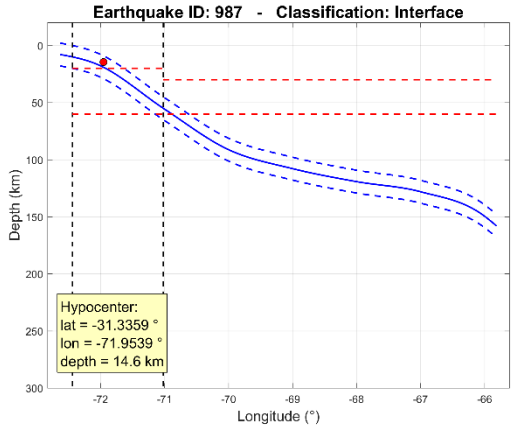

Figure B. 347: Event 987

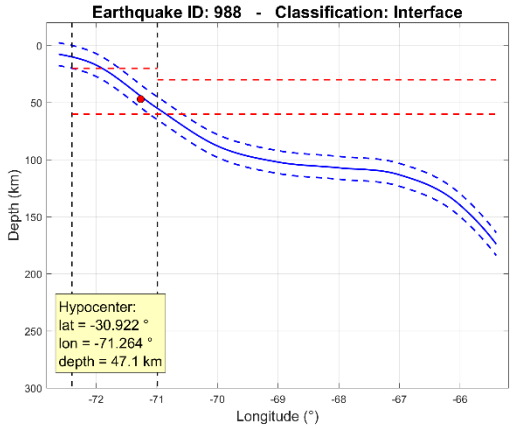

Figure B. 348: Event 988

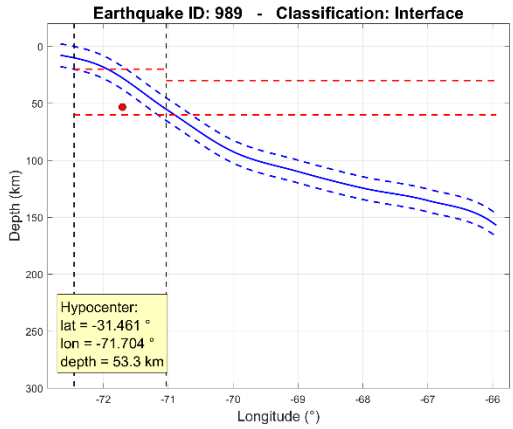

Figure B. 349: Event 989

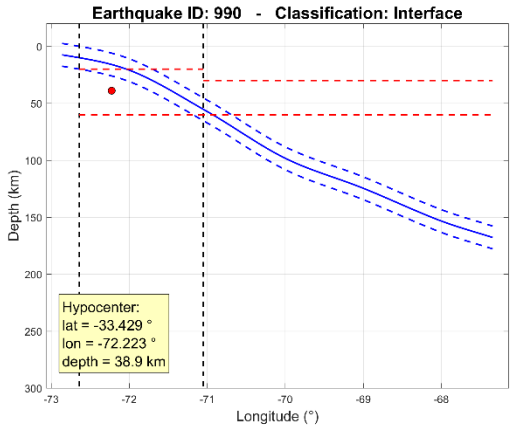

Figure B. 350: Event 990

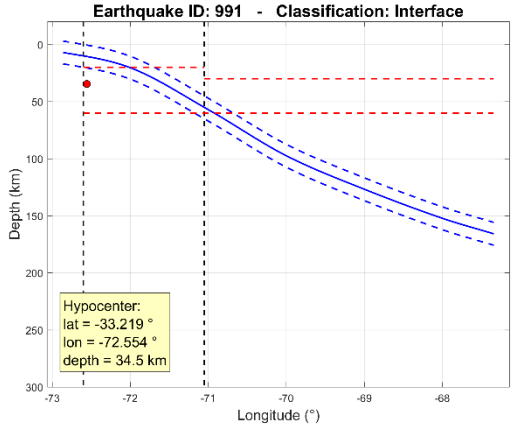

Figure B. 351: Event 991

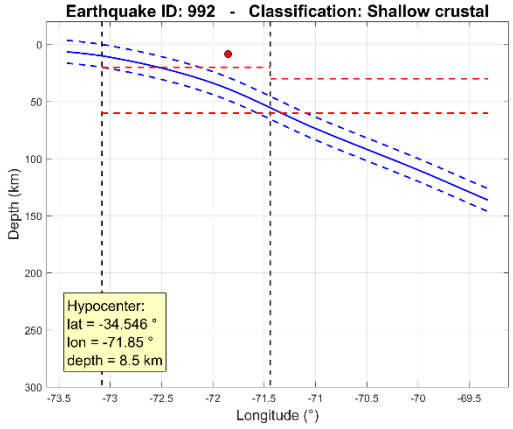

Figure B. 352: Event 992

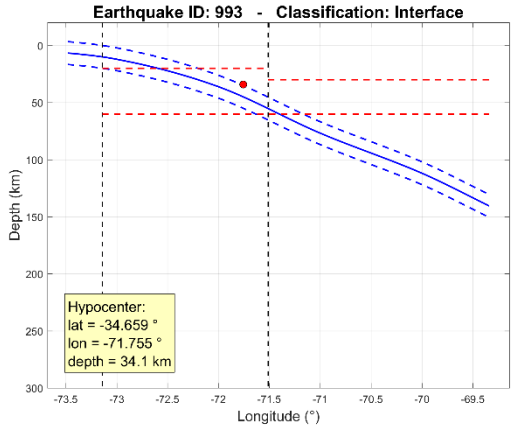

Figure B. 353: Event 993

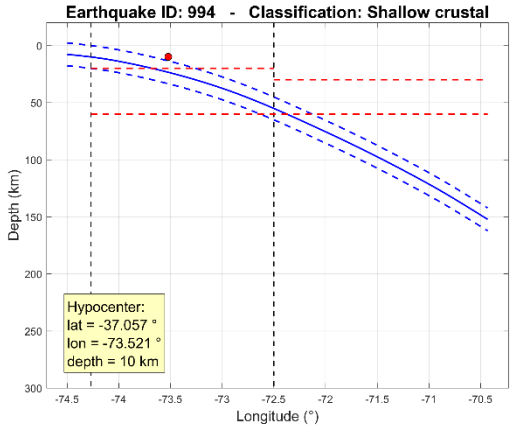

Figure B. 354: Event 994

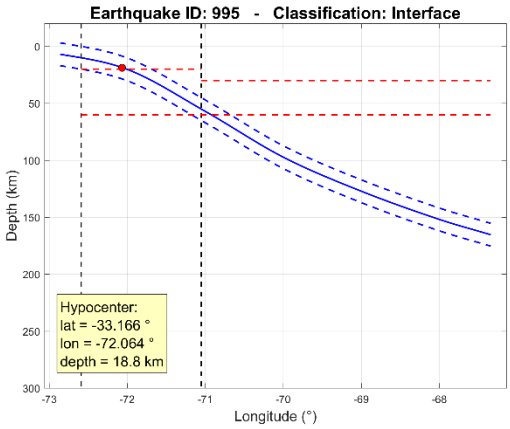

Figure B. 355: Event 995

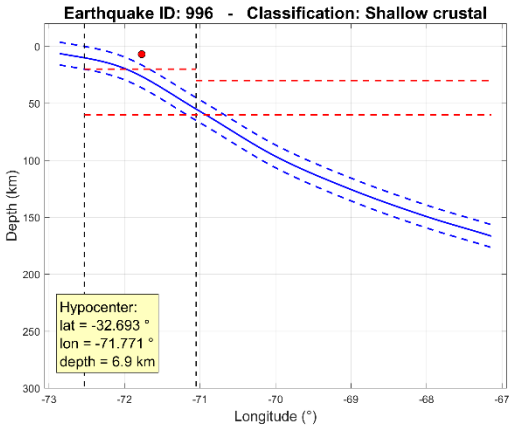

Figure B. 356: Event 996

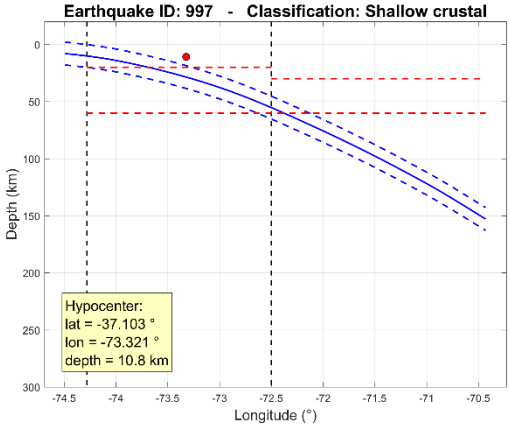

Figure B. 357: Event 997

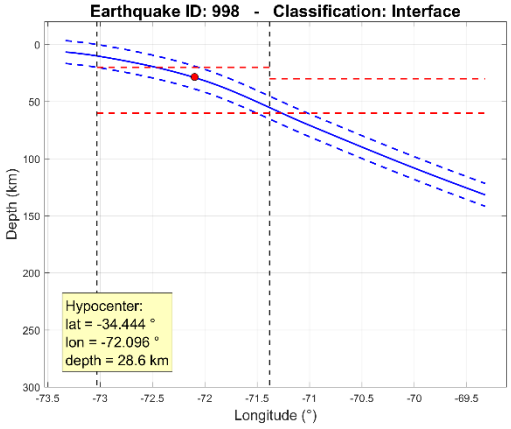

Figure B. 358: Event 998

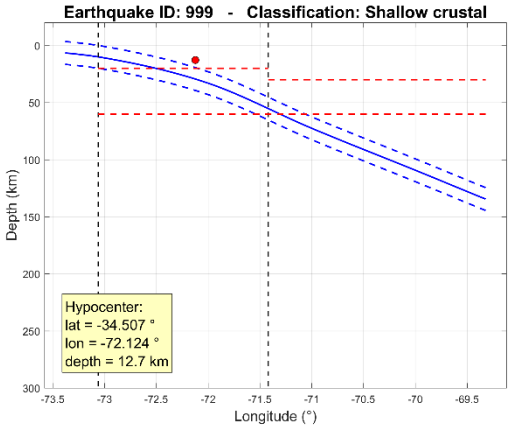

Figure B. 359: Event 999

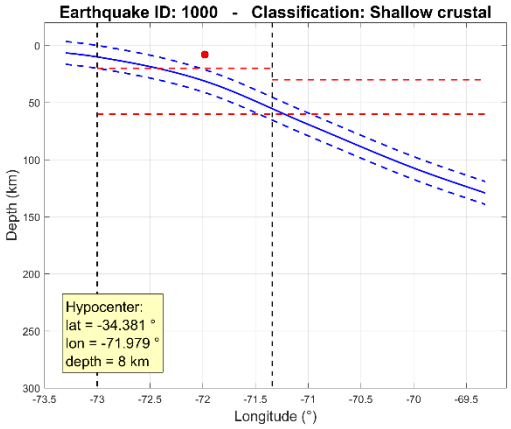

Figure B. 360: Event 1000

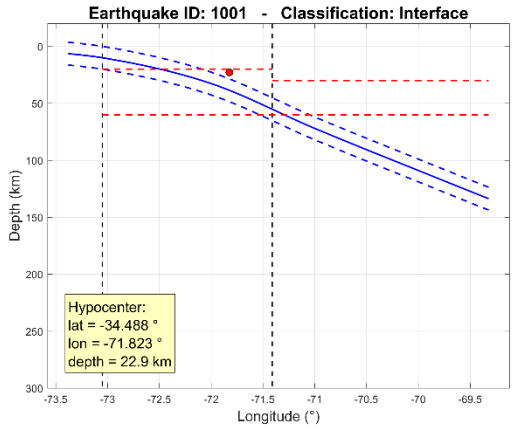

Figure B. 361: Event 1001

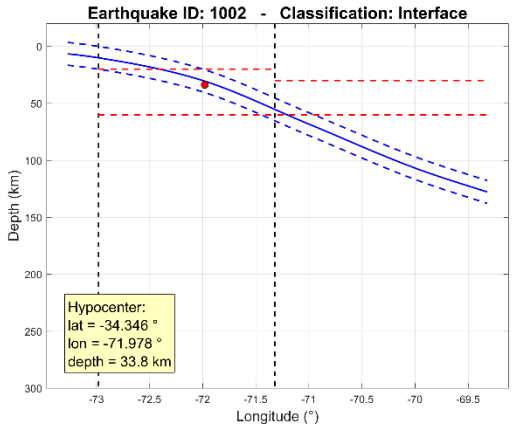

Figure B. 362: Event 1002

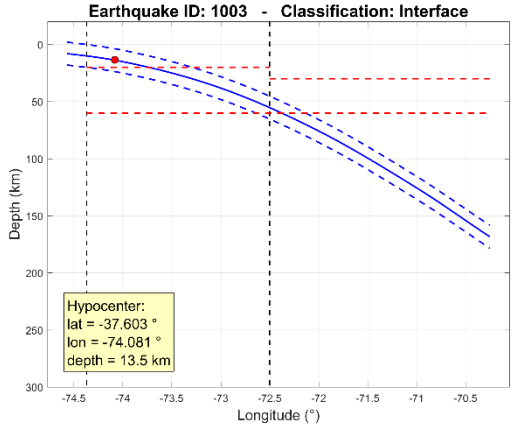

Figure B. 363: Event 1003

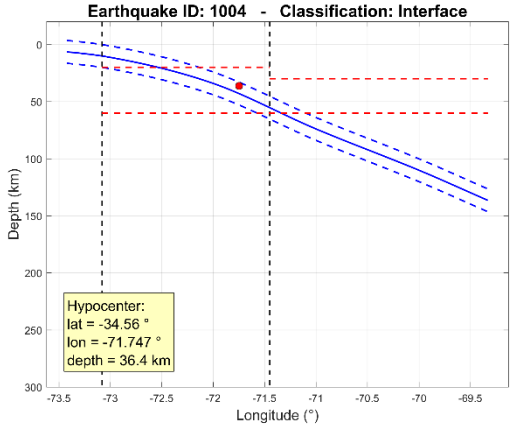

Figure B. 364: Event 1004

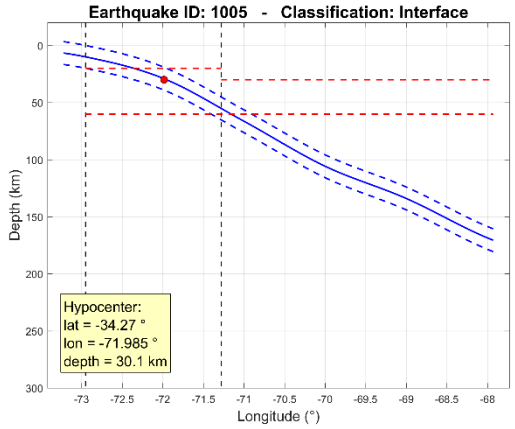

Figure B. 365: Event 1005

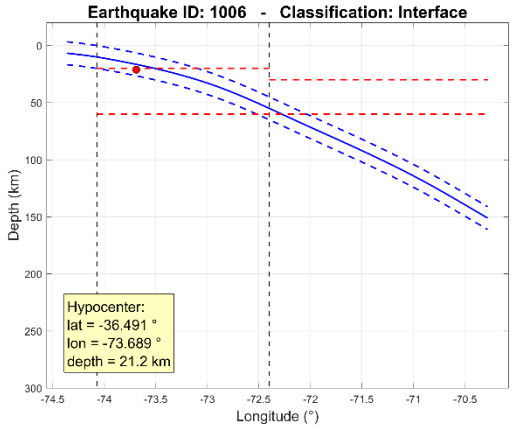

Figure B. 366: Event 1006

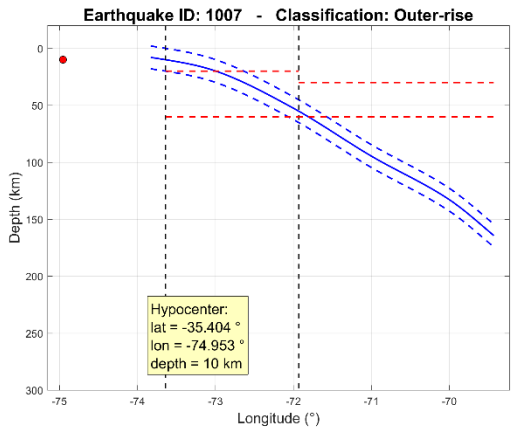

Figure B. 367: Event 1007

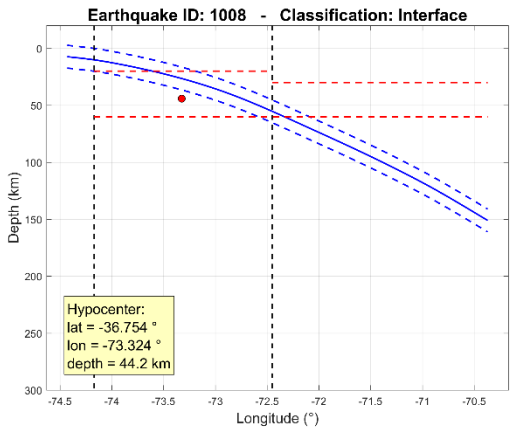

Figure B. 368: Event 1008

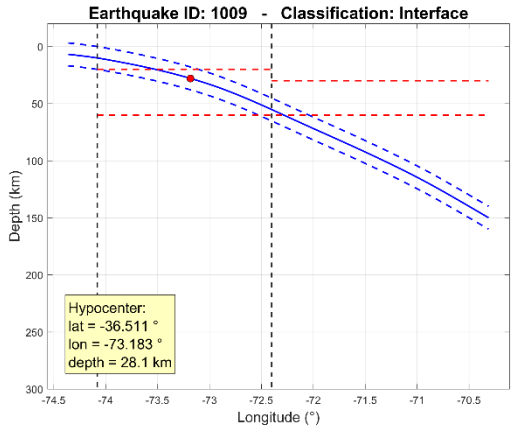

Figure B. 369: Event 1009

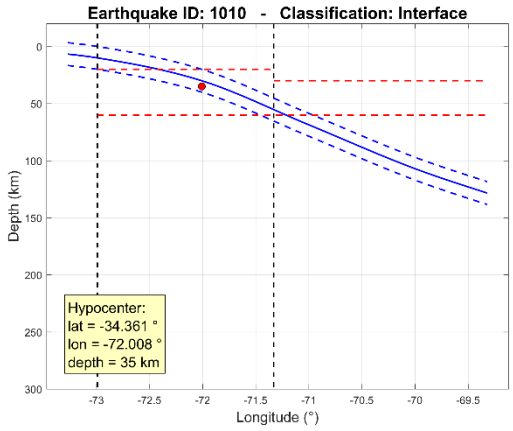

Figure B. 370: Event 1010

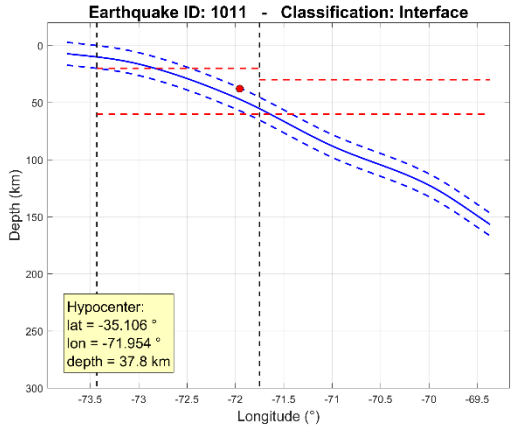

Figure B. 371: Event 1011

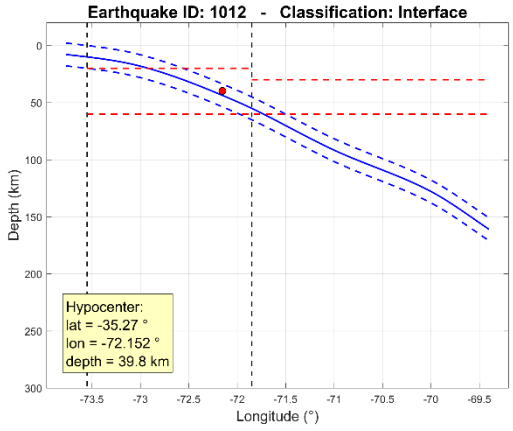

Figure B. 372: Event 1012

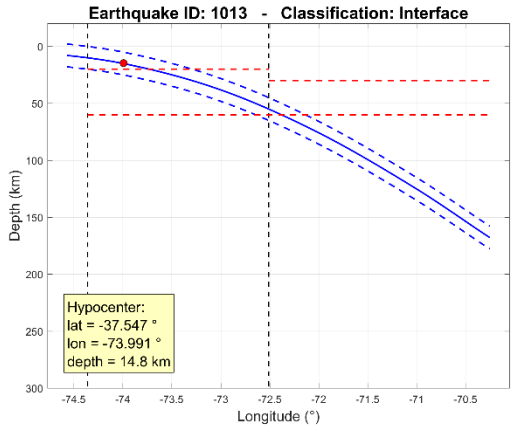

Figure B. 373: Event 1013

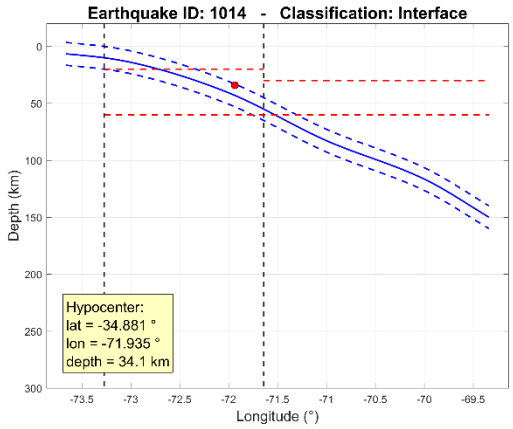

Figure B. 374: Event 1014

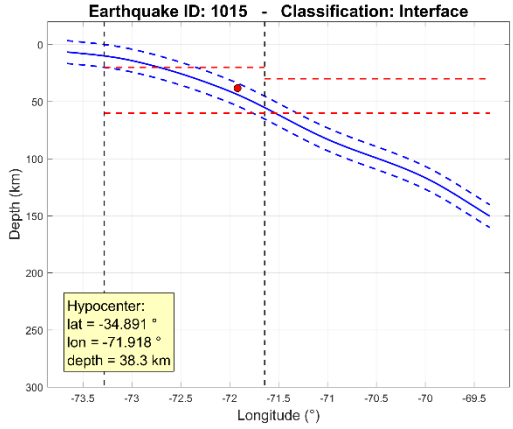

Figure B. 375: Event 1015

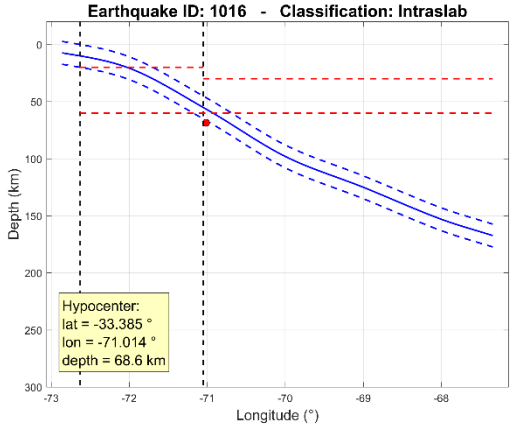

Figure B. 376: Event 1016

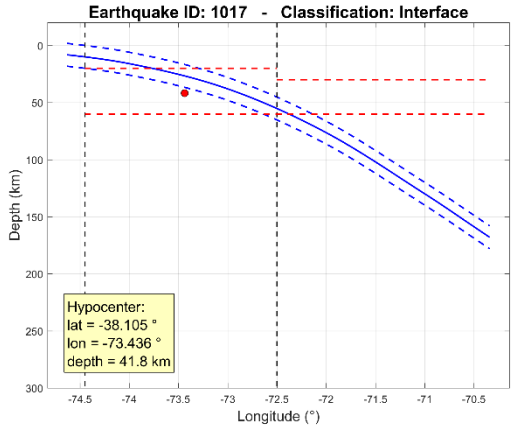

Figure B. 377: Event 1017

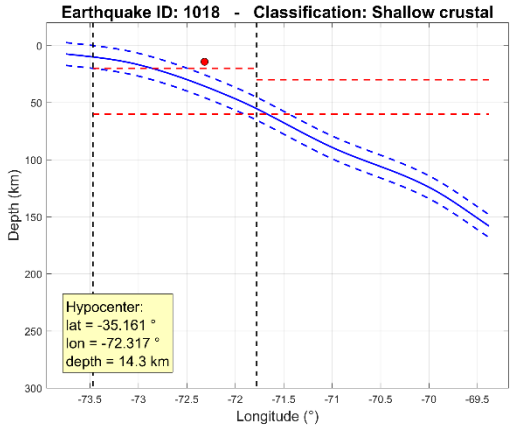

Figure B. 378: Event 1018

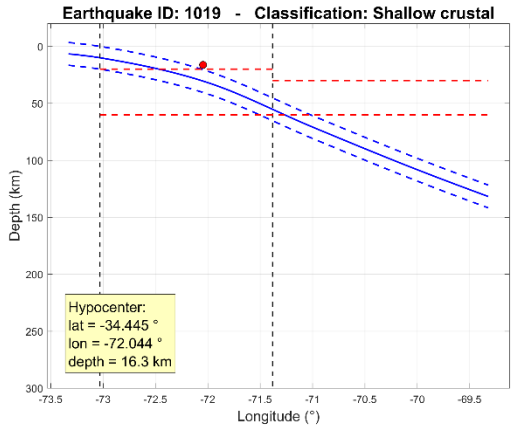

Figure B. 379: Event 1019

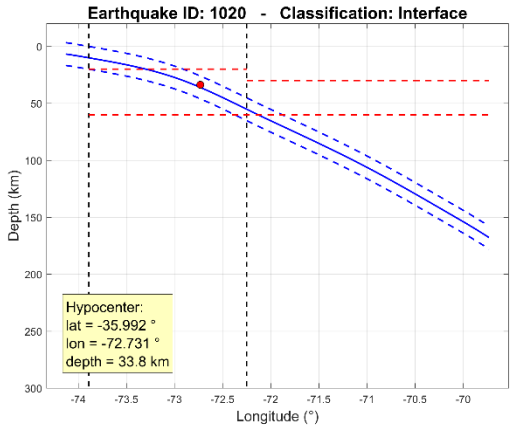

Figure B. 380: Event 1020

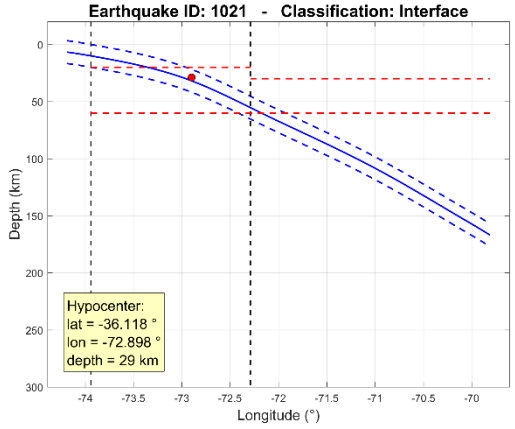

Figure B. 381: Event 1021

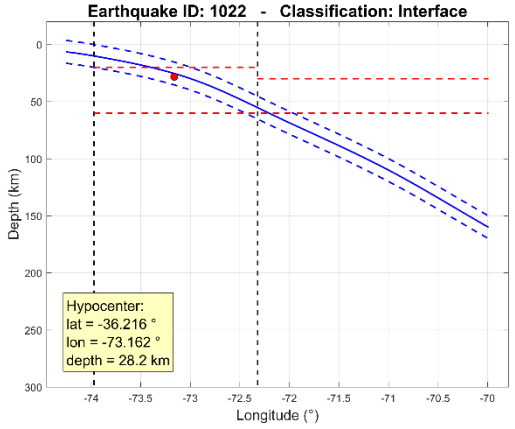

Figure B. 382: Event 1022

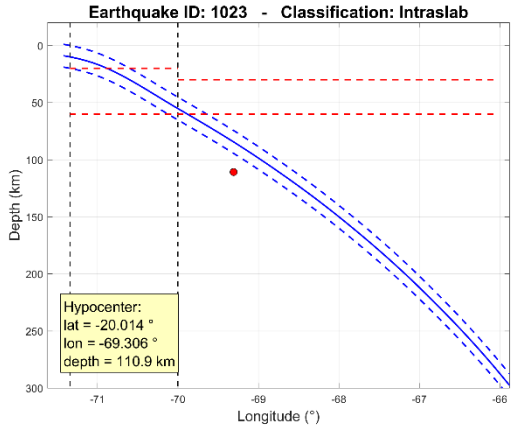

Figure B. 383: Event 1023

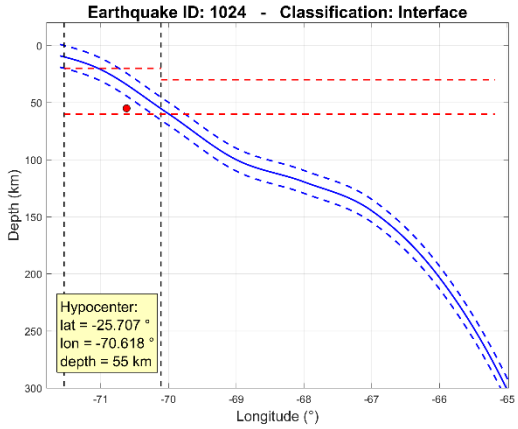

Figure B. 384: Event 1024

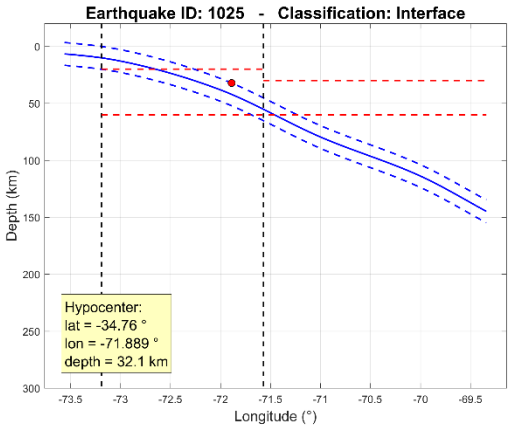

Figure B. 385: Event 1025

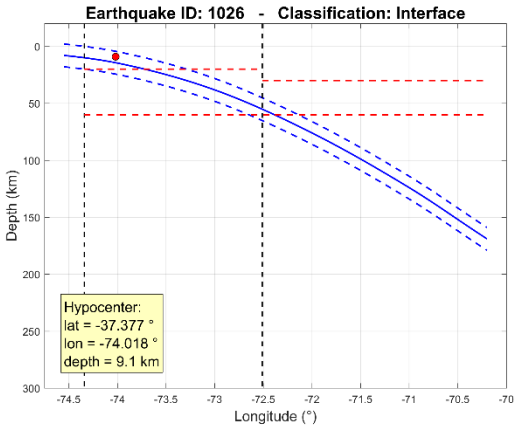

Figure B. 386: Event 1026

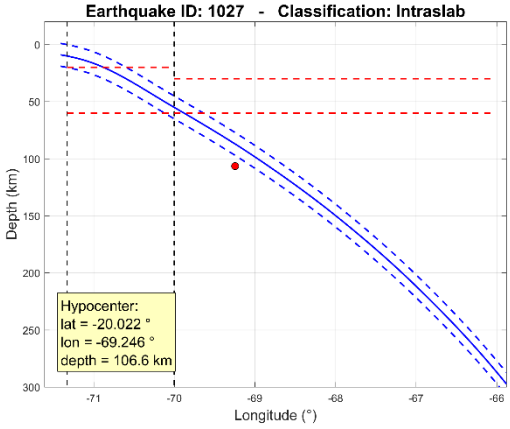

Figure B. 387: Event 1027

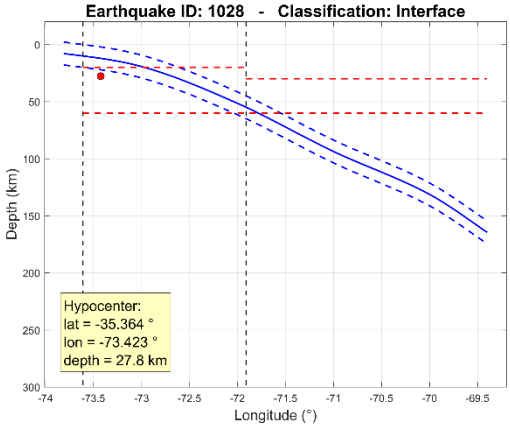

Figure B. 388: Event 1028

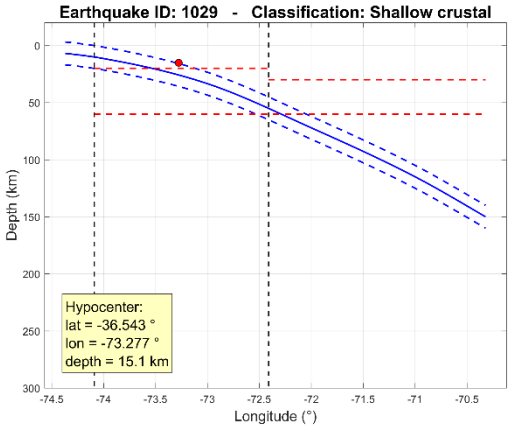

Figure B. 389: Event 1029

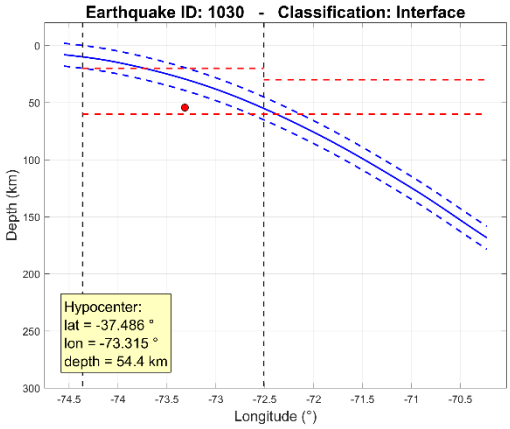

Figure B. 390: Event 1030

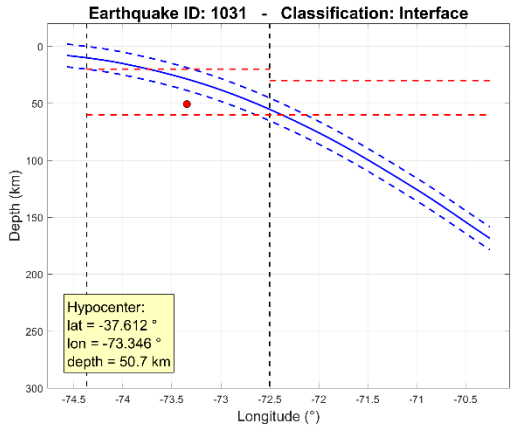

Figure B. 391: Event 1031

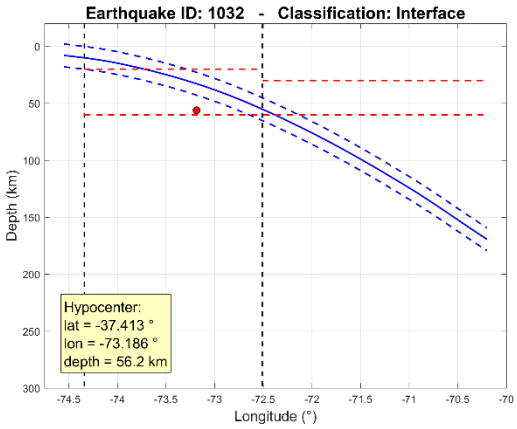

Figure B. 392: Event 1032

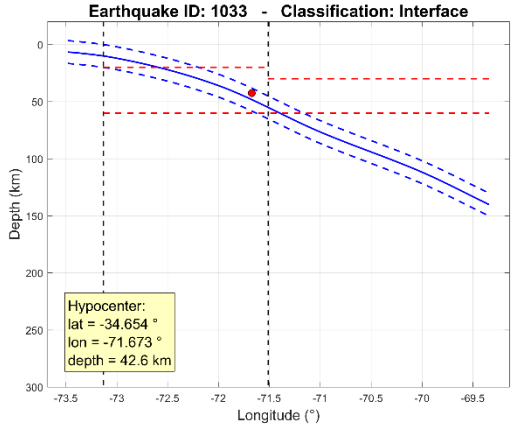

Figure B. 393: Event 1033

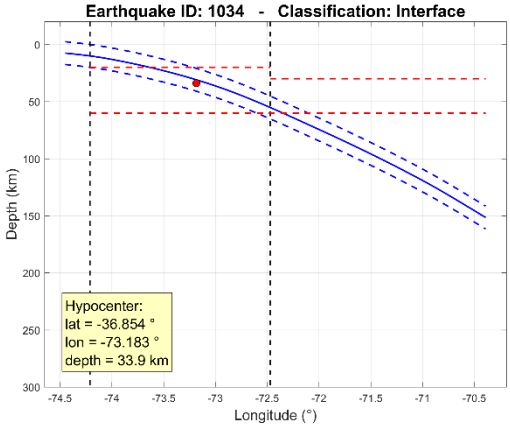

Figure B. 394: Event 1034

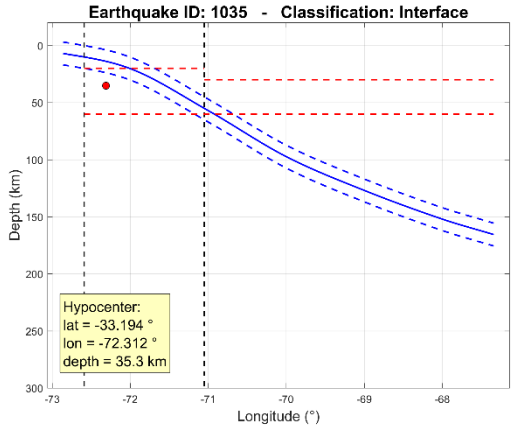

Figure B. 395: Event 1035

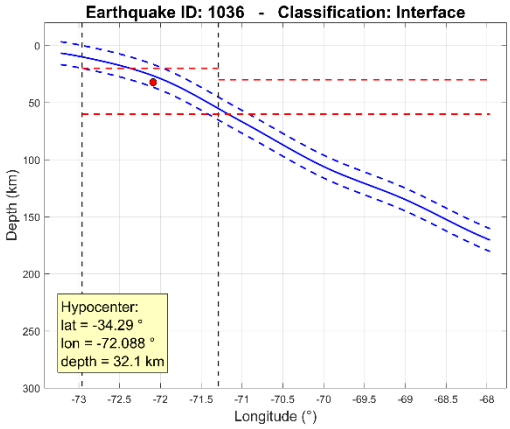

Figure B. 396: Event 1036

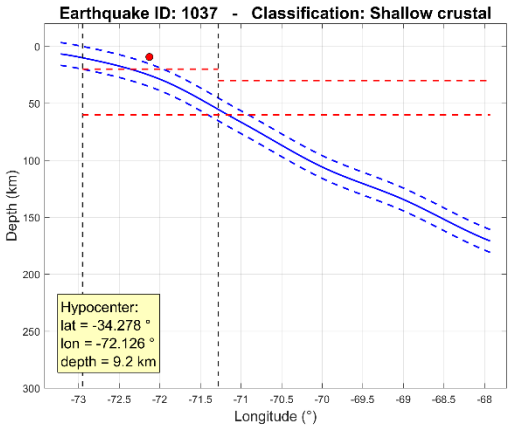

Figure B. 397: Event 1037

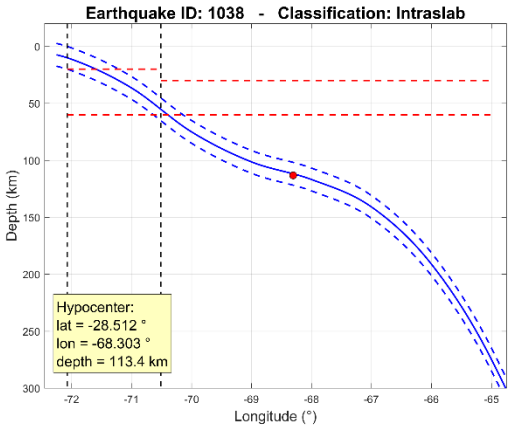

Figure B. 398: Event 1038

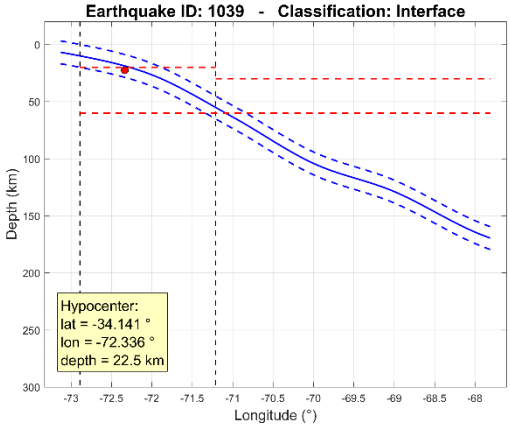

Figure B. 399: Event 1039

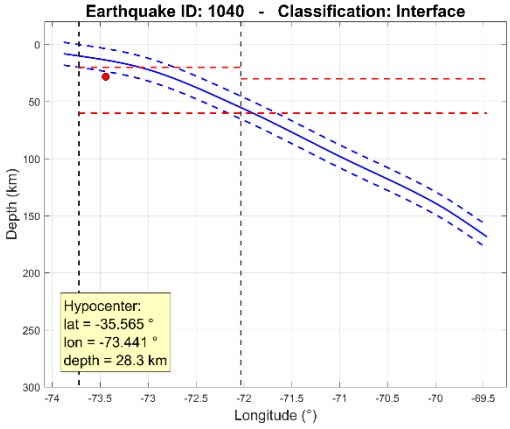

Figure B. 400: Event 1040

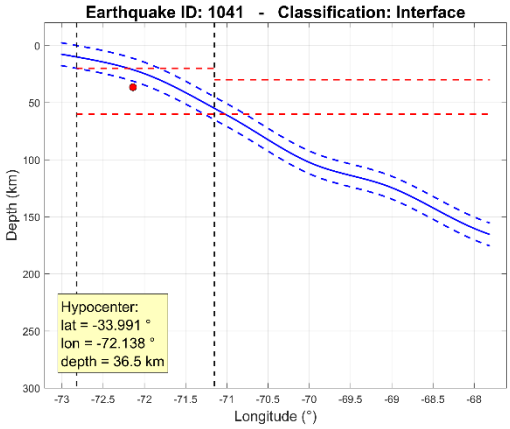

Figure B. 401: Event 1041

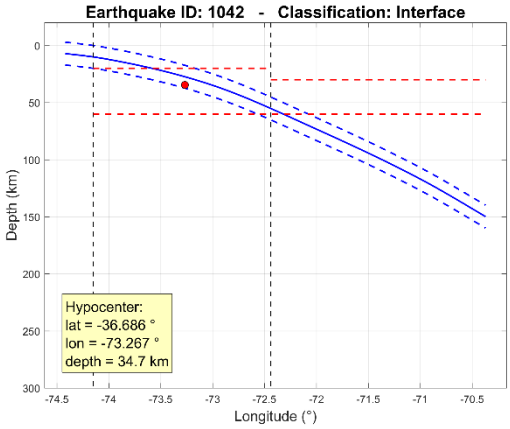

Figure B. 402: Event 1042

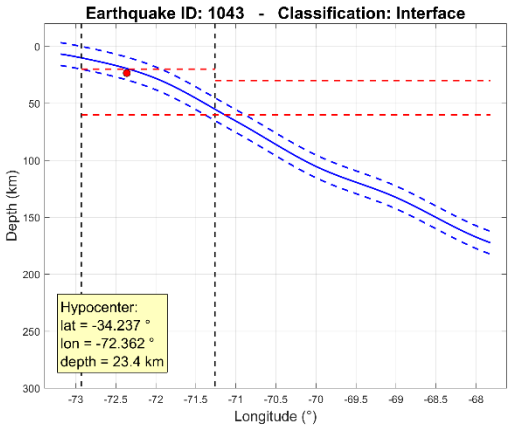

Figure B. 403: Event 1043

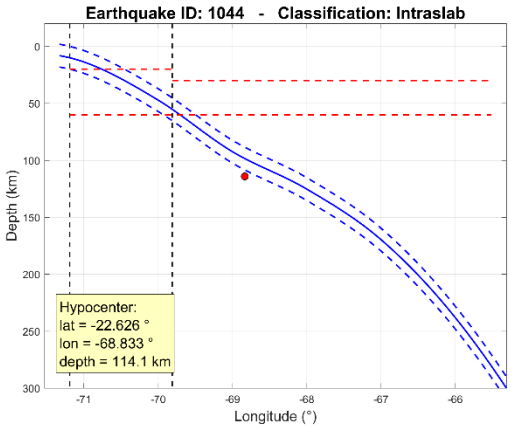

Figure B. 404: Event 1044

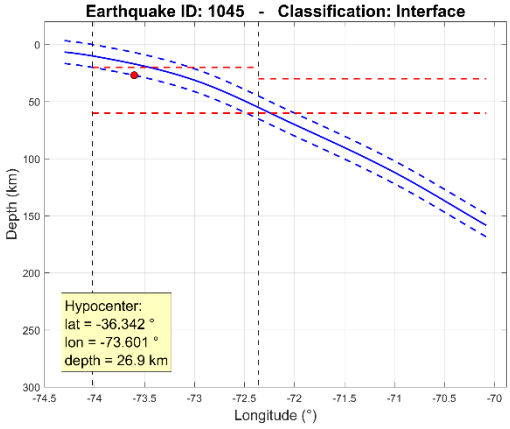

Figure B. 405: Event 1045

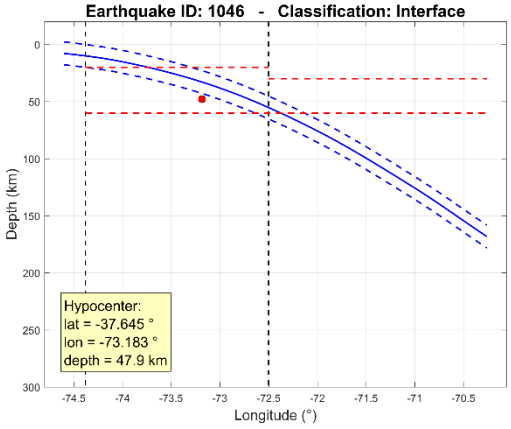

Figure B. 406: Event 1046

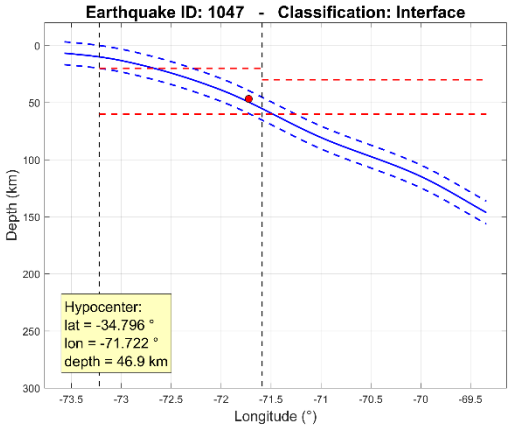

Figure B. 407: Event 1047

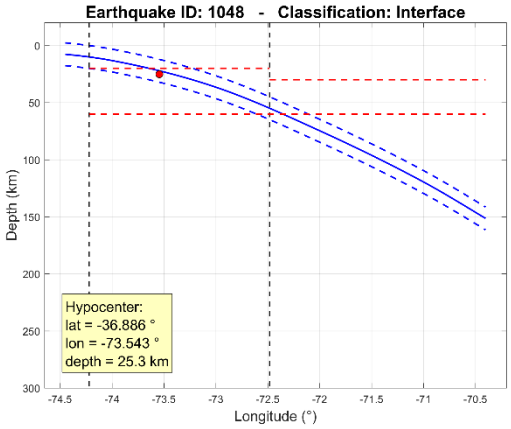

Figure B. 408: Event 1048

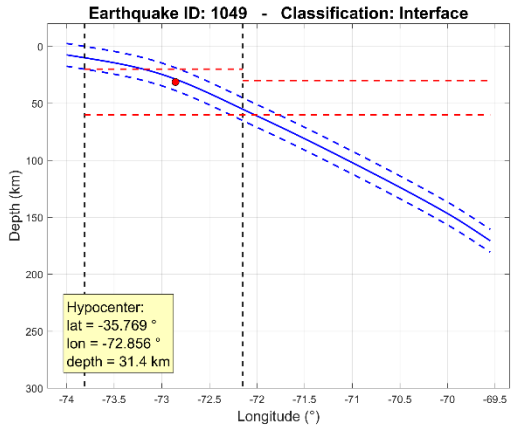

Figure B. 409: Event 1049

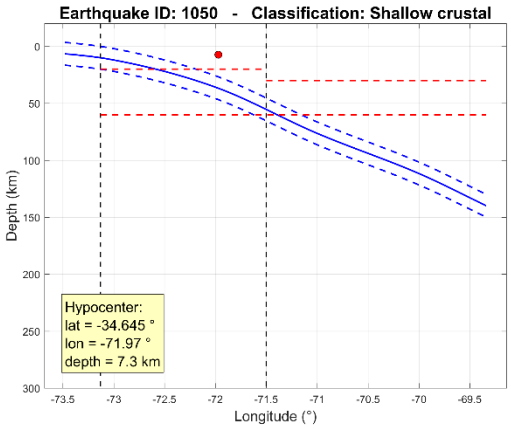

Figure B. 410: Event 1050

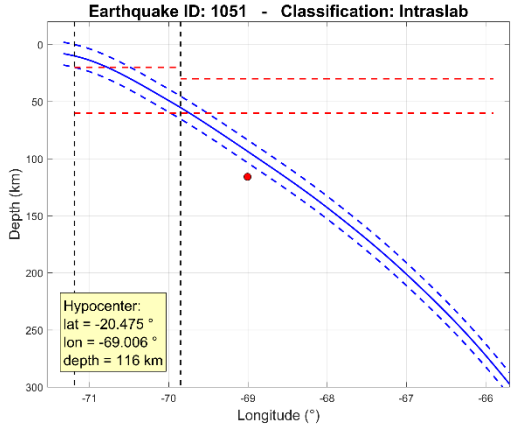

Figure B. 411: Event 1051

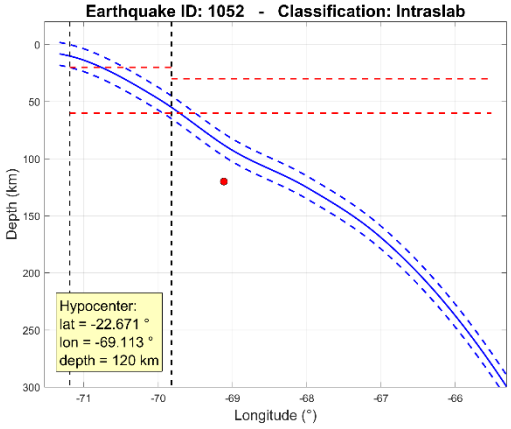

Figure B. 412: Event 1052

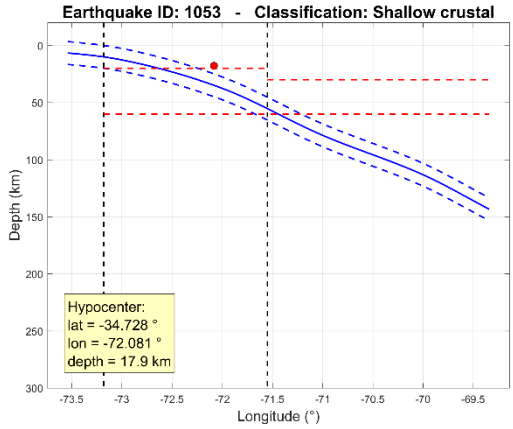

Figure B. 413: Event 1053

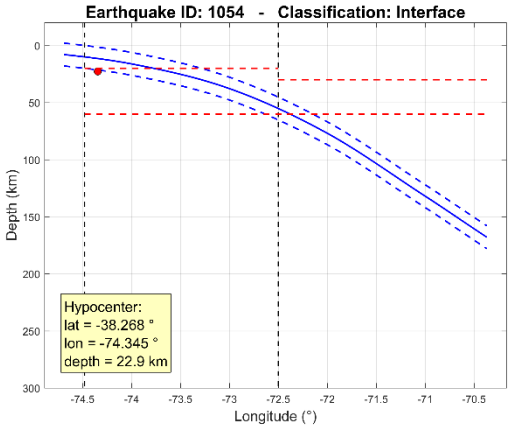

Figure B. 414: Event 1054

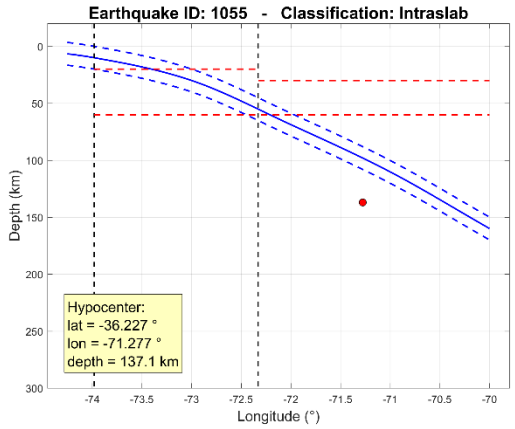

Figure B. 415: Event 1055

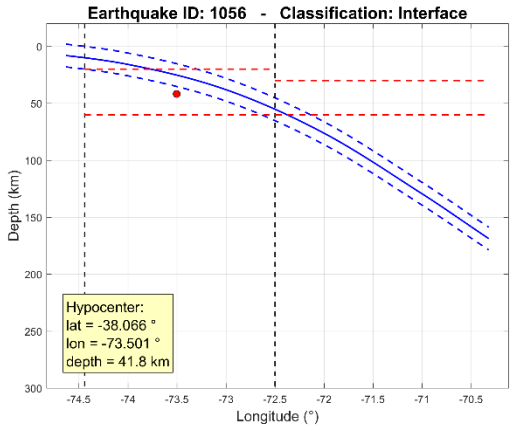

Figure B. 416: Event 1056

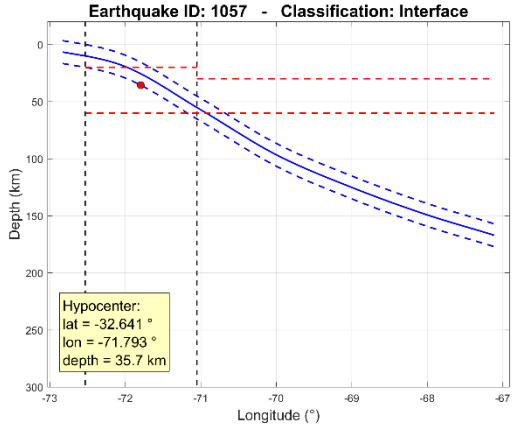

Figure B. 417: Event 1057

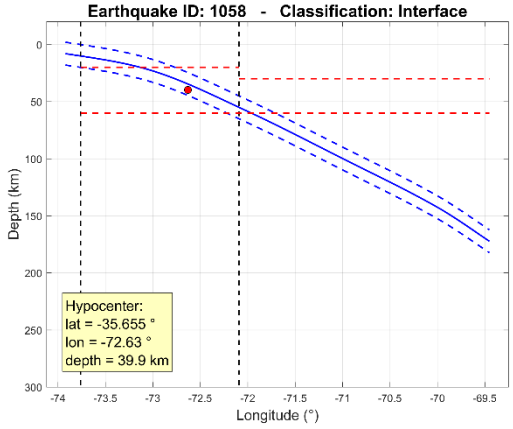

Figure B. 418: Event 1058

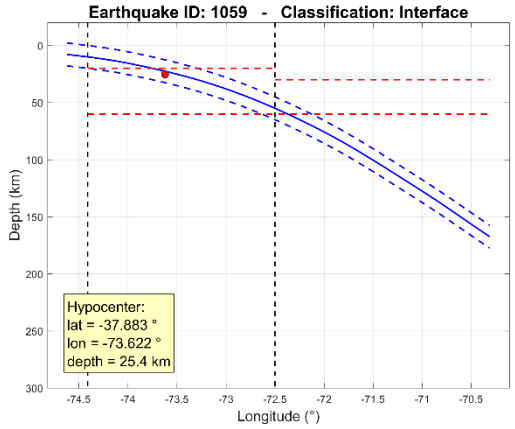

Figure B. 419: Event 1059

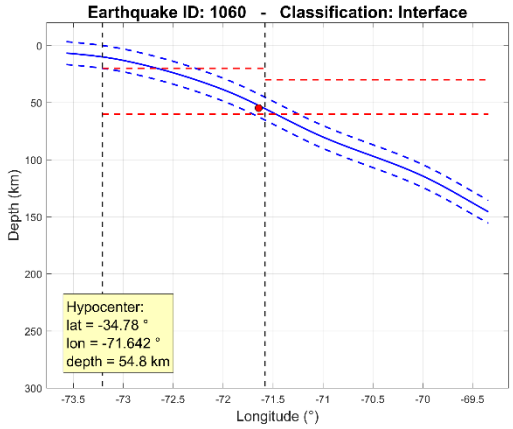

Figure B. 420: Event 1060

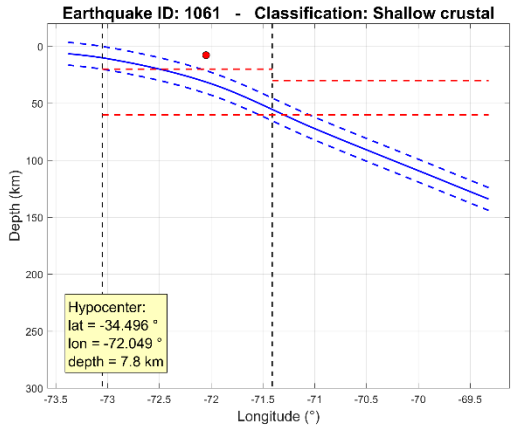

Figure B. 421: Event 1061

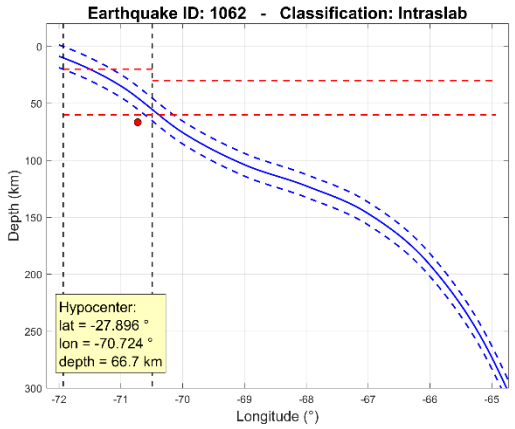

Figure B. 422: Event 1062

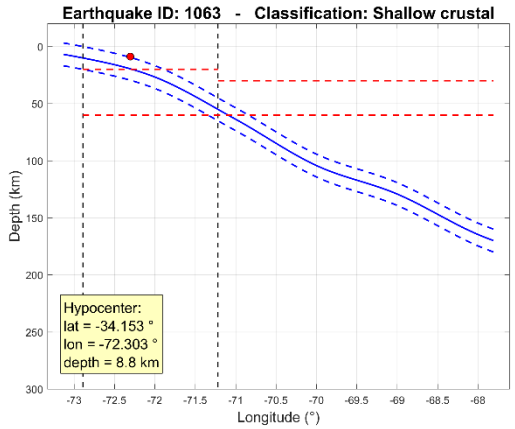

Figure B. 423: Event 1063

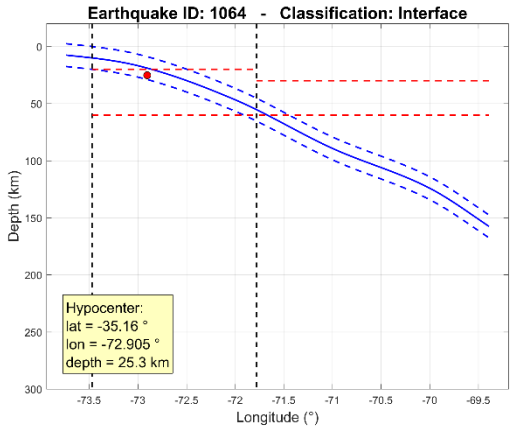

Figure B. 424: Event 1064

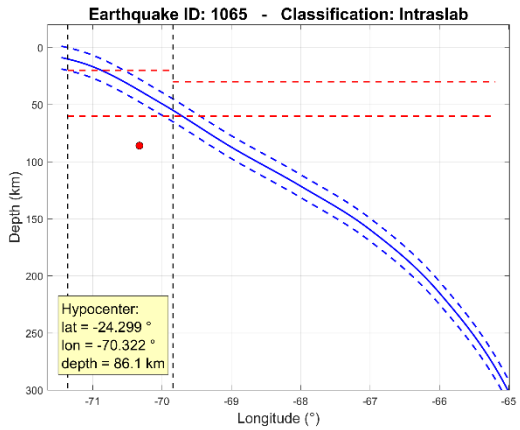

Figure B. 425: Event 1065

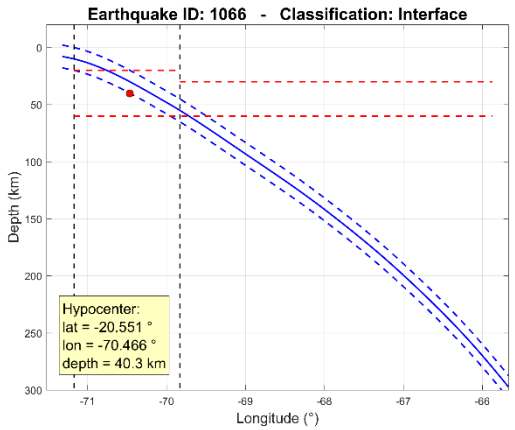

Figure B. 426: Event 1066

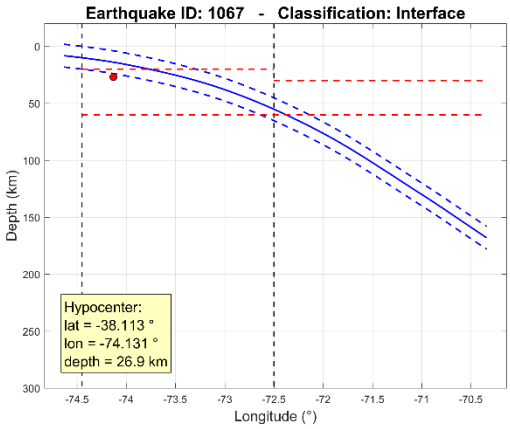

Figure B. 427: Event 1067

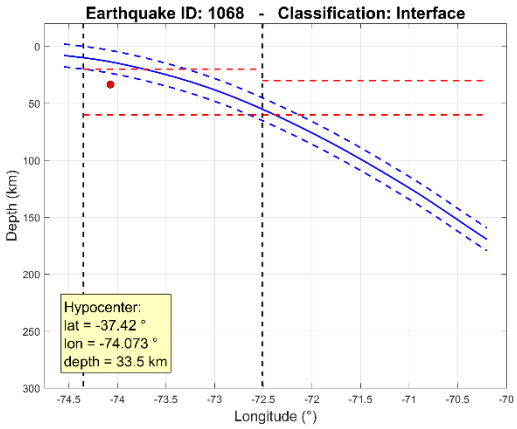

Figure B. 428: Event 1068

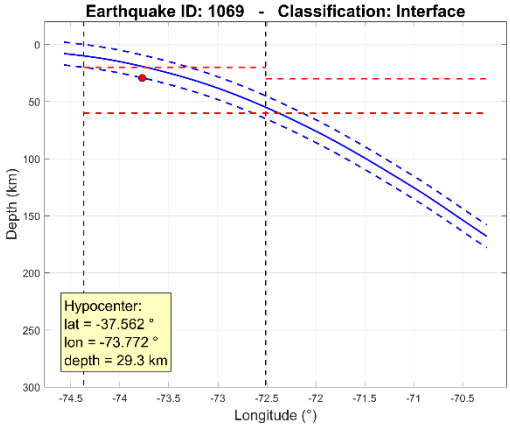

Figure B. 429: Event 1069

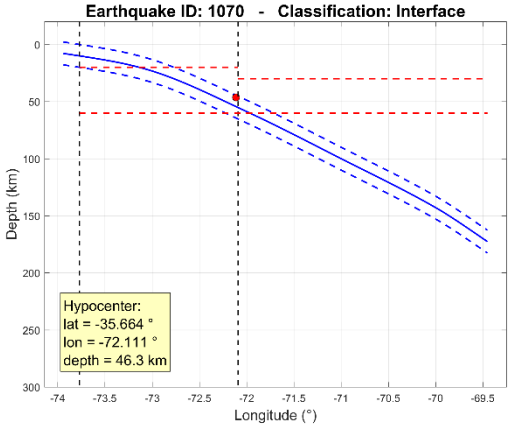

Figure B. 430: Event 1070

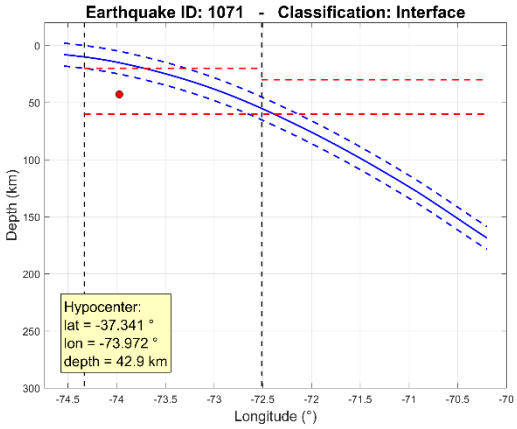

Figure B. 431: Event 1071

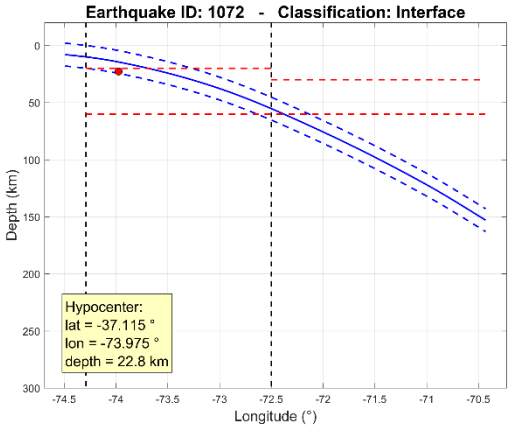

Figure B. 432: Event 1072

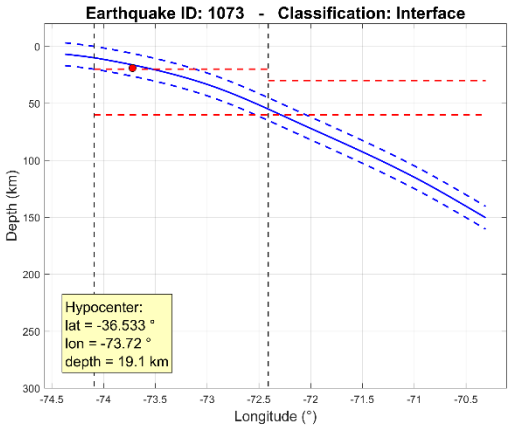

Figure B. 433: Event 1073

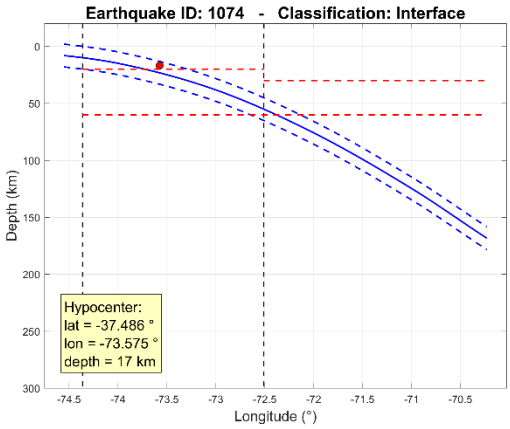

Figure B. 434: Event 1074

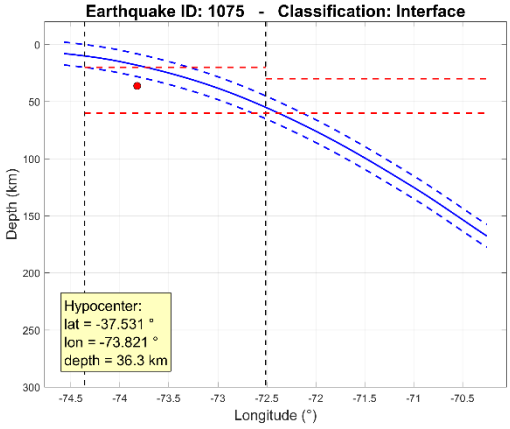

Figure B. 435: Event 1075

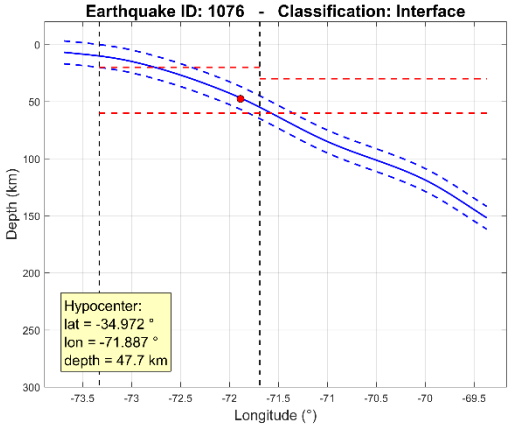

Figure B. 436: Event 1076

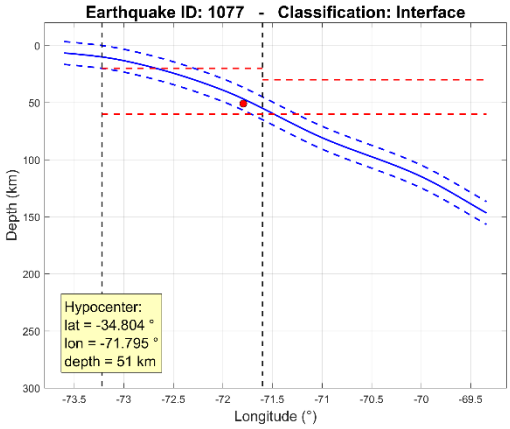

Figure B. 437: Event 1077

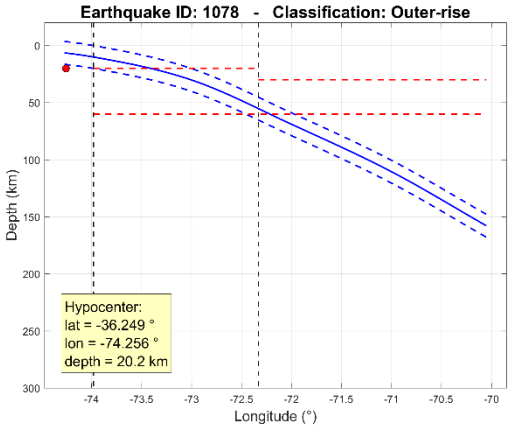

Figure B. 438: Event 1078

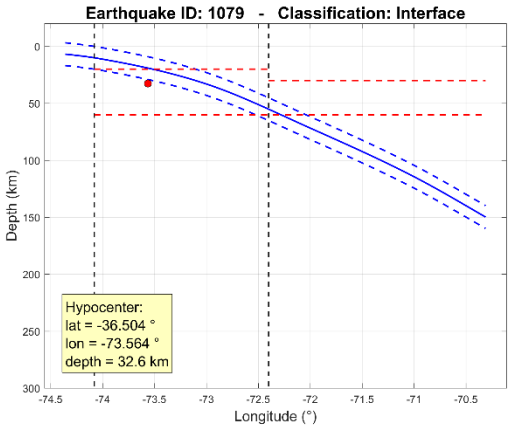

Figure B. 439: Event 1079

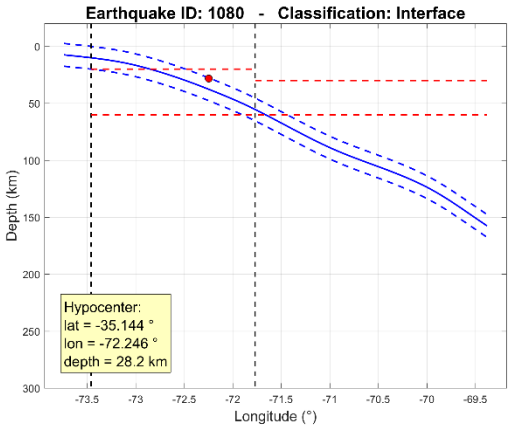

Figure B. 440: Event 1080

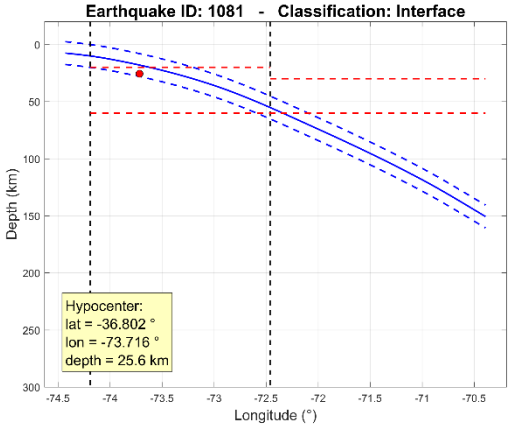

Figure B. 441: Event 1081

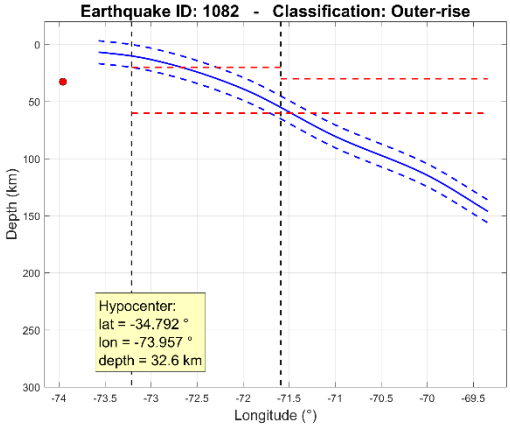

Figure B. 442: Event 1082

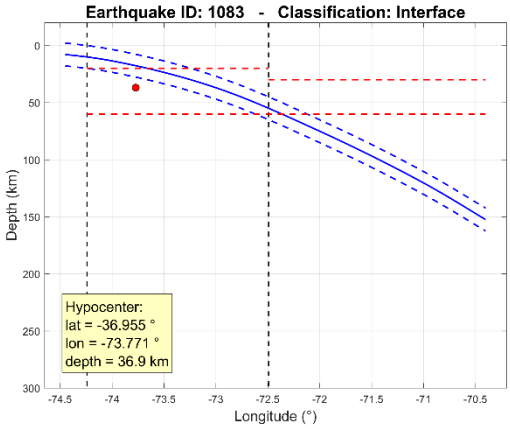

Figure B. 443: Event 1083

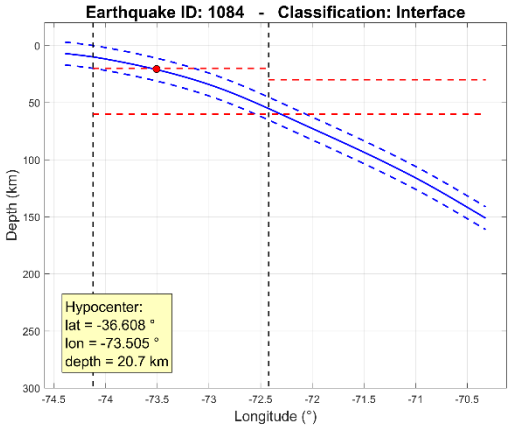

Figure B. 444: Event 1084

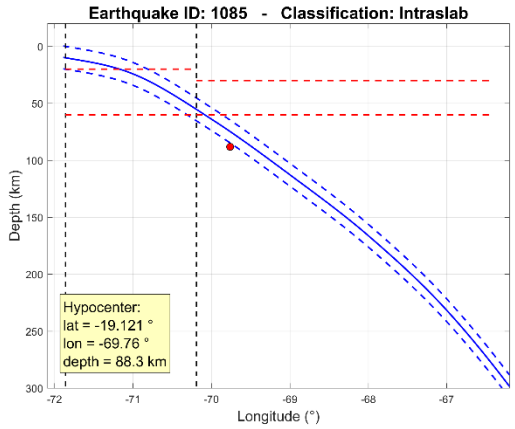

Figure B. 445: Event 1085

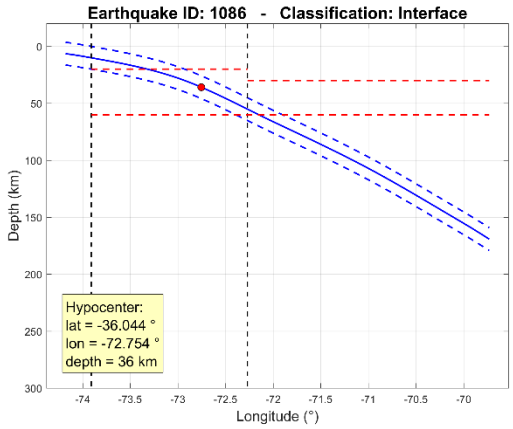

Figure B. 446: Event 1086

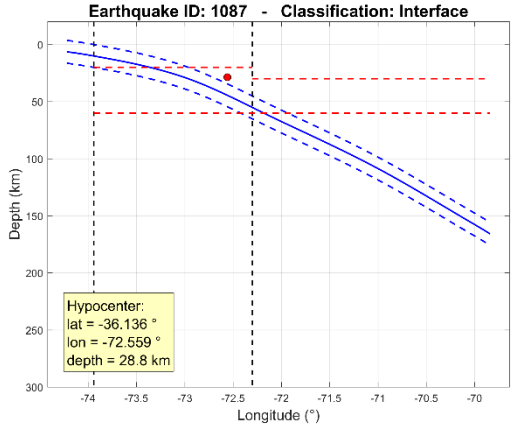

Figure B. 447: Event 1087

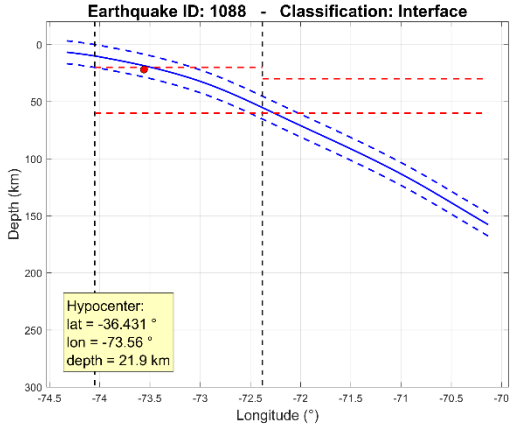

Figure B. 448: Event 1088

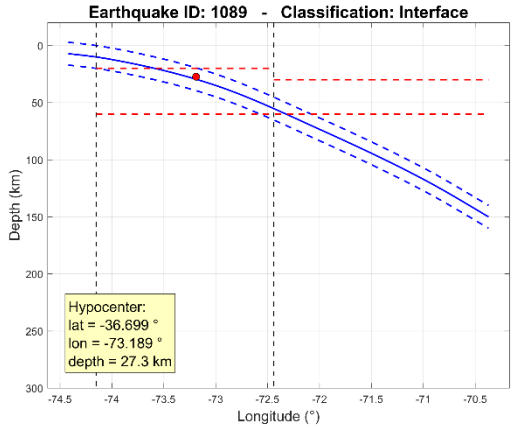

Figure B. 449: Event 1089

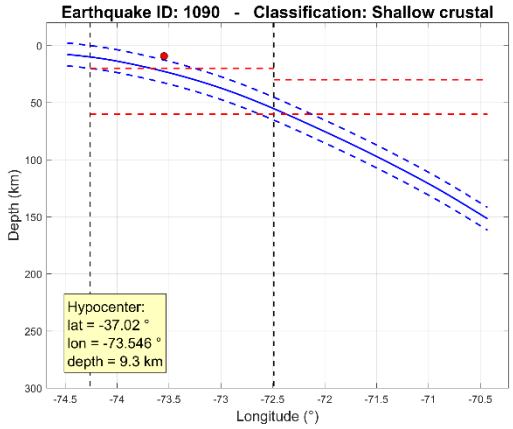

Figure B. 450: Event 1090

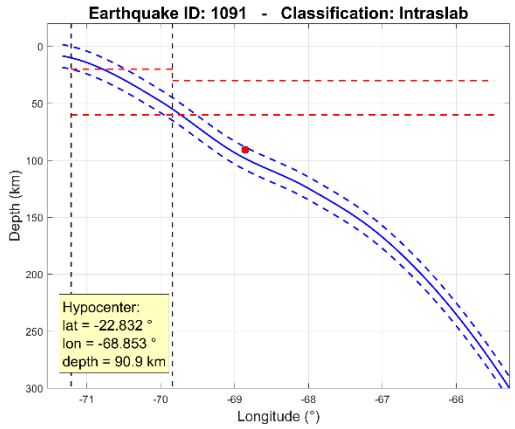

Figure B. 451: Event 1091

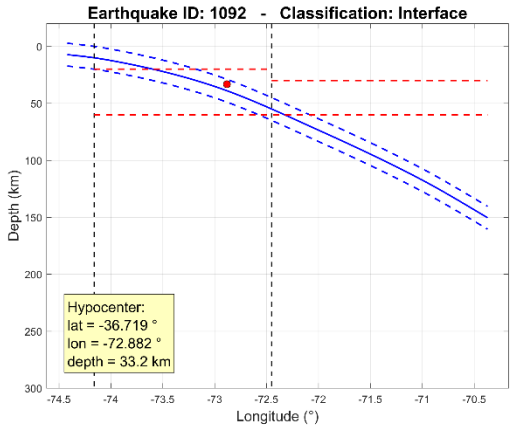

Figure B. 452: Event 1092

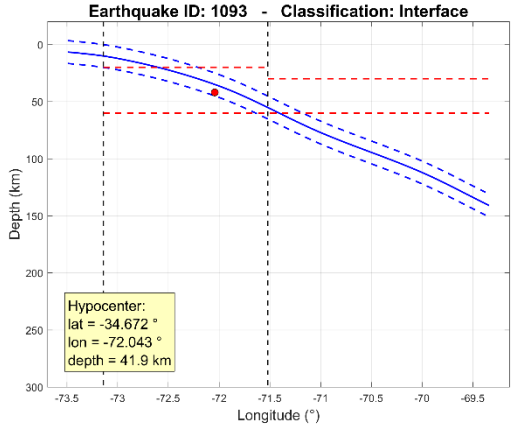

Figure B. 453: Event 1093

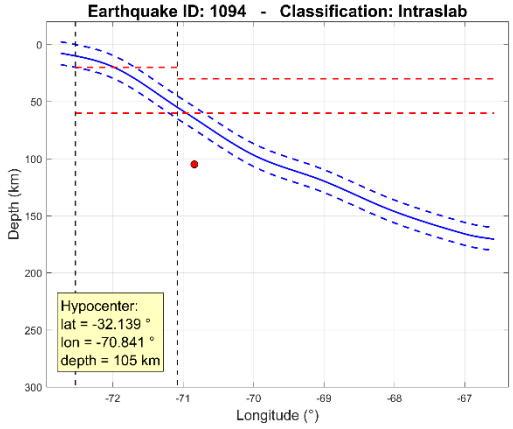

Figure B. 454: Event 1094

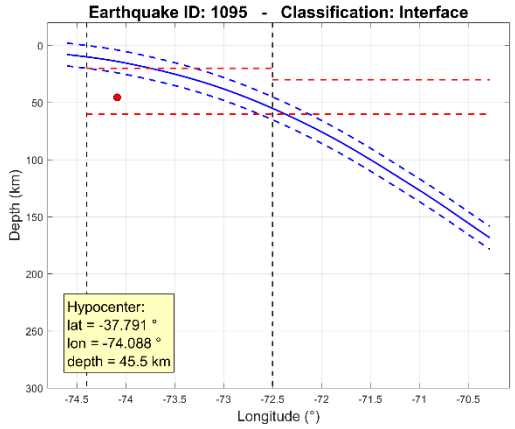

Figure B. 455: Event 1095

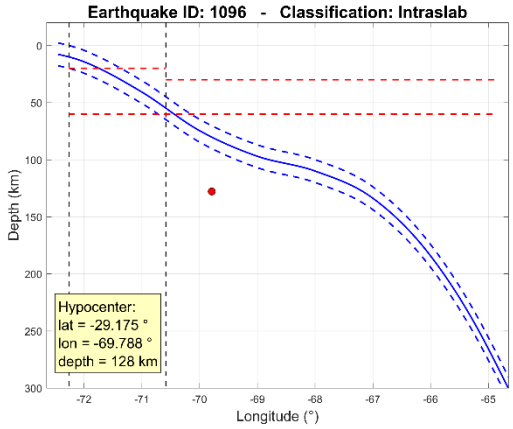

Figure B. 456: Event 1096

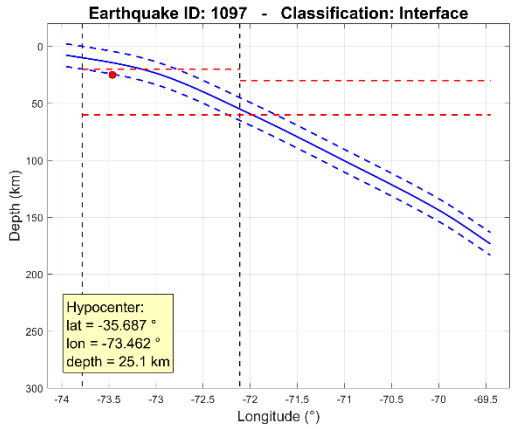

Figure B. 457: Event 1097

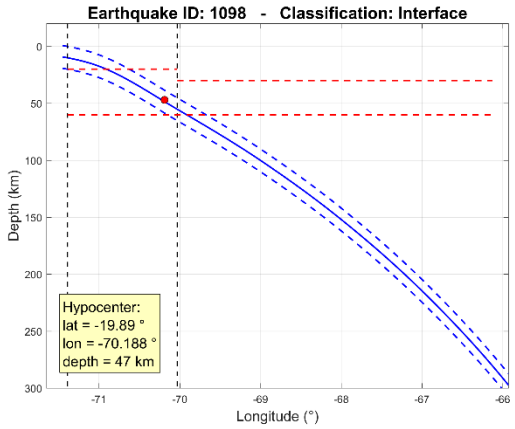

Figure B. 458: Event 1098

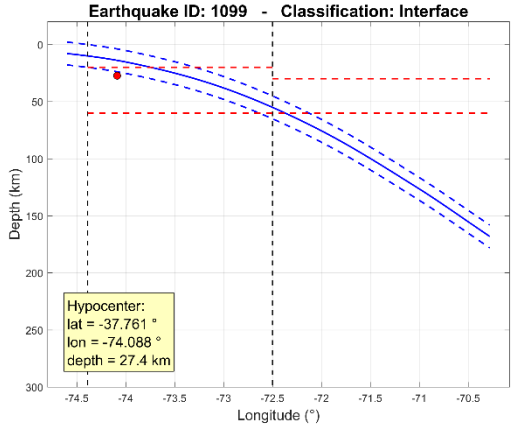

Figure B. 459: Event 1099

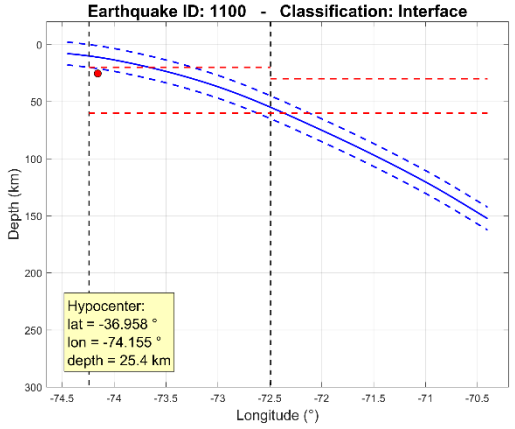

Figure B. 460: Event 1100

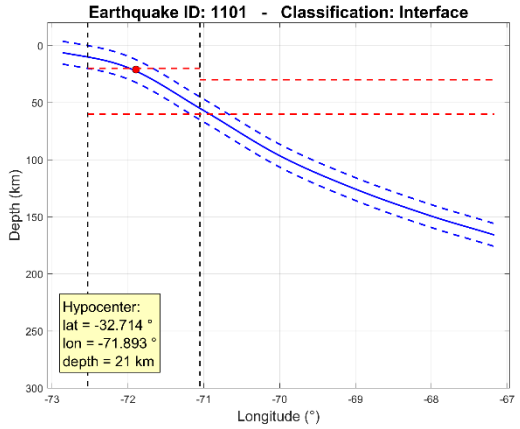

Figure B. 461: Event 1101

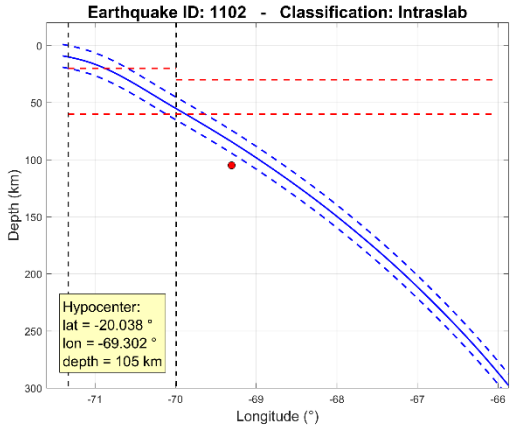

Figure B. 462: Event 1102

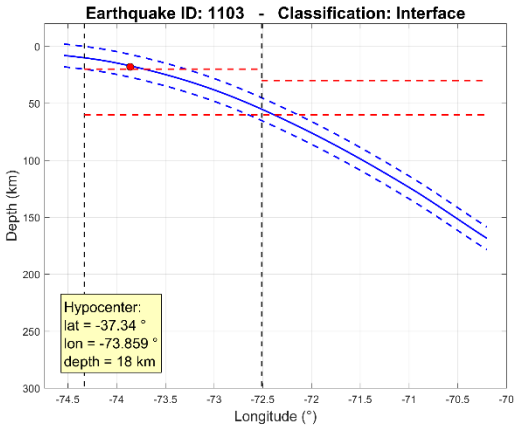

Figure B. 463: Event 1103

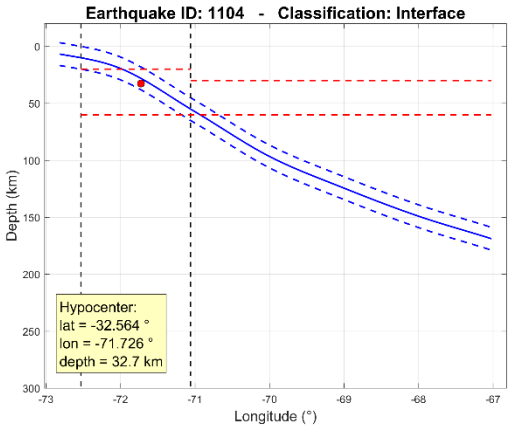

Figure B. 464: Event 1104

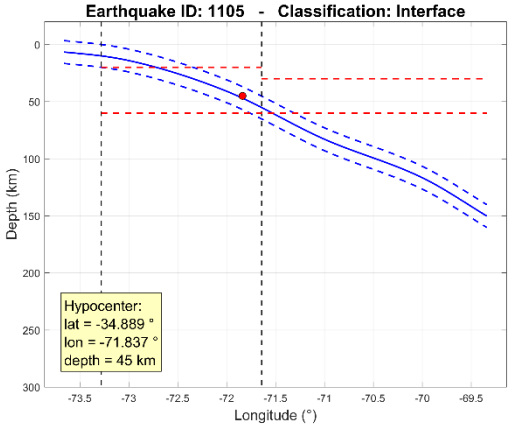

Figure B. 465: Event 1105

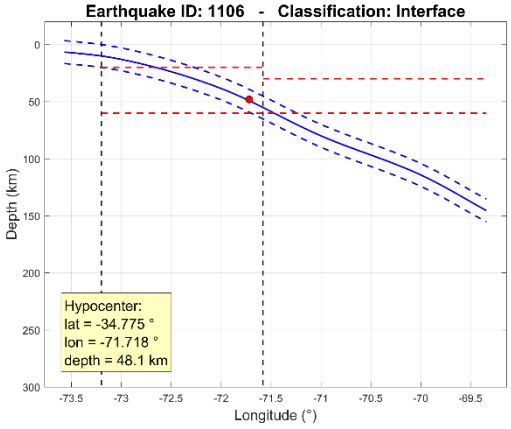

Figure B. 466: Event 1106

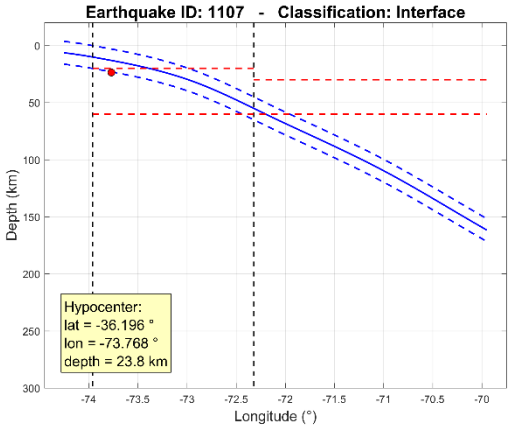

Figure B. 467: Event 1107

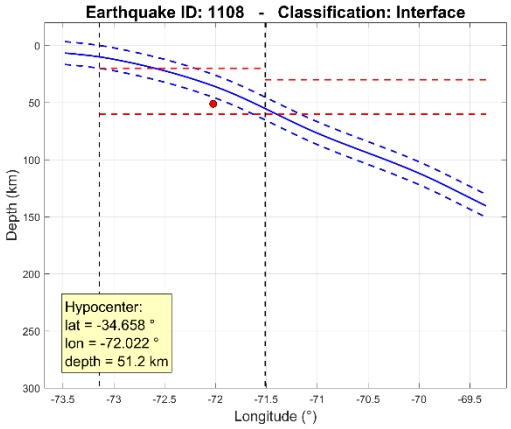

Figure B. 468: Event 1108

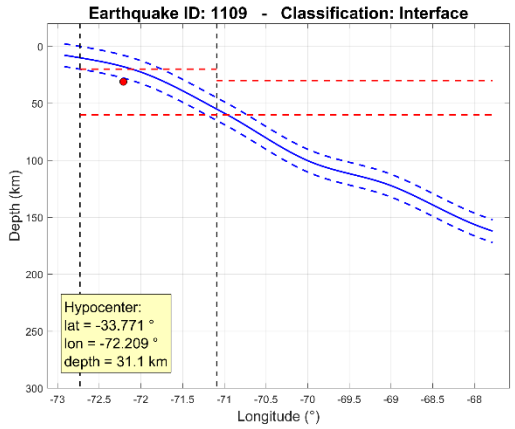

Figure B. 469: Event 1109

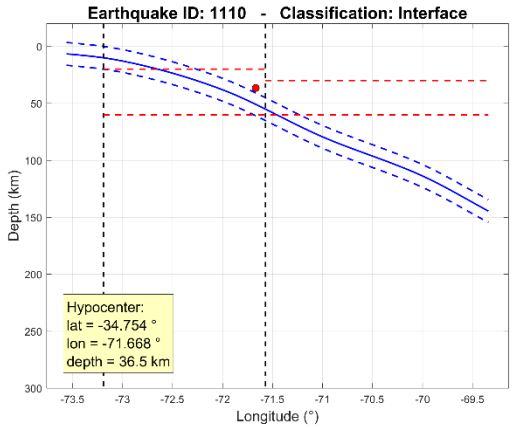

Figure B. 470: Event 1110

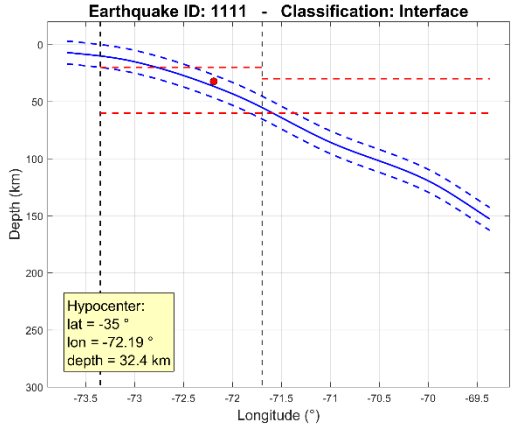

Figure B. 471: Event 1111

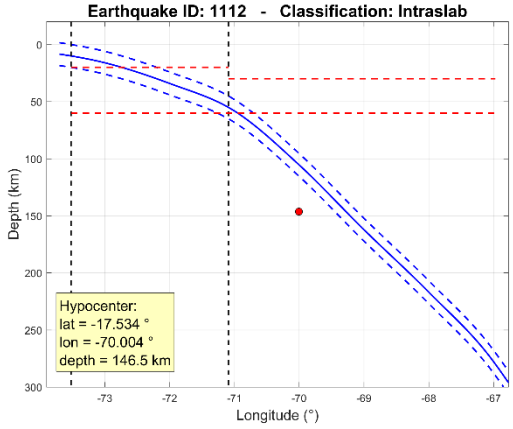

Figure B. 472: Event 1112

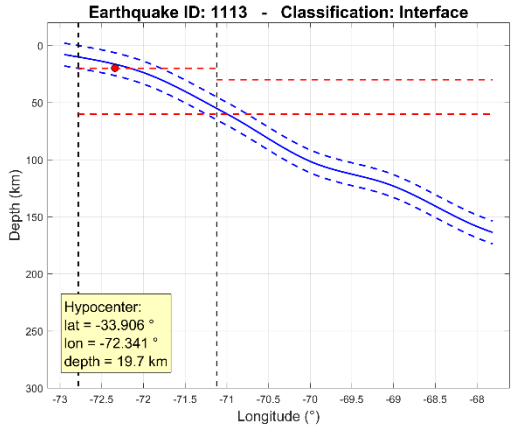

Figure B. 473: Event 1113

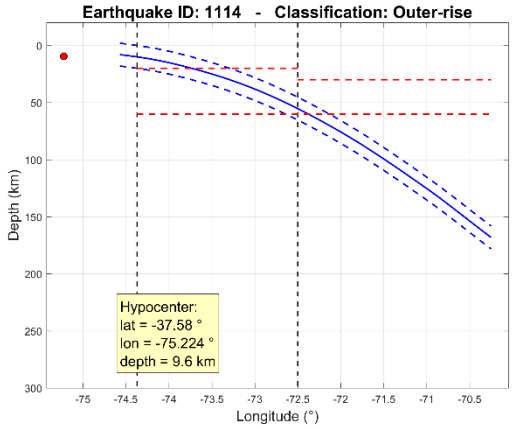

Figure B. 474: Event 1114

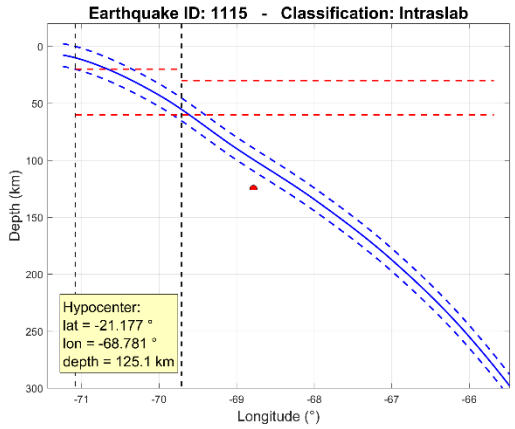

Figure B. 475: Event 1115

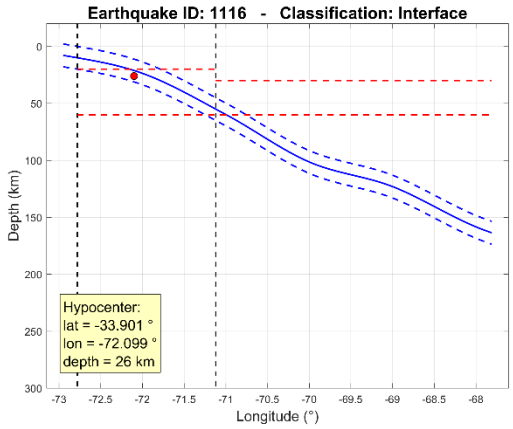

Figure B. 476: Event 1116

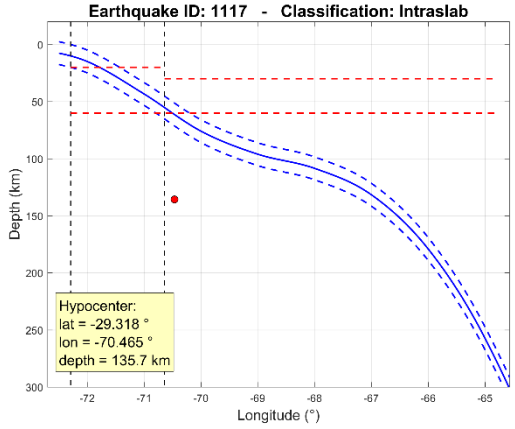

Figure B. 477: Event 1117

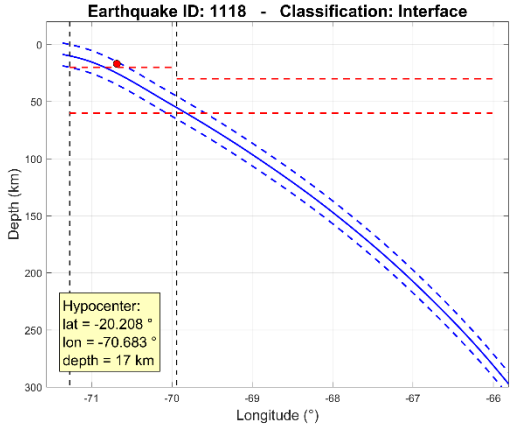

Figure B. 478: Event 1118

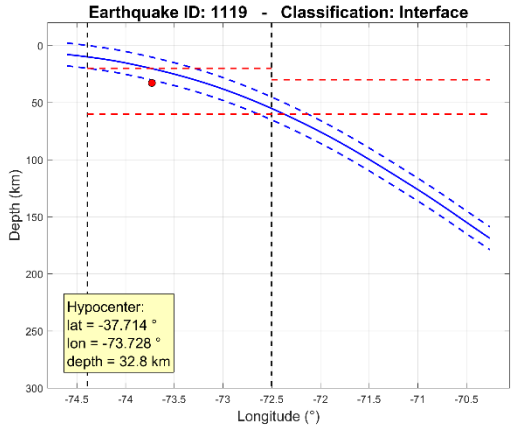

Figure B. 479: Event 1119

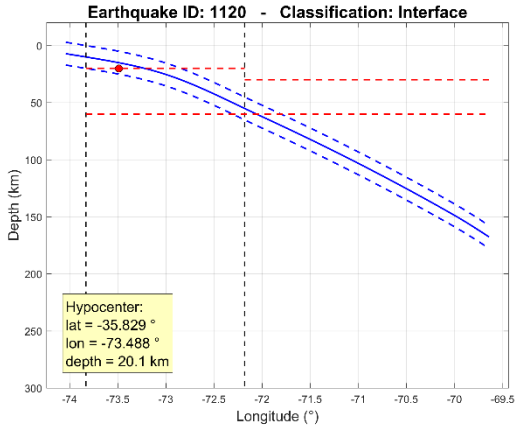

Figure B. 480: Event 1120

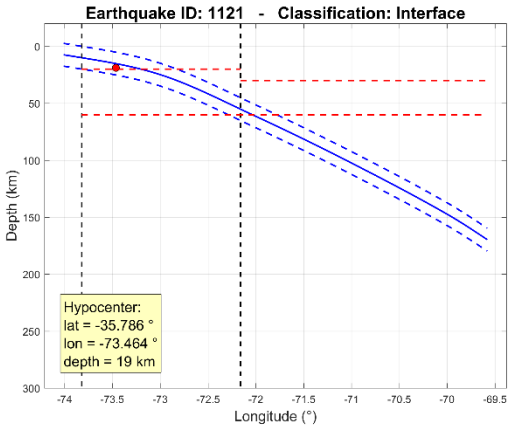

Figure B. 481: Event 1121

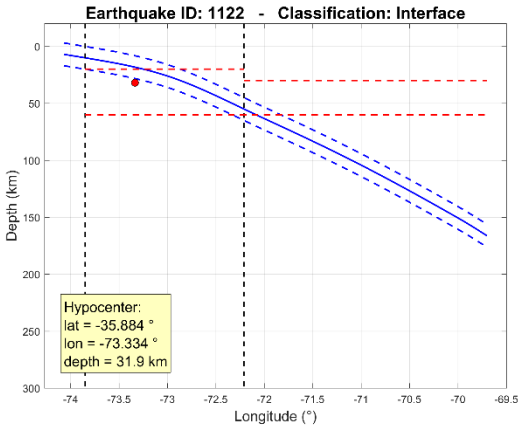

Figure B. 482: Event 1122

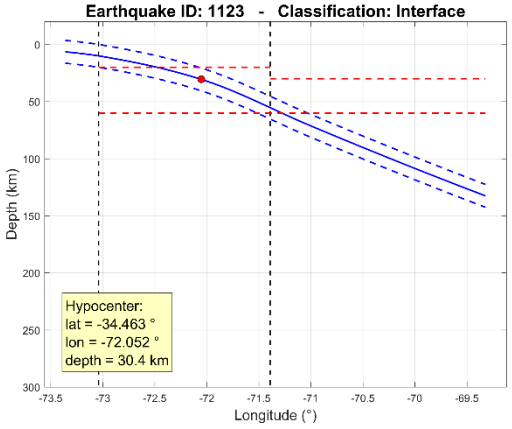

Figure B. 483: Event 1123

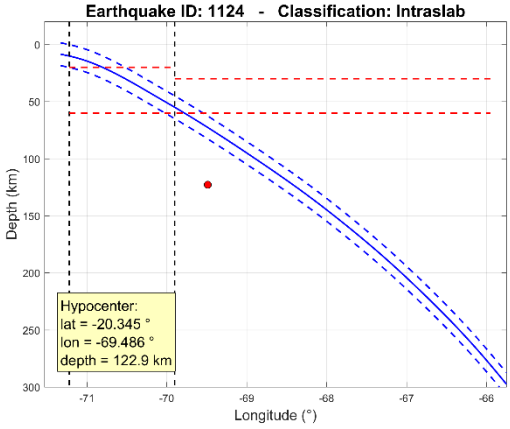

Figure B. 484: Event 1124

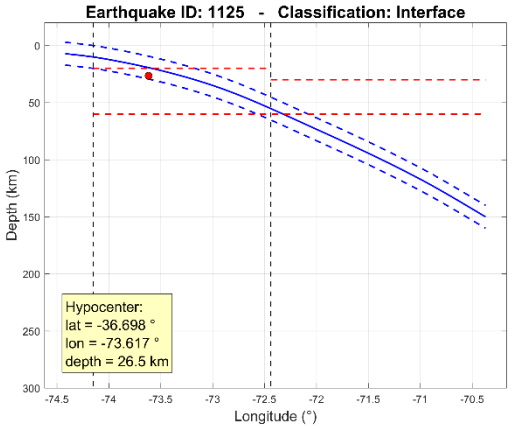

Figure B. 485: Event 1125

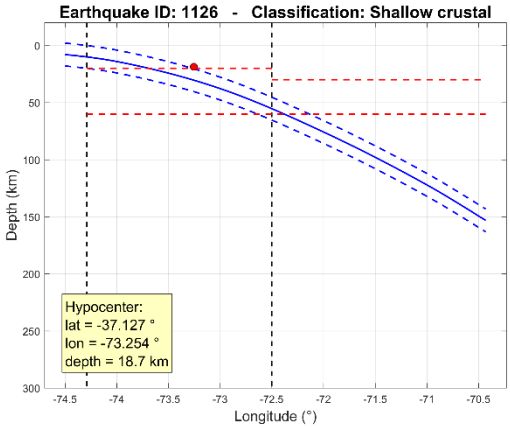

Figure B. 486: Event 1126

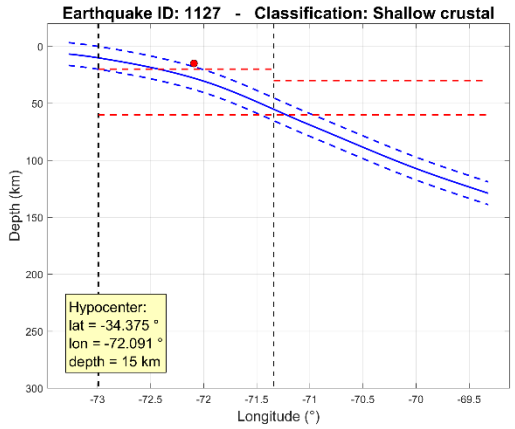

Figure B. 487: Event 1127

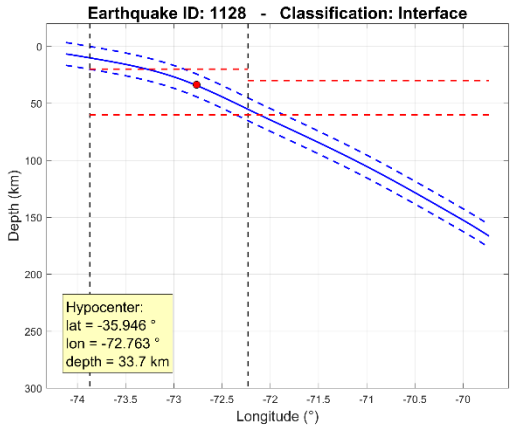

Figure B. 488: Event 1128

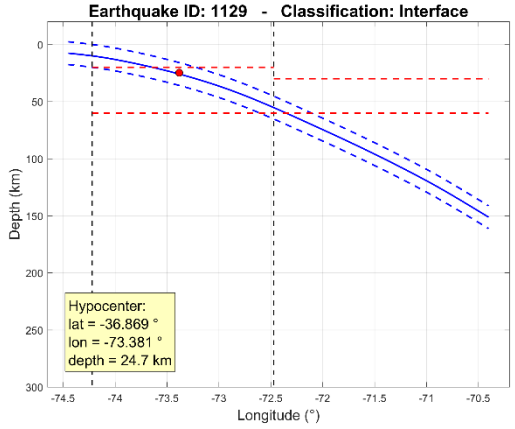

Figure B. 489: Event 1129

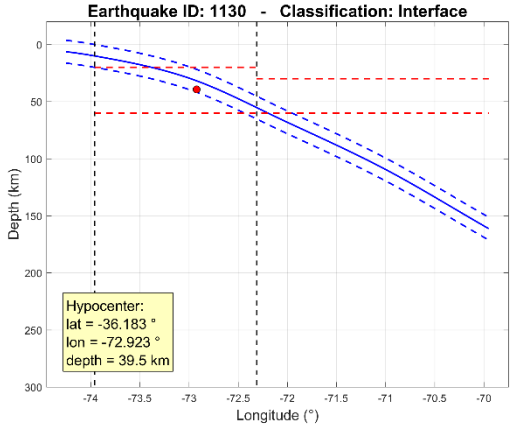

Figure B. 490: Event 1130

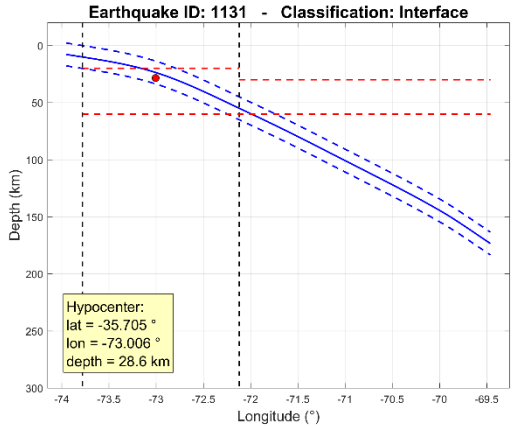

Figure B. 491: Event 1131

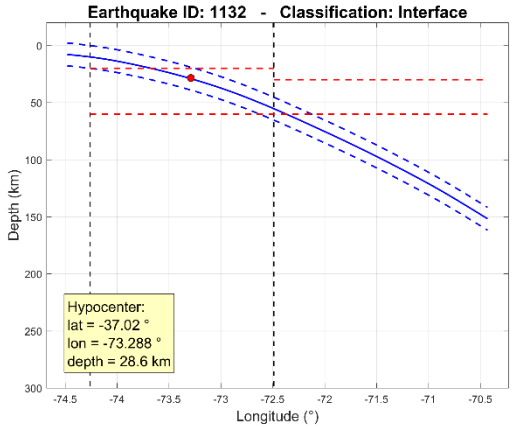

Figure B. 492: Event 1132

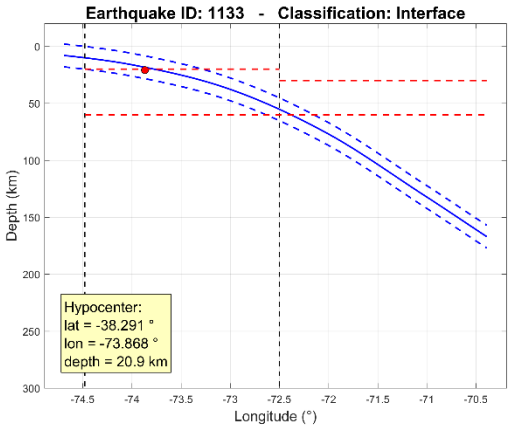

Figure B. 493: Event 1133

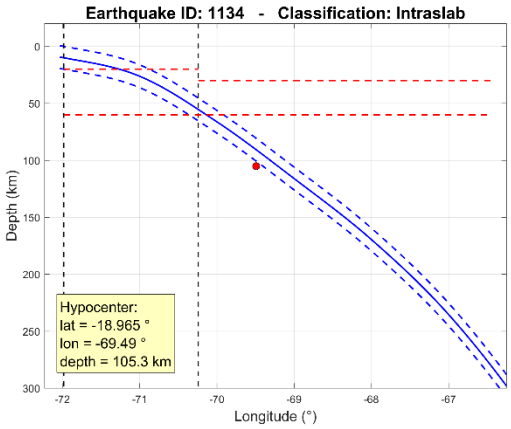

Figure B. 494: Event 1134

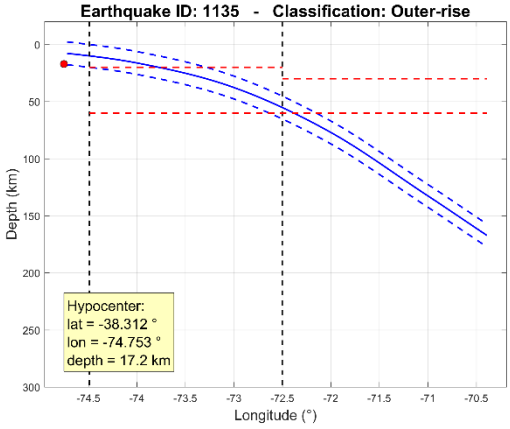

Figure B. 495: Event 1135

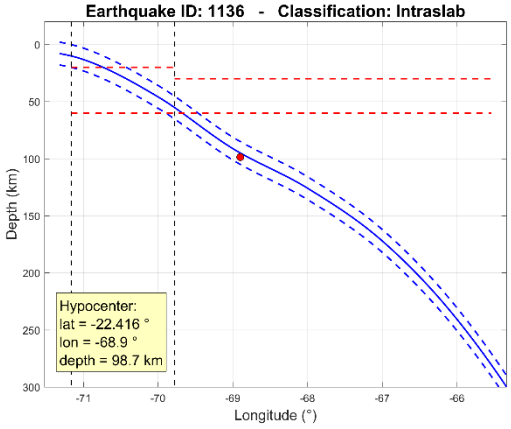

Figure B. 496: Event 1136

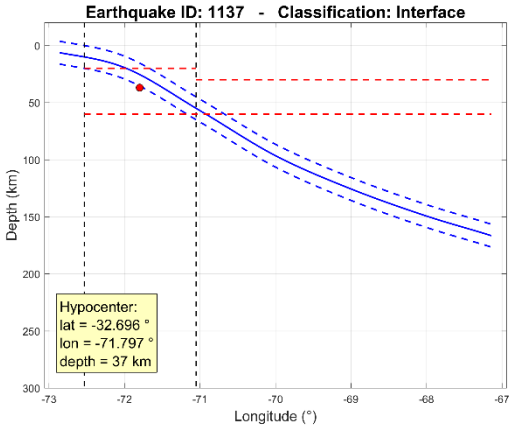

Figure B. 497: Event 1137

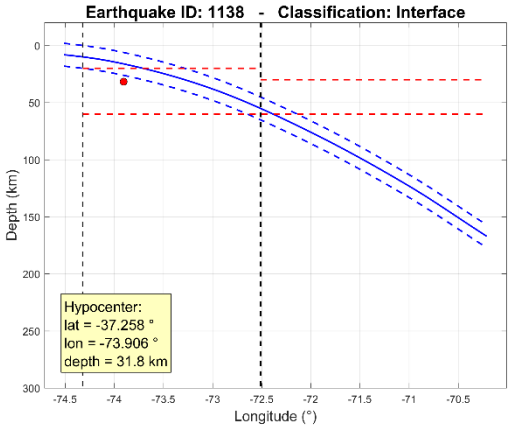

Figure B. 498: Event 1138

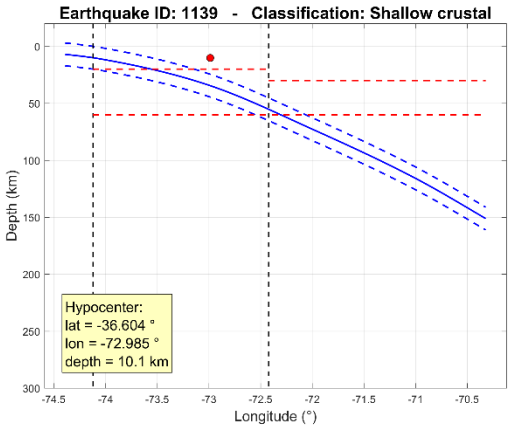

Figure B. 499: Event 1139

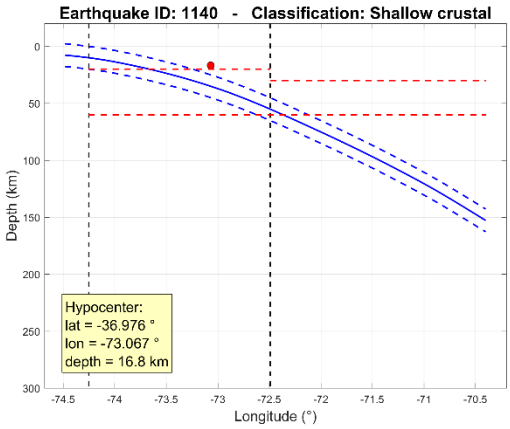

Figure B. 500: Event 1140

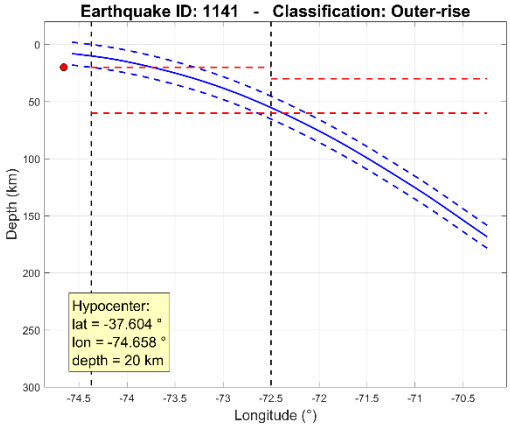

Figure B. 501: Event 1141

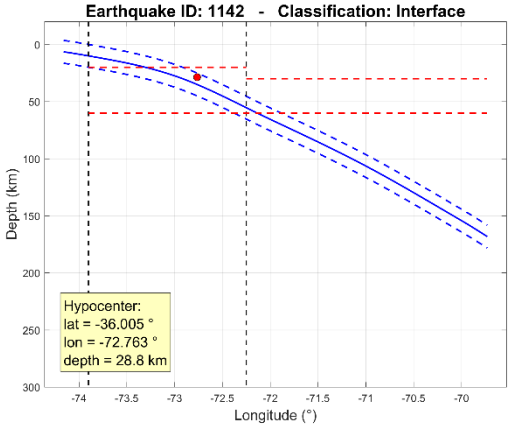

Figure B. 502: Event 1142

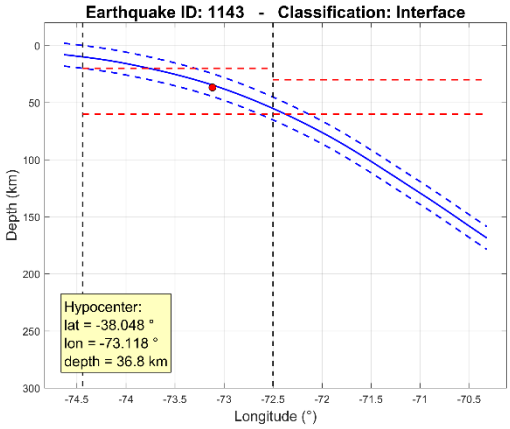

Figure B. 503: Event 1143

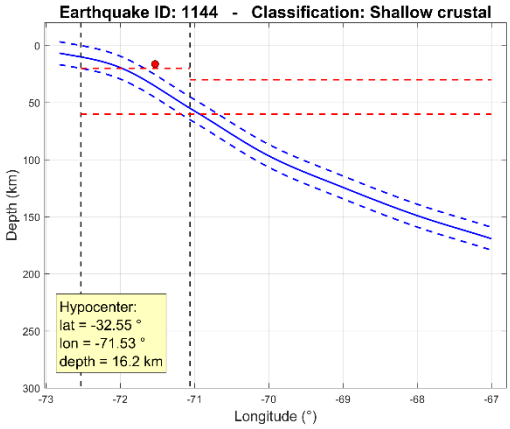

Figure B. 504: Event 1144

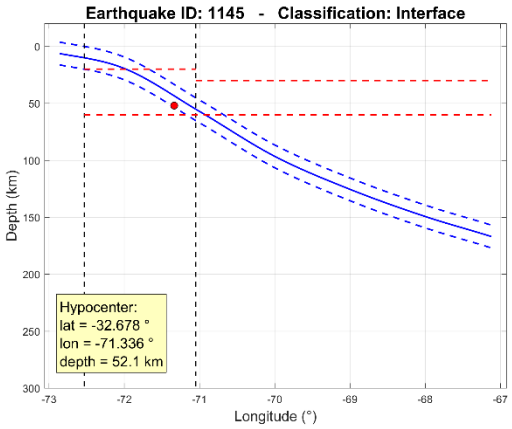

Figure B. 505: Event 1145

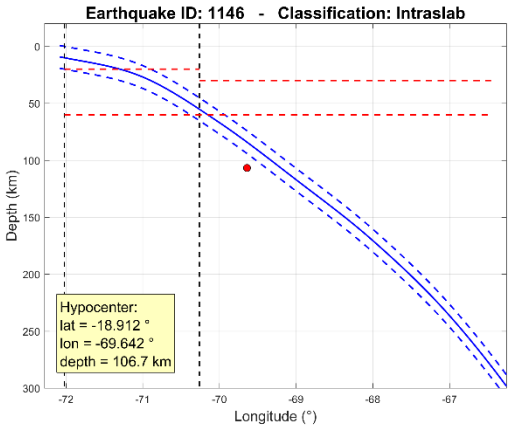

Figure B. 506: Event 1146

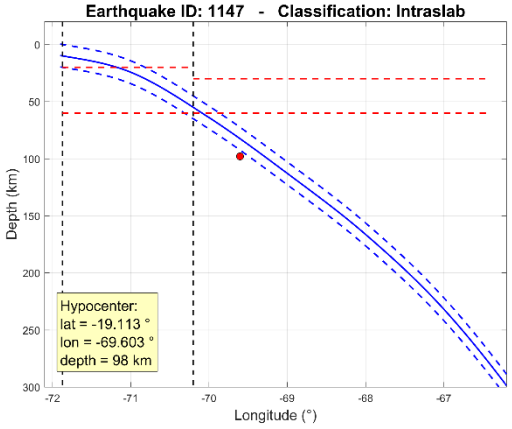

Figure B. 507: Event 1147

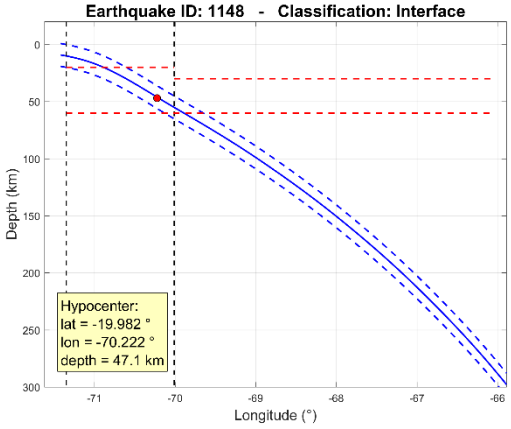

Figure B. 508: Event 1148

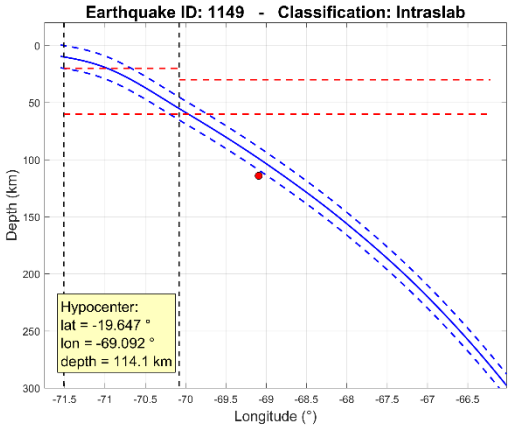

Figure B. 509: Event 1149

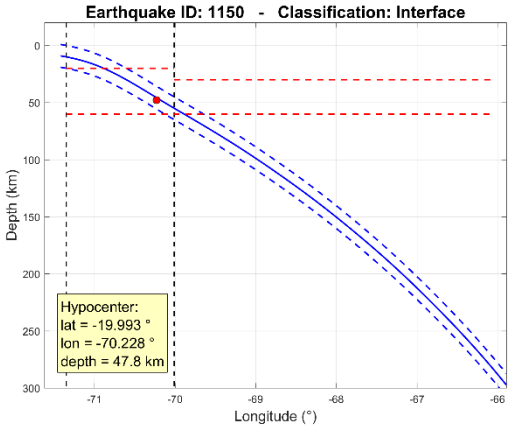

Figure B. 510: Event 1150

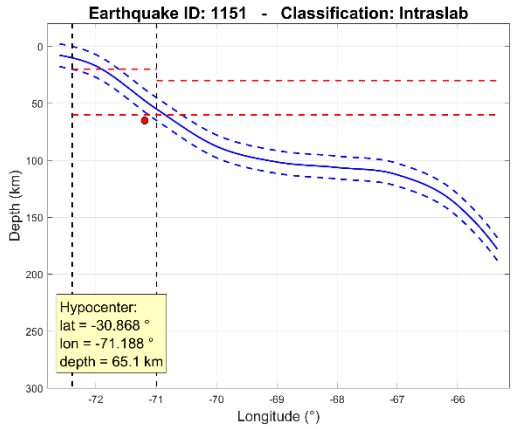

Figure B. 511: Event 1151

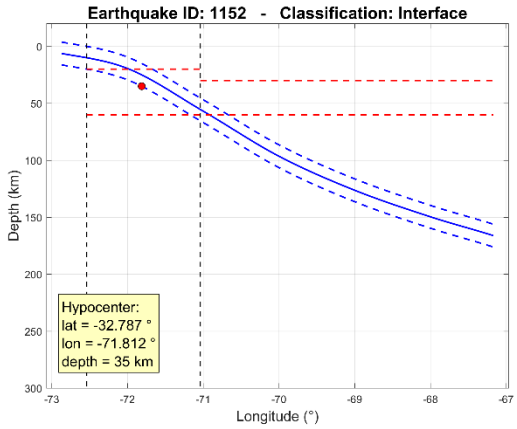

Figure B. 512: Event 1152

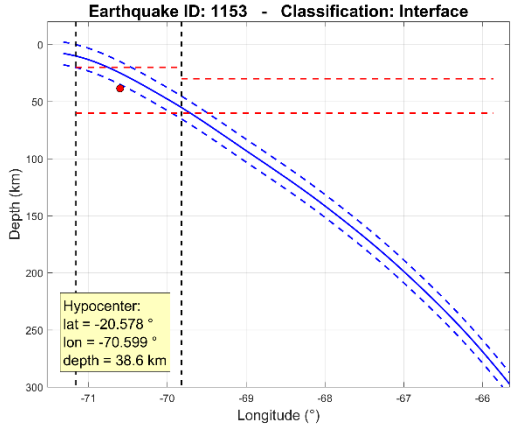

Figure B. 513: Event 1153

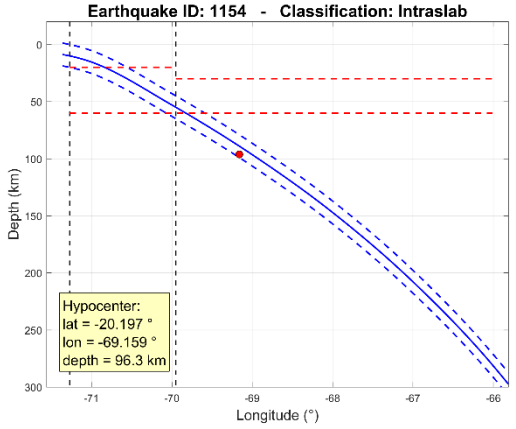

Figure B. 514: Event 1154

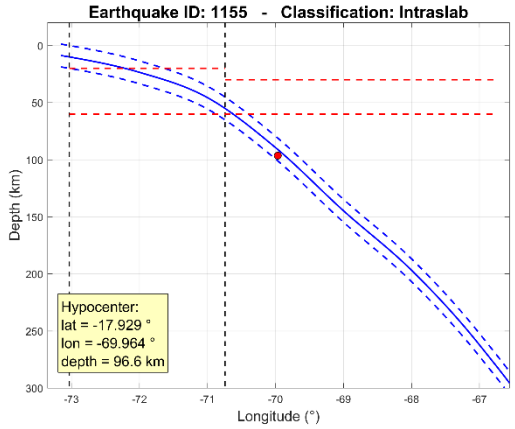

Figure B. 515: Event 1155

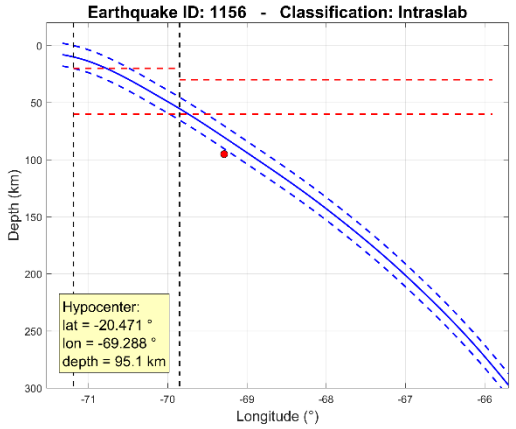

Figure B. 516: Event 1156

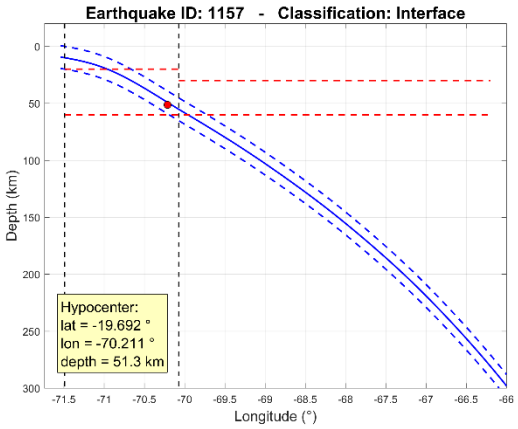

Figure B. 517: Event 1157

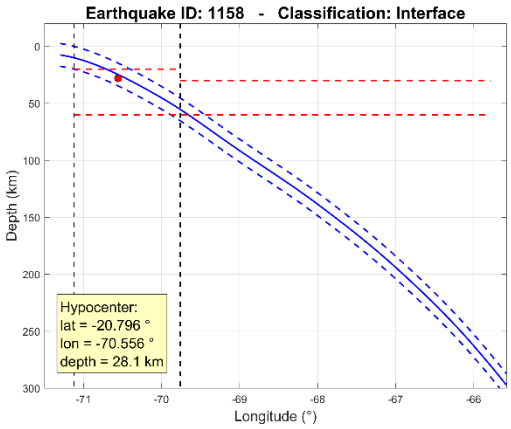

Figure B. 518: Event 1158

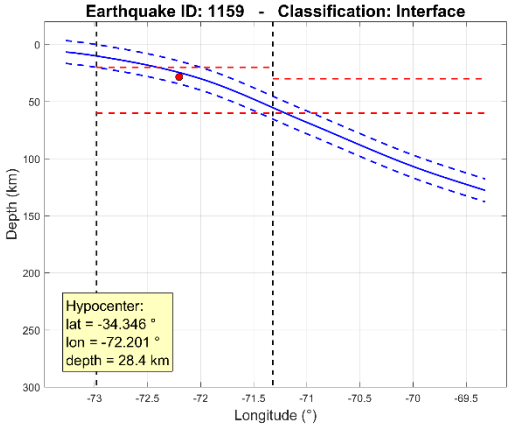

Figure B. 519: Event 1159

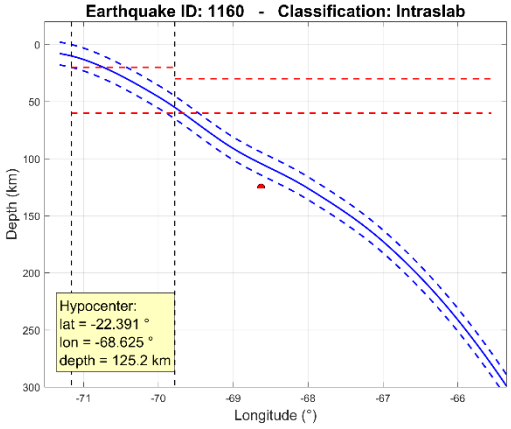

Figure B. 520: Event 1160

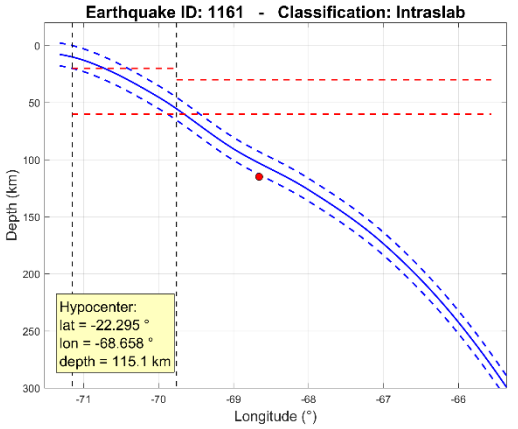

Figure B. 521: Event 1161

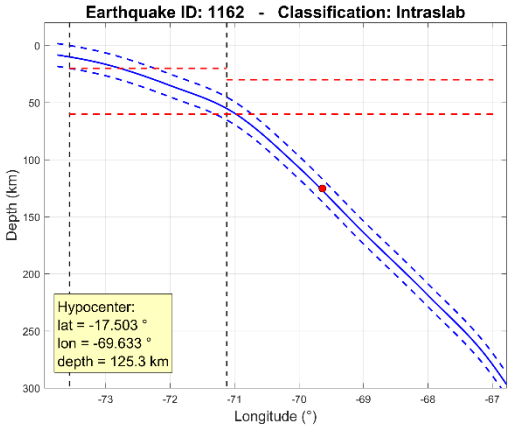

Figure B. 522: Event 1162

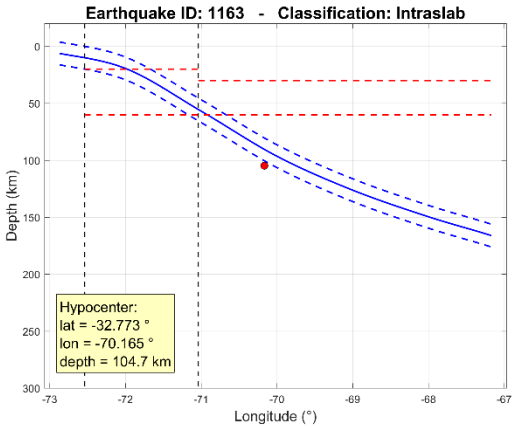

Figure B. 523: Event 1163

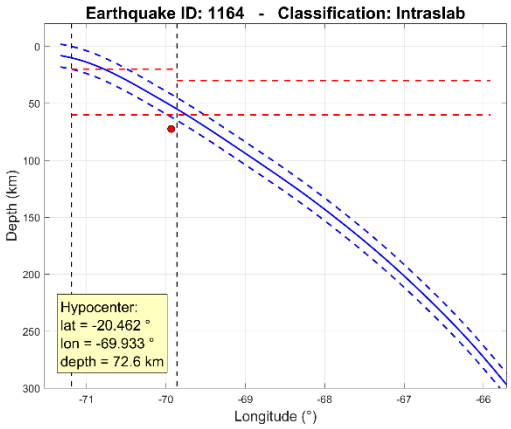

Figure B. 524: Event 1164

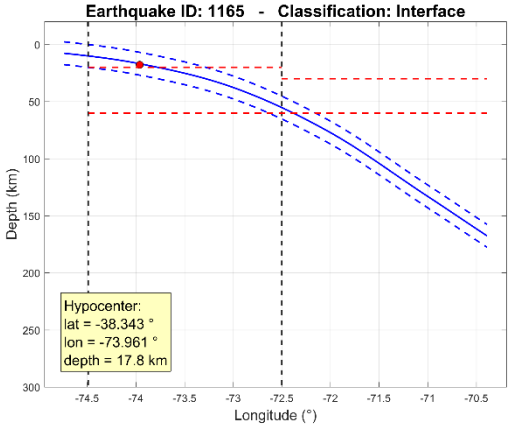

Figure B. 525: Event 1165

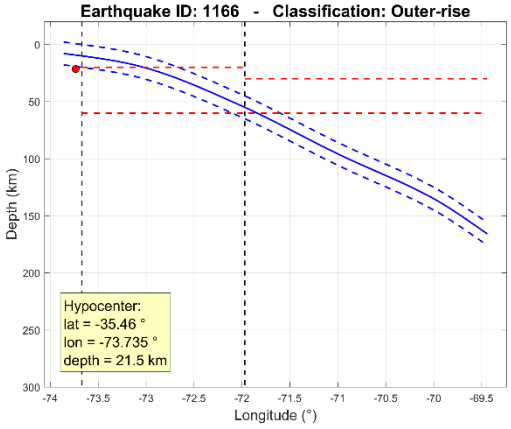

Figure B. 526: Event 1166

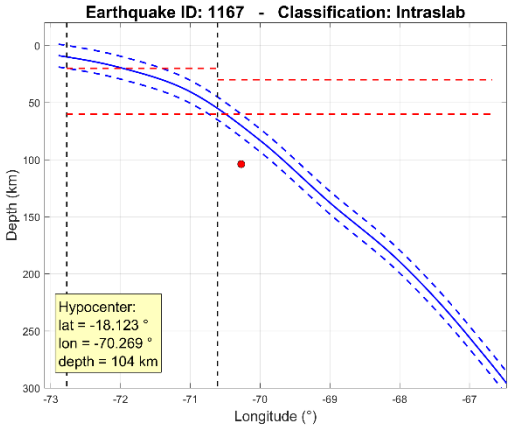

Figure B. 527: Event 1167

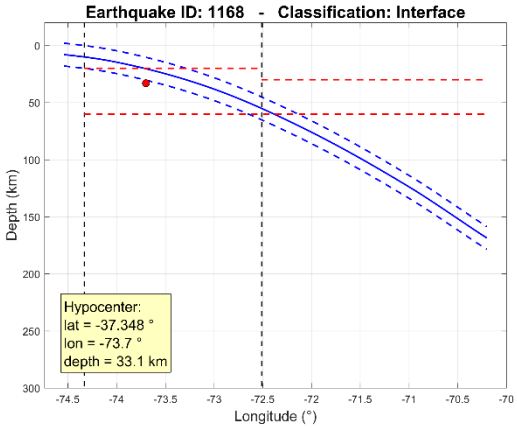

Figure B. 528: Event 1168

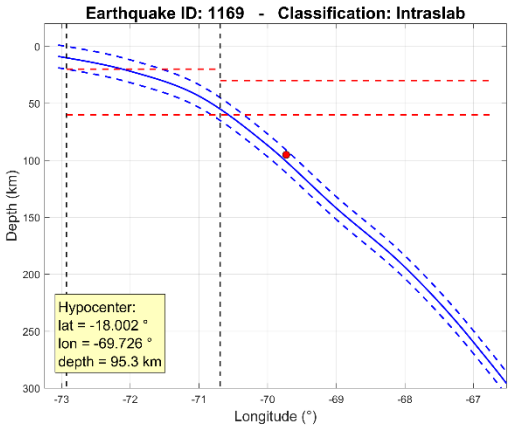

Figure B. 529: Event 1169

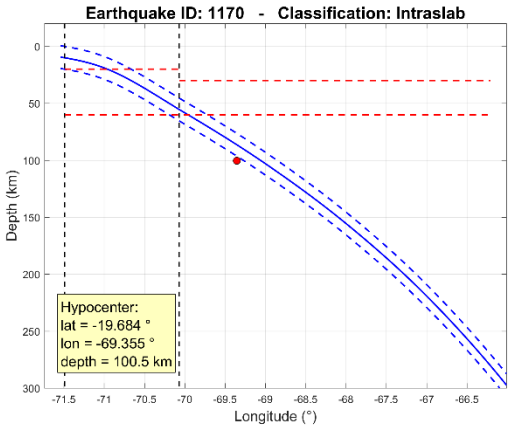

Figure B. 530: Event 1170

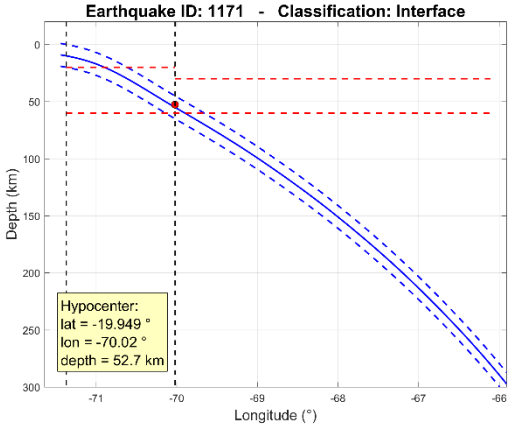

Figure B. 531: Event 1171

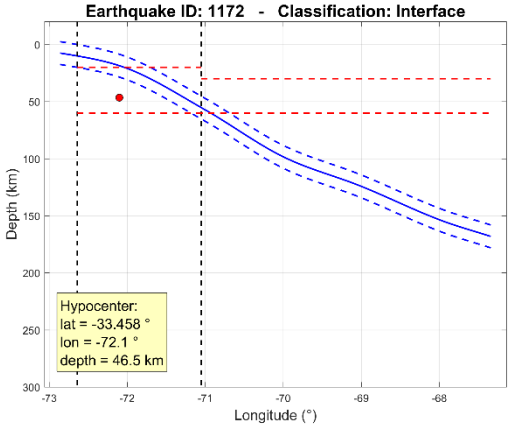

Figure B. 532: Event 1172

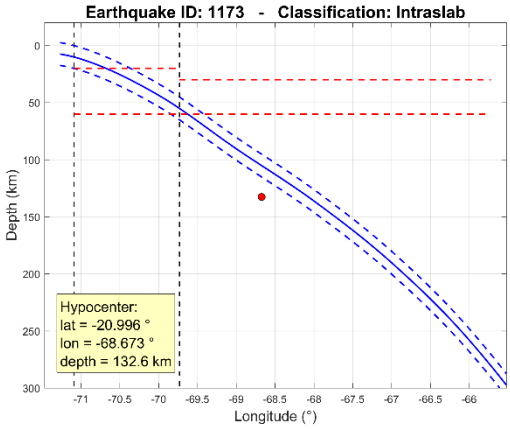

Figure B. 533: Event 1173

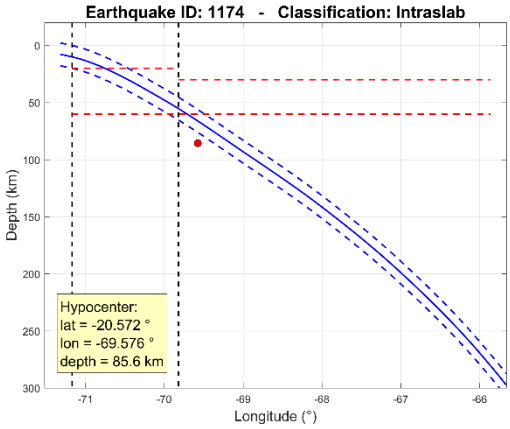

Figure B. 534: Event 1174

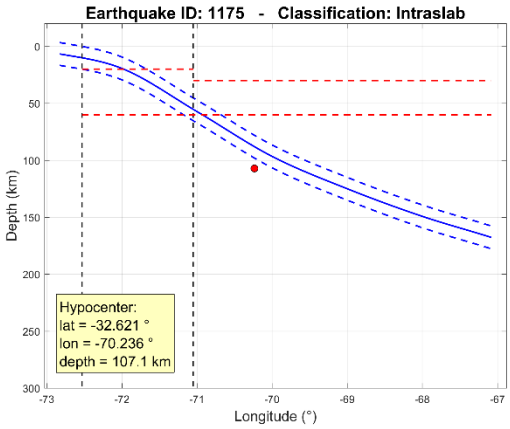

Figure B. 535: Event 1175

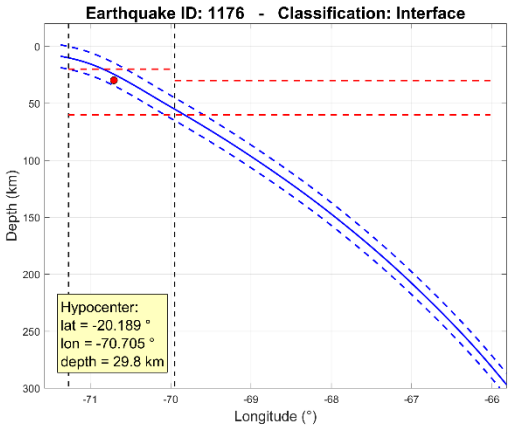

Figure B. 536: Event 1176

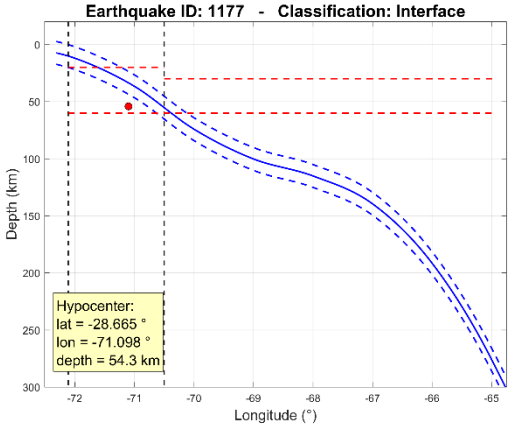

Figure B. 537: Event 1177

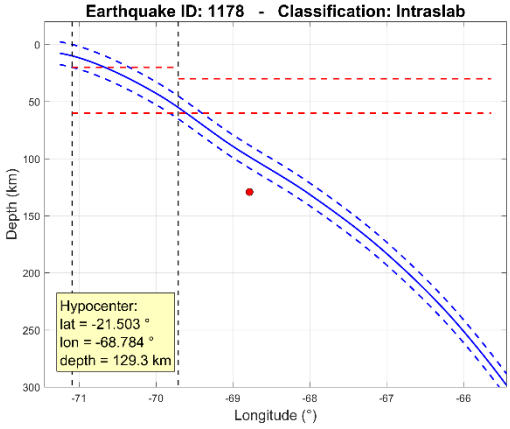

Figure B. 538: Event 1178

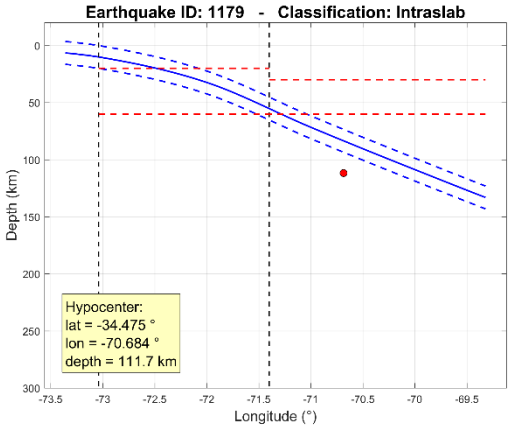

Figure B. 539: Event 1179

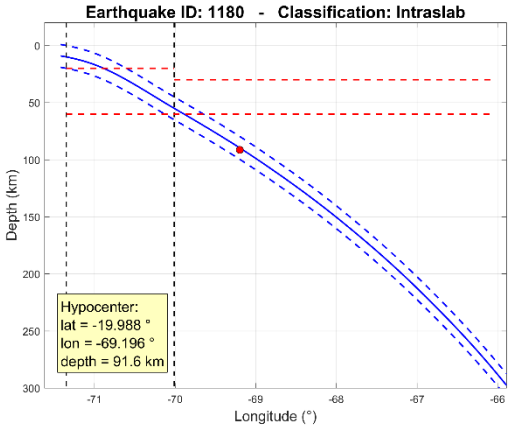

Figure B. 540: Event 1180

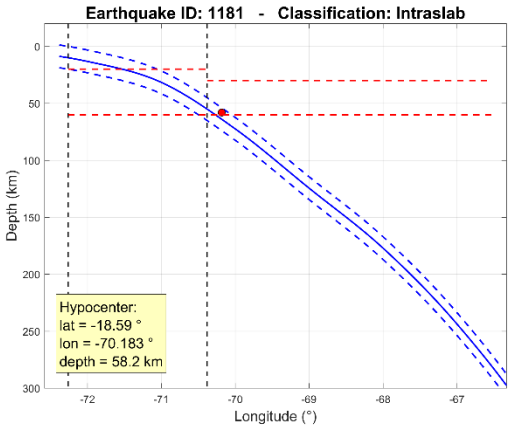

Figure B. 541: Event 1181

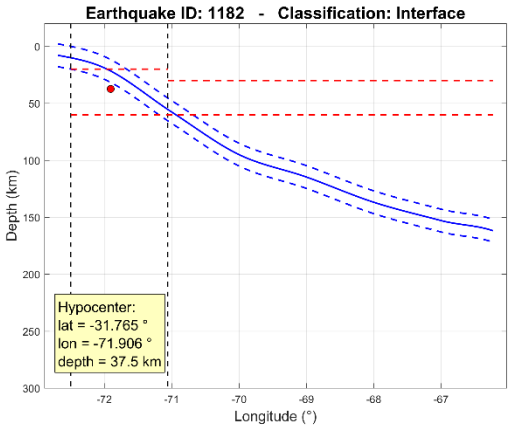

Figure B. 542: Event 1182

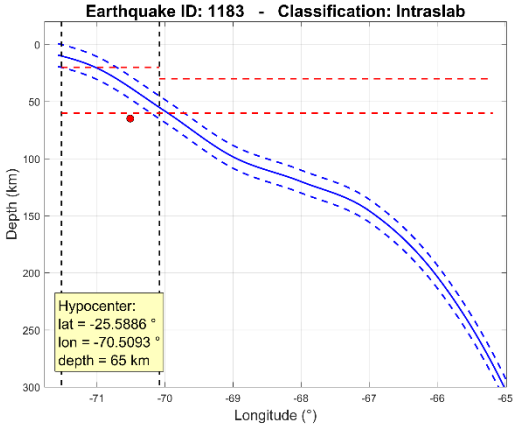

Figure B. 543: Event 1183

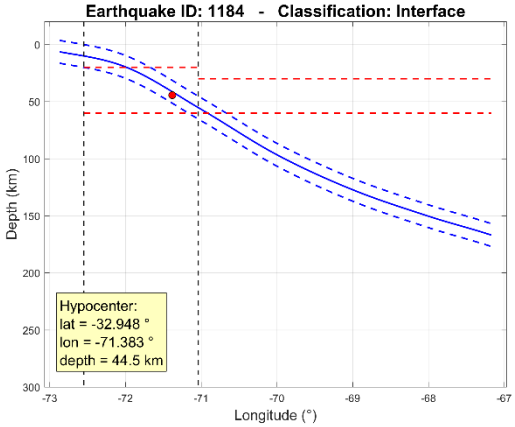

Figure B. 544: Event 1184

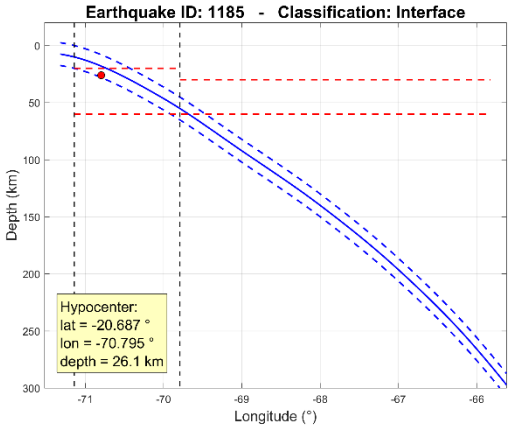

Figure B. 545: Event 1185

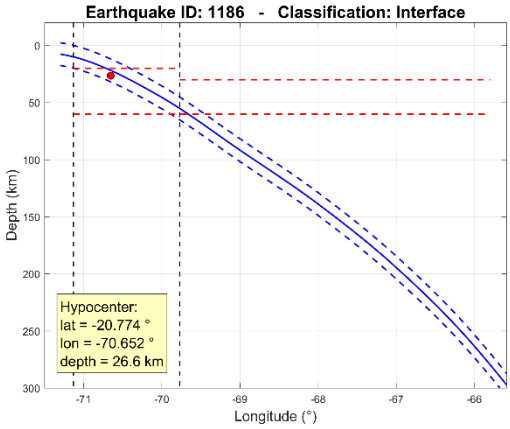

Figure B. 546: Event 1186

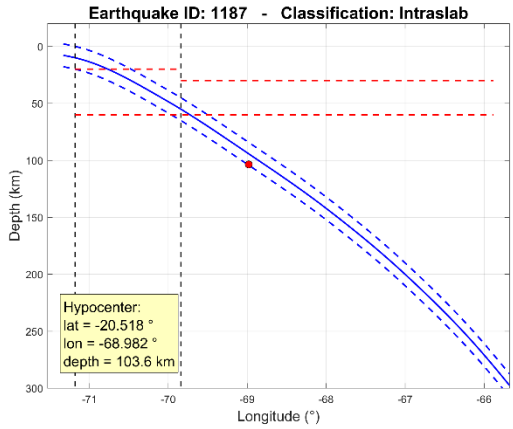

Figure B. 547: Event 1187

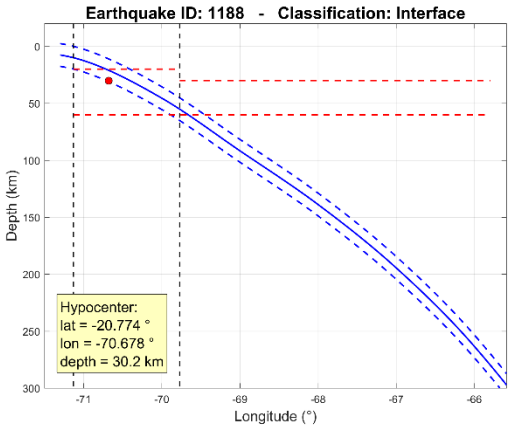

Figure B. 548: Event 1188

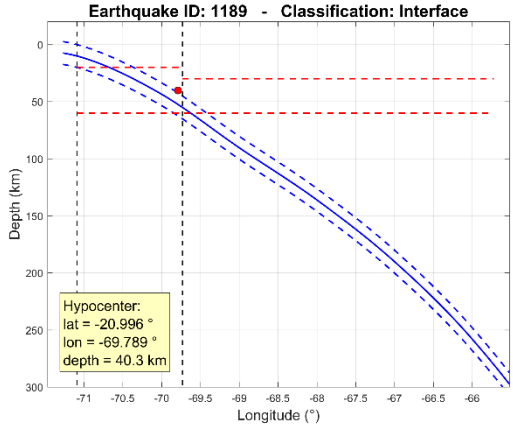

Figure B. 549: Event 1189

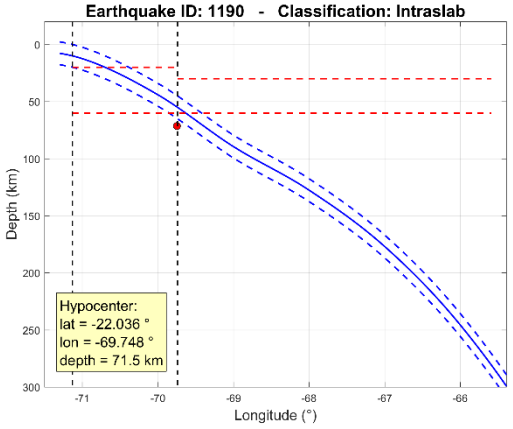

Figure B. 550: Event 1190

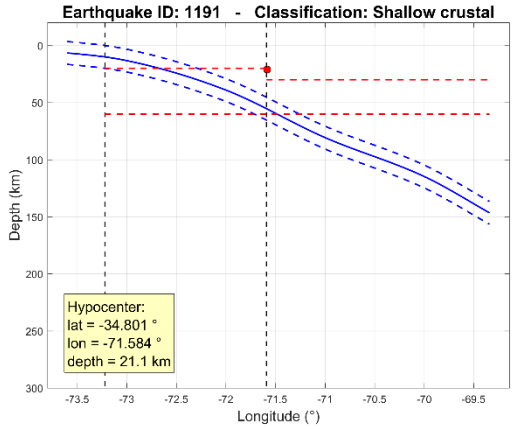

Figure B. 551: Event 1191

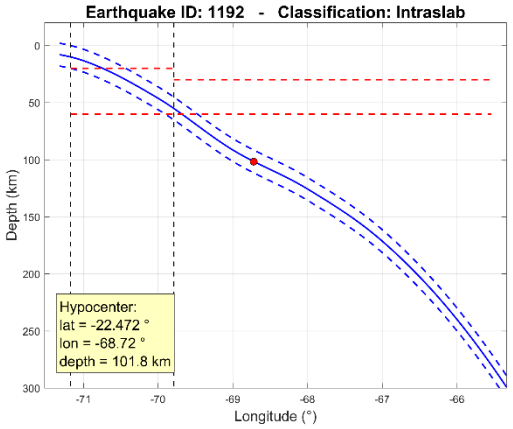

Figure B. 552: Event 1192

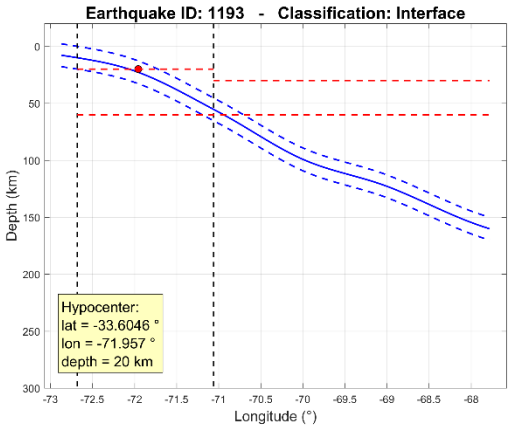

Figure B. 553: Event 1193

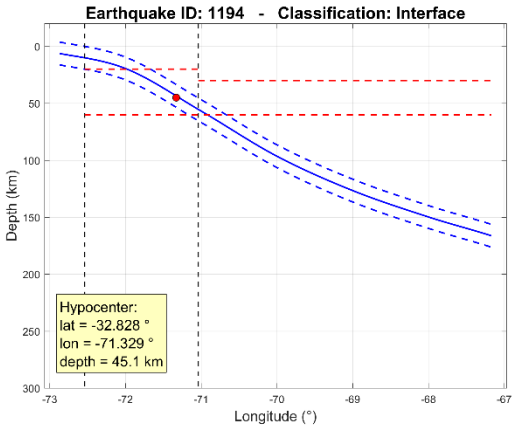

Figure B. 554: Event 1194

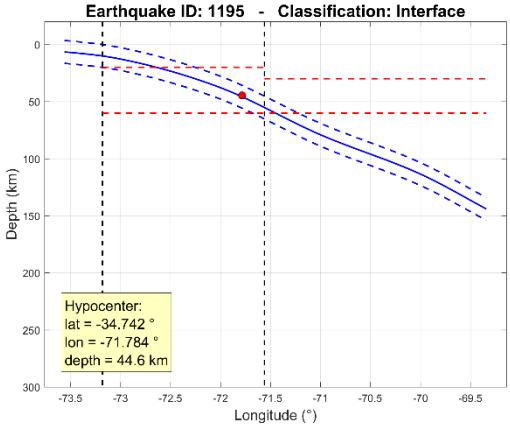

Figure B. 555: Event 1195

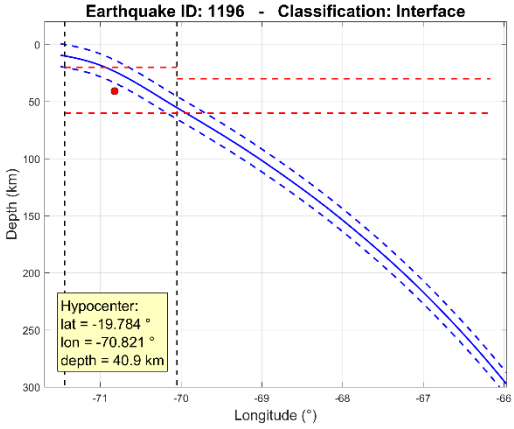

Figure B. 556: Event 1196

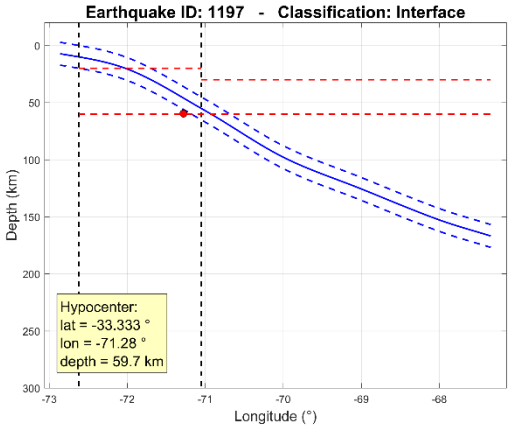

Figure B. 557: Event 1197

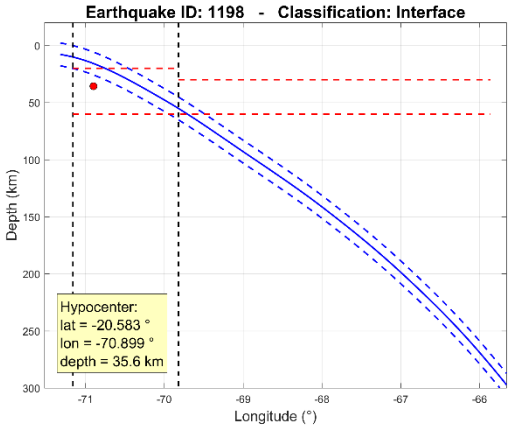

Figure B. 558: Event 1198

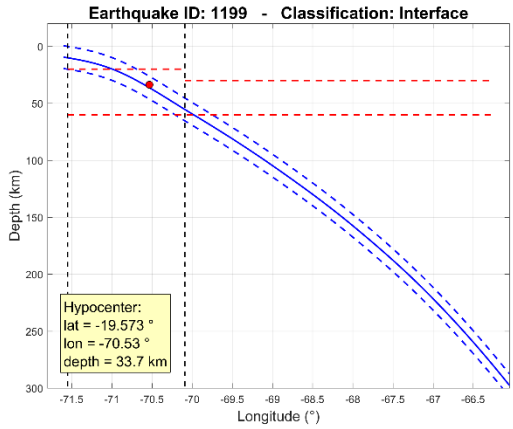

Figure B. 559: Event 1199

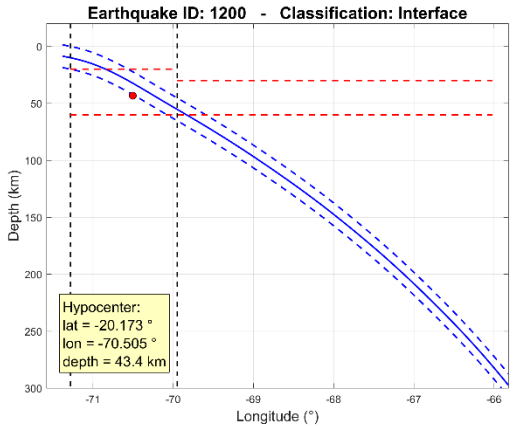

Figure B. 560: Event 1200

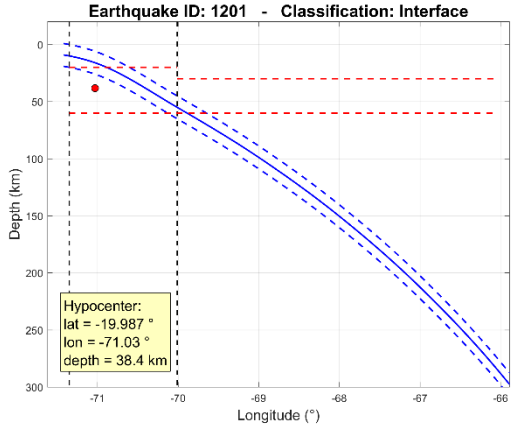

Figure B. 561: Event 1201

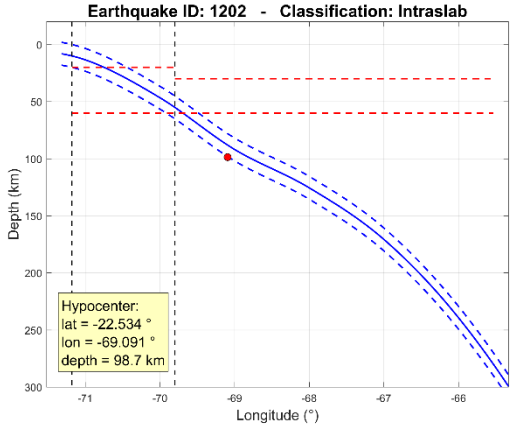

Figure B. 562: Event 1202

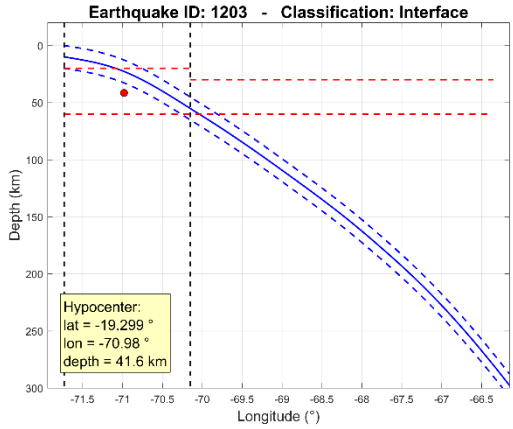

Figure B. 563: Event 1203

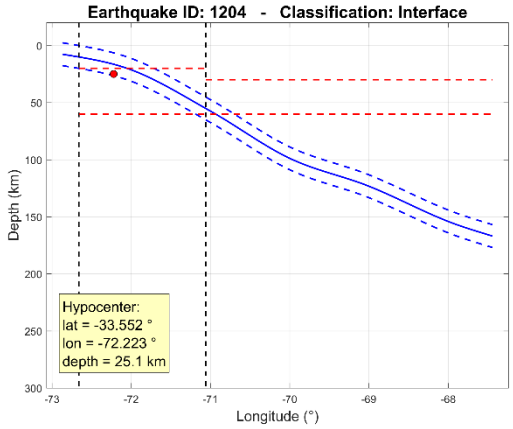

Figure B. 564: Event 1204

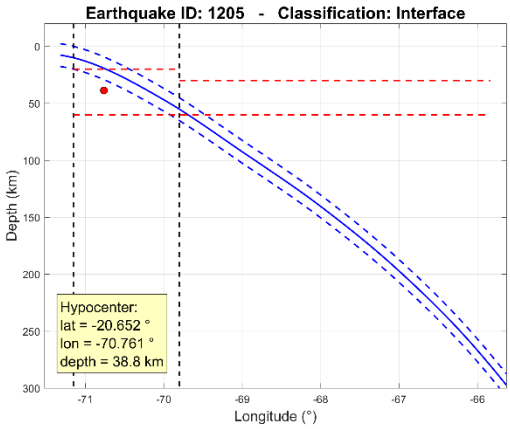

Figure B. 565: Event 1205

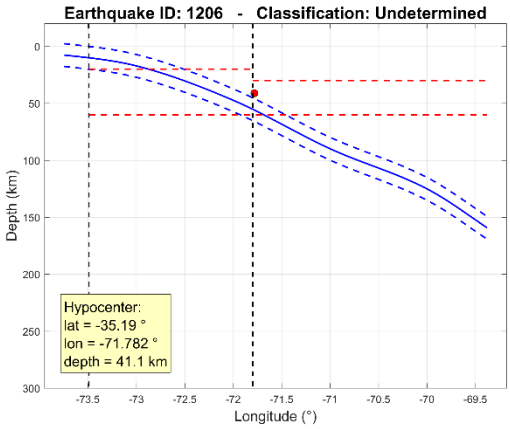

Figure B. 566: Event 1206

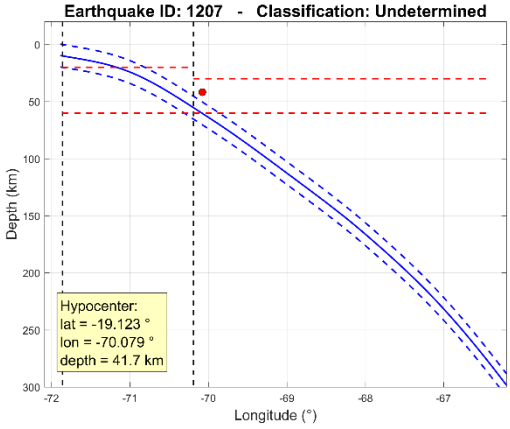

Figure B. 567: Event 1207

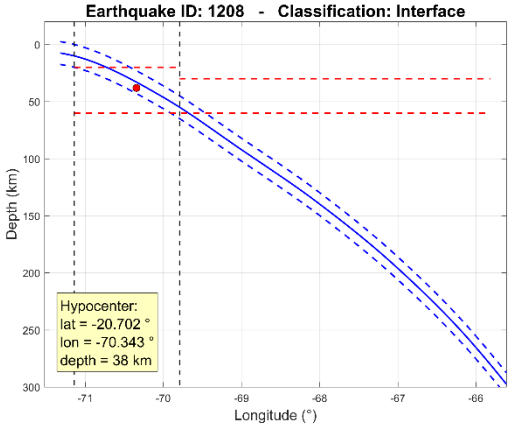

Figure B. 568: Event 1208

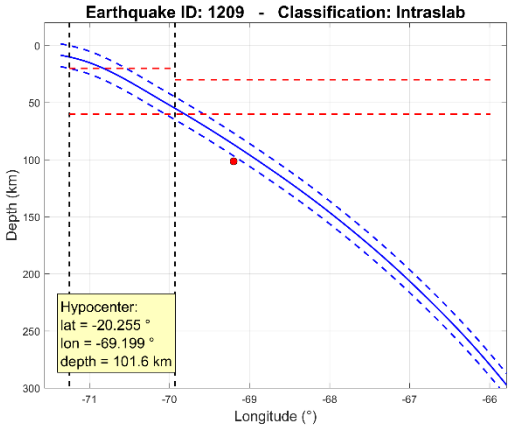

Figure B. 569: Event 1209

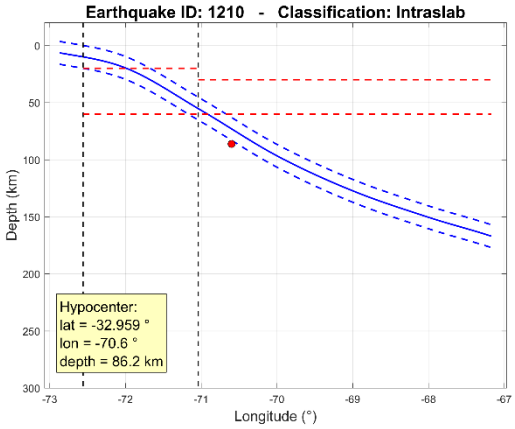

Figure B. 570: Event 1210

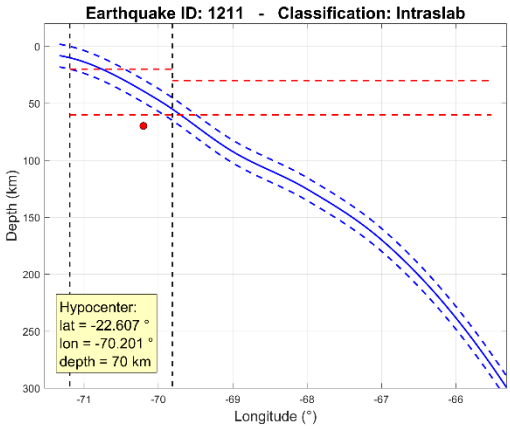

Figure B. 571: Event 1211

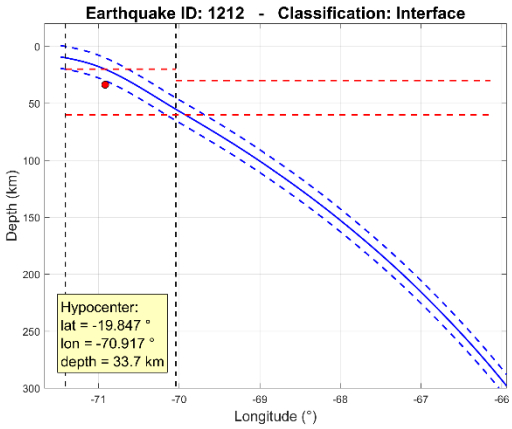

Figure B. 572: Event 1212

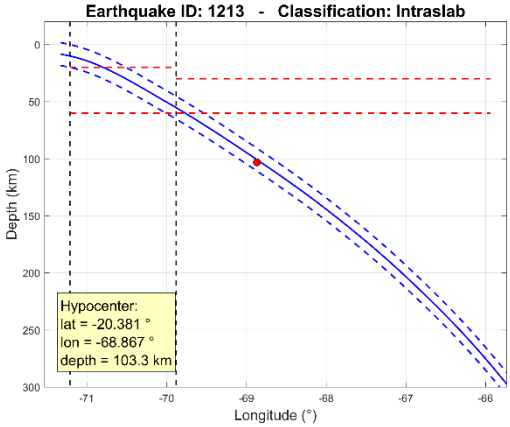

Figure B. 573: Event 1213

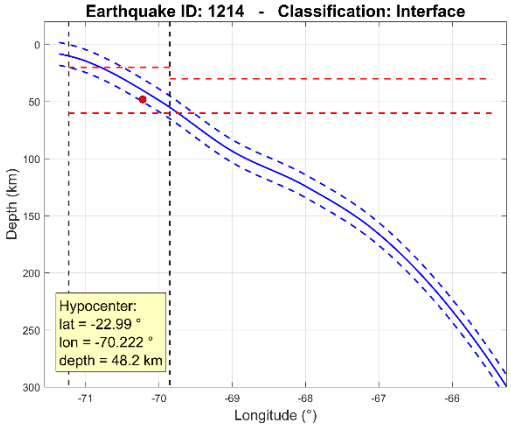

Figure B. 574: Event 1214

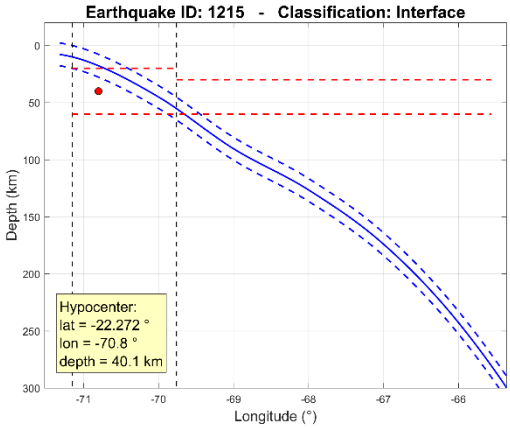

Figure B. 575: Event 1215

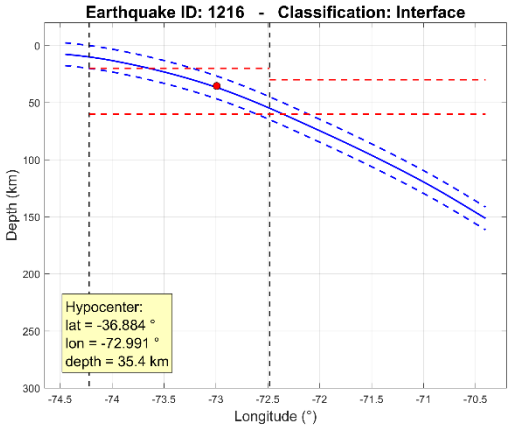

Figure B. 576: Event 1216

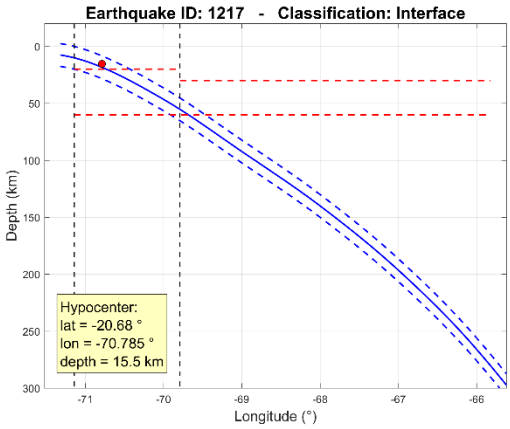

Figure B. 577: Event 1217

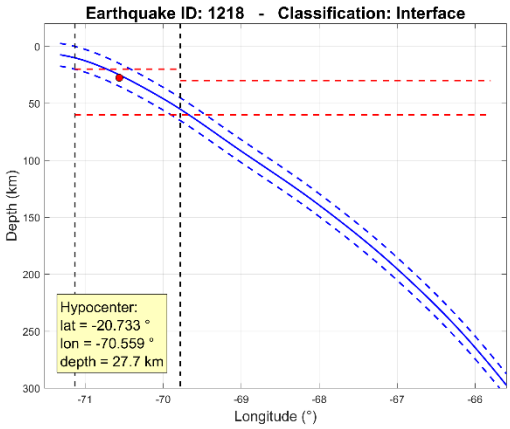

Figure B. 578: Event 1218

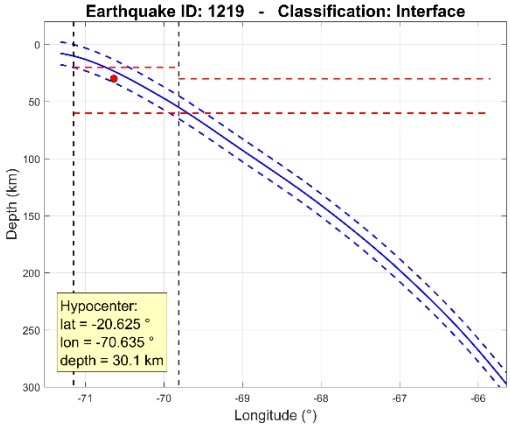

Figure B. 579: Event 1219

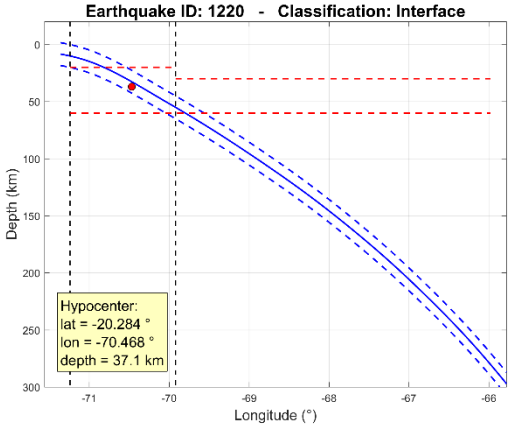

Figure B. 580: Event 1220

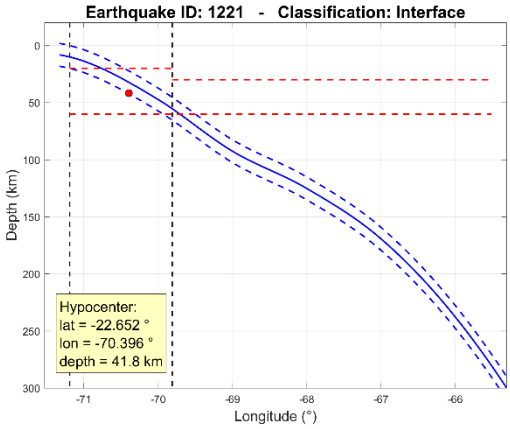

Figure B. 581: Event 1221

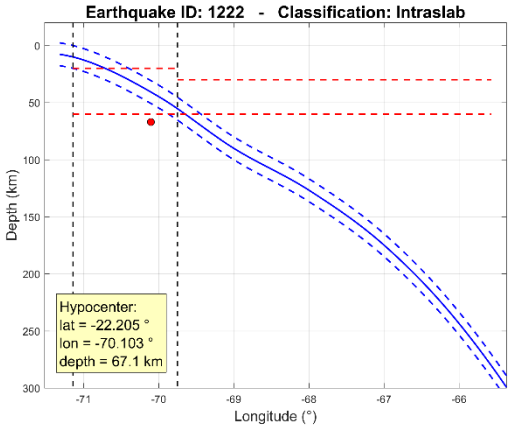

Figure B. 582: Event 1222

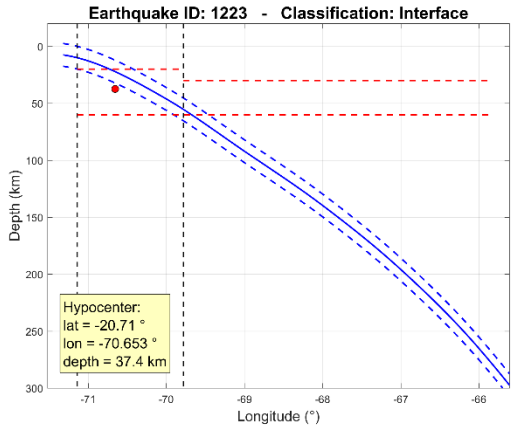

Figure B. 583: Event 1223

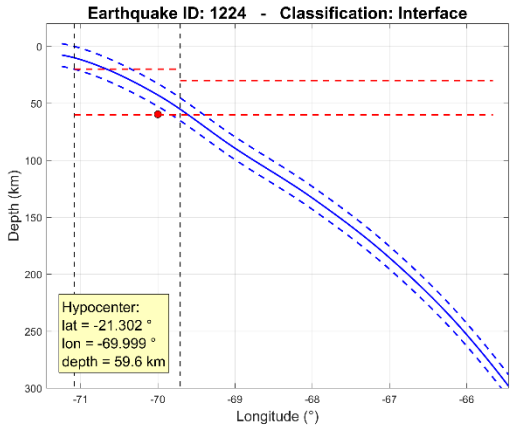

Figure B. 584: Event 1224

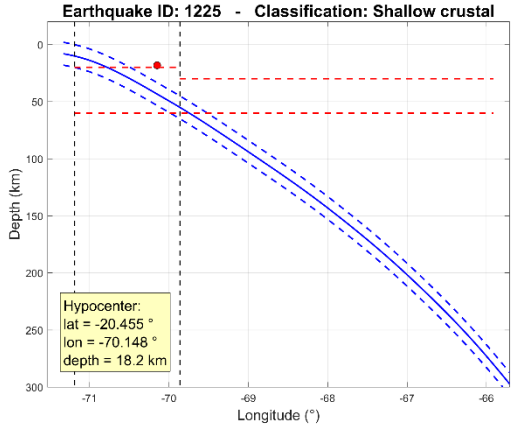

Figure B. 585: Event 1225

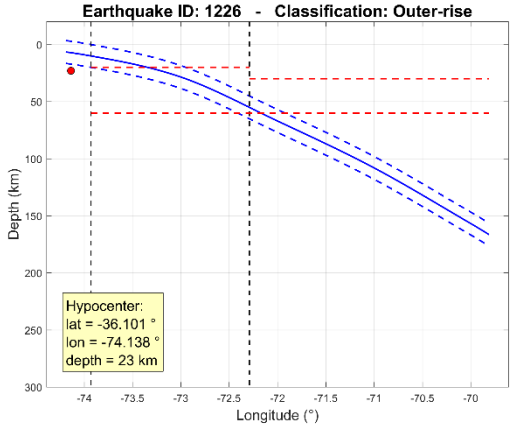

Figure B. 586: Event 1226

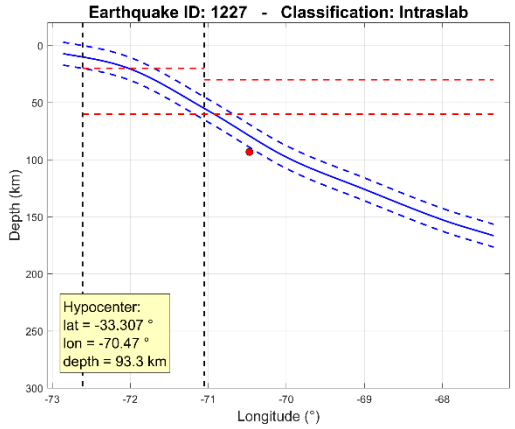

Figure B. 587: Event 1227

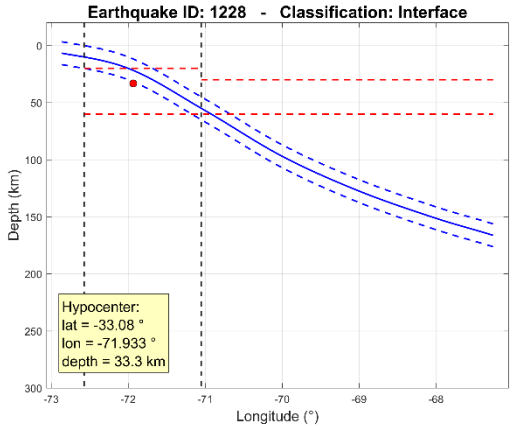

Figure B. 588: Event 1228

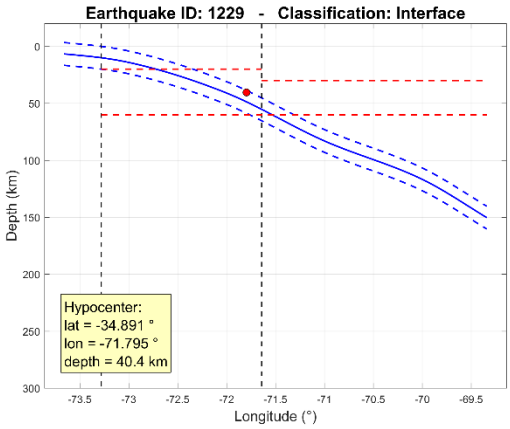

Figure B. 589: Event 1229

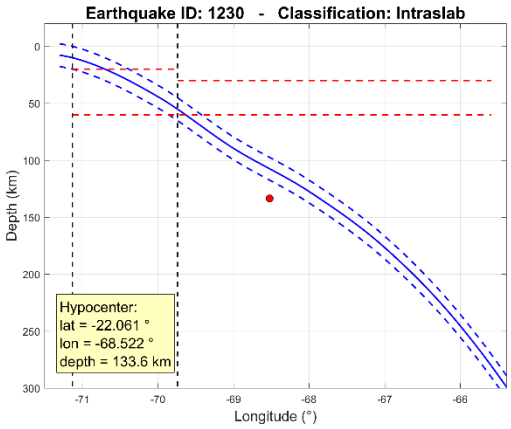

Figure B. 590: Event 1230

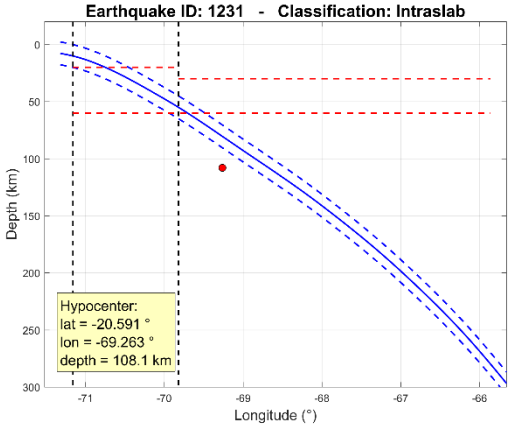

Figure B. 591: Event 1231

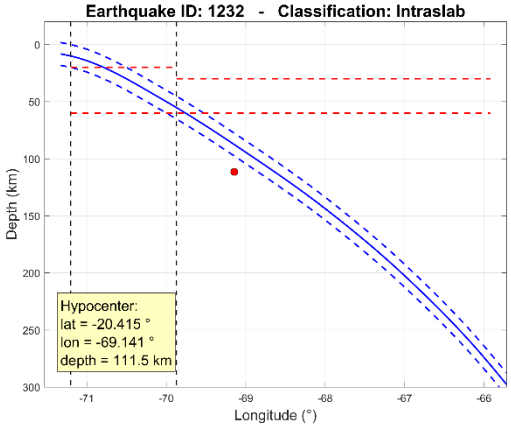

Figure B. 592: Event 1232

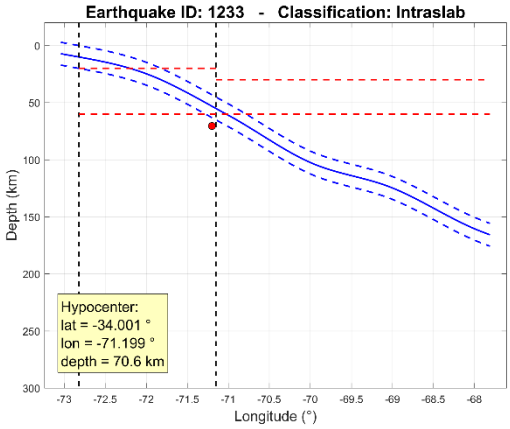

Figure B. 593: Event 1233

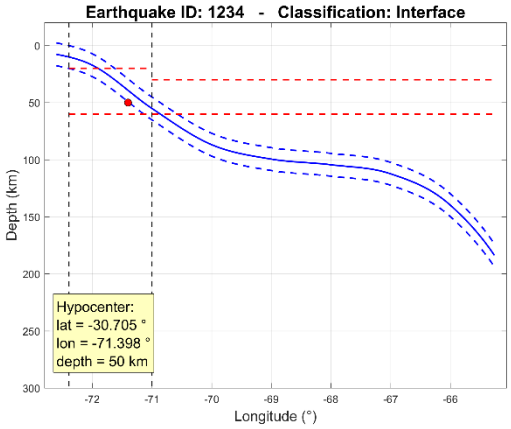

Figure B. 594: Event 1234

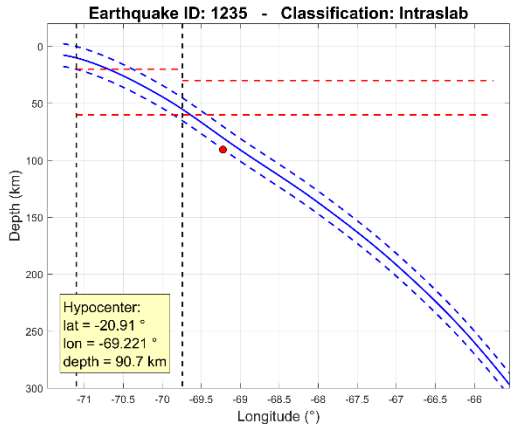

Figure B. 595: Event 1235

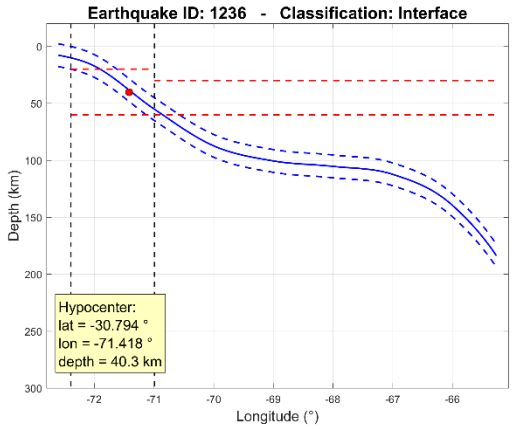

Figure B. 596: Event 1236

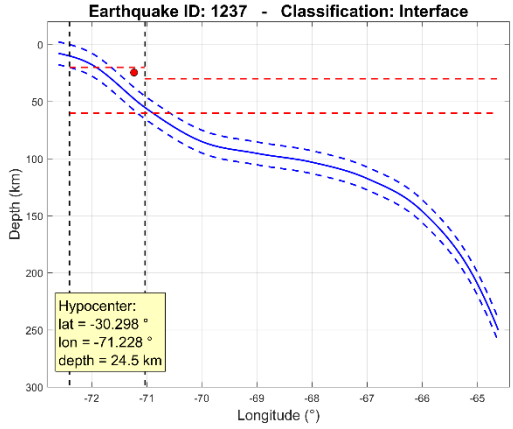

Figure B. 597: Event 1237

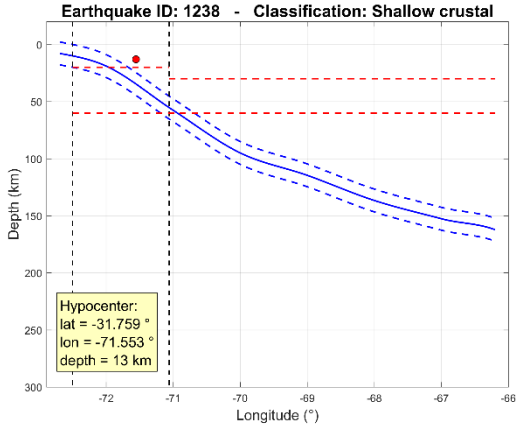

Figure B. 598: Event 1238

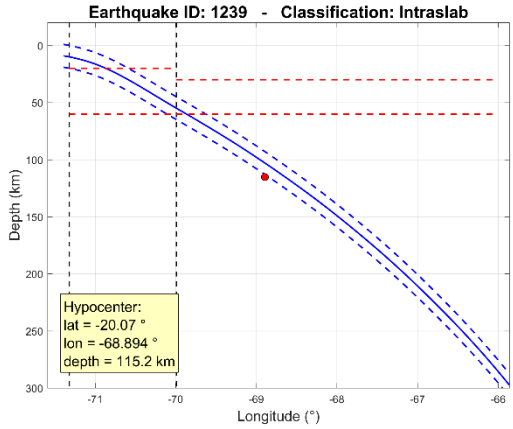

Figure B. 599: Event 1239

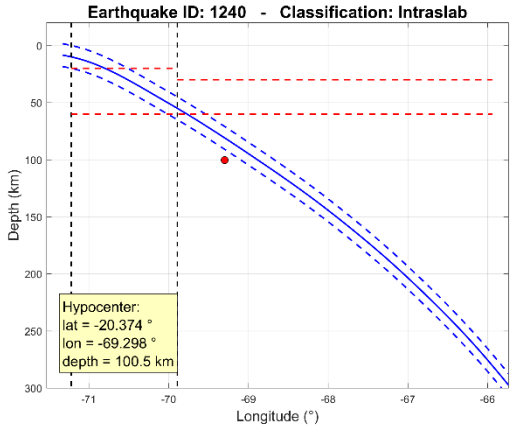

Figure B. 600: Event 1240

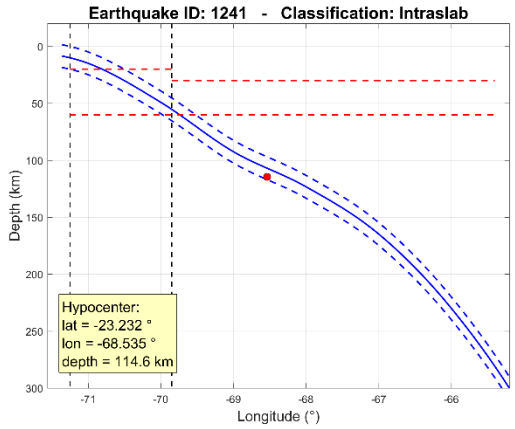

Figure B. 601: Event 1241

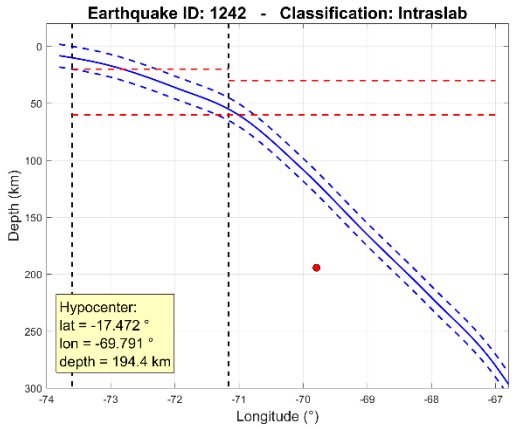

Figure B. 602: Event 1242

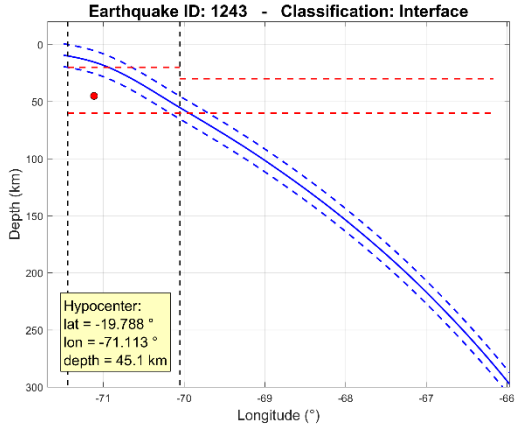

Figure B. 603: Event 1243

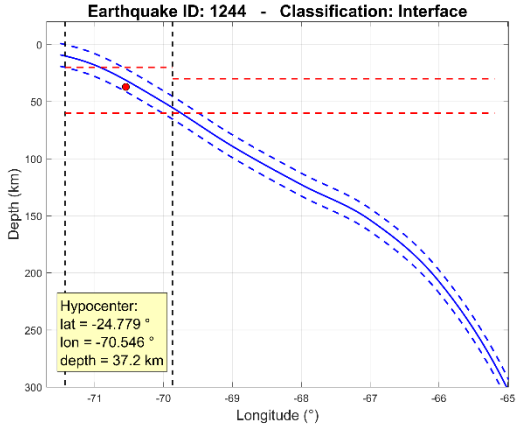

Figure B. 604: Event 1244

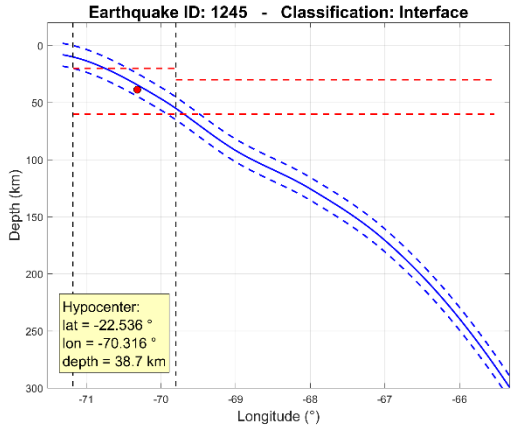

Figure B. 605: Event 1245

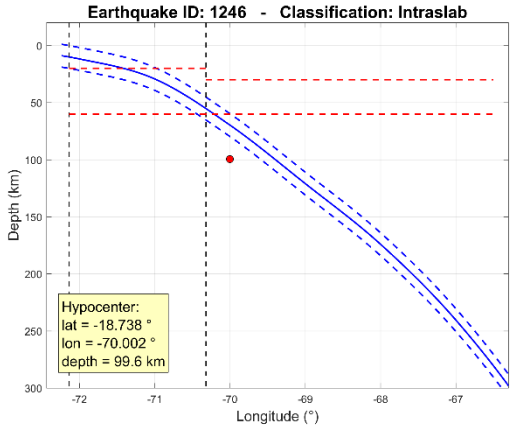

Figure B. 606: Event 1246

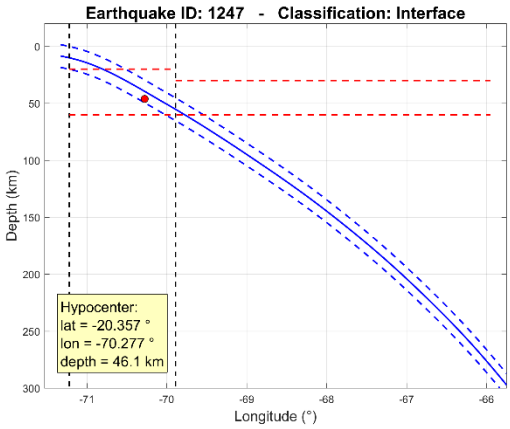

Figure B. 607: Event 1247

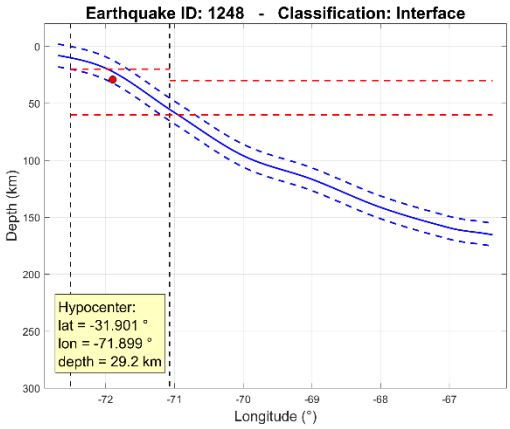

Figure B. 608: Event 1248

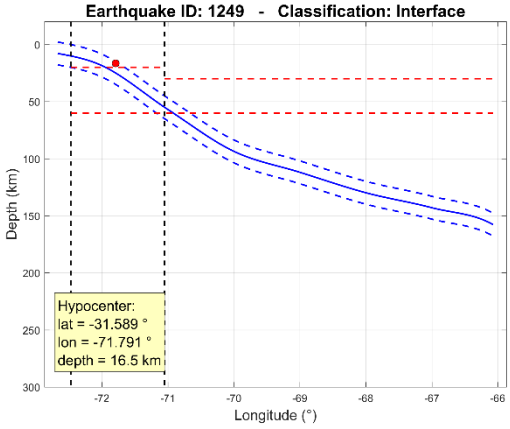

Figure B. 609: Event 1249

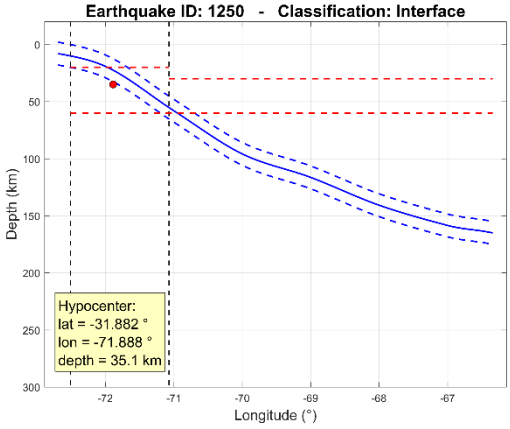

Figure B. 610: Event 1250

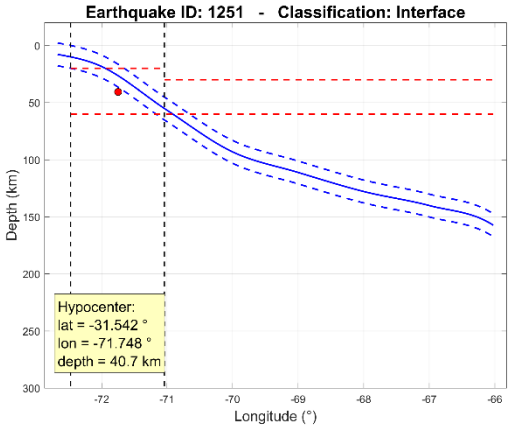

Figure B. 611: Event 1251

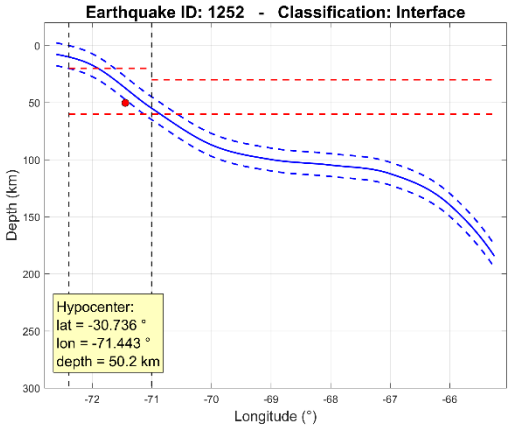

Figure B. 612: Event 1252

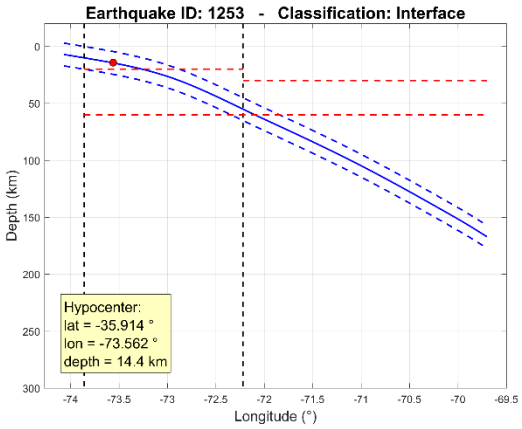

Figure B. 613: Event 1253

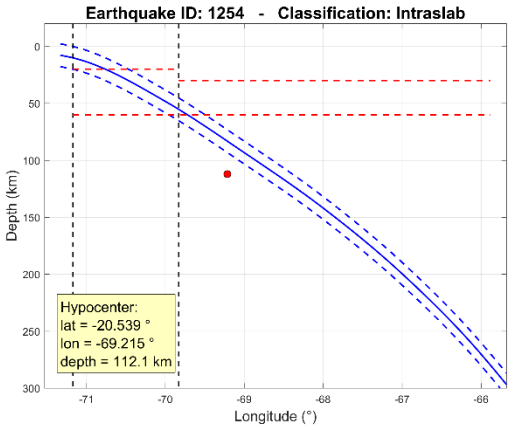

Figure B. 614: Event 1254

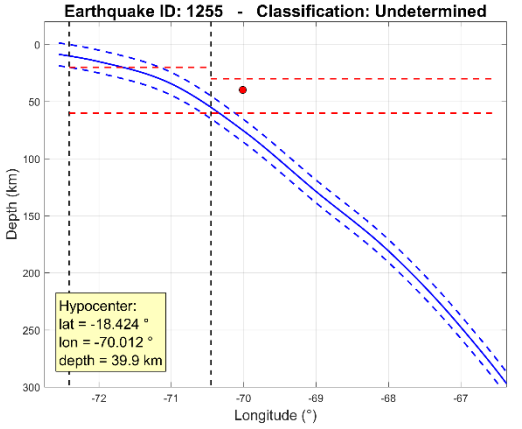

Figure B. 615: Event 1255

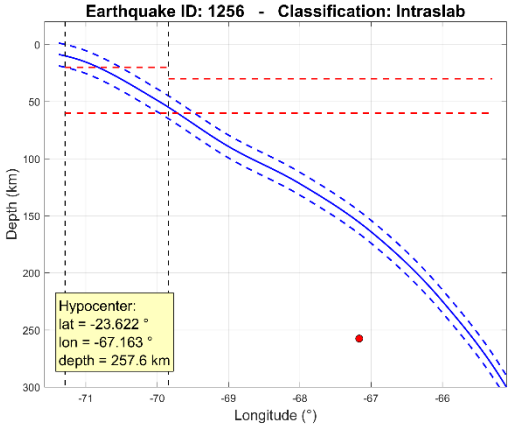

Figure B. 616: Event 1256

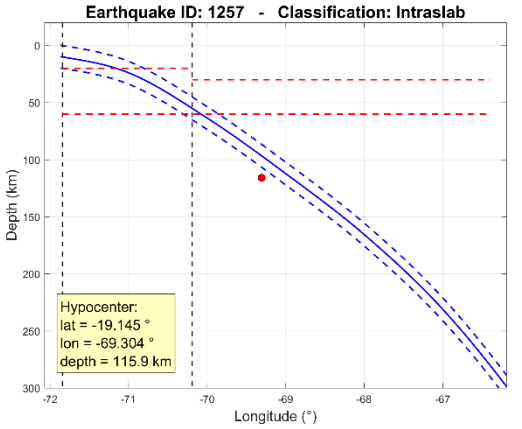

Figure B. 617: Event 1257

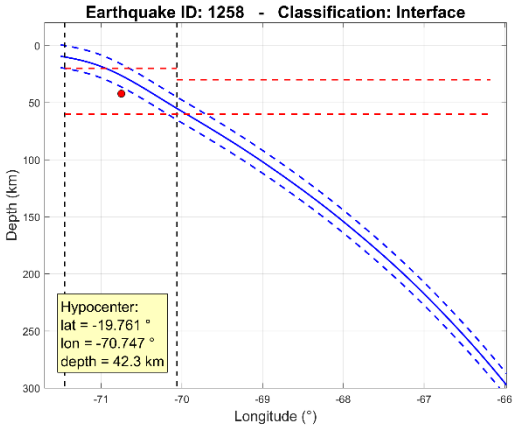

Figure B. 618: Event 1258

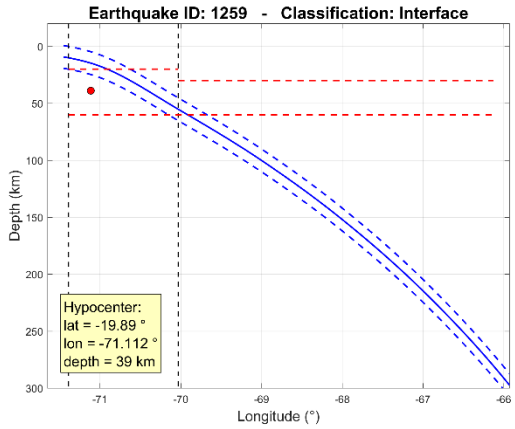

Figure B. 619: Event 1259

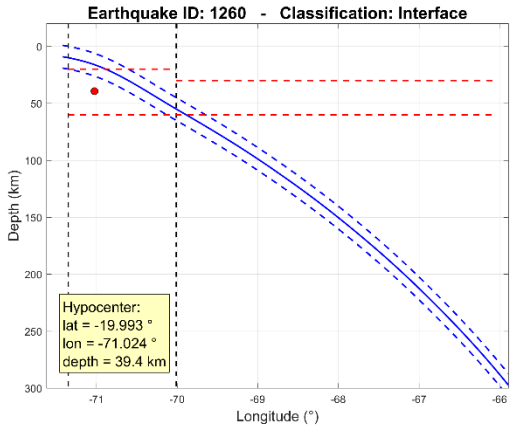

Figure B. 620: Event 1260

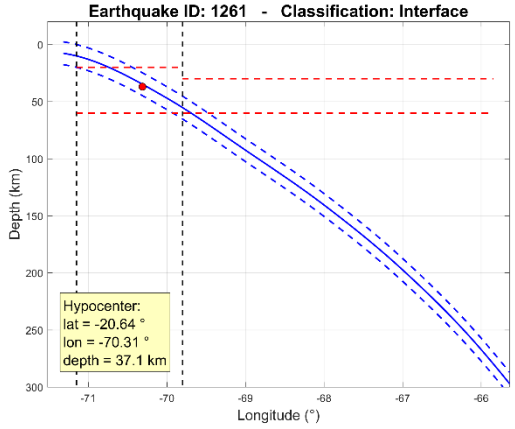

Figure B. 621: Event 1261

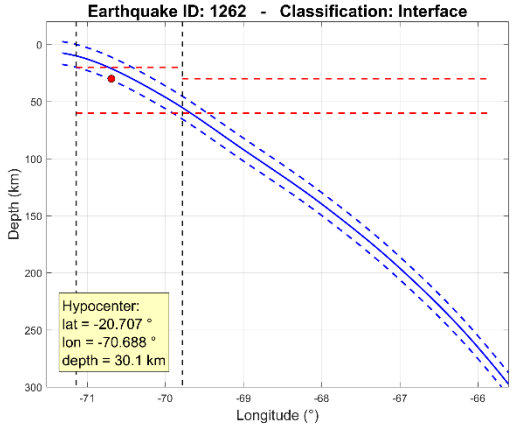

Figure B. 622: Event 1262

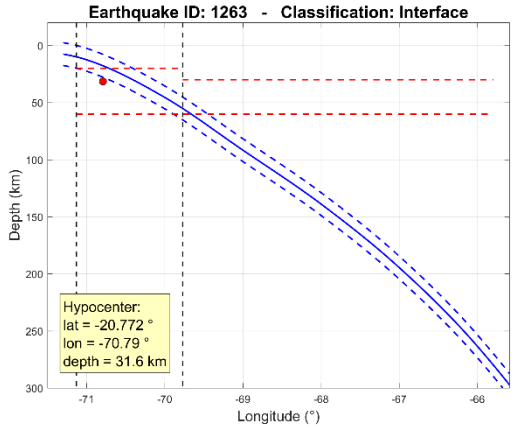

Figure B. 623: Event 1263

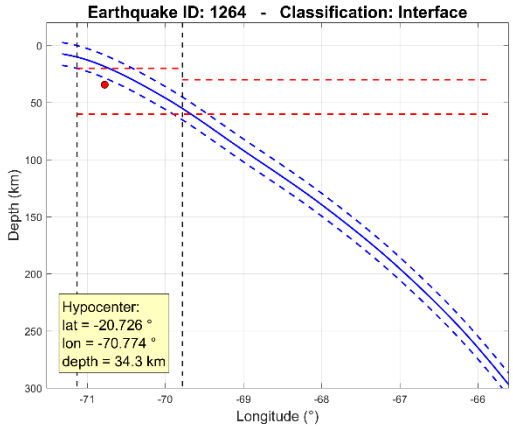

Figure B. 624: Event 1264

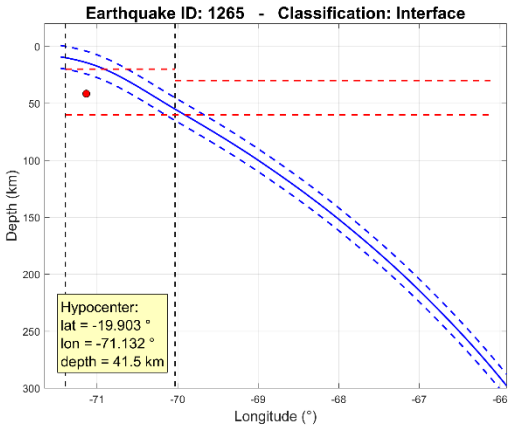

Figure B. 625: Event 1265

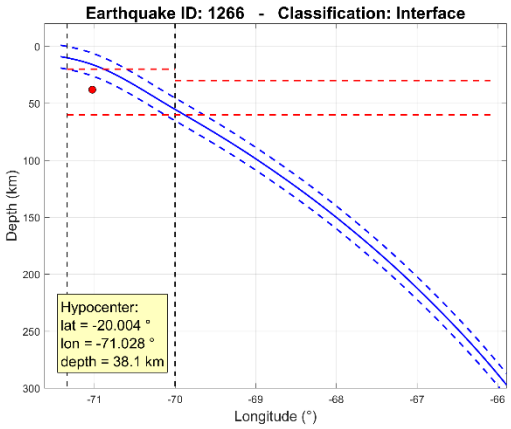

Figure B. 626: Event 1266

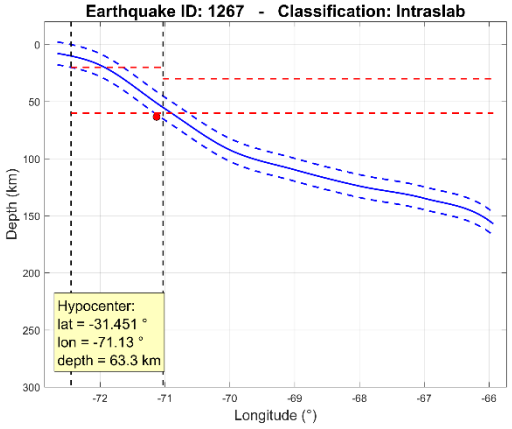

Figure B. 627: Event 1267

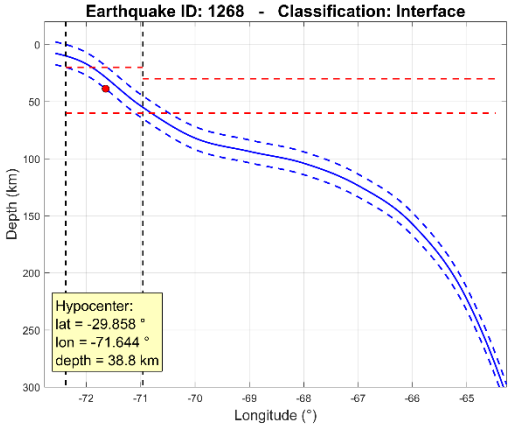

Figure B. 628: Event 1268

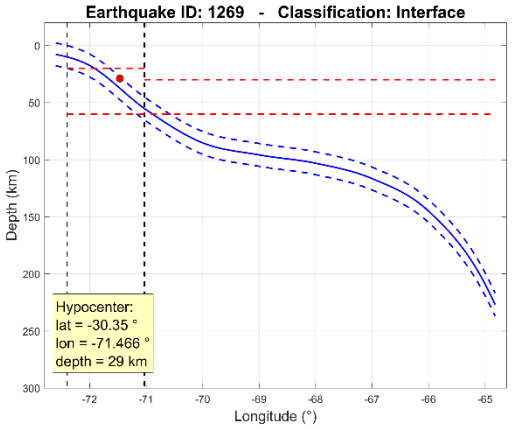

Figure B. 629: Event 1269

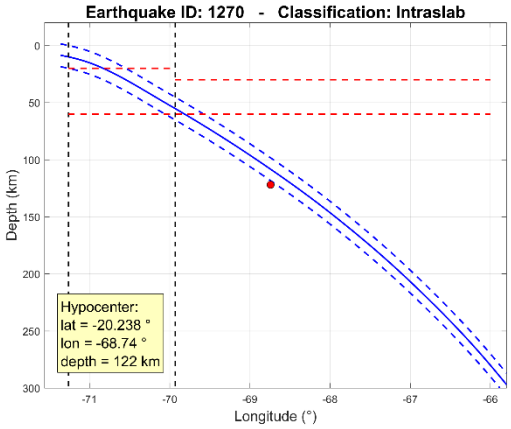

Figure B. 630: Event 1270

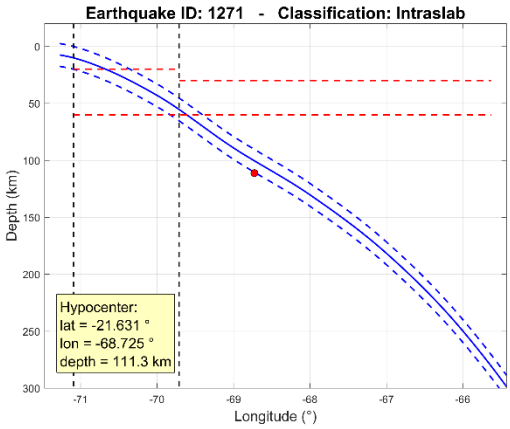

Figure B. 631: Event 1271

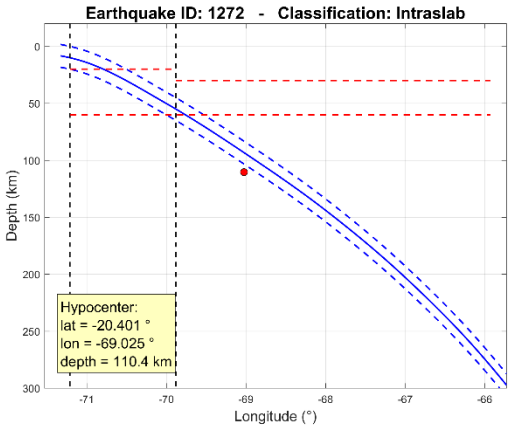

Figure B. 632: Event 1272

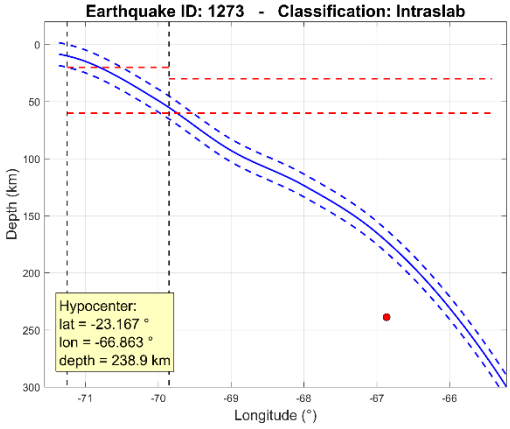

Figure B. 633: Event 1273

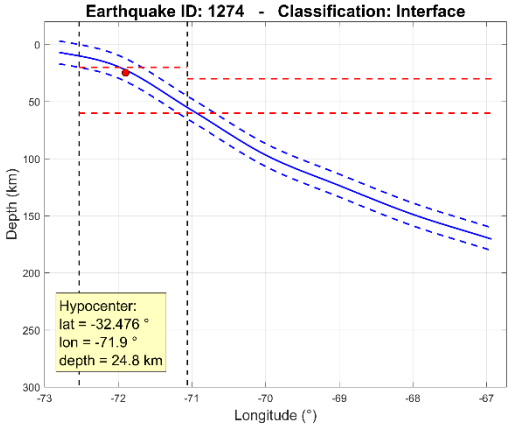

Figure B. 634: Event 1274

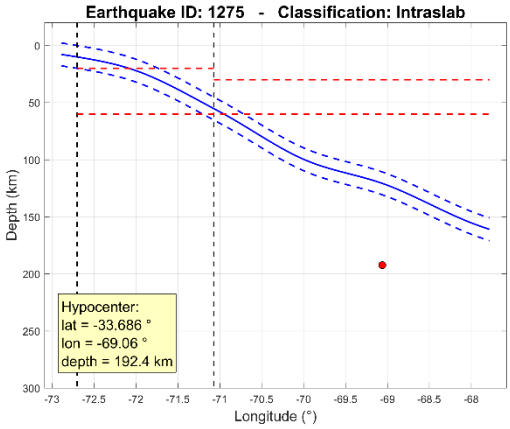

Figure B. 635: Event 1275

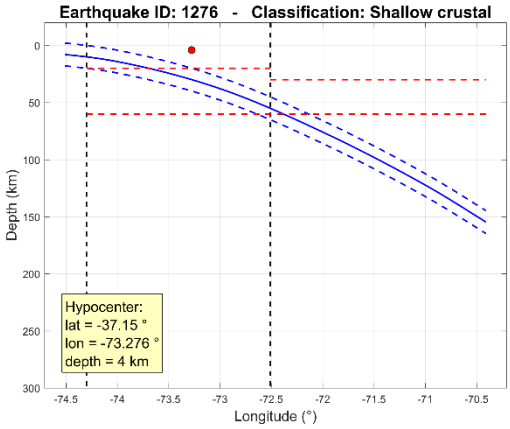

Figure B. 636: Event 1276

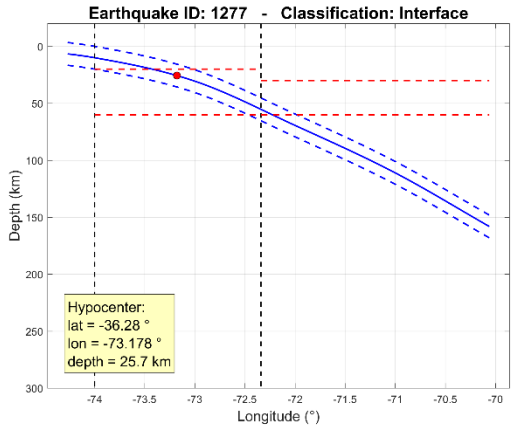

Figure B. 637: Event 1277

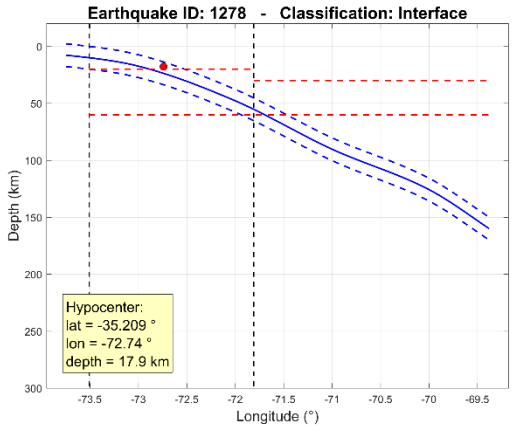

Figure B. 638: Event 1278

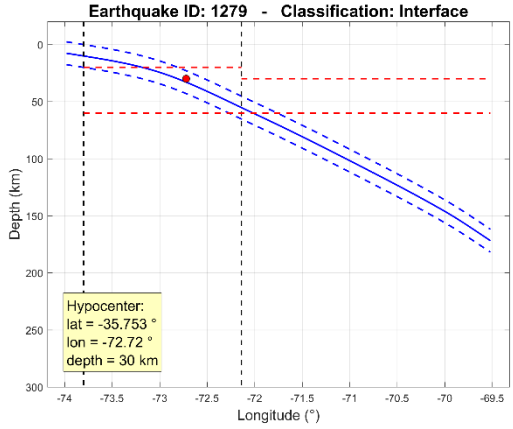

Figure B. 639: Event 1279

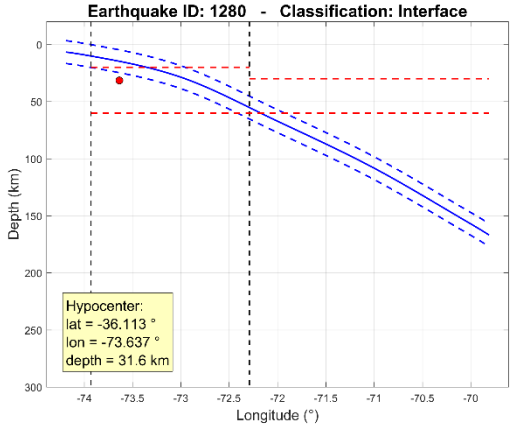

Figure B. 640: Event 1280

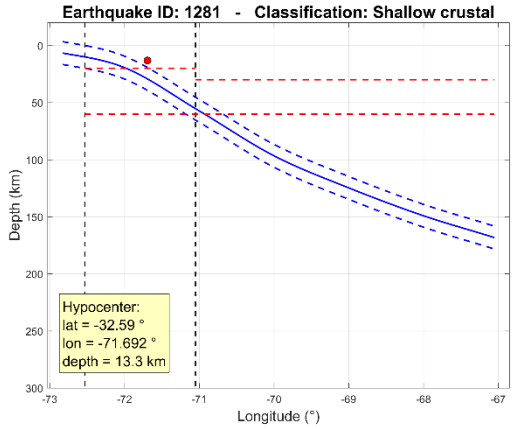

Figure B. 641: Event 1281

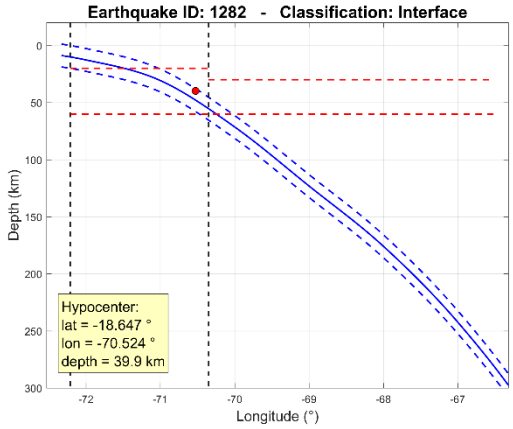

Figure B. 642: Event 1282

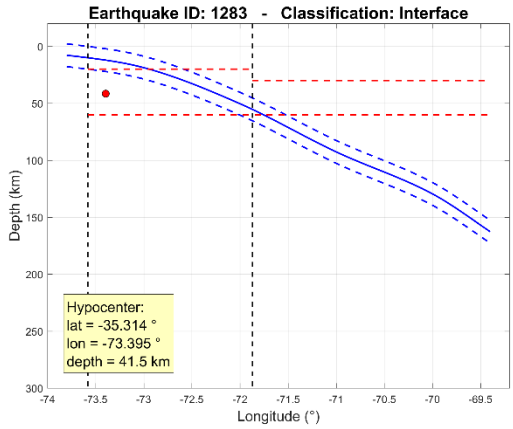

Figure B. 643: Event 1283

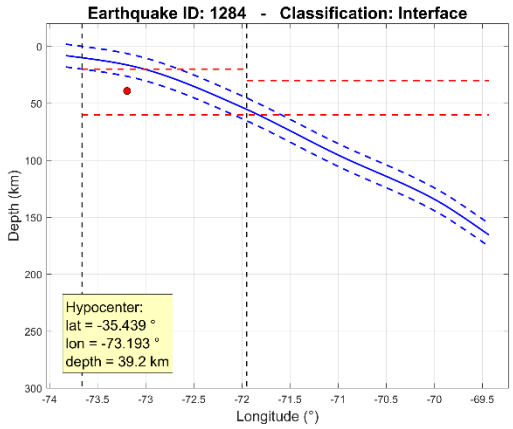

Figure B. 644: Event 1284

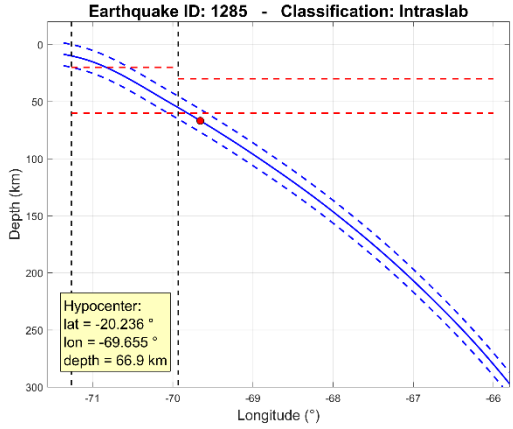

Figure B. 645: Event 1285

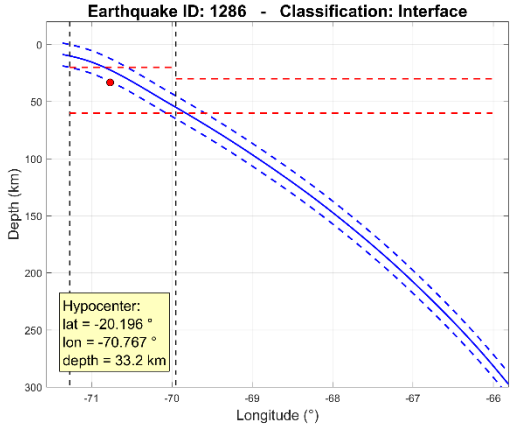

Figure B. 646: Event 1286

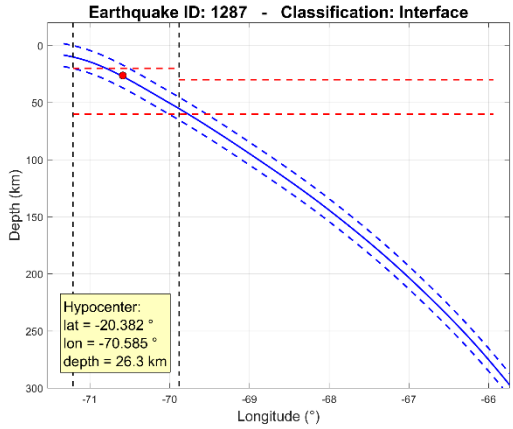

Figure B. 647: Event 1287

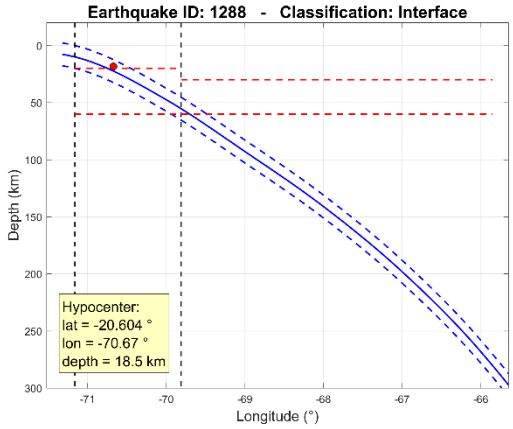

Figure B. 648: Event 1288

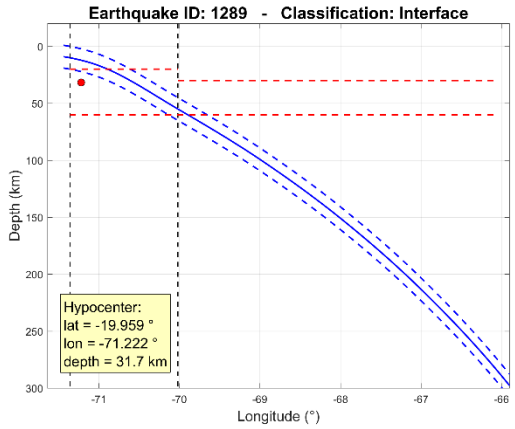

Figure B. 649: Event 1289

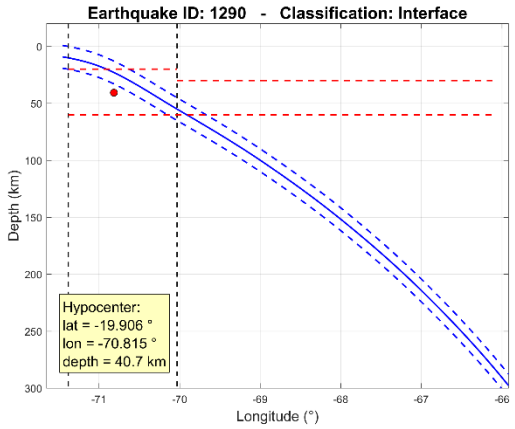

Figure B. 650: Event 1290

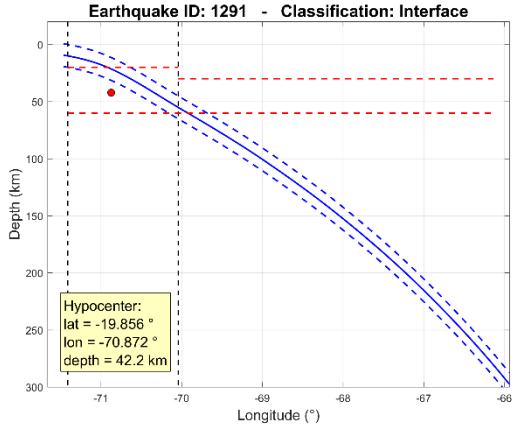

Figure B. 651: Event 1291

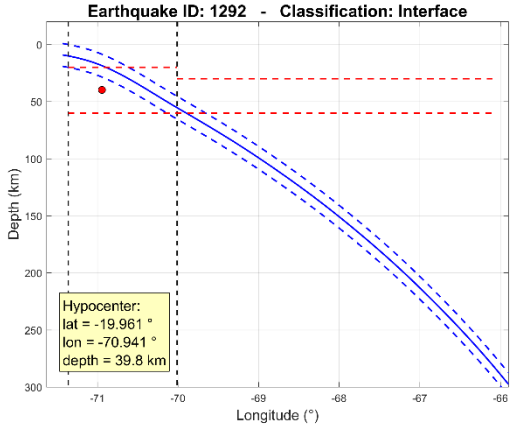

Figure B. 652: Event 1292

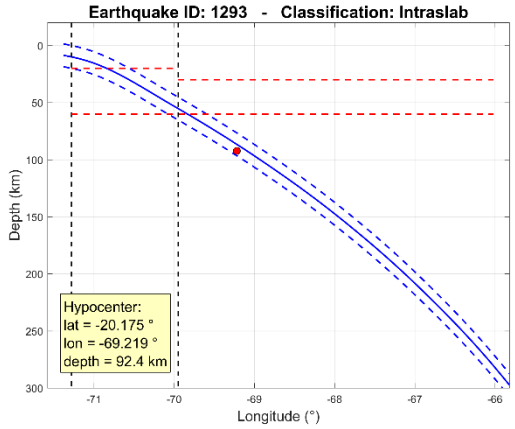

Figure B. 653: Event 1293

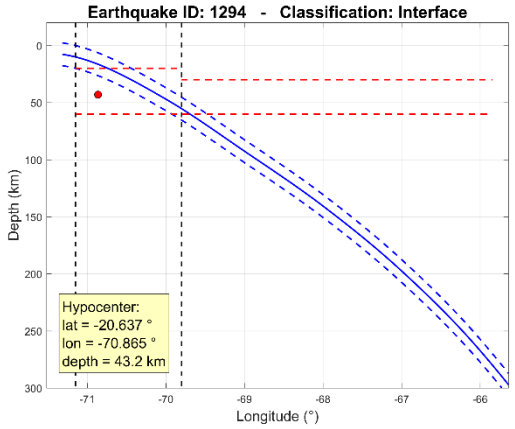

Figure B. 654: Event 1294

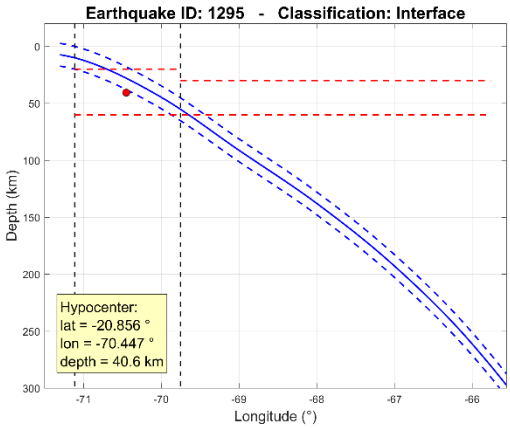

Figure B. 655: Event 1295

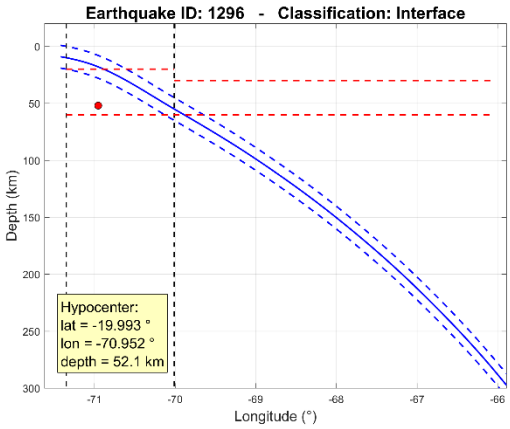

Figure B. 656: Event 1296

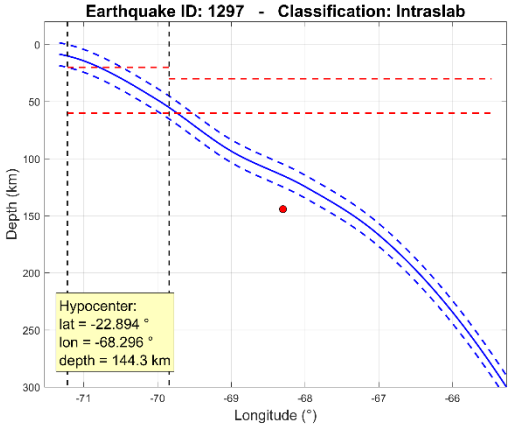

Figure B. 657: Event 1297

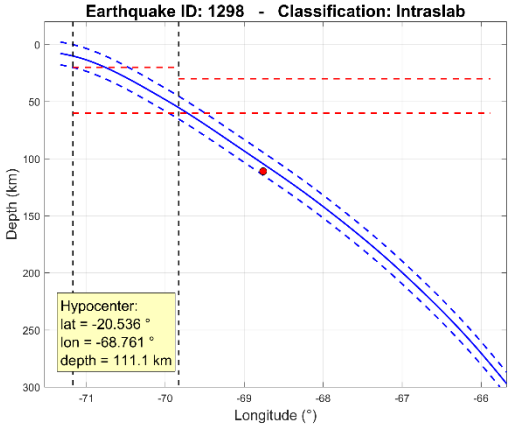

Figure B. 658: Event 1298

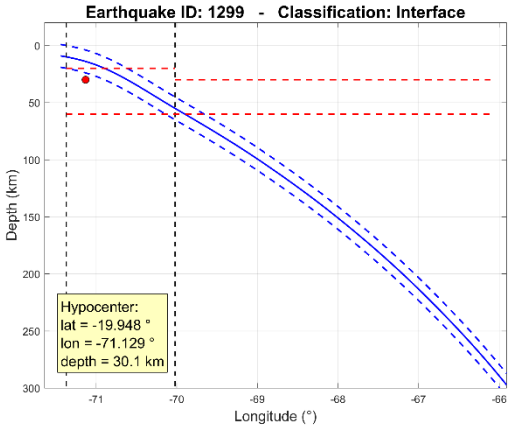

Figure B. 659: Event 1299

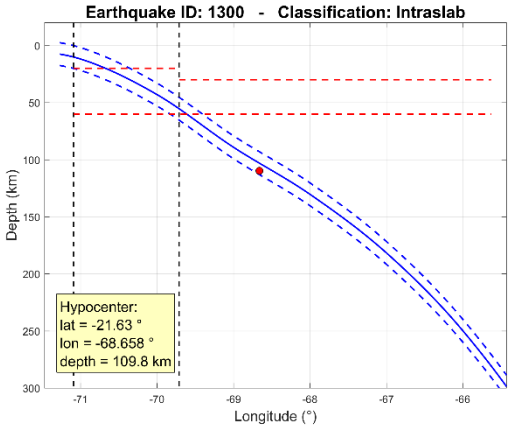

Figure B. 660: Event 1300

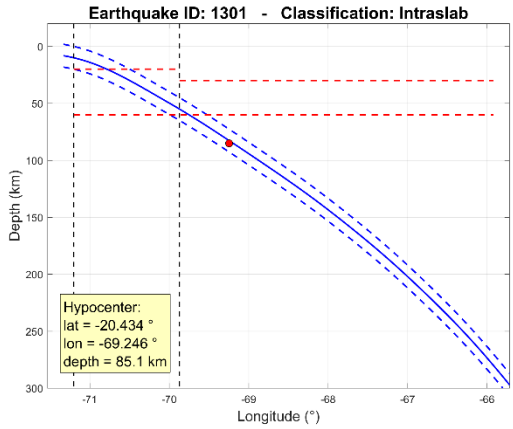

Figure B. 661: Event 1301

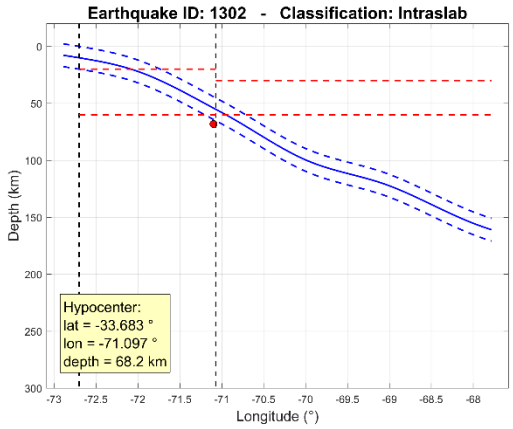

Figure B. 662: Event 1302

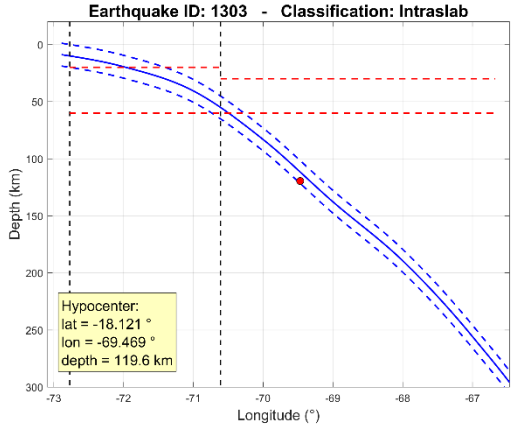

Figure B. 663: Event 1303

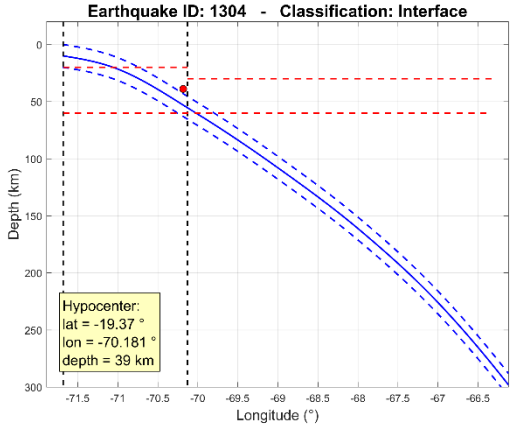

Figure B. 664: Event 1304

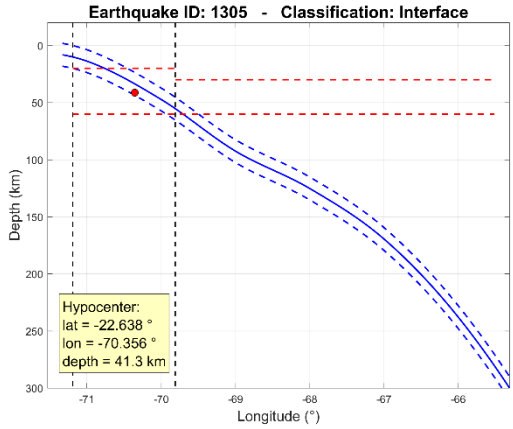

Figure B. 665: Event 1305

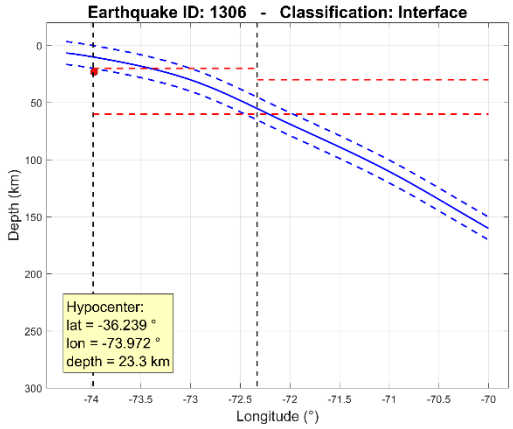

Figure B. 666: Event 1306

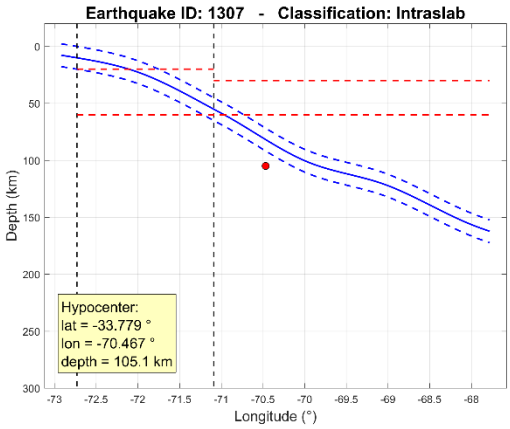

Figure B. 667: Event 1307

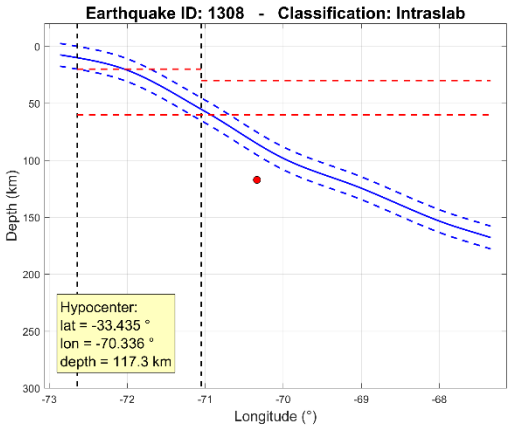

Figure B. 668: Event 1308

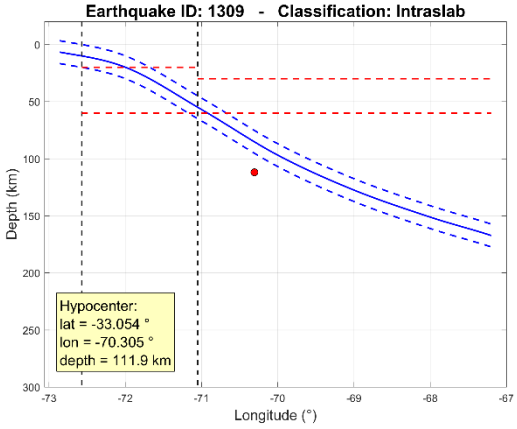

Figure B. 669: Event 1309

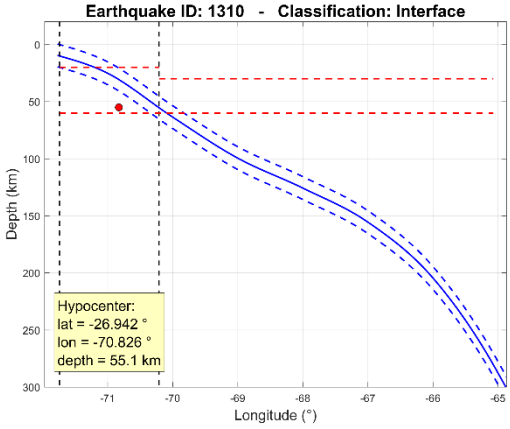

Figure B. 670: Event 1310

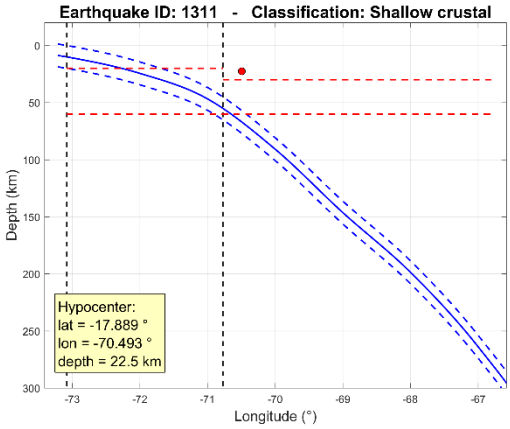

Figure B. 671: Event 1311

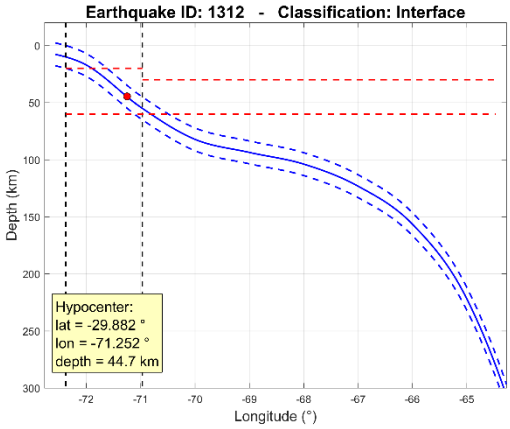

Figure B. 672: Event 1312

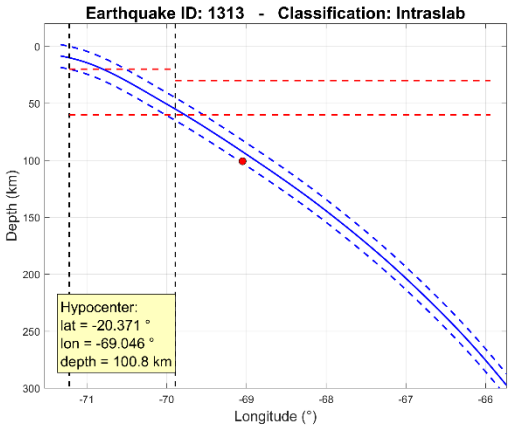

Figure B. 673: Event 1313

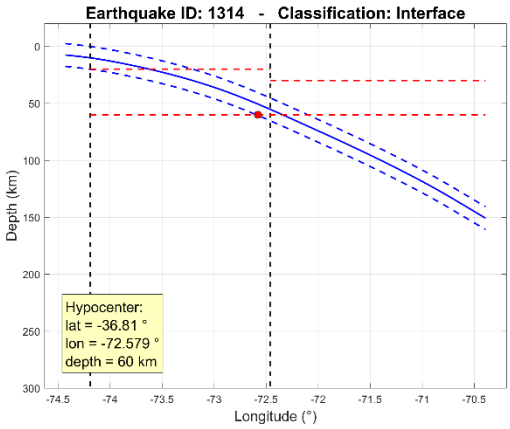

Figure B. 674: Event 1314

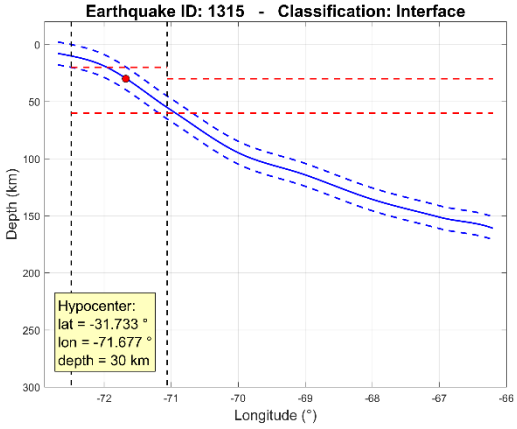

Figure B. 675: Event 1315

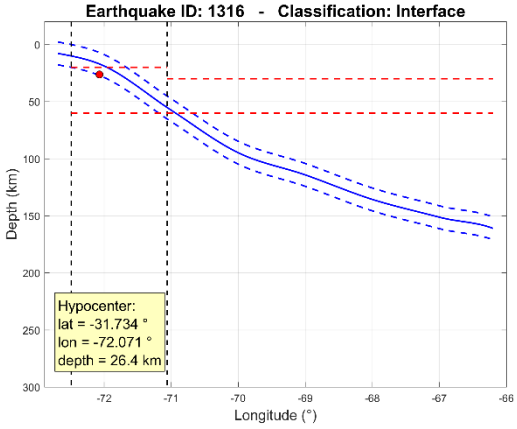

Figure B. 676: Event 1316

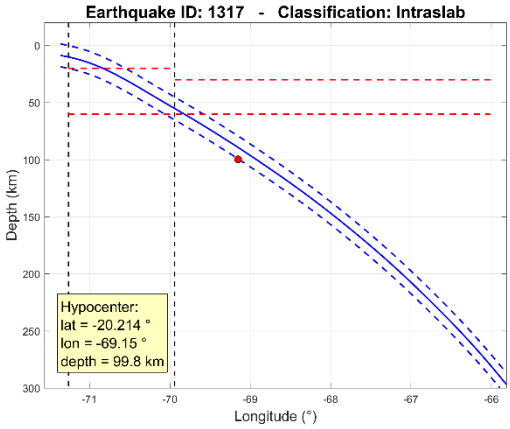

Figure B. 677: Event 1317

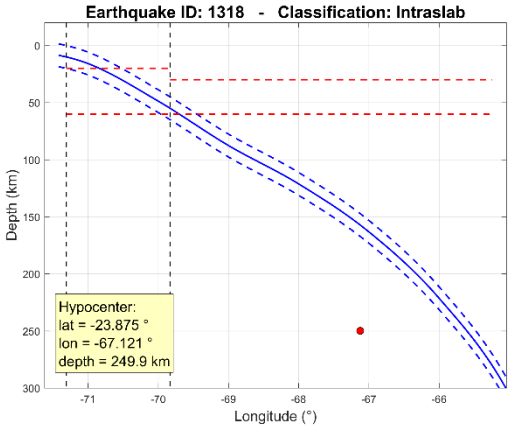

Figure B. 678: Event 1318

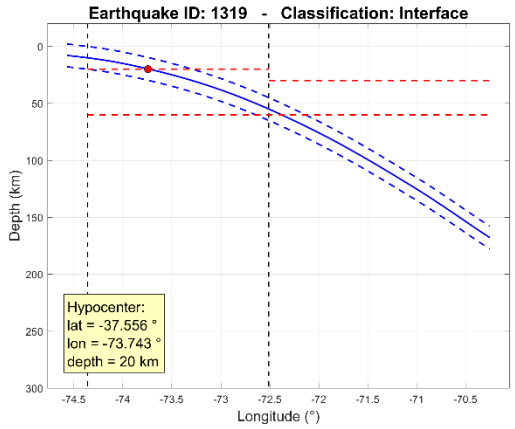

Figure B. 679: Event 1319

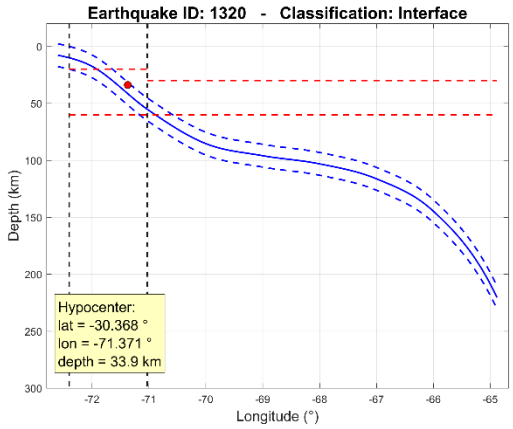

Figure B. 680: Event 1320

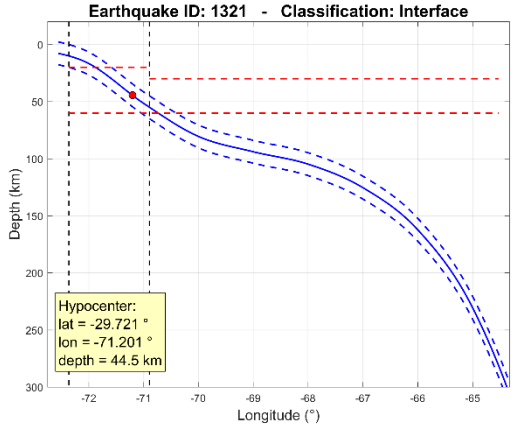

Figure B. 681: Event 1321

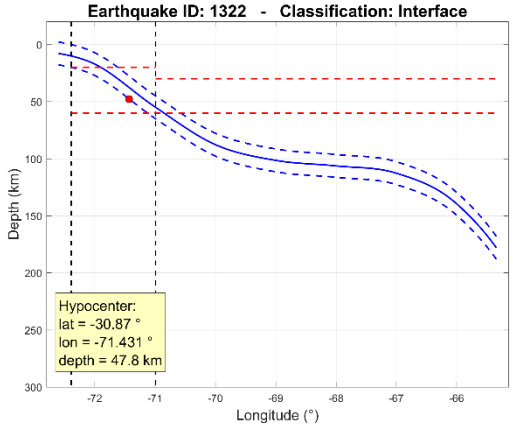

Figure B. 682: Event 1322

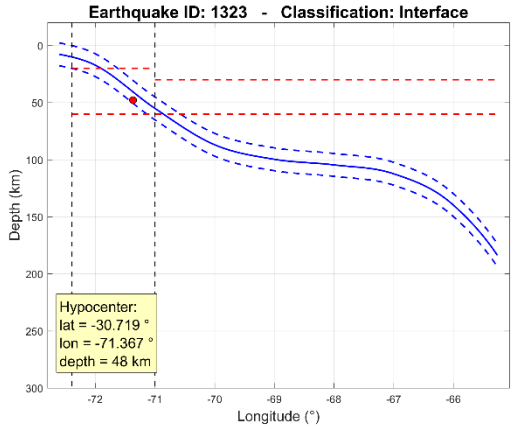

Figure B. 683: Event 1323

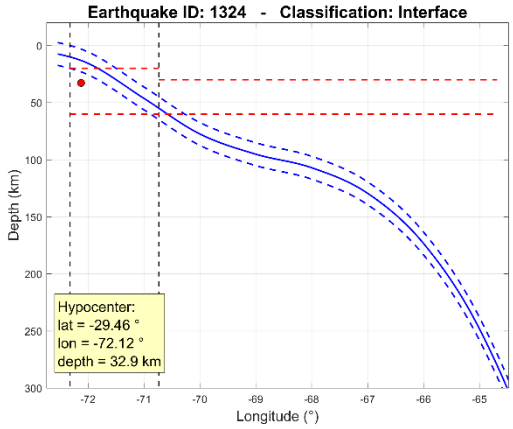

Figure B. 684: Event 1324

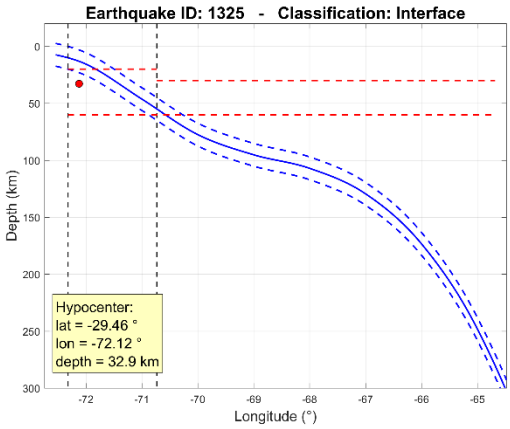

Figure B. 685: Event 1325

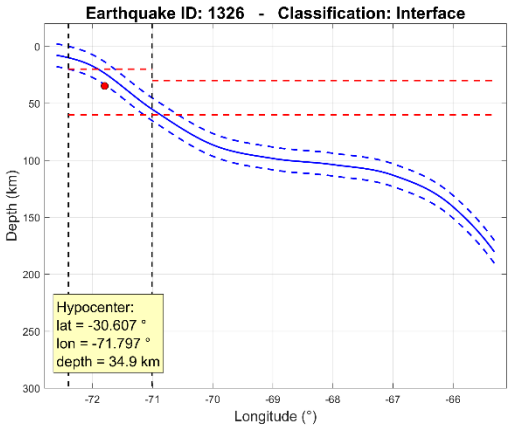

Figure B. 686: Event 1326

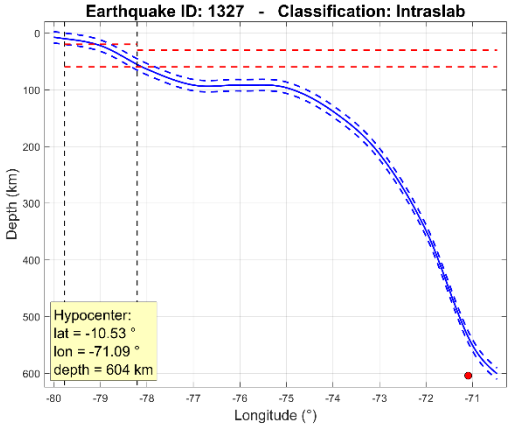

Figure B. 687: Event 1327

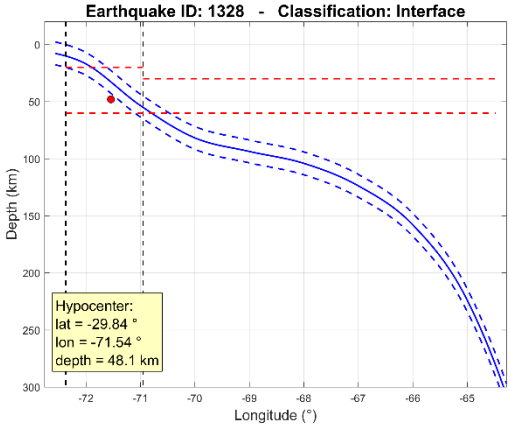

Figure B. 688: Event 1328

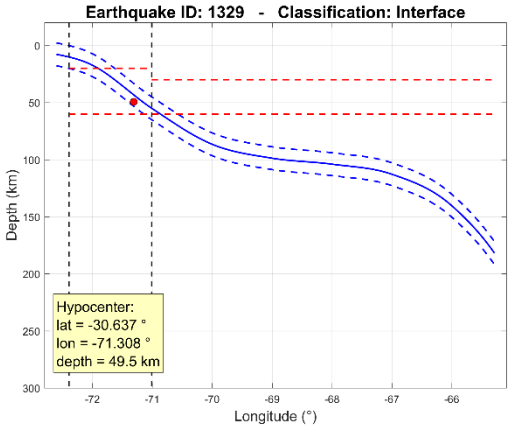

Figure B. 689: Event 1329

REFERENCES

Abrahamson N., Gregor N., and Addo K. (2016). BC Hydro ground motion prediction equations for subduction earthquakes, *Earthq. Spectra* 32(1), 23–44.

Ahdi S. K., Ancheta T. D., Contreras V., Kishida T., Kwak D. Y., Kwok A. O., Parker G. A., Bozorgnia Y., Stewart J. P. (2017). NGA-Subduction Site Database, *16th World Conf. on Earthq. Eng., 16WCEE,* Santiago, Chile, Jan. 9th to 13th.

Algermissen S. T., Kausel E., Hanson S., and Thenhaus P. C. (1992). Earthquake hazard in Chile, *Geophysics Journal*, 37, 195–218.

Arango M. C., Strasser F. O., Bommer J. J., Boroscheck R., Comte D., and Tavera H. (2011). A strong-motion database from the Peru-Chile subduction zone, *Journal of Seismology* 15, 19–41.

Atkinson, G. M. and Boore D. M. (2003). Empirical ground-motion relations for subduction-zone earthquakes and their application to Cascadia and other regions, *Bull. Seismol. Soc. Am.* 93, 1703-1729.

Atkinson, G. M. and Boore D. M. (2008). Erratum to empirical ground-motion relations for subduction-zone earthquakes and their application to Cascadia and other regions, *Bull. Seismol. Soc. Am.* 98, 2567–2569.

Barrientos, S. (2014). Technical report: Iquique earthquake, Mw=8.2, April 1st, 2014, *CSN*, available at http://www.csn.uchile.cl/wp-content/uploads/2016/06/Informe_Terremoto_Iquique_Abr_2014.pdf (In Spanish; last accessed May 2017).

Bastías N. and Montalva G. A. (2016). Chile strong ground motion flatfile, *Earthq. Spectra* 32(4), 2549–2566.

Béjar-Pizarro M., Carrizo D., Socquet A., Armijo R., Barrientos S., Bondoux F., Bonvalot S., Campos J., Comte D., de Chabalier J. B., Charade O., Delorme A., Gabalda G., Galetzka J., Genrich J., Nercessian A., Olcay M., Ortega F., Ortega I., Remy D., Ruegg J. C., Simons M., Valderas C., and Vigny C. (2010). Asperities and barriers on the seismogenic zone in North Chile: state-of-the-art after the 2007 Mw 7.7 Tocopilla earthquake inferred by GPS and InSAR data, *Geophysical Journal International*, 183: 390–406.

Bilek S. L. (2010). Invited review paper: Seismicity along the South American subduction zone: Review of large earthquakes, tsunamis, and subduction zone complexity, *Tectonophysics* 495 (2010) 2–14.

Boroschek R., Contreras V., Kwak D. Y., and Stewart J. P. (2012). Strong ground motion attributes of the 2010 Mw 8.8 Maule Chile Earthquake, *Earthquake Spectra* 28, S19–S38.

Bozorgnia Y., Abrahamson N. A., Al Atik L., Ancheta T. D., Atkinson G. M., Baker J. W., Baltay A., Boore D. M., Campbell K. W., Chiou B. S.-J., Darragh R., Day S., Donahue J., Graves R. W., Gregor N., Hanks T., Idriss I. M., Kamai R., Kishida T., Kottke A., Mahin S. A., Rezaeian S., Rowshandel B., Seyhan E., Shahi S., Shantz T., Silva W., Spudich P., Stewart J. P., Watson-Lamprey J., Wooddell K., and Youngs R. (2014). NGA-West2 Research Project, *Earthquake Spectra*, 30(3), 973-987.

Castillo L. F., Dimaté C., Drouet S., Fernandez G. A., Montalva G., Bastias N., Morales C., Pirchiner M., Singaucho J. C., and Weatherill G. (2016). A South American Strong Motion Database and Selection of ground motion prediction equations (GMPEs) for seismic hazard analysis in South America, *Research topic 6 (RT6), wiki of the SARA project (GEM)*, available at https://sara.openquake.org/hazard_rt6 (last accessed May 2017).

Chiou, B. S.-J., Darragh R., and Power M. (2005). Documentation of the NGA West project, PDF file, available at http://peer.berkeley.edu/ngawest/nga_models.html (last accessed May 2017).

Chiou, B. S.-J. and Youngs R. R. (2008). NGA Model for Average Horizontal Component of Peak Ground Motion and Response Spectra, PEER report 2008/09.

Contreras (2009). Curvas de atenuación para sismos chilenos, *Thesis work to obtain the degree of Civil Engineer,* University of Chile, Santiago, Chile. (In Spanish).

Contreras V. and Boroschek R. (2012). Strong ground motion attenuation relations for Chilean subduction zone interface earthquakes, *Proceedings of the 15th World Conference on Earthquake Engineering 15WCEE*, Lisboa, Portugal.

Contreras V. and Boroschek R. (2015). Response spectral attenuation relations for Chilean earthquakes, *Proceeding at XI Congreso Chileno de Sismologia e Ingenieria Sismica ACHISINA 2015*, March 18-20, Santiago, Chile. (In Spanish).

Crouse, C. (1991). Ground-motion attenuation equations for Cascadia subduction zone earthquakes, *Earthquake Spectra*, Vol. 7, pp. 201–236.

De la Llera J. C., Rivera F., Mitrani-Reiser J., Jünemann R., Fortuño C., Ríos M., Hube M., Santa María H., and Cienfuegos R. (2016). Data collection after the 2010 Maule earthquake in Chile, *Bull. Earthquake Eng.*, Volume 15, Issue 2, pp 555–588.

Delouis B. and Legrand D. (2007). Mw 7.8 Tarapaca intermediate depth earthquake of 13 June 2005 (northern Chile): Fault plane identification and slip distribution by waveform inversion, *Geophys. Res. Lett.*, 34, L01304.

Delouis B., Monfret T., Dorbath L., Pardo M., Rivera L., Comte D., Haessler H., Caminade J. P., Ponce L., Kausel E., and Cisternas A. (1997). The Mw = 8.0 Antofagasta (northern Chile) earthquake of 30 July 1995: A precursor to the end of the large 1877 gap, *Bull. Seismol. Soc. Am.*, 87(2):427-445.

Delouis B., Nocquet J.-M., and Vallée M. (2010). Slip distribution of the February 27, 2010 Mw = 8.8 Maule Earthquake, central Chile, from static and high-rate GPS, InSAR, and broadband teleseismic data, *Geophys. Res. Lett.*, 37, L17305.

Delouis B., Pardo M., Legrand D., and Monfret T. (2009). The Mw 7.7 Tocopilla Earthquake of 14 November 2007 at the Southern Edge of the Northern Chile Seismic Gap: Rupture in the Deep Part of the Coupled Plate Interface, Bull. Seismol. Soc. Am., 99(1) 87-94.

Duputel Z., Jiang J., Jolivet R., Simons M., Rivera L., Ampuero J.-P., Riel B., Owen S. E., Moore A. W., Samsonov S. V., Ortega Culaciati F., and Minson S. E. (2015). The Iquique earthquake sequence of April 2014: Bayesian modeling accounting for prediction uncertainty, *Geophys. Res. Lett.*, 42, 7949–7957.

Ekström G., Nettles M., and Dziewonski A. M. (2012). The global CMT project 2004-2010: Centroid-moment tensors for 13,017 earthquakes, *Phys. Earth Planet. Inter.*, 200-201, 1-9, 2012.

FDSN (2017). International Federation of Digital Seismograph Networks (FDSN): Networks Codes, available at http://www.fdsn.org/networks (last accessed May 2017).

Fischer, T., Álvarez, M., De la Llera, J. C., Riddell, R. (2002). An integrated model for earthquake risk assessment of buildings, *Engineering Structures* 24, 979–998.

Fuentes M., Riquelme S., Hayes G., Medina M., Melgar D., Vargas G., González J., and Villalobos A. (2016). A Study of the 2015 Mw 8.3 Illapel Earthquake and Tsunami: Numerical and Analytical Approaches, *Pure Appl. Geophys.*, 173: 1847.

Garcia J., Pagani M., Rodriguez L., and Weatherill G. (2016). Creation of a new PSHA input model for South America and calculation of results, *Research topic 7 (RT7), wiki of the SARA project (GEM)*, available at https://sara.openquake.org/hazard_rt7 (last accessed May 2017).

Gardi A., Lemoine A., Madariaga R., and Campos J. (2006). Modeling of stress transfer in the Coquimbo region of central Chile, *J. Geophys. Res.*, 111, B04307.

Goulet C. A., Kishida T., Ancheta T. D., Cramer C. H., Darragh R. B., Silva W. J., Hashash Y. M. A., Harmon J., Stewart J. P., Wooddell K. E., Youngs R. R. (2014). PEER NGA-East Database, *Pacific Earthquake Engineering Research Reports*, No. 2014/17.

Hayes G. (2010). Updated Result of the Feb 27, 2010 Mw 8.8 Maule, Chile Earthquake, *NEIC*, available at http://earthquake.usgs.gov/earthquakes/eqinthenews/2010/us2010tfan/finite_fault.php (last accessed August 19, 2013).

Hayes, G. P., Wald D. J., and Johnson R. L. (2012). Slab1.0: A three-dimensional model of global subduction zone geometries, *J. Geophys. Res.* 117, no. B01302.

Hayes G. (2017a). Preliminary Finite Fault Results for the Feb 27, 2010 Mw 8.9 -36.2200, -73.1740 Earthquake (Version 1), *NEIC*, available at https://earthquake.usgs.gov/earthquakes/eventpage/official20100227063411530_30#finite-fault (last accessed May 2017).

Hayes G. (2017b). Preliminary Finite Fault Results for the Sep 16, 2015 Mw 8.2 -31.5952, -71.6728 Earthquake (Version 1), *NEIC*, available at https://earthquake.usgs.gov/earthquakes/eventpage/us20003k7a#finite-fault (last accessed May 2017).

Hayes G. (2017c). Preliminary Finite Fault Results for the Jun 13, 2005 Mw 7.7 -20.0100, -69.2400 Earthquake (Version 1), *NEIC*, available at https://earthquake.usgs.gov/earthquakes/eventpage/usp000dsw1#finite-fault (last accessed May 2017).

Hayes G. (2017d). Preliminary Finite Fault Results for the Nov 14, 2007 Mw 7.7 -22.2500, -69.8900 Earthquake (Version 1), *NEIC*, available at https://earthquake.usgs.gov/earthquakes/eventpage/usp000fshy#finite-fault (last accessed May 2017).

Heidarzadeh M., Murotani S., Satake K., Ishibe T., and Gusman A. R. (2016). Source model of the 16 September 2015 Illapel, Chile, Mw 8.4 earthquake based on teleseismic and tsunami data, *Geophys. Res. Lett.*, 43, 643–650.

Husid R. (1973). Earthquakes: spectral analysis and characteristics of accelerograms as a basis of earthquake-resistant design, *Editorial Andrés Bello* [c1973], Santiago, Chile, 447 p.

Idini B., Rojas F., Ruiz S., and Pastén C. (2017). Ground motion prediction equations for the Chilean subduction zone, *Bull. Earthquake Eng.* 15:1853–1880.

IRIS (2017). Peru-Chile Subduction Zone: Earthquakes & Tectonics, *Incorporated Res. Institutions for Seism.*, animation available at https://www.iris.edu/hq/inclass/animation (last accessed May 2017).

IRISDMC (2017). IRIS Data Management Center, *Incorporated Res. Institutions for Seism.*, available at http://ds.iris.edu/ds/nodes/dmc (last accessed May 2017).

International Seismological Centre (2014). On-line Bulletin, http://www.isc.ac.uk, *Internatl. Seismol. Cent.*, Thatcham, United Kingdom (last accessed May 2017).

Ji C. (2007). Preliminary Result of the Nov 14, 2007 Mw 7.81 ANTOFAGASTA, CHILE Earthquake, *UCSB*, available at http://www.geol.ucsb.edu/faculty/ji/big_earthquakes/2007/11/anto/anto.html (last accessed August 11, 2013).

Kishida T., Bozorgnia Y., Abrahamson N., Ahdi S., Ancheta T., Boore D., Campbell K., Chiou B., Darragh R., Gregor N., Kamai R., Kwak D., Kwok A., Lin P., Magistrale H., Midorikawa S., Parker G., Si H., Silva W., Stewart J., Tsai C., Wooddell K., and Youngs R. (2017). Development of the NGA-Subduction Database, *16th World Conf. on Earthq. Eng., 16WCEE,* Santiago, Chile, Jan. 9th to 13th.

Kuge K., Kase Y., Urata Y., Campos J., and Perez A. (2010). Rupture characteristics of the 2005 Tarapaca, northern Chile, intermediate-depth earthquake: Evidence for heterogeneous fluid distribution across the subducting oceanic plate?, *J. Geophys. Res.*, 115, B09305.

Lay T., Ammon C. J., Hutko A. R., and Kanamori H. (2010). Effects of Kinematic Constraints on Teleseismic Finite-Source Rupture Inversions: Great Peruvian Earthquakes of 23 June 2001 and 15 August 2007, *Bull. Seismol. Soc. Am.*, 100: 969-994.

Lay T., Yue H., Brodsky E. E., and An C. (2014). The 1 April 2014 Iquique, Chile, Mw 8.1 earthquake rupture sequence, *Geophys. Res. Lett.*, 41, 3818–3825.

Lee S.-J., Yeh T.-Y., Lin T.-C., Lin Y.-Y., Song T.-R. A., and Huang B.-S. (2016). Two-stage composite megathrust rupture of the 2015 Mw8.4 Illapel, Chile, earthquake identified by spectral-element inversion of teleseismic waves, *Geophys. Res. Lett.*, 43, 4979–4985.

Lemoine A., Madariaga R., and Campos J. (2001). Evidence for earthquake interaction in central Chile: the July 1997–September 1998 Sequence, *Geophys. Res. Lett.*, 28(14), 2743–2746.

Leyton F., Pastén C., Montalva G., Hurtado G., Leopold A., Ruiz S., and Sáez E. (2017). Towards a geophysical characterization of the Chilean strong-motion stations, *16th World Conf. on Earthq. Eng., 16WCEE*, Santiago, Chile, Jan. 9th to 13th.

Leyton F., Ruiz S., and Sepúlveda S. A. (2009). Preliminary re-evaluation of probabilistic seismic hazard assessment in Chile: from Arica to Taitao Peninsula, *Advances in Geosciences*, 22, 147–153.

Li B. and Ghosh A. (2016). Imaging Rupture Process of the 2015 Mw 8.3 Illapel Earthquake Using the US Seismic Array, *Pure Appl. Geophys.,* 173: 2245.

Li L., Lay T., Cheung K. F., and Ye L. (2016). Joint modeling of teleseismic and tsunami wave observations to constrain the 16 September 2015 Illapel, Chile, Mw 8.3 earthquake rupture process, *Geophys. Res. Lett.*, 43, 4303–4312.

Lorito S., Romano F., Atzori S., Tong X., Avallone A., McCloskey J., Cocco M., Boschi E., and Piatanesi A. (2011). Limited overlap between the seismic gap and coseismic slip of the great 2010 Chile earthquake, *Nature Geoscience*, 4, 173–177.

Luttrell K. M., Tong X., Sandwell D. T., Brooks B. A., and Bevis M. G. (2011). Estimates of stress drop and crustal tectonic stress from the 27 February 2010 Maule, Chile, earthquake: Implications for fault strength, *Journal of Geophysical Research: Solid Earth* (1978–2012), 116(B11).

Mai P. M. and Thingbaijam K. K. (2014). SRCMOD: An online database of finite-fault rupture models, *Seismological Research Letters* 85, 1348–1357.

Marot M. M., Monfret T., Pardo M., Ranalli G., and Nolet G. (2012). An intermediate-depth tensional earthquake (M_W 5.7) and its aftershocks within the Nazca slab, central Chile: A reactivated outer rise fault?, *Earth and Planetary Science Letters* 327–328 (2012) 9–16.

Martin A. (1990). Towards a new regionalization and calculation of seismic hazard in Chile, *Thesis work to obtain the degree of Civil Engineer*, *Department of Civil Engineering, Faculty of Physics and Mathematical Sciences, University of Chile*, Santiago, Chile. (In Spanish).

Melgar D., Fan W., Riquelme S., Geng J., Liang C., Fuentes M., Vargas G., Allen R. M., Shearer P. M., and Fielding E. J. (2016). Slip segmentation and slow rupture to the trench during the 2015, Mw8.3 Illapel, Chile earthquake, *Geophys. Res. Lett.*, 43, 961–966.

Mendoza C., Hartzell S., and Monfret T. (1994). Wide-Band Analysis of the 3 March 1985 Central Chile Earthquake - Overall Source Process and Rupture History, *Bull. Seis. Soc. Am.*, 84 (2):269-283.

Montalva et al. (2016). Unpublished, adaptation of the Abrahamson et al. (2016) BC Hydro GMPE, calibrated to Chilean strong motion data.

Montalva G. A., Bastías N. and Rodriguez-Marek A. (2017). Ground-Motion Prediction Equation for the Chilean Subduction Zone, *Bull. Seismol. Soc. Am.*, 107 (2), Early Edition.

Motagh M., Schurr B., Anderssohn J., Cailleau B., Walter T. R., Wang R., and Villotte J.-P. (2010). Subduction earthquake deformation associated with 14 November 2007, Mw 7.8 Tocopilla earthquake in Chile: Results from InSAR and aftershocks, *Tectonophysics*, 490, 60–68.

Murotani S., Satake K., and Fujii Y. (2013). Scaling relations of seismic moment, rupture area, average slip, and asperity size for M~ 9 subduction-zone earthquakes, *Geophys. Res. Lett.* 40, 1–5.

Núñez I., Boroschek R., Comte D., and Contreras V. (2015). New seismic hazard for Chile, *Proceeding at XI Congreso Chileno de Sismologia e Ingenieria Sismica ACHISINA 2015*, March 18-20, Santiago, Chile. (In Spanish).

Okuwaki R., Yagi Y., Aránguiz R., González J., and González G. (2016). Rupture Process During the 2015 Illapel, Chile Earthquake: Zigzag-Along-Dip Rupture Episodes, *Pure Appl. Geophys.*,173: 1011.

Pardo M., Comte D., Monfretb T., Boroschek R., Astroza M. (2002). The October 15, 1997 Punitaqui earthquake (Mw=7.1): a destructive event within the subducting Nazca plate in central Chile, *Tectonophysics*, 345(1–4): 199–210.

Peyrat S. and Favreau P. (2010). Kinematic and spontaneous rupture models of the 2005 Tarapacá intermediate depth earthquake, *Geophys. J. Int.*, 181 (1): 369-381.

Poblete (2008). Determinación experimental de la Intensidad de Mercalli Modificada para Chile, *Thesis work to obtain the degree of Civil Engineer,* University of Chile, Santiago, Chile. (In Spanish).

Pollitz F. F., Brooks B., Tong X., Bevis M. G., Foster J. H., Bürgmann R., Smalley R., Vigny C., Socquet A., Ruegg J. C., and Campos J. (2011). Coseismic slip distribution of the February 27, 2010 Mw 8.8 Maule, Chile earthquake, *Geophys. Res. Lett.*, 38, L09309.

Power M., Chiou B., Abrahamson N., Bozorgnia Y., Shantz T., and Roblee C. (2008). An Overview of the NGA Project, *Earthquake Spectra*, 24(1), 3–21.

Ruiz S., Klein E., del Campo F., Rivera E., Poli P., Metois M., Vigny C., Baez J. C., Vargas G., Leyton F., Madariaga R., and Fleitout L. (2016). The Seismic Sequence of the 16 September 2015 Mw 8.3 Illapel, Chile, Earthquake, *Seismol. Res. Lett.*, 87 (4), 789-799.

Ruiz S., Metois M., Fuenzalida A., Ruiz J., Leyton F., Grandin R., Vigny C., Madariaga R., and Campos J. (2014). Intense foreshocks and a slow slip event preceded the 2014 Iquique Mw 8.1 earthquake, *Science*, 345:1165–1169.

Ruiz S. and Saragoni G. (2005). Attenuation equations for subduction-zone earthquakes in Chile considering two seismogenic mechanisms and site effects, *IX Jornadas Chilenas de Sismología e Ingeniería Antisísmica*, Concepción, Chile, 16–19 November 2005 (*In Spanish*).

Schurr B., Asch G., Rosenau M., Wang R., Oncken O., Barrientos S., Salazar P., and Vilotte J.-P. (2012). The 2007 M7.7 Tocopilla northern Chile earthquake sequence: Implications for along-strike and downdip rupture segmentation and megathrust frictional behavior, *J. Geophys. Res.*, 117, B05305.

Shao G. and Ji C. (n.d.). Preliminary Result of the Jul 30, 1995 Mw 8.14 Antofagasta Earthquake, *UCSB*, available at http://www.geol.ucsb.edu/faculty/ji/big_earthquakes/1995/07/chile.html (last accessed May 2017).

Shao G. and Ji C. (2001). Preliminary Result of the Jun 23, 2001 Mw 8.4 Peru Earthquake, *UCSB*, available at http://www.geol.ucsb.edu/faculty/ji/big_earthquakes/2001/06/smooth/2001peru.html (last accessed May 2017).

Shao G., Li X., Liu Q., Zhao X., Yano T., and Ji C. (2010). Preliminary slip model of the Feb 27, 2010 Mw 8.9 Maule, Chile Earthquake, *UCSB*, available at http://www.geol.ucsb.edu/faculty/ji/big_earthquakes/2010/02/27/chile_2_27.html (last accessed September 24, 2013).

Skarlatoudis A. A., Somerville P. G., Thio H. K., and Bayless J. R. (2015). Broadband Strong Ground Motion Simulations of Large Subduction Earthquakes, *Bull. Seismol. Soc. Am.*, 105: 3050-3067.

Skarlatoudis A. A., Somerville P. G., and Thio H. K. (2016). Source-Scaling Relations of Interface Subduction Earthquakes for Strong Ground Motion and Tsunami Simulation, *Bull. Seismol. Soc. Am.*, Vol. 106, No. 4, pp. 1652–1662.

Sladen A. (2007). Preliminary Result 11/14/2007 (Mw 7.7), Tocopilla Earthquake, Chile, *Source Models of Large Earthquakes, Caltech*, available at http://www.tectonics.caltech.edu/slip_history/2007_tocopilla/tocopilla.html (last accessed July 1, 2013).

Sladen A. (2010). Preliminary Result, 02/27/2010 (Mw 8.8), Chile, *Source Models of Large Earthquakes, Caltech,* available at http://www.tectonics.caltech.edu/slip_history/2010_chile/index.html (last accessed May 2017).

Stewart J. P., Midorikawa S., Graves R. W., Khodaverdi K., Kishida T., Miura H., Bozorgnia Y., and Campbelle K. W. (2013). Implications of the M_W9.0 Tohoku-Oki Earthquake for Ground Motion Scaling with Source, Path, and Site Parameters, *Earthquake Spectra*, Vol. 29, No. S1, pages S1–S21.

Strasser F. O., Arango M. C., and Bommer J. J. (2010). Scaling of the source dimensions of interface and intraslab subduction-zone earthquakes with moment magnitude, *Seismol. Res. Lett.* 81, 941–950.

Tilmann F., Zhang Y., Moreno M., Saul J., Eckelmann F., Palo M., Deng Z., Babeyko A., Chen K., Baez J. C., Schurr B., Wang R., and Dahm T. (2016). The 2015 Illapel earthquake, central Chile: A type case for a characteristic earthquake?, *Geophys. Res. Lett.*, 43, 574–583.

Villablanca R. and Riddell R. (1985). Assessment of the seismic risk in Chile, Report DIE 85-4, *Department of Struct. and Geotech. Eng., Pontifical Catholic University of Chile*, Santiago, Chile. (In Spanish).

Wald L. (2016). South America tectonic summary, *USGS Earthquake Hazards Program website*, available at https://earthquake.usgs.gov/earthquakes/tectonic/images/southamerica_tsum.pdf (last accessed May 2017).

Wei S. (2014). Apr./0.1/2014 (Mw 8.1), Iquique, Chile. *Source Models of Large Earthquakes, Caltech*, available at http://www.tectonics.caltech.edu/slip_history/2014_chile/index.html (last accessed May 18, 2014).

Ye L., Lay T., Kanamori H., and Koper K. D. (2016). Rapidly Estimated Seismic Source Parameters for the 16 September 2015 Illapel, Chile Mw 8.3 Earthquake, *Pure Appl. Geophys.*, 173: 321.

Youngs R. R., Chiou S. J., Silva W. J., and Humphrey J. R. (1997). Strong ground motion attenuation relationships for subduction zone earthquakes, *Seismol. Res. Lett.* 68, 58–73.

Zeng Y., Hayes G. and Ji C. (2007). Preliminary Result of the Nov 14, 2007 Mw 7.7 Antofagasta, Chile Earthquake, *USGS Online Model*, available at http://earthquake.usgs.gov/earthquakes/eqinthenews/2007/us2007jsat/finite_fault.php (last accessed August 20, 2013).

Zhang Y., Zhang G., Hetland E. A., Shan X., Wen S., and Zuo R. (2016). Coseismic Fault Slip of the September 16, 2015 Mw 8.3 Illapel, Chile Earthquake Estimated from InSAR Data, *Pure Appl. Geophys.*, 173: 1029.

Zhao J. X., Zhang J., Asano A., Ohno Y., Oouchi T., Takahashi T., Ogawa H., Irikura K., Thio H. K., Somerville P. G., et al. (2006). Attenuation relations of strong ground motion in Japan using site classification based on predominant period, *Bull. Seismol. Soc. Am.* 96, 898–913.